UNITED STATES AIR FORCE

GRADUATE STUDENT RESEARCH PROGRAM
1990
PROGRAM TECHNICAL REPORT
UNIVERSAL ENERGY SYSTEMS, INC.
VOLUME 1 OF 3

PROGRAM DIRECTOR, U. E. S.
RODNEY C. DARRAH

PROGRAM ADMINISTRATOR, U. E. S.
SUSAN K. ESPY

PROGRAM MANAGER, A. F. O. S. R.
LT. COL. CLAUDE CAVENDER

SUBMITTED TO
AIR FORCE OFFICE OF SCIENTIFIC RESEARCH
BOLLING AIR FORCE BASE
WASHINGTON, DC

DECEMBER 1990

REPORT DOCUMENTATION PAGE

Form Approved
OMB No. 0704-0188

1. AGENCY USE ONLY (Leave blank)	2. REPORT DATE	3. REPORT TYPE AND DATES COVERED
	5 June 1991	Annual/Final 1 Sep 89-31 Aug 90

4. TITLE AND SUBTITLE
United States Air Force Graduate Student Research Program
1990 Volume 1of3
Program Technical Report ~~(w/atch 1 & 2)~~

5. FUNDING NUMBERS
F49620-88-C-0053

6. AUTHOR(S)
Mr Rodney Darrah

7. PERFORMING ORGANIZATION NAME(S) AND ADDRESS(ES)
Universal Energy Systems (UES)
4401 Dayton-Xenia
Dayton OH 45432

AFOSR-TR- 91 0957

8. PERFORMING ORGANIZATION REPORT NUMBER

9. SPONSORING/MONITORING AGENCY NAME(S) AND ADDRESS(ES)
AFOSR/NI
Bldg 410
Bolling AFB DC 20332-6448

Lt Col V. Claude Cavender

10. SPONSORING/MONITORING AGENCY REPORT NUMBER

11. SUPPLEMENTARY NOTES

12a. DISTRIBUTION/AVAILABILITY STATEMENT
UNLIMITED

12b. DISTRIBUTION CODE

13. ABSTRACT (Maximum 200 words)

The Summer Faculty Research Program (SFRP) was initiated in 1982. The Graduate Student Research Program (GSRP) is an adjunct effort to the Summer Faculty Research Program. Its purpose is to provide opportunities for selected graduate students to perform summer research at Air Force laboratories with supervising professors who hold concurrent SFRP appointments or with Air Force researchers.

The program is available to graduate students enrolled in either Masters Degree or Doctorate Programs. It has proven especially beneficial to the students who are starting their academic research programs.

14. SUBJECT TERMS

15. NUMBER OF PAGES

16. PRICE CODE

17. SECURITY CLASSIFICATION OF REPORT	18. SECURITY CLASSIFICATION OF THIS PAGE	19. SECURITY CLASSIFICATION OF ABSTRACT	20. LIMITATION OF ABSTRACT
UNCLASSIFIED	UNCLASSIFIED	UNCLASSIFIED	UL

UNITED STATES AIR FORCE

GRADUATE STUDENT RESEARCH PROGRAM

1990

PROGRAM TECHNICAL REPORT

UNIVERSAL ENERGY SYSTEMS, INC.

VOLUME I of III

Program Director, UES
Rodney C. Darrah

Program Administrator, UES
Susan K. Espy

Program Manager, AFOSR
Lt. Col. Claude Cavender

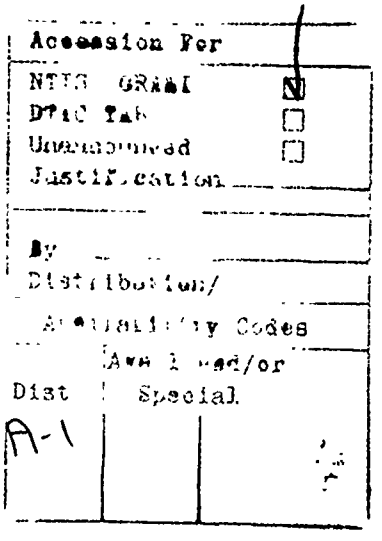

Submitted to

Air Force Office of Scientific Research

Bolling Air Force Base

Washington, DC

December 1990

TABLE OF CONTENTS

Section	Page
Preface	i
List of Participants	ii
Participant Laboratory Assignment	xx
Research Reports	xxiv

PREFACE

The United States Air Force Graduate Student Resarch Program (USAF-GSRP) is conducted under the United Air Force Summer Faculty Research Program. The program provides funds for selected graduate students to work at an appropriate Air Force facility with a supervising professor who holds a concurrent Summer Faculty Research Program appointment or with a supervising Air Force Engineer/Scientist. This is accomplished by the students being selected on a nationally advertised competitive basis for a ten-week assignment during the summer intersession period to perfrom research at Air Force laboratories/centers. Each assignment is in a subject area and at an Air Force facility mutually agreed upon by the students and the Air Force. In addition to compensation, travel and cost of living allowances are also paid. The USAF-GSRP is sponsored by the Air Force Office of Scientific Research, Air Force Systems Command, United States Air Force, and is conducted by Universal Energy Systems, Inc.

The specific objectives of the 1990 USAF-GSRP are:

(1) To provide a productive means for the graduate students to participate in research at Air Force Laboratories/Centers;

(2) To stimulate continuing professional association among the graduate students and their professional peers in the Air Force;

(3) To further the research objectives of the United States Air Force;

(4) To enhance the research productivity and capabilities of the graduate students especially as these relate to Air Force technical interests.

During the summer of 1990, 121-graduate students participated. These researchers were assigned to 23 USAF laboratories/centers across the country. This three volume document is a compilation of the final reports written by the assigned students members about their summer research efforts.

LIST OF 1990 PARTICIPANTS

NAME / ADDRESS	DEGREE, SPECIALTY, LABORATORY ASSIGNED
Ben Abbott Vanderbilt University Electrical Engineering Dept. Nashville, TN 37240 (615) 343-8302	Degree: MS Specialty: Computer Engineering Assigned: Arnold Engineering Development Center
Gregory Addington Colorado - Boulder, Univ. of Campus Box 429, Dept. of Aerospace Eng. Boulder, CO 80310 (303) 492-7559	Degree: BS Specialty: Aerospace Engineering Assigned: Frank J. Seiler Research Lab.
Magna Altamirano New Orleans, Univ. of Lakefront New Orleans, LA 70148 (504) 286-6652	Degree: BS Specialty: Civil Engineering Assigned: Flight Dynamics Laboratory
Joseph Baldonado California State Univ. Dept. of Mechanical Eng. Long Beach, CA 90840 (213) 985-5471	Degree: BS Specialty: Electrical Engineering Assigned: Astronautics Laboratory
Theodore Bapty Vanderbilt University Electrical Eng. Dept. Nashville, TN 37240 (615) 322-3455	Degree: BS Specialty: Computer Engineering Assigned: Arnold Engineering Development Center
Janis L. Baird Alabama, Univ. of A.B. Moore Hall, Box 870312 Tuscaloosa, AL 35487 (205) 348-6075	Degree: MS Specialty: Physiology Assigned: School of Aerospace Medicine

NAME / ADDRESS	DEGREE, SPECIALTY, LABORATORY ASSIGNED
Joseph Bernardo Scranton, Univ. of Chemistry Dept. Scranton, PA 18510 (717) 961-6286	Degree: BS Specialty: Biochemistry Assigned: Engineering & Services Ctr.
Laura Bernhofen Syracuse U. Crouse-Hinds School of Mgmt. Syracuse, NY 13210 (315) 475-1418	Degree: MS Specialty: Statistics Assigned: Human Resources Laboratory Manpower & Personnel Div.
Ronald Blume Tennessee, Univ. & Space Inst. Aerospace Eng. Dept. Tullahoma, TN 37388 (615) 455-0631	Degree: BS Specialty: Aerospace Engineering Assigned: Arnold Engineering Development Center
Andrew Bonas Duke University Dept. of Civil Eng. PO Box 4264DS Durham, NC 27706 (919) 684-167J	Degree: BS Specialty: Civil Engineering Assigned: Occupational & Environmental Health Laboratory
George Boynton Miami, Univ. of Dept. of Physics, PO Box 248046 Coral Gables, FL 33124 (305) 284-2323	Degree: MS Specialty: Physics Assigned: Armament Laboratory
Dora Brenner Auburn University Dept. of Zoology & Wildlife Auburn, AL 36830 (205) 844-9245	Degree: MS Specialty: Chemistry Assigned: School of Aerospace Medicine
Thomas Broersma Texas-Austin, Univ. of EDB 244 Austin, TX 78712 (512) 471-4285	Degree: MS Specialty: Arts Assigned: School of Aerospace Medicine

NAME / ADDRESS	DEGREE, SPECIALTY, LABORATORY ASSIGNED	
Joseph Brogan Scranton, Univ. of Dept. of Biology Scranton, PA 18510 (717) 961-6338	Degree: Specialty: Assigned:	BS Biochemistry School of Aerospace Medicine
Robert Byers Texas A&M Univ. Aerospace Eng. Dept. College Station, TX 77843 (409) 845-0745	Degree: Specialty: Assigned:	MS Aerospace Engineering Astronautics Laboratory
Eric Byrne Kansas State Univ. 234 Nichols Hall Manhattan, KS 66502 (913) 532-6350	Degree: Specialty: Assigned:	MS Computer Science Avionics Laboratory
Jordan Cahn Univ. of Tennessee Space Inst. Dept. of Applied Mathematics Tullahoma, TN 37388 (615) 455-0631	Degree: Specialty: Assigned:	BS Aerospace Engineering Arnold Engineering Development Center
Ann Canfield Utah State Univ. Dept. of Instructional Technology Logan, UT 84321 (801) 752-1398	Degree: Specialty: Assigned:	BS Instructional Technology Human Resources Laboratory Training Systems
Robert Carlin New York at Buffalo, Univ. of Mechanical & Aerospace Eng. Buffalo, NY 14261 (716) 636-4006	Degree: Specialty: Assigned:	BS Aerospace Engineering Frank J. Seiler Research Lab.
Leonard Carter Boston Univ. 705 Commonwealth Ave. Boston, MA 02215 (617) 353-5611	Degree: Specialty: Assigned:	MS Engineering Geophysics Laboratory

NAME / ADDRESS	DEGREE, SPECIALTY, LABORATORY ASSIGNED	
Frank Chavez Arizona State Univ. Dept. of Mech. & Aerospace Eng. Tempe, AZ 85287 (602) 965-3291	Degree: Specialty: Assigned:	BS Aerospace Engineering Flight Dynamics Laboratory
Alan Coleman Indiana Univ. of Pennsylvania Dept. of Physics Wey. Hall Indiana, PA 15705 (412) 357-2370	Degree: Specialty: Assigned:	BS Physics Electronic Technology Lab.
Tammie Confer Akron, Univ. of Dept. of Physics Akron, OH 44325 (216) 375-7078	Degree: Specialty: Assigned:	BS Physics Electronic Technology Lab.
Rand Conger Washington S. Univ. Dept. of Mech. & Materials Eng Pullman, WA 99163 (509) 332-1622	Degree: Specialty: Assigned:	BS Aerodynamics Frank J. Seiler Research Lab.
Brian Cull Kent State Univ. Kent Campus E Main and Lincoln Kent, OH 44242 (216) 672-2880	Degree: Specialty: Assigned:	BS Physics Materials Laboratory
Gary Cunning Colorado-Colorado Spr., Univ. of PO Box 7150 Colorado Springs, CO 80933 (719) 548-0602	Degree: Specialty: Assigned:	BS Electrical Engineering Frank J. Seiler Research Lab.
James Day Kentucky, Univ. of Dept. of Physics, Room 177 Lexington, KY 40506 (606) 257-1397	Degree: Specialty: Assigned:	BS Physics Geophysics Laboratory

NAME / ADDRESS	DEGREE, SPECIALTY, LABORATORY ASSIGNED	
Melissa Dittmer New Mexico, Univ. of Dept. of Physics & Astronomy Albuquerque, NM 87131 (505) 277-6088	Degree: Specialty: Assigned:	BS Physics Weapons Laboratory
Christina Estep Virginia Poly. Inst. & S. Univ. Dept. of Engineering Mechanics Blacksburg, VA 24060 (703) 951-0563	Degree: Specialty: Assigned:	BS Mechanical Engineering Aerospace Medical Research Laboratory
Joan Estes St. Mary's Univ. 1830 Bandera #826 San Antonio, TX 78228 (512) 436-2613	Degree: Specialty: Assigned:	BS Psychology Wilford Hall Medical Center
Paul Fayfich Texas-Austin, Univ. of College of Education Austin, TX 78712 (512) 471-5211	Degree: Specialty: Assigned:	MS Operations Research Human Resources Laboratory Manpower & Personnel Div.
Michael Findler Arizona State Univ. Computer Science Dept. Tempe, AZ 85387 (602) 965-3190	Degree: Specialty: Assigned:	MS Computer Science Avionics Laboratory
James Fitzgerald New Jersey, S. Univ. of Dept. of Biology 202 Boyden Hall Newark, NJ 07102 (201)648-1076	Degree: Specialty: Assigned:	BS Biology School of Aerospace Medicine
Blaise Fitzpatrick Rhode Island, Univ. of Civil and Envir. Eng. Kingston, RI 02881 (401) 792-2692	Degree: Specialty: Assigned:	BS Civil Engineering Engineering & Services Ctr.

NAME / ADDRESS	DEGREE, SPECIALTY, LABORATORY ASSIGNED	
Kenneth Fleming Rensselaer Poly. Inst. Dept. of Psychology Troy, NY 12180 (518) 276-6000	Degree: Specialty: Assigned:	BS Psychology Human Resources Laboratory Operations Training Division
Patrick Fourspring Pennsylvania S. Univ. 211-16 Easterly Parkway State College, PA 16801 (814) 867-3602	Degree: Specialty: Assigned:	MS Structural Engineering Flight Dynamics Laboratory
Joan Fuller Birmingham-Southern College P O Box 670 BSC Birmingham, AL 35254 (205) 780-4231	Degree: Specialty: Assigned:	BS Chemistry Frank J. Seiler Research Lab.
Robert Gabruk Virginia Poly. Inst. Dept. of Mechanical Eng. Blacksburg, VA 24061 (703) 231-7295	Degree: Specialty: Assigned:	BS Mechanical Engineering Aero Propulsion Laboratory
Shawn Gaffney Notre Dame, Univ. of Dept. of Electrical & Comp. Eng. Notre Dame, IN 46556 (219) 239-7596	Degree: Specialty: Assigned:	BS Physics Weapons Laboratory
Andrew Galasso Worcester Poly. Inst. Dept. of Physics Worcester, MA 01609 (508) 831-5313	Degree: Specialty: Assigned:	BS Physics Rome Air Development Ctr.
Michael Geer Pennsylvania State Univ. Civil Engineering Dept. State College, PA 16801 (814) 863-0576	Degree: Specialty: Assigned:	BS Civil Engineering Weapons Laboratory

NAME / ADDRESS	DEGREE, SPECIALTY, LABORATORY ASSIGNED
James Golden Tennessee Space Inst., Univ. of Dept. of Aerospace Eng. Tullahoma, TN 37388 (615) 455-0631	Degree: MS Specialty: Computer Science Assigned: Arnold Engineering Development Center
Ellen Goldey Miami Univ. Dept. of Zoology Oxford, OH 45056 (513) 529-3184	Degree: MS Specialty: Zoology Assigned: Aerospace Medical Research Laboratory
Randy Gove Alabama, Univ. of Dept. of Physics Huntsville, AL 35899 (205) 895-6276	Degree: BS Specialty: Physics Assigned: Armament Laboratory
Thomas Haas Kentucky, Univ. of Dept. of Electrical Eng. Lexington, KY 40502 (606) 257-2943	Degree: BS Specialty: Electrical Engineering Assigned: Materials Laboratory
David Harper Bowling Green S. Univ. Dept. of Psychology Bowling Green, OH 43402 (419) 372-2301	Degree: BS Specialty: Psychology Assigned: Aerospace Medical Research Laboratory
Craig Harwood North Carolina S. Univ. Dept. of Civil Eng., 208 Mann Raleigh, NC 27695 (919) 737-2331	Degree: BS Specialty: Civil Engineering Assigned: Flight Dynamics Laboratory
Dollena Hawkins Tennessee Tech. Univ. Box 5054 TTU Cookeville, TN 38505 (615) 372-3441	Degree: BS Specialty: Mechanical Engineering Assigned: Arnold Engineering Development Center

NAME / ADDRESS	DEGREE, SPECIALTY, LABORATORY ASSIGNED
Gregory Herdt Denver, Univ. of Dept. of Engineering Denver, CO 80208 (303) 871-2102	Degree: BS Specialty: Materials Science Assigned: Astronautics Laboratory
John Holman Iowa, Univ. of W35 Seashore Hall Iowa City, IA 52242 (319) 335-2502	Degree: MS Specialty: Sociology Assigned: Human Resources Laboratory Manpower & Personnel Div.
Michael Houts Massachusetts Inst. of Tech. 77 Massachusetts Ave. Rm. 24-302 Cambridge, MA 02139 (617) 253-3720	Degree: BS Specialty: Nuclear Engineering Assigned: Weapons Laboratory
Tonia Howe Wright S. Univ. Applied Behavioral Science Dept. Dayton, OH 45435 (513) 873-2089	Degree: BS Specialty: Psychology Assigned: Human Resources Laboratory Logistics & Human Factors
Johnny Hurtado Texas A&M Univ. Dept. of Aerospace Engineering College Station, TX 77840 (409) 846-9583	Degree: BS Specialty: Aerospace Engineering Assigned: Astronautics Laboratory
Leonard Isaacs Wyoming, Univ. of 804 University #1 Laramie, WY 82070 (307) 766-4221	Degree: BS Specialty: Mathematics Assigned: Armament Laboratory
Stacey Johnson Meharry Medical College 944 21st Ave. N. Apt. 109 Nashville, TN 37208 (615) 320-5484	Degree: BS Specialty: Biology Assigned: Wilford Hall Medical Center

NAME / ADDRESS	DEGREE, SPECIALTY, LABORATORY ASSIGNED
Lisa Jones Meharry Medical College 1005 D.B. Todd Blvd. Nashville, TN 37208 (615) 327-6000	Degree: BS Specialty: Biology Assigned: School of Aerospace Medicine
Susan Jones St. Mary's Univ. One Camino Santa Maria San Antonio, TX 78284 (512) 436-3011	Degree: BS Specialty: Psychology Assigned: Wilford Hall Medical Center
Christopher Kardish Florida, Univ. of 300 MEB/CIMAR Gainesville, FL 32611 (904) 392-0814	Degree: MS Specialty: Mechanical Engineering Assigned: Engineering & Services Ctr.
George Kim Trinity Univ. 715 Stadium Dr. San Antonio, TX 78284 (512) 736-7231	Degree: BS Specialty: Biology Assigned: School of Aerospace Medicine
James Kime Alabama, Univ. of Box 870312 Tuscaloosa, AL 35487 (205) 348-6075	Degree: BS Specialty: Fitness Management Assigned: School of Aerospace Medicine
Everett King Alabama, Univ. of 4527 18th Ave. East Tuscaloosa, AL 35405 (205) 556-1654	Degree: BS Specialty: Aerospace Engineering Assigned: Arnold Engineering Development Center
John Klinge Colorado, Univ. of Campus Box 429 Boulder, CO 80309 (303) 492-7559	Degree: BS Specialty: Physics Assigned: Frank J. Seiler Research Lab.

NAME / ADDRESS	DEGREE, SPECIALTY, LABORATORY ASSIGNED
Christopher Kocher Illinois, Univ. of 216 Talbot Lab 104 S. Wright St. Urbana, IL 61801 (217) 333-2322	Degree: MS Specialty: Mechanical Engineering Assigned: Astronautics Laboratory
Thomas Kuchar Boston Univ. 725 Commonwealth Ave. Boston, MA 02215 (617) 353-4884	Degree: MS Specialty: Physics Assigned: Geophysics Laboratory
David LaGraffe Syracuse Univ. 201 Physics Bldg. Syracuse, NY 13244 (315) 443-5966	Degree: MS Specialty: Physics Assigned: Rome Air Development Ctr.
Peter LaRose Northwestern Univ. 2145 Sheridan Rd. Evanston, IL 60208 (708) 491-7848	Degree: BS Specialty: Mathematics Assigned: Aero Propulsion Laboratory
John Lair New Orleans, Univ. of Dept. of Mech. Eng. Lake Front Cam New Orleans, LA 70148 (504) 286-6652	Degree: BS Specialty: Mechanical Engineering Assigned: Flight Dynamics Laboratory
Davis Lange Arizona, Univ. of Optical Sciences Center Tucson, AZ 85721 (602) 621-9104	Degree: BS Specialty: Electrical Engineering Assigned: Armament Laboratory
Richard Lareau Worcester Poly. Inst. 100 Institute Rd. Worcester, MA 01609 (508) 831-5000	Degree: BS Specialty: Electrical Engineering Assigned: Rome Air Development Ctr.

NAME / ADDRESS	DEGREE, SPECIALTY, LABORATORY ASSIGNED
James Lasche (To Be Determined)	Degree: BS Specialty: Optics Assigned: Weapons Laboratory
Jeffery Layne Ohio State Univ. 205 Dreese Laboratories Columbus, OH 43210 (614) 292-2572	Degree: BS Specialty: Electrical Engineering Assigned: Avionics Laboratory
Minh Le Calif.-Long Beach, S. Univ. of Mechanical Eng. Dept. Long Beach, CA 90840 (213) 985-4407	Degree: BS Specialty: Chemical Engineering Assigned: Astronautics Laboratory
Teresa Lee Western Illinois Univ. Dept. of Sociology Macomb, IL 61455 (309) 298-1056	Degree: MS Specialty: Sociology Assigned: Aerospace Medical Research Laboratory
Toby Martin Illinois, Univ. of Dept. of Aeronautical Eng. Champaign, IL 61820 (217) 351-1935	Degree: BS Specialty: Aeronautical Engineering Assigned: Weapons Laboratory
Margo McDowell Nebraska, University of Civil Engineering Lincoln, NE 68588 (402) 472-2354	Degree: BS Specialty: Mechanical Engineering Assigned: Materials Laboratory
Michael Montegut Rensselaer Poly. Inst. Psychology Dept. Troy, NY 12180 (518) 276-6472	Degree: BS Specialty: Psychology Assigned: Human Resources Laboratory Operations Training Division

NAME / ADDRESS	DEGREE, SPECIALTY, LABORATORY ASSIGNED	
John Moore Texas-Austin, Univ. of Dept. of Elect. Eng. 3914 Ave D Austin, TX 78751 (512) 458-9674	Degree: Specialty: Assigned:	MS Electromagnetic Rome Air Development Ctr.
Kyle Nash Alabama, Univ. of Dept. of Aerospace Eng. Tuscaloosa, AL 35405 (205) 556-2842	Degree: Specialty: Assigned:	BS Aerodynamics Arnold Engineering Development Center
Kelly Neville Rice University Dept. of Psychology Houston, TX	Degree: Specialty: Assigned:	BS Psychology School of Aerospace Medicine
Keith Newman Pennsylvania State Univ. 209 Steidle Bldg. University Park, PA 16802 (814) 865-5446	Degree: Specialty: Assigned:	MS Metallurgical Engineering Materials Laboratory
Hung Nguyen California State Univ. Mechanical Eng. Dept. Long Beach, CA 90840 (213) 985-4111	Degree: Specialty: Assigned:	BS Mechanical Engineering Astronautics Laboratory
John Noto Tufts Univ. Dept. of Physics & Astronomy Medford, MA 02155 (617) 628-5000	Degree: Specialty: Assigned:	BS Physics Geophysics Laboratory
Allen Olheiser North Dakota State Univ. 1017 N. 10 Street Fargo, ND 58102 (701) 237-4636	Degree: Specialty: Assigned:	BS Computer Engineering Aero Propulsion Laboratory

NAME / ADDRESS	DEGREE, SPECIALTY, LABORATORY ASSIGNED	
Kristina Pawlikowski Ohio S. Univ. Dept. of Civil Eng. Columbus, OH 43212 (614) 299-9323	Degree: Specialty: Assigned:	BS Civil Engineering Flight Dynamics Laboratory
Tanya Payne New Mexico, Univ. of Psychology Dept. Albuquerque, NM 87131 (505) 277-4805	Degree: Specialty: Assigned:	BS Psychology Weapons Laboratory
Christine Perry Pennsylvania S. Univ. Dept. of Aerospace Eng. State College, PA 16801 (814) 867-7877	Degree: Specialty: Assigned:	BS Aerospace Engineering Astronautics Laboratory
James Perry Florida Inst. of Tech. 150 West University Blvd. Melbourne, FL 32901 (407) 768-8000	Degree: Specialty: Assigned:	BS Electrical Engineering Avionics Laboratory
Brett Pokines New York, State Univ. of 1068 Richmond Quad Buffalo, NY 14260 (716) 636-5541	Degree: Specialty: Assigned:	BS Mechanical Engineering Frank J. Seiler Research Lab.
George Proicou Ohio State Univ. Biomedical Center 270 Bevis Hall Columbus, OH 43210 (614) 292-5570	Degree: Specialty: Assigned:	BS Aeronautical Engineering School of Aerospace Medicine
Jenny Rawson Washington S. Univ. Dept. of Elect. & Comp. Eng. Pullman, WA 99164 (509) 335-6602	Degree: Specialty: Assigned:	MS Electrical Engineering Flight Dynamics Laboratory

NAME / ADDRESS	DEGREE, SPECIALTY, LABORATORY ASSIGNED
Keith Redmill Ohio State Univ. Dept. of Elect. Eng. 201 Dreese Lab Columbus, OH 43210 (614) 292-2572	Degree: BS Specialty: Electrical Engineering Assigned: Flight Dynamics Laboratory
Mary Reid Arizona, Univ. of Shantz Blvd. #429 Tucson, AZ 85721 (602) 621-1646	Degree: BS Specialty: History Assigned: Engineering & Services Ctr.
Brahm Rhodes Boston Univ. Aero/Mech. Office 110 Cummington Boston, MA 02215 (617) 353-1285	Degree: MS Specialty: Mechanical Engineering Assigned: Geophysics Laboratory
Edward Riegelsberger Ohio State Univ. Dept. of Electrical Eng. Columbus, OH 43201 (614) 291-0899	Degree: BS Specialty: Electrical Engineerig Assigned: Aerospace Medical Research Laboratory
Joseph Rigney Case Western Reserve Univ. Cleveland Hts., OH 44106 (216) 321-1114	Degree: BS Specialty: Materials Science Assigned: Materials Laboratory
Dawnlee Roberson Texas-San Antonio, Univ. of SB 3.01.37 San Antonio, TX 78228 (512) 691-5665	Degree: BS Specialty: Biology Assigned: School of Aerospace Medicine
Robyn Robinson Meharry Medical College 1005 D.B. Todd Blvd. Nashville, TN 37208 (615) 327-6413	Degree: BS Specialty: Biology Assigned: School of Aerospace Medicine

NAME / ADDRESS	DEGREE, SPECIALTY, LABORATORY ASSIGNED	
Steve Romaniuk South Florida, Univ. of Dept. of Computer Science Tampa, FL 33620 (813) 974-3921	Degree: Specialty: Assigned:	MS Computer Science Avionics Laboratory
Arthur Ryan Wright State Univ. Dept. of Psychology Dayton, OH 45435 (513) 873-2451	Degree: Specialty: Assigned:	BS Psychology Aerospace Medical Research Laboratory
Robert Sabatini Scranton, Univ. of Dept. of Biology Scranton, PA 18510 (717) 961-6117	Degree: Specialty: Assigned:	BS Biology School of Aerospace Medicine
Gregory Schoeppner Ohio State Univ. 470 Hitchcock Hall Columbus, OH 43210 (614) 292-2771	Degree: Specialty: Assigned:	MS Civil Engineering Flight Dynamics Laboratory
John Sebghati Tennessee Space Inst. Box 55 Tullahoma, TN 37388 (615) 454-1087	Degree: Specialty: Assigned:	BS Aerospace Engineering Arnold Engineering Development Center
Charles Shank Syracuse Univ. Dept. of Elec. & Computer Eng. Syracuse, NY 13210 (315) 443-4229	Degree: Specialty: Assigned:	BS Electrical Engineering Rome Air Development Ctr.
David Shehee Eastern Kentucky Univ. Chemistry Dept. Richmond, KY 40475 (606) 677-1456	Degree: Specialty: Assigned:	BS Chemistry Aero Propulsion Laboratory

NAME / ADDRESS	DEGREE, SPECIALTY, LABORATORY ASSIGNED	
Scott Short Dayton, Univ. of 300 College Park Dayton, OH 45469 (513) 229-2627	Degree: Specialty: Assigned:	MS Material Science Materials Laboratory
Sveta Singh Texas-San Antonio, Univ. of Dept. of Life Sciences San Antonio, TX 78285 (512) 691-5493	Degree: Specialty: Assigned:	BS Biology School of Aerospace Medicine
Janet Solomon Alabama, Univ. of Health & Human Perform. Box 870312 Tuscaloosa, AL 35487 (205) 348-6075	Degree: Specialty: Assigned:	MS Physiology School of Aerospace Medicine
Carol Soule Georgia, Univ. of Dept. of Educational Psychology Athens, GA 30602 (404) 542-4110	Degree: Specialty: Assigned:	MS Educational Psychology Human Resources Laboratory Manpower & Personnel Div.
Thomas Starchville Pennsylvania State Univ. Dept. of Aerospace Eng. University Park, PA 16802 (814) 865-2569	Degree: Specialty: Assigned:	BS Aerospace Engineering Astronautics Laboratory
Anne Stephenson Dayton, Univ. of Aerospace Engineering Dept. Dayton, OH 45469 (513) 228-3891	Degree: Specialty: Assigned:	BS Aerospace Engineering Flight Dynamics Laboratory
Julia Stephenson North Texas, Univ. of 505 Eagle #8 Denton, TX 76201 (817) 565-3110	Degree: Specialty: Assigned:	BS Economics Human Resources Laboratory Training Systems

NAME / ADDRESS	DEGREE, SPECIALTY, LABORATORY ASSIGNED	
Velma Velazquez Wright State Univ. Dept. of Psychology Dayton, OH 45435 (513) 873-2391	Degree: Specialty: Assigned:	BS Psychology Human Resources Laboratory Logistics & Human Factors
Andrew Walsh Colorado State Univ. Dept. of Civil Eng. Fort Collins, CO 80523 (303) 491-6603	Degree: Specialty: Assigned:	BS Civil Engineering Engineering & Services Ctr.
Jennifer Wang Rensselaer Poly. Inst. Computer Science Dept. Troy, NY 12180 (518) 276-8291	Degree: Specialty: Assigned:	BS Computer Science Human Resources Laboratory Operations Training Division
Christopher Wanstall Alabama, Univ. of Dept. of Engineering Mechanics Tuscaloosa, AL 35487 (205) 348-7241	Degree: Specialty: Assigned:	BS Oceanography Armament Laboratory
Grant Watson Florida Inst. of Tech. 150 West University Melbourne, FL 32901 (407) 768-8000	Degree: Specialty: Assigned:	BS Mechanical Engineering Arnold Engineering Development Center
Melody Welch Texas A&M Univ. Dept. of Biology 715 Stadium Dr. San Antonio, TX 78212 (512) 736-7231	Degree: Specialty: Assigned:	BS Biology School of Aerospace Medicine
David Welter Dayton, Univ. of Dept. of Mechanical Eng. 300 College Park Drive Dayton, OH 45469 (513) 229-2875	Degree: Specialty: Assigned:	BS Mechanical Engineering Aero Propulsion Laboratory

NAME / ADDRESS	DEGREE, SPECIALTY, LABORATORY ASSIGNED	
William Wilk Alabama, Univ. of Dept. of Aerospace Engineering Tuscaloosa, AL 35486 (205) 348-7987	Degree: Specialty: Assigned:	BS Aerospace Engineering Arnold Engineering Development Center
William Yee Ohio State Univ. 142 Townshend Hall 1885 Neil Ave. Columbus, OH 43210 (614) 292-1123	Degree: Specialty: Assigned:	BS Psychology Aerospace Medical Research Laboratory
Timothy Young Central Florida, Univ. of MEAS Dept., Box 25000 Orlando, FL 32816 (407) 275-2416	Degree: Specialty: Assigned:	BS Mechanical Engineering Aero Propulsion Laboratory

PARTICIPANT LABORATORY ASSIGNMENT

C. PARTICIPANT LABORATORY ASSIGNMENT (Page 1)

1990 USAF/UES GRADUATE STUDENT RESEARCH PROGRAM

AERO PROPULSION LABORATORY (WRDC/APL)
(Wright-Patterson Air Force Base)

1. Robert Gabruk
2. Peter LaRose
3. Allen Olheiser
4. David Shehee
5. David Welter
6. Timothy Young

ARMAMENT LABORATORY (ATL)
(Eglin Air Force Base)

1. George Boynton
2. Randy Góve
3. Leonard Isaacs
4. Davis Lange
5. Christopher Wanstall

HARRY G. ARMSTRONG AEROSPACE MEDICAL RESEARCH LABORATORY (AAMRL)
(Wright-Patterson Air Force Base)

1. Christina Estep
2. Ellen Goldey
3. David Harper
4. Teresa Lee
5. Edward Riegelsberger
6. Arthur Ryan
7. William Yee

ARNOLD ENGINEERING DEVELOPMENT CENTER (AEDC)
(Arnold Air Force Base)

1. Ben Abbott
2. Theodore Bapty
3. Ronald Blume
4. Jordan Cahn
5. James Golden
6. Dollena Hawkins
7. Everett King
8. Kyle Nash
9. John Sebghati
10. Grant Watson
11. William Wilk

ASTRONAUTICS LABORATORY (AL)
(Edwards Air Force Base)

1. Joseph Baldonado
2. Robert Byers
3. Gregory Herdt
4. Johnny Hurtado
5. Christopher Kocher
6. Minh Le
7. Hung Nguyen
8. Christine Perry
9. Thomas Starchville

AVIONICS LABORATORY (Avionics Laboratory)
(Wright-Patterson Air Force Base)

1. Eric Byrne
2. Michael Findler
3. Jeffrey Layne
4. James Perry
5. Steve Romaniuk

C. PARTICIPANT LABORATORY ASSIGNMENT (Page 2)

ELECTRONIC TECHNOLOGY LABORATORY (ETL)
(Wright-Patterson Air Force Base)

1. Alan Coleman
2. Tammie Confer

ENGINEERING AND SERVICES CENTER (ESC)
(Tyndall Air Force Base)

1. Joseph Bernardo
2. Blaise Fitzpatrick
3. Christopher Kardish
4. Mary Reid
5. Andrew Walsh

FLIGHT DYNAMICS LABORATORY (FDL)
(Wright-Patterson Air Force Base)

1. Magna Altamirano
2. Frank Chavez
3. Patrick Fourspring
4. Craig Harwood
5. John Lair
6. Kristina Pawlikowski
7. Jenny Rawson
8. Keith Redmill
9. Gregory Schoeppner
10. Anne Stephenson

FRANK J. SEILER RESEARCH LABORATORY (Frank J. Seiler Research Lab.)
(USAF Academy)

1. Gregory Addington
2. Robert Carlin
3. Rand Conger
4. Gary Cunning
5. Joan Fuller
6. John Klinge
7. Brett Pokines

GEOPHYSICS LABORATORY (Geophysics Laboratory)
(Hansom Air Force Base)

1. Leonard Carter
2. James Day
3. Thomas Kuchar
4. John Noto
5. Brahm Rhodes

HUMAN RESOURCES LABORATORY
(Brooks, Williams and Wright-Patterson Air Force Bases)

1. Laura Bernhofen
2. Ann Canfield
3. Paul Fayfich
4. Kenneth Fleming
5. John Holman
6. Tonia Howe
7. Michael Montegut
8. Carol Soule
9. Julia Stephenson
10. Velma Velazquez
11. Jennifer Wang

C. PARTICIPANT LABORATORY ASSIGNMENT (Page 3)

MATERIALS LABORATORY (ML)
(Wright-Patterson Air Force Base)

1. Broam Cull
2. Thomas Haas
3. Margo McDowell
4. Keith Newman
5. Joseph Rigney
6. Scott Short

OCCUPATIONAL AND ENVIRONMENT HEALTH LABORATORY (OEHL)
(Brooks Air Force Base)

1. Andrew Bonas

ROME AIR DEVELOPMENT CENTER (Rome Air Development Center)
(Griffiss Air Force Base)

1. Andrew Galasso
2. David LaGraffe
3. Richard Lareau
4. John Moore
5. Charles Shank

SCHOOL OF AEROSPACE MEDICINE (School of Aerospace Medicine)
(Brooks Air Force Base)

1. Janis Beaird
2. Dora Brenner
3. Thomas Broersma
4. Joseph Brogan
5. James Fitzgerald
6. Lisa Jones
7. George Kim
8. James Kime
9. Kelly Neville
10. George Proicou
11. Dawnlee Roberson
12. Robyn Robinson
13. Robert Sabatini
14. Sveta Singh
15. Janet Solomon
16. Melody Welch

WEAPONS LABORATORY (Weapons Laboratory)
(Kirtland Air Force Base)

1. Melissa Dittmer
2. Shawn Gaffney
3. Michael Geer
4. Michael Houts
5. James Lasche
6. Toby Martin
7. Tanya Payne

WILFORD HALL MEDICAL CENTER (Wilford Hall Medical Center)
(Lackland Air Force Base)

1. Joan Estes
2. Stacey Johnson
3. Susan Jones

RESEARCH REPORTS

RESEARCH REPORTS

1990 GRADUATE STUDENT RESEARCH PROGRAM

Technical Report Number	Title	Graduate Researcher
Volume I		
Armament Laboratory		
1	Two-Dimensional Simulation of Railgun Plasma Armatures *** Same Report as Dr. Manuel Huerta ***	George Boynton
2	Infrared Laser Polarimetry	Randy Gove
3	Computing Circumcenters	Leonard Issacs
4	High Speed Video Systems for Munitions Testing	Davis Lange
5	Physical Aspects of the Penetration of Reinforced Concrete Slabs *** Same Report as Dr. Eugene Carden ***	Christopher Wanstall
Arnold Engineering Development Center		
6	High-Speed Parallel Signal Processing	Ben Abbott
7	High Speed Parallel Signal Processing *** Same Report as Ben Abbott ***	Theodore Bapty
8	Graphics for Turbine Math Models	Ronald Blume
9	s90 Graphing System	Jordan Cahn
10	A Neural Network for the Analysis of Test Data from the Aeropropulsion Systems Test Facility	James Golden
11	AI Applications for Gas Turbine Engine Testing	Dollena Hawkins
12	Investigations of Acoustic Resonance Phenomena Using Computer Animation Postprocessing	Everett King
13	Exhaust Plume Prediction Method for Underexpanded Nozzles in Supersonic External Flows	Kyle Nash

Volume I

14	Application of an Expert System to Compressor Stall Warning	John Sebghati
15	On the Hazard of Combustion Chamber Oscillations in a Large Freejet Test Cell *** Same Report as Dr. John Russell ***	Grant Watson
16	Uniform Rain/Ice Environment in the Aerothermal Wind Tunnel	William Wilk

Astronautics Laboratory

17	Control Design of Astrex Test Article *** Same Report as Dr. Hung Vu ***	Joseph Baldonado
18	Estimation of Time-Optimal Control Switching Times for Arbitrary Reorientation Maneuvers of a Rigid Spacecraft	Robert Byers
19	Van der Waals Forces in Capillary Tubes	Gregory Herdt
20	Design and Analysis of Reaction Wheel Actuators for ASTREX *** Same Report as Prof. Thomas Pollock ***	Johnny Hurtado
21	The Effects of Elevated Temperature Exposure on the Strength and Microstructure of 2-D Carbon-Carbon	Christopher Kocher
22	Investigating the Loading Rate Effect on the Crack Growth Behavior in a Composite Solid Propellant *** Same Report as Dr. Hsieng Yeh ***	Minh Le
23	Control Design of Astrex Test Article *** Same Report as Dr. Hung Vu ***	Hung Nguyen
24	Introductory Study of Compression-Shear Interaction in 3-D Carbon-Carbons	Christine Perry
25	A Survey of Distributed Sensor Systems for the Control of a Vibrating Cantilevered Beam	Thomas Starchville

Volume I
Engineering and Services Center

26	Identification of Metabolites of Various Pseudomonad Species From Growth on Isomers of Nitrotoluene	Joseph Bernardo
27	A Specimen Preparation Technique for Miscrostructural Analysis of Unsaturated Soil *** Same Report as Dr. George Veyera ***	Blaise Fitzpatrick
28	Remote Control of the Rapid Runway Repair Excavator	Christopher Kardish
29	Rate-Limited Mass Transfer and Solute Transport	Mary Reid
30	Centrifuge Modeling of Explosive Induced Stress Waves in Unsaturated Sand *** Same Report as Prof. Wayne Charlie ***	Andrew Walsh

Frank J. Seiler Research Laboratory

31	Comparisons of the Unsteady Flow Fields Elicited by Constant Rate and Sinusoidal Pitching Motions of an Airfoil	Gregory Addington
32	Control of a Complex Flexible Structure Utilizing Space-Realizable Linear Reaction Mass Actuators *** Same Report as Dr. Ephrahim Garcia ***	Robert Carlin
33	Particle Image Displacement Velocimetry (PIDV) Measurements in Dynamic Stall Phenomena *** Same Report as Dr. Ngozi Kamalu ***	Rand Conger
34	A Preliminary Analysis of Symbolic Computational Technique for Prediction of Unsteady Aerodynamic Flows *** Same Report as Dr. S. A. Kassemi ***	Gary Cunning
35	Transition Metal Carbonyl Complexes in Ambient-Temperature Molten Salts and Alkali Metal Reductions at Tungsten and Mercury Film Electrodes in Buffered Neutral Aluminum Chloride: 1-Methyl-3-Ethylimidazolium Chloride Molten Salts *** Same Report as Dr. Richard Carlin ***	Joan Fuller
36	The Effect of Wall Dynamics on the Flow Field Near the Root of an Oscillating Wing	John Klinge

Volume I

37	Control of a Complex Flexible Structure Utilizing Space-Realizable Linear Reaction Mass Actuators *** Same Report as Dr. Ephrahim Garcia ***	Brett Pokines

Geophysics Laboratory

38	Calculated Plasma Drift Velocities and Comparison with DE-2 Satellite Data	Leonard Carter
39	Optimum Observing Techniques for Detection of OH	James Day
40	IRAS Correlations with Galactic H II Regions	Thomas Kuchar
41	Infrared Spectroscopy of the Becklin-Neugebaurer object and Omicron Ceti	John Noto
42	A New Formal Hierarchy for Multiple Scattering	Brahm Rhodes

Rome Air Development Center

43	Low Temperature Properties of Dilute Tunneling Quadrupoles	Andrew Galasso
44	Absolute Surface Temperature Calibration in Semiconductor Processing	David LaGraffe
45	Optical Simulations of Guided-Wave Structures *** Same Report as Dr. Lionel Freidman ***	Richard Lareau
46	Spectral Integral Formulation Applied to Scattering by Conductor-Backed Dielectric Gaps	John Moore
47	Exploiting Parallel Architectures within a Distributed Computational Environment *** Same Report as Dr. Gary Craig ***	Charles Shank

Weapons Laboratory

48	A Phenomenological Model for the Magnetic Reconnection in Compact Toroid Formation	Melissa Dittmer
49	SEPS: Stimulated Emission Pump Spectroscopy of IF	Shawn Gaffney
50	Analysis of Centrifuge Cratering	Michael Geer

Volume I

51	Shield and Reflector Materials for Out-of-Core Thermionic Space Nuclear Reactors	Michael Houts
52	Applying Post-Detection Aberration Correction to an Imaging System *** Technical Memorandum ***	James Lasche
53	Variable Structure Control Pointing and Tracking of Flexible Structures	Toby Martin
54	Back Propagation Neural Network Simulation on a VAX Class Machine for Identification of Angles of Arrival from Cardioid Patterns *** Submitted as a Technical Memorandum ***	Tanya Payne

Volume II
Wright Research Development Center
Aero Propulsion Laboratory

55	Characterization of the Flowfield of a Dump Combustor	Robert Gabruk
56	"Chaotic" Microfaucets and the Prediction of Droplet Distributions	Peter LaRose
57	Aircraft HVDC Power System - Stability Analysis *** Same Report as Dr. K. S. Rao ***	Allen Olheiser
58	Analysis of Thermal Oxidation of Jet Fuels	David Shehee
59	Effect of Evaporation on the Driving Capillary Pressure in Capillary Pumped Aerospace Thermal Management Systems *** Same Report as Dr. Kevin Hallinan ***	David Welter
60	A Computer Simulation of Thermionic Convertor Performance of Tungsten (110) and Rhenium (0001) Cesium Diminiodes	Timothy Young

Avionics Laboratory

61	Overview of a Software Re-engineering Process Model	Eric Byrne
62	Laser Communications: Extending the Envelope (Airy Disk and Angle of Incidence Measurements)	Michael Findler
63	Integrated Terrain Access and Retrieval System Processor Loading	Jeffery Layne
64	Probabilistic IR Evidence Accumulation *** Same Report as Prof. R.H. Cofer ***	James Perry
65	Machine Learning Applied to High Range Resolution Radar Returns *** Same Report as Dr. Lawrence Hall ***	Steve Romaniuk

Electronic Technology Laboratory

66	Electronic Structure and Deep Impurity Levels in GaAs Related Compound Semiconductors and Superlattices *** Same as Dr. Devki Talwar ***	Alan Coleman
67	Surface Studies Using Scanning Tunneling Miscroscopy	Tammie Confer

Volume II
Flight Dynamics Laboratory

68	Experimental Method, Study, and Investigation of High Energy Absorbtion of AS4/3502 Graphite/Epoxy Panels	Magna Altamirano
69	Method of Characteristics Applied to Supersonic/ Hypersonic Panel Flutter	Frank Chavez
70	Preliminary Investigation of the Structural Durability of Aircraft Tires	Patrick Fourspring
71	Ballistic Damage of Aircraft Structures: Detection of Damage Using Vibration Analysis *** Submitted as Technical Memorandum*** *** Same as Dr. Vernon Matzen ***	Craig Harwood
72	Study of Impact of Carbon Graphite Composite Plates	John Lair
73	Delamination of Laminated Composites	Kristina Pawlikowski
74	H_{∞} Design Based on Loop Transfer Recovery and Loop Shaping *** Same Report as Dr. Chin Hsu ***	Jenny Rawson
75	Parallel Implementation of Structural Analysis and Control Synthesis Algorithms	Keith Redmill
76	Composite Laminate Stress Fields During Dynamic Loading	Gregory Schoeppner
77	Influence of Static and Dynamic Aeroelastic Constraints on the Optimal Structural Design of Flight Vehicle *** Same Report as Dr. Franklin Eastep ***	Anne Stephenson

Materials Laboratory

78	A Comparison of the Analytical and Numerical Solutions of the Nonlinear Diffusion Equation and a Preliminary Investigation into a Specific Case of Second Harmonic Generation	Brian Cull
79	Eddy Current Testing in Nondestructive Evaluation *** Same Report as Dr. P.K. Kadaba ***	Thomas Haas
80	Microcrack Initiation and Growth During Fatigue Cycling by Surface Acoustic Wave Scattering	Margo McDowell

Volume II

81	The Effect of Evaporated Aluminum Overlayers on the Compressive Strength of High-Performance Polymer Fiber Poly-(p-phenylene benzobisthiazole)	Keith Newman
82	Loading Rate Effects on Ductile-Phase Toughening in In-Situ Niobium Silicide-Niobium Composites	Joseph Rigney
83	Analysis of Interlaminar Shear Failures in Brittle-Matrix Composite Flexure Specimens	Scott Short

Volume III
Human Systems Divisions Laboratories
Harry G. Armstrong Aerospace Medical Research Laboratory

84	Simulation of Head/Neck Response to -G_x Impact Acceleration *** Same Report as Dr. Amit Patra ***	Christina Estep
85	Gestational and Lactational Transfer of Hexachlorobenzene from the Maternal Rat Dosed Prior to Breeding	Ellen Goldey
86	Decision-Making Under System Failure Conditions *** Same Report as Dr. Bonnie Walker ***	David Harper
87	Statistical Analysis of Civil Disorders: 1964-1989	Teresa Lee
88	Speaker Normalization and Vowel Recognition using Neural Networks *** Same Report as Dr. A. Krishnamurthy ***	Edward Riegelsberger
89	Cardio-Respiratory Measures of Workload During Continuous Manual Performance *** Same Report as Dr. Richard Backs ***	Arthur Ryan
90	Development of a Localization Performance Paradigm for RHAW Applications	William Yee

Human Resources Laboratory

91	A Comparative Analysis of a 4-Group and 6-Group Job Classification *** Same Report as Dr. Pinyuen Chen ***	Laura Bernhofen
92	A Pilot Study of the Naming Transaction Shell	Ann Canfield
93	Automating the Administration of USAF Occupational Surveys *** Same Report as Dr. Delayne Hudspeth ***	Paul Fayfich
94	Psychophysical Measurement of Spectral Attenuation in the Human In Vivo Ocular Media: Method and Results *** Same Report as Dr. Gillray Kandel ***	Kenneth Fleming
95	An Examination of Factors Influencing Air Force Enlisted Retention	John Holman

Volume III

96	Cognitive Representations of Teams *** Same Report as Dr. Joan Rentsch ***	Tonia Howe
97	Peripheral vs. Foveal Contour Processing in Humans	Michael Montegut
98	Cognitive Determinants of Graph Reading Skill	Carol Soule
99	Survival Analysis: A Training Decision Application *** Same Report as Dr. Stanley Stephenson ***	Julia Stephenson
100	Predicting the Impact of Automation on Performance and Workload in C^2 Systems *** Same Report as Dr. Pamela Tsang ***	Velma Velazquez
101	Peripheral vs. Foveal Contour Processing in Humans *** Same Report as Michael Montegut ***	Jennifer Wang

Occupational and Environmental Health Laboratory

102	Development of Groundwater Modeling in the Air Force Installation Restoration Program	Andrew Bonas

School of Aerospace Medicine

103	Effects of Repeated Days of Light Work at Moderate Temperatures in the Protective Clothing *** Same Report as James Kime and Janet Solomon ***	Janis Beaird
104	Predisposition of Mammalian Cell Cultures Treated with Aflatoxin B1 to Potential Radiation Effects *** Same Report as Dr. Paul Lemke ***	Dora Brenner
105	Organizational Learning and Aircrew Performance	Thomas Broersma
106	PCR Analysis of Ureaplasma urealyticum and Mycoplasma hominis *** Same Report as Dr. Vito DelVecchio ***	Joseph Brogan
107	The Effects of Propranolol on Thermoregulation During Radiofrequency Radiation-Induced Heating and the Examination of Host/Graft Integration in the Rat Hippocampus Using Multiple Site Optical Recording	James Fitzgerald

Volume III

108	An Electrophoretic Comparison of the Effects of Various Carboxylesterase Inhibitors on Cholinesterase and Carboxylesterase Activities	Lisa Jones
109	No Report Submitted *** Would have been Same as Dr. Rex Moyer***	George Kim
110	Effects of Repeated Days of Light Work at Moderate Temperatures in the Protective Clothing *** Same Report as Janis Beaird and Janet Solomon ***	James Kime
111	Human Performance Model of Fatigue	Kelly Neville
112	Aortic Input Impedance Calculation in Supine and Upright Baboon	George Proicou
113	A. Laser Protective Material Evaluation: Data Acquisition and Management System B. Characterization of Nanosecond Laser Pulses Through Laser Eye Protection Materials	Dawnlee Roberson
114	The Effect of Microwave Radiation on the Eye	Robyn Robinson
115	PCR Analysis of Ureaplasma urealyticum and Mycoplasma hominis *** Same Report as Dr. Vito DelVecchio ***	Robert Sabatini
116	Sodium Dodecyl Sulfate Polyacrylamide Gel Electrophoresis for the Resolution of Light Induced FOS-Related Proteins in the Hamster Suprachiasmatic Nuclei	Sveta Singh
117	Effects of Repeated Days of Light Work at Moderate Temperatures in the Protective Clothing *** Same Report as Janis Beaird and James Kime ***	Janet Solomon
118	Physiological Effects of Whole-Body Exposure to Millimeter Waves and Physiological Effects of Alpha-antagonist Tolazoline During Whole-Body Exposure to 2.45 GHz Radiofrequency Radiation	Melody Welch

Volume III
Wilford Hall Medical Center

119	Interrelationships of Tobacco, Caffeine, and Alcohol Use Among Participants of an Air Force-Sponsored Health Promotion Program	Joan Estes
120	The Effect of Race on Birthweight and Outcome in Premature Infants	Stacey Johnson
121	Detection of the Interaction Between Stress and Malingering Among Basic Trainees Using the MMPI-2	Susan Jones

1990 USAF - UES SUMMER FACULTY RESEARCH PROGRAM

Sponsored by the

AIR FORCE OFFICE OF SCIENTIFIC RESEARCH

Conducted by the

Universal Energy Systems, Inc.

FINAL REPORT

Two-Dimensional Simulation of Railgun Plasma Armatures

Prepared by:	Manuel A. Huerta, Ph. D.	and G. Christopher Boynton
Academic Rank:	Professor	Graduate Student
Department and	Physics Department	
University:	University of Miami	
Research Location:	AFATL/SAH	
	Eglin AFB, FL 32542-5000	
Effort Focal Point:	Mr. Kenneth K. Cobb	
Address:	AFATL/SAH	
	Eglin AFB, FL 32542-5434	

Date: 22 August 1990

Contract No: F49620-88-C-0053

Same Report as
Prof. Manuel Huerta
(Report # 7)

1990 USAF-UES SUMMER FACULTY RESEARCH PROGRAM/

GRADUATE STUDENT RESEARCH PROGRAM

Sponsored by the

AIR FORCE OFFICE OF SCIENTIFIC RESEARCH

Conducted by the

Universal Energy Systems, Inc.

FINAL REPORT

INFRARED LASER POLARIMETRY

Prepared by:	Randy Gove
Academic Rank:	Graduate Student
Department and	Physics Department
University:	University of Alabama in Huntsville
Research Location:	USAF AFATL/AGA
	Eglin AFB, FL 32542
USAF Researcher:	Dr. Dennis Goldstein
Date:	22 Aug 1990
Contract No:	F49620-88-C-0053

INFRARED LASER POLARIMETRY

by

Randy Gove

ABSTRACT

The Mueller matrix for a rotating retarder infrared laser polarimeter was theoretically derived. Which included error terms which accounted for the nonideal optical elements used in the experimental polarimeter. The error terms accounted for were nonideal retardance and diattenuation of the retarders, and orientational errors of the retarders and second polarizer with, respect to the x-axis. The inclusion of error terms in the Mueller matrix allows for error compensation to be made in the experimentally determined Mueller matrix. A program was written to experimentally determine the retardance and diattenuation of a sample which is rotated between two fixed polarizers. Beam wander during experimental measurements was also reduced by installing and callibrating a new detector with a larger detector surface area. Mueller matrix measurements were also made on a sample of cadmium telluride with an applied electric field.

ACKNOWLEDGMENTS

I wish to acknowledge the Air Force Office of Scientific Research for sponsoring the program and Universal Energy Systems for their effective handling of administrative matters. Graditude is extended to members of AGA's infrared technology section, namely Lynn Diebler, Tom Davis, David Gray, Otto Martinez, Maggie Fenton, Jeff Barnes, Phyllis Williams, Lisa Collins, and Danielle Walker for their assistance and making me feel at home. A thank you also goes to the special projects laboratory personel Howard McCormick, Michael VanTassel, Voncile Houston, David Onuffer, and Linda Lau for their help and friendship. My deepest appreciation goes to my effort focal point Dr. Dennis Goldstein for making this project possible, educational, and enjoyable. Finally thanks go to Fred Gibson for sharing the summers experiences with me.

I. Introduction

Work in experimental infrared laser polarimetry has been on going at the Air Force Armament Laboratory (AFATL) since the summer of 1988, when Dr. Dennis Goldstein and Mr. David Chenault assembled the polarimeter. A description of the operation of the polarimeter and some of the first measurements made are contained in Mr. Chenault's final report to UES.[1] Additional work on the polarimeter was performed by Mr. Randall Hodgson during the summer of 1989. This work included steps to reduce measurement and data processing errors. A record of this is contained in Mr. Hodgson's final report to UES.[2]

Infrared laser polarimetry is a method for obtaining the polarization properties of a material which is transparent to infrared radiation. These properties are represented by a Mueller matrix for a given sample. The reason for performing polarimetry experiments is to gain a better understanding of infrared crystalline optics, supplying a data base for infrared polarization properties of materials, and most importantly, testing materials to see if they would make a potentially good electrooptic modulator material. By developing better electrooptic modulators improvements can be made in target simulation systems, optical processing

systems, image processing systems, and eventually optical computing. Additional information on polarimetry and characterizing potential electrooptic modulator materials can be found in Dr. Goldstein's dissertation.[3]

I have just completed my first year as a graduate student at the University of Alabama in Huntsville, where I am pursuing a Ph.d in physics, concentrating in optics. During the spring of 1990 I was involved with a reasearch project under the supervision of Dr. Russell Chipman. Experiments were conducted using an infrared spectropolarimeter, which utilizes the same techniques as the infrared laser polarimeter over a spectrum of frequencies. Retardance, diattenuation, and transmittance measurements were taken on an Optics for Research infrared polarizer. The measurements where made from the 3 to 25 micron range to see if this polarizer had achromatic retardance, diattenuation, and transmittance properties. This polarizer was a candidate to be an element in the spectropolarimeter itself. This experience familiarized me with the techniques of polarimetry.

II. Objectives

The first goal of this summers research project was to install a new detector for the purpose of reducing beam wander. In addition to this it was desirable to have a computer program which experimentally determined the retardance and diattenuation of a sample by rotating it between two fixed polarizers. Another goal was to obtain the Mueller matrix for a sample in terms of fourier coefficients, the orientational errors of the optical elements, and the nonideal retardance and diattenuation of the optical element retarders. Once these objectives are achieved measurements of a cadmium Telluride sample with applied electric field could be made.

III. Beam Wander

The first objective worked on, during this summers research effort, was to eliminate the problem of beam wander. Beam wander is the term used to describe the laser beam wandering around on, or possibly off of the surface of the detector. Since the data taken during a laser polarimetry experiment consists of intensity measurements at the detector, beam wander can lead to erroneous results.

Beam wander arises from having the beam strike the retarders nonnormal to the retarders surface. Since the retarders are being rotated the refracted beam tends to wander around on the detector. It is very difficult to align the retarders so the beam strikes normal to its surface for the full 360 degree of rotation. Therefore, an attempt to reduce the beam wander problem was made by installing an integrating sphere with an aperture of .5 inches, and a new detector with a larger detector surface area. The new NERC dewars mounted HgCDTe photoconductive detector has a surface area of $16mm^2$, where-as the previous detector had a surface area of $1mm^2$.

Although the new detector set-up has a larger surface area and certainly reduces beam wander, it does not have the sensitivity of the old detector. This is generally not a problem when using the laser to take measurements, however, a blackbody source is often used to calibrate the optical system, since it is more stable than the laser. The blackbody doesn't emit as much power as the laser so the old detector is used for calibration purposes.

IV. Retardance Diattenuation Program

The second objective for this summers research project was to write a computer program which would experimentally determine the retardance and diattenuation of a sample which is rotated between two fixed polarizers. The scheme used for this program was obtained from a paper by Mr. David Chenault.[4]

The data aquisition and data reduction techniques were the same as those used for finding the Mueller matrix of a sample. In determining the Mueller matrix, the sample is fixed between two rotating retarders, which are also situated between two fixed linear polarizers. In the retardance, diattenuation program there are no retarders and the sample is rotated between two fixed polarizers. In order to obtain the Mueller matrix it was necessary to evaluate all the fourier coefficients a_0, a_1, $\cdots$ a_{12}, and b_1, b_2, $\cdots$ b_{12}. However, in the retardance and diattenuation program the principal transmittances, retardance, and diattenuation can be obtained from the a_0, a_2, and a_4 coefficients. The orientation of the principal transmittances with respect to the x-axis can also be obtained with the additional evaluation of the b_2 and b_4 coefficients. Since the data aquisition and data reduction

techniques are the same for both programs it was only necessary to modify the subroutine of the Mueller matrix program which evaluated the fourier coeffients and performed the calculations. The equations used in the retardance diattenuation program are as follows.

Principal Transmittances

$$K_1 = a_0 + a_2 + a_4 \tag{1}$$

$$K_2 = a_0 + a_4 - a_2 \tag{2}$$

Diattenuation

$$D = \frac{a_2}{a_0 + a_4} \tag{3}$$

Retardance

$$\cos\delta = \frac{a_0 - 3asub4}{[(a_0 + asub4)^2 - a_2^2]^{.5}} \tag{4}$$

Orientations of principal transmittances with respect to the x-axis

$$\tan(2\phi_2) = \frac{b_2}{a_2} \tag{5}$$

$$\tan(4\phi sub4) = \frac{b_4}{a_4} \tag{6}$$

Although the a_1, a_3, a_5, b_1, b_3 and b_5 are not used in any calculations they are evaluated. An optical system with no errors would make each of these coefficients equal to zero. Therefore, a nonzero value for any of these coefficients can

give information on errors present in the optical system such as beam wander, misalignment of elements, and laser or detector fluctuations.

V. Inversion of complete Mueller matrix expression

Some theoretical work was also performed during the summer research project. It was desirable to have the Mueller matrix elements not only in terms of the Fourier coefficients but also include error terms for the misalignment of the optical elements and the nonideal retardance and diattenuation of the retarders. These additional terms where desirable since experimental determination of the magnitudes of these terms would allow for error compensation to be made on the experimentally determined Mueller matrices of samples.

Figure 1 shows the optical system of a polarimeter, along with the error terms associated with it.

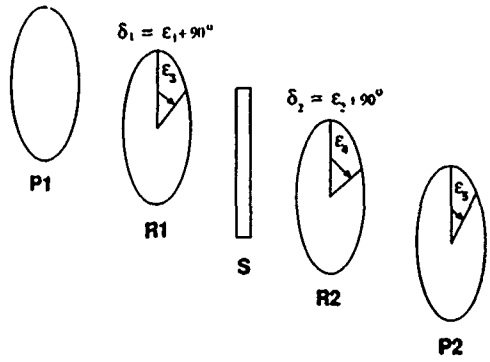

Figure 1 Optical System

All orientational errors are referenced from the polarization axis of the first linear polarizer. The Mueller matrix elements of the sample are encoded on the signal by modulating it with the rotation of the two retarders. The Mueller matrix equation for the system is

$$L_2 R_2(\theta) M R_1(\theta) L_1 \qquad (7)$$

where L_1 is a linear horizontal polarizer

$$\begin{pmatrix} 1 & 1 & 0 & 0 \\ 1 & 1 & 0 & 0 \\ 0 & 0 & 0 & 0 \\ 0 & 0 & 0 & 0 \end{pmatrix}$$

Ideally R_1 is a linear quarter wave retarder at arbitrary angle θ. k_1 and k_2 account for any diattenuation, $\delta = 90 + \epsilon_1$ accounts for nonideal retardance, and ϵ_3 is the orientational error of the fast axis from the x-axis. R_1 is given by

$$\begin{pmatrix} \frac{k_1+k_2}{2} & \frac{k_1-k_2}{2}\cos 2(\theta+\epsilon_3) & 0 \\ \frac{k_1-k_2}{2}\cos 2(\theta+\epsilon_3) & \frac{k_1+k_2}{2}\cos^2 2(\theta+\epsilon_3)+(k_1)^{.5}(k_2)^{.5}\cos\delta\sin^2 2(\theta+\epsilon_3) & -(k_1)^{.5}(k_2)^{.5}\sin\delta\sin 2(\theta+\epsilon_3) \\ \frac{k_1-k_2}{2}\sin 2(\theta+\epsilon_3) & \frac{k_1+k_2}{2}\cos 2(\theta+\epsilon_3)\sin 2(\theta+\epsilon_3)-(k_1)^{.5}(k_2)^{.5}\cos\delta\cos 2(\theta+\epsilon_3)\sin 2(\theta+\epsilon_3) & (k_1)^{.5}(k_2)^{.5}\sin\delta\cos 2(\theta+\epsilon_3) \\ 0 & (k_1)^{.5}(k_2)^{.5}\sin\delta\sin 2(\theta+\epsilon_3) & (k_1)^{.5}(k_2)^{.5}\cos\delta \end{pmatrix}$$

$$\begin{pmatrix} \frac{k_1-k_2}{2}\sin 2(\theta+\epsilon_3) & 0 \\ \frac{k_1+k_2}{2}\cos 2(\theta+\epsilon_3)\sin 2(\theta+\epsilon_3)-(k_1)^{.5}(k_2)^{.5}\cos\delta\cos 2(\theta+\epsilon_3)\sin 2(\theta+\epsilon_3) & -(k_1)^{.5}(k_2)^{.5}\sin\delta\sin 2(\theta+\epsilon_3) \\ \frac{k_1+k_2}{2}\sin^2 2(\theta+\epsilon_3)+(k_1)^{.5}(k_2)^{.5}\cos\delta\cos^2 2(\theta+\epsilon_3) & (k_1)^{.5}(k_2)^{.5}\sin\delta\cos 2(\theta+\epsilon_3) \\ -(k_1)^{.5}(k_2)^{.5}\sin\delta\sin 2(\theta+\epsilon_3) & (k_1)^{.5}(k_2)^{.5}\cos\delta \end{pmatrix}$$

and M is the sample Mueller matrix

$$\begin{pmatrix} m_{11} & m_{12} & m_{13} & m_{14} \\ m_{21} & m_{22} & m_{23} & m_{24} \\ m_{31} & m_{32} & m_{33} & m_{34} \\ m_{41} & m_{42} & m_{43} & m_{44} \end{pmatrix}.$$

Ideally R_2 is a linear quarter wave retarder at arbitrary angle θ. k_1 and k_2 account for any diattenuation, $\delta = 90 + \epsilon_2$ accounts for nonideal retardance, and ϵ_4 is the orientational error of the fast axis from the x-axis. R_2 is given by

$$\begin{pmatrix} \frac{k_1+k_2}{2} & \frac{k_1-k_2}{2}\cos 2\theta+\epsilon_4) & \frac{k_1-k_2}{2}\sin 2\theta+\epsilon_4) & 0 \\ \frac{k_1-k_2}{2}\cos 2\theta+\epsilon_4) & \frac{k_1+k_2}{2}\cos 2\theta+\epsilon_4)+(k_1)^{.5}(k_2)^{.5}\cos\delta\sin^2 2\theta+\epsilon_4) & \frac{k_1+k_2}{2}\cos 2\theta+\epsilon_4)\sin 2\theta+\epsilon_4)-(k_1)^{.5}(k_2)^{.5}\cos\delta\cos 2\theta+\epsilon_4)\sin 2\theta+\epsilon_4) & (k_1)^{.5}(k_2)^{.5}\sin\delta\sin 2\theta+\epsilon_4) \\ \frac{k_1-k_2}{2}\sin 2\theta+\epsilon_4) & \frac{k_1+k_2}{2}\cos 2\theta+\epsilon_4)\sin 2\theta+\epsilon_4)-(k_1)^{.5}(k_2)^{.5}\cos\delta\cos 2\theta+\epsilon_4)\sin 2\theta+\epsilon_4) & \frac{k_1+k_2}{2}\sin^2 2\theta+\epsilon_4)+(k_1)^{.5}(k_2)^{.5}\cos\delta\cos^2 2\theta+\epsilon_4) & -(k_1)^{.5}(k_2)^{.5}\sin\delta\cos 2\theta+\epsilon_4) \\ 0 & -(k_1)^{.5}(k_2)^{.5}\sin\delta\sin 2\theta+\epsilon_4) & (k_1)^{.5}(k_2)^{.5}\sin\delta\cos 2\theta+\epsilon_4) & (k_1)^{.5}(k_2)^{.5}\cos\delta \end{pmatrix}$$

L_2 is a linear polarizer with a small angular error ϵ_5 from the x-axis

$$\begin{pmatrix} 1 & \cos 2\epsilon_5 & \sin 2\epsilon_5 & 0 \\ \cos 2\epsilon_5 & \cos^2 2\epsilon_5 & \cos 2\epsilon_5\sin 2\epsilon_5 & 0 \\ \sin 2\epsilon_5 & \cos 2\epsilon_5\sin 2\epsilon_5 & \sin^2 2\epsilon_5 & 0 \\ 0 & 0 & 0 & 0 \end{pmatrix}$$

The detected intensity takes the form of

$$\mathbf{I} = c\mathbf{AMP} \tag{8}$$

where $\mathbf{P} = \mathbf{R_1L_1S}$ is the Stokes vector of light leaving the polarizing optics with $\mathbf{S}$ being the Stokes vector of the light from the source, $\mathbf{A} = \mathbf{L_2R_2}$ is the Mueller matrix of the analyzing optics, $\mathbf{M}$ is the Mueller matrixs of the sample, and c is a proportionality constant. The intensity can also be written as

$$I = c\sum_{i,j=1}^{4} a_i p_j m_{ij} \tag{9}$$

or

$$I = c \sum_{i,j=1}^{4} u_{ij} m_{ij} \tag{10}$$

the a_i being the elements of **A**, the p_j are the elements of **P**, the m_{ij} are the elements of the Mueller matrix **M**, and where

$$u_{ij} = a_i p_j \tag{11}$$

Since the detector is not polarization sensitive only the top row of the matrix **A** is involved in the calculations. Thus multiplying through the intensity is given by[5]

$$\begin{aligned} I = {} & a_1(m_{11}p_1 + m_{12}p_2 + m_{13}p_3 + m_{14}p_4) \\ & + a_2(m_{21}P_1 + m_{22}p_2 + m_{23}P_3 + m_{24}p_4) \\ & + a_3(m_{31}p_1 + m_{32}p_2 + m_{33}p_3 + m_{34}p_4) \\ & + a_4(m_{41}p_1 + m_{42}p_2 + m_{43}p_3 + m_{44}p_4) \end{aligned} \tag{12}$$

An example of a u_{ij} is

$$u_{11} = \left[\frac{k_{21}+k_{22}}{2} + \frac{k_{21}-k_{22}}{2}\cos 2epsilon_5 \cos 10(\theta+\epsilon_4) + \frac{k_{21}-k_{22}}{2}\sin 2epsilon_5 \sin 10(\theta+\epsilon_4)\right] \times \left[\frac{k_{11}+k_{12}}{2} + \frac{k_{11}-k_{12}}{2}\cos 2(\theta+\epsilon_3)\right]$$

The u_{ij} can be expanded into a Fourier series, the coefficients of each of the harmonic frequencies can be grouped together with the coefficients of the same harmonics in the other u_{ij} to give the Fourier coefficients. Since there are twelve harmonic frequencies we are left with

twenty five equations (Fourier coefficients) in sixteen unknowns (Mueller matrix elements). The next step is to invert the expressions so the Mueller matrix elements are a function of the Fourier coefficients. Although the solution is unique there are several ways to express the results. The inversion process can also be simplified by using a small angle aproximation on the error terms. Since the expressions for the Mueller matrix elements are quite lengthy, the elements will be written in terms of other matrix elements and Fourier coefficients.

$m_{11} = m_{32}, m_{31}, m_{22}, m_{12}, a_0$

$m_{12} = m_{32}, m_{22}, a_4, b_4$

$m_{13} = m_{33}, m_{23}, a_4, b_4$

$m_{14} = m_{33}, m_{32}, m_{23}, m_{22}, m_{21}, m_{31}, m_{24}, m_{34}, m_{12}, m_{13}, m_{11}, a_2$

$m_{21} = m_{22}, a_{20}, b_{20}$

$m_{22} = m_{33}, m_{32}, m_{23}, b_{16}$

$m_{23} = m_{32}, m_{33}, a_{16}, b_{24}$

$m_{24} = m_{32}, m_{23}, m_{31}, a_{22}, b_{22}$

$m_{31} = m_{32}, a_{20}, b_{20}$

$m_{32} = a_{16}, b_{16}, a_{24}, b_{24}$

$m_{33} = a_{16}, b_{16}, a_{24}, b_{24}$

$m_{41} = m_{32}, m_{22}, m_{21}, m_{31}, m_{12}, m_{11}, m_{42}, a_{10}$

$m_{42} = m_{33}, m_{32}, m_{23}, m_{22}, m_{12}, m_{13}, m_{43}, a_{14}$

$m_{43} = m_{33}, m_{32}, m_{23}, m_{22}, m_{12}, m_{13}, a_6$

$m_{44} = m_{33}, m_{32}, m_{23}, m_{22}, m_{21}, m_{24}, m_{34}, m_{12}, m_{13}, m_{11}, m_{43}, m_{42}, m_{41}, a_{12}$

m_{33} and m_{32} are solved completely and the other elements must be solved for in the following order: $m_{23}, m_{22}, m_{21}, m_{31}, m_{24}, m_{34}, m_{12}, m_{13}, m_{11}, m_{43}, m_{42}, m_{41}, m_{14}, m_{44}$ It should be noted that these Mueller matrix elements are also functions of the error terms. Now that these equations have been derived they can be used in the data reduction program to obtain experimental results.

VI. Cadmium Telluride Measurement

Mueller matrix measurements of a cadmium telluride sample with an applied electric field across the crystal were made. Measurements where taken from 1800 through 2800 volts in increments of 100 volts. A linear regression was performed on four sets of data consisting of inverse trigonometric functions of experimental Mueller matrix elements versus phase as a function of voltage. The slope of the line is $n^3 r_{41}$ where n is the index of refraction and r_{41} is the electrooptic tensor coefficient. This quantity is the most important quantity in determining a materials potential as an electrooptic modulator. The results of the

measurements appear in the following table.

y-axis	x-axis	slope= $n^3 r_{41}$
$arccos(m_{44})$	$\frac{2\pi}{\lambda}\frac{VL}{d}$	1.030×10^{-10}
$arccos(m_{22}+m_{33}-1)$	$\frac{2\pi}{\lambda}\frac{VL}{d}$	1.109×10^{-10}
$arcsin(m_{42}^2+m_{43}^2)^{.5}$	$\frac{2\pi}{\lambda}\frac{VL}{d}$	6.625×10^{-10}
$arcsin(m_{24}^2+m_{34}^2)^{.5}$	$\frac{2\pi}{\lambda}\frac{VL}{d}$	5.027×10^{-10}

The average slope of all four data sets is 8.261×10^{-11} with a standard deviation of 2.904×10^{-10}. This differs from the quantity found in the literature of $n^3 r_{41} = 1.00\times10^{-10}$ by seventeen percent. This difference can be attributed to experimental error or error in the quantity given in the literature.

VII. Recommendations

The first recommendation would be the aquisition of a new CO_2 laser. The laser in use now suffers from instability. It will often take several hours to stabilize and some days it will not stabilize at all. When the laser does stabilize an instability of one to five percent can be expected over a five minute time interval, which is the time it takes to make a Mueller matrix measurement. This large fluctuation causes errors in the Mueller matrixs measurements. These errors also cannot be compensated for. With this laser a large amount of time is spent monitoring the laser stability, time that could be used for taking measurements. Also with the aquisition of a more stable laser, measurements with considerable accuracy could be made.

A recommendation can also be made on how to invoke error compensation on the measured Mueller matrix now that the Mueller matrix elements have been derived containing the principal transmittances of the retarders and the other error terms. The Mueller matrix for no sample is the identity matrix. Setting the diagonal elements to one and the off diagonal elements to zero in the Fourier coefficient expressions the number and complexity of these equations

will be reduced. The remaining equations can be used to solve for the nine error terms, in terms of the Fourier coefficients. When a Mueller matrix measurement is made the error terms can be calculated and substituted back into the Mueller matrix element expressions thus compensating for the errors.

As far as follow-on work is concerned, the laser polarimeter can be used to conduct research on depolarization properties of materials and thin films. This area of research has had limited exploration, however it is an important consideration for materials and thin films which find application in devices which utilize polarization.

REFERENCES

1. Chenault, David B., "Mueller Matrix Infrared Polarimetry", Final Report for the 1988 USAF-UES Graduate Student Research Program, 22 August 1988.

2. Hodgson, Randall R., "Laser Polarimetry Development", Final Report for the 1989 USAF-UES Graduate Student Research Program, 17 August 1989.

3. Goldstein, Dennis H., "Polarization Modulation in Infrared Electrooptical Materials", Dissertation, University of Alabama in Huntsvlle, 1990.

4. Chenault, David B., Russell A. Chipman "Linear Diattenuation and Retardance Measurements in an IR Spectropolarimeter" Proc. Polarimetry conference, University of Alabama in Huntsville, Huntsville, AL, May 1990.

5. Goldstein, Dennis H., "Polarization Modulation in Infrared Electrooptical Materials", Dissertation, University of Alabama in Huntsvlle, 1990.

1990 USAF-UES SUMMER FACULTY RESEARCH PROGRAM

GRADUATE STUDENT RESEARCH PROGRAM

Sponsored by the

AIR FORCE OFFICE OF SCIENTIFIC RESEARCH

Conducted by the

Universal Energy Systems, Inc.

FINAL REPORT

Computing Circumcenters

Prepared by:	Leonard H. Isaacs
Academic Rank:	Graduate Student
Department and University:	Mathematics Department, University of Wyoming
Research Location:	AFATL/FXA, Eglin AFB, FL 32542-5000
USAF Researcher:	Bruce Simpson
Date:	20 Aug 90
Contract No.:	F49620-85-C-0013

Computing Circumcenters

by

Leonard H. Isaacs

ABSTRACT

A Fortran code allows the inputting of three arbitrary points in two dimensions and computes the center of the circle on which the three points lie. The first two points are classified as forming a vertical, horizontal or diagonal line segment and the third point determines what type of triangle is formed by the points. The types are degenerate, right or other. If the type is degenerate such as that formed by three collinear points the set of points is flagged. If the type is right triangle or other the center coordinates are computed by analytical methods.

If a point is repeated in a set of 2-tuples that set is flagged.

Acknowledgements

I would like to thank the Air Force Systems Command, Air Force Office of Scientific Research and Universal Energy Systems for their sponsorship and guidance of this program.

Individually, I would like to express my appreciation for the efforts of Dr. Yen Tu and Jr. Bruce Simpson of the Air Force Armament Laboratory at Eglin AFB and to my advisor, Dr. Jack George, who has guided my research.

I. INTRODUCTION:

The Computational Fluid Dynamics Section of the Aeromechanics Division of the USAF Armament Lab at Eglin AFB, is concerned with modeling aerodynamic flows over a body by using computational fluid dynamics techniques. These techniques include the generation of a grid system that simulates the body in question, and the use of flow solvers to determine the aerodynamics of the body.

My interests are in unstructured grid generation techniques and numerical methods of increasing the speed at which solutions are found by the flow solver. One grid generation technique I focused on was the so-called unstructured grid system. This system is particularly efficient at conforming to the boundaries of a body which is a desirable property in that it yields more realistic modeling of aerodynamic flows.

II. OBJECTIVES OF THE RESEARCH EFFORTS:

The goal of the research done at the CFD section is to automatically generate a grid system that accurately models an arbitrary three dimensional body and determine the aerodynamics of the body quickly and efficiently with a computer.

My assignment, as a part of the CFD research effort was to develop a computer code that implements a step in an unstructured grid algorithm. Essentially, the step in the grid algorithm finds the center of the circumcircle of three arbitrary grid points in two dimensions.

III.

a. The unstructured grid algorithm needs to be able to accommodate an arbitrary set of points. With this in mind the circumcenter subroutine must allow any triplet of 'two-tuples' and calculate the center of the circle on which those points lie. Any degenerate cases such as collinear points must be noted so that the degeneracy does not affect the gridding algorithm.

The approach taken to develop the subroutine was to classify the first two coordinates entered into the subroutine as forming either a horizontal, vertical or diagonal line segment. Then the third coordinate could be placed at any position on a circle

around the line segment formed by the first two points. The placement of the third point could lead to a degeneracy or a triangle deemed solvable, in terms of finding a circumcenter. Once the triangle was classified as degenerate or solvable the points could be flagged as degenerate or the center would be calculated.

b. The result of the research has been a code written in Fortran that interactively allows the inputting of any set of three 2-tuples and computes the center of their circumcircle or flags the points as degenerate.

The code allows the inputting of three points that are either vertically, horizontally or diagonally collinear and flags them as degenerate. It also detects any points that are entered more than once in a set of three two-tuples and notifies the user.

The code uses predominantly logical statements to identify the type of triangle formed by the points so that arithmetic operations are kept to a minimum in determining the center of a circumcircle. The center points are given as x and y coordinates and are exact.

IV. RECOMMENDATIONS:

a. The subroutine, although it is a research version, could be

easily added to existing software. Ideally, points would be read from an input file and then the subroutine would be called to find the circumcenter of the points. Any degenerate points would be flagged and that information passed to the main program.

b. Further research would be warranted to determine if the circumcenter of the generalized boundary nodes, as described by Kennon (1989) could be found without use of the Newton-Raphson method which gives only an approximate answer and requires multiple iterations.

REFERENCES

Kennon, S.R., "A New Look at Finite-Volume Methods," Final Report, SBIR Contract F08635-89-C-0211, MDA Engineering Inc., Arlington, Texas, July, 1989.

1990 USAF-UES SUMMER FACULTY RESEARCH PROGRAM/GRADUATE STUDENT RESEARCH PROGRAM

SPONSORED BY THE
AIR FORCE OFFICE OF SCIENTIFIC RESEARCH
CONDUCTED BY THE
UNIVERSAL ENERGY SYSTEMS, INC

FINAL REPORT

HIGH SPEED VIDEO SYSTEMS FOR MUNITIONS TESTING

Prepared by: Davis Alan Lange

Academic Rank: Research Assistant

Department: Optical Sciences Center

University: University of Arizona

Research Location: Air Force Armament Laboratory
AFATL/AGI Eglin AFB

USAF Researcher: Donald Snyder

Date: September 21, 1990

Contract No: F49620-88-C-0053

HIGH SPEED VIDEO SYSTEMS FOR MUNITIONS TESTING

by:
Davis Lange

Abstract:

The testing of munitions systems is critical to ensure proper operation , safety of crew and aircraft, and as a feedback to design engineers on how well they have performed their job. With the present state of advanced weapon systems, the need for accurate and calibrated data is essential. Presently this job is being facilitated by the use of high speed film cameras using essentially 16mm format film. The film is then digitized onto an elaborate computer system for data reduction and analysis.

Recently, an interest has been expressed in the use of Solid State Sensor technology to enhance munitions testing capability. In this report, we report preliminary findings on experimental data using the present procedure. We then use a simple model to predict the performance of a proposed Solid State Sensor system. We compare the predicted results of the 2 systems and show the advantages and disadvantages of the proposed system versus the present standard.

ACKNOWLEDGEMENTS

The author would like to acknowledge the USAF for supporting university research through this program. I also acknowledge the men and women of AFATL/AGI for their incredible enthusiasm and support over the past summer. I acknowledge the support from the SVERDRUP TEAS group at Elin AFB, the people at Freeman Math Laboratories and the people at DYNCORP. I would also like to thank Universal Energy Systems for their outstanding service and management over the entire duration of this program. I would especially like to thank Don Snyder, Rodney Powell, Howard McCormick, Jeffrey Rowe, and Gene Schenette for making the summer enjoyable as well as productive.

INTRODUCTION:

The history of my particular interest in Focal Plane Array Technology started as a result of my past work experience as an Electronics Engineer in the USAF at Hanscom AFB. My research effort was in the developement of Platinum Silicide and Iridium Silicide devices to enhance infra-red Focal Plane Array capabilities. At present , I have been developing a test station for High Speed/ High Resolution Visible FPA's. My coursework has a solid foundation in optical detectors and radiometry.

Eglin AFB was interested in developing the same type of FPA's for their munitions testing requirements. The technology and process to develope these visible imagers will be instrumental in developing High Speed Sensor arrays for the IR spectrum as well.

OBJECTIVES OF THE RESEARCH EFFORT

It was the goal of both AFATL/AGI and us to establish some basis and foundation for the use of Solid State Sensor technology for munitions testing applications. This was to be accomplished by a theoretical analysis of what qualities a device must possess in order to meet the requirements of testing engineers. We also wanted to perform an analysis on the present systems capabilities for comparison purposes. The bulk of this report will address this issue. After the requirements for the system were determined, we wanted to do a feasibility study on the ability of present technology to meet these demands.

THE PRESENT SYSTEM

Munitions testing at present is done with in-flight wingtip cameras that have been accurately mapped prior to departure for calibration purposes. During a munitions test, the camera may be remotely activated and quickly runs up to speeds of around 200 frames per second to capture and detail target flight information. The film is then developed in a photolab under a standard processing procedure with special processing available if required. A contact or optical print of the original film is then made, where the original is stored for future reference. The contact print is then delivered to data capture engineers who perform the digitization of the data. By means of previous calibration, the data will give information about the position of the munition as a function of flight time as well as information related to the flight dynamics of the subject under test.

A controlled experiment was required in order to characterize the performance of the above described process. A Photosonics 1-PL high speed camera which is used in actual flight testing was used with a standard 10mm flight lens to image a calibrated CTF chart at a typical flight setting of f-stop 8. The camera incorporates a spinning wedge which with the film transfer rate determines the shutter speed.

$$\text{Shutter Speed} = \text{FPS} \times 360/\text{wedge angle(in degrees)} \qquad \text{eqn.1}$$

The calibrated CTF chart was imaged at various shutter speeds to chech the properties of the system as a function of exposure level. The film used, KODAK VNF, is standard for the majority of flight tests. The lighting on the chart was typical mid-day lighting conditions.

The film was processed by the photolab under standard procedures, and a contact print of the original was made with both available for analysis. This film was then digitized under the standard procedures.

The system used for digitization of the film is known as GADS and was developed by ERIM in Michigan. The unit consists of a VIDEK ccd imager whose pixels are digitized to 8 bits and stored in an image file. The

system then uses a complex software package which interacts with a analysis engineer to calibrate the data for future reference. The ERIM group is working on an more automated software package which will reduce the data using pixel morphology and image processing techniques. For our analysis, we will only require the imager information since the software can be used on any applicable data set. The sensor characteristics are given in Table 1.

TABLE 1

Resolution	1320 V x 1035H pixels
Pixel Pitch	6.8 microns square
Active area	8.98mm x 7.04mm
Fill Factor	100 %

In order to characterize the system performance, we use the CTF (Contrast Transfer Function) figure of merit. This gives the "visibility" of an object frequency pattern as imaged by the system. In the following, we develop three distinct functions: a theoretical function, a function based on individually measured values of components, and a function based on preliminary information from experimental data. The MTF(CTF) of a system can be determined by breaking the system into individual components and the system MTF(CTF) is given by the product of their individual functions.*

$$CTF(system) = CTF(1) * CTF(2) *... *CTF(n) \qquad \text{eqn. 2}$$

In order to determine the CTF of the system, the frequency in cycles per mm onto the film plane will be used as the reference for the entire analysis. The active film plane of the 1-PL camera in its largest dimension is approximately 10.5mm. This active film area is imaged onto the VIDEK ccd camera in 1180 pixels of 6.8 microns pitch. The remaining pixels of the imager are used for alignment purposes of the film plane. The active dimension of the Videk is then approximately 8mm. Hence the videk system modulates a frequency onto its focal plane of 10.5mm/8mm or 1.3 times the equivalent film plane frequency.

* note: assume that the CTF and MTF are approximately equal

THEORETICAL TRANSFER FUNCTION

There are four individual elements in the present system that contribute to the overall system CTF; the film lense L(film), the film plane F(vnf), the imager lens L(ccd), and the ccd focal plane F(ccd). Their theoretical CTF transfer functions can be approximated as follows.

L(film), L(ccd)	CTF=(1-lf/F#) (diffraction limited)	eqn 3.
F(vnf)	CTF=(1-f/f(cutoff))	eqn. 4
F(ccd)	CTF=(sin(3.14 fx)/(3.14 fx)	eqn. 5

F# = f-stop number of lens
f = spatial frequency (cyc/mm)
x = pixel pitch (dimension in mm)
l = wavelength (mm)

Using an approximate cutoff for the film at 100 cyc/mm and 200 cyc/mm, and F# of 8 (given as average by test engineers), and using an F# of 8 for the imager lens (what is used in general), we obtain using eqn 2. the following :

CTF(system) = (1-(5e-4*f/8))*(1-f/f(cutoff))*(1-(5e-4*1.3*f/8))*
(sin(3.14*f*1.3*6.8e-3)/(3.14*f*1.3*6.8e-3) eqn. 6

** a wavelength of 500 nm was assumed for average value**

A plot of the above function is given in figure 1.

A SEMI-THEORETICAL APPROACH

The next function uses data taken from various sources of the individual CTF of the system components. The film lens, L(vnf) will be assumed ideal since measured data could not be obtained. Values taken for the other CTF curves are given in table 2. A plot of the resultant system transfer function is given in figure 2. The data used for the film was taken from a Kodak specification sheet(1). The data for the Videk imager and the Nikkor 55mm/f 2.8 lens (used on the GADS system) was taken from an SPIE journal(2). We have ignored the magnification factor in this

analysis, so the data is somewhat better than we would get in the present system

TABLE 2

Frequency (cyc/mm)	VNF film	Videk ccd	Nikkor lens
0	1	1	1
10	.85	.98	.95
15	.60	.97	.88
20	.50	.96	.85
25	.37	.95	.81
30	.30	.92	.78
35	.25	.89	.75
40	.20	.85	.72
45	.17	.80	.70
50	.15	.75	.69
55	.13	.67	.68
60	.12	.62	.66

EXPERIMENTAL DATA

Calibrated data to perform a system wide CTF analysis was taken with a typical camera used for in-flight photography. The image data was processed under the standard methods and a digital image format was obtained. A sample of images is shown in Figures A and B. The film data was digitized using the GADS system shown in figure C. A line scan was done to obtain a histogram as a function of line number. From the histogram, a CTF function was tabulated using the following relationship(7):

$$CTF(system) = ((max\ value) - (min\ value))/((min\ ) + (max)) \qquad \text{eqn 7}$$

The data obtained from the screen is given in Appendix A. A plot of 4 random data sets is given in figure 3. It can be readily seen that the data is fairly consistent from image to image. Each of these data sets was from a different exposure of the film. The result is that the visibility of objects is independent of mean exposure level for underexposing of film by up to 3 stops. This is ideally suited for the mission requirements at present since

mean exposure level must be set on the ground prior to flight. Conditions of lighting on the aircraft are constantly changing during the flight. The above result helps alev iate problems that could otherwise have existed due to this variable.

THE PROPOSED SOLID STATE SENSOR SYSTEM

A proposal to use a solid state imaging sensor in place of a film camera for in-flight target imaging has been suggested. The proposed system would need to meet the abilities of the present system in order to be a viable alternative. The big advantage of the proposed system in terms of resolution is that only two components contribute to the CTF of the system. The imager would perform all the functions of the previous mentioned process.

A simple model to determine the expected resolution of the proposed system consists of a lens and a ccd imager. The CTF function for the Lens and Imager are given by eqns 3 and 5 respectively. We make use of eqn 2. to give:

$$CTF(system) = (1-l*f/8)*(\sin(3.14*f*x)/(3.14*f*x) \qquad \text{eqn 8}$$

In figure 4, the theoretical results for imagers with pixel pitch of 7.5, 10 and 15 microns are presented. We choose the F# of the lens to be 8 to allow fair comparison to our experimental data on the present system. At this time we introduce a reality of descrete sampling functions (eg. ccd arrays, analog to digital converters, CD players) known as aliasing. As in electronics, a discrete sampling function must sample an analog signal at twice the analog frequency in order to reproduce the signal accurately. Similarly, a ccd must sample the spatial frequency on its array in order to accurately reproduce the signal. We now propose that the limit of FPA resolution be that for which a frequency can be exactly reproduced. For a ccd array, this frequency corresponds to 1/2 of the first zero crossing frequency of the CTF function. The values of 33,50, and 66 cycles per mm are obtained for the 15, 10 and 7.5 micron pixel devices respectively. Also since actual CTF values do not drift from theoretical values until higher frequencies, eqn 8 yields good agreement with measured values for well behaved systems with diffraction limited optics.

To increase the accuracy of the predicted performance of our model, we take the values of measured CTF for the Nikkor lens in table 2 which will help account for the effects of aberrations that will be encountered in any real lens system. The new transfer function is plotted in figure 5

COMPARISON OF PRESENT AND PROPOSED SENSOR SYSTEM

By comparison of figures 3 and 5, one can see that the proposed system on a one to one comparison will outperform the present system in all formats (7.5,10 and 15 micron pixel pitch). To allow for worst case analysis, the 15 micron pitch will be used for the rest of this analysis.

Up until now, the analysis has dealt only with the spatial frequencies incident on the recording medium of the in-flight system. The analysis must now be moved to the domain of the objects spatial frequency in object space since that is what is important for the final product. For a given object space, we map this onto the size of the detector (the active area) surface as in figure 6. Since the proposed detector resolution is expected to be 1000 pixels in one dimension, with a 15 micron pixel, this will give 15 mm of active image area in one dimension. Since the film plane has an active dimension of only 10.5 mm, the equivalent frequency for a given object spatial frequency is as follows:

$$f(film)/f(ccd) = freq(obj) * x/xx \,/\, (freq(obj) * y/yy) \qquad \text{eqn 9}$$

Therfore the frequency ratio between the 16 mm film and the proposed sensor system is 1.4. We now give a criterion for the minimum acceptable CTF for useful imagery of 0.20. Using the experimental data shown in figure 3, an agreement of the four curves of approximately 17 cyc/mm as the 0.20 modulation point. The corresponding value of frequency for the ccd imager is 17 cyc/mm divided by the 1.4 factor which gives 12 cyc/mm. The proposed system would give a modulation of approximately 0.85 which is substaintailly better. Another way to approach the problem is to calculate the number of pixels required to equal the resolution of the present system. A value of 0.20 modulation from figure 5 gives a corresponding spatial frequency of 50 cyc/mm. Using equation 9. and substituting the appropriate frequencies, and solving for yy gives a value of 3.6 mm. Since we used a 15 micron pixel, this value corresponds to a resolution of 240 elements in one

dimension. We are assuming in the above calculations that a lens with the corresponding Field of View and format are available. This is a good assumption since the largest image field used thus far, 15 by 15 mm is smaller than a standard 35mm film lens format.

For the 1000 element system with the 15 pixel, the equivalent film plane aliasing frequency is at (33 x 1.4 = 46 cyc/mm) using the results of equation 9. The aliasing frequency of the present system with respect to the film plane is given by (73.5 / 1.3 = 56.6 cyc/mm). Therefore the present system could have an advantage as far as aliasing is concerned. At the frequencies we are considering, the modulation is so low that useful imagery cannot be achieved so the advantage is lost (see figure 4).

The obvious question that would arise from the above analysis is to increase the film size up from a 16mm format. This would indeed improve the resolution of the system for a given object frequency. The problem encountered deals with the mechanics of the high speed film cameras. A larger film size would require a higher inertia to get the film up to full speed in a reasonable time and the size of the camera would be increased. The ccd imager would also have to image a larger film plane so that some of the improvement would be negated by the increase in equivalent frequency of 1.3 to approximately 2.5 for a 35 mm film format. However, this does offer a possibility for improving the present systems capabilities.

Solid State sensors also incorporate a variety of features that allow a lot of flexibilty in use. One of these features is the variable electronic shutter. This is also incorporated into many home video camera systems availble today. By recalling equation 1, we see that the film camera is analogous to this in its operation. This feature could be used with a light sensor to establish a mean exposure level on the ccd to allow the system to adapt to changes in lighting conditions. This would guarantee quality imaging and it would no longer be a trial and error judgement as in the film case.

The other flexibility a Solid State sensor can offer is once the data has been captured and stored it can be transferred to the GADS system without the time of film processing or digitizing of the film data coming into the sequence. Therefore data analysis can be completed in much less time and Analysis Engineers will be able to decipher and correct design errors and perform flight safety tests in much shorter periods of time

For the final comparison, the film plane has an advantage. The long term storage of data for future use is done very compactly on a 16 mm reel of film. Almost 5000 pictures can be stored on a 5 inch diameter roll of film. An equivalent amount of digital data for the same roll of film with a 1k by 1k resolution assumed is 5 gigabytes for binary and 20 gigabytes for a standard file. This presents an intense demand on data storage technology. The propable solution is to use an optical data storage system.
Of course, advances in data storage capability should minimize this problem in the future. An advantage that digital storage could provide which standard film storage could not is instant access to data in seconds compared to searching film reel libraries.

FEASIBILITY OF SOLID STATE SENSOR SYSTEM

By analyzing the technology of today, can a solid state sensor system such as that described in the previous analysis be constructed? In analyzing the requirements for a 1000 by 1000 element, 15 micron pixel structure array running at frame rates of 200+ frames per second, the answer is that it can indeed be accomplished. Ford and Tektronik have both reported solid state arrays with 1 million plus pixels (3,4) . Ford has fabricated a 64 output device that has the potential of 1000 frame per second operation. These devices are being tested at the University of Arizona(6). A full analysis was conducted at Eglin AFB which showed that a sensor could be constructed to accomodate the requirements of munitions testing(5). The biggest problems facing the development of such a system proved to be power dissipation of the FPA, and the construction of adequate clock driver electronics. With these problems currently being dealt with, there should be advanced solid state sensors complementing the high speed film cameras in future munitions testing.

RECOMMENDATIONS:

1. To improve present system resolution, the major cause of CTF degredation should be found by future testing and replaced or dealt with appropriately. (A good place to start would be the lens used on the VIDEK imager since it was not specifically designed for the way in which it is being used) Film samples are available for microdensitometer scans which can predict the CTF performance up till the point of digitization.

2. Emphasis on determining the exact requirements of the Air Force munitions testing should be established so that a Solid State Sensor can be identified and designed to meet those needs.

3. Since the data for the experimental CTF function was obtained using an approximation method, the data should be revisited and an actual determination should be made for future reference.

4. The CTF data taken was done for the static case only. An experiment should be run on the present system for dynamic CTF and an analysis of the theoretical dynamic CTF for the proposed system should be established for comparison. (See reference 7 for further information)

APPENDIX A

(cyc/mm)	1	2	3	4	5	6
3.5	78	64	57	55	54	52
5.0	67	60	55	53	51	49
7.0	56	53	52	52	45	42
10	44	39	37	37	28	31
14	32	18	18	17	18	15
20	7	7	7	7	7	5
28	4	3	4	5	4	2
40	2	-	-	-	-	-

REFERENCES

1. KODAK EKTACHROME VIDEO NEWS FILM, 2239 ESTAR BASE EASTMAN KODAK COMPANY, 1981

2. MARTIN, WOMACK, and FISCHER, "A HIGH RESOLUTION CCD CAMERA FOR SCIENTIFIC AND INDUSTRIAL IMAGING APPLICATIONS", PROCEEDINGS OF SPIE, CURRENT DEVELOPMENTS IN OPTICAL ENGINEERING II, FISCHER, SMITH, AUGUST 1987, SAN DIEGO.

3. BREDTHAUER, "64 OUTPUT 1024X1024 PIXEL IMAGER FOR HIGH FRAME RATE APPLICATIONS, PROCEEDINGS OF SPIE, ULTRAHIGH SPEED AND HIGH SPEED PHOTOGRAPHY PHOTONICS AND VIDEOGRAPHY, AUGUST 1989.

4. BLOUKE, YANG, ET AL., "TEKTRONIK FOUR QUADRANT READOUT 1024X1024 CCD IMAGER: FINAL TEST RESULTS, PROCEEDINGS OF SPIE, 1071.

5. DERENIAK, "SOLID STATE SENSOR REPLACEMENTS FOR HIGH SPEED FILM CAMERAS", UES SUMMER REPORT.

6. DERENIAK, GRAEVE, OPTICAL SCIENCES CENTER, UNIVERSITY OF ARIZONA

7. FELTZ, KARIM, "MODULATION TRANSGER FUNCTION OF CHARGE COUPLED DEVICES", APPLIED OPTICS, VOL 29, NO. 5 10 FEBRUARY 1990.

FIGURE A

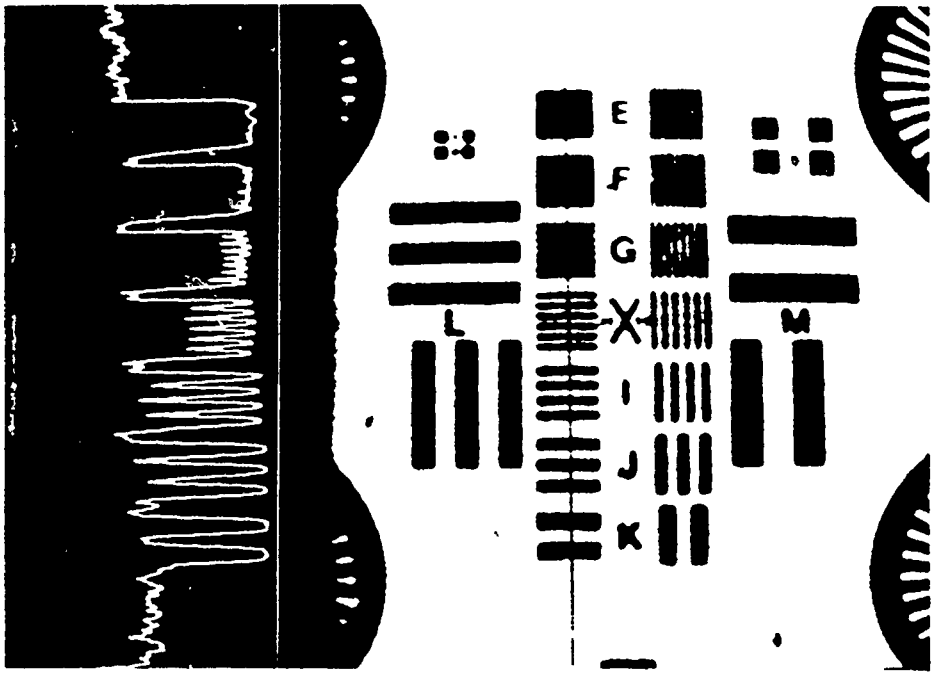

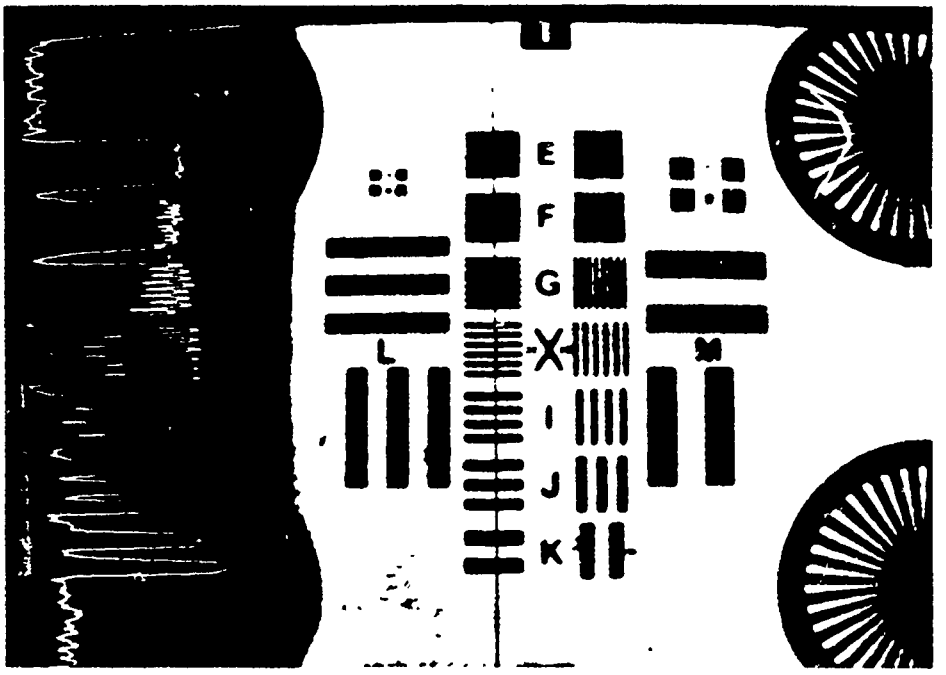

FIGURE B

FIGURE C

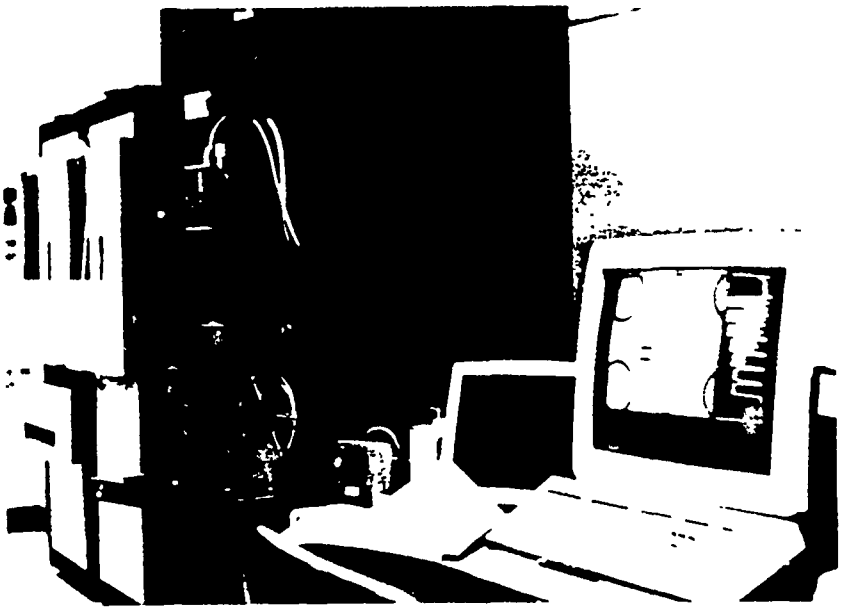

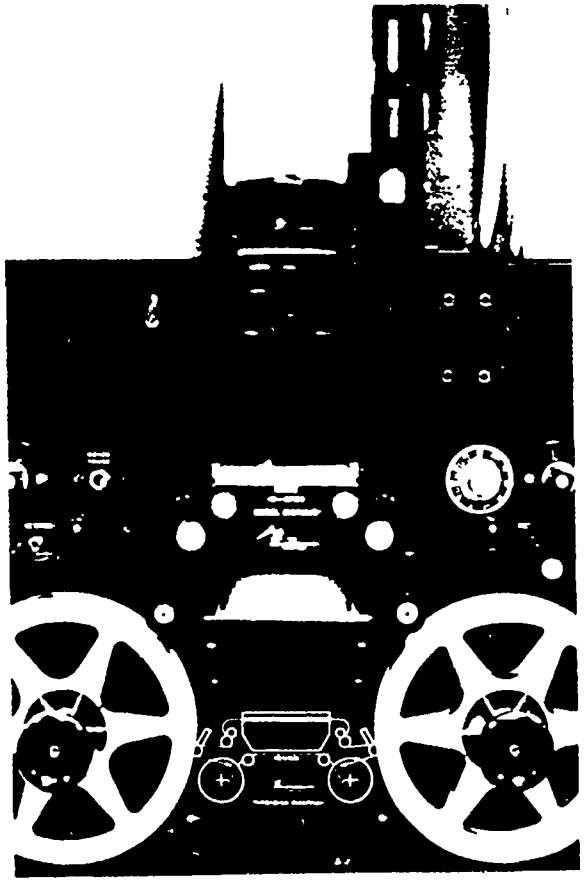

Figure 1

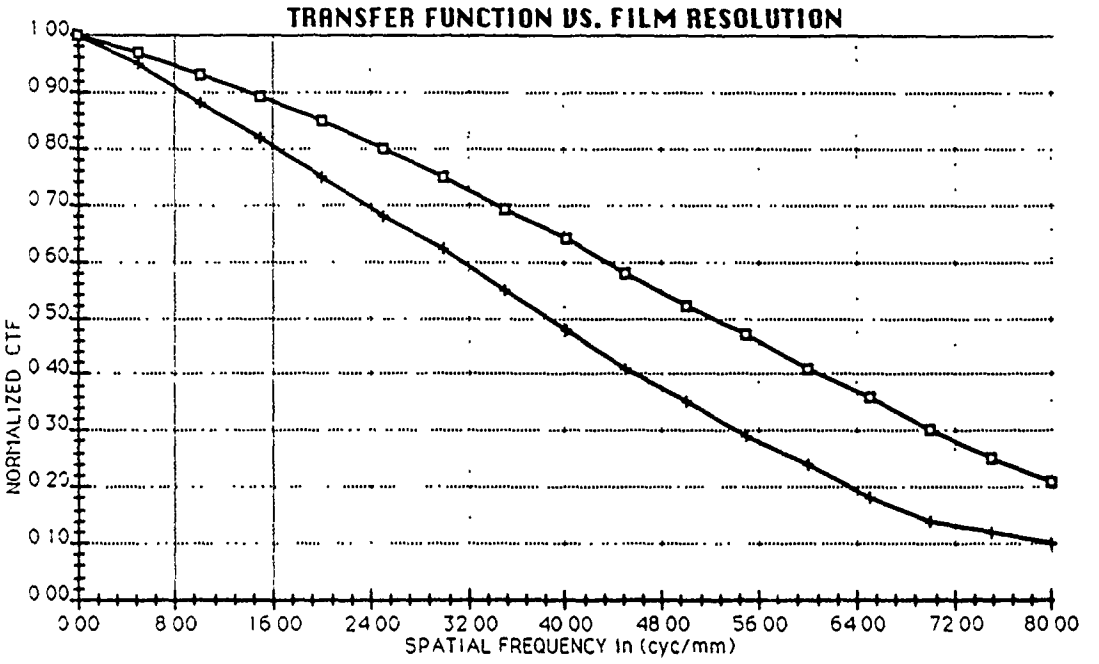

Figure 2

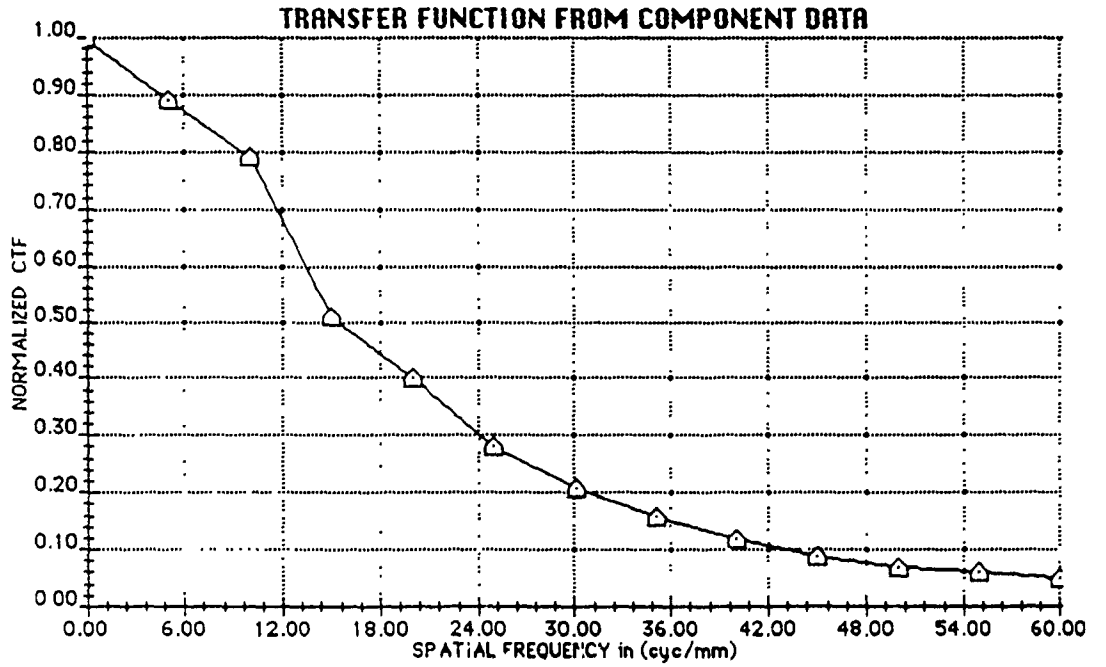

Figure 3

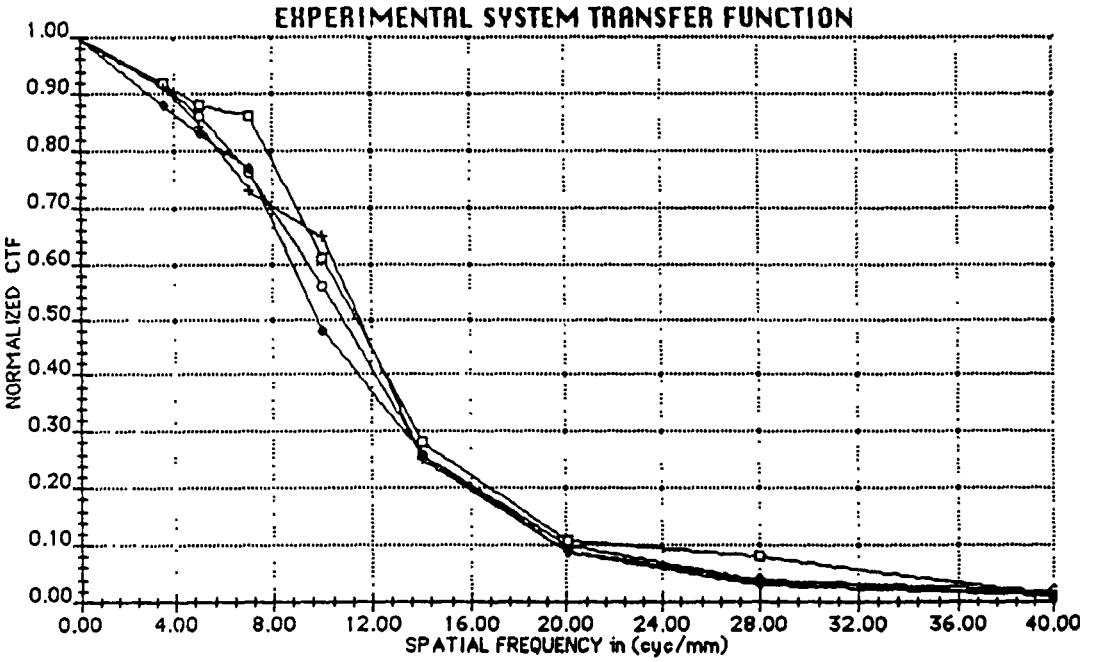

Figure 4

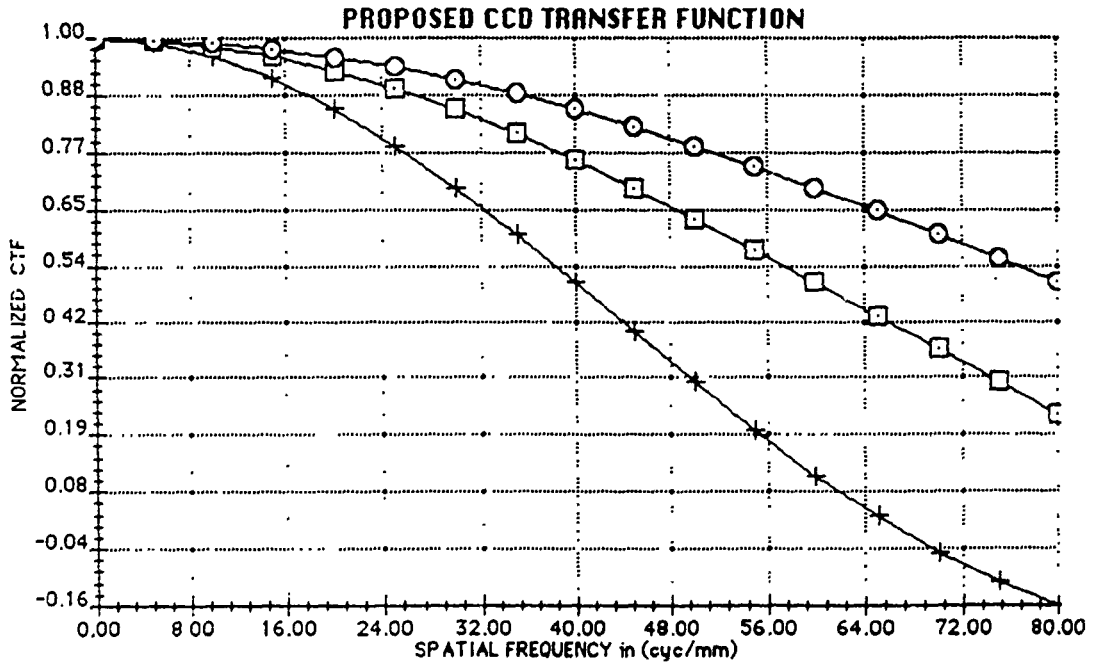

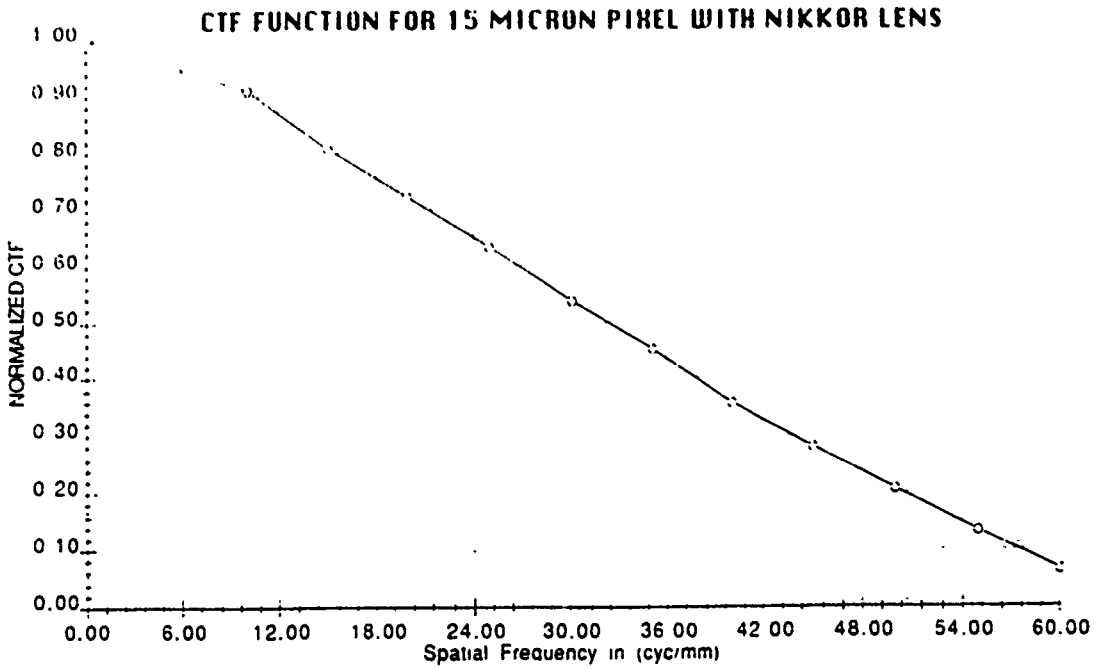

FIGURE 5

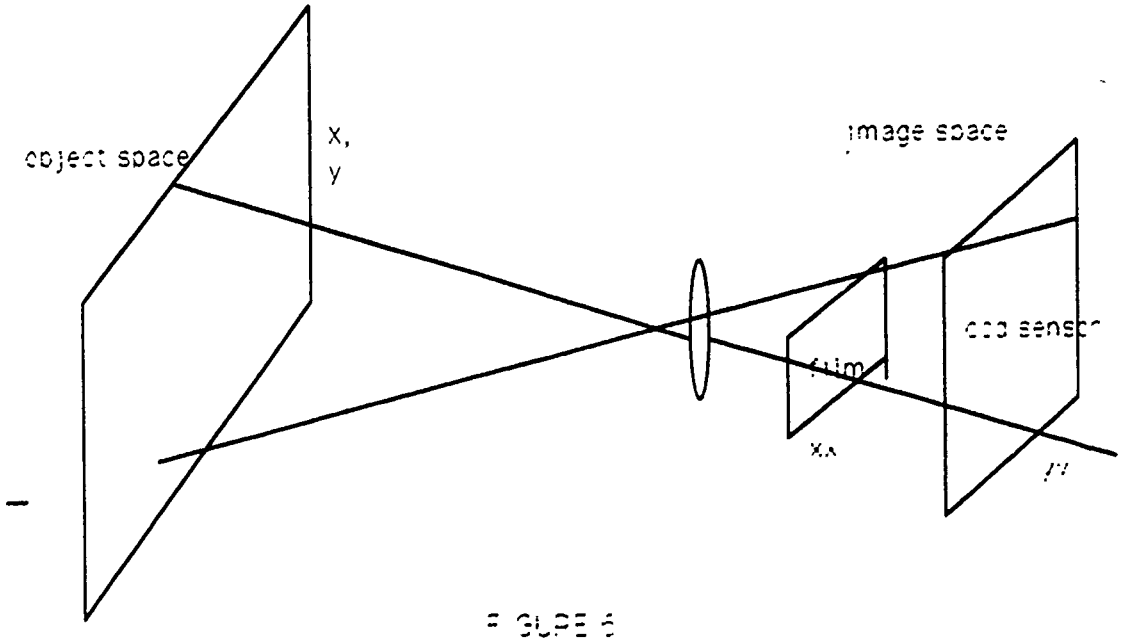

FIGURE 6

1990 USAF-UES SUMMER FACULTY RESEARCH PROGRAM

GRADUATE STUDENT RESEARCH PROGRAM

Sponsored by the

AIR FORCE OFFICE OF SCIENTIFIC RESEARCH

Conducted by the

Universal Energy Systems, Inc.

FINAL REPORT

Physical Aspects of the Penetration of Reinforced Concrete Slabs

Prepared by: A. Eugene Carden, Ph.D.
C. R. Wanstall, B.S.

Academic Rank: Professor and Graduate Student

Department: Engineering Mechanics

University: The University of Alabama

Research Location: USAF/AFATL/SAA
Eglin AFB FL 32542-5434

USAF Researcher: John Collins

Date: 13 July 1990

Contract Number: F49620-88-C-0053, Project #210

Same Report as
Prof. Eugene Carden
(Report # 2)

1990 USAF-UES SUMMER FACULTY RESEARCH PROGRAM/

GRADUATE STUDENT RESEARCH PROGRAM

sponsored by the

AIR FORCE OFFICE OF SCIENTIFIC RESEARCH

conducted by the

Universal Energy Systems, Inc.

FINAL REPORT

High-Speed Parallel Signal Processing

Prepared by:	Ben A. Abbott
	Ted A. Bapty
Academic Rank:	Graduate Student
Department:	Department of Electrical Engineering
University:	Vanderbilt University
Research Location:	AEDC/DOTR
USAF Researcher:	Lt. Greg Nordstrom
Date:	8-10-90
Contract No:	F49620-88-C-0053

High-Speed Parallel Signal Processing

by

Ben Abbott
Ted Bapty

ABSTRACT

Turbine Engine testing generates massive volumes of data at very high rates. Complete storage of all acquired data, if possible, would require unobtainable system capacity. Data must be processed on-line, at the speed of acquisition. This extraction of information effectively compresses the data.

In addition to data compression, on-line processing of these signals is critical to the testing process. The results from the on-line computations must be available to enable mid-test decisions, interactive test planning and catastrophe avoidance.

The reduction of data by extraction of information from these signals requires high-computation algorithms. Performing these computations and displaying the results in an interactive format requires an extremely high processing rate. An aggregate sustained computation rate in the GFLOPS range is necessary to meet requirements.

The high computational requirements and natural parallelism make parallel processing a cost-effective hardware approach. A transputer-based, heterogeneous parallel processing system has been designed to meet the system goals. A software methodology has been developed to ease the programming tasks and to increase the flexibility of application software.

Acknowledgements

We wish to thank the Air Force Systems Command and the Air Force Office of Scientific Research for sponsorship of this research. Universal Energy Systems must also be commended for their concern and help to us in all administrative and directional aspects of this program. Our experience was rewarding and enriching because of many different influences. Lt. Greg Nordstrom provided us with support, encouragement, and a truly enjoyable working atmosphere. The help Tom Tibbals was invaluable in overcoming many technical roadblocks. Jason Scott of the High School program did a terrific job. Finally, we would like to thank Carlos Tirres for all his help in insuring that our experiences at AEDC would be memorable.

I. INTRODUCTION:

When testing turbine engines, an engine is installed in a test cell to simulate a wide variety of conditions. To analyze the dynamic vibrations, stress sensors are placed on the turbine fan blades. A typical stress test instruments the engine with several hundred of these stress sensors along with a variety of temperature. pressure, flow and revolution per minute sensors(Figure 1). Stress sensors can generate signals with bandwidths in the tens of kilohertz.

Turbine Engine testing generates massive volumes of data at very high rates. A single engine may have several thousand sensors, with bandwidths up to tens of kilohertz. Test periods last for several hours. Complete storage of all acquired data, if possible, would require system capacity in the tera-byte range. This approach is prohibitive in terms of cost and technology. These limits mandate the reduction of data on-line, at the speed of acquisition. The reduction of data by extraction of information from these signals requires high-computation algorithms. This extraction of information effectively compresses the data.

In addition to data compression, on-line processing of these signals is critical to the testing process. The results from the on-line computations must be available to enable mid-test decisions, interactive test planning. The on-line examination of information can assist in catastrophe avoidance, by enabling the detection of pathological engine conditions.

In order to convey the results of the data reduction. a high-speed display device is required. Adequate resolution is needed to display the multitude of sensors. Updates must occur smoothly, to avoid operator fatigue. and to minimize the chance of missing a physical engine event.

Performing these computations and displaying the results in an interactive format requires an extremely high processing rate. Typical algorithms include frequency transformation. peak detection and validation and correlation. The majority of algorithms are applied independently to each of the channels. An aggregate sustained computation rate in the GFLOPS range is necessary to meet requirements.

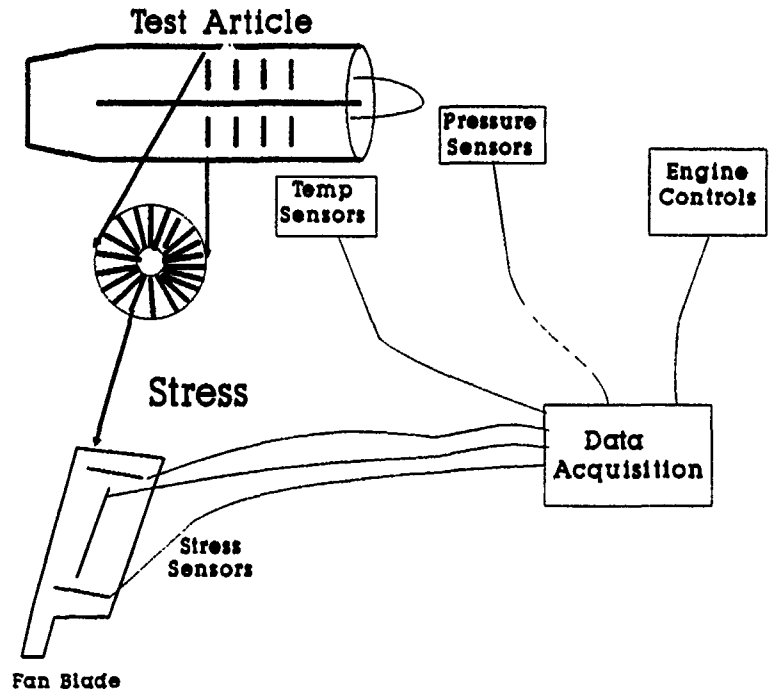

Figure 1: Turbine Engine Instrumentation

The aggregate data input is in the tens of MWords per second.

The high computational requirements and natural parallelism make parallel processing a cost-effective hardware approach. To achieve the multi-GFLOPS goal, a large number of processors must be applied. The distributed memory Transputer architecture matches these requirements. The bare Transputer however, lacks the computational capabilities required. At 2 MFLOPS (Peak) execution speed, over 1000 processors are needed to achieve the 2 GFLOPS requirement. The intermediate storage of results exceed the reasonable capacity for semiconductor memory. Also, the bare transputer has no graphics output capability.

Project History

Under previous AEDC effort, a transputer-based, prototype heterogeneous parallel processing system has been designed to meet the system goals. While the full scale system has not yet been implemented, all processor modules are functional:

1. **The Numeric Processing Element** uses a **T800** and a **Zoran floating point Vector Signal Processor** [6] to supply the bulk of the computational horsepower.

2. **The Graphics Processing Element** incorporates a **Texas Instruments TMS34010** [5] with a dual-page frame buffer. This processing element performs quick, smooth display of dynamic signals.

3. **The Storage Processing Element** uses a DMA-equipped **SCSI** interface to store large quantities of information.

4. **The I/O Processing Element** provides a variety of RS233, Centronics, IEEE-488 and configurable digital parallel I/O lines.

A Transputer is used in conjunction with each of the processing nodes. It provides the general message passing and control fabric of the system. A typical application of these processors to on-line test data processing requires a mix of approximately 100 processors. Figure 2 shows a typical full-scale system. The prototype consists of a handful of processing elements of each type.

Summer Research Focus

The state-of-the-art in software development for large scale parallel processing is still quite primitive. Programming this system with standard, mono-processor software technologies is labor-intensive and error-prone.

In an effort to confront these software development difficulties, Vanderbilt researchers have developed the Multigraph Kernel (MGK) [1]. The MGK provides a

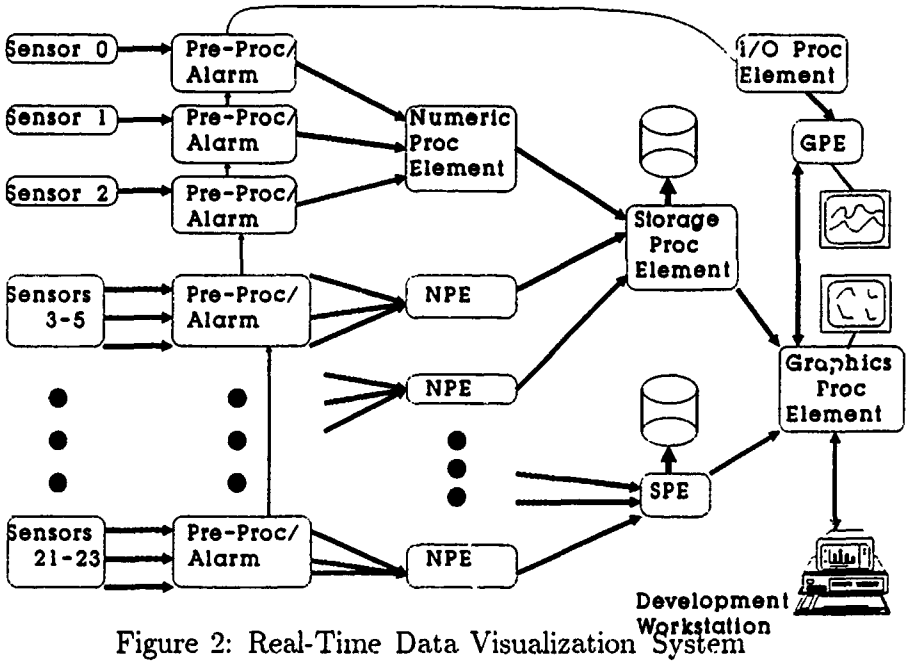

Figure 2: Real-Time Data Visualization System

generic execution environment for parallel programs built by various tools comprising the Multigraph Programming Environment (MPE). This environment provides an extremely high level of programmer interface. The user normally works with interactive graphical languages allowing him to concentrate on declaring a system model rather than program functions and control flow. These high level tools subsequently map the user's model of the required system into a parallel graph computation to be executed under the MGK. The MGK hides the underlying parallel hardware structure by providing a virtual machine, the Multigraph Virtual Machine (MVM).

The summer research focussed on the AEDC/CADDMAS specific use of Multigraph Programming Environment.

II. OBJECTIVES OF THE RESEARCH EFFORT:

At the beginning of the summer term, the basic research objectives were stated as:

- Develop a methodology to ease the programming difficulty of the large-scale, heterogeneous-element parallel processing system of the CADDMAS project.
- The environment should allow dynamic reconfiguration of processing algorithms and displays.
- Apply these concepts to the development of a demonstration system for the CADDMAS hardware.

Along with these objectives, a framework of the approach to be taken was sketched out as follows:

1. Develop a conceptual model for the development of large-scale, interactive, parallel signal processing systems. The model should have characteristics that enable on-line reconfiguration of algorithms to meet changing user requirements.
2. Analyze the target application, a high-speed, high-bandwidth, many-channel real-time data analysis system for on-line analysis of turbine engine test data. Apply the parallel processing model to this system.
3. Develop software to implement a demonstration system. This software should execute on the AEDC-developed parallel processor.

Before the demonstration system could be built, each of the basic processing elements needed a set of run-time library routines to be generated.

This paper continues as follows:

1. The required run-time libraries generated are described: **Numeric Processing Element** and **Graphics Processing Element**.

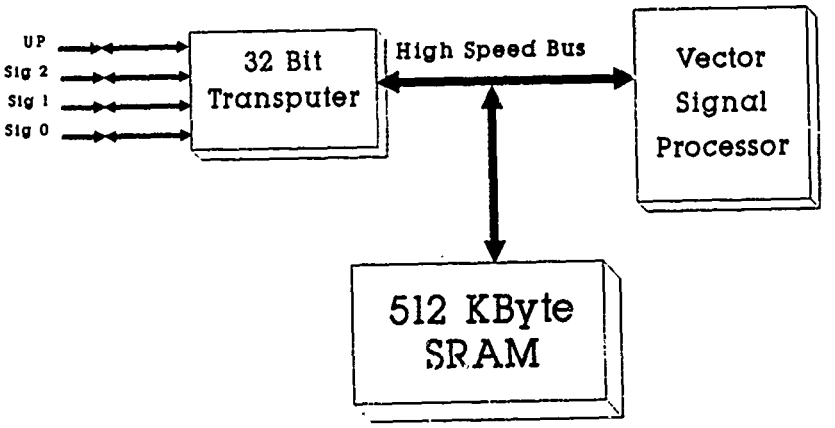

Figure 3: Numeric Processing Element Block Diagram

2. The conceptual model for the development of large-scale, interactive, parallel signal processing systems is described in terms of the software environment mandated.

3. Recommendations for further work are given.

III. NUMERIC PROCESSING ELEMENT:

The Numeric Processing Element uses a 20 MHz T800 for communications and control (see figure 3). The Transputer has access to 512K Bytes of static memory. The Zoran Vector Signal Processor can also be a bus master to allow access to this memory.

The VSP is modeled after an array processor architecture. The VSP has 512 bytes of high speed internal memory. An internal i/o processor transfers data in and out of the internal memory. The execution unit is decoupled from the external bus, to allow concurrent processing with the host T800. The internal RAM memory of the VSP can be divided into two sections to allow overlap of numeric processing and data movement. This internal memory can contain 64 complex vector elements, or

128 real values. In addition, a coefficient look table contains sine and cosine tables for use by VSP instructions.

The VSP fetches and executes its program independently from the Transputer. The VSP program is loaded into the shared memory. Program execution is initiated by the Transputer. Execution commences with the VSP fetching data from the shared memory, processing the data, and returning results to the shared memory. While the VSP is executing its programs, the Transputer is free to continue its processing. The Transputer is preempted when bus activity is required by the VSP. This mechanism is implemented using the Transputer MemRequest/MemGranted interface. Memory bus arbitration overhead is minimized by prefetch FIFO's on instruction and data fetches. With the VSP executing algorithms such as the FFT, approximately 40% of the bus bandwidth is available to the Transputer.

The VSP implements IEEE standard 32 bit floating point. Its instruction set includes high-level routines that support common signal processing tasks. Vector addition multiplication, polynomial expansion, min/max, accumulate, int to FP, and FP to int are single instructions. There are also instructions that implement FIR and IIR filtering. Frequency transformation primitives (DFT and FFT butterfly) are also single instructions. The internal sine/cosine tables support 1024 point FFT' with no external twiddle factors.

The primary goal of the software interface between the Transputer and the VSP is to keep the VSP busy. Since the VSP is an order of magnitude faster for arithmetic operations, the greatest throughput is achieved with maximum VSP execution. Refer to table 1 for execution benchmarks.

The device driver implements a queuing mechanism. Low priority tasks send requests to the high priority driver. If the VSP is currently busy, the request is entered into the queue. When the VSP program completes, the Transputer is signalled via the Event interface. The device driver can then begin execution with the next request in the queue. Using the channel interface allows the device driver to lay dormant until service is requested or the VSP becomes free(i.e. OCCAM ALT). Although not legal in OCCAM, the machine language allows a single channel to

TABLE 1

NUMERIC PROCESSING ELEMENT BENCHMARKS

Algorithm	Execution Time
1024 point Real FFT	2.25 msec
1024 point Complex FFT	2.35 msec
128 point Complex FFT	0.55 msec
Complex Mag(per output)	1.9 usec
Division (per output)	0.9 usec
Natural Log(per output)	2.1 usec
T800-20/LSC 1024 Complex FFT	100.5 msec

service several processes.

A single channel is used as the input to the queue mechanism of the VSP. Since the queue handling process runs in a high priority state the queuing requests will always be handled before another request can be submitted. The driver is in one of three states: 1) waiting for a request or VSP-Complete event(i.e. OCCAM ALT); 2) responding to an event, and starting a new vsp execution; or 3) placing a VSP request in the queue. Since the driver is a high priority task, and the clients are low priority, there clearly cannot be any requests submitted while the driver is in states 2 or 3 because a high priority task cannot be preempted by a low priority task. If the driver is ALT'ing on the event and the incoming channel, then immediately after receiving a enqueue request, the process enters state 3, in which case the driver is the only process executing, disallowing any more requests from the low priority clients.

IV. GRAPHICS PROCESSING ELEMENT:

Online data processing places stiff demands on the system's graphics processing capabilities. While no graphics device can keep up with all of the data processed,

the GPE must provide a low-latency display with smooth updates. If an operator must concentrate on the display for several hours, there should be a minimum of flicker. In addition, the display must support a resolution capable of showing several graphs concurrently. Color must be available to highlight objects and to enable data overlays.

The Graphics Processing Element(GPE) provides a high performance, high resolution, color display interface. This processor receives processed information from a multitude of sensors and integrates the data into a dynamic display. System users need high resolution graphics to display data from the large number of sensors. The engineers need high-speed rendering to display dynamically changing information with an operator perception of continuous time (approximately 10 updates/sec). This device integrates information from several clusters of Numeric Processing Elements.

The GPE is a dual-CPU computer. with high bandwidth communication, high-speed general purpose computation, and high-speed, high resolution color graphics. Aggregate input bandwidth is the T800's 6 4M bytes/sec. Aggregate general purpose computation rates are 16 MIPS and 2.5 MFLOPS(peak). The peak line drawing rate of the 34010 is 1.2 million pixels per second. The graphics resolution is 1024x768 with 16 simultaneous colors. The GPE implements dual frame buffers to reduce flicker (See figure 4).

The Graphics System Processor is a general purpose processor with graphics extensions. The GSP controls two local busses, and is a slave device on the Transputer bus . All busses are decoupled. allowing full speed operation of all devices. The GSP Bus handles the graphics processor's program and working data. The serial video bus transfers high speed data at the 65 MHz necessary to refresh the display.

The GSP has 256K Bytes of DRAM for program and data storage functions. There is enough video memory (768I bytes) for dual frame buffers. With the double buffering technique, all drawing can occur in the invisible screen. Only completely

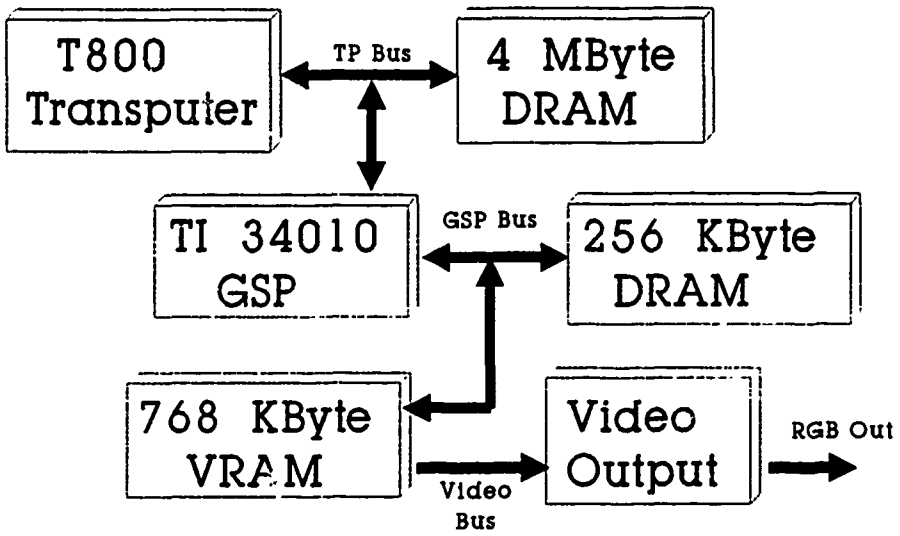

Figure 4: Graphics Processing Element Block Diagram

drawn images are visible on the display. This reduces the flicker caused by repeated clearing and redrawing of the graphics screen.

The GSP supplies the video timing. The video logic converts the digital pixel value information into an analog Red-Green-Blue(RGB) signal for display on a CRT monitor.

The Transputer interfaces to the GSP via the host interface port on the 34010. This interface provides a method for reading and writing directly into the GSP address space. Transputer accesses to GSP memory are transparent to the software operating on the 34010. The GSP cannot access Transputer memory. It is a slave to the T800, that operates asynchronous from the transputer.

The software on the TI34010 processor implements a display list processor. Buffers passed from the T800 contain commands and data to be plotted. Dual buffers allow the T800 to be loading a buffer while the GSP is interpreting the previous list. Buffers are marked with a status. to determine when the memory is free.

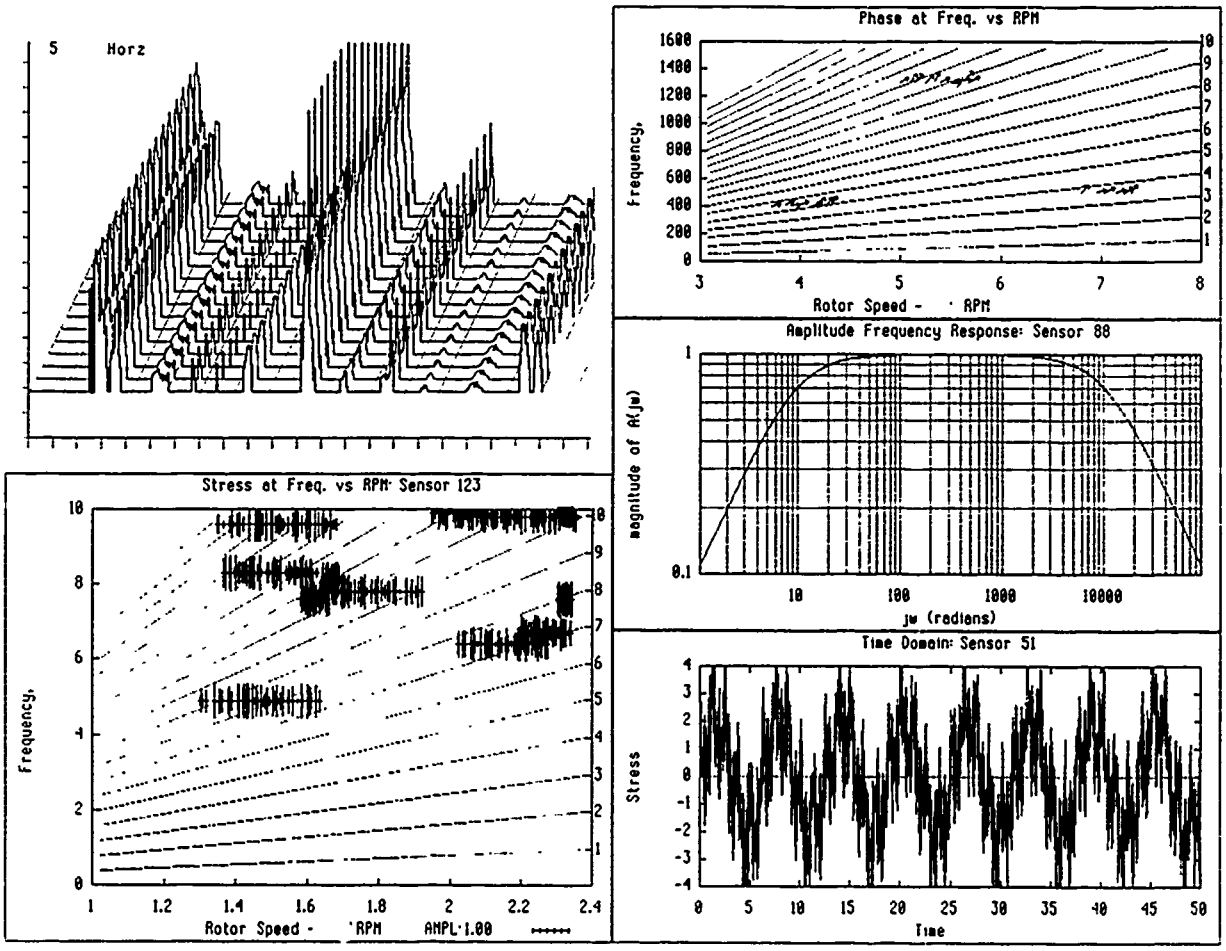

Figure 5: Typical Graphics Display

The display list processor supports low level operations such as point, line, box, and text operations. It also implements higher level functions such as axis and grid drawing. There are functions for line, bar, and waterfall plots. The high level functions are implemented to reduce communication time. The display list processor supports non-overlapping, tiled windows. Drawing operations are clipped outside the currently selected window.

A library for the transputer implements the display list generation and communication. This library insulates the programmer from the complexities of the TS00-TI34010 hardware/software interface. Since the GSP has no hardware sup-

port for floating point, scaling, if necessary, is done on the T800 or at the data source in a distributed fashion.

In addition to the display list generation library, GNUPLOT from the Free Software Foundation, has been ported to the GPE. The GNU software runs on the T800, with a special TI34010 device interface to translate plot calls to display list commands. Figure 5 contains an example system display. This plotting package offers a simple, fast, device-independent method of data presentation.

By using GNUPLOT, we gain the advantages of data portability. Post-processing and output generation can be accomplished at the engineer's personal computer in an environment similar to the on-line system. That is, after a test, an engineer can take a copy of a certain section of the test data he is interested in back to his personal computer and view it using a PC or Workstation version of GNUPLOT.

The GNUPLOT program was modified to allow several additional functions that AEDC test engineers need:

- Multiple window support for the CADDMAS GPE.
- Subroutines to plot campbell and phase campbell diagrams were added. These are plots with frequency on the y-axis, rotor speed on the x-axis, and stress on the z-axis. The z-axis is represented as vertical lines with varying amplitudes on the graph. In a phase campbell there is phase data instead of stress data. In a phase campbell the phase data is represented with a arrow tip pointing in the relative direction of the phase.
- Engine order line options were provided for the campbell plots.
- A campbell label which includes a scale for engineers to measure the data, a label for the scale, and the scale value that the graph is drawn to were also added.

All additions were developed in the spirit of GNUPLOT's original ability in that they allow auto-scaling, device independent display, etc. The campbell routines

were written in a general fashion so as to allow the identical routine to perform a modified campbell plot. That is, the x-axis may actually have any data (e.g. temperature) the engineer desires.

V. SOFTWARE ENVIRONMENT:

While hardware can and has been constructed to meet these requirements,the software engineering can be very difficult and expensive. The problem is compounded by the requirement for in situ algorithm reconfiguration. Handling the large number of possible configurations can be an enormous task. With thousands of inputs, and multiple algorithms to execute, there is a combinatorial explosion of possible configurations. The static configuration of all necessary computation configurations is impossible.

Further, the interactive environment requires the capability to reconfigure the signal processing algorithms on-line. While most analysis methods are known before testing, events occurring during the test can change the analysis requirements. Engineers must have the flexibility to change and/or add new processing methods to the signal processing system. The system must adapt dynamically to these changing requirements. The adaptation is required to enable engineers to examine changing phenomena with flexible analysis methods. This adaptation must occur in-situ, without affecting other ongoing computations.

A structured environment can ease the development for these large scale. dynamic parallel processing systems. We have developed a system modeled after the familiar laboratory bench. This system. which we call the Probes Environment. is constructed from three basic types of objects: Signals. Probes. and Displays.

Signals are data sources. They can be interfaces to sensors, function generators. or signal simulators. Minimal preprocessing of the signals is assumed. Signals are always producers of information. and are never consumers.

Displays are the outputs of the system. They can be windows in a graphics display. ports to hard copy devices. or other physical output devices. Displays are always consumers of information.

Probes make up the bulk of the system. Probes connect to producers of informa-

tion, perform some user-specified computation, and produce an output signal. The probe can perform any algorithm, including storage of the signal. The outputs of the probe can handle any user-supported data format (e.g. integer, float, complex, array).

Probes are defined graphically using the Hierarchical Description Language developed at Vanderbilt University [4]. These probes are constructed by connecting primitive computational elements, termed Primitive Actors, together in a hierarchical structure to produce a computational structure. These Primitives are implemented in a standard programming language (C,Fortran,Ada,...) with a small amount of code to interface to the Multigraph kernel. Since the probe is built from small, independent modules, it can be a parallel structure in itself. The internal complexity of the probe is hidden from the end user.

The probe is designed in an object-oriented manner. The probe object contains information about processing algorithms, supported data types, required resources, processor assignment hints, initialization requirements, etc. The object's information can be used for automated processor placement. The probe object also knows how to install an instance of itself on the target architecture.

Signal processing systems are constructed by connecting the various types of objects in an arbitrary structure. Type checking is performed on connections to assure a consumer can support its producer's format. A resource manager is charged with constructing the processing structures.

The resource manager is a generic program that supports many different types of Signals, Probes, and Displays. As new applications are developed, new probes and displays will be added. Consequently, the Resource Manager should be generic enough to handle any type of probe without modification. The approach chosen here is to contain the probe-specific information inside the probe. The resource manager need not know about the internal structures of a probe. The probe is able to install itself, carrying out any required initialization, modify itself, or remove itself. Initialization parameters are acquired by the installation procedures of the particular probe. The resource manager handles the inter-object connection. The

system continues operation while structures are being added.

The user interface allows the user to install and connect probes and displays in the signal processing system. The user interface can be a graphical display, in which the user sees representations of the available signals, displays, and probes. New signal flows are built by installing probes and displays, and connecting between them in the desired order, and installing the signal flow. This interface can also take the form of a text-based menu interface.

The on-line reconfiguration of the Probes Environment assumes the ability to interactively install programs on a specific processor and the ability to connect data channels across arbitrary networks of transputers. The Multigraph Kernel provides these services [2].

The Probes Environment is currently under development and will continue under the CADDMAS/Vanderbilt consulting funds. A C-based prototype version is partially coded. However, it is expected that the final version will be a C++ implementation due to the object-oriented nature of the Probes and the user interface required.

VI. RECOMMENDATIONS:

In summary, engine testing applications require extremely demanding computational resources. The structure of these applications is well suited to parallel architectures. The need for dynamic reconfiguration of algorithms complicates matters beyond the usual issues in parallel program development. The probes based approach described in this paper works well in this environment. The user interface is quite natural since it closely matches the laboratory environment familiar to the test engineers.

Further work needs to address the following issues:

- First and foremost, the CADDMAS hardware must be proven. The run time libraries generated during the summer work should be put together such that real engine data may processed. This will prove the hardware and the salability of the system. The probes interface should be simulated during this work

to keep future compatibility and yet speed progress.

- A graphical user interface to the Probes environment has been described. It needs to be implemented. The work of the HDL [4] can be used as a starting point.

- Due to the Probes based user interface, feasibility investigation is needed to see if a C++ type of graphics environment (e.g. MIT's InterViews) would be useful. It is beneficial to have this work on a variety of platforms including the GPE.

- Future modifications needed for the GNUPLOT functions include:

  - Integration with the MGK dataflow to allow high performance plot data input.
  - Integration with the application system user interface.
  - Multiple window display for PC and workstation versions.
  - 3-D extensions for surface plots.

- Future tests for the CADDMAS hardware need to be planned.

- Load balancing, performance monitoring, and debugging tools are needed to approach the optimum utilization of the CADDMAS hardware. This research should be accomplished within the framework of the Probes environment so as to use the knowledge of the problem at hand when making decisions about processor placement or information flow.

- Issues of dynamic processor/sensor replacement and management should be investigated due to the large number of sensor failures in real aero-mechanical tests.

References

[1] Biegl, C.: "Design and Implementation of an Execution Environment for Knowledge-Based Systems" Ph.D. thesis, Department of Electrical Engineering, Vanderbilt University, Nashville, TN., Dec., 1988.

[2] Abbott, B., Biegl, C., Sztipanovits, J.: "Multigraph for the Transputer", Proceedings of the Third Conference of The North American Transputer Users Group, Santa Clara, Calif., April 1990.

[3] INMOS Limited: Transputer Reference Manual, 1989.

[4] Karsai, G.: "Hierarchical Description Language (HDL) User's Manual" Dept. of Electrical Engineering, Vanderbilt University, Technical Report #87-004, 1987.

[5] Texas Instruments Incorporated: **TMS34010 User's Guide.**

[6] Zoran Corporation: **ZR34345 32-Bit IEEE Floating-Point Vector Signal Processor User's Manual.**

1990 USAF-UES SUMMER FACULTY RESEARCH PROGRAM/

GRADUATE STUDENT RESEARCH PROGRAM

sponsored by the

AIR FORCE OFFICE OF SCIENTIFIC RESEARCH

conducted by the

Universal Energy Systems, Inc.

FINAL REPORT

High-Speed Parallel Signal Processing

Prepared by:	Ben A. Abbott
	Ted A. Bapty
Academic Rank:	Graduate Student
Department:	Department of Electrical Engineering
University:	Vanderbilt University
Research Location:	AEDC/DOTR
USAF Researcher:	Lt. Greg Nordstrom
Date:	8-10-90
Contract No:	F49620-88-C-0053

Same Report as
Ben Abbott
(GSRP)
(Report # 6)

1990 USAF-UES SUMMER FACULTY RESEARCH PROGRAM

GRADUATE STUDENT RESEARCH PROGRAM

Sponsored by the

AIR FORCE OFFICE OF SCIENTIFIC RESEARCH

Conducted by the

Universal Energy Systems, Inc.

FINAL REPORT

Graphics for Turbine Math Models

Prepared by:	Ronald J. Blume
Academic Rank:	Graduate Student
Department and	Aerospace Engineering
University:	University of Tennessee Space Institute
Research Location:	AEDC/DOT Arnold AFB Tullahoma, TN., 37388
USAF Researcher:	Dr. Milton Davis
Date:	16 July 1990
Contract No:	F49620-88-C-0053

Graphics for Turbine Engine Models

by

Ronald J. Blume

ABSTRACT

Turbine engine math modeling often requires visual representation in order to detect data trends. This plotting program was designed to be incorporated in an existing graphics package. It is modular and capable of running independently when interfaced with a program written by the user. This program uses PLOT88 subroutines which can be used on personal computers.

The program allows for multiple: plots, plots per column, curves and colors, axis labels and titles and ledgers with text and color coded symbols. Presently, the program is capable of multiple surface plots per page.

Acknowledgements

I wish to thank the Air Force Systems Command and the Air Force Office of Scientific Research for sponsorship of the research. Administrative aspects of this program where undertaken by Universal Energy Systems.

Special thanks goes to Dr. Milt Davis and Alan Hale of Sverdrup,AEDC. Dr. Davis was instumental in choosing me for this project. Mr. Hale dedicated much of his precious time giving me the technical and programming support and mental attitude needed for this assignment.

I. INTRODUCTION:

Engineers use graphical output to analyze problems and to compare trends. Often they need plotting capabilities tailored to the job being performed or a program which may embody the plotting package.

A plotting program, ATDAPT was developed by Alan Hale at AEDC. It is capable of drawing X-Y, Surface and Contour plots. There is a need to run ATDAPT on personal computers for the purpose of portability and if main frames are not available. ATDAPT was written using subroutines from a commercial graphing package called DISSPLA. DISSPLA is expensive and too large for personal computers. Therefore, an alternative package of subroutines must be used to replace DISSPLA.

II. OBJECTIVES OF THE RESEARCH EFFORT:

First, I investigated alternative packages to DISSPLA. Only two packages, GraphicC and PLOT88, were explored. The program was written to be modular and stand alone and easily embodied into the ATDAPT program. Because of the program's structure it is possible to provide a host of possible future applications.

Iil. APPROACH

a.) The approach was to develop a plotting program using subroutines which are commercially available in plotting packages. The ATDAPT program used DISSPLA subroutines. DISSPLA is a commercial packages which resides in the Center's main frames, but could not be used on a work station due to its large memory. Therefore, two alternate packages were investigated, GraphicC and Plot 88. GraphicC is written in C language while ATDAPT is in FORTRAN. In the past when GraphicC was used with other programs written in FORTRAN, great difficulties were encountered, and I was advised not to try to make the two languages compatible with one another. To ensure modularity subroutines were called through argument lists only and subroutines communicate through common statements.

b.) PLOT88 like ATDAPT was written in FORTRAN and after researching PLOT88's abilities it was decided that it was capable of replacing DISSPLA.

IV. RESULTS

a.) Work was done in two areas, X-Y and Surface plot capabilities. The MAIN subroutine was written only to emulate the portions of ATDAPT which would later drive my subroutines with the added ability to test all the options in mind.

To insure that the program is user friendly a menu of commonly used variables appears in a default menu with their values. Within DEFMENU another subroutine DEFCHANG is called. The subroutine GRAPHIT creates the plots. The last subroutine called in Main is GRAPHLEG. This subroutine creates ledgers which appear on every plot. I did not start the surface plotting effort until the end of the research period. Therefore, to speed development, a separate program was created using a loop structure similar to the X-Y approach.

b.) It was assumed at the onset that the Main subroutine would be supplied by the user for their own specific purposes. To achieve this multi-purpose generality the program was written to be modular (stand alone). This was achieved by calling the subroutines from Main through argument lists only. Inter-communication of variables between subroutines was accomplished by the use of common statements which, by definition, make default variables common to all subroutines which contain the common statement (see box 1 and 2 figure 1).

The subroutine which generates the menu is named DEFMENU and also prompts the user to change any of its thirty four values by typing the variables corresponding number followed by its new value. DEFCHANG allows for the default changes to be placed into memory without the need to recompile the current values (as shown in figure 2).

GRAPHIT allows for multiple: plots per columns; curves and colors, and axis labels; and page titles. Within GRAPHIT the area of the page is defined and broken down into plotting windows in which and X and Y axis will occupy. This is how automatic

scaling is performed. Next, GRAPHIT, knowing the number of plots, columns and plots per column, calculates the window position where the plot is to reside. The axis, axis numbering, labeling, and plotting of the curves with symbols are performed for one plot at a time (see figure 3).

GRAPHLEG is totally independent of GRAPHIT and can be called before or after GRAPHIT. If ledgers are not wanted, the call may be omitted. GRAPHLEG creates a box at the lower right hand corner of the plot, which contain symbols corresponding to each curve. To the right of every ledger is a description of the plot curve. An interesting feature of the ledger is that it is scaled in both directions by changing default values or if the height or width of the box exceeds axis length, the box is scaled in both directions and its contents shrunk automatically (See figure 4).

The Surface plot program (see figure 5) includes multiple: plots, plots per column and multiple surfaces. The user can change menu values for rotation and elevation angle to view plots at any perspective. Due to lack of time, axis, axis labeling and numbering, and contouring were not developed.

V. RECOMMENDATIONS

In the future a new manual and automatic scaling and axis drawing subroutine should be written allowing for numbers to be placed at increments other than one inch. The X-Y, Surface and contouring plots need to be developed fully and integrated into an executable library to avoid frequent compiling.

REFERENCES

Young T.L. and Van Woert M.L., Plot 88 - Software Library Reference Manual, Plotworks Inc., 1989.

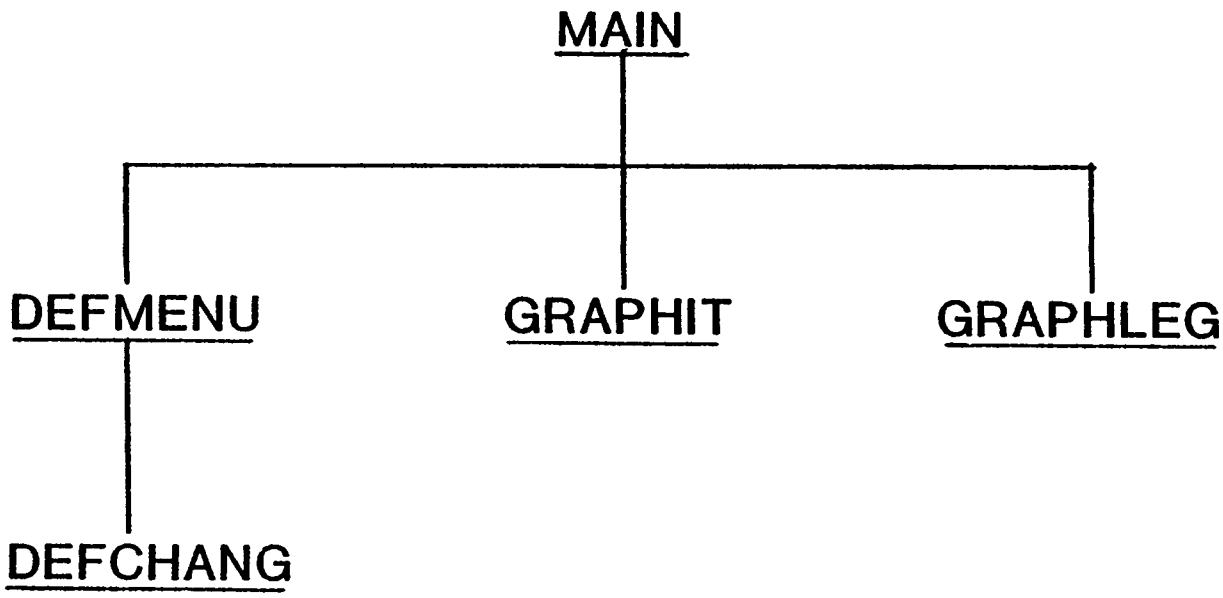

Fig 1. SUBROUTINE STRUCTURE

```
********************************* DEFAULT MENU ***********************************
*   1 - XPGSIZE   ( 9.9)      2 - YPGSIZE    ( 7.7)     3 - TOP SPACE  (1.00) *
*   4 - PLOT MAR. ( .90)      5 - RT. MAR.   ( .50)     6 - LT. MAR.   (1.00) *
*   7 - BOTT. MAR ( .20)      8 - CENTER MAR (1.00)     9 - STRING     (   9) *
*  10 - LAB STRING(   6)     11 - PEN UP,DN  (   2)    12 - NUM HEIGHT ( .20) *
*  13 - LABEL HGT ( .20)     14 - EXPONT HGT ( .12)    15 - X HEADER   ( 3.5) *
*  16 - Y HEADER  ( 7.0)     17 - HEADER HGT (  .3)    18 - WINDOW PEN (   1) *
*  19 - HEADER PEN(   3)     20 - AXIS PEN   (   1)    21 - CURVE PEN  (   1) *
*  22 - SMB SPACE ( .10)     23 - SMB HEIGHT ( .20)    24 - HGT/SPACE  ( .50) *
*  25 - DECIMAL   (   2)     26 - TERMINAL IO(  97)    27 - TERM. MODEL(  97) *
*  28 - PRINTER IO(   0)     29 - PRNT MODEL (  60)    30 - OUTPUT     (   1) *
*  31 - LINE TYPE (   1)     32 - LINE HGT   ( .10)    33 - SMB ANGLE  (  0.) *
*  34 - SMB DNSTY (   1)                                                      *
**********************************************************************************

TO CHANGE INPUT : NUMBER,VARIABLE -- / TO TERMINATE
```

Fig 2. DEFAULT MENU

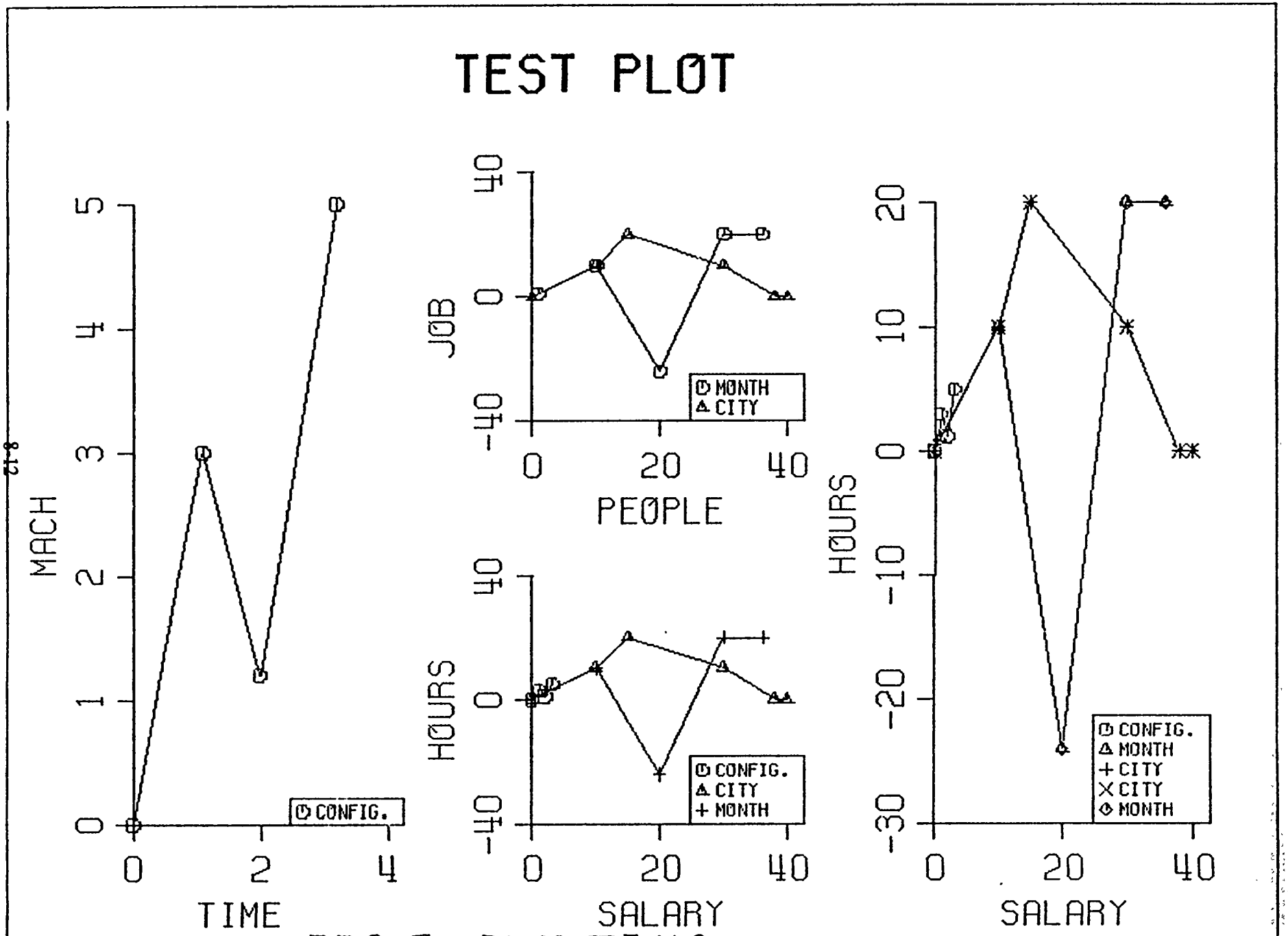

FIG. 3. PLOTTING

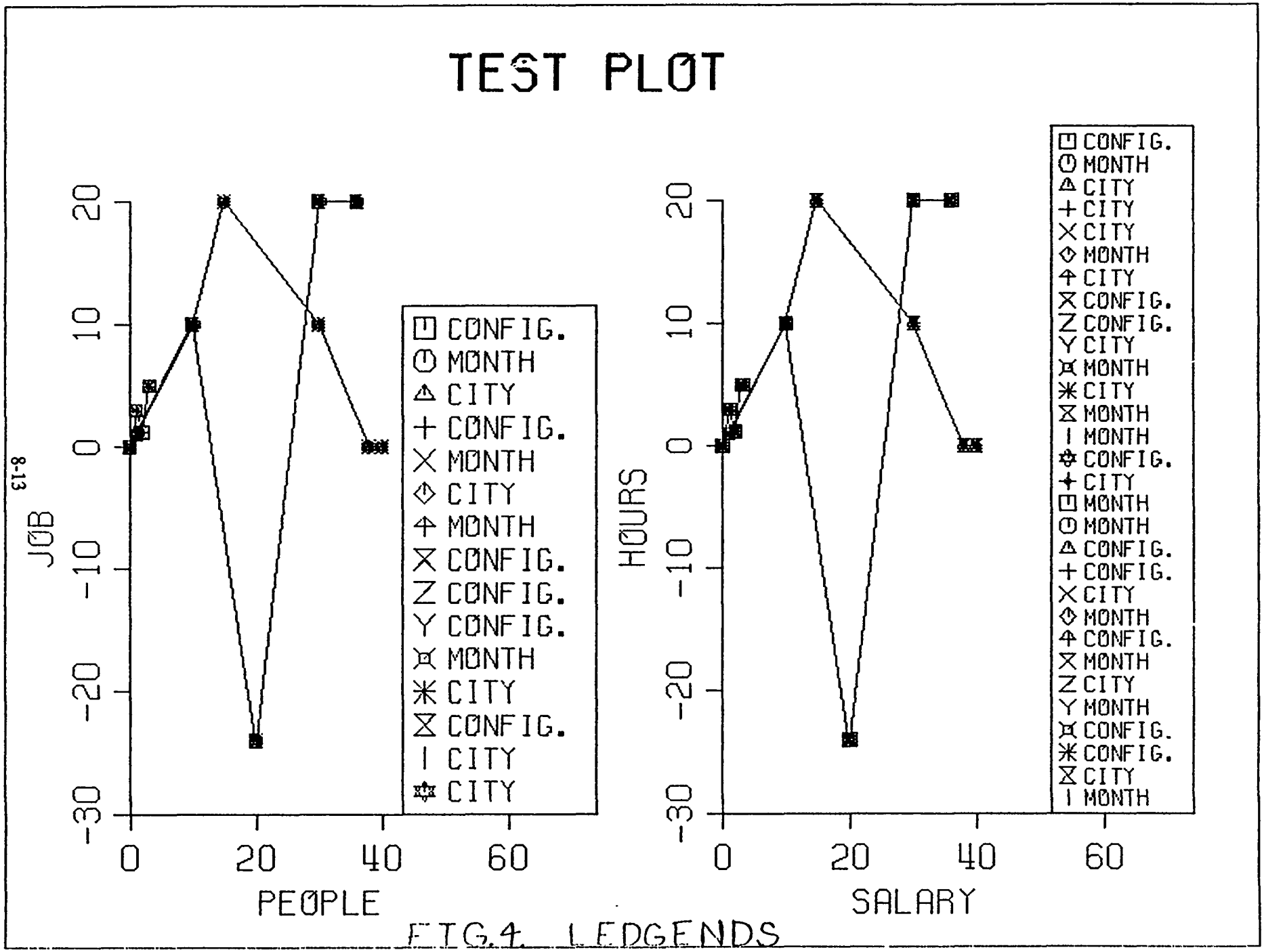

FIG.4 LEDGENDS

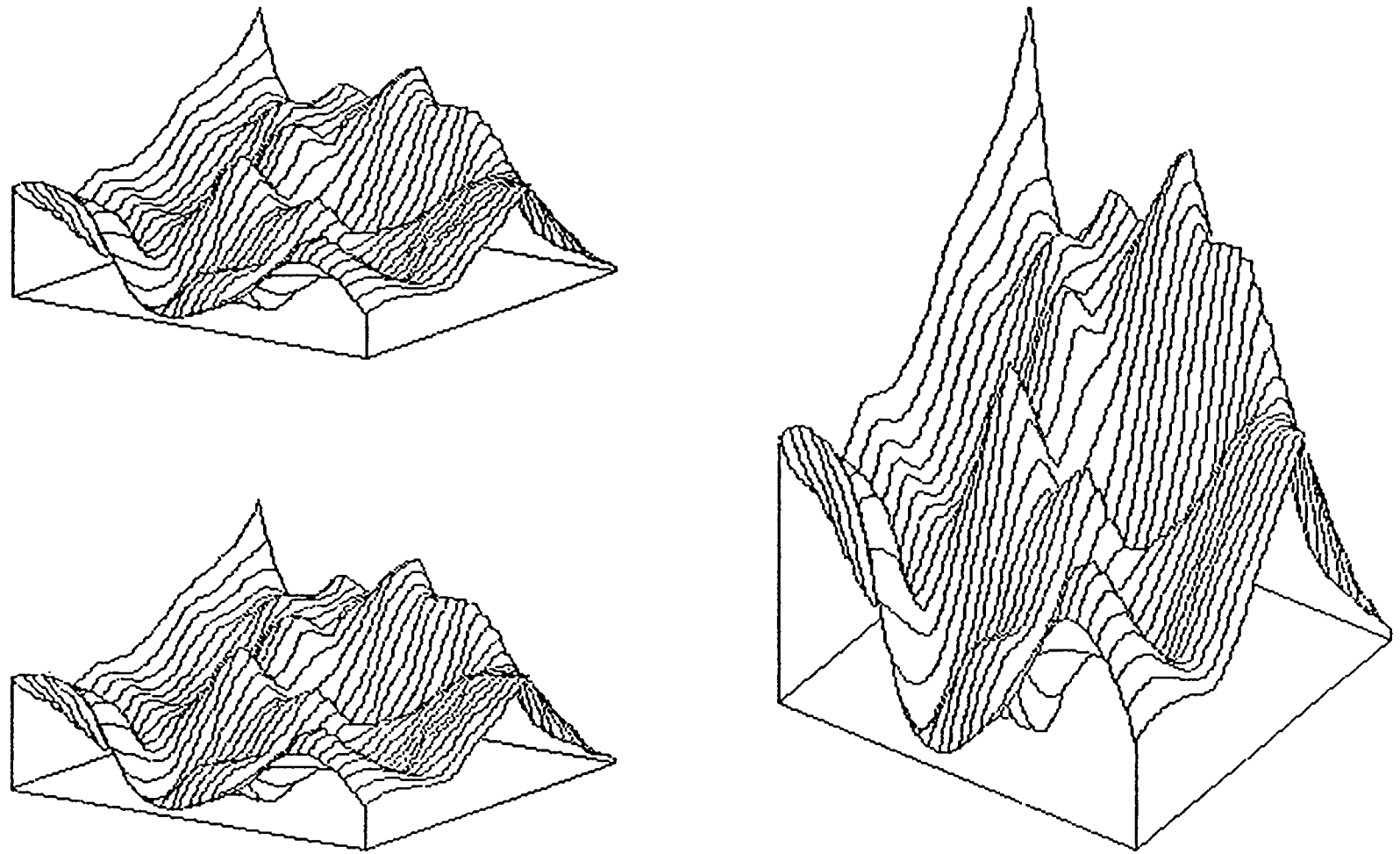

Fig. 5 SURFACE PLOTS

1990 USAF-UES SUMMER FACULTY RESEARCH PROGRAM
GRADUATE STUDENT RESEARCH PROGRAM

Sponsored by the
AIR FORCE OFFICE OF SCIENTIFIC RESEARCH
Conducted by the
Universal Energy Systems, Inc.

FINAL REPORT

s90 Graphing System

Prepared by:	Jordan Cahn
Academic Rank:	Masters Candidate
Department and University:	Applied Mathematics Department, University of Tennessee Space Institute
Research Location:	Calspan Corporation/AEDC Operations, Arnold Air Force Base, TN 37389
USAF Researcher:	Peter Hoffman
Date:	20 September 1990
Contract No:	F49620-88-C-0053

s90 Graphing System

by

Jordan Cahn

Abstract

The Graphing System s90 is used to draw two or three dimensional graphs of theoretical or experimental data. The code was written in the C language to run on a Unix operating system. s90 calls the Unix library plot to execute screen commands. Telnet facilities enable hard copy printing of the graphs. s90 features dynamic allocation of data arrays and a separate parameter file for quick changes in graph appearance.

Acknowledgements

I wish to thank Air Force Systems Command for sponsoring my research through the kind auspices of the Air Force Office of Scientific Research and the Arnold Engineering Development Center. Also, thanks go to to Universal Energy Systems for their effective management of the summer research program.

I would like to express my utmost appreciation for aid and guidance given to me by Peter Hoffman, Jack Benek and Peggy Palmer of Calspan, and Allen Buck of OAO. Further, the help of Fred Shope, Bill Thomson, Rob Tramel and Theresa Cates was invaluable.

Finally, I would like to thank Dr. K. C. Reddy of UTSI for helping me get into the program and Carlos Tirres for all his aid since I've been at AEDC.

I. Introduction

Currently, The Arnold Engineering Development Center is in the process of switching their computers to Unix based operating systems. There are reservations among the staff about this decision. Some researchers are worried that many of the programs and facilities they need will not be available in the new Unix environment.

Calspan's CFD department is obviously very dependent on the base computers to accomplish their aims. The head of the department decided it was necessary to show that switching to Unix systems was feasible and to begin the process.

I received my Bachelors Degree in Aerospace Engineering and I am currently working on a Masters in Applied Math. With this background I was familiar with the tools and goals of Computational Fluid Dynamics. Further, I had programmed in FORTRAN and C languages. Since I had never worked with a Unix operating system, my experience in adapting to it would give the department some idea of what to expect. We decided that a graphing system that works in a Unix environment would be a useful and feasible facility for me to create.

II. Objectives of the Research Effort

The objective of my summer research was the production of a computer program to create graphs. An inflexible qualification of this objective was to write the program for Unix based operating systems. The department requirements for the system were that it display two or three dimensional graphs, that the data file format be easily produced and that the user didn't need to count the number of data points. Further, it was requested that the program not be menu driven. My goal was to be able to produce graphs that were of high enough quality and format to place in reports and papers.

III. s90 Graphing System

Overview

s90 is a graphics program designed to run on mainframe computers. The mainframe must have a Unix operating system and support a C compiler, C libraries and Tektronics 4014 emulation. s90 will take a suitably formatted data file and plot it on a terminal screen.

Telnet is equipped to write the display off the screen as a postscript file, which can be printed upon a laser printer. The graphics system was written for an ULTRIX operating system on a Microvax computer.

s90 needs three parts to run: s90.c - the source code, p.c - the parameter file, and d.dat the data file. The data file must be assembled by the user to the correct format and be named "d.cat." The parameter file tells the program all the particulars of the display. This parameter file will be either p2.c or p3.c, (for two and three dimensional graphs respectively) or an alteration of one of these, renamed as p.c. The source code s90.c should not need changing except when running on other computers.

Datafile

The data must be formatted but the format is rather loose. The numbers may be integer, floating point, or exponential. They may be either positive or negative. The numbers must be separated by a space. They may be separated by more than one space. They may be on separate lines. The numbers may be followed by a comma, but this is not necessary.

The data will be read as sets of numbers defining a point, X value then Y value then, if 3-D, Z value. This will repeat until the end of the file. Data must be edited before moving the file to "d.dat."

To display data as separate lines, line end flags must be entered. To do this insert in the data after the last point of the line a point which is all LINEND values, two or three #'s depending on dimensions. I have set LINEND equal to -111, but it is available to change in the parameter file. It is necessary to put line end flags after the last point in the data file.

The finished datafile "d.dat" should have no header, title, or other entries except the data and line end values.

Parameter File

The parameter file contains choices for the style of display and some simple processing of data. It is a separate file from the source code. When the source code is executed the parameter file will be appended to the program. The file the source code appends is called "p.c." Therefore, the parameter file "p.c." must be named before executing the program.

I have provided two files, "p2.c" and "p3.c," which contain my preferred output style for two and three dimensions. The easiest way to use the system is to, as I have, maintain two parameter files and before running s90 rename the proper file "p.c." After seeing the resulting graph, fine tune it to best present the data by changing the values in "p.c." and running s90.

Source Code

The source code is called s90.c. It first appends the parameter file. Then it reads in the data file. It continues by putting the grid and axes on the screen. Then it graphs the data. Finally it labels the axes.

Execution

To run the system, after having written data file "d.dat" and parameter file "p.c," type s90. The source code will compile, the terminal will shift to graphics mode, and the graph will be drawn on the screen.

Printing The Graph

After the exact graph is displayed on the terminal screen, the screen display may be written as a Post Script file. To do this press ALT-G. This is a Telnet function that returns a graphics menu. Press F-1 to write the screen to file "ps.out." Telnet will write the file on the hard disk of the terminal. While it is writing the hard disk and Telnet are not available. Once it has written on the hard disk, use FTP to transfer the file to a computer that is connected to a laser printer. Print the file from that computer. Note that complicated graphs may take a while to print out. A graph with 10,000 points takes approximately 5 minutes to write and 15 minutes to print.

Exiting s90

After displaying the graph and possibly writing a Post Script file, type any character and then the RETURN button. This will recall the UNIX environment. If the terminal is still in graphics mode press the HOME button.

Running S90 - condensed version

1) Name a suitably formatted data file "d.dat"
2) Name a parameter file "p.c."
3) Type "s90" and hit RETURN button
4) Wait until graph appears
5) To print graph, hit ALT-G then F-1
6) Send "ps.out" to a laser printer
7) Type any character and RETURN to exit

IV. Recommendations

a. To run s90 in an Unix operating system it is necessary to have the math library and the plot library with Tektronics 4014 emulation. It should be ascertained that both these pieces of software are included with any new Unix operating system.

b. An investigation should be made into the possibility of sending graphs from the program directly to a printer, bypassing the screen and the terminal hard disk.

c. A short presentation should be developed to inform the researchers of the useful features of Unix operating systems and of the Telnet.

REFERENCES

McGilton, H., Morgan, R., Introducing the Unix System, New York, New York, McGraw-Hill Book Company, 1983.

National Center for Supercomputing Applications, NCSA Telnet for the PC, U. of Illinois at Urban-Champaign, NCSA Documentation and Publications Department, July 1988.

Plauger, P. J., Brodie, J., Standard C, Redmond, Washington, Microsoft Press, 1989.

1990 USAF-UES SUMMER FACULTY RESEARCH PROGRAM

GRADUATE STUDENT RESEARCH PROGRAM

Sponsored by the

AIR FORCE OFFICE OF SCIENTIFIC RESEARCH

Conducted by the

Universal Energy Systems, Inc.

FINAL REPORT

A Neural Network for the Analysis of Test Data from the Aeropropulsion Systems Test Facility

Prepared:	James B. Golden, III
Academic Rank:	Graduate Student
Department and	Computer Science
University:	University of Tennessee Space Institute
Research Location:	AEDC Arnold Engineering Development Center Arnold Air Force Base, TN 37389
USAF Researcher:	Art Mantone
Date:	10 August 1990
Cont-act No.:	F49620-88-C-0053

A Neural Network for the Analysis of Test Data from the Aeropropulsion Systems Test Facility

by

James B. Golden III

ABSTRACT

With the advent of the USAF's Advanced Tactical Fighter and NASA's National Aerospace Plane, demands for concise test data reduction and interpretation will increase beyond the capabilities of current methodologies. As mission complexity increases it becomes apparent that real time data analysis for flight safety, mission control and test conduct becomes a necessary tool.

A neural network is a biologically inspired mathematical model, which can be represented by a directed graph, that has the ability to learn through training. Neural networks have many advantages over current aviation computing systems including the ability to learn and generalize from their environment. The results of this research show that a neural network can be used for fault diagnosis in an engine test cell when the problem of fault monitoring and diagnosis is seen as one of pattern recognition.

ACKNOWLEDGEMENTS

I wish to thank the Air Force Systems Command and the Air Force Office of Scientific Research for sponsorship of this research. Universal Energy Systems must be mentioned for their concern and help to me in all administrative and directional aspects of this program. I would like to thank Carlos Tirres for all his help in assisting me with this fellowship. I am indebted to Dr. Virgil Smith and Art Mantone of Sverdrup Technology for all their assistance in data collection and a free flow of ideas. I owe a debt of gratitude to Dr. Bruce Whitehead who exhibited both patience and enthusiasm throughout the course of this research.

It must be noted that parts of this report are extracts from my masters thesis 'A Neural Network for the Analysis of Test Data from the Aeropropulsion Systems Test Facility', copyright 1990.

CHAPTER I

INTRODUCTION

(1.1) Problem Statement

Simulated flight tests conducted in the Aeropropulsion Systems Test Facility (ASTF) produce large quantities of sensor data at rates that overwhelm flight test personnel. The task of monitoring signals from test cell sensors and watching for the onset of possible fault situations requires significant experience and a number of test cell personnel. Because of the variety and quantity of test cell data, extensive knowledge and experience is required for accurate differentiation of data types. A neural network architecture that could accurately diagnose the onset of fault situations and alert test cell engineers would result in a significant savings in personnel, downtime because of damaged equipment, and improve test cell safety.

(1.2) Approach

The main approach of this research is to design and analyze a network architecture to monitor sensor data from the ASTF to detect data that falls outside learned parameters, thus signifying a fault. In this research, diagnostic problems in general are conceptualized as a mapping of an input pattern (representing sensor data) to an output pattern which is interpretable as a diagnosis.

A neural network is a biologically inspired mathematical model, which can be represented by a directed graph, that has the ability to learn through training. The action of a neural net may be viewed principally as a mapping through which points in the input space are transformed into corresponding points in the output

space on the basis of designated attribute values (of which class membership might be one) (Pao,1989). It is the goal of this research to design a neural network architecture that can classify ASTF test data as part of a nominal engine test or as data from a system in failure. The words neural network, network, net, and network model will be used interchangeably throughout this thesis.

Three major subsystems that make up the ASTF instrumentation and control systems are the Plant Instrumentation and Control System (PICS), Test Instrumentation System (TIS), and the Automatic Test Control System (ATCS). The ATCS provides facility and engine status monitoring for the detection of unsafe operating conditions having a potential for causing damage to the engine or the test facility (Polce, 1982). Currently, many engineers are needed to monitor data output from the ATCS to check for abnormal operating conditions during a test.

The ATCS is used to control test conditions inside the test cell, control of engine operating conditions, and the detection of abnormal plant and engine operating conditions. Because these tend to be problems in parameter estimation and the detection of events outside expected parameters, the ATCS was chosen as the initial test bed for the network.

CHAPTER II

PROBLEM ANALYSIS

(2.1) The ASTF Domain

The Aeropropulsion Systems Test Facility is designed for testing airbreathing engine propulsion systems over a wide range of altitudes and Mach numbers. Simulated flight tests conducted in the facility will determine the operational and performance characteristics of aeropropulsion systems; thus, the time required for flight tests is shortened, and the risks and expense of flight tests are minimized (Polce, 1982).

The ASTF was designed to permit development and surveillance tests of large airbreathing, jet propulsion engines throughout their operational envelopes by providing the capability for true simulation of flight altitude and flight Mach number conditions. The facility is capable of performing direct-connect testing of turbojet and high-bypass (8:1) turbofan engines up to 75,000 pound-rated, sea level, static thrust throughout the appropriate engine operating envelopes (Polce, 1982). The facility is designed to allow testing in both direct-connect and freejet modes.

In Polce's (1982) thesis he describes different types of tests that will be conducted in the ASTF. These test types require the capability of transient testing, e.g., engine power transients, flight profile transients, or combinations of the two. The facility operating conditions and the corresponding engine operating conditions for testing in the ASTF are:

(1) Steady Environment — Steady Engine Power Setting.

(2) Steady Environment — Transient Engine Power Setting.

(3) Transient Environment — Steady Engine Power Setting.

(4) Transient Environment — Transient Engine Power Setting (Mission Profile Simulation) (Polce, 1982).

Looking at the testing requirements that the ASTF must perform, it becomes obvious that systems within the test cell must be able to alter both pressures and temperatures, along with a number of valve openings, to regulate test cell conditions. As the system increases in complexity, it becomes an overwhelming task to supervise all the sensors that monitor the facility. Instrumentation and data handling equipment must be provided to measure, transmit, acquire, display, and process those measurements which are required to determine the performance of the test article. The measurement capability for each test cell includes 970 pressure measurements, 820 temperature measurements, and 152 miscellaneous measurements, such as forces, flows, speeds, geometries, vibrations, accelerations, and strains (Polce, 1982).

As stated in (1.2), three major subsystems make up the ASTF instrumentation and control system. They are the Plant Instrumentation and Control System (PICS), The Test Instrumentation System (TIS) and the Automatic Test Control System (ATCS) [see Figure 1].

The ATCS performs a number of control functions inside the test cell. The ATCS is used to:

(1) Control test conditions.

(2) Control engine operating conditions.

(3) Coordinate control of test and engine operating conditions with plant configuration changes.

(4) Detect abnormal plant and engine operating conditions and their response thereto.

(5) Communicate with facility operators (Polce, 1982).

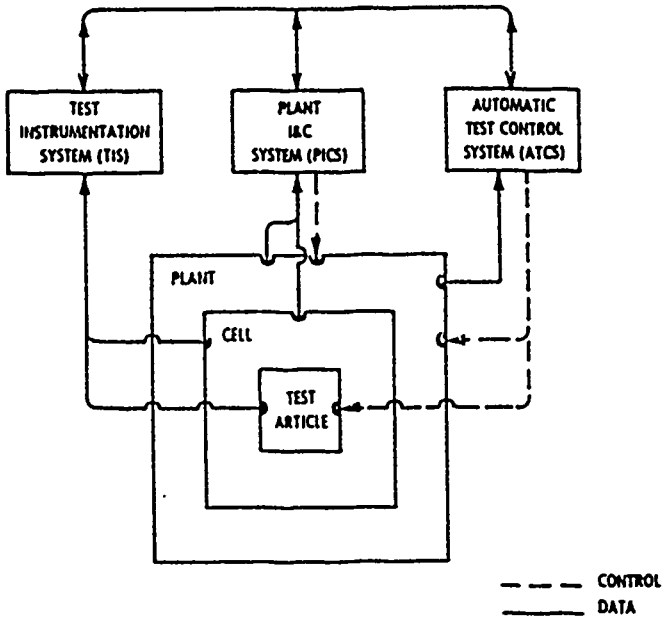

Figure 1. ASTF Instrumentation and Control Interface Diagram.

Because of the importance of the ATCS and because it is used for detection of abnormal conditions inside the test cell, this research concentrates on applying neural network technology to enhancing the ATCS.

The ATCS controls the parameters which establish a desired test condition by positioning forty-six of the facility configuration and control valves. The ATCS is used to control various engine controls and the interface to the test cell engineers is effected at a panel in the test building control room. Pertinent test information is communicated to test cell personnel through four CRT terminals. It is the end goal of this research to establish a better means of monitoring test data from the ATCS.

(2.2) Fault Monitoring and Diagnosis

In order to apply neural networks to fault monitoring and diagnosis, the task of fault detection must be seen as one of pattern recognition. In approaching the ASTF we will say that fault detection is observing data that fall outside expected parameters previously regarded as "normal" operation. Sensor data that fall outside normal boundaries do not necessarily indicate that the system is beginning to fail, but it does indicate that an abnormal occurrence is taking place inside the system that is being studied and warrants further attention. As stated previously, in this research diagnostic problems are viewed as a mapping of an input pattern representing sensor data to an output pattern which is interpretable as a diagnosis.

Analysis of a complex system should use an opportunistic strategy — there is no computationally feasible "legal move generator" that defines the space of solutions in which pruning and steering take place as in classical AI systems (Nii and Feigenbaum, 1978). Bits and pieces of information must be used as the opportunity arises to (relatively) slowly build a coherent picture of the world (system). This is one way in which neural networks are better than current AI methods at analyzing signal data from complex systems.

CHAPTER III

RESULTS

(3.1) A Two Layer Semilinear Feed–Forward Neural Network: A Generalized Perceptron Approach

The Automatic Test and Control System (ATCS) in the ASTF uses 33 sensor values for diagnosis of the health of the facility. Eleven of those are commands values from the test cell engineers for changing the test cell environment. The other 22 are sensors that monitor the conditions of the engine and the test cell. In order to catch all possible faults that occur in the ASTF it is necessary to monitor all 22 data sensors. The network was trained using a training set of 60 scaled vectors composed of 20 normal followed by 40 abnormal vectors made up of 22 sensor values and their desired outputs. The network was allowed to iterate 1000 times over the training set to achieve the lowest possible total system error while still achieving 1000 iterations. Finalized connection weights for the input nodes (sensors) to the output node ranged between -1.61 and 3.78. The sensors with the strongest connection weights (highest absolute value) were a pressure sensor (P0) with a weight of 3.78, pressure sensor PL3H with a weight of 3.57 and a valve opening sensor (LVC1B) with a connection weight value of 2.02. The final threshold for the input nodes was -0.46. The hyperplane formed by the two layer network is shown in Figure 2.

In order to interpret exactly what the network found, other than by testing it on new data sets, we can look at how the final weights converged and try to decide if the weight values are telling us anything about the system being analyzed.

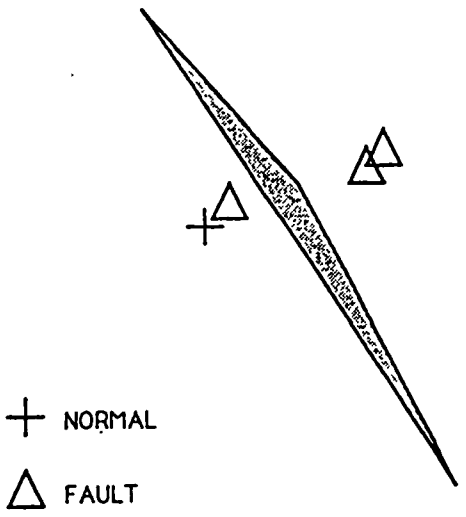

Figure 2. Hyperplane Formed by a Two Layer Neural Network in Three Dimensions (Sensor PO, Sensor PL3H and Sensor LVC1B)

Graphing the final weights in Figure 3 we can see the pattern of connection weights with peaks at sensors P0, PL3H and LVC1B. As far as this two layer network is concerned, the majority of relevant information as to the health of the system can be gained from these sensors. In other words, these sensor values give the best indications as to the status of the system.

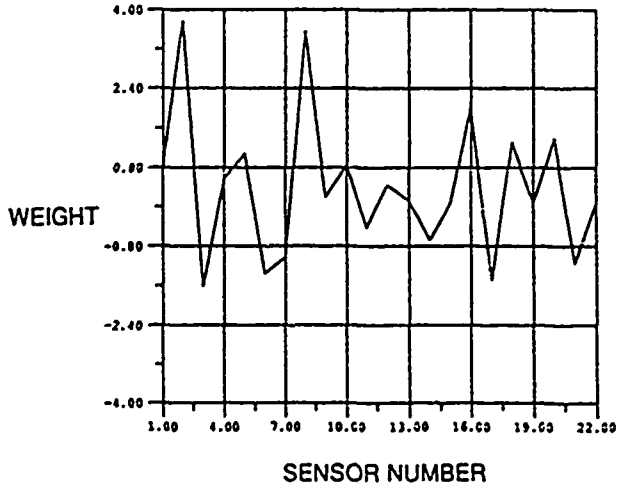

Figure 3. Final Connection Weights for a Two Layer Neural Network

The two layer neural network was tested on seven data sets composed of ten vectors made up of 22 sensor values. Two of those sets were from the training set in order to judge whether or not the system was working correctly. The other five were composed of arbitrary input vectors from the ASTF simulator representing engine test runs new to the network. As expected, the network computed a low output node value for the normal vectors extracted from the training set (0.013) and a high output node value for the vectors representing faulty data taken from the training set (0.999). This is not surprising since we would expect the network to correctly identify input vectors it has seen before. The true test of the system, of course, is its ability to make an accurate diagnosis of the health of the system based on some unknown input. When a set of normal ASTF sensor vectors was presented to the network the value of the output node value was 0.014, a correct diagnosis. Four new data sets composed of faulty sensor vectors was presented to the network and the output node achieved values of 0.990, 0.998, 0.936 and 0.990 respectively. These output values correctly indicate that the system is in failure. This shows that the network architecture is making accurate diagnosis and generalizing over the space spanned by the input variables. A summary of the output values for the network tested on various data sets is given in Figure 6.

To confirm that the network was indeed accurately classifying ASTF sensor data from any sensor in the ASCS, the network was trained using a new training set composed of vectors different from those in the original training set. The network was tested against test vectors extracted from the training set. As expected the system achieved high diagnostic accuracy with a mean output value of 0.997 for vectors representing faults and a mean output value of 0.0004 for vectors representing a normal test run. To test the network for generalizability over all sensors

from the ASTF two unknown (not part of the training set) faults were presented to the network from unspecified locations in the test cell. The first vector was an unknown representing a turbine trip at an undisclosed location in the ASTF and the second vector represented a compressor failure in an unspecified leg of the test cell. The network achieved an output value of 0.998 for the first vector and 0.992 for the second vector.

(3.2) A Three Layer Semilinear Feed–Forward Neural Network: A Multilayer Perceptron Approach

A network was constructed using a hidden layer composed of three and five processing elements. Tests were run for each type of network, both on the vectors extracted from the training set and on the same unknown test vectors as for the two layer network. Since a two layer network gave accurate responses, the three layer network should be thoroughly scrutinized to see if it enhances the amount of information gained from the network. Since adding a layer adds computational complexity and adds to the time necessary to train and test the network, a hidden layer should be able to detect hidden features in the patterns of input data not seen by the two layer network, and be able to generalize over many different test sets in order to make it economically worthwhile.

The first three layer neural network used three processing elements in the hidden layer. Connection weights from the input nodes to the first hidden node ranged from–1.60 to 0.76 with highest (absolute value) weights from sensors P0 (–1.55), PL3H (–1.60). Only these two sensors had connection weight strenghts greater than 1.0. Connection weights from the input nodes to the second hidden node ranged from –1.59 to 0.71 with greatest weight strengths from sensors P0 (–

1.30) and PL3H (–1.59). Again, only these two sensors had weights whose absolute value was greater than 1.0. Connection weights to the last hidden node ranged from–1.27 to 2.50 with the strongest connections from sensors P0 (2.28), PL3H (2.50) and LVC2A (–1.27). By adding a hidden layer new information was gained on diagnosing the health of the test cell, namely the significance of data from sensor LVC2A. In the two layer neural net the connection strength between LVC2A and the output node was high (1.48), but its relative importance in diagnosing the status of the system was best seen in studying the connection weights between the input layer and the third hidden node. The hyperplanes formed by the three hidden nodes can be seen in Figure 4. The addition of the hidden layer produced enough hyperplanes to form a more complex region to better classify the data.

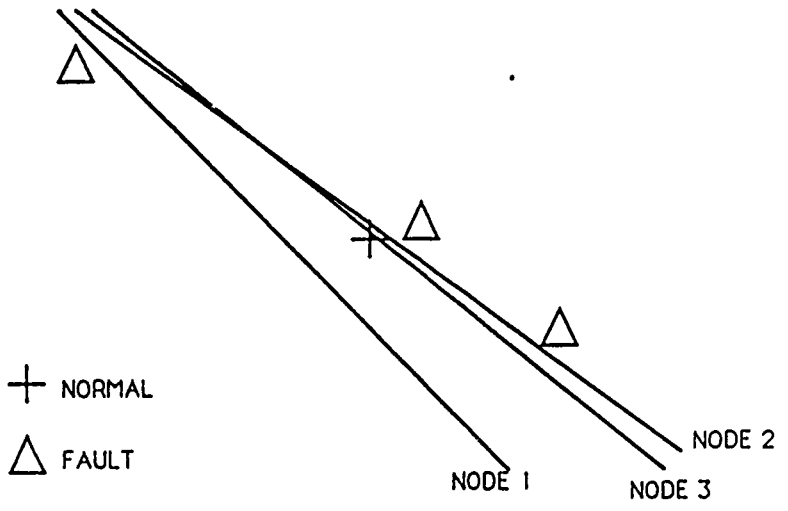

Figure 4. Hyperplanes Formed by Three Hidden Nodes Graphed in Three Dimensions (Sensor PO, Sensor PL3H and Sensor TL1H)

A three layer neural network with five hidden processing elements was also

explored. For all five hidden nodes the strongest connections between the input layer and the hidden layer were from nodes representing sensors P0, PL3H, LVC1B and LVC2A. Based on the finalized weights of the multilayer network, four sensors give the strongest indication as to the health of the ASTF. A summary of connection weights can be seen in Figure 5.

The three layer neural network with three and five hidden processing elements (PEs) was tested on the same data sets as the two layer network in order to compare diagnostic accuracy. A summary of the results is given in Figure 5. Computing the output for the network with three nodes in the middle layer using data sets composed of normal and faulty vectors extracted from the training set, resulted in an output node value of 0.010 and 0.996 respectively. For the test set composed of new normal sensor data the value on the output node was 0.011. For the four faulty sensor data sets the network achieved the following values: 0.991, 0.994, 0.973 and 0.991. By comparing these values with the outputs from the two layer network it can be seen that diagnostic accuracy was increased somewhat in four out of five test cases by the addition of the hidden layer.

Testing the three layer system with five hidden PEs, the network computed output values of 0.011 for the normal test case extracted from the training set and 0.997 for the abnormal test case similarly derived. For the new unknown test cases the network achieved values on the output node of 0.013 for the normal vectors and 0.992, 0.996, 0.944 and 0.992 for the fault cases respectively. This architecture did better than the two layer system in the same four out of five test cases as the system with three hidden PEs, but achieved a higher diagnostic accuracy then the other three layer network in only three out of five cases.

SENSORS	HIDDEN NODES								
	0	3			5				
	0	1	2	3	1	2	3	4	5
PT2	0.88	-0.79	-0.60	0.70	-0.35	-0.50	-0.40	0.18	0.69
PO	3.78	-1.55	-1.30	2.28	-0.05	-0.97	-1.21	0.98	2.75
TT2	-1.61	0.03	0.16	-0.97	-0.54	0.08	0.10	-0.13	-0.33
PLA	0.56	0.49	0.36	-0.02	0.44	0.38	-0.09	-0.01	0.07
PHC1V	1.10	-0.27	-0.07	0.40	0.00	0.00	-0.46	0.01	0.84
PL1H	-1.35	0.76	0.69	-0.91	-0.02	0.54	0.56	-0.81	-1.01
PL2H	-1.02	0.22	0.16	-0.21	-0.33	0.06	0.72	-0.53	-0.64
PL3H	3.57	-1.60	-1.59	2.50	-0.15	-1.27	-0.87	1.45	1.90
P0EC1	0.20	0.32	-0.20	-0.08	0.3	-0.14	-0.05	-0.03	0.09
TL1H	0.84	-0.87	-0.83	0.92	-0.43	-0.75	-0.04	0.32	0.45
TL2H	-0.42	-0.42	0.29	0.49	-0.42	0.29	0.49	-0.23	0.03
TL3H	0.45	-0.26	-0.01	0.04	-0.08	0.05	-0.40	0.58	-0.14
THC1V	0.13	0.30	-0.10	0.28	0.22	-0.09	0.38	0.21	0.07
TC12	-0.68	-0.44	-0.38	-0.34	-0.40	-0.26	-0.41	-0.40	0.25
LVC1A	0.07	0.34	0.14	0.36	0.37	0.25	0.31	0.32	-0.40
LVC1B	2.02	-0.28	-0.54	0.98	0.46	-0.34	-0.64	0.95	1.13
LVC2A	-1.48	0.73	0.71	-1.27	-0.14	0.52	0.35	-0.29	-1.40
LVC2B	1.33	-0.42	0.00	0.86	0.00	0.07	-0.10	0.21	1.18
LVC3A	0.08	0.24	0.09	-0.41	0.13	0.09	-0.30	-0.14	0.21
LVC3B	1.41	-0.15	-0.83	0.07	0.25	-0.75	-0.81	0.47	0.82
LVTC1	-1.14	0.41	0.61	-0.47	-0.24	0.41	0.74	-0.48	-0.63
LV100	0.09	0.09	0.45	0.05	0.06	0.49	0.04	0.41	0.09

Figure 5. Final Connection Weights from Input Nodes to Nodes of Hidden Layer Based on Number of Hidden Nodes

Number Of Nodes In Middle Layer	Normal (train)	Fault (train)	Normal (test)	Fault 1 (test)	Fault 2 (test)	Fault 3 (test)	Fault 4 (test)
0	0.013	0.999	0.014	0.990	0.998	0.936	0.990
3	0.010	0.996	0.011	0.991	0.994	0.973	0.991
5	0.011	0.997	0.013	0.992	0.996	0.944	0.992

Figure 6. Final Output Values for Test Data Based on the Number of Nodes in the Hidden Layer

The results of these tests prove that the network is achieving accurate diagnosis of the health of the ASTF over arbitrary inputs and that the network is able to generalize over all possible faults in this instance. Based on the comparisons in Figure 6, it can be seen that a three layer neural network with three hidden nodes achieves a slightly more accurate diagnosis than a two layer neural network. The addition of two more nodes in the hidden layer only results in a small increase in performance, but significantly increases the time needed to train the network. Tests conducted using the two layer network seem to indicate that data coming from the ASTF sensors is linearly separable. Based on the increased run time and greater computational complexity it appears that a two layer network is able to di-

agnose the status of the engine test cell with high enough diagnostic accuracy not to warrant the addition of a middle layer, specifically the addition of five hidden nodes. However, in this case a multilayer neural net proved useful in discovering sensor information that give important insight into monitoring the health of the test cell. Also Figure 2 clearly shows that a two layer neural network is unable to seperate all classes of data, especially in the presence of noise.

The strongest connection weights from the first hidden node to the output node were from sensors PL3H (-1.60), PO (-1.55), and TL1H (-0.87). Using these weights to calculate the intercepts of the hyperplane on a three dimensional graph clearly shows that a multi-layer neural network with three hidden processing elements seperates data that was non-linearly separable. The addition of a middle layer adds diagnostic accuracy to the network.

CHAPTER IV

CONCLUSIONS AND RECOMMENDATIONS

This research has shown that a neural network can be used to differentiate between patterns of data representing a normal test run of the Aeropropulsion Systems Test Facility and sensor data coming from a test cell that is in failure. A network was also built to classify the type of fault that is occuring. For simulated ASTF data a near optimal diagnosis can be achieved using a two layer neural network (generalized perceptron). However, for simulated data with noise such as would occur in actual engine test cell data, a multilayer neural network with three hidden processing elements yields a more accurate diagnosis. The neural network architecture described in this report diagnoses the health of the ASTF with a high degree of accuracy after being exposed to an input vector representing sensor data from only one time slice (0.2 sec) and an even higher accuracy after averaging ten time slices, or two seconds, worth of data.

In addition, by monitoring the converging weights of the input processing elements it was seen that the most relevant information used by the 22 input node network comes from four sensors, P0, PL3H, LVC1B and LVC2A based on connection strengths. Graphing the node connection weights and the total system error for various network parameters shows whether the weights oscillate while approaching error minima.

This research has demonstrated the usefulness of neural networks for fault monitoring and diagnosis. Further research and implementation of neural network based systems will give test personnel a new tool in the anlysis of critical test data. This system will help take neural network technology out of the laboratory

and help create commercial systems for the analysis of complex systems. The most significant potential benefit of the system which has been developed is the improved safety of test cell personnel by rapid detection of faulty conditions. This will be of extreme importance as testing begins on more advanced systems such as the National Aerospace Plane and the Advanced Tactical Fighter.

1990 USAF-UES SUMMER FACULTY RESEARCH PROGRAM/

GRADUATE STUDENT RESEARCH PROGRAM

Sponsored by the

AIR FORCE OFFICE OF SCIENTIFIC RESEARCH

Conducted by the

Universal Energy Systems, Inc.

FINAL REPORT

AI APPLICATIONS FOR GAS TURBINE ENGINE TESTING

Prepared by:	Dollena S. Hawkins
Academic Rank:	Master's Degree Candidate
Department and	Mathematics Department
University:	Tennessee Technological University
Research Location:	Turbine Engine Division, AEDC,
	Arnold Air Force Base
USAF Researcher:	Major J. A. Davis, Lt. R. S. Hauser
Date:	August 10, 1990
Contract No.:	F49620-88-C-0053

AI APPLICATIONS FOR GAS TURBINE ENGINE TESTING

by

Dollena S. Hawkins

ABSTRACT

Expert systems and neural networks have been investigated to determine the feasibility of applying such technology to gas turbine engine testing. This research was accomplished by a literature search and detailed discussions with Arnold Engineering Development Center (AEDC) Air Force and contractor personnel. Findings indicate that applications may result from continued development of research efforts currently planned or in progress. It is recommended that AEDC carefully integrate artificial intelligence (AI) as a technological tool. Judicious and successful implementation of expert systems and neural networks depends upon the organizations' (1) increased knowledge of the capabilities and limitations of the technology and (2) support of research efforts.

I. INTRODUCTION:

The Directorate of Propulsion Test (DOPT) test gas turbine engines by simulating altitude and mach number within test cells. Their work contributes to the qualification of turbine engines for flight, demonstration of advanced turbomachinery, improvement to hardware and software components, establishment of performance levels prior to production, and troubleshooting of problems with operational systems. Advanced testing techniques and instrumentation are paramount to the testing of turbine engines that are on the leading edge of technology.

Articles in scientific journals and the media in general have contributed to a heightened interest in AI because of its potential benefits to the technological world. Within DOPT the natural question has arisen, "Can AI techniques be applied to enhance the testing of gas turbine engines?" This question initiated the research discussed in this paper. My appointment was a result of my educational background, BSME and current pursuit of a masters in mathematics.

II. OBJECTIVES OF THE RESEARCH EFFORT:

During testing of gas turbine engines, massive quantities of data are collected and stored. Part of the data is processed during the testing operation and returned to the test cell control room in a variety of media forms, such as digital readouts, computer printouts, and graphs. Other sensory data is recorded in analog form during testing and is digitized and converted to plots and graphs for in-depth analysis days after the test. The initial task was to determine if expert systems could be used to aid in the identification of "significant data" (i.e. identifying that portion of the data needing further analysis). Assume a system could monitor sensor outputs and indicate the occurrence of a significant event while the test was being run. Then, for example, in the case of analog data, only the data recording the significant event would need to be digitized. This would result in reduction of the amount of data handled and stored while still maintaining a thorough analysis of test results. If research findings were to support such an application of an expert system to turbine engine testing, then an implementation plan would be developed.

Results of the initial literature search revealed that little research has been conducted in the specific area described above and that AI technology is not limited to expert systems. Therefore, the objective was redefined to be -- determine the feasibility of using expert systems and neural networks in gas turbine engine testing (not just data collection and storage).

In addition to identifying engine test requirements suitable for such applications, a secondary objective -- to identify management considerations in applying AI technology -- was added.

III. Approach and Findings:

The approach to achieve both objectives consisted of synthesizing information collected from a literature search of AI and from detailed discussions with AEDC Air Force and contractor personnel concerning gas turbine engine testing, data collection, and data analysis. The following summarizes the findings.

Feasibility of Applications:

Based on extensive review of the referenced literature, there currently exists no ready to implement neural network or expert system for use in gas turbine engine testing. Researchers are currently pursuing the following areas:

* gas turbine engine health monitoring
* diagnostic expert systems for gas turbine engine maintenance
* prototype expert systems and neural networks for the Space Shuttle Main Engine
* AEDC development of prototype expert systems and neural networks

In addition, Fox (1990), Helton (1990), and Keyes (1989), as well as others, have written about key management issues

regarding application of AI technology. The following describes these findings in more detail.

Gas Turbine Engine Health Monitoring:

Research efforts are contributing specifically to the improvement of fault diagnosis and health monitoring of gas turbine engines, but primarily without the use of neural networks or expert systems. Such is the case with Merrington's (1989) work which outlines a method for extracting dynamic characteristics from gas turbine engine transient data. Similarly, Muir, Saravanamuttoo, and Marshall (1989) detail a stage-stacking method, using generalized stage characteristics, to create a realistic compressor model which can estimate variable geometry effects at the state level. Their work has been used to produce a comprehensive mathematical model of the GE LM2500. Also, Aker and Saravanamutto (1989) have completed a model that predicts gas turbine performance degradation due to compressor fouling.

Diagnostic Expert System for Gas Turbine Engine Maintenance:

While expert systems and neural networks have not been applied to the testing of developmental gas turbine engines, such technology has definite use in maintenance applications. Doel and LaPierre's (1989) paper provides an overview of diagnostic expert systems for gas turbine engines. According to Doel and LaPierre, most of the developed systems are ground based and are designed to assist maintenance personnel in troubleshooting and fault isolation. Of the few systems actually built,

all have been derived from military programs. For example, the LEADER system described by Shurtleff (1988) is designed to support the troubleshooting process throughout the AFT1500 production engine facility.

Troubleshooting and fault isolation are often integral parts to development of a new engine. It would seem, therefore, that an expert system would be helpful in gas turbine engine testing at AEDC. The very fact that the engines tested at AEDC are of a developmental nature precludes such a use of an expert system. An expert system requires a database of expertise knowledge that is not available on a new engine. It may be argued that the F100 family of engines have been tested at AEDC for about 20 years and that the expertise does exist for development of a knowledge base system. Modifications to the F100, however, make the F100-PW-100 quite different then the F100-PW-229 engine. Thus, the changes are too significant to say that a "constant" knowledge base could be established.

In contrast, a maintenance expert system does have applications in AEDC's Plant Operations. The equipment used to support engine tests at AEDC requires routine maintenance as well as emergency repairs. As with any organization, maintenance experts are relied on for troubleshooting faulty equipment; and, that expertise is lost due to retirements and other forms of attrition. Development of expert systems for diagnosing faults of critical equipment could be most beneficial. In addition, some generic expert systems are already on the

market that could be useful. See Harmon, Maus, and Morrissey (1988) for details on available software.

Prototype Expert Systems and Neural Networks for the Space Shuttle Main Engine:

A variety of research efforts have been directed toward using expert systems and neural networks in various applications involving the Space Shuttle Main Engine (SSME). Ali and Perrera's (1990) work involves development of an intelligent diagnostic expert system for use during SSME testing that monitors and integrates high frequency steady state sensor information from the SSME's high pressure oxygen turbopump to detect faults during their early development stages. Specifically, the system monitors bearing wear patterns and deterioration of inner and outer races. Similar work was done by Garcia (1987) for the high pressure liquid hydrogen turbopump. Also, Tarn (1988) describes a prototype expert system for analyzing rotordynamic data from the low and high pressure fuel and oxidizer turbopumps on the SSME. Ali and Crawford (1988) detail the design of a propulsion control and monitoring system for the SSME that also utilizes an expert system.

One expert system developed for the SSME has also been tested for use with jet engines. Dietz, Kiech, and Ali. (1988)

> outline an architecture for a . . . diagnostic expert system capable of accommodating noisy, incomplete, and possibly erroneous input data, and present results from prototype systems applied to jet and rocket engine fault diagnosis

The jet engine fault diagnosis portion of the testing used

data from an engine simulation program called ATEST (Advanced Turbine Engine Simulation Technique). Fuel interruptions and bearing failures were the two fault conditions tested. Testing and evaluation of the system focused not only an accurate fault diagnosis but also on the ability of the system to correctly identify varying degrees of fault severity and duration. Dietz, Kiech, and Ali (1989) describe follow-on work of this research. The developed neural network topology was found to have a major weakness in that when presented with fault patterns different than those for which it was trained, erroneous responses would occur. This problem was resolved by changing the neural network architecture and is described in a second paper by Dietz, Kiech, and Ali (1989). No additional work on the jet engine application has been reported in literature. Whitehead, Kiech, and Ali (1990) continued work on the neural network architecture with emphasis on prototype testing for rocket engine fault diagnosis.

Whitehead, Ferber, and Ali (1990) used a second type of neural network to develop a health monitoring system for the SSME. Rather than diagnosing the type of fault, their objective was to detect anomalies. This emphasis on detection rather than diagnosis is paving the way for their development of a neural network that trains solely on normal data. The network architecture described by Whitehead, Ferber, and Ali was designed for steady state sensor inputs; but, future direction of their research effort includes development of a system to monitor transient modes of the SSME.

AEDC Development of Prototype Expert Systems and Neural Networks:

It does appear that with modification or further development some applications of expert systems and/or neural networks seem likely. For example, Golden (1990) has developed a prototype neural network for fault monitoring of the ASTF test facility. Fault detection is limited to diagnosing normal running conditions, loss of one air side compressor during a ramp in test conditions, loss of air side compressors during idle, a turbine trip, or some unknown fault. Testing of the system has been limited to simulated data including added noise in order to closer approximate real engine test data. It has thus far yielded positive results. The benefits of such a system would be improved test cell safety and faster response time to fault situations. Additional testing using real data is currently in progress. ASTF data is highly linearly separable and it is Golden's opinion that other technology may be used for monitoring with equal success and less cost. In a situation where sensory data is not linearly separable, however, Golden's work seems promising.

In addition to Golden's work with neural networks, AEDC is currently involved in a variety of efforts to develop working expert systems. The reader is referred to Lo (1990) for broader descriptions of the following expert systems which are in developmental/prototype stages:

*a system for building expert systems to monitor ground test facility equipment which utilizes a dynamical

knowledge base

*an expert system for designing diffuser systems in propulsion ground test facilities that utilizes a hypertext manual and advisory system which captures experts' knowledge and experience

*a system to assist in the design and placement of boundary-layer trips on wind tunnel models during the planning of a wind tunnel test

*a system that diagnoses problems associated with drying air used in AEDC's 16-ft transonic wind tunnel

In a second paper by Lo (1990), the first of these efforts is detailed. The design of the research effort is to incorporate expert systems, neural networks, and hypertext into the construction of a monitoring system. Compressor stall monitoring and vibration analysis for rotating equipment are the two areas identified for possible application. Lo and Sebghati (1990) have iniated work to develop the compressor stall monitoring system.

Management Considerations:

More applications have been developed for expert systems than for neural networks. Both are developing technologies with on-going research efforts. Neural networks primarily remain a research field; whereas, expert systems are already being used in the business world. Accordingly, different strategies are needed for implementation of the two technologies. Further development of neural network applications requires research

support. Implementation of expert systems requires a business strategy.

Authorities do not agree on a single definition of AI. Neither do authorities agree on a single approach to implementing expert systems. One representative approach is that given by Helton (1990). Helton's approach is called **infusion** -- developing mainstream acceptance of expert systems as tools of automation to be used in the right place at the right time. Helton details infusion as encompassing four phases: awareness, early implementation, acceptance, and intensification.

Awareness is gained by having someone track the technology or in other words, become the technology champion. Awareness also means educating the organization as to "What is AI?" and "How can this technology be beneficial?". Early implementation means developing a small number of successful applications. This demonstrates the legitimate value of the technology and leads to acceptance. Intensification is achieved when expert system technology has moved into the mainstream thinking. When a considerable number of employees know when and where to exploit this technology the necessary level of support and funding will become more likely.

In order to develop successful applications, it is important to know how to pick a good problem. Keyes (1989) cites some critical considerations when selecting a problem area for use of an expert system. Her recommendations include picking a

problem where there is a readily accessible expert who can explain how to solve the problem; information does not change continually; and, it demonstrates a worth, such as increased productivity or lowered costs. Rowan (1989) summarizes,

> knowledge-based systems . . . (become beneficial when) . . . expertise is scarce, vague, and dispersed and should be preserved, made precise, focused and applied continuously.

Recognize that if there is no expert, then there is no expert system. The quality of the domain expert's knowledge and ability to communicate/capture that knowledge is the cornerstone of a valid and accurate expert system. Note, too, that developed systems will not work once completed without user support.

IV. RECOMMENDATIONS:

By identifying the capabilities and limitations of expert systems and neural networks DOPT will best be in a role to capitalize on these two forms of AI technology. Since limited work in applying expert systems and neural networks to gas turbine engine testing has been completed, these tools of tomorrow will be realized through funding of research today. Vibration monitoring, fault diagnosis, and health monitoring are the research areas most likely to yield viable applications.

Expert system research has progressed farther than neural network research. Accordingly, organizations are already

benefiting from utilization of expert systems; but, management must use care and discretion in selection of projects. The more knowledgeable one becomes regarding expert systems, the more capable one will be in identifying potential applications. A key way to accumulate this knowledge within the organization is to identify an individual or group to stay abreast of this growing branch of AI. A judicious eye is needed to separate misnomers and misrepresentations from the truth about expert systems. Reading current literature, attending AI conferences, and participating in the AI work group at AEDC will enable the technology champion to be knowledgeable. When information is passed on through memos, letters, and presentations the infusion process will begin to establish expert systems and neural networks alongside the current tools at the disposal of engineers, managers, and technicians who make engine testing a reality at AEDC.

V. ACKNOWLEDGMENTS:

I wish to thank the Air Force Systems Command, the Air Force Office of Scientific Research, and the Arnold Engineering Development Center for sponsorship of this research. A special thanks to Major J. Davis and Lieutenant S. Hauser for their patience and guidance throughout this effort. Gratitude is also extended to Universal Energy Systems, Inc. for their helpfulness in administrative matters.

REFERENCES

Aker, G.F. and H.I.H. Saravanamuttoo, "Predicting Gas Turbine Performance Degradation Due to Compressor Fouling Using Computer Simulation Techniques," Journal of Engineering for Gas Turbines and Power, Vol. 111 (April 1989), pp. 343-350.

Ali, Dr. Moonis, and Dr. Roger Crawford, "Rocket Engine Control and Monitoring Expert System," AIAA/ASME/SAE/ASEE 24th Joint Propulsion Conference, Boston, MA, July 1988.

Dietz, W.E., E.L. Kiech, and M. Ali, "Pattern-Based Fault Diagnosis Using Neural Networks," The First International Conference on Artificial Intelligence and Expert Systems, UTSI, Tullahoma, TN, June 1988, pp. 13-23.

-----, "Jet and Rocket Engine Fault Diagnosis in Real Time," Journal of Neural Network Computing, Vol. 1, Number 1, (Summer 1989), pp. 5-18.

-----, "Classification of Data Patterns Using an Autoassociative Neural Network Topology," The Second International Conference on Industrial and Engineering Applications of Artificial Intelligence & Expert Systems IEA/AIE-89, UTSI, Tullahoma, TN, June 1989, pp. 1028-1036.

Doel, David L., and Lee R. LaPierre, "Diagnostic Expert Systems for Gas Turbine Engines - Status & Prospects," AIAA/ASME/SAE/ASEE 25th Joint Propulsion Conference, Monterey, CA, July 1989.

Fox, Mark S., "AI and Expert System Myths, Legends, and Facts," IEEE Expert (February 1990), pp. 8-19.

Garcia, Jr., Raul C, "A Expert System to Analyze High Frequency Dependent Data for the Space Shuttle Main Engine Turbopumps," Third Annual Conference on Artificial Intelligence for Space Applications, Huntsville, AL, Nov. 1987, pp. 213-220.

Golden, J., "A Neural Network for the Analysis of Test Data from the Aeropropulsion Systems Test Facility," Master Thesis, The University of Tennessee, 1990.

Harmon, Paul, Rex Maus, and William Morrissey, Expert Systems: Tools & Applications, New York, John Wiley & Sons, 1988.

Helton, Tom, "AI Infusion: Getting Your Company Involved," AI Expert (March 1990), pp. 54-59.

Keyes, Jessica, "Why Expert Systems Fail," AI Expert (November 1989), pp. 50-53.

Lo, C.F., "Application of Neural Network Based Expert Systems to Monitoring Systems," Unpublished, UTSI, Tullahoma, TN, 1990.

-----, "An Overview of Intelligent Systems for Aerospace Ground Testing," 16th Aerodynamic Ground Testing Conference, Seattle, Washington, June 1990.

Merrington, G.L., "Fault Diagnosis of Gas Turbine Engines from Transient Data," Journal of Engineering for Gas Turbines and Power, Vol 111 (April 1989), pp. 237-242.

Muir, D.E., H.I.H. Saravanamuttoo, and D.J. Marshall, "Health Monitoring of Variable Geometry Gas Turbines for the Canadian Navy," Journal of Engineering for Gas Turbines and Power, Vol. 111 (April 1989), pp. 244-250.

Perrera, Lisa, Untitled and Unpublished Master Thesis, The University of Tennessee, 1990.

Rowan, Duncan A., "On-Line Expert Systems in Process Industries," AI Expert (August 1989), pp. 30-38.

Sebghati, John, "Application of Expert Systems to Compressor Stall Warning", Unpublished, UTSI, Tullahoma, TN, 1990.

Shurtleff, J.S., "LEADER: An Automatic, Real-Time Diagnostic Knowledge System," SAE, Aerospace Technology Conference and Exposition, Anaheim, CA, Oct. 1988.

Tarn, Robert B., "Rocketdyne Automated Dynamics Data Analysis and Management System," 58th Shock and Vibration Symposium, Huntsville, AL, Oct. 1987, pp. 151-164.

Whitehead, Bruce A., Earl L. Kiech, and Moonis Ali, "Rocket Engine Diagnostics Using Neural Networks," AIAA/SAE/ASME/ ASEE 26th Joint Propulsion Conference, Orlando, FL, July 1990.

Whitehead, Bruce A., Harry J. Ferber II, and Moonis Ali, "Neural Network Approach to Space Shuttle Main Engine Health Monitoring", AIAA/SAE/ASME/ASEE 26th Joint Propulsion Conference, Orlando, FL, July 1990.

1990 USAF-UES SUMMER FACULTY RESEARCH PROGRAM

GRADUATE STUDENT RESEARCH PROGRAM

Sponsored by the

AIR FORCE OFFICE OF SCIENTIFIC RESEARCH

Conducted by the

Universal Energy Systems, Inc.

FINAL REPORT

Investigations of Acoustic Resonance Phenomena Using Computer Animation Postprocessing

Prepared by:	E. Gordon King, Jr.
Academic Rank:	Graduate Student
Department and University:	Aerospace Engineering Department The University of Alabama, Tuscaloosa
Research Location:	AEDC/DOT Arnold Engineering Development Center Arnold Air Force Base, TN 37389
USAF Researcher:	Dr. R. Jones, Sverdrup/AEDC Group
Date:	22 July, 1990
Contract No:	F49620-88-C-0053

Investigations of Acoustic Resonance Phenomena Using Computer Animation Postprocessing

by

E. Gordon King, Jr.

ABSTRACT

Acoustic pressure flowfields can be a complex combination of standing and propagating waves. The corresponding wave behavior and effects are difficult to understand and convey using conventional methods such as two dimensional graphs.

A field variable visualization tool, or animation postprocessor, has been developed to allow near real-time animation of any set of discretized flowfield data. Among its many capabilities, is the ability to view the flowfield from any perspective and animate acoustic pressure amplitude and phase on any computational planes of interest.

Acknowledgements

I wish to thank the Air Force Systems Command and the Air Force Office of Scientific Research for sponsoring of the Graduate Student Research Program. Furthermore, the program was made more enjoyable by the courteous and prompt direction given by the staff at Universal Energy Systems.

Special thanks must go to Dr. Ralph Jones who organized an interesting and challenging summer project and supplied many needed technical suggestions. Also, the graphics programming skills of Dr. Mike Stokes were invaluable in overcoming some difficult coding obstacles. In general, thanks goes to all of the members of the Propulsion Computational Technology Section at Sverdrup/AEDC for making my stay at AEDC a pleasant and productive one.

I. INTRODUCTION:

The Aeropropulsion Systems Test Facility (ASTF) at Arnold Engineering Development Center (AEDC) is designed to test a wide range of turbojet and turbofan engines. Today's complex engines, with two dimensional thrust vectoring and thrust reversing capabilities, pose a unique challenge to the designers and operators of such modern engine test facilities.

One test experience which highlights such challenges resulted from a unique coupling of the fluid dynamic characteristics of the engine exhaust plume and the acoustic characteristics of the facility exhaust system. As a result of this coupling, an acoustic resonance mode in the exhaust portion of the C-2 test cell was excited. Coupled with the exhaust from the test article, this resonance phenomenon produced a low frequency, high amplitude pressure field in the exhaust ducting resulting in movement of the entire exhaust portion of the test cell. Such motion, should it go unchecked, could inflict serious structural damage to the test facility.

In general, since the acoustic wave movement in the facility exhaust system is a complex combination of standing and propagating waves, it is difficult to understand and convey the nature of the resonance phenomenon using conventional means such as two dimensional graphs. It was proposed that a means to visually display the acoustic pressure field in

the test cell, as it varies in time, would be a valuable tool in the analysis of the C2 phenomenon.

Through the Graduate Student Research Program, I was selected to begin work on an animation postprocessor that would allow visualization of discretized acoustic field variables (i.e., amplitude and phase).

My areas of research interest include propulsion optimization techniques applied to a two dimensional thrust vectoring nozzle design. Also, I have been involved with several projects to utilize computer generated imagery in Computational Fluid Dynamics.

II. OBJECTIVES OF THE RESEARCH EFFORT:

At the onset of the 1990 Graduate Student Research Program (GSRP) a basic set of objectives for the animation postprocessor were defined. Since it would eventually be used as a general purpose animation tool, the input data format should be flexible enough to allow input from a number of sources (i.e., experimentally, analytically, and numerically generated data). Thus, the input format was established as a discrete three dimensional array of acoustic amplitude and phase data in either cartesian, cylindrical or spherical coordinate systems. Also, since visualization of acoustic interactions were desired on computational planes other than those defining solid surfaces, it was necessary to have the capability for the user to define which set of planes are of interest. The postprocessor was to also give the user the option of viewing the body from different perspectives (i.e., allow flowfield rotation and translation about all axes). In addition, so that the animation postprocessor could be modified easily after the short GSRP contracting term, the source code was to be written to be as modular as possible. Finally, it was evident that some means of validation of the animation techniques being incorporated would be necessary. To do this, several analytically derived model problems would be considered.

III. Image Manipulation

a. Once the basic postprocessor environment had been constructed, a simple, non-animated cylindrical model was used to test the ability to manipulate the body/flowfield. Using a set of "slider bars" appropriately scaled (see figure 4), the user could choose to modify either the X, Y, and Z spatial location, or the x, y, and z body rotation angles.

b. The mouse controlled "slider bars" proved to be an excellent method by which to change the orientation of the body/flowfield. Also, the implementation of a "reset button" allowed the flowfield to be reset to its default orientation.

IV. Test Case Modelling

a. Acoustic field models were constructed using various coordinate systems. The first set of models used a simple monopole point source to produce an acoustic pressure field[2]. To test the generality of the postprocessor, various models including cubes, concentric cylinders, and spheres were immersed in the acoustic field to test the use of cartesian, cylindrical and spherical coordinate systems as shown in figures 4, 6 and 8. In all the models, the location of the source could be moved to yield different

acoustic pressures throughout the domain. For further verification, a hemispherical model was constructed and situated in a dipole source generated flowfield.

b. Using the various models, it was determined that the animation techniques being employed were aptly suited for the task. However, when using models with longer wavelength sources, the color shading technique was seen to have some limitations depending on the aspect ratio of the polygon representing the surface. If the aspect ratio of the polygon comprising the faceted surface was too large, it would visually convey that a wavefront was moving perpendicular to usual wavefront patterns. This led to a general limitation, namely, that the computational grid aspect ratio should be kept less than 2.0. Even so, aspect ratios of 3.0 were tested with little color degradation leading to false wavefronts. All the models appeared consistent with analytical results and produced easily distinguishable wavefronts for even the offset dipole generated model.

V. Test Cell Modelling

After the project had progressed past the verification phase, a numerical solution modelling the C2 phenomenon was used. The numerical FORTRAN solution was done under contract by The University of Tennessee Space Institute[1]

amplitude dropped to near zero values, the phase angle wavefronts could still be seen.

c. The new animations were compared with instantaneous pressure amplitude and phase angle data generated in the afore mentioned contract. Figures 9 and 10 show phase angle and pressure amplitude data generated numerically which compares directly to a "still frame" image taken from the animation postprocessor.

d. It was found that a "still frame" image generated by the animation postprocessor and the instantaneous data from the UTSI contract conveyed the same accustic wave information. Also, using the animation postprocessor, the acoustic field could be animated so that standing as well as propagating wave behavior was easily distinguished. Furthermore, viewing computational planes other than those defining the body showed decisively the rotational movement of the waves through the exhaust duct for the cases of rotational acoustic modes.

VI. RECOMMENDATIONS:

a. While undertaking verification processes and animating the numerical solutions for the C2 test cell, it was obvious that the total number of flowfield points should be kept to a minimum for smooth, continuous animation. For discretized acoustic fields with less than 30,000 points, animation rates are on the order of 30 frames per second. The frame rate can drop to 3-7 frames per second for a flowfield containing 100,000 points. Therefore, it is recommended that if animation of a large number of points is desired, the domain be broken into subsets for use by the animation postprocessor.

b. For this particular GSRP project, the animation postprocessor was used exclusively for visualization of acoustic pressure field variables. However, due to the generic nature of the input data file, the animation postprocessor could be used to animate any number of time-dependant variables on a discretized domain with only minor modifications.

c. Currently, the animation postprocessor maps the acoustic pressure amplitude and phase angle information into one of 16 million screen colors. This creates color bands and patches of varying intensity. Another useful method to display acoustic pressure data would be to display pressure

amplitude as various colors, but use "isolines" to display phase angle contours.

d. An important capability of the animation postprocessor is the ability of the user to re-orient the displayed image to view the animation from a different perspective. However, it is recommended that the rotations be changed from a body axes reference to that of a "screen" or global reference.

References

(1) Caruthers, J. E., and A. D. Vakili, "Investigation of resonant phenomena in an engine test cell", Sverdrup Technology Project no. DD22EW, 1989

(2) Kinsler, L. E., et. al., Fundamentals of Acoustics, John Wiley & Sons, Inc., 1982

(3) Morse, P. M., and K. U. Ingard, Theoretical Acoustics, McGraw-Hill, Inc., 1968

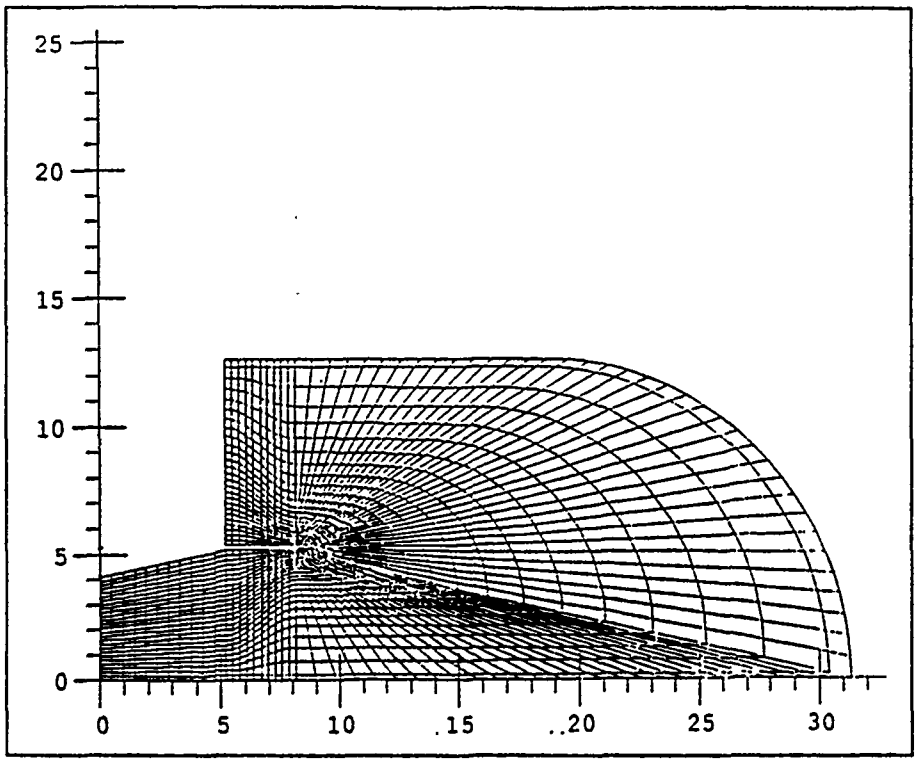

Figure 1: Body Fitted Grid

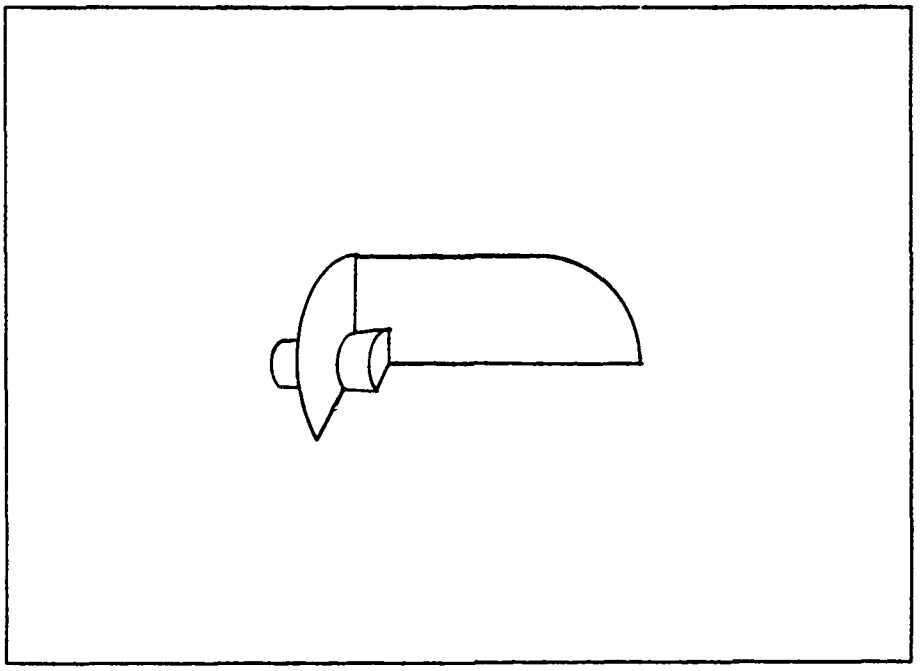

Figure 2: C2 Model Orientation in Postprocessor

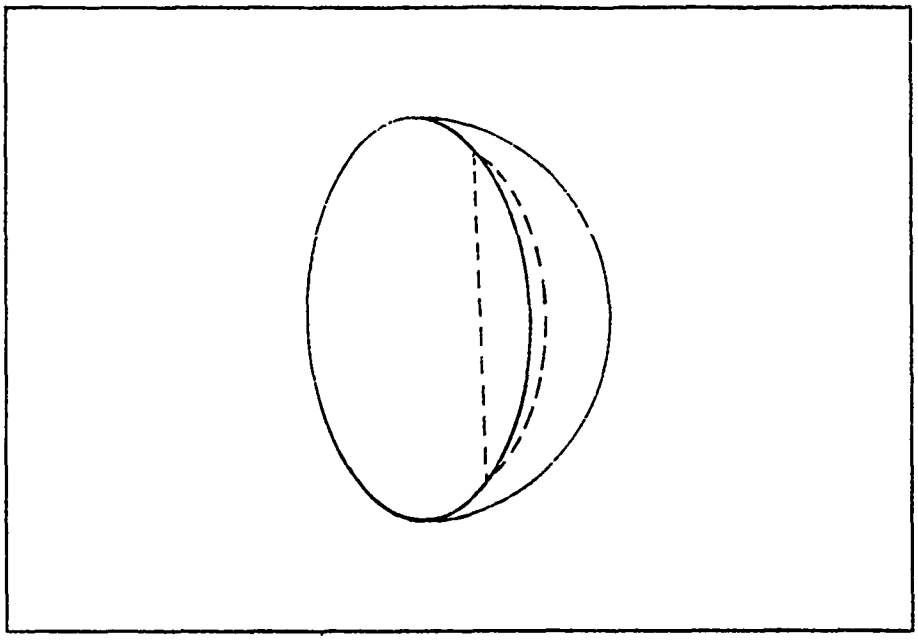

Figure 3: Spherical Model Orientation in Postprocessor

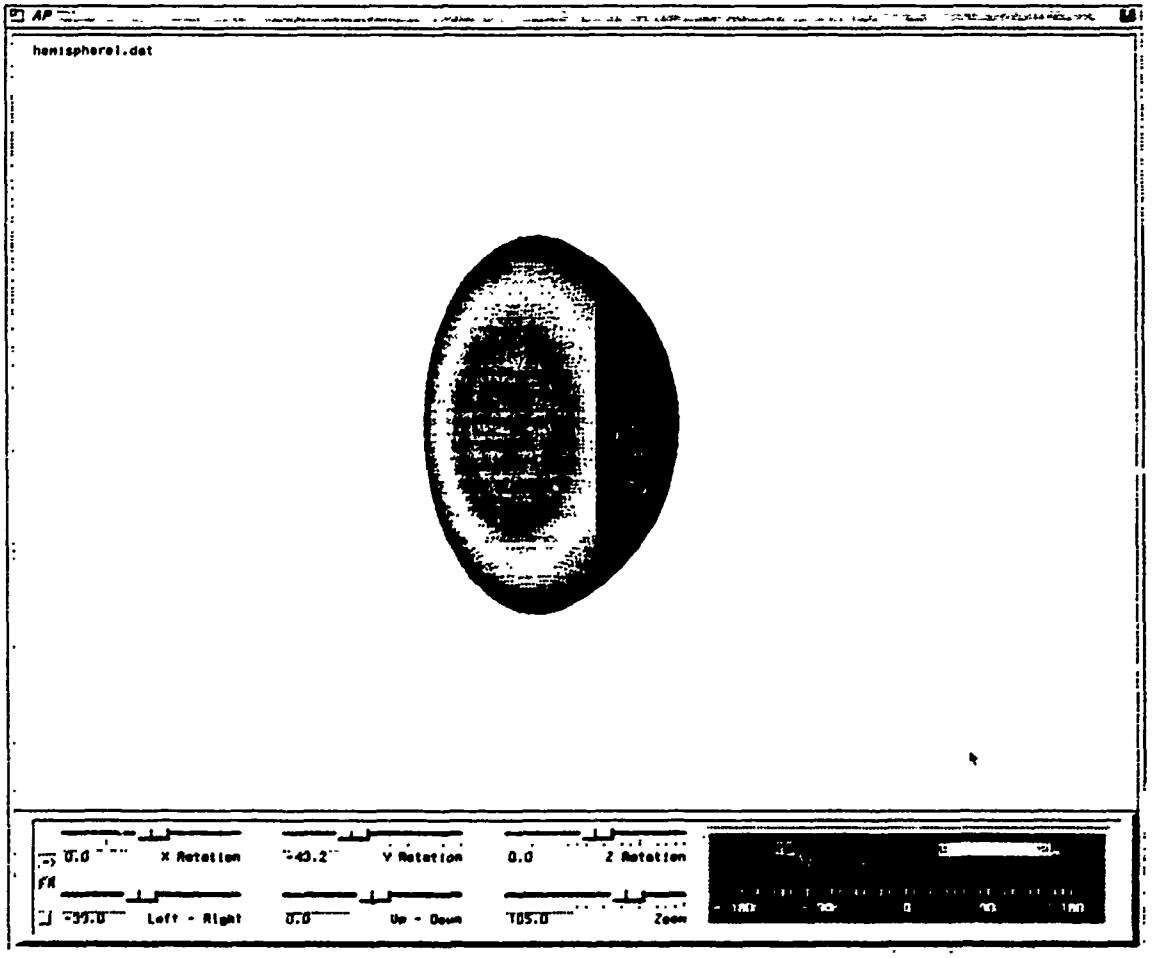

Figure 4: Spherical Model "Still Frame" from Postprocessor

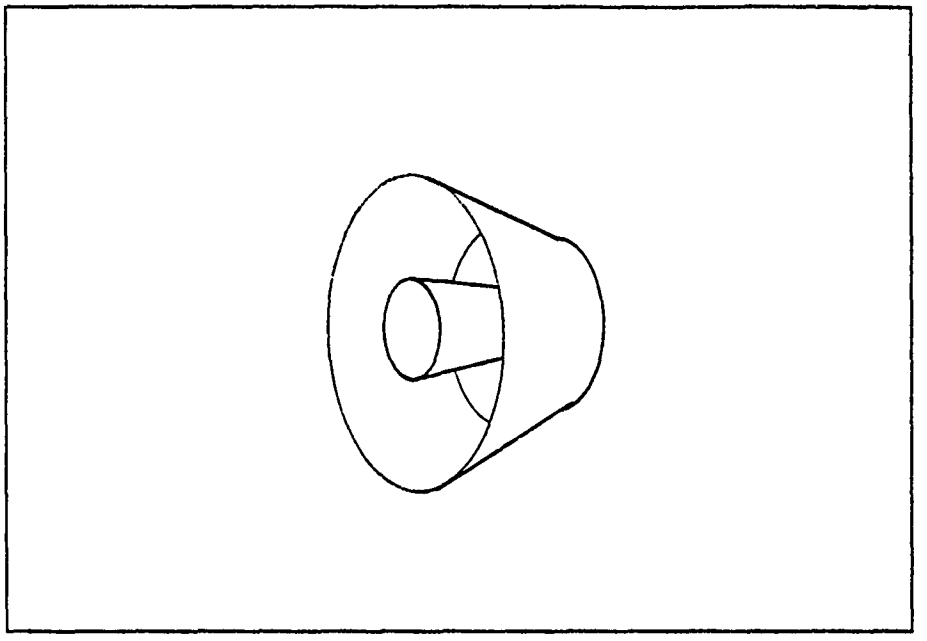

Figure 5: Cylindrical Model Orientation in Postprocessor

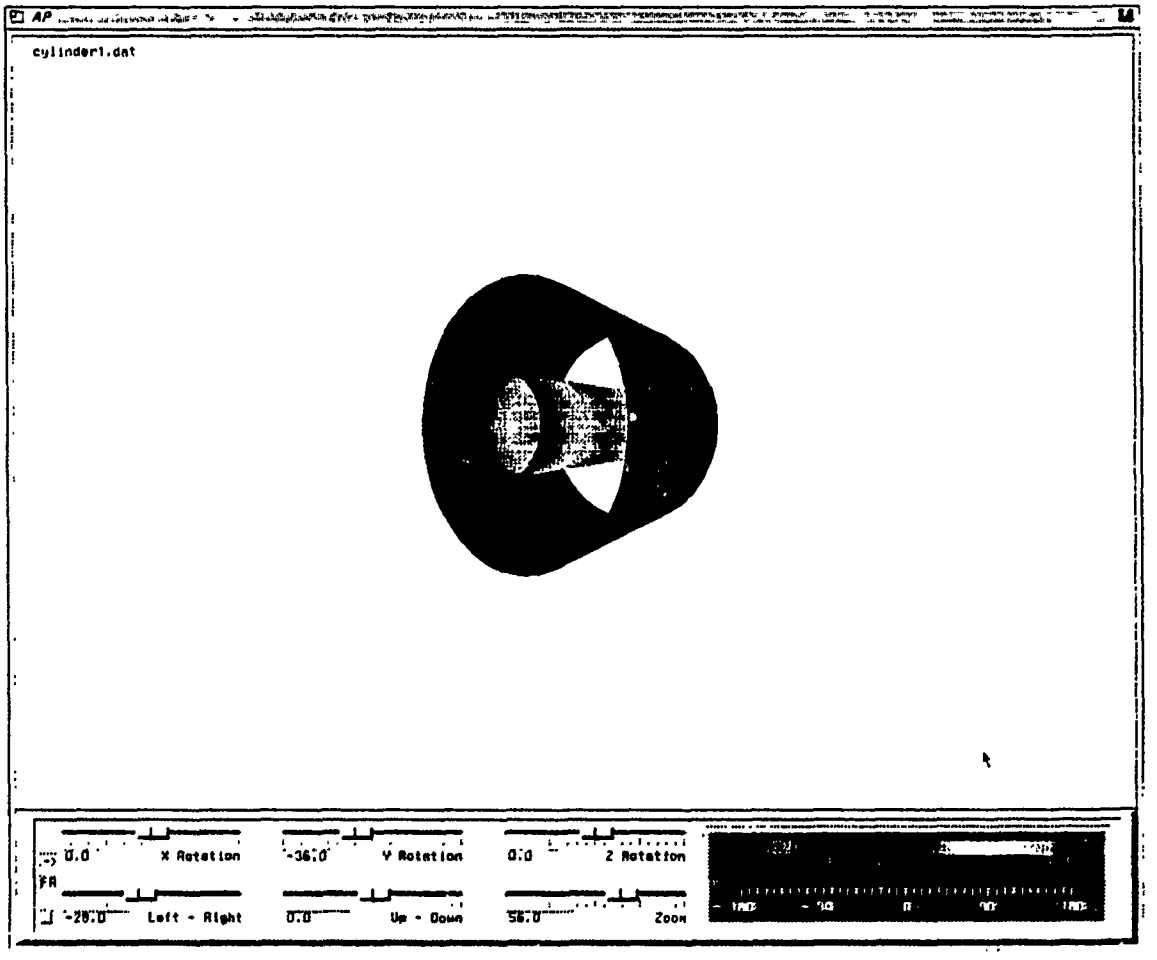

Figure 6: Cylindrical Model "still frame" from Postprocessor

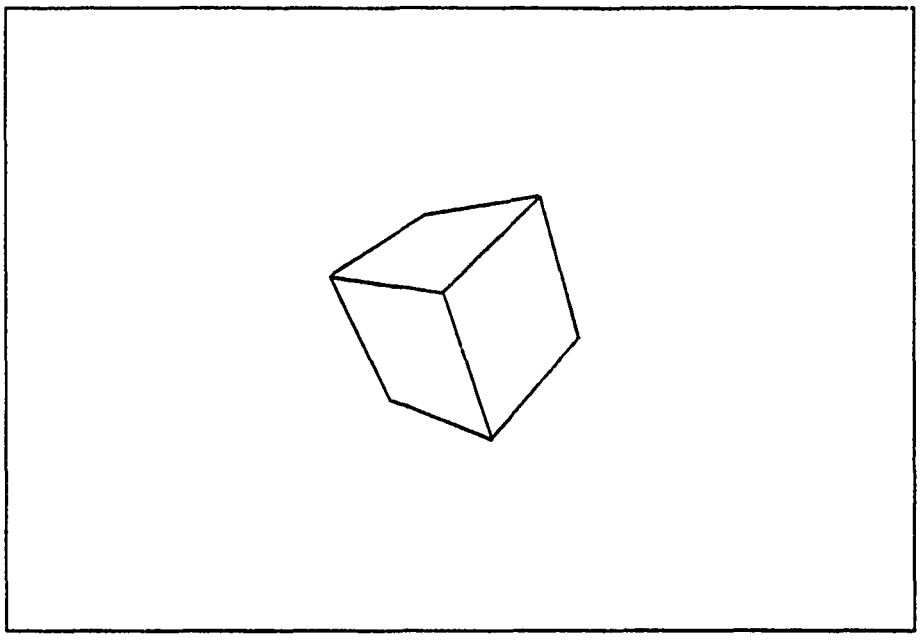

Figure 7: Cube Model Orientation in Postprocessor

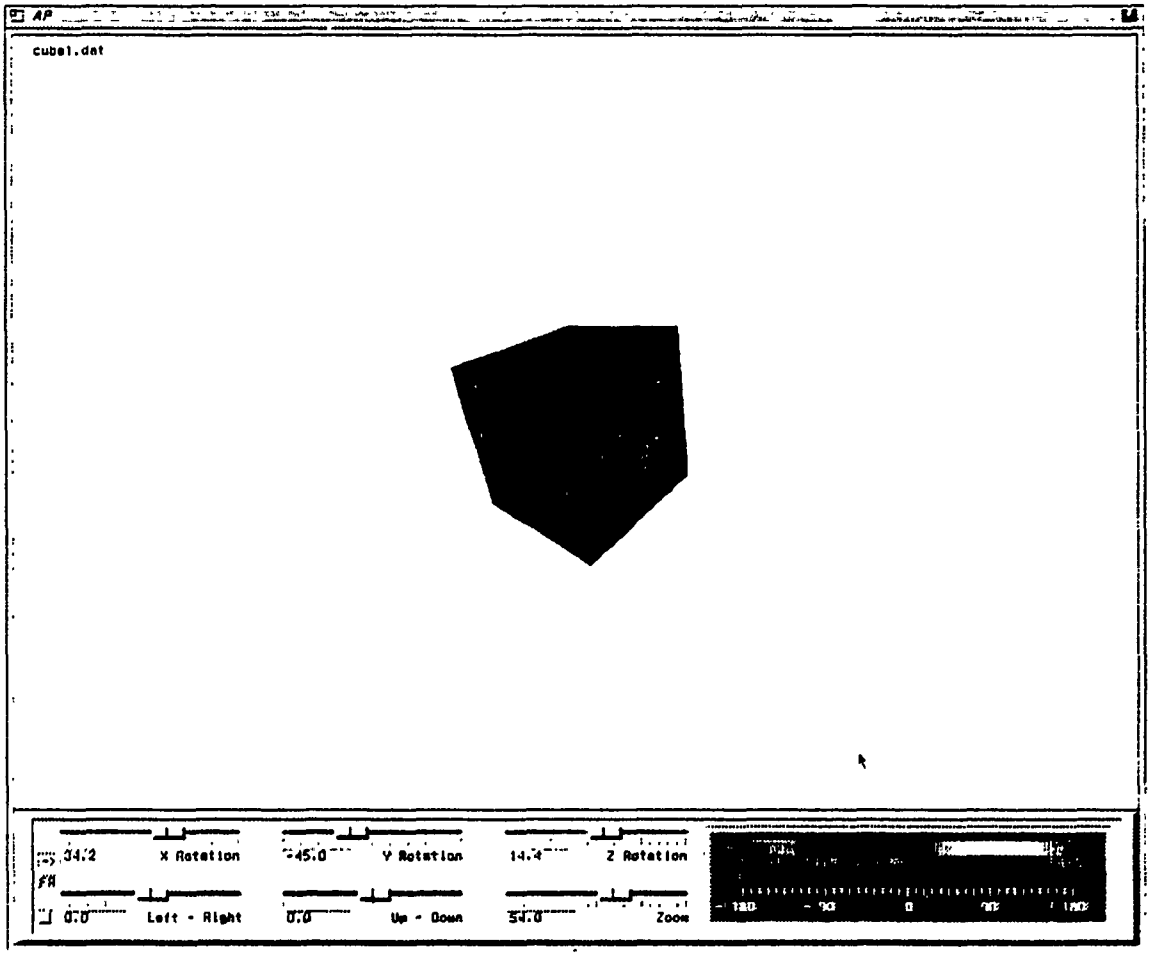

Figure 8: Cartesian Model "Still Frame" from Postprocessor

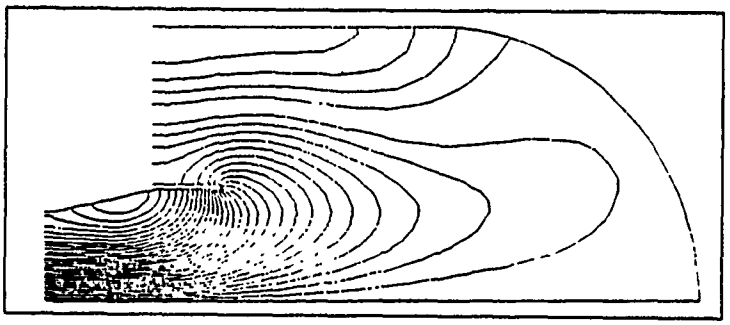

Acoustic Pressure Amplitude Contour Lines

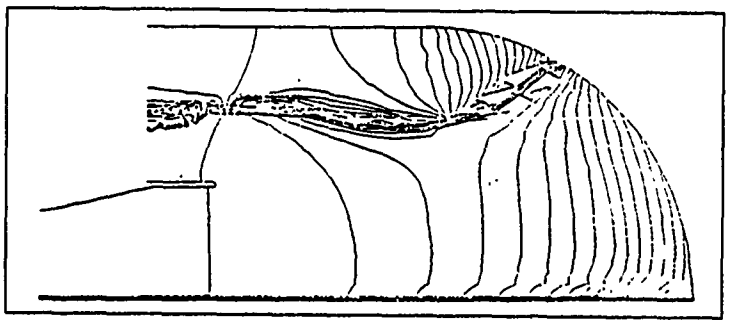

Acoustic Pressure Phase Angle Contour Lines

Reduced freqency:
2.2
Theta mode:
1
Data taken from [1]

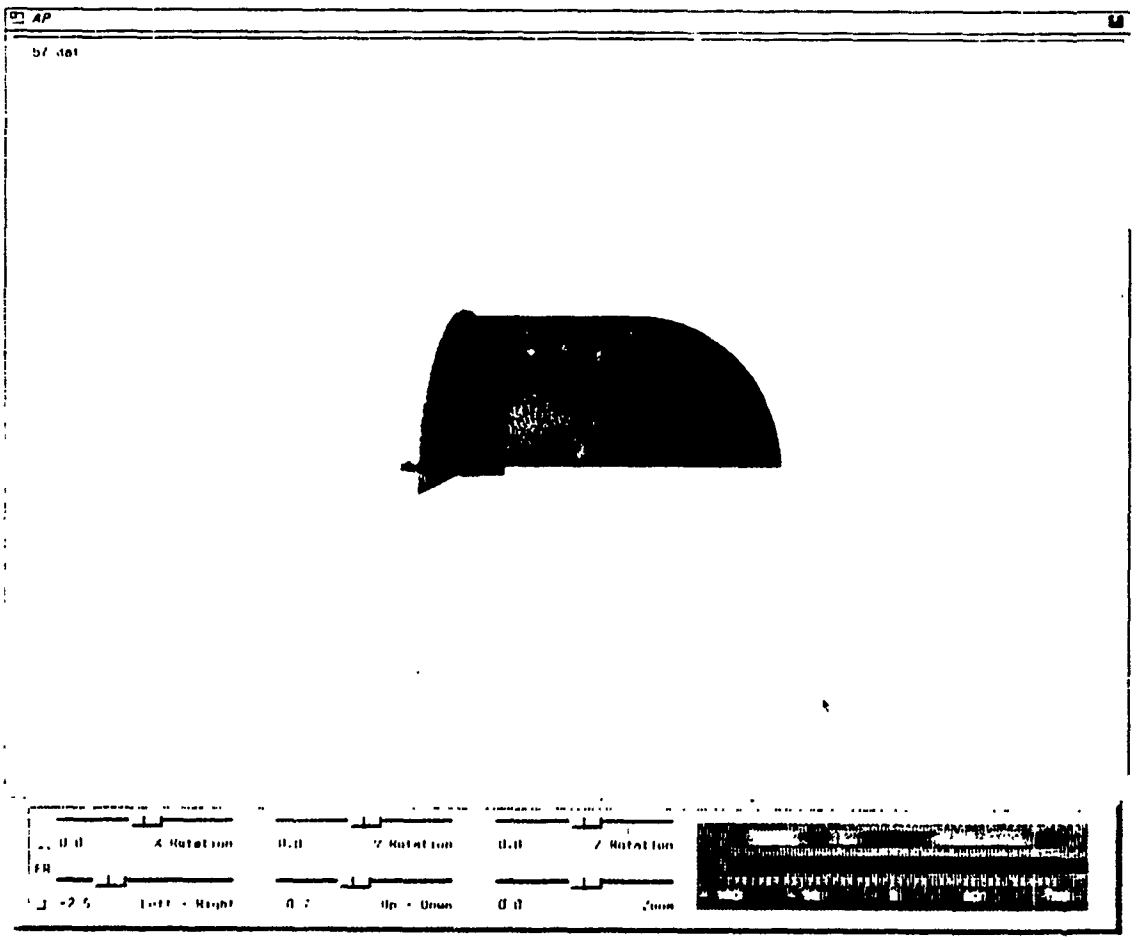

Figure 9 : C2 Model in Animation Postprocessor

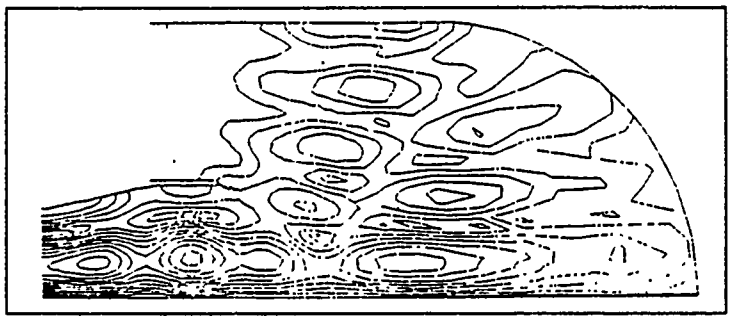

Acoustic Pressure
Amplitude Contour
Lines

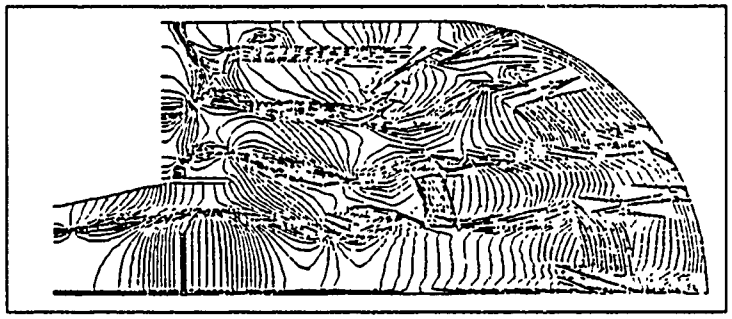

Acoustic Pressure
Phase Angle
Contour Lines

Reduced frequency:
6.58
Theta mode:
1
Data taken from [1]

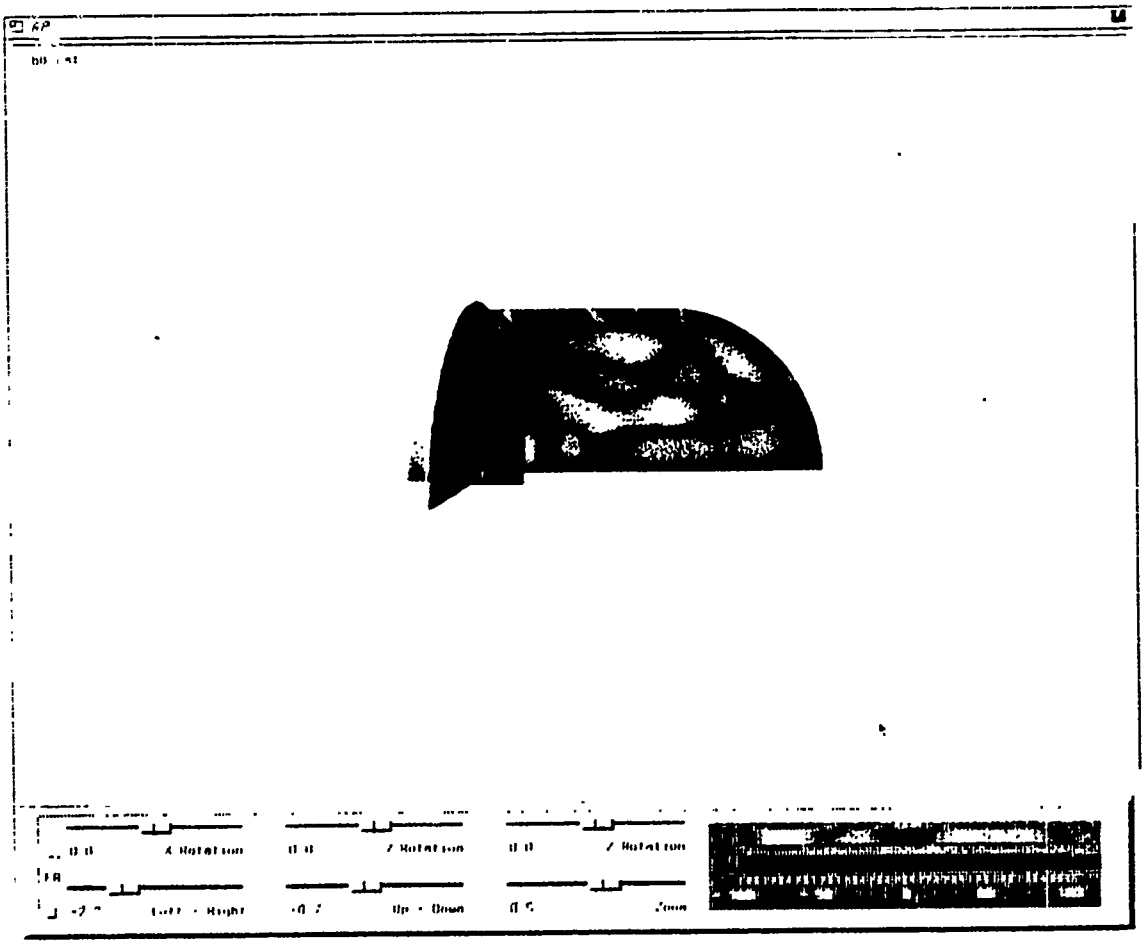

Figure 10 : C2 Model in Animation Postprocessor

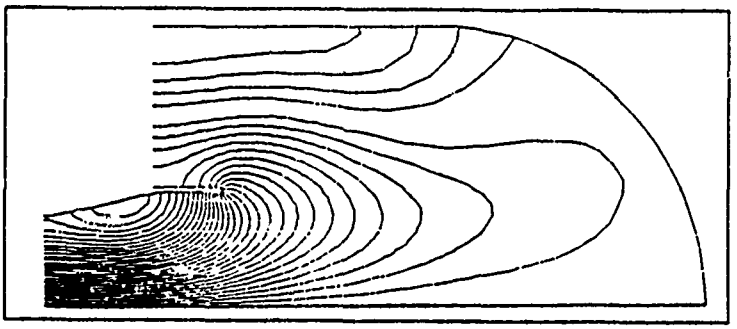

Acoustic Pressure Amplitude Contour Lines

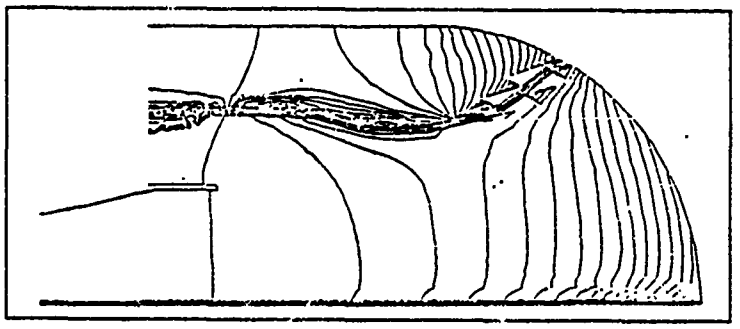

Acoustic Pressure Phase Angle Contour Lines

Reduced freqency:
2.2
Theta mode:
1
Data taken from [1]

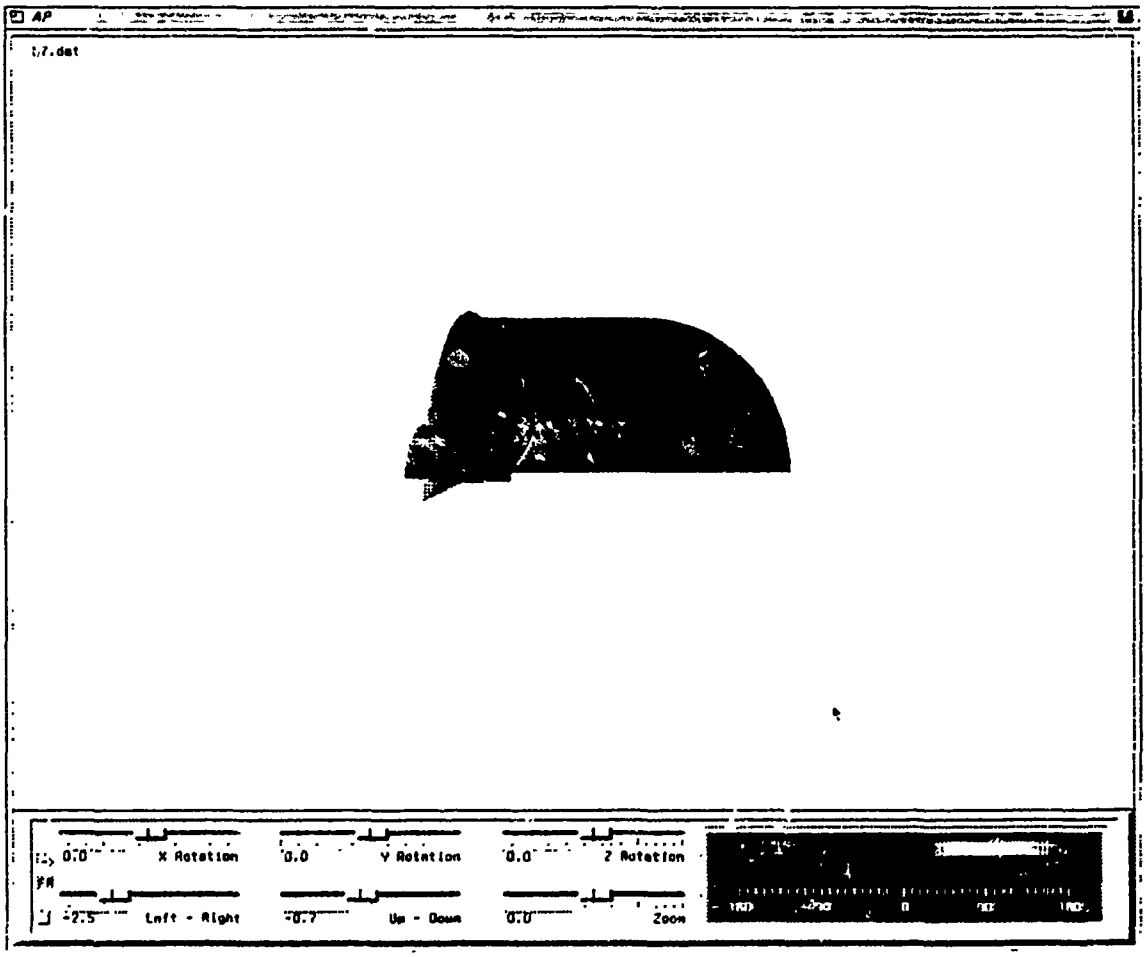

Figure 11: C2 Model in Animation Postprocessor

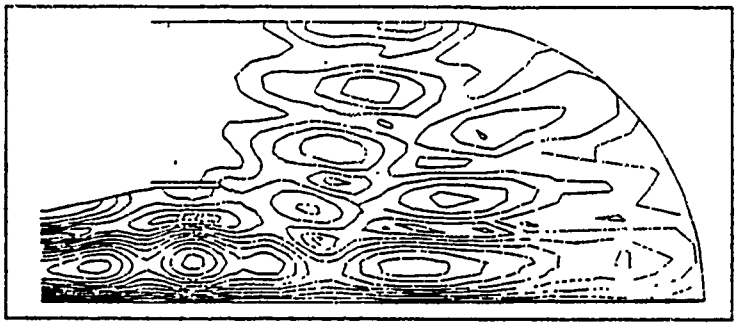

Acoustic Pressure
Amplitude Contour
Lines

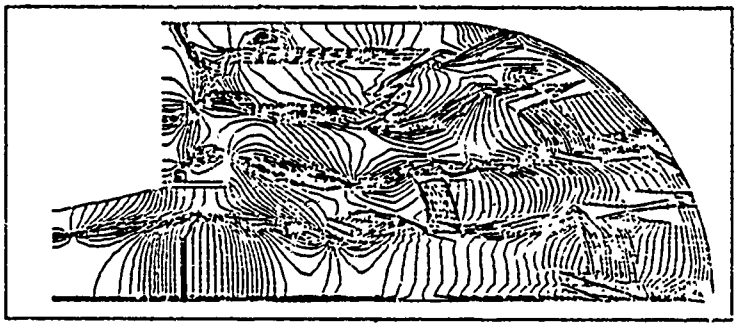

Acoustic Pressure
Phase Angle
Contour Lines

Reduced frequency:
6.58
Theta mode:
1
Data taken from [1]

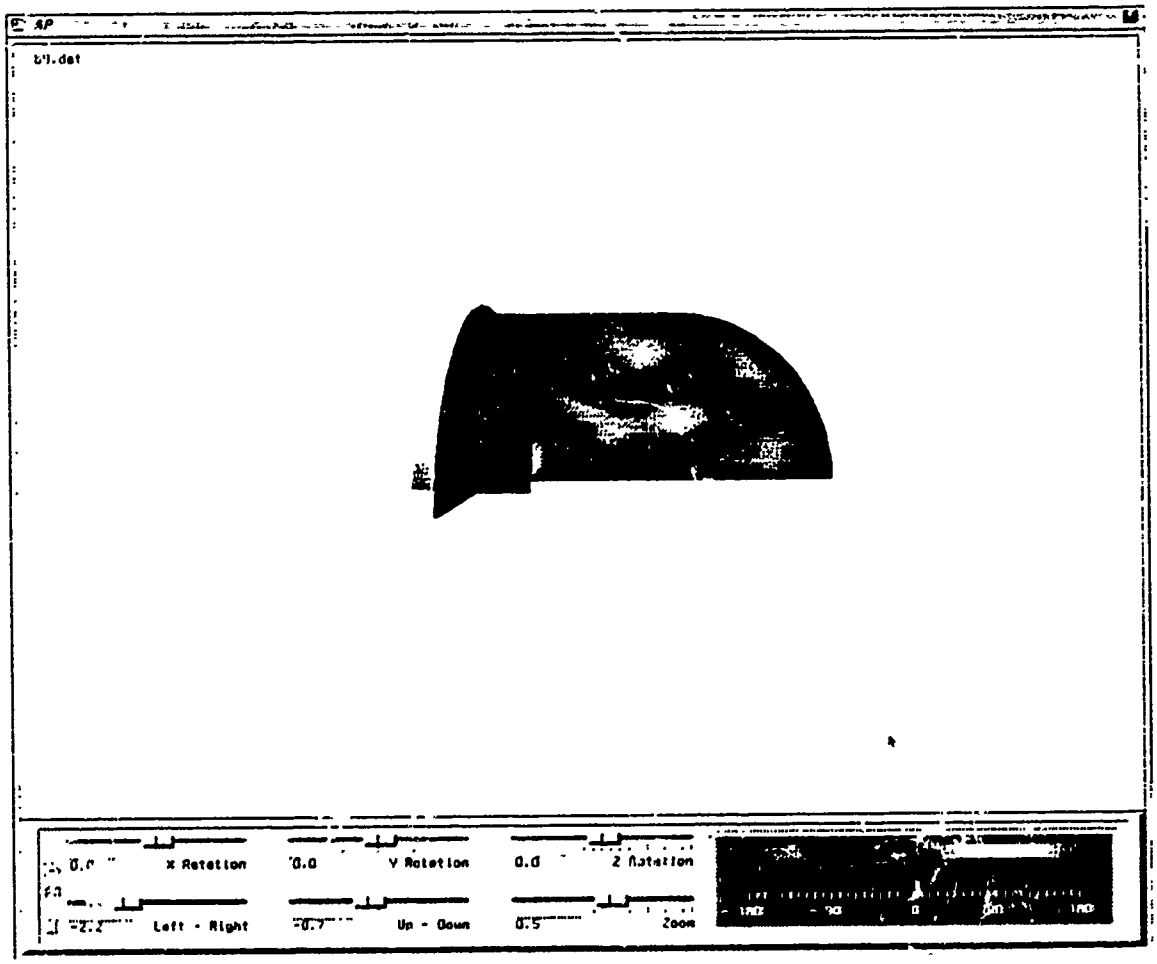

Figure 12: C2 Model in Animation Postprocessor

1990 USAF-UES SUMMER FACULTY RESEARCH PROGRAM

GRADUATE STUDENT RESEARCH PROGRAM

Sponsored by the

AIR FORCE OFFICE OF SCIENTIFIC RESEARCH

Conducted by the

Universal Energy Systems, Inc.

FINAL REPORT

Exhaust Plume Prediction Method for Underexpanded Nozzles in Supersonic External Flows

Prepared by:	Kyle L. Nash
Academic Rank:	Graduate Student
Department and University:	Department of Aerospace Engineering The University of Alabama
Research Location:	Arnold Engineering Development Center Arnold AFB, TN 37389
USAF Researcher:	Brian Wettlaufer Sverdrup Technology, Inc., AEDC Group
Date:	1 August 1990
Contract No:	F49620-88-C-0053

Exhaust Plume Prediction Method for Underexpanded Nozzles in Supersonic External Flows

by

Kyle L. Nash

ABSTRACT

Screening of various diffusers for an engine ground test facility requires in-depth knowledge about the flowfield the diffuser must capture. Generally, information about the geometry of the engine exhaust plume, as well as the Mach number and pressure of the exhaust flowfield are required. The objective of this project has been the development of an analysis tool (computer program) for the prediction of underexpanded exhaust plumes discharging into supersonic external streams. Due to the expense of utilizing an advanced CFD approach on a supercomputer, a PC-based prediction that provides quick approximations was desired. Once the screening for the appropriate diffuser has been carried out, the results may then be validated through application of a more advanced Navier-Stokes solution on a supercomputer. Initial results of the analysis tool exhibit excellent agreement with experimental data.

Acknowledgements

I wish to thank the Air Force Systems Command and the Air Force Office of Scientific Research for sponsoring this research. I also wish to thank Universal Energy Systems for their excellent administration of this program which was greatly facilitated by the efforts of Carlos Tirres at Arnold Engineering Development Center.

My work under this program was greatly facilitated by the knowledge shared and advice given by Brian Wettlaufer. Also, the assistance received from Terri Brock was invaluable. Finally, I wish to thank Brent Bates for his encouragement and technical advice in the course of my work at AEDC.

I. INTRODUCTION:

As a premier testing facility, Arnold Engineering Development Center (AEDC) will be instrumental in testing to support the National Aerospace Plane (NASP) Program development. One of the most important aspects of the program will be testing of the newly developed SCRAMjet engines. The testing of these full-scale engines is expected to be carried out in the Aeropropulsion Systems Test Facility (ASTF) at AEDC. Significant modifications to the C-1 test cell of ASTF are required to support this advanced test project. Due to the complexity and scale of these modifications, it was decided that a sub-scale version of the modified hardware would provide useful information as well as confidence in the design before the full-scale modifications were implemented.

One of the most important components of the facility is the diffuser that will capture the exhaust from the test article, as well as the external flow around the test article. A unique requirement for the facility is that a region of subsonic flow be maintained in the diffuser. This provision will allow the test cell pressure to be controlled by adjusting the back pressure following the diffuser. Also, this diffuser must operate over the entire test range of the SCRAMjet engine. As a starting point in diffuser design, the plume shape and characteristics must be known.

II. OBJECTIVES OF THE RESEARCH EFFORT:

To support preliminary design of a diffuser, a personal-computer based program capable of approximating engine exhaust plumes was needed. The "first-cut" exhaust plume data determined by this program could then be used to screen various diffuser designs. More accurate analysis could be performed as a final step using a supercomputer-based analysis.

The exhaust flow of interest would be emitted from a two-dimensional nozzle into a supersonic external stream. The general arrangement of the freejet nozzle, test article, and diffuser is shown in Figure 1.

III. APPROACH:

Many computer simulations of exhaust plumes are currently available. Codes based on the method of characteristics (MOC) have existed for a number of years. Given the correct boundary conditions, these codes normally provide good solutions. Unfortunately, the MOC approach is cumbersome due to its complexity. It is also somewhat slow in execution. Another alternative is a parabolized Navier - Stokes solution method available at AEDC. This code would likely provide excellent solutions over the entire test cell; however, it requires a powerful supercomputer. Thus, the expense of the solutions forbids any type of parametric study that would require several runs of the code.

A simple approach that could be implemented in a code run inexpensively (i.e. on a personal computer) was needed. The most suitable candidate found was the Latvala method (Reference 5) which was based on initial research discussed in Reference 1. This method was originally developed for the prediction of underexpanded exhaust plumes from axisymmetric nozzles. The restriction to underexpanded exhaust plumes was decided to be acceptable since the test article would operate primarily in this range and since underexpansion represents the most severe case of exhaust spreading. The application of an axisymmetric method to a two-dimensional nozzle was also determined to be acceptable. Studies have found that two-dimensional plumes become rounded a short distance downstream and begin to behave similar to axisymmetric plumes (Reference 2). Also, for the sub-scale system being designed, the nozzle is nearly rectangular; therefore, the plume becomes rounded much closer to the nozzle exit plane.

The final concern was in accounting for the external supersonic flow which the Latvala method neglected. To solve this problem, a simplification of the flowfield was required (see Figure 2). If the underexpanded exhaust plume is treated as a solid boundary which turns the incoming supersonic external flow, an oblique shock is produced. An important parameter in determining the initial plume shape is the nozzle to freestream static pressure ratio. When the

oblique shock is encountered, the pressure ratio is altered; thus, resulting in a different plume shape. The new plume shape will in turn produce an oblique shock of different strength. Clearly, the process becomes iterative where there is one correct plume shape and oblique shock relationship. It is important to note that for the simplified flowfield, an average plume slope, θ is used to determine the correct oblique shock angle, β. By treating the plume as a solid boundary inclined at an angle θ to the freestream flow moving at Mach number M_∞, simple oblique shock theory yields the appropriate shock angle.

IV. LATVALA METHOD

A complete description of the Latvala Method may be found in Reference 5. A brief description is included here.

If a very small section of the plume boundary is considered (Figure 3), the relationship between the variables is given by:

$$\frac{\Delta X}{r_n} = \left(\frac{r_{n+1}}{r_n} - 1\right) \cot(\alpha_n - \delta/2) \qquad (1)$$

If the angle, α_n, is known at one point on the plume boundary and a turning angle δ is specified, the unknowns in equation 1 are $\Delta x/r_n$ and r_{n+1}/r_n.

For isentropic flow, the angle through which a flow

turns is the difference between the Prandtl-Meyer angles at two points in the flow. Thus, if the Prandl-Meyer angle, ν_n, is known at one point on the boundary, the Prandtl-Meyer angle at the adjacent point is equal to the original Prandtl-Meyer angle plus the angle through which the boundary turns, $\nu_{n+1} = \nu_n + \delta$. The Prandtl-Meyer angle of the boundary at the nozzle exit, after expanding to the ambient pressure, can be determined from the pressure ratio across the plume boundary. Therefore, the Prandtl-Meyer angle at any point along the boundary may be determined. For each Prandtl-Meyer angle there is a corresponding area ratio, A/A^*. If the area ratio is considered to be a spherical area ratio, then the radius ratio, r_{n+1}/r_n, is given as follows:

$$r_{n+1}/r_n = \frac{(A/A^*)_{n+1}(1 + \cos \alpha_{n+1})}{(A/A^*)_n \ (1 + \cos \alpha_n \ )} \qquad (2)$$

The values specified to start the computations are the nozzle exit Mach number, M_{noz}, ratio of specific heats, γ, nozzle angle, θ_N, and the ambient to stagnation pressure ratio, P_∞/P_0. The initial flow inclination is given by:

$$\alpha_1 = \nu_1 - \nu_j + \theta_N \qquad (3)$$

where ν_1 is the Prandtl-Meyer angle corresponding to the specified pressure ratio and ν_j is the Prandtl-Meyer angle corresponding to the nozzle exit Mach number. The area ratio, A/A^* is that which corresponds to ν_1. Once α_1 and

A/A^* are determined, the plume boundary point can be determined. The remaining points are found through the specified turning angle, δ, with the following relationships:

$$\nu_{n+1} = \nu_n + \delta \qquad (4)$$

$$\alpha_{n+1} = \alpha_n - \delta \qquad (5)$$

This process is repeated until the inclination is zero.

V. RESULTS

The first stage of this project was to utilize the original Latvala method to develop a program for predicting plume expansion into a quiescent environment. Once validation was complete on the first stage, the external flow handling method was added. As mentioned earlier, an average plume slope is required in this iterative process. It was found that the determination of this average plume slope could have a significant effect on the resulting plume shape solution. If only the first several boundary points were used in determining the plume slope, the oblique shock produced would be of high strength, resulting in a large rise in the external pressure. This pressure rise would in turn prevent the plume from expanding correctly further downstream. Studies on this effect indicated that the best results were obtained by using the slope of a line from the nozzle lip to points approximately six nozzle exit radii downstream. A possible explanation of these results is that

plume boundaries with fairly similar pressure ratios tend to be similar in geometry near the nozzle exit. The differences occur further downstream where the plume boundaries begin to approximate straight lines. If this more important (and larger) area is used to dictate the plume slope, then better results are obtained.

The code was validated with both experimental and theoretical data (Refs. 3, 4 and 6). It was found to provide excellent plume approximations (see Figure 4), particularly at lower freestream Mach numbers where it will be applied in the sub-scale system design program. Also, the code quickly generates the plume boundaries, an important asset when performing parametric studies (Figure 5). Based on the code validation studies as well as those of E. K. Latvala, the plume approximations can be considered accurate to approximately seven nozzle exit radii downstream.

VI. RECOMMENDATIONS

An important area that may be worth further study is that of two-dimensional exhaust plumes. Appropriate 2-D exhaust plume data was not available in the course of this research; thus, preventing an investigation of the assumption that an axisymmetric method could yield good approximations. If greater accuracy were desired, there are methods of refining a predicted axisymmetric plume to obtain

a 2-D plume solution (Reference 2). This approach could prove beneficial.

REFERENCES

1. Adamson, T.C., Jr., J.A. Nicholls, "On the Structure of Jets From Highly Underexpanded Nozzles Into Still Air," Journal of Aero/Space Sciences, January 1959, pp. 18-24.

2. Brooke, D., D.J. Dusa, A.P. Kuchar, B.M. Romine, "Initial Performance Evaluation of 2DCD Ejector Exhaust Systems," AIAA-86-1615, June 1986.

3. Henson, J.R., J.E. Robertson, "Methods of Approximating Inviscid Jet Boundaries for Highly Underexpanded Supersonic Nozzles," AEDC-TDR-62-7, May 1962.

4. Herron, R.D., "Investigation of Jet Boundary Simulation Parameters for Underexpanded Jets in a Quiescent Atmosphere," AEDC-TR-68-108, September 1968.

5. Latvala, E.K., "Spreading of Rocket Exhaust Jets at High Altitudes," AEDC-TR-59-11, June 1959.

6. Pindzola, M., "Jet Simulation in Ground Test Facilities," AGARDograph 79, November 1963.

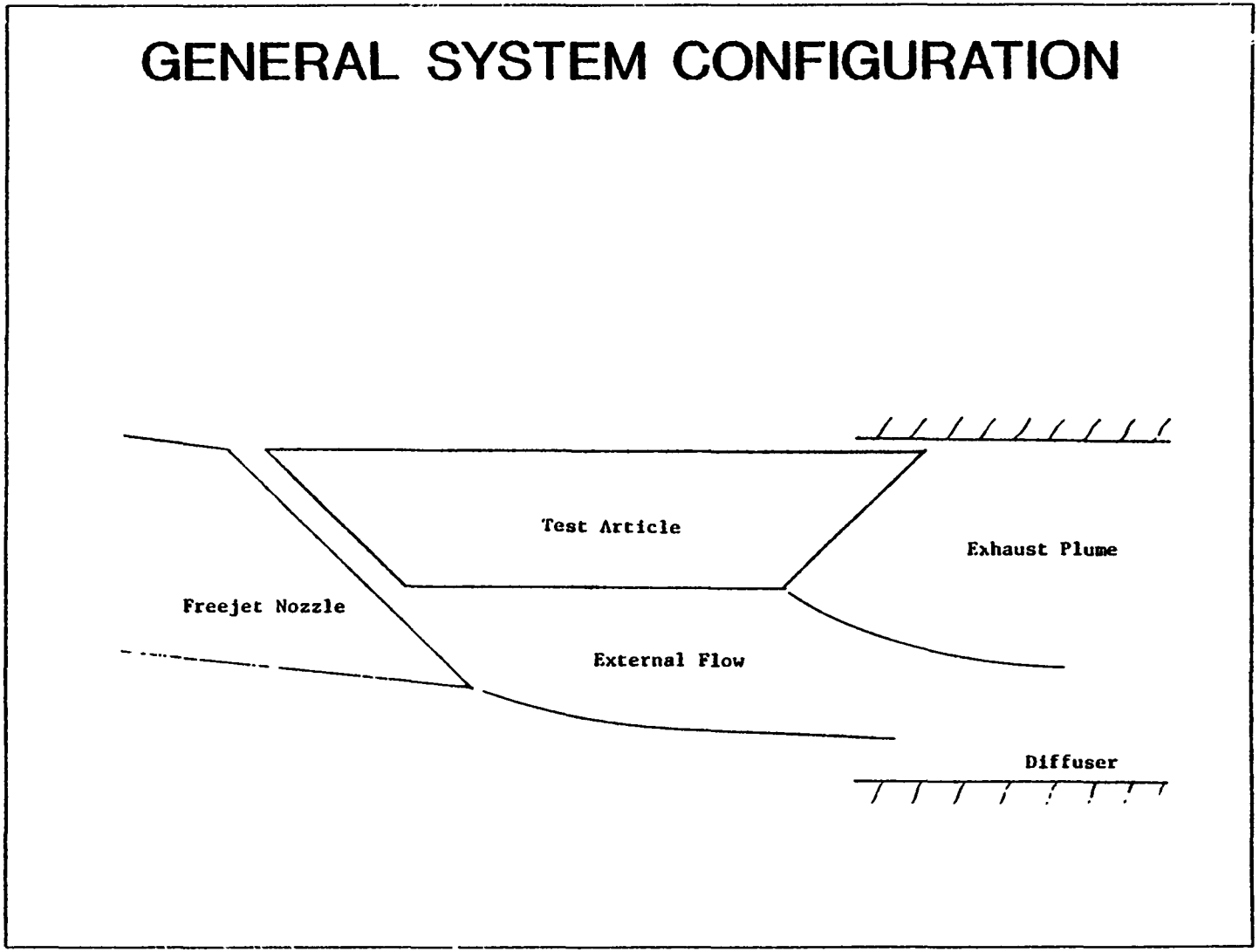
GENERAL SYSTEM CONFIGURATION
Test Article
Exhaust Plume
Freejet Nozzle
External Flow
Diffuser

FIGURE 1

SIMPLIFIED FLOWFIELD MODEL

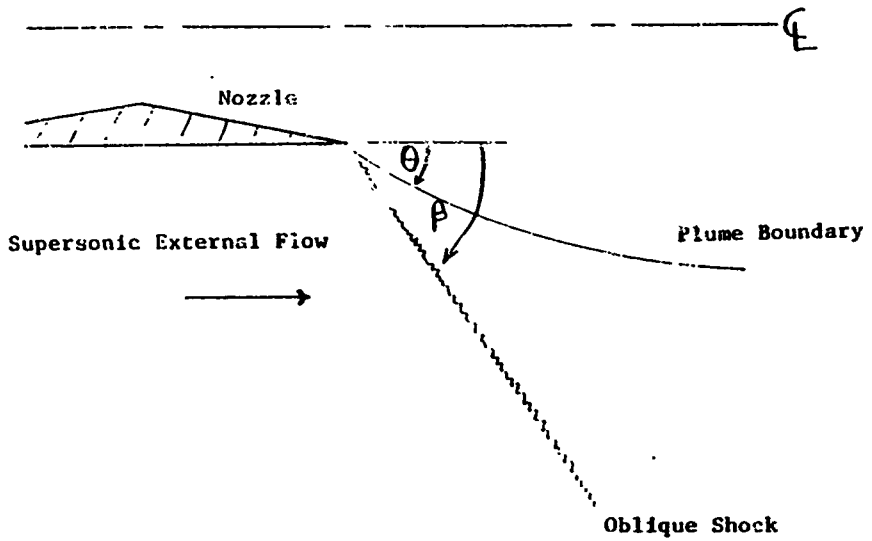

FIGURE 7

LATVALA PLUME PREDICTION METHOD

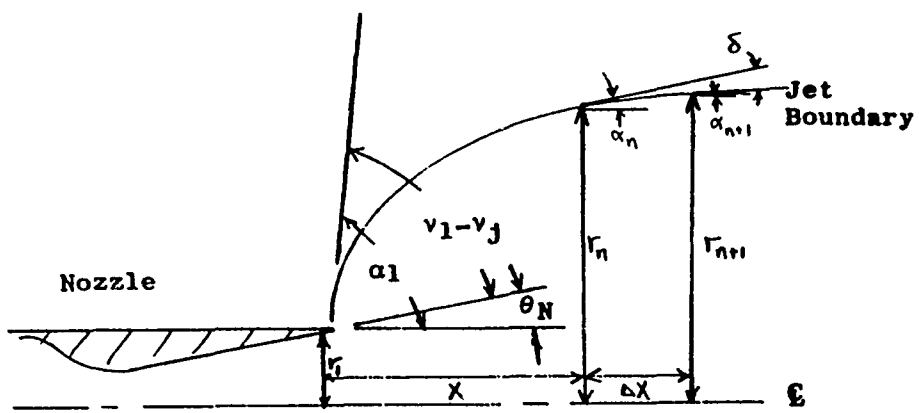

FIGURE 3

THIS
PAGE
IS
MISSING
IN
ORIGINAL
DOCUMENT

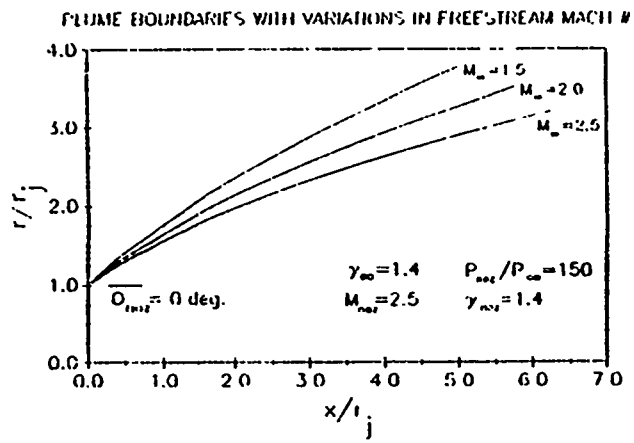
PLUME BOUNDARIES WITH VARIATIONS IN FREESTREAM MACH #
4.0
3.0
2.0
1.0
0.0
r/r_j
M_∞=1.5
M_∞=2.0
M_∞=2.5
γ_∞=1.4
P_noz/P_∞=150
θ_noz= 0 deg.
M_noz=2.5
γ_noz=1.4
0.0 1.0 2.0 3.0 4.0 5.0 6.0 7.0
x/r_j

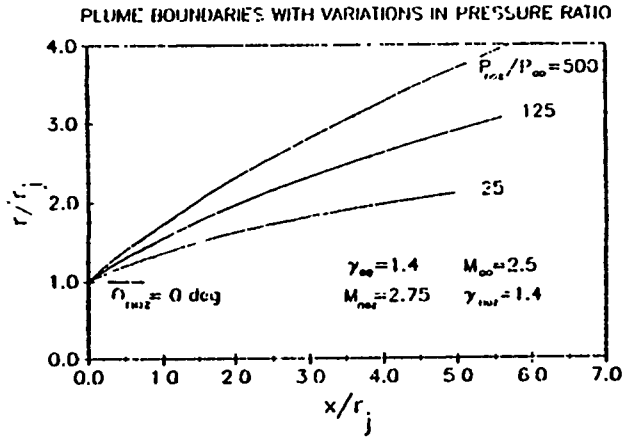
PLUME BOUNDARIES WITH VARIATIONS IN PRESSURE RATIO
4.0
3.0
2.0
1.0
0.0
r/r_j
P_noz/P_∞=500
125
25
γ_∞=1.4
M_∞=2.5
θ_noz= 0 deg
M_noz=2.75
γ_noz=1.4
0.0 1.0 2.0 3.0 4.0 5.0 6.0 7.0
x/r_j

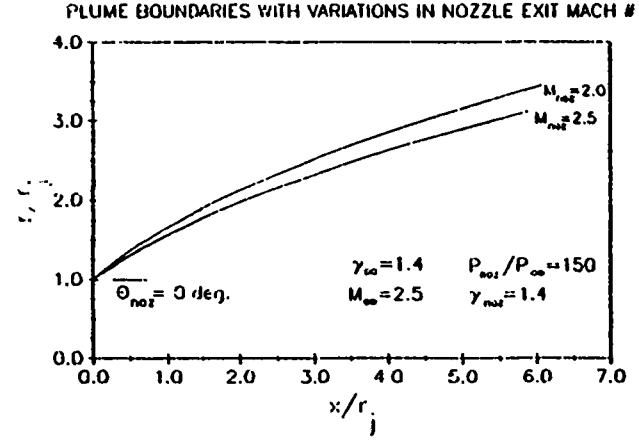
PLUME BOUNDARIES WITH VARIATIONS IN NOZZLE EXIT MACH #
4.0
3.0
2.0
1.0
0.0
M_noz=2.0
M_noz=2.5
γ_∞=1.4
P_noz/P_∞=150
θ_noz= 0 deg.
M_∞=2.5
γ_noz=1.4
0.0 1.0 2.0 3.0 4.0 5.0 6.0 7.0
x/r_j

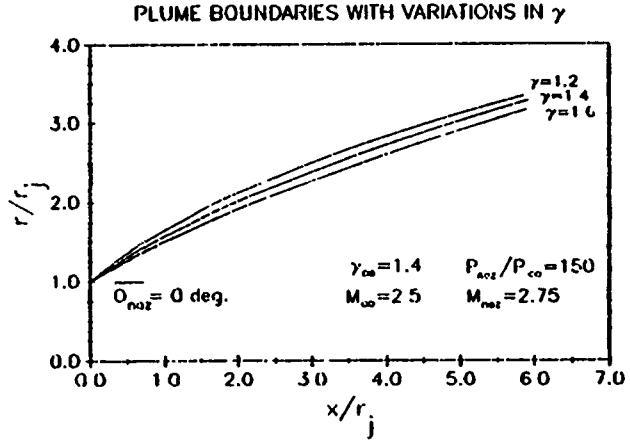
PLUME BOUNDARIES WITH VARIATIONS IN γ
4.0
3.0
2.0
1.0
0.0
r/r_j
γ=1.2
γ=1.4
γ=1.6
γ_∞=1.4
P_noz/P_∞=150
θ_noz= 0 deg.
M_∞=2.5
M_noz=2.75
0.0 1.0 2.0 3.0 4.0 5.0 6.0 7.0
x/r_j

FIGURE 5

1990 USAF-UES SUMMER FACULTY RESEARCH PROGRAM/

GRADUATE STUDENT RESEARCH PROGRAM

Sponsored by the

AIR FORCE OFFICE OF SCIENTIFIC RESEARCH

Conducted by the

Universal Energy Systems, Inc.

FINAL REPORT

Application of an Expert System to Compressor Stall Warning

Prepared by:	John M. Sebghati
Academic Rank:	Master's Degree candidate
Department and	Aerospace Engineering
University:	University of Tennessee Space Institute
Research Location:	Arnold Engineering Development Center
	Arnold AFB, TN 37389
USAF Researcher:	Richard G. Womack
Date:	17 Sept 90
Contract No:	F49620-88-C-0053

Application of an Expert System to Compressor Stall Warning

by

John M. Sebghati

ABSTRACT

Stress data from a select number of compressor blades in a 16 ft. transonic wind tunnel located at the Arnold Engineering Development Center (AEDC), Arnold Air Force Base, was collected and, along with some synthesized stall stress data, used by an expert system to construct a knowledge base. The expert system and its knowledge base were then tested, showing a high degree of accuracy. With this system, a more accurate method of detecting stalls in a wind tunnel's compressor is available.

Acknowledgements

I wish to thank the Air Force Systems Command and the Air Force Office of Scientific Research for sponsorship of this research. Also, thanks should go to Universal Energy Systems for aiding me in all administrative and directional aspects of this program.

The experience I gained during this program has aided me immensely on account of a number of people. Dr. Ching F. Lo from the University of Tennessee Space Institute provided me with the overall guidance and direction. Richard Womack's help in some of the detailed aspects of my research has proven to be invaluable. Thanks must also go to Gary Jarrell, Walter Bishop, and Zhi "George" Shi for passing along some of their wisdom onto me in a number of areas.

I. INTRODUCTION:

The detection of a stall in the compressor of a wind tunnel is not an easy task. The current method being used at the Arnold Engineering Development Center (AEDC) involves the use of strain gauges located on a select number of compressor blades, and their continuous monitoring by a human operator. The onset of a stall may go unnoticed for a period of time on account of the difficulty for a human eye in detecting a change in the stress trace and through human error, a normal stress trace can be found in Figure 1. The results of a stall could prove disastrous, with major damage occurring to the compressor blades and the wind tunnel's structure, along with the possibility of human injury.

AEDC houses a large number of wind tunnels, including 16 ft. transonic and supersonic tunnels. They are concerned with the damage that may occur as a result of a compressor stall going undetected. A diagram of the transonic wind tunnel's compressor, C1, can be found in Figure 2. As a result of this, a more sensitive and accurate method for detecting stalls was desired.

My research interests have included the construction of an expert system developer through the use of artificial intelligence technology. Dr. Ching F. Lo from the University of Tennessee Space Institute has a contract with AEDC for the construction of this developer. This developer would allow the user to build specific "monitoring type" expert systems which would examine the various equipment used in propulsion systems' ground testing

facilities and accrues system performance information in a dynamic knowledge base. The resultant expert system would have the capability of monitoring the performance of ground support equipment for testing facilities. It would be able to analyze the information for possible abnormalities, display it for on-line monitoring, and/or archive it for future examination. This system would use a form of pattern recognition, like the nearest neighbor rule, to classify the performance of the equipment as being normal or with fault. The result of this interest led to my assignment at the Arnold Engineering Development Center.

Through this system, the life of machine components would be increased through a greater awareness of machine conditions. It would provide engineers with diagnostic information enabling them to make informed decisions on machinery repair. It would also be able to provide tools for the establishment of a more cost-effective maintenance approach.

II. OBJECTIVES OF THE RESEARCH EFFORT:

Stress data from a select number of wind tunnel compressor blades was needed for input into an expert system in order to create a knowledge base. It was my assignment as a participant in the 1990 Graduate Student Research Program (GSRP) to initiate the acquisition of the appropriate data and to convert it to the compatible format required for utilization by this expert system. Once the knowledge base is created, further stress data is needed for testing and modifying the expert system in order to check its accuracy.

III.

a. Stress data from a select number of compressor blades was recorded on magnetic tape during some tests in the 16 ft. transonic wind tunnel at a Mach number of 0.6. This data was then run through a Spectrum Analyzer resulting in a frequency spectrum. The Spectrum Analyzer was connected to a personal computer and "snapshots" of the frequency spectrum were recorded to disk as Ascii files using a piece of commercial software entitled STAR. In Figure 3, one of these "snapshots" can be found for a compressor operating under normal conditions. Peaks can be seen at 10 Hz, which is the rotational speed of the compressor, and at the harmonics of 10 Hz. The natural frequency for this compressor is 27.5 Hz, which accounts for the dominate frequency at 30 Hz.

There was a desire to incorporate off-the-shelf software in the construction of the expert system. The Arnold Engineering Development Center desired that the system be IBM compatible. This led to the use of an expert system builder entitled VP-Expert. A basic expert system was constructed by Zhi "George" Shi at the University of Tennessee Space Institute.

In order to form a knowledge base and to test the system, stress data from normal operating conditions and from stall conditions was needed. The normal operating condition stress data was already available but there was no room in the tunnel's schedule for the acquisition of data during stall conditions. In order to gain this data for the knowledge base, a

computer program was written which modified normal stress data into what stall stress data roughly looks like. This was done with the aid of Richard Womack who from experience was able to show what the stress data would look like during stall conditions by taking an example of normal data and sketching over it. The program, utilizing this example, then turned out data like that of Figure 4. This is a frequency spectrum of stress data from a simulated run during a compressor stall. The differences between this figure and Figure 3 can easily be seen: the natural frequency dominates the graph, the amplitudes at 6.5 Hz and 12.5 Hz grow, and the 70 Hz amplitude diminishes.

The expert system utilizes a program which picks out the amplitudes at certain frequencies, the harmonics of 10 Hz and those amplitudes that are significantly changed by the onset of a stall. These amplitudes are then formed into a n-dimensional vector, n being the number of amplitudes picked out. Using normal stress data the expert system forms a normal region in space, and likewise with the stall stress data forms a stall region. This then makes up the knowledge base. A form of pattern recognition, called the nearest neighbor classification rule, is then used to check the new data. This method equally divides the n-dimensional space into regions dominated by the normal and stall stress data. When deciding how to classify new data, as normal or stall, its vector location in space is checked. It is then classified according to which region it falls in. Points on the boundary would be classified as unknown and left to the operator to decide.

b. The result of this is a basic expert system which can be used to monitor a wind tunnel's compressor. This system is hooked up to strain gauges through the Spectrum Analyzer. A knowledge base is then formed by training the system with some previously recorded stress data from normal operating and stall conditions. The system would now be able to distinguish between these two conditions. Actual data, after being processed by the Spectrum Analyzer, is passed on to the expert system. The system will examine its knowledge base of known classes and decide whether or not it can identify the class that the data falls in. If it can decide, it offers the operator an opportunity to view the data and then continues to monitor the compressor blades through the stain gauges. If the expert system cannot identify the class, it informs the operator and offers a frequency spectrum view of the data. Once the class has been decided on, it is added to the knowledge base and the expert system continues in its monitoring.

Initial tests on the expert system have been completed with favorable results. The system identified the correct class almost every single time using a completely new set of stress data.

IV RECOMMENDATIONS:

a. Because of equipment problems and the lack of time, my assignment wasn't completed. There is a need for some true stall data for incorporation into the knowledge base and this will have to be accomplished when there is time to run the compressor at stall conditions. Up until now only synthesized stall data has been used.

b. More testing and modification of the expert system is needed.

c. Once the system is fully functional, it can be incorporated into the compressor monitoring system and taught the difference between normal and stall stress data. It will then be able to complement the human operator in monitoring the compressor during wind tunnel operations.

d. Eventually, a generic expert system produced from the modification of the current system will have the ability to be set up so as to monitor equipment besides a wind tunnel's compressor and for characteristics other than stress.

REFERENCES

Cover, Thomas M., "Estimation by the Nearest Neighbor Rule", IEEE Transactions on Information Theory, Vol. IT-14, January 1968, pp. 50-55.

Cover, Thomas M., and P.E. Hart, "Nearest Neighbor Pattern Classification", IEEE Transactions on Information Theory, Vol. IT-13, January 1967, pp. 21-27.

Harmon, Paul, and David King, Expert Systems, Taipei, Taiwan R.O.C., Distinguishing Book Company, 1985.

Tou, J.T., and Rafael C. Gonzalez, Pattern Recognition Principles, Reading, Massachusetts, Addison-Wesley Publishing Company, 1974.

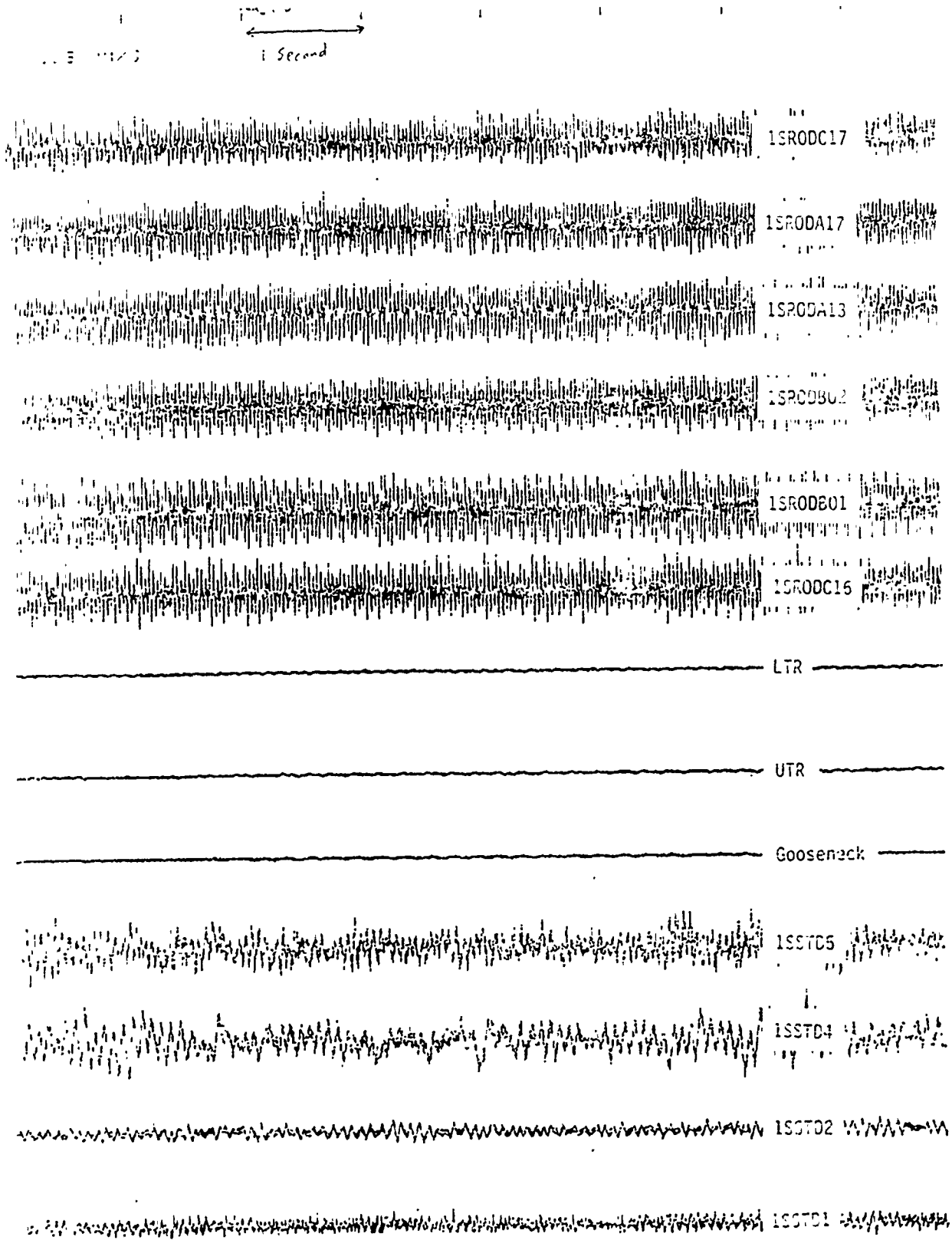

Figure 1 Typical Compressor C1 Stress Traces (25mm/sec)

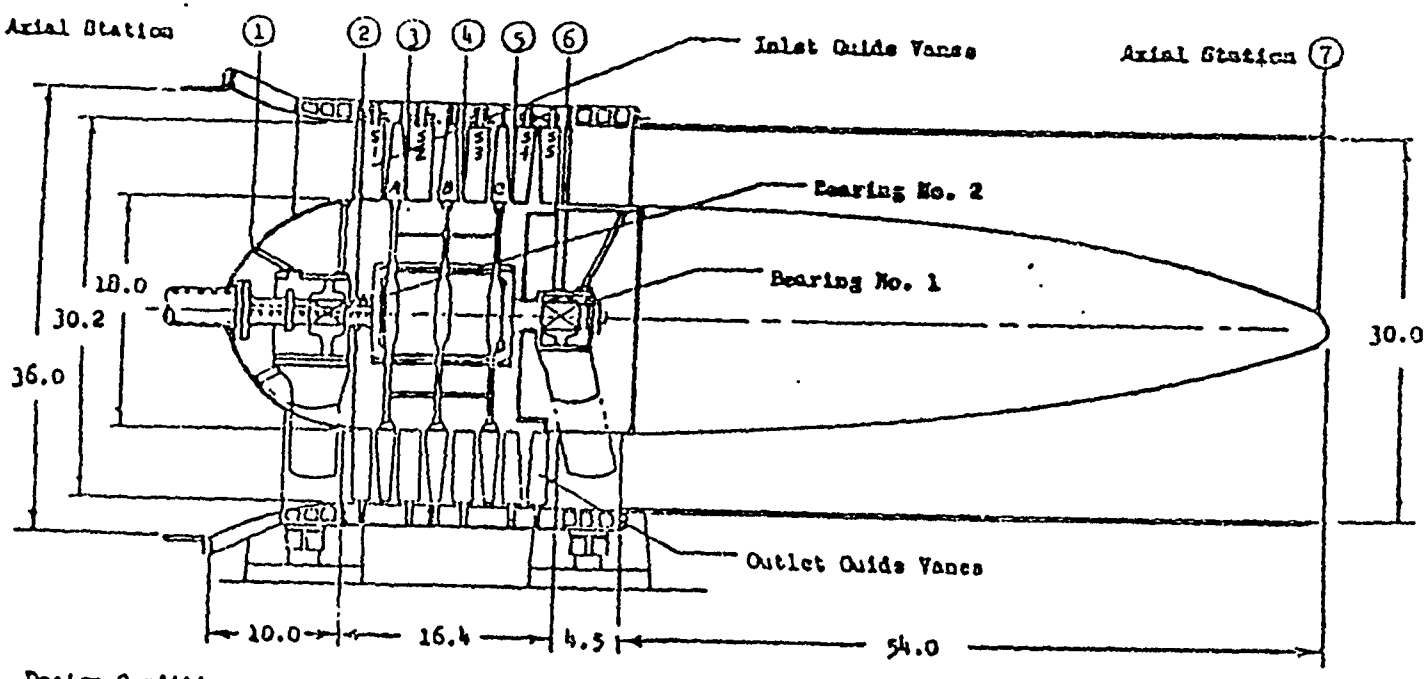

Design Conditions

Tip Speed 942 ft/sec (Absolute)
Hub Speed 565 ft/sec (Absolute)
Design Pressure Ratio 1.385
Design Inlet Volume Flow 200,000 cfs
Flow Coefficient 0.47
Work Coefficient 0.308
Inlet Axial Velocity 442 ft/sec

Figure 2 Compressor C1

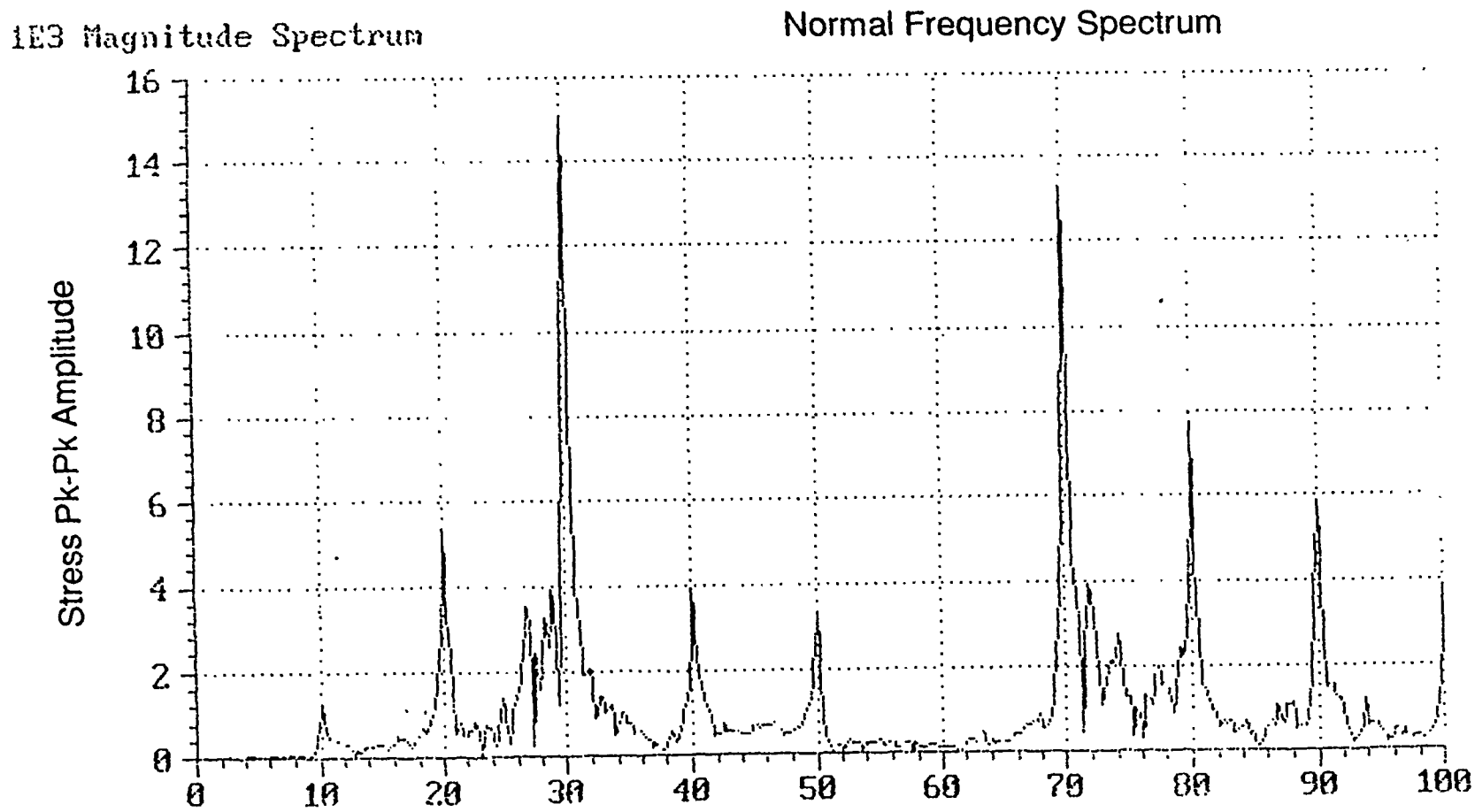
1E3 Magnitude Spectrum
Normal Frequency Spectrum
Stress Pk-Pk Amplitude
16
14
12
10
8
6
4
2
0
0
10
20
30
40
50
60
70
80
90
100
Frequency, Hz

Figure 3

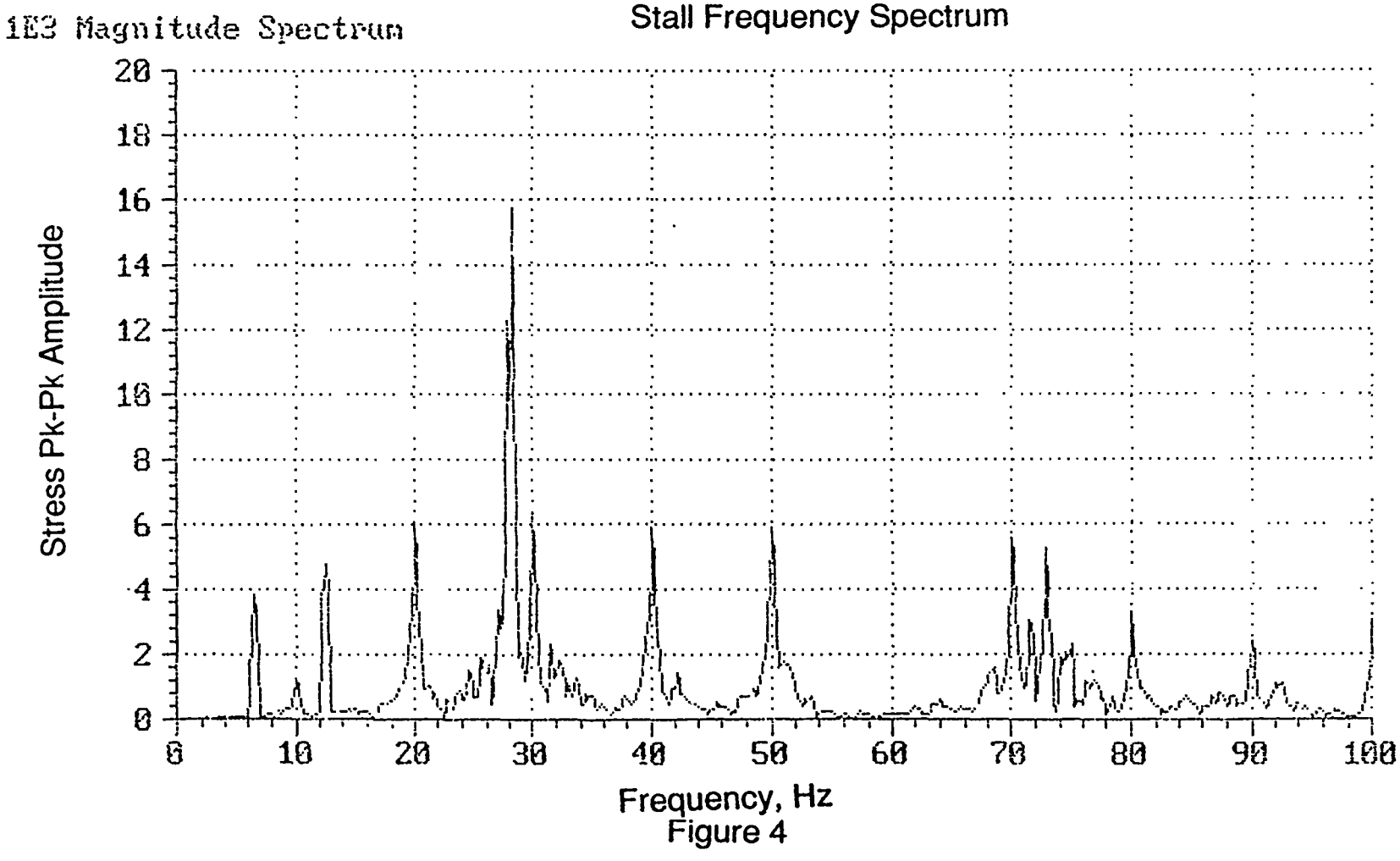
1E3 Magnitude Spectrum
Stall Frequency Spectrum
Stress Pk-Pk Amplitude
20
18
16
14
12
10
8
6
4
2
0
0
10
20
30
40
50
60
70
80
90
100
Frequency, Hz

Figure 4

1990 USAF-UES SUMMER FACULTY RESEARCH PROGRAM

GRADUATE STUDENT RESEARCH PROGRAM

Sponsored by the

AIR FORCE OFFICE OF SCIENTIFIC RESEARCH

Conducted by the

Universal Energy Systems, Inc.

FINAL REPORT

On the Hazard of Combustion Chamber Oscillations in a Large Freejet Test Cell

Prepared by:	John M. Russell, Sc.D. and Grant M. Watson, B.S.
Academic rank:	Associate Professor and Graduate Student, resp.
Department and	Mechanical and Aerospace Engineering
University:	Florida Institute of Technology
Research Location:	USAF/AEDC Arnold AFB Tennessee 37389
USAF Researcher:	Clyde H. Kunz
Date:	24 Aug 90
Contract No:	F49620-88-C-0053

Same Report as
Prof. John Russell
(Report # 16)

1990 USAF-UES SUMMER FACULTY RESEARCH PROGRAM/

GRADUATE STUDENT RESEARCH PROGRAM

Sponsored by the

AIR FORCE OFFICE OF SCIENTIFIC RESEARCH

Conducted by the

Universal Energy Systems, Inc.

FINAL REPORT

Uniform Rain/Ice Environment in the Aerothermal Wind Tunnel

Prepared by:	William Glenn Wilk
Academic Rank:	Graduate Student
Department and University	Aerospace Engineering The University of Alabama
Research Location:	Arnold Engineering Development Center Arnold AFB, TN 37389
USAF Researcher	Dwayne Carver, Calspan Corporation AEDC Division
Date:	July 20, 1990
Contract No:	F49620-88-C-0053

Uniform Rain/Ice Environment in the Aerothermal Wind Tunnel

by

William Glenn Wilk

ABSTRACT

The primary objective of the project was to evaluate new nozzles for an ice injection system to improve the particle spatial uniformity in the wind tunnel test section. The test apparatus records the ice particle distribution and initial velocity using shuttered, foil witness plates dropped vertically along the apparatus guide tracks. At the time of this writing, no tests have been completed; the results included herein are limited to those that document the design and fabrication of the test apparatus.

Acknowledgments

I wish to thank Mr. Dwayne Carver from Arvin Calspan Corporation for giving me guidance and support in achieving the project objectives. I would like to thank Mr Ernie Lucas for providing encouragement, motivation and a conducive work environment. Finally, acknowledgment must be given to the Air Force System Command and the Air Force Office of Scientific Research for providing the research opportunity through the administrative support of Universal Energy Systems, Inc.

I. INTRODUCTION:

The development of a means to study material erosion effects due to rain and ice impacting reentry vehicles, missiles, and supersonic vehicles was recognized by the Naval Aeroballistics Committee because "no existing facility can currently test full scale radomes under multiple particle impact conditions." There is not a theory that accurately predicts erosion on such radomes. Current facilities and techniques such as rocket sleds, whirling arm, ballistic ranges, and sounding rockets lack the capability to provide adequate simulation, eg, proper conditions, model size, loads on specimen, etc. ~~On the other hand, conventional wind tunnel can provide.~~

Engineers at the Arnold Engineering Development Center developed an ice particle injection system for the Aerothermal Wind Tunnel C in the von Karman Gas Dynamics Facility(Fig 1). Laboratory and operational tests have been performed in this facility. Performance aspects of run time, operating pressure and survivability of particles have been determined. At present, the primary deficiency is a nonuniform distribution of the ice particle cloud. The injected ice is concentrated along the center line and not uniformly distributed over the entire test section. Therefore, laboratory tests of new injection nozzles are to be performed in an attempt to correct this deficiency. The design of a moving, shuttered witness plate was

required to gain qualitative results of the new injection nozzles. This report documents the design and fabrication of this effort.

II. OBJECTIVES OF THE RESEARCH EFFORT:

The objective of the project was to evaluate several proposed injection nozzles in a controlled laboratory experiment to determine qualitatively, which new nozzle would improve the ice particle distribution in the wind tunnel test section.

III. APPROACH:

The current injection nozzle is a converging-diverging nozzle with a throat diameter of 0.156in(Fig 2). A slurry of liquid nitrogen and ice particles approximately 500um in diameter is injected into the stilling chamber of the supersonic wind tunnel. Ideally under these conditions, the liquid nitrogen should expand upon exiting the throat and flash to a vapor. Consequently, it should give the ice particles different, initial radial and axial velocities that once entrained in the tunnel flow field, would be distributed uniformly in the test section. However, with the current injection nozzle the liquid nitrogen fails to expand and quickly vaporize.

The simplest modification to the injection system to improve the uniformity is to place a conical center body

in the diverging portion of the nozzle. The point of the center body is placed at the throat of the nozzle. This physically forces the ice particles from the center line, increases the surface area of the liquid nitrogen and decreases the time it takes to flash to a vapor(Fig 3).

The nozzle evaluations required establishing a test apparatus that captured the distribution of the ice particles and if possible determined the velocity of the impacting particles. The design had to minimize any interference with ice particle cloud. Furthermore, the apparatus could not obstruct viewing of the test run.

IV. Apparatus Design:

a. The solution was the development of a wedged-shaped, shuttered, witness plate that fell vertically through a steel channel track as a blade in a guillotine(Fig 4). The characteristics of the ice injection system and the ice particle field, governed the primary design of the test apparatus as follows:

The ice injection system(Fig 1) was designed to deliver approximately five hundred thousand particles per second for thirty seconds. Typically, the number of particles impacting a one inch square area of a stationary foiled witness plate would destroy the witness plate. Therefore, the design included a shutter to control exposure time.

The distribution across any line that crosses the center of the injected particle cloud could be used to provide an accurate representation of the particle distribution of the complete field assuming an axisymmetric flow. Therefore, only the horizontal distribution through the center of the particle field was needed.

To measure the velocity of the ice particles, the entire shuttered witness plate was designed to drop vertically along a guide track. As a free fall apparatus in a 1g environment, the vertical velocity is a direct function of the drop height

$$\text{Velocity} = 2g * \text{Drop Height} \qquad (1)$$

Assuming a constant particle velocity and knowing the vertical velocity, the witness plate distance from the shutter entrance, and the particle impact shift from the "center line", it is possible to calculate the velocity of particles that entered the shutter. This approach to defining particle velocity is shown in figure 5.

The bulk of the lab test apparatus was the twelve foot guide tracks which were a combination of welded steel channels and angles. Beyond providing guidance for the moving witness plate, the channels provided the support for the triggering devise used to open the shutter of the witness plate at the moment it passed through the center of the ice particle cloud. The track had to minimize any horizontal and rotational motion to insure that the shutter

of the witness plate opened fully. Furthermore, the vertical velocity of the witness track was assumed to be the same as a free falling object and did not account for any friction. The vertical track could not restrict the fall of the witness plate(Fig 6).

b. At my departure (July 20), final assembly of the test apparatus, ice injection system, and support equipment was underway. The proposed new nozzles had been constructed. However, the actual experiment to verify the new nozzle designs had not begun.

V. Recommendations:

Following completion of the laboratory test of the new nozzles, additional tests in the Aerthermal Wind Tunnel C in the von Karman Gas Dynamics Facility should be run. The tests will insure that the new nozzle chosen from the initial laboratory test performs as expected under the varying conditions in the wind tunnel.

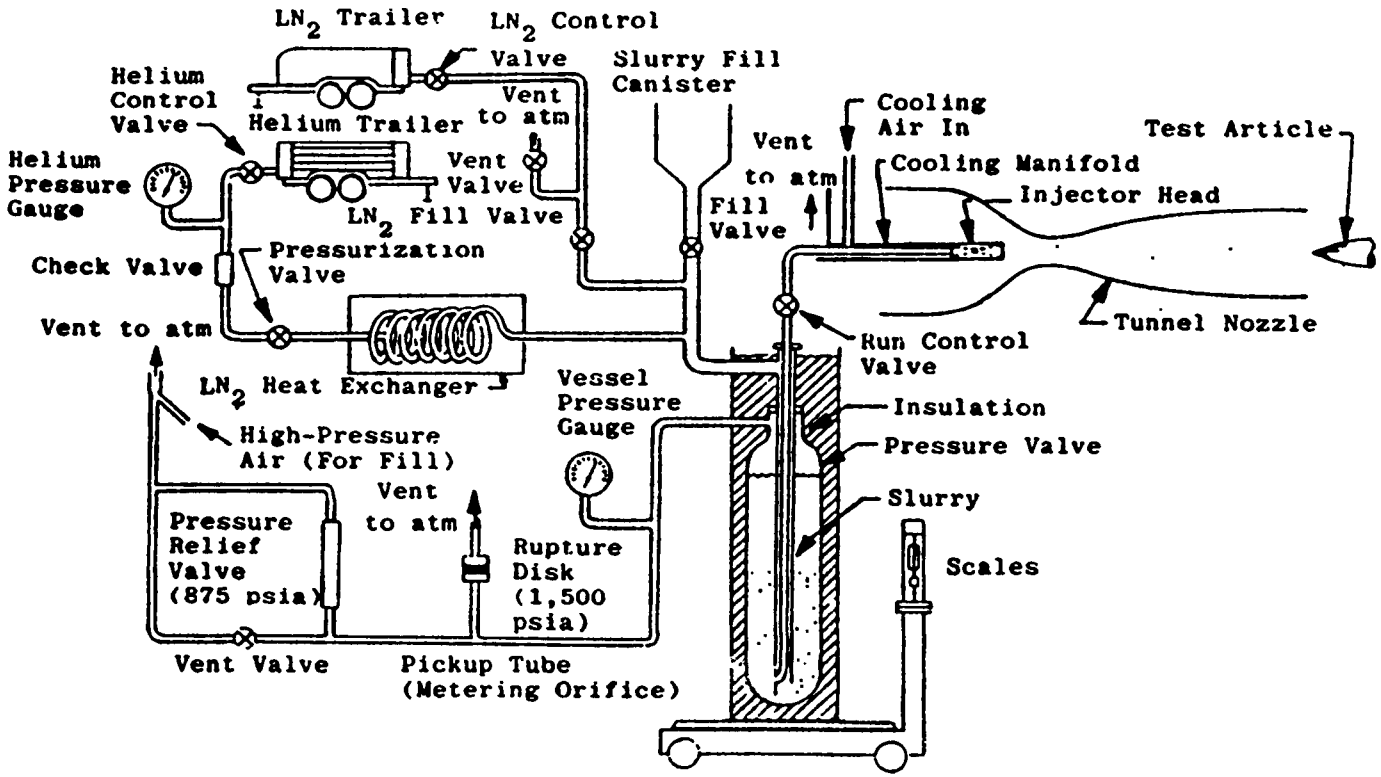

Fig 1. System Schematic

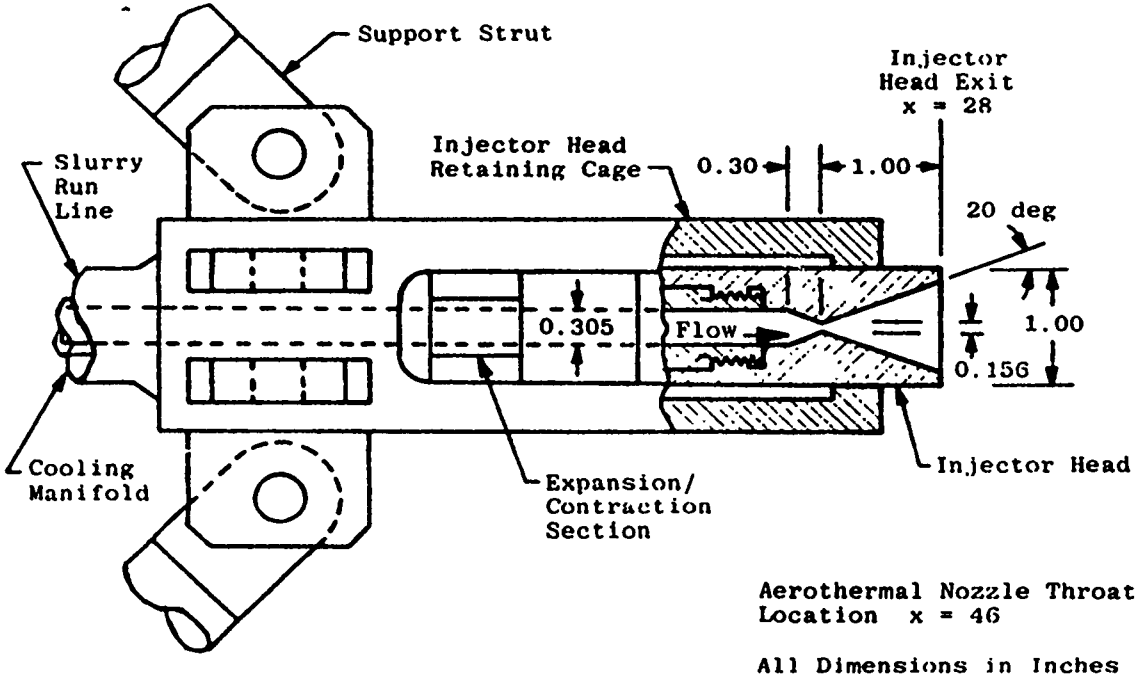

Fig 2. Injector Head Specifications

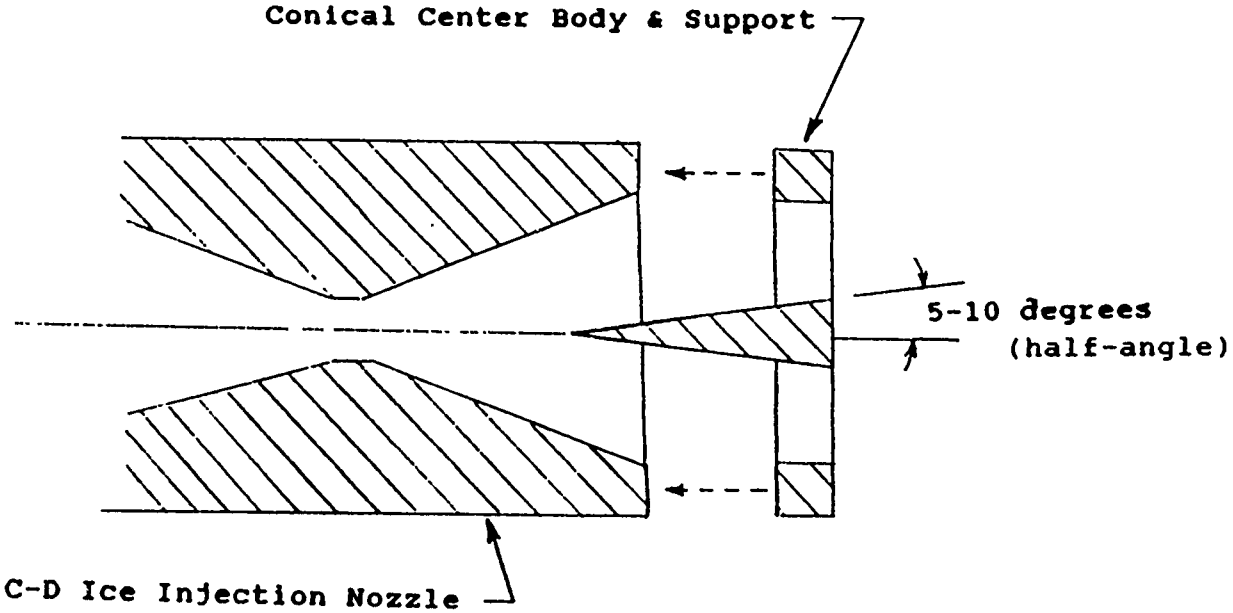

Fig 3. New Injection Nozzle

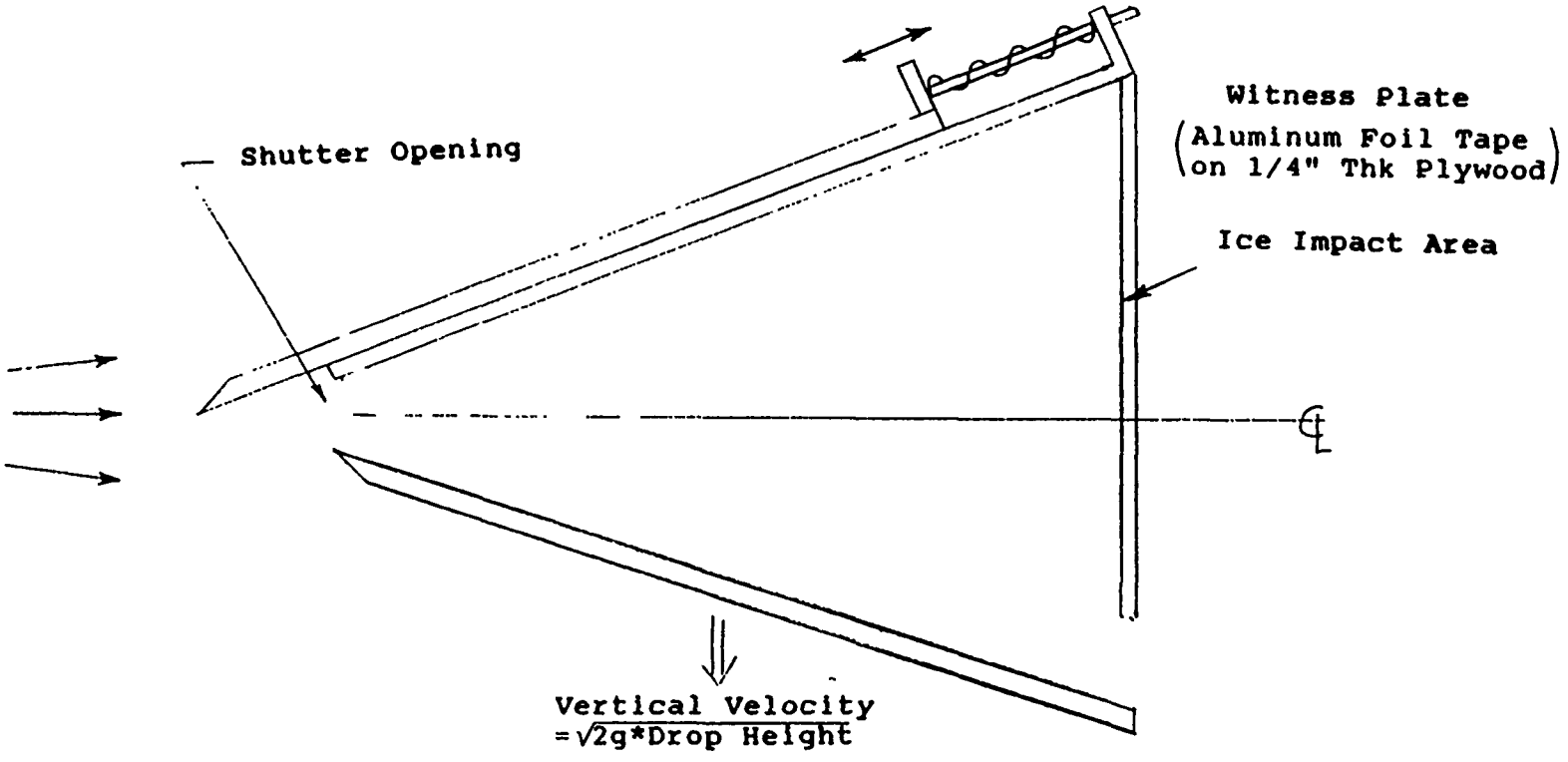

b. Side View

Figure 4. Concluded

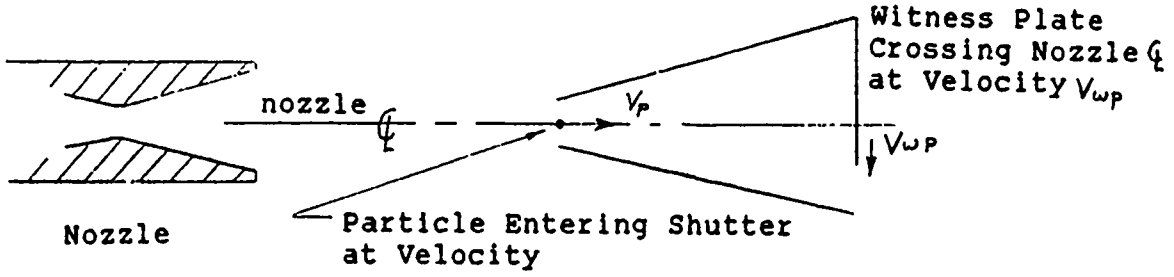

Side View as Particle Enters Shuttter

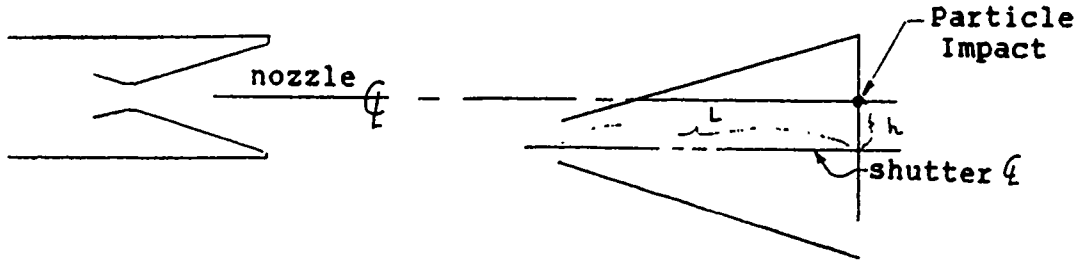

Side View as Particle Impacts Witness Plate

Assuming constant velocity of particle(V_p) and witness plate(V_{wp}) the particle velocity is defined as

$$V_p = \frac{L}{h} V_{wp}$$

Figure 5. Illustration of Particle Velocity Definition from Moving Shutter Witness Plate

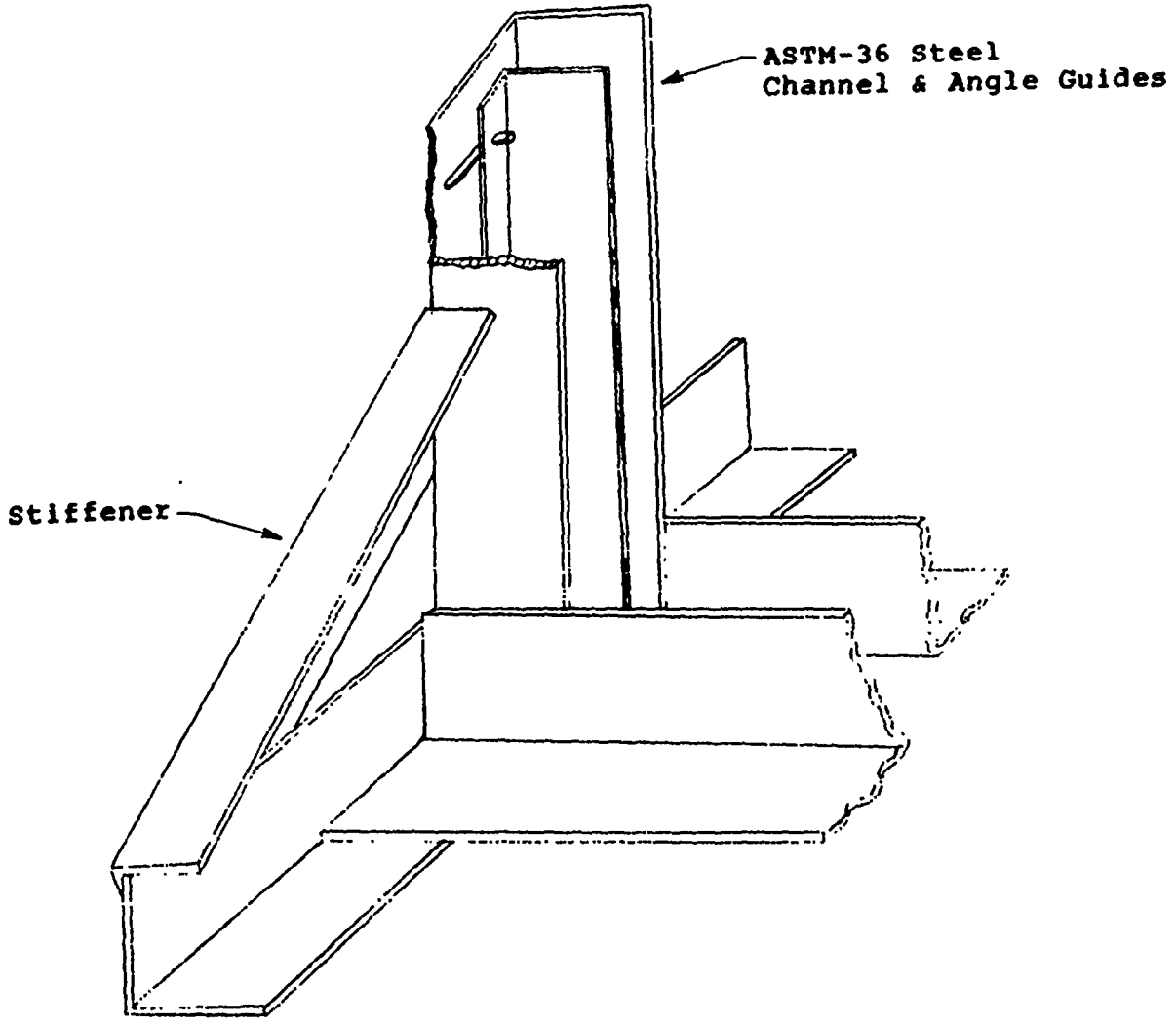

Fig 6. Corner Detail of Vertical Guides

1990 USAF-UES SUMMER FACULTY RESEARCH PROGRAM

GRADUATE STUDENT RESEARCH PROGRAM

Sponsored by the

AIR FORCE OFFICE OF SCIENTIFIC RESEARCH

Conducted by the

Universal Energy Systems, Inc.

FINAL REPORT

CONTROL DESIGN OF ASTREX TEST ARTICLE

Prepared by:	Hung V. Vu, Ph.D., Assistant Professor
	Joseph P. Baldonado, Graduate Student
	Hung M. Nguyen, Graduate Student
Department and	Mechanical Engineering
University:	California State University, Long Beach, CA 90840
Research Location:	Astronautics Laboratory / VSSS
	Edwards AFB, CA 93523
USAF Researcher:	Alok Das, Ph.D.
Date:	September 20, 1990
Contract No:	F49620-88-C-0053

Same Report as
Prof. Hung Vu
(Report # 23)

1990 USAF–UES SUMMER FACULTY RESEARCH PROGRAM/

GRADUATE STUDENT RESEARCH PROGRAM

Sponsored by the

AIR FORCE OFFICE OF SCIENTIFIC RESEARCH

conducted by the

Universal Energy Systems,Inc.

FINAL REPORT

Estimation of Time–Optimal Control Switching Times for Arbitrary Reorientation Maneuvers of A Rigid Spacecraft

Prepared by:	Robert M. Byers
Academic Rank:	Graduate Student
Department and	Aerospace Engineering
University:	Texas A& M University
Research Location:	AFAL/VSSS
	Edwards AFB,CA
USAF Researcher:	Dr. Alok Das
Date:	1 Sept 1990
Contract No:	F49620-88-C-0053

Estimation of Time–Optimal Control Switching Times for Arbitrary Reorientation Maneuvers of A Rigid Spacecraft

by

Robert M. Byers

ABSTRACT

The problem of slewing a rigid body from an initial orientation to an arbitrary target state using bang–bang controls was considered with application to the AFAL ASTREX (Advanced Structure Technology Research Experiment) testbed. A quasi closed–form solution for the control switching times is obtained using a sequential approximation of the state transition matrix. It is compared to an exact solution obtained iteratively using a first order gradient method. The closed form solution gives a very good approximation of the control switching times and can be computed in real–time with only modest computing capability.

Acknowledgements

I wish to thank the Air Force Systems Command, the Air Force Office of Scientific Research, and the Air Force Astronautics Lab for sponsoring this research. I am especially grateful to Dr. Alok Das for his professional oversight of my work. I am also indebted to my academic advisor, Dr. S. R. Valdal whose insights and guidance have been essential to my progress. In addition I greatly appreciate the work done by Mr. Wade Schlaegel in generating computer animated graphics for my presentations.

I. INTRODUCTION

The Advanced Structure Technology Research Experiment (**ASTREX**) is a test bed for various experiments in control methodologies for rapid slewing and vibration suppression in large flexible space structures. Although not rigid, the ASTREX test article is very stiff and will be slewed using a conbination of cold gas thrusters and reaction wheels. Among its research goals is investigating minimum time large angle slewing with either 10 lbf or 200 lbf thrusters as the primary controls. A method of generating the optimal control switch times for a rigid body would have direct application to ASTREX.

I have been investigating minimum time reorientation of rigid bodies as part of my research for a Ph.D. in Aerospace Engineering at Texas A&M University. I had previously written a computer program which generates the open loop solution to this problem and had been working on a closed form solution which can be executed by a computer in real time. My research interests potentially contribute directly to the ASTREX goals and was the primary reason for my assignment to the Astronautics Lab.

II. OBJECTIVES OF THE RESEARCH EFFORT

The problem of slewing a rigid body from an initial rest state to some arbitrary rest state is of general interest. To satisfy the necessary conditions for optimality, the controls are required to be "Bang–Bang". Since the controls are saturated throughout the maneuver, it is necessary only to determine times at which the controls "switch".

For slewing about a principle axis using a single control torque, the problem is

linear and the solution is well understood. However, for an arbitrary rigid body, with multiple controls not necessarily aligned with principle axes, the problem is non-linear and no structure to the solution is readily apparent. Although it is possible to generate a solution using several numerical methods, it has heretofore not been possible to determine the time optimal switch times in "real time". Obviously, a system which has a requirement for minimum time slewing cannot accept any delay in determining the necessary controls to accomplish the desired manuever.

My objectives at the Astronautics Lab were to investigate the nature of the time-optimal slewing maneuver as it applied to ASTREX . Initially, I used a first order gradient algorithm to generate control histories for such maneuvers. I then modified my program so that a smooth cubic spline replaced the instantaneous control switching so as to avoid excitation of the flexible modes of vibration in the structure.

The majority of my time at the Astronautics Lab was devoted to developing a quasi closed-form method of determining the necessary switch times required to perform a maneuver given a sequence of bang-bang control torques. The algorithm I eventually developed generates approximate switch times rapidly enough that large angle maneuvers can be accomplished with small residual pointing error. Significantly, these switch times can be generated with modest computing power in real time, thus making their application practical.

III. EQUATIONS OF MOTION AND NECESSARY CONDITIONS FOR OPTIMALITY

The differential equations for the angular velocity vector are given by Euler's

Equations:

$$\dot{\underline{\omega}} = -\mathbf{I}^{-1}\underline{\omega} \times \mathbf{I}\underline{\omega} + \mathbf{I}^{-1}\mathbf{B}\underline{u} \tag{1}$$

where $\mathbf{I}$ is the (3×3) inertial matrix, $\mathbf{B}$ is the $(3 \times m)$control influence matrix and $\underline{u}$ is the $(m \times 1)$ control vector.

A convenient means of representing spacecraft attitude is via *Euler parameters*, $\underline{\beta}$, where:

$$\beta_i = l_i \sin\left(\frac{\theta}{2}\right) \quad i = 1,2,3 \tag{2a}$$

$$\beta_0 = \cos\left(\frac{\theta}{2}\right) \tag{2b}$$

where $\underline{l}$ is the unit axis about which a rotation of angle θ will bring a body to a given orientation.

The differential equations are given by:

$$\dot{\underline{\beta}} = \frac{d}{dt}\begin{Bmatrix}\beta_1\\ \beta_2\\ \beta_3\\ \beta_0\end{Bmatrix} = \frac{1}{2}\begin{bmatrix}0 & \omega_3 & -\omega_2 & \omega_1\\ -\omega_3 & 0 & \omega_1 & \omega_2\\ \omega_2 & -\omega_1 & 0 & \omega_3\\ -\omega_1 & -\omega_2 & -\omega_3 & 0\end{bmatrix}\begin{Bmatrix}\beta_1\\ \beta_2\\ \beta_3\\ \beta_0\end{Bmatrix}$$

$$= \frac{1}{2}G(\omega)\underline{\beta} \tag{3}$$

We define the state vector as:

$$\underline{x}^T = \left\{\underline{\omega}^T, \underline{\beta}^T\right\}$$

to arrive at the set of differential equations:

$$\underline{f} = \dot{\underline{x}}(x,u,t) \tag{4}$$

We assume that the control is bounded such that

$$|u_i| \leq 1, \quad i = 1,\ldots,m$$

as is the case with on–off thrusters. In the general case of optimal control, we seek to minimize a performance index:

$$J = \int_0^{t_f} \left[L + \underline{\Lambda}^T \left(\underline{f} - \underline{\dot{x}} \right) \right] dt \tag{5}$$

where L is a scalar cost function and $\underline{\Lambda}$ is the (7×1) vector of Lagrange multipliers, while enforcing the terminal constraints:

$$\underline{\psi} = \begin{Bmatrix} x_1(t_f) \\ \vdots \\ x_6(t_f) \end{Bmatrix} = \underline{0}$$

The augmented performance index is:

$$\bar{J} = \underline{\nu}^T \underline{\psi} + \int_0^{t_f} \left[L + \underline{\Lambda}^T \left(\underline{f} - \underline{\dot{x}} \right) \right] dt \tag{6}$$

where $\underline{\nu}$ is a (6×1) vector of constant multipliers to be determined. The Hamiltonian then is:

$$\mathcal{H} = L + \underline{\Lambda}^T \underline{f} \tag{7}$$

Where, for the minimum time problem, $L = 1$. Since the equations of motion are linear in the control (which is bounded), we can use *Pontryagin's Principle* to find the optimal control:

$$u_i = -\text{sign} \left(\frac{\partial \mathcal{H}}{\partial u_i} \right) \tag{8}$$

That is, the control is "bang–bang" except for singular regions where $\mathcal{H}_{u_i} = 0$ for some finite period of time.

IV. OPEN LOOP SOLUTION USING A FIRST ORDER GRADIENT METHOD:

The following disscussion is motivated by Bryson[2] and Meier[3].

For the free final time problem the differential of the augmented performance index is:

$$d\bar{J} = \underline{\nu}^T \psi_x \delta\underline{x}(t_f) + L(t_f)dt_f + \int_0^{t_f} \left[\left(L_x + \underline{\Lambda}^T f_x\right) \delta\underline{x} + \left(L_u + \underline{\Lambda}^T f_u\right) \delta\underline{u} - \underline{\Lambda}^T \delta\dot{\underline{x}} \right] dt \qquad (9a)$$

Integrating by parts, noting that $\delta\underline{x}(t_f) = d\underline{x}(t_f) - \dot{\underline{x}}(t_f)dt_f$ and collecting terms gives:

$$d\bar{J} = \left[\left(L + \underline{\Lambda}^T \underline{f}\right) dt_f + \left(\underline{\nu}^T \psi_x - \underline{\Lambda}^T\right) d\underline{x}_f \right]_{t=t_f} + \underline{\Lambda}^T(t_0)\delta\underline{x}(t_0) + \int_0^{t_f} \left[\left(L_x + \underline{\Lambda}^T f_x + \dot{\underline{\Lambda}}^T\right) \delta\underline{x} + \left(L_u + \underline{\Lambda}^T f_u\right) \delta\underline{u} \right] dt \qquad (9b)$$

We choose $\underline{\Lambda}$ to make the coefficents of δx and $dx(t_f)$ disappear. If we pick

$$\underline{\Lambda} = \underline{p} + R\underline{\nu}$$

we get the differential equations:

$$\dot{\underline{p}} = -L_x - f_x^T \underline{p}, \quad \underline{p}(t_f) = 0 \quad \Rightarrow \underline{p}(t) \equiv \underline{0} \qquad (10a)$$

$$\dot{R} = -f_x^T R, \quad R(t_f) = \left(\frac{\partial \underline{\psi}}{\partial \underline{x}}\right)^T_{t=t_f} \qquad (10b)$$

Substituting gives:

$$d\bar{J} = \left(L + \underline{\nu}^T \underline{f}\right)_{t=t_f} dt_f + \int_0^{t_f} \left[L_u + (R\underline{\nu})^T f_u\right] \delta\underline{u} dt$$

Which gives:

$$\delta\underline{u}(t) = -\mathbf{W}^{-1} \left[L_u + (R\underline{\nu})^T f_u\right]^T \qquad (11a)$$

$$dt_f = -\frac{1}{b} \left[\underline{\nu}^T \underline{f} + L\right]_{t=t_f} \qquad (11b)$$

Where $\mathbf{W}$ is a positive definite weighting matrix and b is a positive scalar. Separating the terms of $d\bar{J} = \underline{\nu}^T d\underline{\psi} + dJ$ gives

$$d\underline{\psi} = \underline{f}(t_f)dt_f + \int_0^{t_f} R^T f_u \delta\underline{u}(t)dt$$

Substituting in the equations for δu and dt_f gives

$$d\underline{\psi} = -\frac{1}{b}\left[\underline{f}\left(\underline{\nu}^T\underline{f} + L\right)\right]_{t=t_f} - \left(I_{\psi J} + I_{\psi\psi}\underline{\nu}\right) \tag{12}$$

where

$$I_{\psi\psi} = \int_0^{t_f} R^T f_u \mathbf{W}^{-1} f_u^T R dt \tag{13a}$$

$$I_{\psi J}^T = \int_0^{t_f} L_u \mathbf{W}^{-1} f_u^T R dt \tag{13b}$$

Solving for ν gives:

$$\underline{\nu} = -\left[I_{\psi\psi} + \frac{1}{b}\underline{f}(\underline{f}^T)\right]^{-1}\left[d\underline{\psi} + I_{\psi J} + \frac{1}{b}L\underline{f}\right]_{t=t_f} \tag{14}$$

Since in the minimum time problem $L = 1, \Rightarrow I_{\psi J} \equiv 0$. If we assume (based on Pontryagin's principle) that the control is always saturated (i.e. $u_i = \pm 1, \quad i = 1, \ldots m$) it is unnecessary to determine $\delta u_i(t)$ at every instant in time. Instead, computational savings can be realized by adjusting only the time of control switches. Thus at some nominal switch time t_{ij} (the jth switch of the ith control) over some correction Δt_{ij}, $\delta u_i = \Delta u$ that is

$$\delta u_i = \begin{cases} \Delta u, & t_{ij} \le t \le t_{ij} + \delta t_{ij}; \\ 0, & \text{otherwise.} \end{cases}$$

where the sign of Δu is determined from $\text{sign}(u(t)_{new} - u(t)_{old})$

Thus it is not necessary to integrate to find $I_{\psi\psi}$ instead:

$$I_{\psi\psi} = \sum_{i=1}^{m} \sum_{j=1}^{ns(i)} R_{ij}^T f_u \mathbf{W}^{-1} f_u^T R_{ij} \tag{15}$$

The increment to the final time dt_f and the vector ν are calculated as before and instead of calculating $\delta u(t)$ we find

$$dt_{ij} = -\frac{W_{ii}^{-1}}{\Delta u_i} \left(\frac{\partial \mathcal{H}}{u_i} \right)_{t=t_{ij}} \tag{16}$$

Step by step the algorithm is given by

1) Guess a nominal control history $u(t)$ and t_f

2) Forward integrate differential equations $\underline{f}$ (Eqs. 4) from $0 \leq t \leq t_f$.

3) Determine R(t) via backward integration of Eq. 10b and simultaneously determine $I_{\psi\psi}$ (Eq. 15)

4) Choose $d\underline{\psi} = -\epsilon\underline{\psi}$ $0 < \epsilon \leq 1$

5) Determine vector of constants $\underline{\nu}$, increment to control $\delta u(t)$ and increment to final time dt_f

6) Repeat steps 2 thru 6 with $u(t) = u(t)_{old} + \delta u(t)$ until solution converges sufficiently.

I have coded this algorithm in FORTRAN with the program name of STOP.FOR (Switch Time Optimization Program)

To start STOP.FOR we need to know approximately when, and how many control switches there are. To accomplish this, the steepest descent algorithm is used with

$$L = 1 + C \sum_{i=1}^{m} (u_i^2 - 1)^2 \tag{17}$$

Although this is an unconstrained control problem the performance index is penalized for $u_i \neq 1$. The sharpness of the control switch is determined by the size of the constant C. Although this program is slow to converge, it actually settles on a final time and switch times fairly quickly.

V. QUASI-CLOSED FORM SOLUTION OF SWITCH TIME INTERVALS

Although the above algorithm will generate the optimal solution to the minimum time slewing problem, it is time–consuming to implement and therefore not of practical use for manueuvering an actual spacecraft. The inherent non–linearity of Euler's Equations is an obstacle to their general solution but for many actual systems they can been linearized. For systems in which:

$$|\underline{\omega} \times \mathbf{I}\underline{\omega}| \ll |\mathbf{B}\underline{u}| \tag{18}$$

the nonlinear term can be ignored and the angular velocity differential equations (Eqs. 1) become:

$$\dot{\underline{\omega}} = \mathbf{K}\underline{u} \tag{19}$$

where $\mathbf{K} = \mathbf{I}^{-1}\mathbf{B}$. For simplicity , assume initially that $\mathbf{K}$ is the (3×3) identity matrix and that $\underline{u}$ is a (3×1) control vector. From the necessary conditions, we know that between switches the control vector $\underline{u}$ is constant which leads to the angular velocity vector being a linear function of time over the interval $t - t_0$:

$$\underline{\omega} = \underline{u}(t - t_0) + \underline{\omega}_0$$

where t_0 is the time of the previous control switch and $\underline{\omega}_0$ is the angular velocity vector evaluated at $t = t_0$. For simplicity the following notational convention is

adopted:

$$\Delta_i = t_i - t_{i-1}$$

$$\underline{\omega}_i = \underline{\omega}(t = t_i)$$

$$\underline{u}_i = \underline{u}(t_i > t > t_{i-1})$$

The angular velocity at $t = t_i$ then is:

$$\begin{aligned} \underline{\omega}_i &= \underline{u}_i \Delta_i + \underline{\omega}_{i-1} \\ &= \sum_{k=1}^{i} \underline{u}_k \Delta_k \end{aligned} \tag{20}$$

For the rest–to–rest reorientation maneuver, $\underline{\omega}_0 = \underline{0}$. After the application of some sequence of non–zero control vectors, the angular velocity at the final time is also the zero vector. Examination of the optimal solution obtained from STOP.FOR for numerous manuevers indicates that the controls switch sequentially, that is, the elements of $\underline{u}$ switch in any order but no control switches twice before all others have switched. Assuming sequential switching and examining the nature of the magnitude of the angular velocity vector, it is found that the rigid body may be brought back to rest after a minimum of five switches (six control intervals) provided that:

$$\underline{u}_{i+3} = -\underline{u}_i \qquad i = 1, 2, 3 \tag{21a}$$

$$\Delta_{i+3} = \Delta_i \tag{21b}$$

This is exactly what is observed in the numerical solution. This observation holds true in the case where the matrix **K** is not the identity matrix. It has been found by Bilimoria and Wie[4] that for small rotations about a principle axis, seven switches gives a very slightly reduced final time. However, this result is not established for a general rotation and the improvement over using five switches is truely miniscule.

Thus, it appears that in general, any reorientation may be accomplished with five switches of bang-bang controls. However, it is also clear that there are several sequences of controls, using five switches, which may accomplish any given rotation. One of the possible sequences of course, will yield the minimum time solution.

Recall Eq.(3)

$$\dot{\underline{\beta}} = \frac{1}{2} G(\omega) \underline{\beta}$$

which has the general solution:

$$\underline{\beta}(t) = \Phi(t, t_0) \underline{\beta}(t_0) \tag{22}$$

where $\Phi(t, t_0)$ is the (4×4) state transition matrix which satisfies the differential equations:

$$\frac{d}{dt} \Phi(t, t_0) = \frac{1}{2} G(\omega) \Phi(t, t_0)$$

with $\Phi(t_0, t_0) =$ the (4×4) identity matrix.

Detailed analysis[5] of the state transition matrix shows that there are only four unique elements:

$$\Phi(t, t_0) = \begin{bmatrix} \phi_0 & -\phi_3 & \phi_2 & -\phi_1 \\ \phi_3 & \phi_0 & -\phi_1 & -\phi_2 \\ -\phi_2 & \phi_1 & \phi_0 & -\phi_3 \\ \phi_1 & \phi_2 & \phi_3 & \phi_0 \end{bmatrix} \tag{23}$$

Solving Eq. (23) for the instantaneous values of the four elements $\underline{\phi}$ gives:

$$\begin{Bmatrix} \phi_1 \\ \phi_2 \\ \phi_3 \\ \phi_0 \end{Bmatrix} = \begin{bmatrix} -\beta_0(t_0) & -\beta_3(t_0) & \beta_2(t_0) & \beta_1(t_0) \\ \beta_3(t_0) & -\beta_0(t_0) & -\beta_1(t_0) & \beta_2(t_0) \\ -\beta_2(t_0) & \beta_1(t_0) & -\beta_0(t_0) & \beta_3(t_0) \\ \beta_1(t_0) & \beta_2(t_0) & \beta_3(t_0) & \beta_0(t_0) \end{bmatrix} \begin{Bmatrix} \beta_1(t) \\ \beta_2(t) \\ \beta_3(t) \\ \beta_0(t) \end{Bmatrix} \tag{24}$$

Setting $\underline{\beta}(t_f) = [0\ 0\ 0\ 1]^T$ gives

$$\underline{\phi}(t_f, t_0) = \underline{\beta}(t_0) \tag{25}$$

Since over the interval Δ_i, $\underline{u}_i$ and $\underline{\omega}_{i-1}$ are constant, an approximate solution of $\Phi(\Delta_i) \equiv \Phi(t_i, t_{i-1})$ is given by:

$$\phi_0 = \cos(\| \underline{M}_i \| \frac{\Delta_i}{2}) \tag{26a}$$

$$\phi_j = \frac{m_{ij}}{\| \underline{M}_i \|} \sin(\| \underline{M}_i \| \frac{\Delta_i}{2}) \qquad j = 1,2,3 \tag{26b}$$

where:

$$\underline{M}_i = \underline{u}_i \frac{\Delta_i}{2} + \underline{\omega}_{i-1}$$

$$= [m_{i1}, m_{i2}, m_{i3}]^T$$

This approximation gives good results where the cross product vector $\underline{r} = \frac{\Delta_i}{2}(\underline{u}_i \times \underline{\omega}_{i-1})$ has small components. For $\underline{r} = \underline{0}$ it is an exact solution.

Since it was shown that only six control intervals are necessary for the optimal maneuver, the state transition matrix can be written as:

$$\Phi(t_f, t_0) = \prod_{k=6}^{1} \Phi(\Delta_k) \tag{27}$$

from which the equations for the elements of $\underline{\phi}$ can be extracted. Four extremely nonlinear equations of the form

$$\underline{f} = \underline{\phi}(t_f, t_0) - \underline{\beta}(t_0) = \underline{0} \tag{28}$$

result. These equations are functions of the sequence of three unique control vectors and the three unique time intervals. If a control sequence is assumed, then we have four equations and three unknowns. Like the Euler Parameters themselves, these equations are not independent; knowledge of any three of them is sufficient to solve for three unknowns and the first three are chosen for this purpose.

There are eight possible combinations of ± 1 in groups of three:

$$\begin{bmatrix} 1 & 1 & 1 & 1 & -1 & -1 & -1 & -1 \\ 1 & 1 & -1 & -1 & -1 & -1 & 1 & 1 \\ 1 & -1 & 1 & -1 & -1 & 1 & -1 & 1 \end{bmatrix}$$

Note that the last four column vectors are merely the negative of the first four. If each of these vectors is considered as the initial control for the system, four of them will cause $\ddot{\beta}_0 < 0$ and can thus be discarded as time optimal possibilities. Of the remaining four vectors, there are 24 combinations of three of them, that is, there are 24 possible control sequences to consider associated with 24 sets of switch times which can potentially perform the desired maneuver. It is not necessary to evaluate all of them. Experience has shown that only two or three are of interest, the others generally require negative time intervals, which is physically unrealizable. To quickly eliminate these, the following method is used: Assuming (contrary to fact) that:

$$G(M_i)G(M_{i-1}) = G(M_{i-1})G(M_i)$$

This assumption permits the simple solution:

$$\phi_0(t_f, t_0) = cos(\| \underline{\gamma} \| \frac{t_3}{2}) = \beta_0(t_0) \tag{29a}$$

$$\phi_j(t_f, t_0) = \frac{\gamma_j}{\| \underline{\gamma} \|} \sin(\| \underline{\gamma} \| \frac{t_3}{2}) = \beta_j(t_0) \qquad j = 1,2,3 \tag{29b}$$

where:

$$\underline{\gamma} = \underline{u}_1\Delta_1 + \underline{u}_2\Delta_2 + \underline{u}_3\Delta_3 = \mathbf{U}\underline{\Delta}$$

$$t_3 = \Delta_1 + \Delta_2 + \Delta_3$$

Using the definition of the Euler Parameters (Eq.(2)) gives the set of equations:

$$t_3\underline{\Delta} = -\psi_0\mathbf{U}^{-1}\underline{l} \tag{30}$$

which are a linear set of equations and are quickly solved. All control sequences (i.e. possible U matrices) requiring that any of the elements of $\underline{\Delta}$ be less than zero are discarded. For the remaining sequences, the solution of these equations yields a good initial guess of the switch time vector $\underline{\Delta}$. Generally, only two or three sequences remain which can then be solved by computing the Jacobian of the three equations numerically (using the chain rule) and solving for the switching intervals using a nonlinear equation solving technique such as Newton's Method. It is then a simple matter to chose the control sequence, and the associated switch time intervals which give the least total time.

The step–by–step algorithm is given below:

1) Determine the four possible initial controls by evaluating $\ddot{\beta}_0(t_0)$

2) Evaluate 24 possible control sequences U via Eq. (30).

3) Those sequences which are not eliminated are used in the solution of Eqs. (28).

4) Select the sequence and associated switch times yielding the minimum time maneuver.

This technique, called Estimation of Linear Velocity Interval Switching is coded in a FORTRAN program ELVIS.FOR.

VI. SIMULATION RESULTS AND DISCUSSION

Two simulated maneuvers are shown using the ASTREX rigid body model. The first is a near single axis maneuver of $\theta_0 = 45°$ about the x-axis. The solution of ELVIS is essentially identical to that of STOP. The second is an arbitrary rotation with $\theta_0 = 45°$ with $\underline{\beta}^T(t_0)$ =(.35 .1 .1181 .923879)

. The solution generated by ELVIS is compared to that given by STOP.

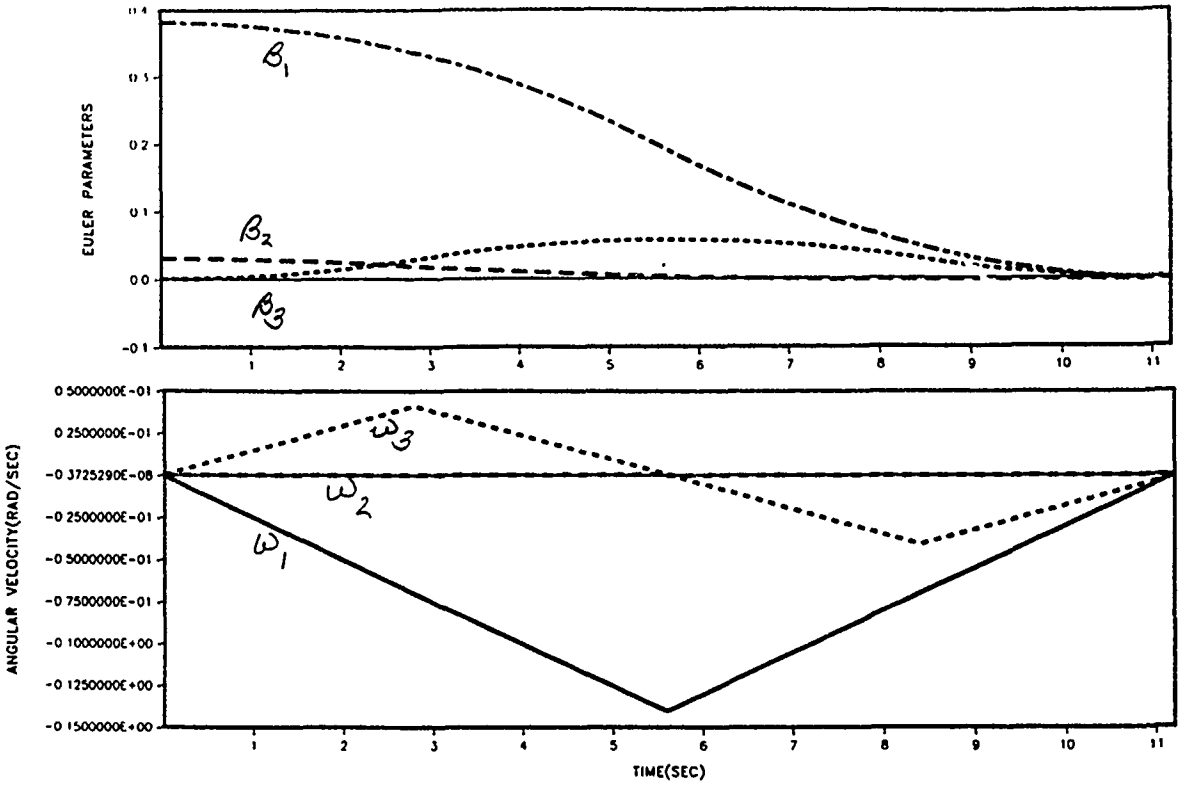

45° Near Single-Axis Rotation
(ELVIS)

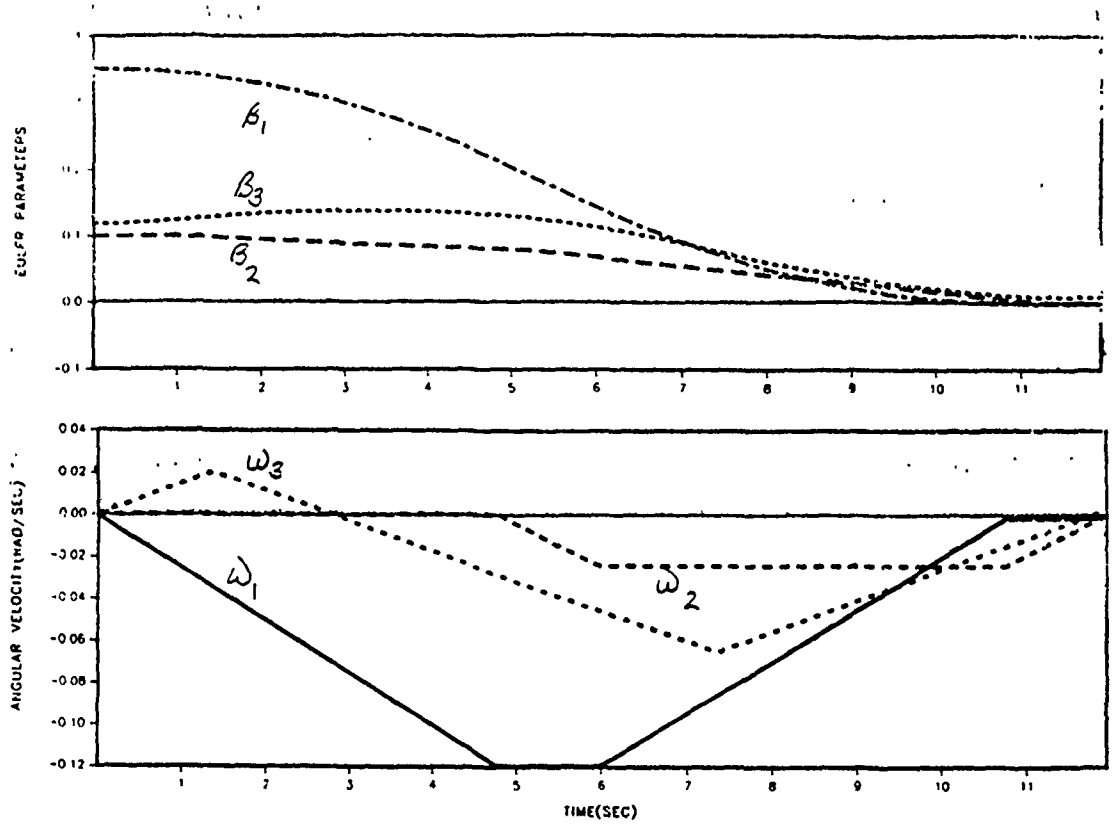

General 45° Rotation
(ELVIS)

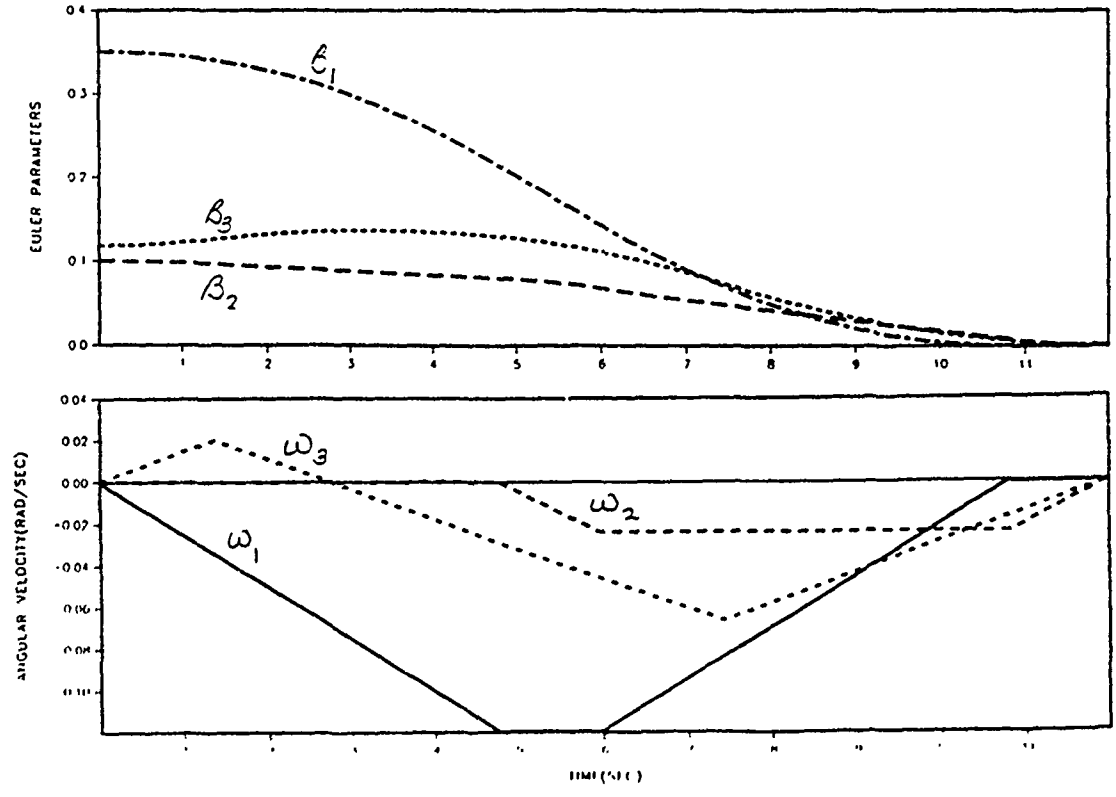

General 45° Rotation (STOP)

ELVIS is an approximate solution with two sources of error. The first is the unmodelled nonlinear terms in Eq. (1). For a spacecraft with three ide. .:cal principle moments of inertia, this term disappears completely. Because of the symmetry of the switch times, the terminal angular velocity will be zero. In ASTREX, the gyroscopic coupling terms are very small due to the similar values of the principal inertias and the low rotation rates encountered. However, there are small contributions resulting in small terminal errors of both angular velocity and orientation. The second source of error is due to the approximate solution to the state transition matrix used. For small rotations, it gives excellent results; as the size of the maneuver increases, it becomes progressively worse. Using the ASTREX model, it was found that rotations of $\theta_0 \leq 45°$ had a terminal orientation error of $\theta(t_f) < 1°$ and a small amount of drift.

VII. RECOMMENDATIONS

ELVIS generates a solution for the control switch times quickly enough so that it can be considered for use in real time. Although the switch times are not exact, the optimal control sequence is chosen and it brings ASTREX to a final state which is well within the bounds of a terminal precision pointing controller. This technique should be implemented on ASTREX when it is equipped with cold-gas thruster in Fall 1990. Initailly, ASTREX will be equipped with small 10 lbf thrusters which will cause only small excitation of the elastic modes.

Prior to actual implementation on ASTREX a terminal controller should be added to correct the terminal state error due to the approximate state transition matrix used.

REFERENCES

1. Turner, J.D. and Junkins, J.L. Optimal Spacecraft Rotational Maneuvers. New York, Elsevier Scientific Publishing Co.,1985.

2. Bryson, A.E. and Ho, Y.-C.Applied Optimal Control New York, Hemisphere Publishing Corp., 1985.

3. Meier, E.B. and Bryson, A.E., "An Efficient Algorithm for Time Optimal Control of a Two–Link Manipulator", AIAA Paper 87-2263

4. Bilimoria, K.D., and Wie, B. "Minimum Time Large Angle Reorientation of a Rigid Spacecraft" AIAA Paper 90-3486,Guidance, Navigation & Control Conference Portland, Oregon, August 1990.

5. Kane, T.R., "Solution of Kinematical Diffential Equations for a Rigid Body", Journal of Applied Mechanics, March 1973, pp. 109–113.

1990 USAF-UES SUMMER FACULTY RESEARCH PROGRAM

GRADUATE STUDENT RESEARCH PROGRAM

Sponsored by the

AIR FORCE OFFICE OF SCIENTIFIC RESEARCH

Conducted by the

Universal Energy Systems, Inc.

FINAL REPORT

Van der Waals Forces in Capillary Tubes

Prepared by:	Gregory Herdt
Academic Rank:	M.S. Candidate
Department and University:	Engineering Department University of Denver
Research Location:	USAF Astronautics Laboratory Edwards AFB
USAF Researcher:	Michael Powell
Date:	30 Aug 90
Contract No:	F49620-88-C-0053

Van der Waals Forces in Capillary Tubes

by

Gregory Herdt

ABSTRACT

A theoretical model of van der Waals forces in smooth capillary tubes was developed using the method of surface mode analysis. Preliminary calculations using a computer program described in the text indicate that these forces should be strong enough to play a significant role in capillary pumping in metal heat pipe wicks. These results suggest that heat pipe performance can be optimized by appropriate materials selection and processing.

Acknowledgements

This research was sponsored by the Air Force Systems Command and the Air Force Office of Scientific Research. I wish to thank them and Universal Energy Systems, Inc. both for the support provided and for an opportunity to undertake this study. I also wish to express my appreciation to Mike Powell and the Vehicle Systems Division at the USAF Astronautics Laboratory, who made my tenure as a GSRP fellow both pleasant and productive. My advisor, Dr. Larry Swanson, encouraged me to pursue this problem and to apply for the fellowship. His support has most certainly been appreciated. Finally, the editorial assistance of my wife Vicki is gratefully acknowledged.

I. INTRODUCTION:

Optimization of capillary pumping in heat pipe wicks holds great promise for enhancing heat pipe performance. Models of capillary pumping must necessarily incorporate microscopic interfacial phenomena in their description of the vapor-liquid interface near the vapor-liquid-solid contact line (interline) in capillary tubes. In particular, van der Waals forces play an important role because they are long range, charge independent forces. Wayner originally pioneered the application of these forces to heat transfer problems [1-4]. This approach has recently been incorporated in a theoretical model of the evaporating meniscus in a capillary tube developed by Dr. Larry Swanson of the University of Denver [5]. His work has shown a clear correlation between mass transfer rates and the van der Waals dispersion forces in a capillary tube.

Currently there is much interest in developing high performance heat pipes for space power applications. Heat pipes are particularly well suited to space power applications because they utilize a passive capillary pumping mechanism and hence are not subject to the weight and reliability penalties posed by actively pumped systems. It is evident, however, that a great deal of research is needed to attain optimum performance in heat pipes. Improving heat pipe performance by increasing the mass transfer rate in the heat pipe wicks effectively increases the capacity of the heat pipes. This is an area of interest to the Space Power Section of the Vehicle Systems Division at the USAF Astronautics Laboratory, located at Edwards AFB, where my research was conducted.

My work on van der Waals forces in capillary tubes has been motivated by Dr. Larry Swanson, who is currently conducting research on heat pipes with the support of an AFOSR Mini Grant. Dr. Swanson encouraged me to pursue this problem by applying for a Summer Graduate Student Research fellowship. This work will also be the basis for my M.S. thesis in Materials Science at the University of Denver.

II. OBJECTIVES OF THE RESEARCH EFFORT:

The primary objective of my research effort was to develop a theoretical expression for the van der Waals force at the vapor-liquid interface of an absorbed liquid layer on the inner surface of a smooth capillary tube. This work is useful both in gauging the magnitude of van der Waals forces in heat pipe wicks and as the basis for a more sophisticated description of these forces. It is necessary to include the capillary tube geometry, which has a substantial effect for small (on the order of $10\mu m$) capillary radii, in such descriptions.

A second objective of the study was to evaluate the effect of surface media on the van der Waals forces. This phase of the study is important due to the potential for optimizing capillary pumping by appropriate selection of heat pipe wick materials. This work is currently being extended to include capillary tubes with a layer of material on the surface, which will be used to study the effects of oxide layers and possible coating materials on the van der Waals forces.

These objectives reflect the overall motive for this study, which is to evaluate the impact of material properties on the performance of capillary heat pipe wicks.

III. BACKGROUND:

The theory of van der Waals forces has been reviewed in several excellent textbooks [6-8]. Van der Waals forces are long range attractive forces which are always present between atoms. There are three types of interaction which are responsible for van der Waals forces [8]. These are the Debye, Keesom, and dispersion interactions. The Keesom interaction is due to the presence of permanant dipoles in a medium, whereas the Debye interaction arises from induced dipole moments. Although the time average dipole moment of an atom or molecule may be zero, the instantaneous dipole moment is non-zero. Neighboring atoms and molecules are polarized by this instantaneous dipole moment, which leads to the attrac-

tive dispersion interaction between atoms and molecules.

Van der Waals forces between macroscopic bodies were originally studied by Hamaker [9], who assumed that the interatomic dispersion energies are pairwise additive. The interaction energy between macroscopic bodies can then be expressed in terms of volume integrals over the bodies in question. One difficulty with this approach is that it neglects many-body forces between atoms which play a significant role in condensed media. This method also does not properly account for the attenuation or retardation of the van der Waals forces by an intervening medium. The Hamaker approach further assumes that a single frequency constitutes the dominant contribution to the van der Waals forces, thereby oversimplifying the optical behavior of the media involved [6].

These problems where remedied by Lifshitz [10,11] in the late fifties. The Lifshitz theory treats van der Waals forces as a consequence of fluctuating electromagnetic fields between macroscopic bodies. This approach lends itself to the calculation of van der Waals forces in condensed media, including liquid films [12]. The surface mode analysis method of van Kampen [13], which is equivalent to the Lifshitz theory, has become the preferred approach for calculating van der Waals forces between macroscopic bodies because of its mathematical and conceptual simplicity.

In the surface mode analysis approach, each medium is treated as an ensemble of simple harmonic oscillators. The van der Waals energy of interaction between media is then given by the difference between the sum of the zero point energies of the media in contact and the media in isolation. A method for explicitly doing this has been developed by Ninham, Parsegian and Weiss [14]. One advantage of this formalism is that it accounts for the temperature dependence of van der Waals forces. By solving the Maxwell equations for the surface modes of a system and applying the appropriate boundary conditions, a set of secular determinants is obtained whose roots are the normal modes of the system. These are used in the above formalism to obtain the van der Waals energy of interaction per unit area between media.

IV. THEORY:

The van der Waals forces in a smooth capillary tube have previously been studied by Philip [15,16] using the Hamaker theory. Because the absorbed layer in a capillary tube can be relatively thick (greater than 1000 A), retardation effects have a significant impact on the van der Waals interaction at the vapor-liquid interface in a capillary tube. The temperature dependence of the van der Waals forces is also an important factor in assessing their role in capillary pumping for heat pipe applications. Clearly the need exists for a theory of retarded van der Waals forces in a capillary tube. In this section of the report, I shall outline my contribution to this work.

A number of assumptions have been made in my formulation of this problem. I have not included the effects of surface impurities and defects, porosity, and surface roughness. Effects due to surface charges (the electric double layer) are also not discussed, as they entail the seperate problem of solving the Boltzmann-Poisson equation. All short-range surface forces (i.e. hydrogen bonding) have been omitted from this work.

Solution of the Maxwell equations for the surface electromagnetic modes is most easily accomplished by introducing a superpotential, with Fourier components $\mathbf{Z}_\omega$ defined by

$$\phi_\omega = -\nabla \cdot \mathbf{Z}_\omega \qquad \mathbf{A} = -i\mu\varepsilon\omega\left(1+\frac{i\sigma}{\varepsilon\omega}\right)\mathbf{Z}_\omega, \tag{1}$$

where ϕ_ω is the Fourier component of the scalar potential and $\mathbf{A}_\omega$ is the Fourier component of the vector potential. This procedure is illustrated in a paper by Richmond and Ninham [17]. For the problem at hand, these superpotentials satisfy an equation of the form

$$(\nabla^2 - \rho_i^2)\,\mathbf{Z}(\mathbf{k};r) = 0, \tag{2}$$

in each of the media and satisfy the boundary conditions between the media. Throughout this paper the subscript i will refer to the medium in question. Specifically, an i value of 1 will refer to the capillary tube medium, 3 will denote the liquid absorbed layer, and 2 will

denote the vapor phase above the liquid. It is also important to bear in mind that the dielectric permitivity of each of these media will be a function of frequency, $\varepsilon_i = \varepsilon_i(\omega)$. In eqn. (2) we have

$$\rho_i^2 = k^2 - \mu\varepsilon_i\omega^2\left(1 + \frac{i\sigma}{\omega\varepsilon_i}\right), \tag{3}$$

and

$$\mathbf{Z}_\omega(\mathbf{r}) = \sum_{k_z=-\infty}^{+\infty}\sum_{m=-\infty}^{+\infty} e^{i(k_z z + m\theta)}\mathbf{Z}(\mathbf{k};r). \tag{4}$$

Solutions to eqn. (2) have the general form

$$\mathbf{Z}(\mathbf{k};r) = \mathbf{A}_m K_m(\rho_i r) + \mathbf{B}_m I_m(\rho_i r). \tag{5}$$

By matching fields and potentials at the boundaries, a system of equations for the components of the coefficients in eqn. (5) results. Non-trivial solutions of these systems are subject to the requirement that their secular determinant be equal to zero. The secular determinant corresponding to the radial components of these coefficients reduces to

$$D_1(\omega; k_z, m) = 1 - \bar{\Delta}_{13}\bar{\Delta}_{23}\frac{I_m(\rho_3 r_c)K_m(\rho_3 r_c)}{K_m(\rho_3 r_i)I_m(\rho_3 r_i)}. \tag{6}$$

The two components that are tangential to the surface of the capillary tube yield identical secular determinants of the form

$$D_2(\omega; k_z, m) = 1 - \Delta_{13}\Delta_{23}\frac{I_m(\rho_3 r_i)K_m(\rho_3 r_c)}{K_m(\rho_3 r_i)I_m(\rho_3 r_c)}. \tag{7}$$

In eqns. (6) and (7) the delta terms are defined as follows :

$$\bar{\Delta}_{13} = \frac{\rho_1\varepsilon_3 - \rho_3\varepsilon_1\dfrac{K'_m(\rho_3 r_c)K_m(\rho_1 r_c)}{K_m(\rho_3 r_c)K'_m(\rho_1 r_c)}}{\rho_1\varepsilon_3 - \rho_3\varepsilon_1\dfrac{I'_m(\rho_3 r_c)K_m(\rho_1 r_c)}{I_m(\rho_3 r_c)K'_m(\rho_3 r_c)}}, \tag{8}$$

$$\bar{\Delta}_{23} = \frac{\rho_2\varepsilon_3 - \rho_3\varepsilon_2\dfrac{I'_m(\rho_3 r_i)I_m(\rho_2 r_i)}{I_m(\rho_3 r_i)I'_m(\rho_2 r_i)}}{\rho_2\varepsilon_3 - \rho_3\varepsilon_2\dfrac{K'_m(\rho_3 r_i)I_m(\rho_2 r_i)}{K_m(\rho_3 r_i)I'_m(\rho_2 r_i)}}, \tag{9}$$

$$\Delta_{13} = \frac{\rho_1 - \rho_3 \dfrac{K'_m(\rho_3 r_c) K_m(\rho_1 r_c)}{K_m(\rho_3 r_c) K'_m(\rho_1 r_c)}}{\rho_1 - \rho_3 \dfrac{I'_m(\rho_3 r_c) K_m(\rho_1 r_c)}{I_m(\rho_3 r_c) K'_m(\rho_3 r_c)}}, \tag{10}$$

$$\Delta_{23} = \frac{\rho_2 - \rho_3 \dfrac{I'_m(\rho_3 r_i) I_m(\rho_2 r_i)}{I_m(\rho_3 r_i) I'_m(\rho_2 r_i)}}{\rho_2 - \rho_3 \dfrac{K'_m(\rho_3 r_i) I_m(\rho_2 r_i)}{K_m(\rho_3 r_i) I'_m(\rho_2 r_i)}}. \tag{11}$$

Note that the primes on the modified Bessel functions in these equations denote derivatives with respect to r. In the limit of large capillary radii, eqns. (6-11) asymptotically approach the Lifshitz results for a flat plate geometry, as they should. This can be easily shown by substituting the asymptotic forms of the modified Bessel functions and their derivatives into eqns. (6-11) and cancelling terms as necessary.

The electromagnetic surface modes given by eqns. (6) and (7) are directly incorporated in a state density sum which yields an expression for the van der Waals interaction energy per unit area. Following the approach of Ninham, Parsegian, and Weiss [14], we see that the free energy of interaction per unit area, F(l,T), is given by

$$F(l,T) = \frac{1}{(2\pi)^2} \sum_{m=-\infty}^{+\infty} \int_{-\infty}^{+\infty} dk_z \, [G_l(k_z) - G_\infty(k_z)], \tag{12}$$

where l is the absorbed layer thickness and T is temperature. In this expression

$$G_l(k_z) = K_B T \sum_{n=0}^{\infty}{}' \ln [\sinh(\beta h \nu_n / 2)] \tag{13}$$

represents the free energy contribution from the allowed surface modes of the system. Here K_B is the Boltzmann constant and $\beta = 1/K_B T$. The prime on the sum indicates that only half of the n = 0 term contributes to the sum. In the above equation, Eqn. (13) can be reduced to

$$G_l(k_z) = K_B T \sum_{n=0}^{\infty}{}' \ln D(i\xi_n; k_z, m). \tag{14}$$

Details pertaining to this last step can be found in ref. [14]. Where the sum is now taken over imaginary frequencies $i\xi_n = n(2\pi)^2 K_B T/h$. Note that $D(i\xi_n; k) = D_1(i\xi_n; k) D_2(i\xi_n; k)$. Using this fact and the results given in eqns. (12-14), one obtains an expression of the form

$$F(l,T)=\frac{K_BT}{(2\pi)^2}\sum_{n=0}^{\infty}{}'\sum_{m=-\infty}^{+\infty}\int_{-\infty}^{+\infty}dk_z\,[\ln D_1(i\xi_n;k_z,m)+\ln D_2(i\xi_n;k_z,m)]\,. \tag{15}$$

Eqn. (15) represents the interaction free energy per unit area due at the vapor-liquid interface for a smooth capillary tube geometry. The flat plate Lifshitz result for interaction energy per unit area is recovered from eqn. (15) in the appropriate limit. This follows from the fact that eqns. (6-11) go to the flat plate limit for large capillary radii, and because the sum over m in eqn. (15) becomes an integral in this limit. By use of the prescription

$$\sum_{m=-\infty}^{+\infty}\int_{-\infty}^{+\infty}dk_z\rightarrow 2\pi\int_0^{\infty}dk\,k\,, \tag{16}$$

we can then recover the Lifshitz expression.

Evaluation of eqn. (15) is clearly a computationally intensive undertaking. A computer program is currently being developed to evaluate this expression. A major obstacle in this undertaking has been the development of numerical routines to evaluate modified Bessel functions over a broad range of orders and arguments. Such routines must be designed to properly incorporate the asymptotic expressions for the modified Bessel functions given in Abramowitz and Stegan [18]. Care must also be taken to avoid floating point overflow when evaluating expressions such as eqns. (6-11) on a computer. By grouping the terms so that expressions of roughly equal magnitude divide one another, this difficulty can be averted.

The above mentioned program has several key parts. Routines are needed to evaluate the dielectric functions $\varepsilon_l(i\xi_n)$ and the deltas given by eqns. (8-11), which utilize the Bessel function routines. These routines are called by a function which is numerically integrated using an adaptive simpson method of the form described in Burden and Faires [19]. The main body of the program consists of a nested loop corresponding to the double sum within which the numerical integration is carried out. All calculations are done in double precision because of the wide range of values of Bessel functions generated in the infinite integral. Error trapping and early out tests have been incorporated in the code to insure that necessary tolerances are attained for the shortest possible run-time.

V. RECOMMENDATIONS

This work has established the preliminary theoretical framework necessary to evaluate van der Waals forces in capillary tubes. A clear need exists for refinement of the model to account for the characteristics of real surfaces. Factors which might be considered in extending the current work include better modeling of material properties and an extension of the theory to include surface coatings and impurities, porous media, surface defects, and rough surfaces.

Modeling of the frequency dependent dielectric behavior of materials of interest has posed a major difficulty in this study. The dielectric behavior of liquids of interest can be approximated using a procedure developed by Ninham and Parsegian [20]. However, some care must be used in applying this method, as Hough and White [21] have observed. Some information has been published on the frequency dependent dielectric behavior of common materials [3,23], but results have not been published for most materials of interest. The dielectric response of solids can be extracted from their optical spectra. Data on the optical spectra of many pure metals are readily available [22], but complete data for metal oxides and other materials are more difficult to obtain. The approach taken by Parsegian and Weiss [23] is most appropriate for modeling $\varepsilon(\omega)$ for conducting materials because it has a sound physical basis. The least squares fit recommended in this paper, however, is somewhat difficult to implement because it entails the solution of a complicated nonlinear algebraic system, which may lead to unstable solutions.

A great deal of work remains to be done on the effects of surface coatings and impurities on the van der Waals forces. I am currently engaged in extending the theory presented here to include surface coatings and surface impurity layers, including oxides. Although this effort is initially aimed at calculating the effect of a homogeneous layer of a single species, I hope to be able to incorporate impurity concentrations in my later models.

Surface roughness effects are also not considered in this study. Early on in this work it

was recognized that accounting for surface roughness effects would be a study in its own right. Past works [24,25] have incorporated surface roughness effects by using the Hamaker method of calculating van der Waals forces. Although this method is conceptually easy, several difficulties arise in practical applications. The first of these difficulties is that no adequate analytical model of rough surfaces currently exists. Recent work in fractal modeling of surfaces may be applicable in solving this problem [26]. A more serious difficulty is that the Hamaker approach does not account for retardation and many-body forces which makes the Hamaker approach a poor method for studying surface roughness effects in the presence of an absorbed layer.

An alternative to the Hamaker approach would be application of the surface mode analysis method. This method could be applied using a perturbation approach for thick absorbed layers. A layer is considered thick when the average asperity height is much less than the absorbed layer thickness. For other cases, the finite element approach might be used to calculate surface modes on rough surfaces. This approach could also be used to account for porous media and the presence of voids. Such a study would, however, be computationally intensive.

In conclusion, the present work has refined previous efforts to evaluate van der Waals forces in capillary tubes. This effort constitutes an essential step in evaluating the role of van der Waals forces in capillary pumping. Preliminary calculations indicate that, despite retardation by the absorbed layer, these forces will be significant in metal capillary tubes. More study will be required to determine whether or not optimization of capillary pumping in heat pipe wicks by appropriate materials selection and processing is viable. I am hopeful that many of these questions will be answered during the course of my thesis research, of which this study was a part.

REFERENCES

1. Wayner, P.C. Jr., Kao, Y.K. and LaCroix, L.V.,"The Interline Heat-Transfer Coefficient of an Evaporating Wetting Film," International Journal of Heat and Mass Transfer, V. 19, 1976, pp. 487-492.

2. Preiss, G. and Wayner, P.C. Jr.,"Evaporation from a Capillary Tube," Journal of Heat Transfer, V. 98, No. 2, 1976, pp. 178-181.

3. Wayner, P.C. Jr.,"The Effect of the London-van der Waals Dispersion Force on Interline Heat Transfer," Journal of Heat Transfer, V. 100, No. 1, 1978, pp. 155-159

4. Wayner, P.C Jr.," Effect of Thin Film Heat Transfer on Meniscus Profile and Capillary Pressure," AIAA Journal, V. 17, No. 7, 1979, pp. 772-776.

5. Swanson, L.W. and Herdt, G.C.,"Model of the Evaporating Meniscus in a Capillary Tube," Submitted to the 3rd ASME-JSME Thermal Engineering Joint Conference.

6. Mahanty, J. and Ninham, B.W., Dispersion Forces, New York, Academic Press, 1976.

7. Langbein, D., Van der Waals Attraction, Berlin, Springer-Verlag, 1974.

8. Israelachvili, J.N., Intermolecular and Surface Forces with Applications to Colloidal and Biological Systems, New York, Academic Press, 1985.

9. Hamaker, H.C., Physica, V. 4, 1937, pp. 1058-1072.

10. Lifshitz, E.M., Soviet Physics JETP, V. 2, 1956, pp. 73-83.

11. Dzyaloshinskii, I.E., Lifshitz, E.M., and Pitaevskii, L.P., Advances in Physics, V. 10, 1960, pp. 165-209.

12. Dzyaloshinskii, I.E., Lifshitz, E.M., and Pitaevskii, L.P.,"Van der Waals Forces in Liquid Films," Soviet Physics JETP, V. 37, No. 1, 1960, pp. 161-170.

13. Van Kampen, N.G., Nijboer, B.R.A., and Schram, K.,"On the Macroscopic Theory of van der Waals Forces," Physics Letters, V. 26A, No. 7, 1968, pp. 307-308.

14. Ninham, B.W., Parsegian, A.V., and Weiss, G.H.,"On the Macroscopic Theory of Temperature-Dependent van der Waals Forces," Journal of Statistical Physics, V. 2, No. 4, 1970, pp. 323-328.

15. Philip, J.R.,"Absorption and Geometry : The Boundary Layer Approximation," Journal of Chemical Physics, V. 67, No. 4, 1977, pp. 1732-1741.

16. Philip, J.R.,"Unitary Approach to Capillary Condensation and Absorption," Journal of Chemical Physics, V. 66, No. 11, 1977, pp. 5069-5075.

17. Richmond, P. and Ninham, B.W.,"A Note on the Extension of the Lifshitz Theory of van der Waals Forces to Magnetic Media," Journal of Physics C, V. 4, 1971, pp. 1988-1993.

18. Abramowitz,M. and Stegan,I.A., Handbook of Mathematical Functions, New York, Dover Publications, Inc., 1972, pp. 377-378.

19. Burden,R.L. and Faires,J.D., Numerical Analysis, 3rd ed., Boston, Prindle, Weber and Schmidt, 1985, pp. 172-175.

20. Ninham, B.W. and Parsegian, A.V.,"Van der Waals Forces", Biophysical Journal, V. 10, 1970, pp. 646-663.

21. Hough, D.B. and White, L.R.,"The Calculation of Hamaker Constants from Lifshitz Theory with Applications to Wetting Phenomena," Advances in Colloid and Interface Science, V. 14, 1980, pp. 3-41.

22. Palik,E.D., ed., Handbook of Optical Constants of Solids, New York, Academic Press, Inc., 1985.

23. Parsegian, V.A. and Weiss, G.H.,"Spectroscopic Parameters for Computation of van der Waals Forces," Journal of Colloid and Interface Science, V. 81, No. 1, 1981, pp. 285-288.

24. Van Bree, J.L.M.J., Poulis, J.A., Verhaar, B.J. and Schram, K.,"The Influence of Surface Irregularities upon the van der Waals Forces Between Macroscopic Bodies," Physica, V. 78, 1974, pp. 187-190.

25. Philip, J.R.,"Absorption and Capillary Condensation on Rough Surfaces," Journal of Physical Chemistry, V. 82, No. 12, 1978, pp. 1379-1385.

26. Hazlett, R.D.,"Fractal Applications: Wettability and Contact Angle," Journal of Colloid and Interface Science, V. 137, No. 2, 1990, pp. 527-533.

1990 USAF-UES SUMMER FACULTY RESEARCH PROGRAM

GRADUATE STUDENT RESEARCH PROGRAM

Sponsored by the

AIR FORCE OF SCIENTIFIC RESEARCH

Conducted by the

Universal Energy Systems, Inc.

FINAL REPORT

Design and Analysis of Reaction Wheel Actuators for ASTREX

Prepared by:	Tom C. Pollock and Johnny E. Hurtado
Academic Rank:	Assoc. Professor and Graduate Student
Department and University:	Aerospace Engineering Department Texas A & M University
Research Location:	Astronautics Laboratory Edwards AFB, CA 93523
USAF Researcher:	Alok Das, Ph.D.
Date:	September 21, 1990
Contract No:	F49620-85-C-0013

Same Report as
Prof. Thomas Pollock
(Report # 21)

1990 USAF-UES SUMMER FACULTY RESEARCH PROGRAM/

GRADUATE STUDENT RESEARCH PROGRAM

Sponsored by the

AIR FORCE OFFICE OF SCIENTIFIC RESEARCH

Conducted by the

Universal Energy Systems, Inc.

FINAL REPORT

THE EFFECTS OF ELEVATED TEMPERATURE EXPOSURE ON THE STRENGTH AND MICROSTRUCTURE OF 2-D CARBON-CARBON

Prepared by:	Christopher G. Kocher
Academic rank:	Graduate Student
Department and	Theoretical and Applied Mechanics
University:	The University of Illinois at Urbana-Champaign
Research Location:	AL/VSSC
	Edwards AFB, CA 93523-5000
USAF Researcher:	Dr. Peter B. Pollock
Date:	August 15, 1990
Contract No:	F49620-88-C-0053

I. INTRODUCTION

As the demand for lightweight, strong, high-temperature materials increases, 2-D carbon-carbon is rapidly becoming a candidate material for primary structural applications. Current uses lie primarily in aerospace, where carbon-carbon is utilized due to its low coefficient of thermal expansion (CTE), high strength-to-weight ratio, resistance to ablative and corrosive environments, and its high-temperature stability. Such applications include space radiators for heat dissipation, mirror substructures, rocket nozzles, and high-temperature surfaces (skins) of advanced aerospace vehicles. Other fields, however, are beginning to see uses for the material as well. In medicine, for instance, carbon-carbon hip joints and bone plates have been successfully tested. In the automotive industry, carbon-carbon is used for high-performance race car brakes and clutches (tribological applications).

As carbon-carbon receives increasing consideration as a candidate material for primary structural elements, it becomes more important that the mechanical response of the material to a variety of mechanical and thermal loadings be understood in detail. Designers of advanced aerospace vehicles must have certain knowledge of the material properties in order to achieve efficient designs which minimize weight while optimizing strength. A high premium is placed on an efficient design when the weight of a structure must be kept to an absolute minimum. Understanding the behavior of the material as well as any effects induced by the service environment can aid in the improvement of the material. If the failure is known to occur in one particularly undesirable manner, the composite can perhaps be altered somehow to eliminate that failure mode with the goal of improving the properties of the material. Composites are unique in that they can be tailored specifically for a given purpose.

Many applications of carbon-carbon involve subjecting the material to extreme heat on the order of several thousand degrees Fahrenheit. Certain behavioral changes

from such an environment are known, qualitatively. Elevated temperature exposure will, for instance, increase the density of cracks in the material and therefore cause an associated degradation in material and thermal properties. Qualitative explanations are not sufficient, and a thorough quantitative study is essential.

To this end, the Composites Lab at the Edwards Air Force Base Astronautics Laboratory has a strong interest in determining the environmental effects on structural carbons and methods of subsequently improving the material through programs aimed at evaluating various fabrication methods.

The research discussed herein dealt with the effects of thermal exposure on the mechanical properties and microstructural characteristics of a 2-D carbon-carbon laminate consisting of carbon fiber bundles woven into an 8-harness satin weave and surrounded by a matrix of pyrolitic carbon deposited by chemical vapor deposition (CVD).

The structure of pyrolitic carbon is generally classified according to its optical texture, i.e its appearance under an optical microscope using crossed polarizers. Such lighting will then reflect colors particular to the orientation of the carbon crystallites relative to the light source. The structures depend on the deposition conditions within the CVD reactor (temperature, pressure, source gas, etc.), but local variations of the deposition conditions within the material can occur producing varying optical textures regardless of the conditions exterior to the composite. Each microstructural form of pyrolitic carbon has different mechanical properties depending on the crystallite size and density. The mechanical properties of a variety of CVD deposits have been reported in the open literature.

It is known that heating carbon-carbon to extreme temperatures induces microcracks within the matrix due to differences in CTE of the longitudinal and transverse bundles. A shear lag phenomena is proposed for the cause of this network of transverse cracks which lie in and are oriented parallel to the fiber bundles. These

transverse cracks reduce both the modulus and CTE of the composite. A second type of microcracking can occur, namely crack formation at the fiber/matrix interface. Interface cracks can propagate completely or only partially around a fiber. Although microcracks can degrade certain mechanical and thermal properties of the composite, they can serve to improve its fracture toughness. A crack propagating through the material may encounter a microcrack, be deflected, stop, and require a considerable increase in strain energy to propagate further.

The differential in temperatures between the temperature at which carbon-carbon materials are processed (near 2000°F) and room temperature is sufficient to induce microcracking within the matrix of the composite; thus, simply from the manufacturing process, a carbon-carbon component is already considerably weaker than the theoretical maximum strength predicted from the properties of the undegraded constituents. If the component is then exposed to temperatures above the processing temperature, then additional microcracking may occur causing further reduction in properties.

A Bachelor's and a Master's degree in engineering mechanics with an emphasis on the mechanics of composite materials, coupled with several years experience performing microstructural studies of carbon-carbon materials provides me with an excellent background to study these materials. The study of composites is a strongly interdisciplinary field in which both microscopic and macroscopic descriptions of material behavior are essential for completeness.

II. OBJECTIVES OF THE RESEARCH EFFORT:

Several objectives were specified at the onset of this work:

(i) determine how elevated temperature exposure in an inert atmosphere affects the tensile (warp and fill), and shear (warp only) strengths and moduli, and fracture strength, of 2-D CVD-matrix carbon-carbon via a comprehensive testing program,

(ii) determine any microstructural changes, in terms of microcracking and crystallite structure, that occured in the material as a consequence of heat treatment,

(iii) correlate microstructural changes with experimental results,

(iv) develop analytical models to complement experimental observations.

Most of the above objectives were satisfied, at least in part, with the exception of the fracture and compression testing, and obtaining the crystallite structure of the matrix material. All of the mechanical tests have been completed and the data reduced. A comprehensive series of microphotomontages were made of the material from each temperature treatment. These were used to make crack density measurements. Analysis is ongoing to correlate microstructural changes and experimental observations with each other.

The fracture and compression testing did not work for this material. In the case of the fracture tests, it was planned to use the compact-tension test to determine the fracture strength of the material across the warp yarns. As it turned out, that specimen geometry was not successful. So, as all of the specimens had been prepared, we decided to convert them to compression specimens to collect compression strength and modulus. This, too, failed due to inaccuracies in the alignment of the load train on the servohydraulic testing machine and its high sensitivity to inaccuracies in specimen machining.

Some new objectives were specified as the project became underway. Upon investigating the montages, evidence appeared that a type of crack not expected was forming, so it became necessary to analyze the mechanism of formation for these cracks. This became the responsibility of another summer student (Rebecca Teders). A second, additional objective arose out of a need to separate the damage induced from mechanical loading from that already present from the thermal loading. This effort, also the responsibility of another summer student (Bruce Hinds III), led to the identification of the tensile failure process in the material. While the mystery surrounding the formation of the "odd" cracks has yet to be solved, the tensile failure process has been determined.

III. MATERIAL DESCRIPTION

The 2-D carbon-carbon laminates used in this study were manufactured by HITCO using their CVD reactors. The cloth consists of T-300 (PAN) fiber bundles with 3000 filaments per bundle woven into an 8-harness satin weave. The weave has 24 bundles per inch in the warp direction and 23 bundles per inch in the fill direction, so the weave is very nearly balanced, i.e. it has the same number of ends in both the warp and fill directions. The cloth was first heat set at 4500°F. This was done so that the effects of heat treatment on the composite could be attributed to changes in the matrix only. Since the fiber structure would change with increased temperature, exposing the cloth to the highest expected temperature prior to composite fabrication "locks in" the microstructure formed at that temperature. Thus, any subsequent HTT up to or below the highest temperature experienced by the fibers will not alter its structure.

Thirty-eight dry plies were cut to approximately 14" x 11.5", stacked, warp aligned, to fabricate each of three laminates. The stacked cloth was then sandwiched

between 11" x 13" x 0.750" graphite plates with a rectangular array of 120 0.125" dia. holes spaced 1" apart in each direction. The assemblies were then infiltrated with a pyrolitic carbon matrix derived from methane through a total of five 125-hour densification cycles. The material (dry plies between graphite plates) was run through two densification cycles. The graphite plates were then removed and the panels were run through another densification cycle. After the third cycle, the panels were taken out of the furnace and machined to 12.1" x 10.1" x 0.325" then put through the two final densification cycles. Although most of the particulars of the deposition process are proprietary, and thus could not be related to us, it was revealed that the deposition temperature was approximately 1800°F, and the same deposition conditions are maintained within the reactor for each cycle. Intermittently between some of the CVD runs, the plates were removed from the furnace, weighed, and measured to calculate the bulk densities. The densities evolved as follows:

	PLATE #1	PLATE #2	PLATE #3
DENSITY AFTER SECOND CYCLE	1.536 g/cc	1.578 g/cc	1.536 g/cc
DENSITY AFTER THIRD CYCLE	1.7068 g/cc	1.6165 g/cc	1.6639 g/cc
AFTER MACHINING TO 12.1" x 10.1" x 0.325"	1.556 g/cc	1.509 g/cc	1.536 g/cc
DENSITY AFTER FOURTH CYCLE	1.604 g/cc	1.593 g/cc	1.597 g/cc
DENSITY AFTER FIFTH CYCLE	1.627 g/cc	1.614 g/cc	1.617 g/cc

HITCO estimated the fiber volume fractions of the plates to be 47%, 41%, and 49%, respectively. These calculations are based on the weight of the dry plies divided by the fiber density (1.92 g/cc) divided by the total volume, 1046 cc (14" x 12" x 0.380").

The fiber volume fractions in each direction of the finished composite, however, can be calculated based on the number of fibers per inch, the thickness of a single ply, and the across-sectional area of a single fiber (using an average radius of 6μm). These calculations yield 31% in the warp direction and 30% in the fill direction, or approximately 60% overall. This value compares well with values obtained using image analysis of high-magnification microphotographs. From this method, a fiber volume fraction of 62.03% ± 0.83% within a bundle, or 31% in that direction.

The same image analysis technique gave a void volume fraction (within a bundle) of 8.07% ± 1.1%. The volume fraction of interbundle voids was not determined.

IV. EXPERIMENTAL PROGRAM

To investigate the changes in material properties and microstructure of the material induced from high temperature exposure, a comprehensive testing plan was devised through which all of the moduli and strengths of the material subjected to various temperature ranges could be determined. It was decided that tension in the warp, fill, and 30° off-axis directions would give all of the in-plane moduli. The Iosipescu shear test was used to give the shear strength data, and the compact tension fracture test would give the fracture toughness of the material.

An appropriate specimen cutting plan was implemented to maximize the number of specimens. The specimen near-net shapes were cut from the panels using a diamond-impregnated band saw blade. The tension specimens were ground to final dimensions

using a high-speed diamond-impregnated router bit and an aluminum template to give uniformity of dimensions. The compact tension specimens were machined on a conventional milling machine using carbide tooling. The Iosipescu shear specimens blanks were sent to Ultracarbon for final machining. To double the number of tensile specimens, all of them were sent to the Permag Corporation where they were sliced along the midplane of the laminate and ground to no more than 0.0005" deviation in thickness along the length of each specimen.

The material was divided into groups for four temperature histories. One group remained as-received, while the remaining groups were subjected to 2700°F, 3500°F, and 4500°F, respectively.

Heat treatment was done in an Astrofurnace manufactured by Astro Industries. Prior to each run the chamber was evacuated to 10^{-5} torr and backfilled with 10-15 psi of helium. Two runs were made to 4500°F. For one run, the heating rate was very fast; the final temperature was reached within 2.5 hrs. A second group of specimens was heated to the same temperature at a slower rate of 200°F per hour. For both runs, the material was allowed to soak at the maximum temperature, then the temperature was decreased to ambient within 3 hours. The furnace is controlled by a programmable controller which was not working properly at the time, so the cooling rates were not controllable. The machine simply shut off the power to the heating elements and cooled the chamber with room temperature water.

Due to nonlinearities in the response of the system, the initial temperature ramp could not be accurately controlled. Hence the chamber reached 2000°F in a shorter time than was anticipated. This was expected not to cause undue thermal shock to the material, since it had already seen a similar temperature during processing.

Ramp rates of approximately 200°F per hour were used for the remaining temperature runs.

Tests were performed using an MTS tension-torsion materials testing machine with a 50,000 lb capacity. Displacement data from the tension tests was taken with a clip-on extensometer. Displacement data was channelled through an amplifier into a data aquisition system. Load output was fed directly into the computer from the MTS machine.

During the tension tests, a clevis joint was used between the upper grip and the crosshead to prohibit the influence of bending or twisting induced by misalignment of the grips. Wedge-type mechanical grips were used to grip the specimens. Great care was taken to insure alignment of the specimens in the grips for all tests. Only 1 or 2 of approximately 30 tension specimens failed near the grips. The gage section dimensions were 0.75" x 0.125 " and 4" long. Aluminum end tabs were bonded to the ends of the specimens using cyanoacrylate-based cement.

Edge replications were made periodically on some of the tension specimens during the loading. Prior to loading, the specimens were polished along one edge down to 0.3 μm using alumina polishing grit. During testing, the load was held fixed and a replication was made. During this time displacement data was not taken. The process involved the application of acetate tape softened with acetone to the edge of the specimen. The replica took a half hour or more to dry, so the material had to be kept under load for that time until the finished replica could be removed. As the test was resumed and extensional data taken again, a drop in load was seen on the stress-strain curve. This particular type of material may be susceptible to creep relaxation over relatively short periods of time. This has not been investigated yet. Attempts were made to obtain replications at or near the time when delamination began to appear. This point on the stress-strain curve was known, since the initiation of delamination cracks produces a sudden reduction in laminate stiffness. As the stress-strain curve for the test was monitored in real time as the test was occurring, this "yield point", or onset of delamination, could be determined and the test held at that point.

Iosipescu shear tests were performed in a special fixture manufactured at the University of Wyoming. Each specimen had a notch radius of 0.1875" and a gage width of 0.400". The thickness of the specimens was 0.33". Due to the difficulty of obtaining strain or displacement data at the highly localized net section, only load and crosshead displacement data were obtained.

In performing the fracture tests, it was discovered that the compression strength of the material was lower than anticipated. Extension of the initial crack did not occur, but rather the material failed in compression at the rear of the specimen. This caused all of the fracture specimens to be converted into compression specimens.

The dimensions of the compression specimens were approximately 0.7" x 1.0" x 1.5". The low area to length ratio was assumed to be adequate to prohibit global buckling of the specimens.

Edge replications were made of some of the compression specimens as well.

To determine the tensile strength and modulus of the matrix material, HITCO provided us with scale from the inside of their CVD furnaces. An attempt was made to try to make tensile specimens out of this material, but it proved to be too difficult a task. Due to the small size of the raw CVD material, the specimens made from it had to be small as well. As brittle as the material was, it was easily broken and so specimens could not be successfully fabricated. It was, however, possible to bond strain gages to the carbon. There had been some question about this matter. More material was requested from HITCO for a later attempt to do these tests.

V. MICROSTRUCTURAL OBSERVATIONS

Samples of the as-received and heat treated material were examined using optical microscopy. Considerable variation in the microstructure of the pyrolitic

carbon matrix was seen in a given sample. Within the bundles, the matrix carbon appeared to have an isotropic texture derived from deposition at high temperatures (>1250°C) and low gas concentrations (>30%), according to Oh and Lee (1988). This is in contradiction to what would be expected from the "known" process temperature. Such a low temperature (980°C), according to Oh and Lee, would produce a smooth laminar structure, regardless of the concentration of the gas. The interbundle matrix, however, possessed the expected smooth laminar structure. A number of boundaries between distinctly different structures were seen within the matrix. It was thought that these boundaries corresponded to the end of one deposition and the beginning of another. This was later found to be false. The optical texture of CVD carbon can change abruptly within a continuous deposit. A hypothesis for this phenomena is that local changes in deposition conditions take place within the component producing a changing microstructure. The abrupt changes in structure may be due to the sudden crossing of a phase boundary as the concentrations of the CVD species changes.

No textural changes in the nature of the CVD coatings was observed with respect to the heat treatment temperature seen by the material, as heat treatment does not alter the optical texture of CVI carbon. Hence other microscopic methods are necessary to determine the qualities of the matrix material. An attempt was made to use X-ray diffraction analysis using a sample of the composite, but the fiber and matrix peaks were inseparable. The broader fiber band covered up the matrix band. Now that we have raw matrix material, an attempt may be made to try the analysis again with pure matrix material. Another method, scanning tunneling microscopy (STM) was tried for this purpose. Samples of both composite and pure matrix were prepared, but the results were not what we wanted. The STM gave us information about the surface of the material, not about its crystal structure. Several other techniques, transmission electron microscopy and laser ramann microprobe analysis, are currently being investigated for the determination of the crystallite parameters l_c and d_{002}. Knowing

these parameters will enable the quantification of microstructural changes brought about by heat treatment and the estimation of the mechanical properties of the matrix material based on data available in the literature.

Photographic montages of all materials were made using an optical microscope at low magnification (50x). From these montages, the crack densities could be determined. The distance between two adjacent cracks was measured with a ruler, and this measurement was repeated 100 times over each specimen taking a random distribution of transverse cracks. The crack density (cracks per inch) was found to vary linearly with temperature from 125 cpi at 1800°F to 195 cpi at 4500°F. No theoretical explanation for this phenomena is as of yet proposed.

Crack widths were also measured for each temperature using an optical microscope at high magnification (1000 x) fitted with a reticle for measurements. A total of 120 measurements for each temperature were made, all by another summer student Deborah Sewell). The trend of the data is that the average crack width increases with temperature to the 3500°F point, then the crack width decreases. No explanation is offered for this phenomena.

In addition to the straight transverse cracks, a number of angle cracks were observed. The study of these cracks using a shear lag model has been undertaken by another summer student (Rebecca Teders) investigating the mechanism of formation of these cracks using finite element analysis to investigate the thermal stresses induced from cooling the composite through a large temperature differential. Several modifications were made to the model, but none of them gave results matching experimental observations. This subject will be addressed in the future.

It is anticipated that porosity measurements will be made. Porosity has been shown to play an important role in the response of carbon-carbon composites. Image analysis indicates that the fiber bundles in the composite contain approximately 8%

voids. This value may vary by one or two percent between different samples, thus explaining some of the scatter in the experimental data.

VI. EXPERIMENTAL OBSERVATIONS

The experiments gave not only the usual quantitative data about strength and modulus, but also a wealth of information regarding the physical behavior of the material. The edge replication method proved to be highly effective in determining the tensile failure process of the carbon-carbon.

Prior to mechanical loading, the material is laden with a network of transverse cracks formed during thermal cycling. These transverse cracks are regularly spaced, a fact which brings to mind the concept of a "saturation crack density." Because of the differences in thermal expansion coefficient in the two fiber (or bundle) directions, discontinuities in normal stress occur between the longitudinal and transverse bundles. This normal stress discontinuity produces a very high shear stress gradient between the crossing bundles. This shear lag phenomena is thought to be responsible for the development of the transverse cracks. It is interesting to note that, for a given sample of material, mechanical loading does not introduce additional transverse cracks within the material. The possibility of the material already having reached its saturation crack density prior to the onset of mechanical loading is discounted because the material exposed to higher temperatures possesses higher crack densities. The material, then, through undergoing a high temperature differential, forms a pattern of transverse cracks, the density of which is related directly to the magnitude of the temperature differential.

As the mechanical loading introduces even greater strain in the material than that incurred during thermal cycling, it is expected that the additional mechanical loading would increase the density of the transverse cracks. This is known not to occur. An edge replication was made of a sample after thermal loading and prior to mechanical loading. Then, the specimen was tested, and another replication was made at 34 ksi. Comparison of the two replications (made of the same region) indicates no increase in the number of transverse cracks. It also may rule out the possibility of crack closure having occurred since the patterns of transverse cracks from the two replicas overlap exactly. The observation that there is no change in the transverse crack density implies a either fundamental difference in the nature of the two types of loading or that a different failure mechanism becomes predominant prior the formation of additional transverse cracks. This difference has yet to be investigated.

Edge replication has revealed the tensile failure process to be as follows:

Because of variations in crimp angle between adjacent longitudinal (parallel to the loading direction) bundles, the two bundles will have different stiffnesses and thus move relative to each other in response to a uniform axial strain. This relative displacement produces a shear stress gradient across the transverse bundle between the two longitudinal bundles. Because of this shear stress, a series of diagonal cracks form at both bundle interfaces and propagate inwards toward existing transverse cracks. When the cracks are linked, the upper and lower portions of the transverse cracks then close (they are no longer visible on the replicas), and the transverse bundle appears then to be saturated with regularly-spaced s-shaped cracks. The matrix material, being brittle, is assumed to fail on a plane of maximum normal stress. Making measurements from the replicas, the angled cracks were oriented at approximately 30° to the loading axis. Based on this angle and the applied axial stress (20 ksi) at the formation of the angled cracks, a maximum principal stress (directed at 60o to the applied load) of 30 ksi was calculated. This value is in the acceptable range, though on the high end, of

known data for the tensile strength of pyrolitic carbon. The shear stress at the bundle interface is then 17.3 ksi.

Once the angled cracks have linked up with the transverse cracks forming the "s-cracks," delaminations initiate at the bundle interface (one of them only) and propagate along the interface, in the direction of the applied load. It is known from previous investigations with composite laminates fabricated from unidirectional material, that the magnitude of the interlaminar normal stress is very high at the free edge. Depending on the particular theory used, for a composite tensile modulus of 16 Msi, the interlaminar normal stress can be between 1.25 and 1.88 times the applied axial stress. These delamination cracks appeared at an axial stress of approximately 25 ksi. The delamination cracks then link with each other causing global separation of the layers. Once the layers have separated, they will share unequal portions of the load and begin to fail in turn until the entire laminate has failed. The delamination was visible not only from the replicas, but was so pronounced as to be easily visible to the naked eye.

The failure surfaces of the specimens were broomed out, virtually eliminating the hope of examining the failure surfaces under an electron microscope. The delaminations ran the entire length of the gage section.

so, it appears that the 8-harness weave behaves very much like a cross-ply laminate fabricated from unidirectional material, at least locally, where the longitudinal bundles are straight.Several failure mechanisms were observed in the 2-D carbon-carbon that are typical of cross-ply laminates:

(i) the formation of regularly-spaced transverse cracks, and

(ii) delamination at the 0-90 interface due to high interlaminar normal stresses.

VII RESULTS

Although not all of the data has been processed, some preliminary results are given. The heat treatment to the highest temperature brought about a 13% decrease in delamination strength, a 22% decrease in shear strength, and a 60% increase in crack density. The tensile moduli did not change (as was expected), but the snear modulus was reduced by 16%. The tensile strength in the warp direction was, on the average, 5% or so higher than the fill strength. This is attributed to differences in crimp angle in the warp and fill directions, and the differences in fiber volume fraction in the two directions (24 bundles per inch in the warp direction vs. 23 bundles per inch in the fill direction). In the weaving process, the warp bundles are kept taught while the fill, or weft, bundles are woven between them. This causes the warp bundles to have less curvature than the fill bundles, but this effect is less pronounced in an 8-harness satin weave.

Only the shear strength across the warp bundles was tested, as they are the strongest. The shear data showed little scatter, while considerable scatter was seen in the tension tests. The data has not been normalized to the porosity, but it is believed that doing so would eliminate a significant portion of the scatter. It is well established that porosity decreases the strength of materials, particularly brittle materials, which are more sensitive to flaws. Much of the porosity in the material was seen from microscopy to have sharp corners which might serve as sights for crack initiation. The more potential sites, the higher the probability of premature failure.

The compression tests have not been completed as of this writing, and it is unknown if they will ever be. A few tests were performed with widely varied results giving cause for concern. It was found that the current compression loading fixture is extremely sensitive to slight misalignments or inaccuracies in specimen dimensions, i.e.

if the upper and lower surfaces are not parallel to within 0.0001". Two new compression test methods are under evaluation.

No study of the failure surfaces of the shear specimens has been undertaken. It would be of interest to examine in detail the failed specimens to ascertain the failure process in shear as well.

VIII RECOMMENDATIONS

Examination of the results gathered thus far has indicated areas requiring further exploration. The tensile failure process has been determined, but the shear failure process should also be determined. Analysis of ultimate failure as related to the crimp angles of the fiber bundles should also be addressed. In general, a good deal of work is required to correlate theory with experimental observations before more definite conclusions can be drawn.

The edge replication technique has proven to be a valuable tool in determining the failure process of this material, but it has some disadvantages. It is hoped that the Composites Lab at Edwards AFB will purchase a video system whereby the failure process can be viewed continuously in real time, recorded on video tape, and the resulting images enhanced through computerized image analysis.

IX ACKNOWLEDGEMENTS

First and foremost, I wish to thank the Air Force Office of Scientific Research and Universal Energy Systems for sponsorship of this research and providing the excellent program allowing myself and many other students and faculty around the country to gain experience ar such highly regarded research institutions.

I would also like to thank Mr. James Wanchek, TSGT. Hamm, and the entire staff of the Composites Lab at Edwards AFB for their continued support of the summer program and their willingness to accommodate our specific needs. In particular, Dr. Peter B. Pollock of the University of Dayton Research Institute, with whom this work was performed, is to be commended for providing me, and a host of other summer students, with such an outstanding opportunity to learn about the business of doing science.

1990 USAF-UES SUMMER FACULTY RESEARCH PROGRAM/

GRADUATE STUDENT RESEARCH PROGRAM

Sponsored by the

AIR FORCE OFFICE OF SCIENTIFIC RESEARCH

Conducted by the

Universal Energy Systems, Inc.

FINAL REPORT

INVESTIGATING THE LOADING RATE EFFECT ON THE CRACK GROWTH BEHAVIOR IN A COMPOSITE SOLID PROPELLANT

Prepared by: HSIEN-YANG YEH, PH.D., MINH D. LE

Academic Rank: ASSOCIATE PROFESSOR

Department and University: MECHANICAL ENGINEERING DEPARTMENT, CALIFORNIA STATE UNIVERSITY, LONG BEACH

Research Location: ASTRONAUTICS LABORATORY
EDWARDS AIR FORCE BASE, CA 93523-5000

USAF Researcher: C.T. LIU, PH.D.

Date: JULY 16, 1990

Contract No: F49620-88-C-0053

Same Report as
Prof. Hsien-Yang Yeh
(Report # 25)

1990 USAF-UES SUMMER FACULTY RESEARCH PROGRAM

GRADUATE STUDENT RESEARCH PROGRAM

Sponsored by the

AIR FORCE OFFICE OF SCIENTIFIC RESEARCH

Conducted by the

Universal Energy Systems, Inc.

FINAL REPORT

CONTROL DESIGN OF ASTREX TEST ARTICLE

Prepared by:	Hung V. Vu, Ph.D., Assistant Professor
	Joseph P. Baldonado, Graduate Student
	Hung M. Nguyen, Graduate Student
Department and	Mechanical Engineering
University:	California State University, Long Beach, CA 90840
Research Location:	Astronautics Laboratory / VSSS
	Edwards AFB, CA 93523
USAF Researcher:	Alok Das, Ph.D.
Date:	September 20, 1990
Contract No:	F49620-88-C-0053

Same Report as
Prof. Hung Vu
(Report # 23)

1990 USAF-UES SUMMER FACULTY RESEARCH PROGRAM/

GRADUATE STUDENT RESEARCH PROGRAM

Sponsored by the

AIR FORCE OFFICE OF SCIENTIFIC RESEARCH

Conducted by the

Universal Energy Systems, Inc.

FINAL REPORT

Introductory Study of Compression-Shear Interaction in 3-D Carbon-Carbons

Prepared by:	Christine A. Perry
Academic Rank:	Graduate Student
Department and	Aerospace Engineering
University:	Pennsylvania State University
Research Location:	AL/VSSC Edwards AFB California 93523
USAF Researcher:	Dr. Peter B. Pollock
Date:	18 Sept 90
Contract No:	F49620-88-C-0053

Introductory Study of Compression-Shear Interaction in 3-D Carbon Carbons

by

Christine A. Perry

ABSTRACT

Testing of 3-D carbon-carbon specimens under pure compression, pure shear applied by torsion, applied shear with constant compressive load, and applied compression with constant shear stresses was planned on an MTS machine capable of applying axial loads and torque. The response of the material to this testing was to expose the types of weave distributions within the fiber bundles. From here, theories on compression-shear interaction could be evaluated. While testing was not performed due to certain obstacles, progress was made in understanding the linear assumptions within the theory of torsion, viewing the untested material via microscopy, and designing a fixture with the ability of applying a combined loading of compression and torsion, while taking into account certain requirements necessary for more precise compression testing.

Acknowledgements

I wish to thank the Air Force Systems Command, the Air Force Office of Scientific Research, and the Air Force Astronautics Laboratory for sponsorship of this research. I would also like to thank Universal Energy Systems for their administrative help.

Dr. Pete Pollock shared his knowledge so that I could expand my knowledge of what "science" and research is all about, for this I wish to express my gratitude. His collaboration and guidance helped me through many an obstacle.

I wish to thank all those (including technicians, fellow student researchers, and supervisors) at the Composites Lab with whom I had the pleasure of working with this Summer. The encouragement of Dr. David W. Jensen and Dr. Roger C. Thompson of the Pennsylvania State University was greatly appreciated. Finally, the unending concern and support of Danniella Muheim Thompson and Dr. Roger C. Thompson during my stay in California will not be forgotten.

I. INTRODUCTION:

Carbon-carbon composites are a material with high temperature capabilities. This feature continues to spark interest in its research for use in areas such as space structures and on the National Aerospace Plane (NASP). It is necessary, for these materials to be used confidently and to their highest potential, to understand and predict their behavior.

Recently at the Air Force Astronautics Laboratory, Dr. Peter Pollock began working on 3-D fine weave carbon-carbon billets received from FMI with the intention of researching the material's behavior under compression/shear combined loading. Through experimental and theoretical research, an understanding of the material can be developed to assess theories on compression-shear interaction, particularly one contained in "Shear Stress-Strain Relation Obtained From Torque-Twist Data" by S.B. Batdorf and Robert W.C. Ko.

The above study requires someone with a background in structures/solid mechanics, as well as an understanding of the mechanics of composite materials. My undergraduate study in Aerospace Engineering provided an extensive background in statics, dynamics, strength of materials, and aerospace structures (both course and laboratory work). Also, as an elective, an introduction to composite materials class supplied the necessary first principles for composite study. My graduate research interests were inspired by this introductory course to include the study of composites and understanding their behavior through analytical and computational methods.

II. OBJECTIVES OF THE RESEARCH EFFORT:

My assignment was to evaluate theories about compression-shear interaction in 3-D rectangular weave carbon-carbon composites through experimental testing. Although compression-shear coupling is currently inadequately understood, it can be very important when the compressive modulus is orders of magnitude greater than the shear modulus. Such is the case for carbon-carbon where the weakness in shear is due to the weak interfaces of the fiber bundles that are only as strong as good graphite.

To understand compression-shear coupling, the types of fiber deformations and interactions under these loadings must be understood. The weave distributions are of particular interest since the nonlinearity of the material in shear is due to exactly what the distributions are. The response of 3-D carbon-carbons to a cylinder torsion test with an applied axial load is expected to expose the nonlinearity response of the material. Keeping this in mind, the experimentation then needs to be understood not only from a mechanical view, related to loads and geometry, but also from a materials view, related to weave distributions and voids within the fiber bundles and matrix.

III. THEORETICAL STUDIES:

a. Since a nonlinear response is expected from carbon-carbons in shear, the research began by deriving the theory of torsion, paying particular attention to the linear assumptions made. Basically, two areas are linearized within the theory: material-related and geometry-related. By understanding the affects of

the linearities, it will be possible to determine when these assumptions are no longer valid.

Looking at figure 1 on the following page, the geometric nonlinearity comes from a small angle assumption. The relations,

$$d = R\theta \tag{1}$$

$$d = \tan\gamma \tag{2}$$

can be linearized at small angles with,

$$\gamma = \tan\gamma \tag{3}$$

The material linearity results from using Hooke's Law, noticing the sheared element in figure 1,

$$\tau = G\gamma \tag{4}$$

From equations (1) - (4), the well-known torsion relations are derived:

$$\tau = Tr/J \tag{5}$$

$$\theta/L = T/GJ \tag{6}$$

After this derivation, the small angle assumption was examined to determine its range of validity. By deriving the theory of torsion without equation (3), a nonlinear equation results from solving with equation (1) and equation (2):

$$T = \frac{2\pi GL^3}{\theta^3}\left[\frac{1}{3}\left(\frac{R\theta}{L}\right)^3 \tan^{-1}\left(\frac{R\theta}{L}\right) - \frac{1}{6}\left(\frac{R\theta}{L}\right)^2 + \frac{1}{3}\ln\sqrt{1+\left(\frac{R\theta}{L}\right)^2}\right] \tag{7}$$

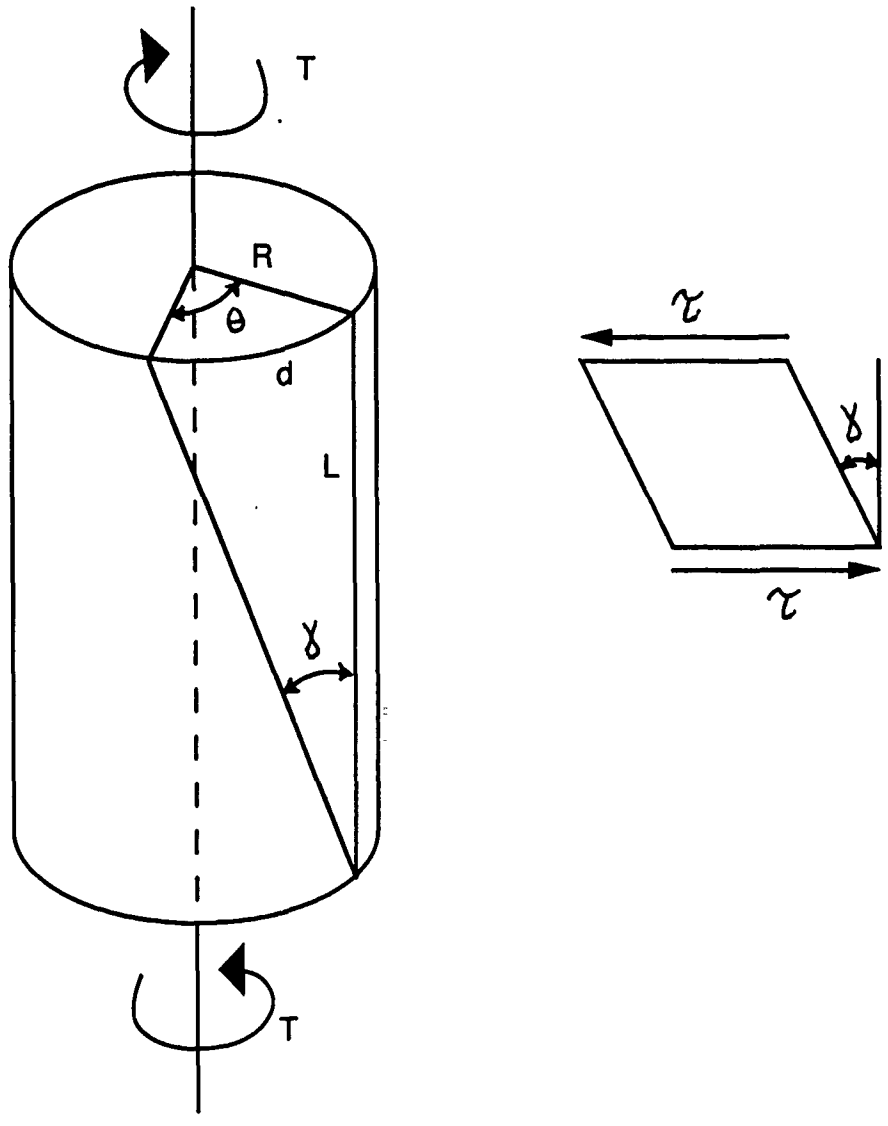

Figure 1. Cylinder and element with applied torque

The material linearity assumption has not been studied. It will be examined after the specimens have been tested by studying the weave distributions (through microscopy and possibly replication methods) and testing results.

b. Two equations were obtained for the angle of twist of a cylinder related to an applied torque. Equation (6) and equation (7) were plotted for a range of θ / L and compared. The results of this comparison determined that, before yield, the geometric linearity was valid for the future testing. For angles of twist up to 124 degrees, the linear equation resulted in less than a 2.5 % error for the carbon-carbon material. Depending on the extent of the twist after yield, the geometric nonlinearity may or may not play as important a role as the material nonlinearity.

IV. EXPERIMENTAL STUDIES:

a. The material obtained for testing was three 3-D fine weave carbon-carbon composite billets received from FMI with approximate dimensions of 2.7 inches by 2.17 inches by 0.67 inches. Because the available material was limited, restrictions on the number of planned tests resulted.

Since the objective was to evaluate theories, particularly one by S.B. Batdorf and Robert W.C. Ko, S.B. Batdorf was contacted by Dr. Pollock to obtain his thoughts concerning what tests might be useful. His reply on April 10, 1990 listed the following: successive loading and unloading in compression, successive loading and unloading in shear, loading in shear in the presence of two different constant compressive loads, and loading in compression in the presence of two different constant shearing stresses. This outline was adopted

and, taking the material limitations into account, two specimens for each type of test would be used with rectangular specimens for the pure compression tests and cylindrical dogbone specimens for the pure torsion and compression/torsion tests.

The actual testing of each specimen would be preformed on an MTS machine capable of applying axial loads and torque. Before any carbon-carbon tests, a steel cylinder was tested under pure compression for calibration purposes. When the correct Young's modulus was not determined from the resulting stress-strain curves, the testing was halted. Basically, two reasons for the inaccurate runs were found. First, end faces of all the specimens must be ground to a higher precision to eliminate uneven loading across the specimen. The original steel cylinder's end faces were machined flat and parallel to an accuracy of one thousandth. Acceptable results, errors under ten percent, were not obtained until the accuracy was increased to one ten-thousandth. Second, alignment of the MTS machine's grips was necessary. Although the misalignment is small (on the order of 0.002 inches per inch), it was enough to produce inaccuracies in the compression testing. For the pure compression tests, this problem was solved using a spherical bearing as one test fixture. This allowed one grip of the machine to align with the other by rotating over a spherical surface contained within the device. The bearing however, would not be used for the torsion tests due to its design.

After the above problems arose, the main research went into designing a testing fixture that took into account the above requirements and could be used for compression/torsion testing.

b. The final design to date, presently being manufactured at the Composites Building of the Astronautics Laboratory, is a combination of steel and epoxy. The fixture is shown in figure 2 on the following page. A thin layer of epoxy will be poured into the well of piece 4. This layer is not initially present but added to the fixture shortly before the experiment is to be performed and cures with piece 3 resting in the layer. By using a layer of epoxy, the misalignment of the MTS machine is corrected. Also, it should be mentioned that the surfaces of piece 1 and piece 3 with which the specimen will be in contact are to be ground to an accuracy of one ten-thousandth.

The exact procedure for this design is not known. However, in general the following will apply. Piece 1 will be placed in the upper grip and piece 4 in the lower grip of the MTS machine. Piece 2 will be placed around the specimen's ends which are to be square and, using screws, attached to piece 1 and piece 3. Depending on the fit, set screws or shims may be necessary to secure the specimen compactly into piece 2. After the specimen is intact, the upper grip will be lowered by the machine until piece 3 is resting in the thin layer of epoxy contained in the well of piece 4. Some type of heating element will be placed around the lower grip to meet the required temperature for the cure cycle of the epoxy. After curing, the test fixture is ready to be used to apply compression and torsion to the specimen.

When applying the desired loadings, the epoxy will be placed in shear. Therefore, it was necessary not only to determine the cure cycle but to determine the shear strength of the epoxy. Although the exact epoxy has not been chosen, preliminary tests were conducted using an epoxy with a quick cure and adhesive abilities that is used at the laboratory for setting microscopy

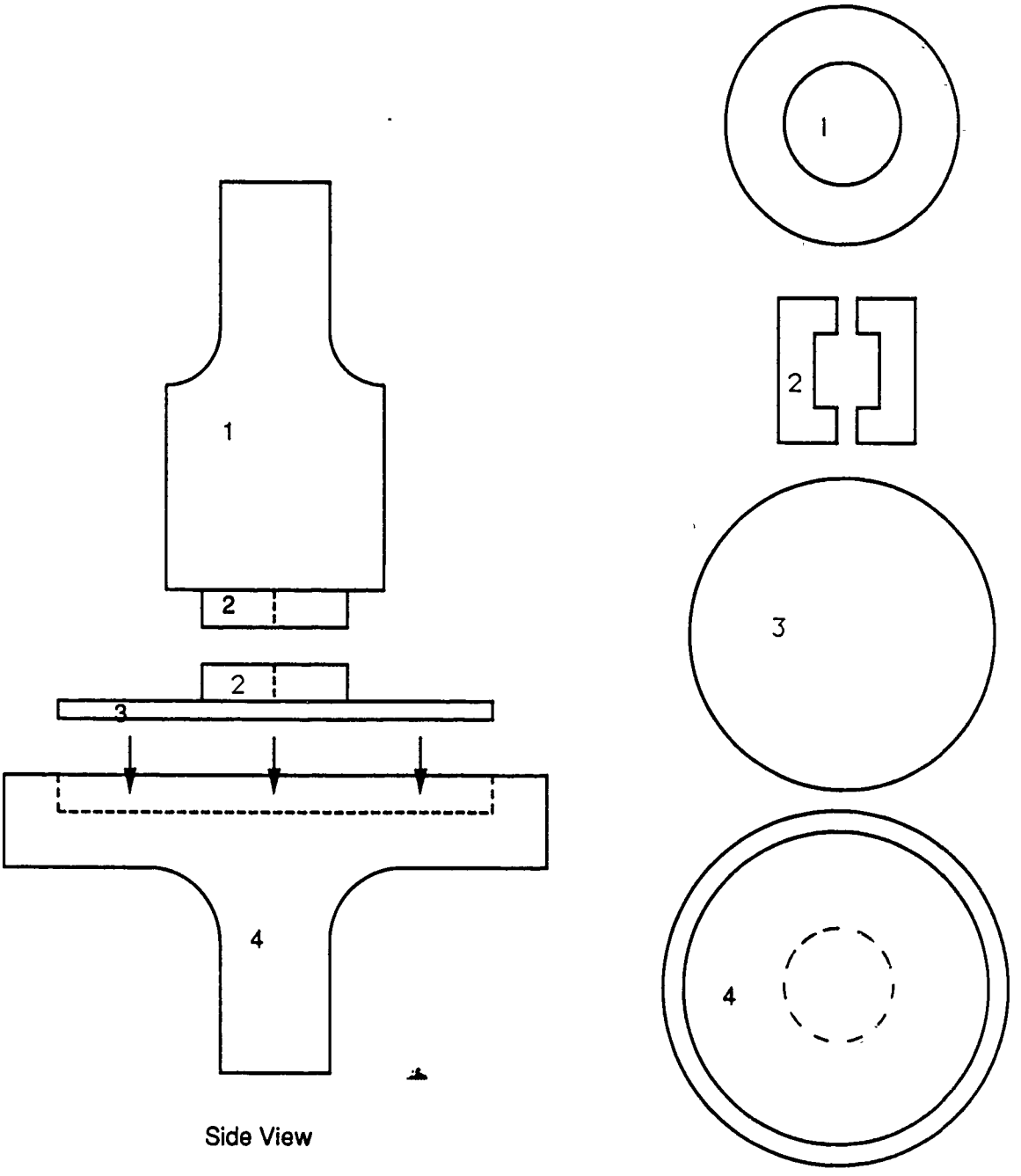

Figure 2. Compression/Torsion Testing Fixture (Not To Scale)

specimens. From double lap shear tests using steel bars, the strength of this epoxy was determined to be over 1000 psi for a cure cycle of 45 minutes at 100 degrees Celsius. Calculations, using approximate dimensions of the test fixture, determined that the epoxy should experience no more than 8 psi in shear.

V. MICROSCOPY STUDIES:

a. Fiber deformations and interactions are to be understood for gathering information about the material nonlinearity. To determine the weave distribution, the tested material will be prepared for microscopy. Although it is the tested carbon-carbon that will contain the distributions, in the initial stages, before testing, the received material also needs to be viewed and photographed to find fiber bundle dimensions, fiber diameters, and characteristics of the material in general. It should be noted that the x-face and y-face are assumed identical when viewing the dimensions and characteristics.

Thin layers along the z-face and x-face were removed from one of the billets and set in epoxy. These specimens were then polished and viewed using a microscope, before being photographed. Photographs were taken using 30X, 50X and 1000X magnification. These photographs enabled measurements to be taken using calipers, noting the magnification. One important factor in all measurements is the averaging needed due to the variation of the material's dimensions within the bundles, matrix, and fibers. Therefore, as many measurements as possible were made and averaged with the available photos. With these dimension, it is possible to: 1) compare data with the manufacturing company, FMI, such as bundles/inch and fiber diameter. 2) obtain the fiber

volume fraction of the material for such uses as rough calculations of the compressive modulus for comparison with the pure compression tests.

b. The z-face was examined first. Some obvious first impressions were the three types of cracks present. These included thermal cracks, interface cracks, and biaxial cracks. The thermal cracks are a result of the material being processed at extremely high temperatures and then being cooled. This procedure introduces thermal stresses which in turn can produce cracks within the fiber bundles and matrix. The interface cracks or voids and matrix deposits between the bundles result from the matrix and fiber bundles not perfectly adhering during fabrication. The biaxial cracks at 45 degree angles within the z-fiber bundles were present only when the sides of the bundle remained attached to the neighboring material of matrix and x- or y- fiber bundles. This is a result most likely of failure in shear where 45 degree angle cracks are characteristic.

Excessive fiber bundle bulging was not noticed in the bundles on the z-face. And although cracks were present, the fibers within the bundles were very compact with good fiber-matrix mixing.

When the x-face was prepared and viewed, surprising results were seen. The matrix had many more voids compared to the z-face and the x-fiber bundles were rarely attached to the adjacent fibers running lengthwise but rather were surrounded on all sides by matrix or a mixture of matrix and voids. Cracks similar to the ones described above were also present.

VI. RECOMMENDATIONS

a. As stated earlier, the objective of this research was to evaluate theories about compression-shear interaction in 3-D rectangular weave carbon-carbon composites. When this goal is achieved, an understanding of how the bundles interact with one another under various loadings will be found. These results can then be applied not only to 3-D rectangular weaves but also to materials with other 3-D and 2-D weaves, with similar volume fractions, and under similar loadings.

b. During the ten-week period, less was accomplished than expected. Future research includes testing the carbon-carbon specimens under the different loadings remembering the requirements for more precise testing. The material available is limited, so testing must be done carefully. It is recommended that other material be tested first for verification of the accuracy of the compression/torsion fixture. As in the case of the compression tests of the steel cylinder, further requirements for more precise testing techniques may result.

REFERENCES

Batdorf, S.B. and Robert W.C. Ko, "Shear Stress-Strain Relation Obtained From Torque-Twist Data," UCLA-ENG-86-41, University of California, Los Angeles, California, January 1986, pp. 1-6.

Pollock, P.B., C.T. Sun, "A Study of Failure in 3-D Carbon-Carbons," AFRPL TR-84-061, Purdue University, West Lafayette, Indiana, September 1984, pp. 13-16.

1990 USAF-UES SUMMER FACULTY RESEARCH PROGRAM

GRADUATE STUDENT RESEARCH PROGRAM

Sponsored by the

AIR FORCE OFFICE OF SCIENTIFIC RESEARCH

Conducted by the

Universal Energy Systems, Inc.

FINAL REPORT

A Survey of Distributed Sensor Systems for the Control Of a Vibrating Cantilevered Beam

Prepared By:	Thomas F. Starchville, Jr.
Academic Rank:	Graduate Student
Department and	Aerospace Engineering
University:	The Pennsylvania State University
Research Location:	AL/VSSS
	Edwards AFB, CA 93523
USAF Researcher:	Dr. Alok Das
Date:	11 November 1990
Contract No:	F49620-88-C-0053

A Survey of Distributed Sensor Systems for the Control Of a Vibrating Cantilevered Beam

by

Thomas F. Starchville, Jr.

ABSTRACT

A survey into the use of distributed sensing devices is conducted for use in controlling a vibrating cantilevered beam. The distributed sensor chosen for the analysis is a piezoelectric film bonded to one side of a cantilevered beam. The primary difference between distributed sensors and discrete sensors is that the distributed sensor produces an output signal proportional to some quantity integrated over the area that it covers. This is unlike a discrete sensor which measures the motion at a singular point. Because of this difference, the modal content must be extracted from the the distributed sensor signal. The process used to perform this is a state estimator known as a Kalman-Bauchy filter. Problems with the actuator chosen for the experiment prohibited experimentation; however, work is continuing.

ACKNOWLEDGMENTS

I wish to thank the Air Force Systems Command and the Air Force Office of Scientific Research for their sponsorship of this research. Furthermore, Universal Energy Systems guided me through the research effort by their help with the administration aspects of the program.

I consider my research performed at the Astronautics Lab at Edwards AFB, CA a very pleasant and rewarding experience. Not only did this program afford me the opportunity to do research for the first time, but also a number of different influences at AL/VSS contributed to my experience. Mr. Wade Schlaegel proved to be invaluable with his support in dealing with laboratory's computer system. Because of this influence I was able to discover different software packages to which I would not have otherwise been exposed. The help of Mr. Angel Cruz and Mr. Joel Berg was an asset in presenting solutions to problems that arose with the project. The encouragement of Dr. Alok Das and Dr. Roger Thompson was well appreciated when aspects of the project became difficult or discouraging.

I. INTRODUCTION:

Vibration control of a simple cantilevered beam using a distributed sensor system is analyzed. Unlike discrete sensors, which measure the dynamic characteristics of a structure at several individual points, distributed sensors produce a signal proportional to some quantity integrated over a continuous path and/or area. This leads to some problems extracting the modal content from the signal. A state estimator, such as a Kalman-Bauchy filter, must be used to aid in extracting the modal content of the motion.

Two proof-mass actuators were considered for providing the force needed to control the motion of the beam. It was found that these actuators exhibited saturation at a frequency which was too low for a planned objective of the experiment. Furthermore, it was found in documentation that the actuators added nonlinear effects to the system (Bailey, 1986).

When controlling the motion of the beam, two types of control systems were considered for comparison -- open-loop and closed-loop (feedback) regulators. The theory behind the optimal regulator was discussed in some detail with colleagues throughout the summer in order to get a better understanding of the subject. This knowledge would be needed for the design of the control system. Comparison between open-loop and closed-loop control systems showed that a closed-loop system is more desirable because the control system is able to correct itself while executing. A computer code was written to solve for the optimal closed-loop control system and tested on a simple dynamic problem for verification.

II. OBJECTIVES OF THE RESEARCH EFFORT:

Vibration control of large flexible structures has become more emphasized in the research community since the introduction of projects such as NASA's Space Station Freedom and the recently completed Air Force project, ASTREX. Technology in distributed sensors has opened a new field of study -- smart structures. Smart structures are a specialized type of structures, meaning that, with the addition of a distributed sensing system, one may monitor the motion of the entire structure, as well as material health. Embedded fiber-optics and piezoelectric films are two types of distributed sensors.

The purpose of participation in the 1990 Graduate Summer Research Program (GSRP) was to become introduced to this new technology, so that the work done at the Astronautics Lab at Edwards AFB, CA might be applied to a masters' thesis. Before any experimentation could be performed using a piezoelectric film sensor system, the theory of optimal control systems was examined. A computer code was written to calculate the control system required for a general dynamic problem which could be later expanded to include the experiment. Furthermore, much emphasis was placed on experimental technique, because this was the author's first project assignment.

Unfortunately, actual experimentation on the piezoelectric system could not take place because of a problem with part of the experimental set-up. An understanding of optimal control theory and the experience gained working on a project has been well worth the minor set backs. The problems encountered throughout the course of the project helped to become creative enough to pose a solution. The project is continuing at Penn State University with certain changes to the original experimental design.

III. EXAMINATION OF EXPERIMENTAL COMPONENTS:

a. The structure chosen for analysis was a portion of the joint Charles Stark Draper Laboratory/Rocket Propulsion Laboratory (CSD/RPL) experiment shown in Figure 1. The CSD/RPL experiment was created to examine the control of a maneuvering spacecraft with four flexible appendages (Bailey, 1986). For research purposes, only one of the aluminum arms was considered and was modeled as a horizontal, cantilevered beam by mounting the central hub assembly to a table. The length of the aluminum beam was approximately four feet. This allowed for a low damping ratio and large, visible motions at low frequencies. The low damping ratio means that the motion can be sustained for a long period of time (on the order of 10 seconds) before it settles.

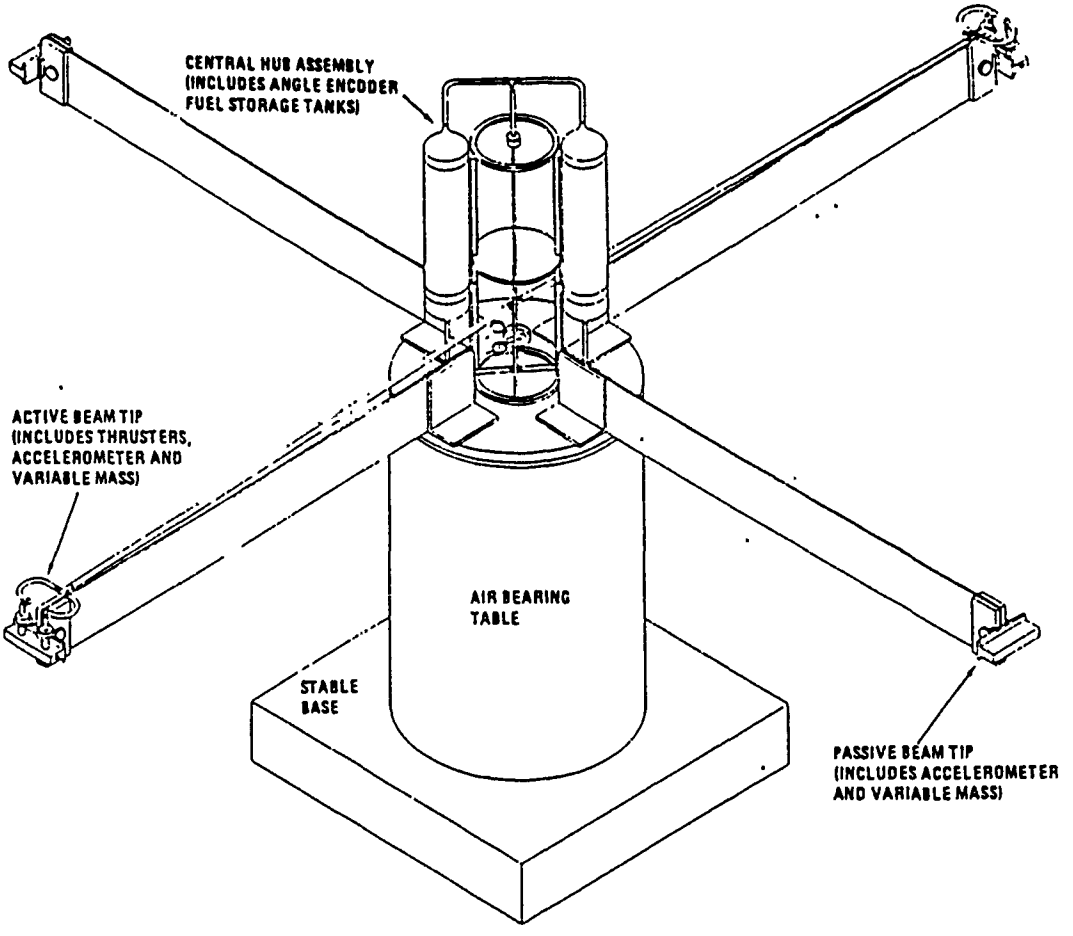

Figure 1. The CSD/RPL Experimental Apparatus (Bailey, 1986).

The horizontal, cantilevered beam posed one major problem due to a characteristic of the beam. The width of the beam was approximately six inches, which caused twisting at the tip to occur when large tip deflections were induced. This twisting was caused by the gravitational force acting perpendicular to the oscillatory motion of the beam. Furthermore, the twisting was increased when the actuator arrangement was added at the tip. There were two primary options to solving this problem: add a compensator to the control system to correct for the twist or mount the assembly so that the beam is cantilevered vertically (see Figure 2). The second solution would have the gravitational force acting longitudinally on the beam decreasing the twist at the tip considerably. This solution was chosen because it was the easiest to implement. Complications to the dynamic model would have resulted if the first solution had been implemented.

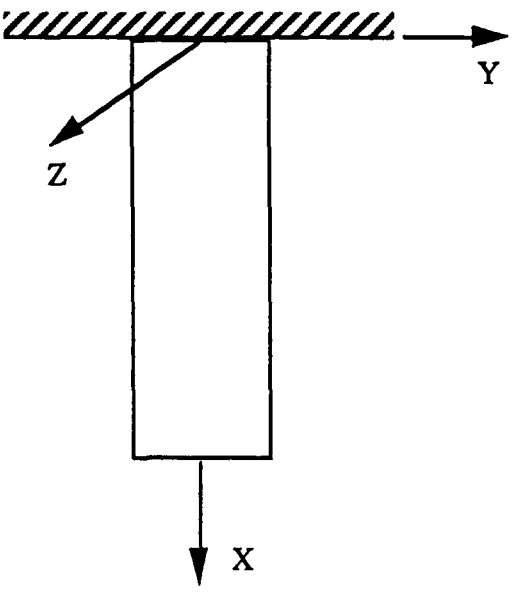

Figure 2. Vertical Cantilevered Beam.

b. A piezoelectric film sensor system had been mounted to one side of the structure from the CSD/RPL experiment. This film spanned the entire length and width of the beam.

Since the film was a distributed system, its output signal was proportional to a quantity integrated over the entire film area. Since the film was mounted directly to the surface of the beam, it was sensing the motion of the beam at its surface. The beam's surface was either in tension or compression during an oscillatory period of the system. Since the film was bonded to the surface, the film material also experienced the same tension and compression. The output signal of the film is in proportion to the strain integrated over the film area. This was the relationship that was needed to link the output of the sensor to the motion of the beam. An expression for the integrated strain of the beam over the sensor area is as follows:

$$\bar{\varepsilon}_{xx} = \Delta y \sum_{i=1}^{5} \frac{t}{2EI_{zz}} q_i \int_{x_1}^{x_2} \phi_i'' \, dx \qquad (1)$$

where Δy is the width of the film, E is the Youngs' Modulus for the beam, I is the Moment of Inertia about the z-axis, t is the thickness of the beam, x_1 and x_2 are the end positions of the film, q_i is a set of generalized coordinates and ϕ_i are the assumed mode shapes.

Though the expression relating the output to the motion had been determined, there was no direct way to analyze the modal content of the output signal. A type of state estimator known as a Kalman filter was examined to provide the modal content needed. This filter would predict the variables at the next time step from present measurements. The estimates that it obtains are optimal in the statistical sense (Kirk, 1970). The sensor signal can be assumed to contain noise, which tends to affect the convergence of a closed-form solution. In the presence of noise, the typical state-space model now contains terms to include state excitation (actuator) noise and sensor noise.

$$\dot{\underline{x}}(t) = A\underline{x}(t) + B\underline{u}(y) + \underline{v}(t)$$
$$y(t) = Cx(t) + w(t) \qquad (2)$$

The noise is defined by $\underline{v}(t)$ and $\underline{w}(t)$ in the state-space model. The matrices A, B, and C are constant throughout the problem. Solving for the Kalman gain matrix that would convert measured quantities to predicted quantities required solution to an algebraic Riccati equation (Meirovitch, 1990).

c. Two proof-mass actuators (PMAs), KIMCO model LA23-43-001, were chosen to provide the force required to control the beam's motion. This type of actuator is called a "moving coil" linear actuator. The moving coil actuators have a typically heavy base which contains the magnet and a lightweight wire coil. If the coil assembly is mounted to the structure, the heavy magnet becomes the proof-mass. By using two PMAs mounted "back to back" and located at the tip, the effective proof mass and peak force are doubled. Furthermore, with the PMAs operating in opposite directions, a reduction in the inherent non-linearities is achieved (Bailey, 1986).

These actuators presented a variety of problems that had to be dealt with. First, the amplification box used to amplify the signal to the PMAs did not work correctly. The device was stripped and rewired the device according to company diagrams; however, correct amplification still could not be achieved. A conversation with an engineer at the Inland Motor Company uncovered a mistake in the wiring diagram that was used to rewire the device, the correction was made, and the amplifiers performed well. Unfortunately, this setback disrupted the time table sufficiently to prevent experimentation on the beam during the summer research program.

Several tests were performed on the PMAs to identify their dynamic characteristics and to determine how to incorporated into the final control system design. It was found that the

PMAs became saturated when the deflections of the tip were larger than three or four inches. Saturation is defined here as the state at which one of the proof-mass actuators has moved completely to the stoppers (see Figure 3), requiring a very large control force to

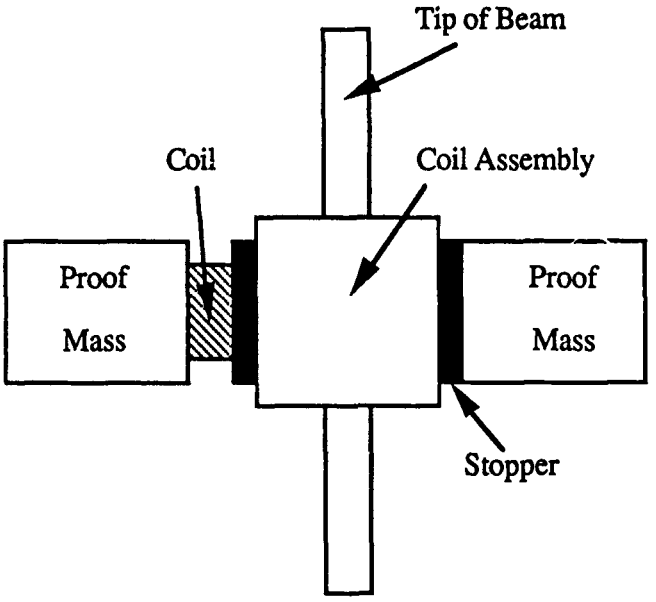

Figure 3. Saturation of the Proof-Mass Actuators.

push the mass away. The gain on the control force was increased; however, this caused the PMAs to hit the stoppers violently and bounce away. Motion of this type was undesirable because the impulse on the beam created by the masses hitting their stoppers disrupted the original simple harmonic motion. If the gain on the PMAs was decreased, the control force did not have enough strength to move the masses. It was therefore concluded that in order to effectively use the proof-mass actuators only small deflections at the tip could be analyzed. This contradicted with the large, visible motion that was desired.

d. Before any of the system identification or analysis was performed, a fundamental understanding of optimal control theory had to be achieved. A computer code was written

to analyze two types of control systems -- open-loop and closed-loop (feedback) regulators. The closed-loop gain matrix was solved by integrating the following Riccati equation backwards through the time interval with a Runge-Kutta routine:

$$\dot{K} = KA + A^T K + Q - KBR^{-1}B^T K \qquad (3)$$

where K is the gain matrix, Q & R are the regulator weighting matrices, and A & B are the state-space model matrices (Kirk, 1970). This Riccati equation is of the same form that the Kalman-Bauchy gain matrix was found. To check the validity of the code, it was tested using a simple dynamic system of two masses attached by two springs. Examining the results of the test case showed that a closed-loop control system performs better than an open-loop one, especially if an impulse is introduced to the system at some point in the analysis. Since the code was written for any simple system, it may easily be applied to the current problem.

IV. RECOMMENDATIONS:

a. Although experimentation on the cantilevered structure did not take place during the research effort as previously anticipated, work has been proceeding at Penn State University to complete the study as part of a masters' thesis. The degree of examination has been expanded to include the motion of the first five modes of the beam. Furthermore, the impact of an embedded fiber-optic sensor system will be analyzed. Other major characteristics of the original experiment have also been changed to achieve a better dynamic model.

b. The beam will still be mounted as a vertical, cantilevered beam to reduce the twisting at the tip due to gravity. To further reduce this tip twisting, the width of the beam will be reduced to one or two inches.

c. Piezoelectric film material will still be used as the preliminary distributed sensor system; however, a smaller area of the beam will contain this film. Recently, a proposal was made to place two piezoelectric film sheets near the tip and root of the beam. In essence, this would be like placing two different sensors on the beam. Two output signals would need to be fed into the Kalman-Bauchy estimator in order to extract the desired modal content from such a set-up.

d. Since the PMAs introduced unwanted complexities to the system, they have been replaced by a motor and reaction wheel combination. With the introduction of the reaction-wheel type of actuator, the previously-mentioned excitation noise will need to be considered more thoroughly, since a reaction-wheel has the inherent characteristic of adding noise to a system.

REFERENCES

Bailey, T., Gruzen, A., and Madden, P. "RCS/Linear Discrete Actuator Study: Interim Technical Report," CSDL-R-1919, The Charles Stark Draper Laboratory, Cambridge, Massachusetts, November 1986, pp. 1-27.

Kirk, D. E., Optimal Control Theory, Prentice-Hall, Inc., Englewood Cliffs, New Jersey, 1970, pp. 184-218, 426.

Meirovitch, L., Dynamics and Control of Structures, John Wiley & Sons, New York, New York, 1990, pp. 193-201, 240-252.

1990 USAF-UES SUMMER FACULTY RESEARCH PROGRAM / GRADUATE STUDENT RESEARCH PROGRAM

Sponsored by the

AIR FORCE OFFICE OF SCIENTIFIC RESEARCH

Conducted by the

Universal Energy Systems, Inc.

FINAL REPORT

Identification of Metabolites of Various Pseudomonad Species From Growth on Isomers of Nitrotoluene

Prepared by: Joseph D. Bernardo

Academic Rank: Candidate, Masters of Arts in Biochemistry

Department and: Chemistry Department

University: University of Scranton,

Scranton, PA, 18510-4626

Research Location: AFESC/RDVW
Tyndall AFB
Panama City, FL, 32404

USAF Researchers: Jim Spain, PhD.
Billy E. Haigler, PhD.

Date: September 10, 1990

Contract No.: F49620-88-C-0053

Identification of Metabolites of Various Pseudomonad Species from Growth on Isomers of Nitrotoluene

by

Joseph D. Bernardo

ABSTRACT

Various Pseudomonad species were grown in the presence of toluene in order to induce enzymes which would metabolize the toluene as the sole carbon source. Using these induced cells, a suitable concentration of a nitrotoluene isomer (1X10 M) was injected into culture fluids and sampled at specified time intervals. These samples were centrifuged and injected into the HPLC. Production of metabolites showed up as different peaks on the HPLC chart. These peaks were then analyzed and an attempt at identification was made. Identification was based on the similarity of standard retention times of compounds and UV spectra, as compared to the unknown compounds. Identified peaks were then analyzed via GC/MS to get positive identification. Once metabolites were identified, a metabolic pathway for each of the species could be mapped out.

I. INTRODUCTION

Various Pseudomonad species are known to be involved in the breakdown of certain aromatic compounds.(1) For example, many soil Pseudomonads contain the genetic information necessary to produce enzymes which are involved in the breakdown of toluene.(2) Thus, it is possible for these Pseudomonads to survive in hostile environments, such as hazardous waste sites, by utilizing only toluene (or some other organic molecule) as its sole carbon source. By utilizing the genetic information which codes for the enzyme to degrade toluene, some Pseudomonads have the ability to metabolize various aromatics, as in the following case: the three isomers of nitro toluene.

The microbiology lab of the Engineering and Services Center at Tyndall Air Force Base, is interested in the breakdown of these halo-aromatics by various Pseudomonad species. They are particularly interested in the biochemical pathways involved in the breakdown of nitro substituted aromatics. Our purpose is to elucidate the biochemical pathways involved in the breakdown of nitro substituted aromatics, such as the nitro toluene. This will help to develop methods for the degradation of these compounds at hazardous waste sites, since these compounds are quite toxic. A second goal is to

determine the biochemical pathways involved in the breakdown of the nitro toluenes. This information will be helpful in developing a process in which these organisms can be used to degrade old stockpiles of explosives, particularly, tri nitro toluene (TNT).

My research involves a study of the biochemical aspects of biodegradative processes by the soil Pseudomonads. This interest, along with some research performed in biochemical pathways led to the assignment at the microbiology lab.

II. OBJECTIVES OF THE RESEARCH EFFORT

Many of the Pseudomonad species which have the capability to degrade toluene as the sole carbon source, have pathways which are relatively well illucidated.(3) However, the pathways (if any), for the breakdown of nitro toluenes are less well known. There has been some studies performed in the microbiology lab at Tyndall Air Force Base (and other places), on this topic, but nothing very comprehensive.(4,5,6,7,8)

My objectives for the Summer Graduate Student Research Program were to obtain various species of Pseudomonads (already under study at the lab), and attempt to compile a comprehensive list of metabolites produced by these Pseudomonads using isomers of nitro toluene as the sole carbon source.

III.

a. The different Pseudomonad species used were:

Pseudomonad sp. JS150, G4, TOL 500
Pseudomonas mendocina, Pseudomonas putida F1 (502)

The species have different metabolic pathways for the catabolism of toluene, with the exceptions of JS150 and 502 which have the same pathways. All organisms were grown on toluene as the sole carbon source prior to the experiments, in order to induce the enzymes for the breakdown of toluene. Organisms were grown on a concentration of a nitro toluene isomer (1×10^{-4} M). The culture fluids were sampled at regular time intervals and were centrifuged to remove cell debris and to halt any biochemical processes. Supernatant was analyzed for metabolites using reversed phase high pressure liquid chromatography (HPLC). Any samples not immediately analyzed were frozen and stored at -10°C.

b. The Pseudomonad sp. with the TOL 500 insert plasmid, revealed different results for each of the isomers of nitro toluene. Growth using the different isomers yielded products which are shown in Figure 1. They were degraded in much the same manner as the known pathway for toluene degradation. For the isomers of nitro toluene, the first few steps of the pathway are the same, however, the last step is not. Normally, a nitro catechol product, following the nitro benzoate, is produced -- this is not the case. What is produced when the organisms use the meta and para nitro toluene; are the meta and nitro phenols respectively.

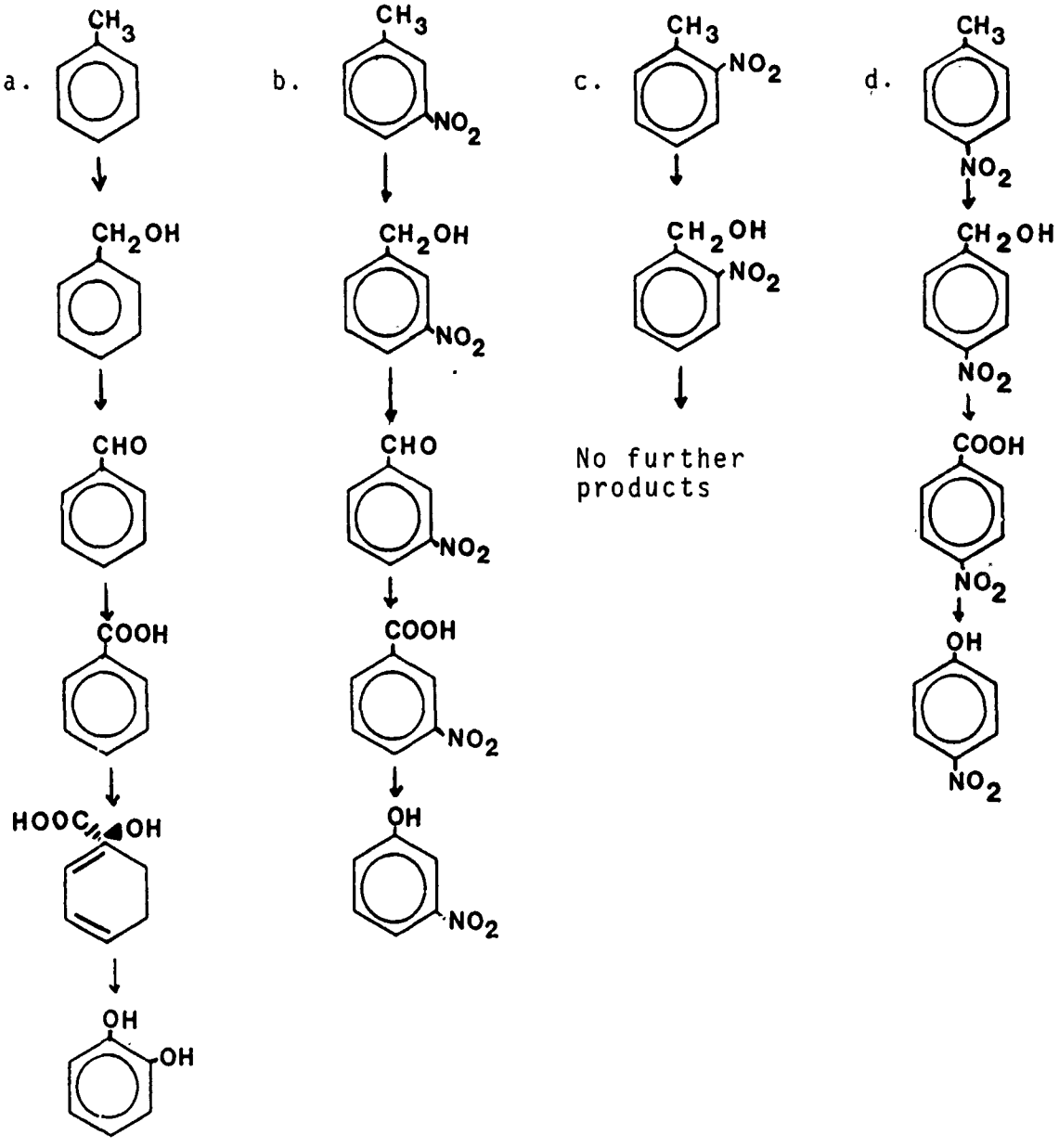

Figure 1: a. Known pathway of toluene degradation by the TOL plasmid. b. Pathway of meta nitro toluene as determined experimentally. c. Ortho nitro toluene pathway. d. Para nitro toluene pathway.

Concerning degradation of the ortho nitro toluene isomer, the organism is unable to break it down any further than nitro benzyl alchohol. The problem here is one of steric hindrance at the active site of the enzyme. The combination of the bulky nitro group with the methyl group in an active site which is quite specific for only a methyl group causes problems when leading to the formation of products. The reaction is one which oxygen is added to the methyl group on the toluene molecule. The presence of a nitro group on the carbon adjacent to the methyl group carbon must cause some steric problems. Another problem may be the fact that the two groups which are adjacent to one another (the methyl and the nitro group), are of a very different nature. The methyl group tends to donate electron density whereas, the nitro group tends to withdrawing electron density.

c. The pathway for strain G4 calls for a monooxygenase to add a hydroxyl group directly to a carbon which is a part of the ring system. This occurs twice, thus making a methyl, nitro catechol. After the organism was incubated in the presence of the nitro toluene isomers, testing was performed on the culture fluids for metabolites as described above. The results were negative -- no metabolites were formed, and no disappearance of the nitro toluene isomers was noticed. The pathway for toluene degradation in this organism, along with the actual results, are shown in figure 2. After analyzing these results, a conversation with Dr. Billy E. Haigler

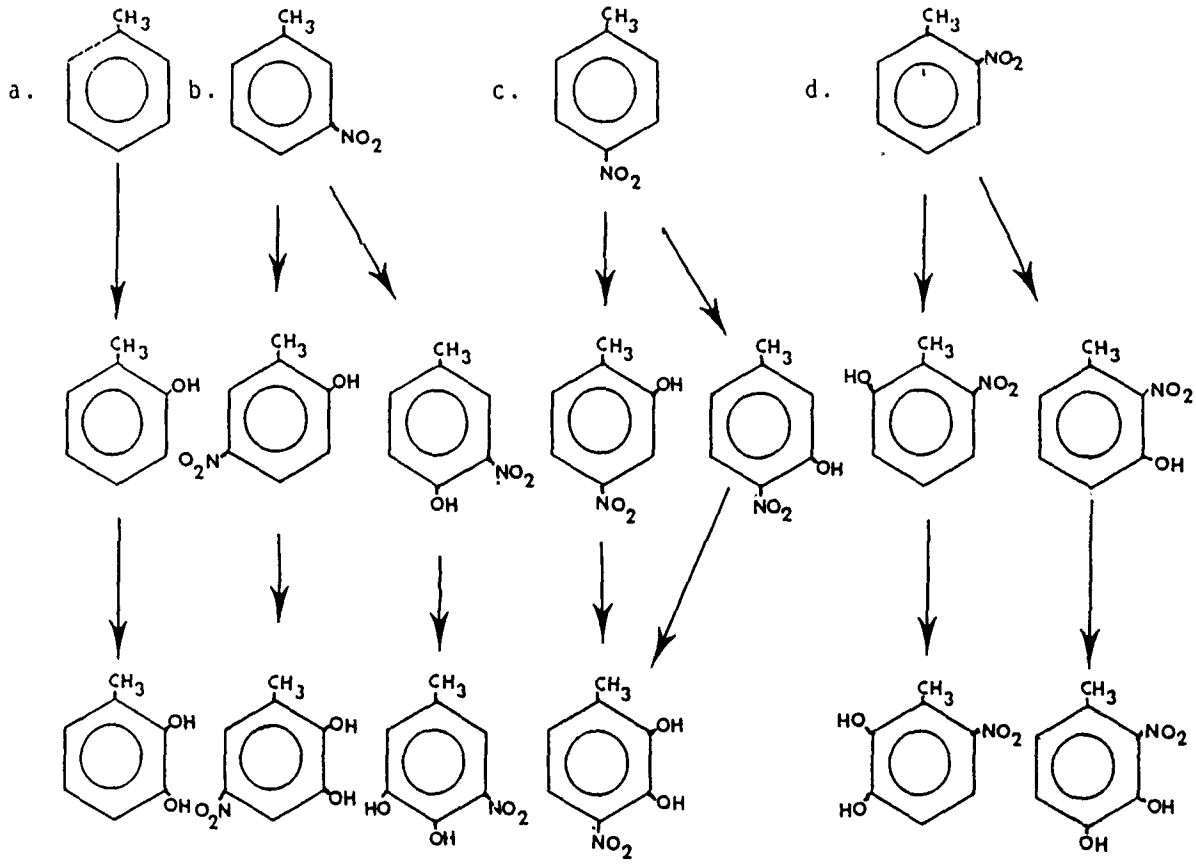

Figure 2: Potential pathways for degradation of nitro toluene by the strain G4. Results were negative. No metabolites produced. a. Pathway for metabolism of tluene. b,c,d: proposed pathways for meta, para, and ortho nitro toluene respectively.

supplied information which stated that strain G4 grown on toluene and tested for growth on nitro benzene resulted in a negative manner also, meaning, no growth for the strain G4 for nitro benzene. With this corellation in results for the same organism, using similar substrates. It was decided that, with the advice of Dr. Haigler and Dr. Spain, that these results were accurate. However, a repeat of the same experiment with strain G4 just to confirm the original results, was required. The results of this experiment: negative.

d. Toluene grown Pseudomonas sp. strains JS150 and 502 gave results which were similar to each other. Strains JS150 and 502 are supposed to have the same metabolites produced when grown on the nitro toluene isomers. In reality, the results obtained are not the same as described above.

(1) For the ortho nitro toluene isomer, the both strains produced a 2- nitro benzyl alchohol. For the JS150 strain, the nitro benzyl alchohol was the only metabolite. The 502 strain produced one other metabolite along with the nitro benzyl alchohol -- the other metabolite is an unknown compound which has a retention time of 7.382 min. This metabolite has not been identified, however, the spectra is known and more work may be performed in order to identify it. The other metabolite, the 2-nitro benzyl alchohol has been positively identified using comparative spectra and retention times via HPLC analysis and GC/MS analysis. For strain JS150, all of

the ortho nitro toluene was metabolized, however, for strain 502, some small concentration of the ortho nitro toluene was left over (see figure 3).

(2) For both strains JS150 and 502, the meta nitro toluene isomer was metabolized again very similarly. Both strains produced the 3-nitro benzyl alchohol. This fact was supported by GC/MS analysis -- for both strains. Strain JS150 produced two other metabolites along with the nitro benzyl alchohol. These were, an unidentified peak at 9.740 min. along with a peak at 6.992 min. which has been identified as 3-nitro benzoic acid via HPLC. Strain 502 did not produce the same two peaks as the JS150, instead, a metabolite was formed which, as of yet, is unidentified. This metabolite had a retention time of 11.253 min. on the HPLC. The strain JS150 totally metabolized all of the meta nitro toluene in the culture fluid, strain 502 did not metabolize all of the meta nitro toluene.(See Figure 4)

(3) For the para nitro toluene isomer, neither strain JS150 nor 502 produced any nitro benzyl alchohol. Strain JS150 produced unidentified peaks at 9.720 min., 11.536 min., and 15.395 min. All of the nitro toluene had been metabolized in this experiment. (For each of the nitro toluene isomers, strain JS150 metabolized the concentrations of these isomers in each sample.) Strain 502 utilized para nitro toluene, and produced two unidentified peaks -- one with a retention time

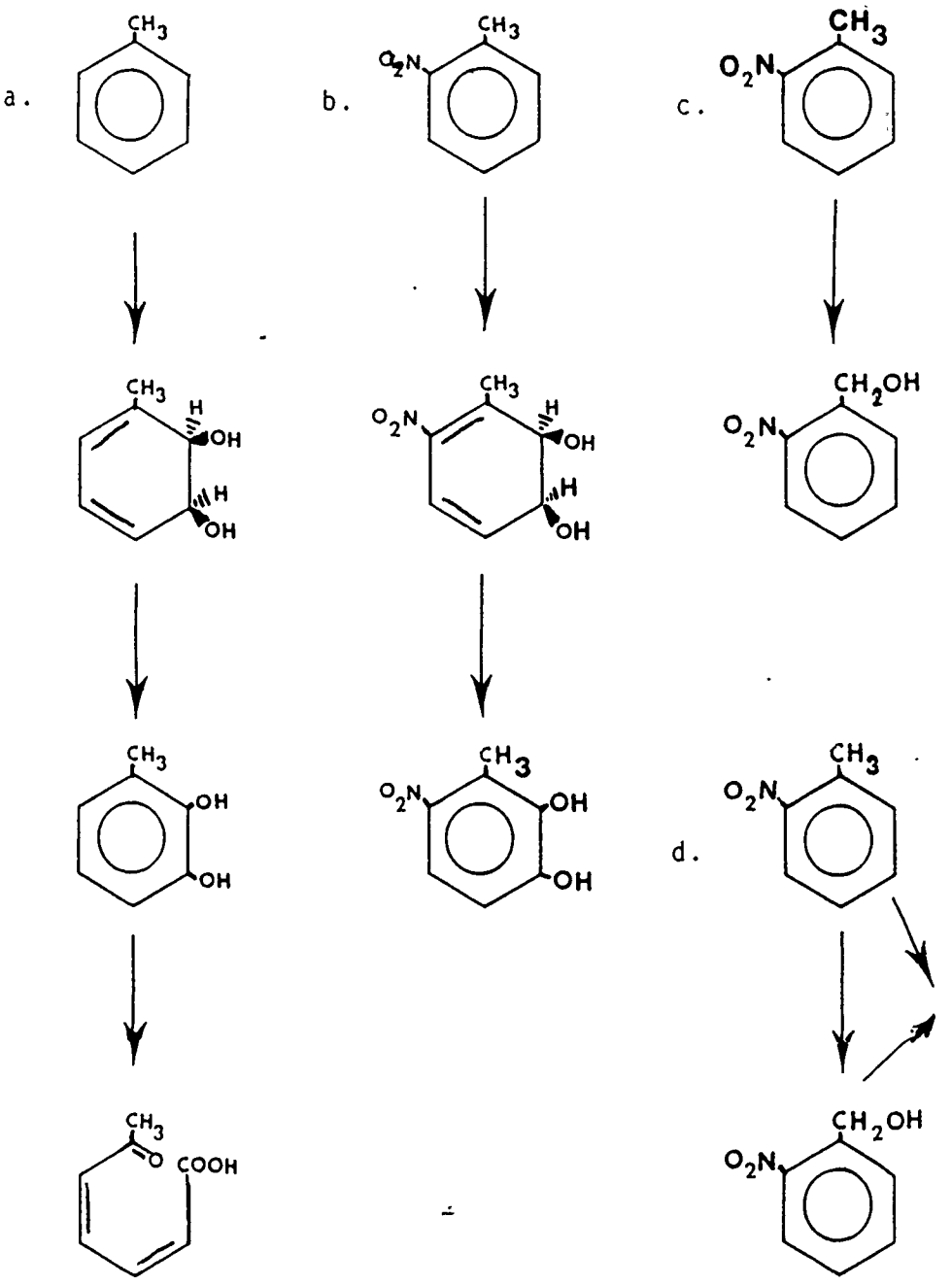

Figure 3: Potential pathways of ortho nitro toluene degradation for JS150 and 502 vs. actual results. a. Pathway for toluene; b. Proposed pathway; c. Actual results for strain JS150; d. Actual results for strain 502.

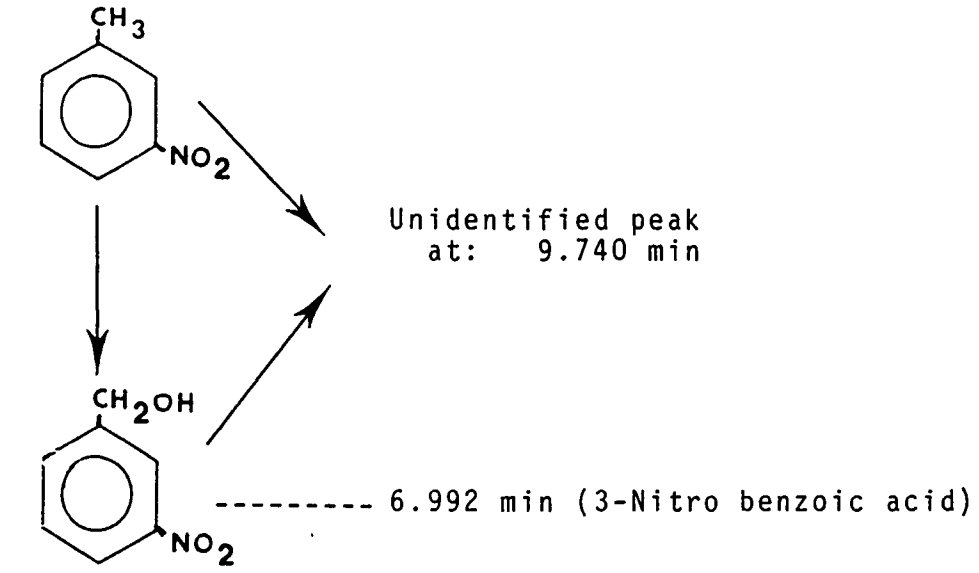

JS150

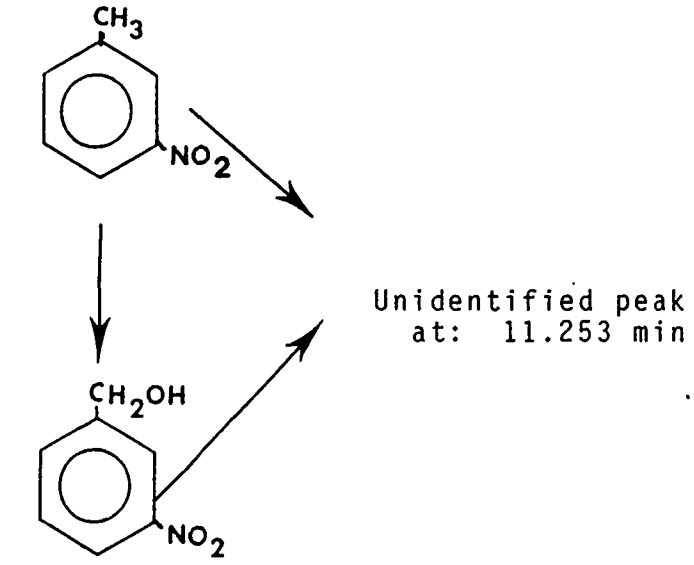

502

Figure 4: Metabolic products of JS150 and 502 when utilizing meta nitro toluene.

of 12.505 min., the other at 15.017 min. For this sample, 502 did not metabolize all of the nitro toluene which was present at the start of the experiment.(See Figure 5)

e. Pseudomonas mendocina was another organism which was used to attempt to determine the possible pathway of metabolism using nitro toluene isomers. The mechanism of the enzymes for toluene degradation in P. mendocina is to first hydroxylate the ring, then to hydroxylate the methyl group. This pathway was the one which was proposed for the action of the organism on the nitro toluene isomers. According to the results of the experiment, this was not the case. When the organism was incubated with the ortho isomer of nitro toluene, it produced as metabolites; 2-nitro benzyl alchohol as the first appearing product, and two other unidentified peaks, one with a retention time of 7.482 min., the other with a retention time of 11.977 min. The 2-nitro benzyl alchohol was identified via HPLC analysis and also by GC/MS analysis. When grown in the presence of meta nitro toluene, the organism produced metabolites of 3-nitro benzyl alchohol, and one unidentified peak at 8.561 min. retention time. Para nitro toluene metabolism yielded only one product -- 4-nitro benzyl alchohol. Also, the para nitro toluene was found in solution throughout the experiment, the same is true of the meta nitro toluene, however, the ortho nitro toluene had been completely metabolized. (See Figure 6) The meta and para isomers of nitro benzyl alchohol were also identified via HPLC and GC/MS

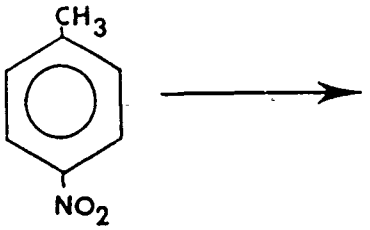

Unidentified peaks
at: 9.720 min
11.536 min
15.395 min

JS150

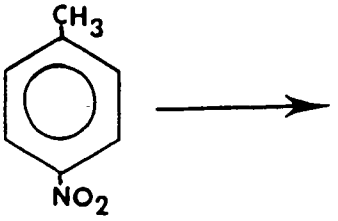

Unidentified peaks
at: 12.505 min
15.017 min

502

Figure 5: Metabolites obtained from strains JS150 and 502 when grown on para nitro toluene.

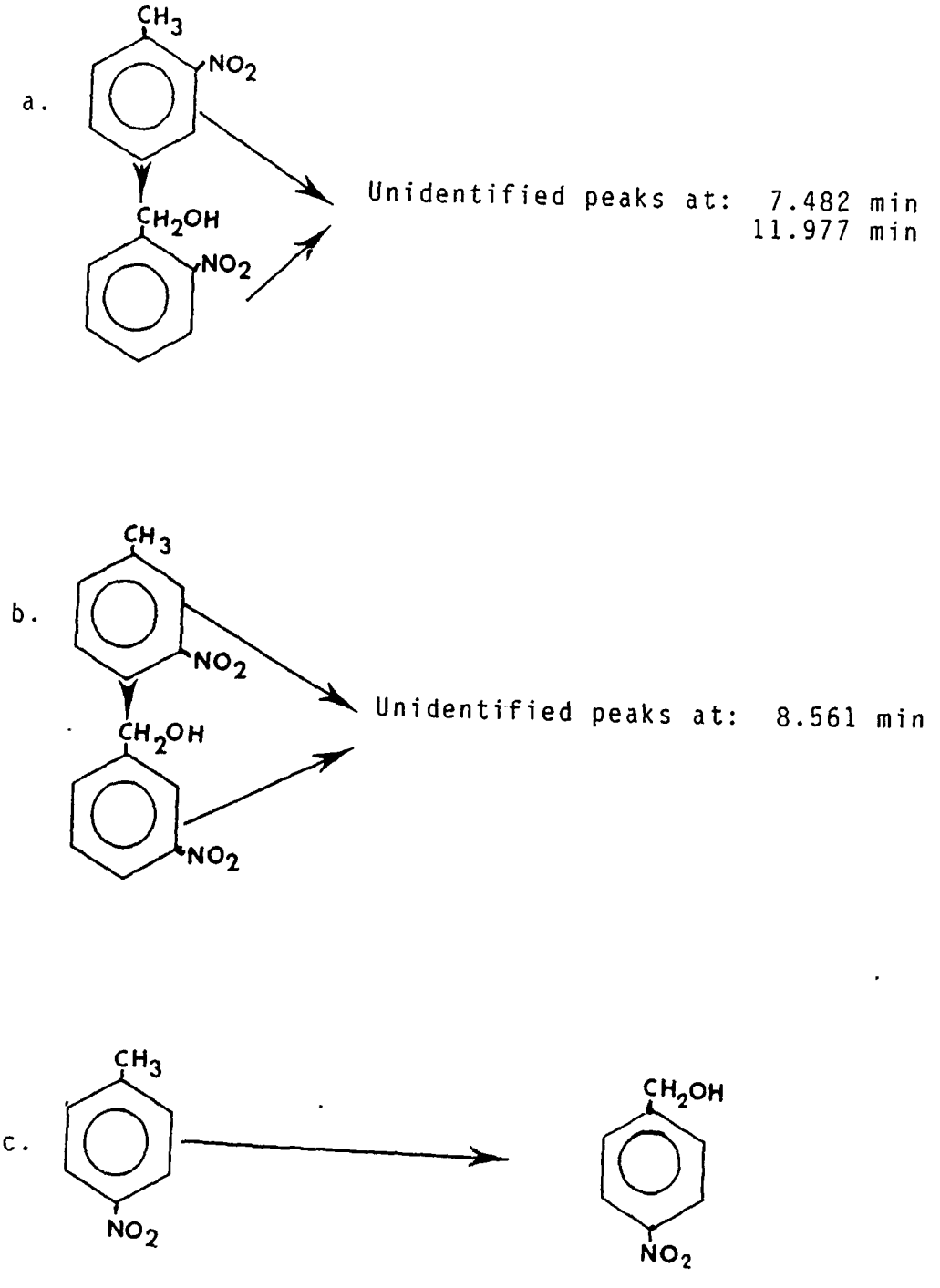

Figure 6: Metabolites obtained from Pseudomonas mendocina when grown on a. Ortho nitro toluene, b. meta nitro toluene, c. para nitro toluene.

analysis.

IV. Using the strain with the Tol 500 plasmid, a few experiments were required to determine whether certain electron donating or electron withdrawing groups have any effect on the metabolism of these molecules. All of the molecules used were benzoic acids -- the only difference in the molecules is that the other group on the molecule was a representative of an electron withdrawing or elecron donating group. The experiments were run in the same manner as all of the experiments utilizing nitro toluene isomers as described above. The molecules used in these experiments were -- chloro benzoic acid, amino benzoic acid, and toluic acid. Each of these molecules were metabolized to a certain degree by the Tol 500 organism, however, there has been no identification of the products of these metabolic pathways as of yet.

V. In addition to the above experiments, a nitro toluene isomer experiment was performed on an organism which arrived at the lab just prior to the completion of the assignment. Dr. Spain suggested running the experiment to determine whether or not the organism, Pseudomonas picketti, was able to metabolize the nitro toluene isomers. The results were -- P. picketti was able to metabolize the nitro toluene isomers into products, however, there was not sufficient time to identify these metabolites.

VI. RECOMMENDATIONS

a. There still remains much work to be done on these different organisms. A recommendation would be to identify all of the unidentifed products of the different organisms. Once these have been identified, the information would be essential in helping to make a decision on whether or not to proceed to investigate further, that organism and its particular pathway. A very good recommendation would be to perform NMR studies on the metabolites of the reations. This would enable us to determine which isomeric form the metabolite is, and possibly would save time in searching thus, freeing time up for more important aspects of the research.

b. Stoichiometric analysis must be performed also for each of the pathways in order to determine exactly how much of the substrate is being metabolized into products.

c. Once these are completed, an idea would be to focus on just one or two of the oranisms in order to complete any detailed research. This would entail the complete analysis of the metabolic pathways of these two organisms. The two organisms which are a good choice to continue studying are; TOL 500 strain and (PpF1) strain 502. This suggestion came from conversations with other members in the lab at Tyndall.

References

(1) Reineke, W., and H.J. Knackmuss. 1988. Microbial Degradation of Haloaromatics. Ann. Rev. Microbiol. 42:263-287.

(2) Ribbons, D.W., and R.W. Eaton. 1982. Biodegradatin and Detoxification of Environmental Pollutants. p.63. CRC Press, Boca Raton, FL.

(3) Reineke, W., and H.J. Knackmuss. ibid.

(4) Yinon, J. 1989. Metabolic Studies of Explosives. Biomedical and Environmental Mass Spectrometry. 18:149-56.

(5) McCormick, N.G., F.E. Feeherry, and H.S. Levinson. 1976. Microbial Transformation of 2,4,6-Trinitrotoluene and Other Nitro Aromatic Compounds. Applied and Environmental Microbiology. 31:949-958.

(6) Sitzmann, M.E. 1974. Chemical Reduction of 2,4,6-Trinitrotoluene - Initial Products. Journal of Chemical and Engineering Data. 19:179-181.

(7) Zylstra, G.J., W.R. McCombie, D.T. Gibson, and R.A. Finette. 1988. Toluene Degradation by Pseudomonas Putida F1: Genetic Organization of the TOD Operon. 1988. Applied and Environmental Microbiology. 54:1498-1503.

(8) Shields, M.S., S.O. Montgomery, P.J. Chapman, S.M. Cuskey, and P.H. Pritchard. 1989. Novel Pathway of Toluene Catabolism in the Trichloroethylene Degrading Bacterium G4. Appl. and Enviro. Microbio. 55:1624-1629.

Acknowledgements

I wish to thank the Air Force Systems Command and the Air Force Office of Scientific Research for sponsorship of this research. Also, many thanks to Universal Energy Systems for the opportunity to perform this research, it has been truly enlightening. The Air Force Engineering and Services Center at Tyndall Air Force Base, should also not go without recognition. They created an environment which was best to perform in. The surroundings were very comfortable and any questions I had were quickly answered.

I would like to thank Perry Sullivan for his wonderful support throughout the program. Also, great thanks to the members of the microbiology lab at the ESC at Tyndall. Especially, Dr. Jim Spain, without whose excellent teaching and suggestions the research would not have been possible. I would also like to thank Shirley Nishino for the technical help she gave in the lab. The help of Mike Henley and Dr. Howard Mayfield in regards to identifying metabolites using the GC/MS was greatly appreciated. Technical assistance also came from Sgt Volnof, who obtained chemicals and other supplies which were needed throughout the experience. The concern of Dr. William Seffens and Dr. Chuck Pettigrew was greatly appreciated. The overall assistance of Dr. Billy E. Haigler during the entire program is very greatly appreciated. His knowledge and guidance truly supported the project. It was a pleasure working with him.

1990 USAF-UES SUMMER FACULTY RESEARCH PROGRAM/
GRADUATE RESEARCH PROGRAM

Sponsored by the

AIR FORCE OFFICE OF SCIENTIFIC RESEARCH

Conducted by the

Universal Energy Systems, Inc.

FINAL REPORT

A SPECIMEN PREPARATION TECHNIQUE FOR MICROSTRUCTRAL ANALYSIS OF UNSATURATED SOIL

Prepared by:	George E. Veyera, Ph.D., Assistant Professor Blaise J. Fitzpatrick, Graduate Student
Department:	Department of Civil and Environmental Engineering
University:	University of Rhode Island
Research Location:	USAF Engineering and Services Center HQ AFESC/RDCM Tyndall AFB Panama City, FL 32403-6001
USAF Researcher:	Dr. C. Allen Ross
Date:	30 September 90
Contract No.:	F49620-88-0053

Same Report as
Prof. George Veyera
(Report # 37)

1990 USAF-UES SUMMER FACULTY RESEARCH PROGRAM/

GRADUATE STUDENT RESEARCH PROGRAM

Sponsored by the

AIR FORCE OFFICE OF SCIENTIFIC RESEARCH

Conducted by the

Universal Energy Systems, Inc.

FINAL REPORT

Remote Control of the Rapid Runway Repair Excavator

Prepared by:	Christopher J. Kardish
Academic Rank:	Graduate Student
Department and University:	Department of Electrical Engineering, University of Florida
Research Location:	HQ AFESC/RDCP Tyndall AFB, FL 32403
USAF Researcher:	Edgar F. Alexander and Allen D. Nease
Date:	7-August-1990
Contract No:	F49620-88-C-0053

Remote Control of the Rapid Runway Repair Excavator

by

Christopher J. Kardish

ABSTRACT

A remote control system for the Rapid Runway Repair excavator has been developed. Digital bit-serial communications have been used for flexibility and interoperability. Operation of the excavator showed no noticable degradation in performance when compared to an on-board operator.

Acknowledgements

The Air Force Systems Command and the Air Force Office of Scientific Research are to be commended for their efforts to bridge the gap between the academic and government research communities. I have benefitted greatly from this opportunity, and praise the foresight which keeps practical research concerns current in the academic arena. The administrative assistance received from the offices of Universal Energy Systems are paramount to the success of my little part of this program.

I owe many of my colleagues at the Air Force's Engineering and Services Center including Mr. Perry Sullivan, coordinator for the summer programs at AFESC. Ms. Lindia McHugh for her efforts to send me where I am going and for directing mail my way. Jeff, who with the permission of Sgt Carl Hollopeter, assisted me with the trials of an extremely dirty computer. Edgar Alexander, who taught me the ins and outs of project management. I also thank Capt Charles Manzione, RDCP branch chief, for his patience and understanding with my occasionally loquacious reports. Finally I must thank Mr. Allen Nease, without whose help and guidance this project would have never come to fruition.

I. INTRODUCTION:

A robot is traditionally operated by a supervisor who leads the robot through a sequence of moves. This sequence of moves can then be replayed by the robot at a rate beyond the capabilities of the supervisor; the supervisor is then needed only to monitor the robot and to rectify any problems that may be encountered.

The Air Base Operating Surfaces Branch (RDCP) of the USAF Engineering and Services Center at Tyndall Air Force Base is responsible for research into the rapid repair of runways after an attack. At the heart of the Rapid Runway Repair (RRR) program is a multi-purpose excavator capable of completely repairing craters with minimal support. Current systems implemented on the excavator include preprogrammed functions (tool changing, digging, jack hammering, compacting and level scraping) and a more traditional position controlled teach-playback system. Both these systems require the presence of an operator on-board the excavator to direct the actions of the excavator. The risk of human life in a post attack scenario makes the presence of the supervisor on-board the excavator impractical. For this reason it is desirable to develop a system by which the excavator can be operated from a remote location.

My research interests in the area of robotics have been pursued through graduate studies at the University of Florida and at Purdue University, as well as through my work with Cybotech, an Indianapolis based robotics company, and earlier RRR work through the

University of Florida. I have worked on the development of robot controllers in both Florida and Indiana. My current research interests are in the area of force feedback of remote systems. This has application to the operations of the excavator including the handling of hazardous materials.

II. OBJECTIVES OF THE RESEARCH EFFORT:

Prior to the summer there was no remote operation capability for the RRR excavator. A commercial product existed for radio operation of the excavator, based on a frequency modulation scheme which decoded frequency commands to control electrohydraulic servo valves on the excavator. This method did not provide the flexibility necessary for the operation of the previously developed control systems, therefore an alternative method needed to be developed. Communications with the excavator were selected to be digital as the systems previously developed interfaced with the on-board computer. Digital communications also provided the flexibility for expansion necessary as the RRR vehicle is still a prototype vehicle and further functions may need to be added.

My assignment as a participant in the 1990 Graduate Student Research Program (GSRP) was to design and implement a remote control system for the RRR excavator based on digital communications. It was determined that the Robotic Vehicle Message Format (RVMF) developed by engineers at the US Army Tank and Automotive Command (TACOM) should be implemented. As the RVMF did not address the presence of a

general purpose manipulator, design and implementation of the RVMF protocol for such a device was a major task. The other task involved writing software to interpret the received RVMF communication packets.

At the completion of my tenure in the 1990 GSRP a remote control system was implemented which provided control over the functions of the excavator arm through a pair of joysticks connected to a base station computer. A qualitative performance evaluation noted no discernable difference from direct manual operation of the excavator.

III. DESIGN OF USER INTERFACE:

A graphical user interface was initially designed to provide control over all desired functions for the excavator (Figure 1). The existing hardware for electronic control supported proportional control for the arm functions. As joysticks were available to provide a simulated control station for operation of the excavator, they were chosen for use for the remote control system. Functions of both the graphic and electric joysticks duplicated the functions on the excavator.

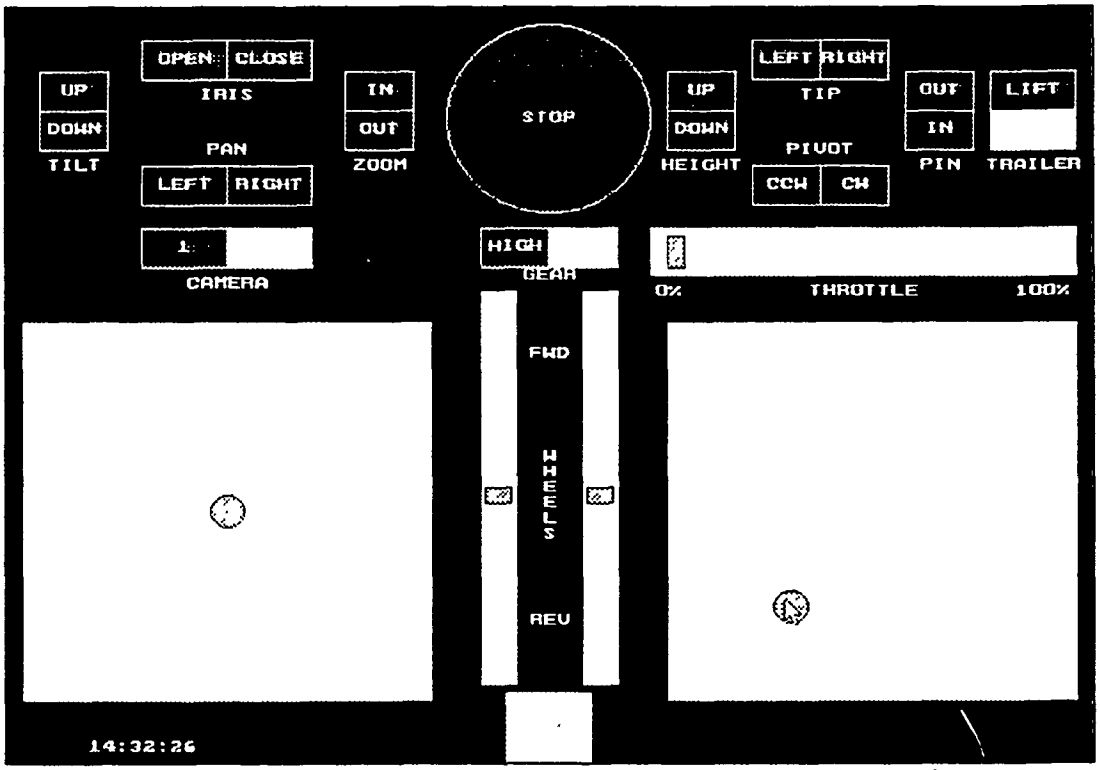

Figure 1: Conceptual User Interface for the Rapid Runway Repair (RRR) Remote Control System

IV. COMMUNICATION SYSTEM DESIGN:

The communication hardware was required to consist of standard, off-the-shelf items. Modularity and expandability considerations dictated the use of an RS-232C bit-serial interface. This permits the future replacement of the hardwired connection between the base and on-board computers with radio modems. Asynchronous communication is preferable as it permits the update of commands dependant only on the readiness of new commands due to changes in the position of the controls. Finally, bi-directional, or full duplex, communications are desirable, permitting the updating of status information at the

base station while sending commands to the remote excavator. These considerations have been independently reached by Mariani (1988) of TACOM.

The communication protocol chosen is the Robotic Vehicle Message Format (RVMF) developed by Mariani and Wong (1989), and permits interoperability with other DOD systems. The RVMF did not address the problem of operating a general purpose manipulator as one of the mission platforms, so I designed an RVMF block to address this problem (Table I).

Block Name Unit Name Attribute Name	Block Address	Unit ID	Attribute Identifier	Parameter Length (Bytes)
Joint Controlled Manipulator	50H			
Joint #n		0(n)H		
Position Command			01H	4
Velocity Command			02H	4
Acceleration Command			03H	4
Torque (Force) Command			04H	4

Table I: RVMF Block Description for Joint Controlled Manipulator

However the RVMF did address several problems relevant to the RRR mission, primarily operation of multiple vehicles, which is not specifically supported by the RVMF, but may be supported by an additional layer added to the message block.

Though several contemporaries in robot control questioned the capabilities of using an IBM AT type backplane for the operation of a remote system, performance showed no need for improvement in the computer architecture. The basis for this question is the bandwidth of the AT backplane, which is limited to 8MHz. While this may be considered slow when compared to other systems, it is more than adequate when compared to the bandwidth of the excavator itself, which is 0.1Hz.

V. RECOMMENDATIONS:

a. The remote control system should be integrated with a complete radio telemetry system. The complete capabilities of the excavator should be reconfigured to operate remotely. Additionally, an audio and video transmission system should be incorporated on the excavator to operate remotely. These will restore many of the senses lost by an operator from a remote station. Thus audio, video and data links will be required.

b. The control of multiple vehicles is of paramount concern for the RRR mission. No digital communication system has yet been demonstrated to operate more than one vehicle at a time. However this technology is available from the areas of computer networks, and can be easily adapted.

c. A remote operator is at an disadvantage when using a telemetry system since human sensory inputs, including balance and depth, may be lost. The recovery of these senses

may not be cost effective, though the incorporation of force feedback to the operator will provide for enhanced materials handling capabilities.

d. Code development required extensive use of interrupt service routines. As this technique of programming does not lend itself to intuitive analysis, it is advisable to use a real time kernel, such as UNIX, VRTX or VX Works, to ease the task of programming the complete system.

REFERENCES

Brendle, B.E., 1990, "Robotic Vehicle Communications Interoperability Protocols," 1990 Autonomous Unmanned Vehicle Systems Conference, Dayton, OH.

Mariani, D., 1988, "Robotic Vehicle Communications Interoperability," RD&E Center Technical Report, US Army Tank-Automotive Command Research, Development and Engineering Center, Warren, MI.

Mariani, D. and Y.M. Wong, 1989, "Robotic Vehicle Message Format," RD&E Center Technical Report, US Army Tank-Automotive Command Research, Development and Engineering Center, Warren, MI.

1990 USAF-UES SUMMER FACULTY RESEARCH PROGRAM/

GRADUATE STUDENT RESEARCH PROGRAM

Sponsored by the

AIR FORCE OFFICE OF SCIENTIFIC RESEARCH

Conducted by the

Universal Energy Systems, Inc.

FINAL REPORT

RATE-LIMITED MASS TRANSFER AND SOLUTE TRANSPORT

Prepared by:	Mary E. Reid
Academic Rank:	Student
Department and University:	Soil and Water Science, University of Arizona
Research Location:	AFESC/RDVC Tyndall AFB, FL
USAF Researcher:	Dave Burris
Date:	2 August 1990
Contract No.:	F49620-88-C-0053

RATE-LIMITED MASS TRANSFER AND SOLUTE TRANSPORT

by

Mark L. Brusseau
and Mary Reid

ABSTRACT

Mass transfer processes such as sorption/desorption and immiscible liquid-aqueous phase transfer can have significant impact on solute transport and remediation of contaminated groundwater, especially when local equilibrium is defied. The objective of the work reported herein was to investigate nonequilibrium sorption of representative organic chemicals by aquifer materials comprised of low organic carbon. The miscible displacement technique was employed for this purpose. Results suggest that the first-order reverse sorption rate constant is log-log linearly related to the sorption equilibrium constant. Furthermore, it appears that nonequilibrium sorption is similar for all five aquifer materials investigated. Thus, the empirical relationship obtained from these data may serve as a means to obtain estimates of sorption rate constants. It is important to note, however, that a time scale effect was observed, such that the sorption rate constant varied with pore-water velocity.

I. INTRODUCTION:

Nonequilibrium sorption can have a significant impact on the transport and fate of contaminants in the subsurface. In addition, remediation of contaminated soils and aquifers can also be constrained by nonequilibrium. In recognition of this importance, the sorption kinetics of organic chemicals has recently become an active area of research. In the investigation and modeling of sorption dynamics it has generally been assumed in the past that the sorption "reaction" was sufficiently fast such that the local equilibrium assumption (LEA) was valid. Recent experimental and theoretical investigations have, however, caused the validity of the LEA to be re-evaluated. Most of the experimental work that has been reported, however, has concerned soils and sediments with relatively high organic carbon contents. Conversely, there has been little work reported on the nonequilibrium sorption of organic chemicals by aquifer materials comprised of low organic carbon (c.f., Lee et al., 1988; Brusseau et al., 1990a; 1990b; 1990c). The objective of the work reported herein was to investigate nonequilibrium sorption of representative organic chemicals by aquifer materials comprised of low organic carbon.

II. OBJECTIVES OF THE RESEARCH EFFORT:

The major objective of the research effort was to investigate the nonequilibrium sorption of organic chemicals by low organic-carbon aquifer materials.

III. MATERIALS AND METHODS:

Experimental apparatus

The techniques employed for the miscible displacement experiments were similar to those utilized by Brusseau et al (1990b). The column apparatus was an Alltech preparative chromatography column made of precision-bore stainless steel, with an internal diameter of 2.25 cm and a length of 7 cm. Bed supports on both ends were stainless steel diffusion mesh of pore size 60 μm. The diffusion mesh enhanced radial distribution of influent solution and also minimized dispersion at the effluent end. The column apparatus was designed to have a minimum void volume in the end plates. Two dual-piston HPLC pumps (Waters 510) were connected to the column with a Rheodyne switching valve to facilitate switching between solutions with and without the solute of interest. The system was designed so that the solute contacted only stainless steel.

Effluent from the column was directed through a flow-through, variable wave-length UV detector (Waters 450) to allow continuous monitoring of the solution-phase concentration of the solute, which was recorded on a strip chart recorder (Soltec 1242). The wavelength to be used for each experiment was determined by selecting for maximum response. Previous miscible displacement studies have usually employed collection of effluent fractions, which were then analyzed by GC or HPLC. For volatile chemicals, this method suffers from the potential for loss by volatization during the fraction collection and analysis steps. The use of the flow-through detection method eliminates this problem. It also

significantly simplifies the analytical process. However, this method is limited to the use of detectors that are suitable for flow-through operation. This constraint will obviously restrict the chemicals that may be used to detector-specific set.

Materials

The following chemicals were employed for the miscible displacement experiments: 1,4-dichlorobenzene, tetrachloroethene, p-xylene, and naphthalene; pentafluorobenzoic acid was employed as a nonsorbing tracer. The following five aquifer materials were used for these experiments: Lula, Borden, Tinker, Columbus, and Barksdale. Properties of these materials are reported by Stauffer (1987).

Experimental procedure

The column was packed in incremental steps with the dry material to establish uniform bulk density. After completion of packing, electrolyte solution (0.005 M $CaSO_4$, 0.02% NaN_3) was pumped through the column until steady-state water saturation was established; this generally required approximately two days. The constancy of column masses (i.e., maintenance of saturated conditions) was monitored periodically throughout the experiments. The measured dead volumes were used to determine the corrected pore volume of the column. The matrix for all solutions was that described above. Saturated stock solutions for each solute were prepared by placing quantities in excess of their solubility limit in contact with the electrolyte solution and stirring the solution for at least 48 hours. Solutions were filter sterilized with 0.45 μm filters prior to use. Aliquots of the stock solution were

diluted with electrolyte solution until the desired concentration was achieved. The concentration values (C_0) of the solutions used for the MDC experiments were generally 10% to 25% of the aqueous solubility.

A typical experiment involved the continuous injection of a pulse of the selected solute, the pulse size being large enough such that the point of $C/C_0 = 1$ was reached. The solute pulse was then displaced with 0.005 M $CaSO_4$ solution until the point of $C/C_0 = 0$. Constancy of flow was periodically checked by collecting effluent fractions. These measured flow rates were checked against the average flow rate determined by collecting and measuring all effluent over the injection period; they compared well in all cases. The flow rates used for the experiments were 2, 1, and 0.1 ml/min (average pore-water velocity = approx. 80, 40, and 5 cm/hr, repectively).

To check for the existence of nonidealities other than nonequilibrium sorption (e.g., nonlinearity), comparisons of the frontal and distal portions of the breakthrough curves were made. The presence of nonlinearity, for example, would result in non-coincident frontal and distal curves. The comparisons showed the two portions to be coincident (see Figure 1 for an example). To check the reproducibility of the method, repeat experiments were occasionaly performed. An example of such is presented in Figure 2. These results suggest a high degree of reproducibility.

Data anlysis

The results of the miscible displacement experiments were analyzed with a first-order bicontinuum model. Models of this

type, where sorption is assumed to be instantaneous for some portion of the porous medium and rate-limited for the remainder, have been presented by Selim et al. (1976) and Cameron and Klute (1977). Sorption is described as follows:

$$S_1 = F\, K_p\, C \qquad (1a)$$

$$dS_2/dt = k_1\, S_1 - k_2\, S_2 \qquad (1b)$$

where C is the solute concentration in the water-phase (M/L^3), S_1 is the sorbed-phase concentration in the equilibrium domain (M/M), S_2 is the sorbed-phase concentration in the kinetic-controlled domain (M/M), K_p is the sorption equilibrium constant, F is the fraction of sorbent for which sorption is instantaneous, and k_1 and k_2 are the forward and reverse sorption rate constants (T^{-1}), respectively. These models can represent each of the three processes, namely physical nonequilibrium, chemical nonequilibrium, and intrasorbent diffusion, responsible for nonequilibrium sorption (Brusseau and Rao, 1989a).

To simulate solute transport, the following two nondimensional equations are employed:

$$\partial C^*/\partial p + (\beta R-1)\,\partial C^*/\partial p + (1-\beta)R\,\partial S^*/\partial p = (1/P)\,\partial^2 C^*/\partial X^2 - \partial C^*/\partial X \qquad (2)$$

$$(1-\beta)R\,\partial S^*/\partial p = \omega (C^* - S^*) \qquad (3)$$

where

$$C^* = C/C_0 \qquad (4a) \qquad\qquad P = vL/D \qquad (4b)$$

$$S^* = S_2/(1-F)K_p \qquad (4c) \qquad\qquad R = 1 + (\rho/\theta)K_p \qquad (4d)$$

$$p = vt/L \quad (4e) \qquad \beta = (1 + F(\rho/\theta)K_p)/R \quad (4f)$$

$$X = x/L \quad (4g) \qquad \omega = k_2(1-\beta)RL/v \quad (4h)$$

and where D is the dispersion coefficient (L^2/T), v is the average pore-water velocity (L/T), x is distance (L), L is column length (L), ρ is bulk density (M/L^3), and θ is volumetric soil-water content. To run the model, knowledge of the following parameters is required: the Peclet number P, which represents the dispersive-flux contribution to transport; the retardation factor R, which represents the effect of sorption on transport; the fraction of instantaneous retardation, β; the Damkohler number ω, which is a ratio of hydrodynamic residence time to characteristic time of the sorption "reaction"; and T_0, the size in pore volumes of the input pulse. The value for P was obtained from the BTC of a nonsorbing solute. The value for R was obtained by moment analysis, i.e., the first, normalized, absolute temporal moment of a dirac pulse (Brusseau et al., 1990b, or from area above the breakthrough curve (Nkedi-Kizza et al., 1987). The value of T_0 is known from measurement. The two unkown parameters are thus β and ω. The nonlinear, least-squares optimization program CFITIM (van Genuchten, 1981) was used under flux boundary conditions to determine values for the two unknowns.

IV. RESULTS AND DISCUSSION:

Pentafluorobenzoic acid breakthrough curves were obtained for the columns to establish their hydrodynamic character and to determine values for P. These BTCs were symmetrical and sigmoidal

in shape and were invariant with pore-water velocity, which suggests the absence of physical nonequilibrium (Brusseau and Rao, 1989a). BTCs for the organic chemicals were, in contrast, asymmetrical (see Figures 1 and 2). This, in conjunction with the symmetrical BTCs obtained for a nonsorbing tracer, is highly suggestive of a sorption-related nonequilibrium process (Brusseau and Rao, 1989a).

The relationship between k_2, values of which were determined by optimization, and K_p was evaluated using the linear-free-energy-relationship technique, in the manner of Brusseau and Rao (1989b). The results for the 2 ml/min velocity experiments are shown in Figure 3, where the regression equation reported by Brusseau and Rao (1989b) is included for comparison. An inverse correlation between k_2 and K_p is evident. In addition, it appears that all five aquifer materials exhibit similar nonequilibrium behavior. This observation that sorbent appears to play only a secondary role on the nature of nonequilibrium sorption was also reported by Brusseau et al. (1990b; 1990c).

The effect of velocity on rate-constant values was investigated by comparing data obtained at the fast velocities to that obtained at 0.1 ml/min. Inspection of Figure 4 reveals that the rate constants appear to vary with velocity. Inspection of Figure 4 also shows that the K_p values did not change significantly with velocity. This suggests that additional sorption is not taking place at the slower velocity and, therefore, that the velocity effect is related to the nature of the first-order model approximation. This time scale effect is important to consider

when determining appropriate rate-constant values for a given situation.

V. RECOMMENDATIONS:

a) The empirical relationship obtained from these data may serve as a means to obtain estimates of sorption rate constants. These would be useful for input to models that may then be used to investigate the relative importance of nonequilibrium sorption on the transport and fate of organic contaminants in the subsurface.

b) One suggested topic of follow-on research is to compare the effect of heterogeneous aquifer properties (e.g., hydraulic conductivity, sorption capacity) to that of nonequilibriunm sorption on the transport of organic chemicals. Another topic would be an investigation of mass transfer of organic contaminants between residual immiscible liquids and water.

ACKNOWLEDGMENTS

I would like to thank Dave Burris and Tom Stauffer for their assistance, as well as that of the RDV staff. I would also like to thank Mary Reid for her help in performing the experiments reported herein.

REFERENCES

Brusseau, M. L. and Rao, P. S. C, Sorption nonideality during

organic contaminant transport in porous media, CRC Critical Reviews in Environ. Control, 19, 33, 1989a.

Brusseau, M. L. and Rao, P. S. C., Evidence for diffusional mass transfer within sorbent organic matter as a cause for sorption nonequilibrium, Chemosphere, 18, 1691, 1989b.

Brusseau, M.L., Larsen, T., and Christensen, T.H., Rate-limited sorption and nonequilibrium transport of organic chemicals in low organic carbon aquifer materials, Water Resour. Res. (in review), 1990a.

Brusseau, M.L., Jessup, R.E., and Rao, P.S.C., Sorption kinetics of organic chemicals: Evaluation of gas-purge and miscible-displacement techniques, Environ. Science Technol., 24, 727, 1990b.

Brusseau, M.L., Jessup, R.E., and Rao, P.S.C., Nonequilibrium sorption of organic chemicals: Elucidation of rate-limiting processes, Environ. Science Technol., (in press), 1990c.

Cameron, D. R., and Klute, A., Convective-dispersive solute transport with a combined equilibrium and kinetic adsorption model, Water Resour. Res., 13, 183, 1977.

Lee, L. S., Rao, P. S. C., Brusseau, M. L., and Ogwada, R. A., Nonequilibrium sorption of organic contaminants during flow

through columns of aquifer materials, Environ. Tox. Chem., 7, 779, 1988.

Nkedi-Kizza, P., Rao, P. S. C., and Hornsby, A. G., The influence of organic cosolvents on leaching of hydrophobic organic chemicals through soils, Environ. Sci. Technol., 21, 1107, 1987.

Selim, H. M., Davidson, J. M., and Mansell, R. S., Evaluation of a two-site adsorption-desorption model for describing solute transport in soils, Proc. Summer Computer Simulation Conf., Washington, D.C., 1976.

Stauffer, T..B., Sorption of nonpolar organics on minerals and aquifer materials, Ph.D. dissertation, College of William and Mary, 1987.

Van Genuchten, M. Th., Non-equilibrium transport parameters from miscible displacement experiments, USDA, US Salinity Lab, Research Report No. 119, 1981.

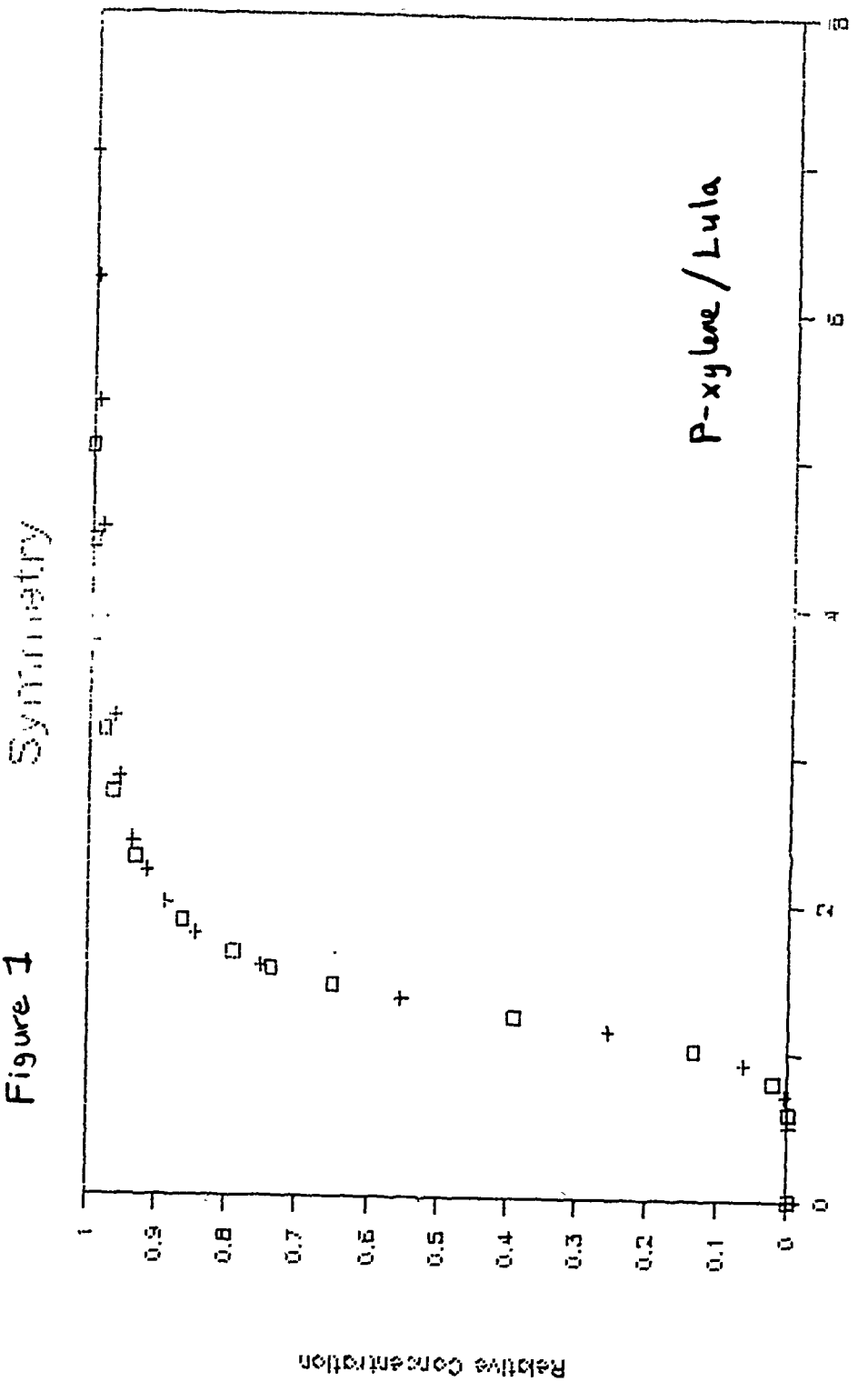
Figure 1
Symmetry
P-xylene / Lula
Relative Concentration
Pore Volumes
Fit
0
0.1
0.2
0.3
0.4
0.5
0.6
0.7
0.8
0.9
1
2
4
6
8

Figure 2 Reproducibility

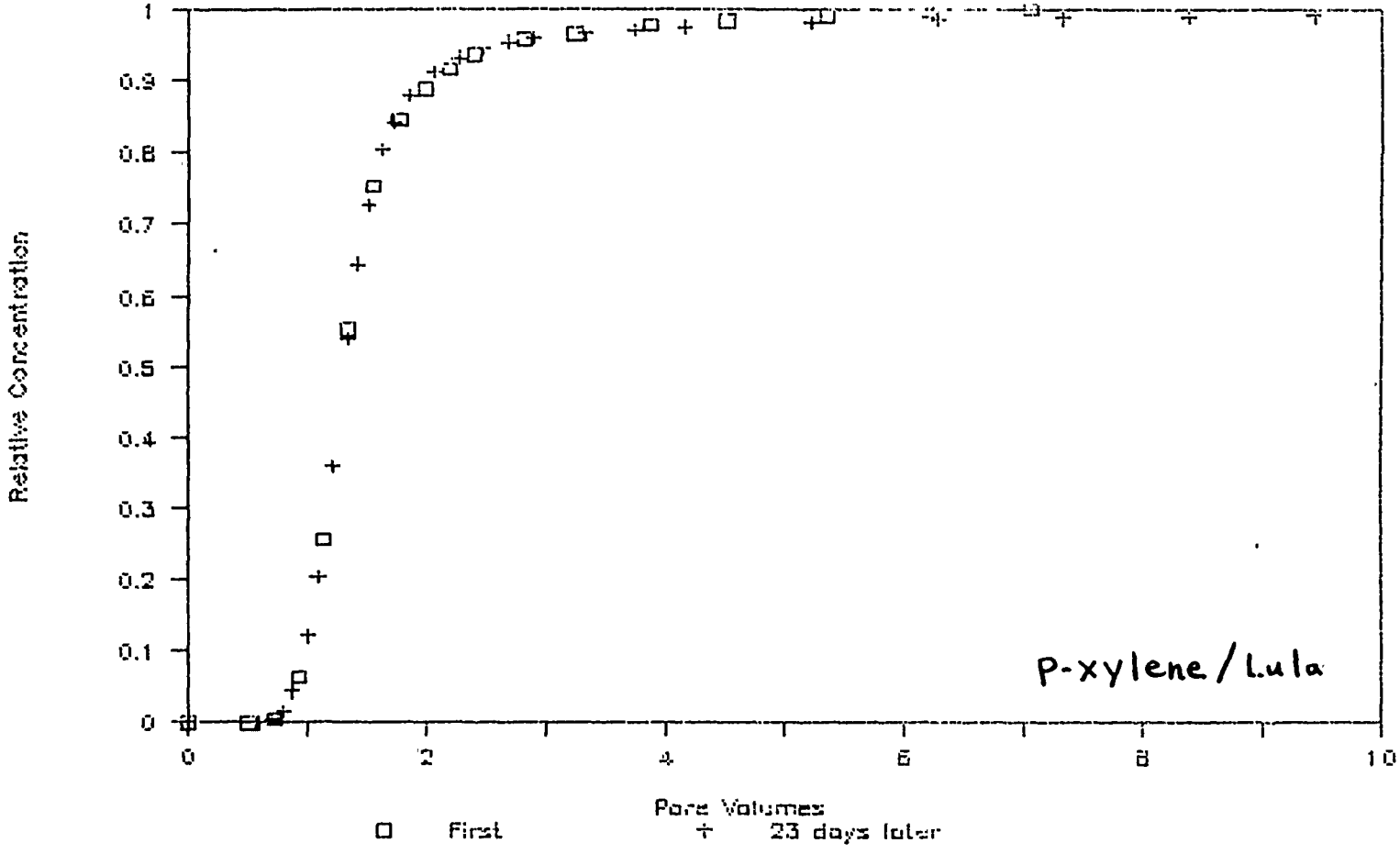

Figure 3. Relationship: k2 vs. Kp

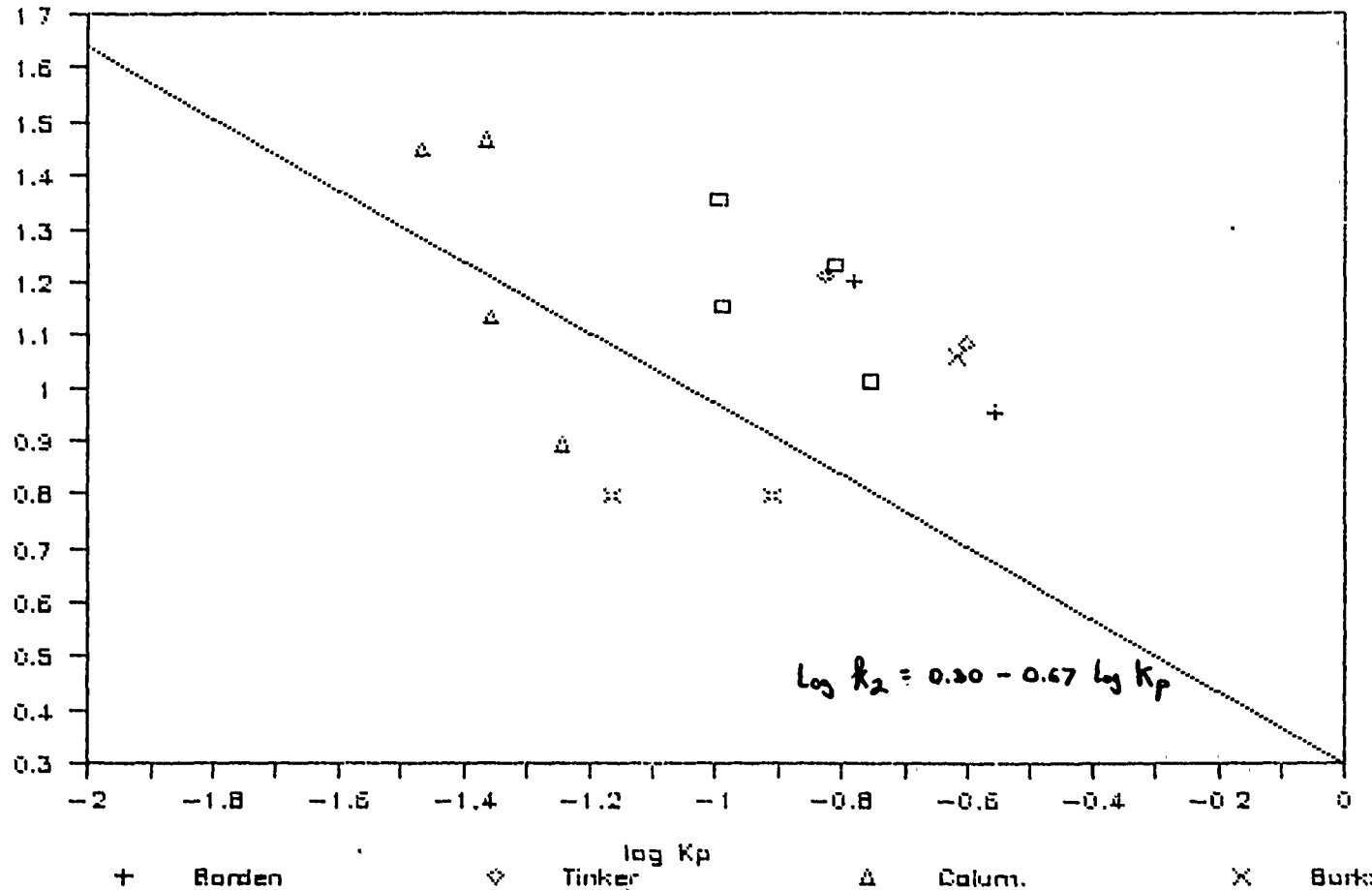

□ Lula + Borden ◇ Tinker △ Calum. × Burks.

Figure 4. Effect of Velocity

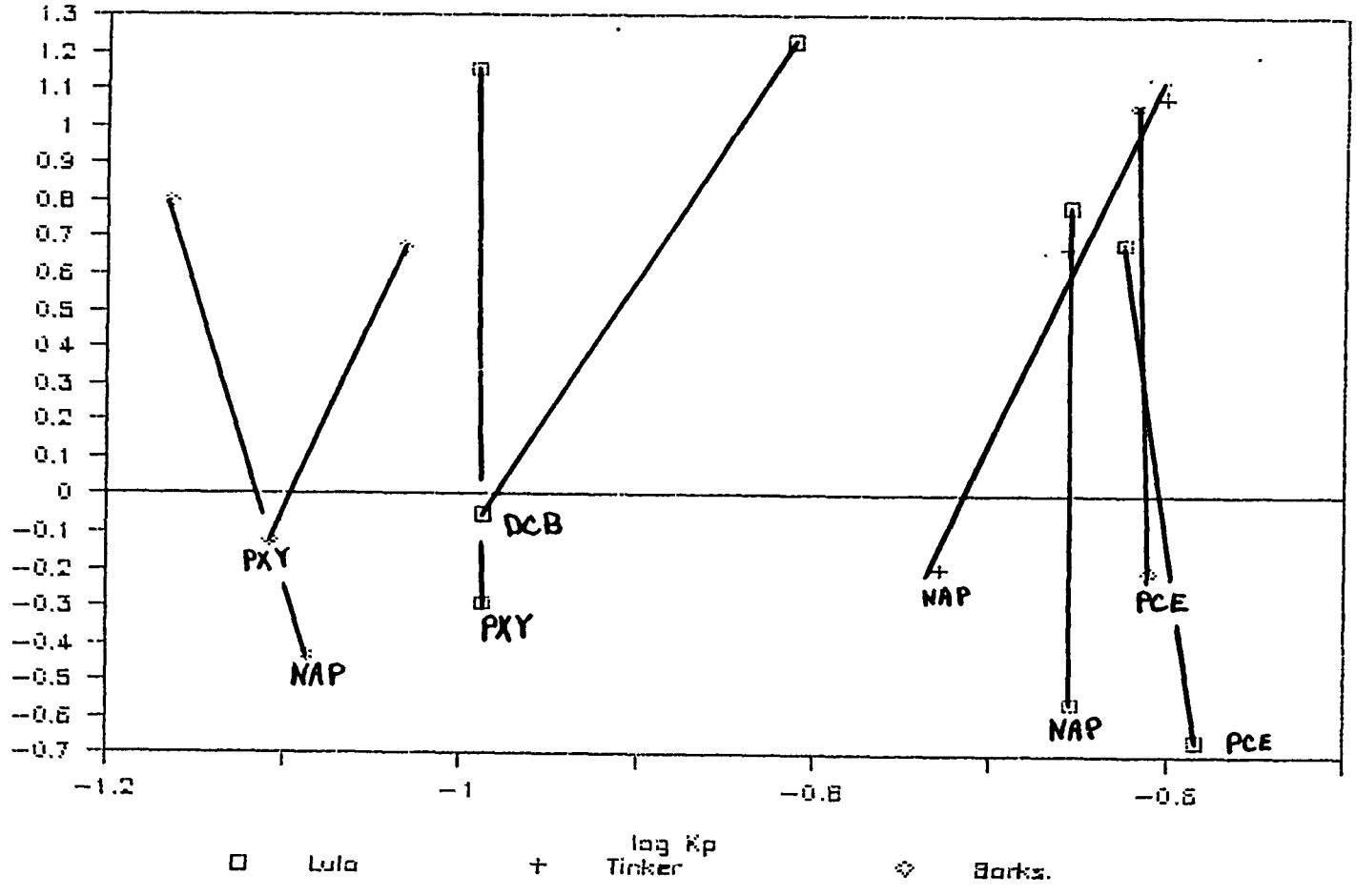

File for Air Force Column Data
Mark Brusseau 14 June 1990

Kp	k2		log Kp	log K2
0.081	17.5	TCE/o	-1.09151	1.243038
0.16	14.4	PXYL/o	-0.79588	1.158362
0.101	22.6	PCE/2-2	-0.99567	1.354108
0.154	17	DCB/2-2	-0.81247	1.230448
0.103	0.89	DCB/2-01	-0.98716	-0.05060
0.176	10.3	NAP/2-2	-0.75448	1.012837
0.102	14.2	PXYL/2-2	-0.99139	1.152288
0.118	7.14	PXYLr/2-2	-0.92811	0.853698
0.164	6.31	PXYL/2-1	-0.78515	0.800029
0.103	0.51	PXYL/2-01	-0.98716	-0.29242
0.222	0.277	NAP/2-01	-0.65364	-0.55752
0.221	6.13	NAP/2-1	-0.65560	0.787460
0.354	1.2	NAP/2s-1	-0.45099	0.079181
0.317	0.146	NAP/2s-01	-0.49896	-0.83564
0.237	4.9	PCE/2-1	-0.62525	0.690196
0.261	0.22	PCE/2-01	-0.58335	-0.65757
0.123	2.1	PCE/5-01	-0.91009	
0.276	9	PCE/5-2	-0.55909	
0.165	15.8	NAP/5-2	-0.78251	
0.128	8.75	PCE/3-1	-0.89279	
0.149	16.2	DCB/3-2	-0.82681	
0.071	12.2	PXYL/3-1	-1.14874	
0.22	4.71	NAP/3-1	-0.65757	
0.25	12.1	NAP/3-2	-0.60205	
0.187	0.637	NAP/3-01	-0.72815	
0.043	29.2	DCB/1	-1.36653	
0.057	7.8	NAP/1	-1.24412	
0.034	28	PCE/1	-1.46852	
0.044	13.6	PXYL/1	-1.35654	
0.241	11.45	PCE/4-2	-0.61798	
0.245	0.63	PCE/4-01	-0.61083	
0.19	15.45	PCE/4-1	-0.72124	
0.0135	6.5	NAPr/4-1	-1.86966	
0.036	3.95	NAP/4-1	-1.44369	
0.082	0.37	NAP/4-01	-1.08618	
0.228	3.4	NAP/P4-1	-0.64206	
0.0684	6.26	NAP/4-2	-1.16494	
0.0023	7.1	DCB/4-2	-2.63827	

APPENDIX : Data

0.139	2.12	DCB/P4-2	-0.85698
0.234	0.17	PXY/P4-01	-0.63078
0.078	0.76	PXY/4-01	-1.10790
0.093	4.69	PXY/4-1	-1.03151
0.123	6.26	PXY/4-2	-0.91009

when determining appropriate rate-constant values for a given situation.

V. RECOMMENDATIONS:

a) The empirical relationship obtained from these data may serve as a means to obtain estimates of sorption rate constants. These would be useful for input to models that may then be used to investigate the relative importance of nonequilibrium sorption on the transport and fate of organic contaminants in the subsurface.

b) One suggested topic of follow-on research is to compare the effect of heterogeneous aquifer properties (e.g., hydraulic conductivity, sorption capacity) to that of nonequilibriunm sorption on the transport of organic chemicals. Another topic would be an investigation of mass transfer of organic contaminants between residual immiscible liquids and water.

ACKNOWLEDGMENTS

I would like to thank Mark Brusseau for his direction of this project. I would also like to thank Dave Burris and Tom Stauffer for their assistance, as well as that of the RDV staff.

REFERENCES

Brusseau, M. L. and Rao, P. S. C, Sorption nonideality during organic contaminant transport in porous media, CRC Critical

1990 USAF-UES SUMMER FACULTY RESEARCH PROGRAM/

GRADUATE STUDENT RESEARCH PROGRAM

Sponsored by the

AIR FORCE OFFICE OF SCIENTIFIC RESEARCH

Conducted by the

Universal Energy Systems, Inc.

FINAL REPORT

Centrifuge Modeling of Explosive Induced Stress Waves in Unsaturated Sand

Prepared by:	Wayne A. Charlie (1) and Andrew J. Walsh (2)
Academic Rank:	(1) Professor and (2) Graduate Student
Department and University:	Department of Civil Engineering Colorado State University
Research Location:	HQ AFESC/RDCM Tyndall AFB FL
USAF Researcher:	Capt Steven T. Kuennen and Dr C. Allen Ross
Date:	September 28, 1990
Contract No:	F4962-88-C-0053

Same Report as
Prof. Wayne Charlie
(Report # 29)

1990 USAF-UES FACULTY RESEARCH PROGRAM/

GRADUATE STUDENT RESEARCH PROGRAM

Sponsored by the

AIR FORCE OFFICE OF SCIENTIFIC RESEARCH

Conducted by the

Universal Energy Systems, Inc.

FINAL REPORT

Comparisons of the Unsteady Flow Fields Elicited by Constant Rate and Sinusoidal Pitching Motions of an Airfoil

Prepared by:	Gregory A. Addington
Academic Rank:	Graduate Student
Department and University:	Department of Aerospace Engineering Sciences University of Colorado at Boulder
Research Location:	FJSRL/NH United States Air Force Academy, CO 80840
USAF Researcher.:	Captain Scott Schreck
Date:	27 September 1990
Contract No:	F49620-88-C-0053

Comparisons of the Unsteady Flow Fields Elicited by Constant Rate and Sinusoidal Pitching Motions of an Airfoil

by

Gregory A. Addington

ABSTRACT

Research into unsteady separated flows about airfoils has largely proceeded along two fronts, one which uses constant rate pitching of the wing and another which uses sinusoidal oscillations of the wing. Both types of motion have their own merits, but to date no study to the author's knowledge has attempted to define a set of matching conditions under which the flow fields elicited by the two motions are comparable. By using smokewire flow visualizations of the centerline and the near surface flows, this study attempts to define a rudimentary set of matching parameters for which similar variances elicit similar differences in the respective elicited flow field, be those differences of either a qualitative or quantitative nature. A refinement of this parameter matching will take place at a later date once surface pressure measurements currently being acquired at FJSRL are available.

I. INTRODUCTION

Research into unsteady separated flows about airfoils has largely progressed along two fronts. On the one hand, sinusoidal oscillations of airfoils can be used to model the effects experienced by helicopter rotor blades and axial flow turbines. On the other hand, a constant rate pitch is thought to be a motion which future "supermaneuverable" combat aircraft will use to enable them to take advantage of possible stall and post-stall maneuvers (Herbst, 1980). Hence, both motions have practical application, but to date, no study has attempted to define any type of matching conditions such that the elicited flow fields are comparable.

The low speed wind tunnel facility of the Frank J. Seiler Research Laboratory (FJSRL) located at the United States Air Force Academy provided an excellent opportunity to experimentally compare these two motions. A computer controlled airfoil driving mechanism which is capable of sequencing airfoil motion to flow visualization equipment and the availability of surface pressure measuring equipment are two factors which make FJSRL a quality location for such a study. Pressure data is not included in the current study but instead will be taken by FJSRL researchers and will be correlated with the presented flow visualization data at a future date.

Current efforts underway at the University of Colorado at Boulder have largely involved flow visualizations and hot wire velocimetery of the flowfields elicited by sinusoidally oscillating airfoils at low Reynolds numbers, although some constant rate pitch work has been performed in the past. With the installment of Captain Scott Schreck, a former University of Colorado doctoral student, at FJSRL, cooperation between the two institutions has been on the rise, which has lead to the study at hand.

II. OBJECTIVES OF THE RESEARCH EFFORT

As discussed earlier, a methodology for the comparisons of constant rate and sinusoidal pitching of an airfoil has not, to this author's knowledge, been arrived upon at any level; however, due to the complexity of unsteady fluid dynamics, a simple flow visualization study would not suffice for this task. Hence, it was decided to base such a comparison on several types of data: first, flow visualizations of an airfoil undergoing both types of motions; second, surface pressure data for both motions; and third, correlating the new data with previously published data to provide the desired comparison protocol.

For the flow visualization segment of this effort, visualizations of both the centerline and near surface flows were taken with the intent of finding, on a relatively qualitative scale, the effect of changing pitching parameters on the flowfields elicited by the airfoil. The parameters selected were, for constant rate pitching, the non-dimensional pitching rate parameter $a+$, the starting angle a_s, and

the pitch amplitude da, and the corresponding parameters for oscillating airfoil of K, a_m and a_w, respectively.

Since the brevity of the summer commission of ten weeks precluded the immediate acquisition of surface pressure data, an emphasis was placed on the flow visualization segment of this correlation outline. Follow-up investigations underway at FJSRL will acquire the necessitated pressure data and the correlations will take place shortly.

III. NOMENCLATURE

General

U	free stream velocity (ft/s)
b	airfoil semi-span (ft)
c	airfoil chord length (ft)
a	airfoil angle of attack (deg)

Constant Rate Pitch

$\dot{a}$	pitch rate (da/dt) (deg/s)
$a+$	non-dimensional pitch parameter (ac/U)
da	pitch amplitude (deg)
a_s	pitch starting angle (deg)
DSV	Dynamic Stall Vortex

Oscillating Pitch

a_m	mean pitch angle (deg)
a_w	pitch amplitude (deg)
w	angular frequency (deg/sec)
K	non-dimensional pitch parameter (wc/2U)

IV. METHODOLOGY

Data was taken in the Frank J. Seiler Research Laboratory's 3 ft x 3 ft low speed wind tunnel located on the campus of the United States Air Force Academy. This wind tunnel has a relatively low test section turbulence level, documented to be $\leq$ 0.15% at U = 30 ft/s. For the acquisition of flow visualization data, U was maintained at 10 ft/s throughout this stage of the experiment.

The airfoil used in this study was a hollow, extruded aluminum NACA 0015 with c = 0.5 ft and b = 1 ft. To one wingtip was fitted a circular spitter plate centered on the airfoil midspan, to the other side of which a dovetail rail was attached so that either one of two driving mechanisms could be employed.

The constant rate pitch mechanism at FJSRL consists of a DC stepper motor linked to a MASSCOMP 5500 computer via the computer's built in digital to analogue converter. Embedded computer routines allowed for the control of $\Delta\alpha$ and $\dot{\alpha}$ with reasonable precision (errors of ± 0.4 deg in α and $\pm 2\%$ $\dot{\alpha}$ were the maximums). The computer was also employed, via a junction box, to control the sequencing of a variable speed 16 mm camera to the motion of the airfoil and high intensity strobe lights to the shutter of the camera. (It is important to note that the camera to airfoil synchronization is for the camera's motor and not its shutter, so the phase of the shutter and the phase of the airfoil in its pitch motion in this system are only randomly related, therefore the exact time any one picture was taken with respect to the airfoil's position is not precisely defined.) For this portion of the procedure, the camera speed was set to 150 frames per second, while $\dot{\alpha}$'s of 115, 286, 573 and 768 deg/s were used to give $\dot{\alpha}+$ of 0.10, 0.25, 0.50 and 0.67, respectively. Because of time limitations, only a $\Delta\alpha$ of 35^{o} was used, while α_s's of 0^{o} and 10^{o} were investigated.

The oscillation mechanism consists of a 3/4 HP DC motor linked to the airfoil via a scotch yoke and reduction gear system. The scotch yoke was designed so to give a reasonably true (2% error) sinusoidal motion. A reference time mark was provided by a magnet and reed switch which triggered a variable delay circuit. This delay circuit then initiated the strobelight pulse which was thusly phase locked to the airfoil motion, enabling multiple exposure (typically 5) 35mm photographs to be taken of the visualized field. For this experiment, ω's of 573, 1146 and 1719 deg/s were employed to give K's of 0.25, 0.50 and 0.75, respectively. Both α_m and α_w were maintained at 10^{o}.

(The ramifications to this study of not varying $\Delta\alpha$ for the constant rate pitching and α_m and α_w for sinusoidal oscillations is discussed in the recommendations section.)

With both motion types, smoke for the visualizations of the flowfield was introduced into the freestream with a 0.005 in diameter tungsten smokewire. For the views of centerline flows, the smokewire was stretched between two copper poles which penetrated the test section so that the wire would be in the plane of the airfoil centerline and orthogonal to the planform. The near surface visualizations were obtained by using an adaptation of the smokewire technique used by Schreck (1989) and Horner et al (1990). For this technique, the smokewire was stretched from a contact plate placed between the airfoil and splitter plate along the leading edge, then turned at the wingtip so to continue the smokewire along the free wingtip to the trailing edge. The distance from the airfoil to the smokewire was maintained at 0.1 in along its entire length. Both smokewires were manually coated with SAE 30 weight motor oil then ohmically heated to vaporize the oil into a thin sheet of smoke.

V. RESULTS AND DISCUSSION

A. Dynamic Stall Vortex/Leading Edge Vortex Comparability

A portion of the flow visualizations collected are presented as Fig.'s 1-6. For reference, frames on Fig.'s 1, 5 and 6 labeled A-T are of midspan visualizations looking from the tip inward to the splitter plate. Frames a-t show the visualizations of the near surface flows at the same, or nearly the same (see the prior note regarding the constant rate pitch sequences), phase angle as A-T. This sequencing is maintained for Fig.'s 1-6. In the cases of constant rate pitches, white dots in the upper right hand corner of the frames indicate , respectively the first frame after the pitching motion has begun and ended. The image denoted as the first frame following motion initiation may differ temporally from the actual instant of motion initiation by no more that 6.7 ms because of the lack of a shutter/motion phase relationship and frame rate used. For oscillation motion visualizations, frames A-J and a-j correspond to the pitching up segment of the motion while K-T and k-t correspond to the airfoil pitching down. A and a show the airfoil at maximum pitch up ($\alpha = 20^{o}$) while K and k show the minimum α (0^{o}). The time and angular displacements between frames is shown as a part of Table 1.

Both the constant rate pitch and the sinusoidally oscillating pitch of the airfoil generate a large vortical structure at the leading edge of the airfoil during some point of the motion as the first large scale indication of the dynamic stall process. For purposes of clarity, that vortical structure as created in the constant rate pitching motion will be termed the "Dynamic Stall Vortex" (DSV), while the corresponding structure in the sinusoidal motion will be termed the "Leading Edge Vortex" (LEV). Three parameters used to characterize the DSV and LEV are the initiation time, convection rate and cohesiveness, which are defined as follows: initiation time is the point in the motion at which the DSV/LEV first becomes apparent; convection velocity is the rate at which the vortex moves with respect to a fixed reference point (in Fig. 7 convection velocity is non-dimensionalized by U); cohesiveness is a qualitative measure of how well or poorly defined the vortex is in its general shape, clarity, etc.

The variation of the dynamic parameter for each motion has a profound effect on the respective primary vortex structure. In the case of the constant rate pitch and its corresponding DSV (see Fig.'s 1-4), increasing $\alpha+$ causes the DSV to initiate later in the motion and be of a more cohesive nature as confirmed by previous studies (Walker et al, 1985; Helin and Walker, 1985), and convects at an increased average rate (Fig. 7). Similarly, increasing K for a sinusoidally oscillating airfoil has like effects on the LEV's relative initiation time, cohesiveness and convection rate, also as demonstrated previously (Schreck and Luttges, 1988; Schreck, 1989).

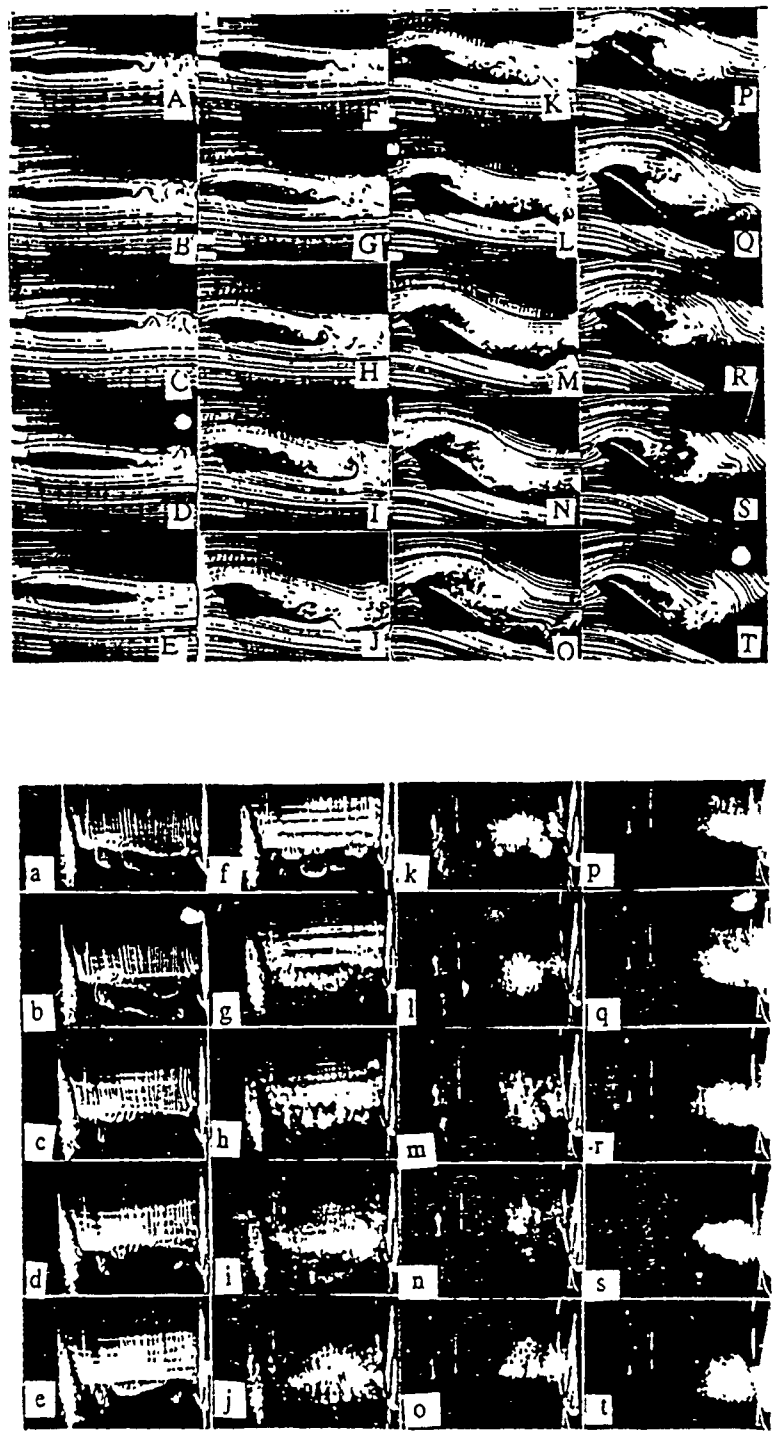

Fig. 1 Visualizations of constant rate pitch motion. $a \div = 0.10$, $a_s = 0^o$. Upper sequence shows centerline flows (airflow from left to right), lower shows near surface flows (airflow from top to bottom, splitter plate at right).

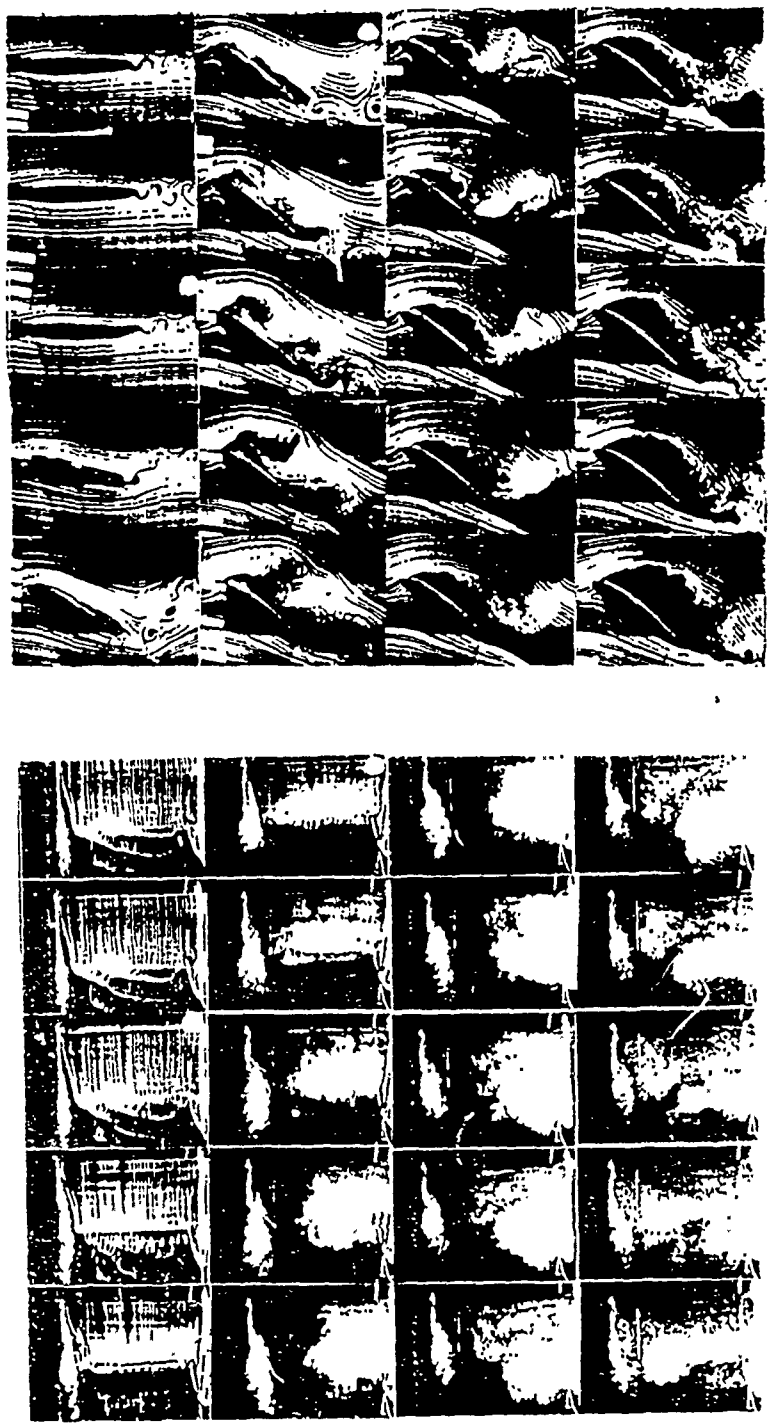

Fig. 2 Visualizations of constant rate pitch motion. $a\dot{+} = 0.67$, $a_c = 0^o$. Upper sequence shows centerline flows (airflow from left to right), lower shows near surface flows (airflow from top to bottom, splitter plate at right).

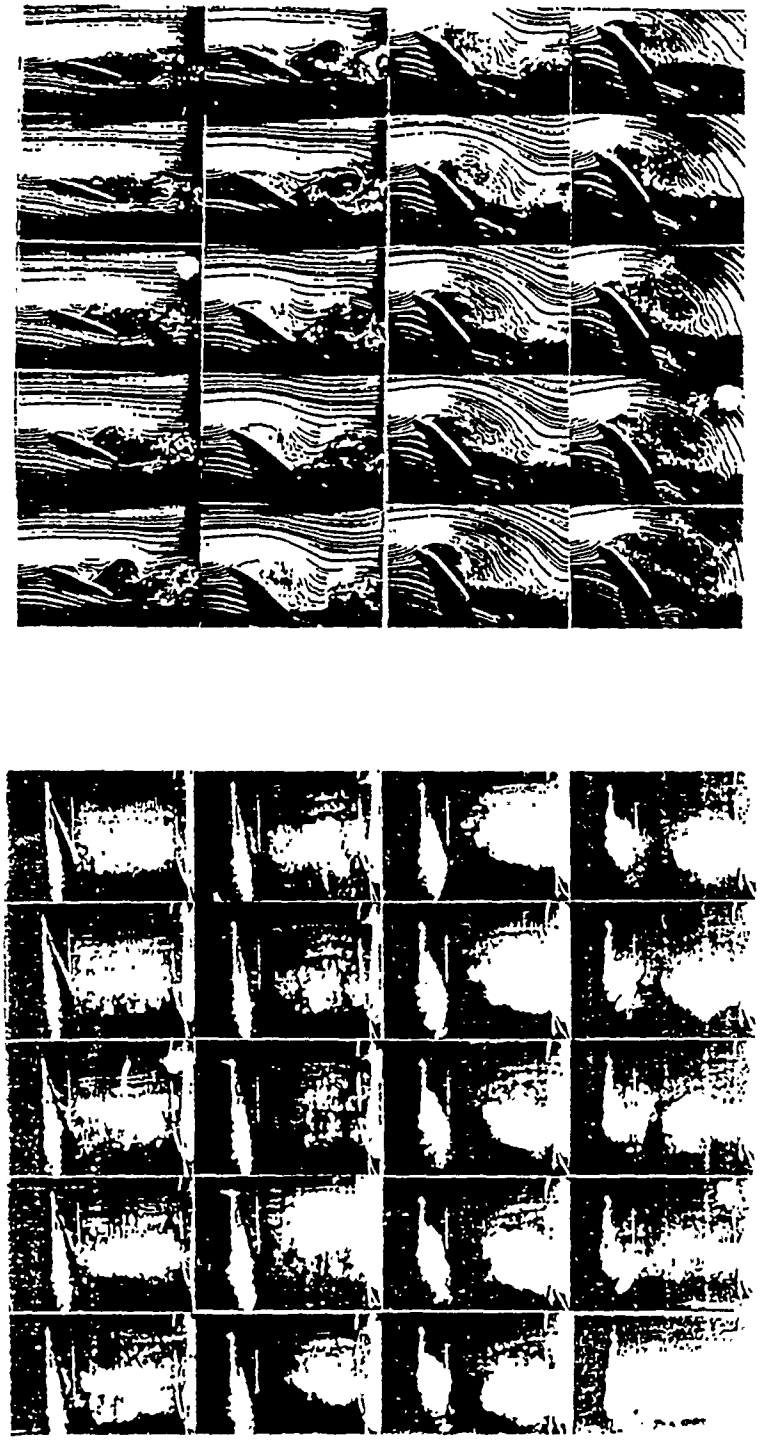

Fig. 3 Visualizations of constant rate pitch motion. $\bar{a} = 0.10$, $a_s = 10^o$. Upper sequence shows centerline flows (airflow from left to right), lower shows near surface flows (airflow from top to bottom, splitter plate at right).

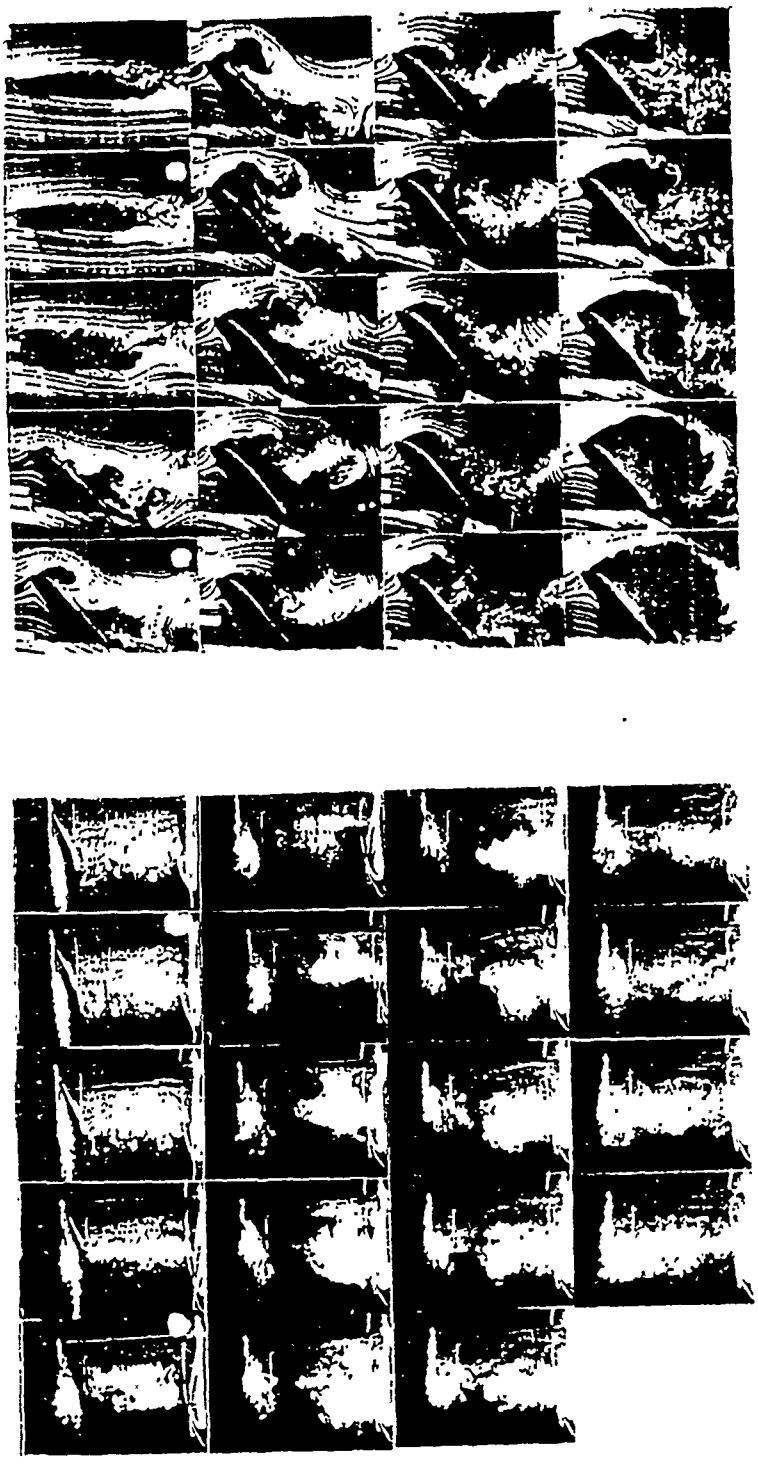

Fig. 4 Visualizations of constant rate pitch motion. $a\dot{+} = 0.67$, $a_s = 10^o$. Upper sequence shows centerline flows (airflow from left to right), lower shows near surface flows (airflow from top to bottom, splitter plate at right).

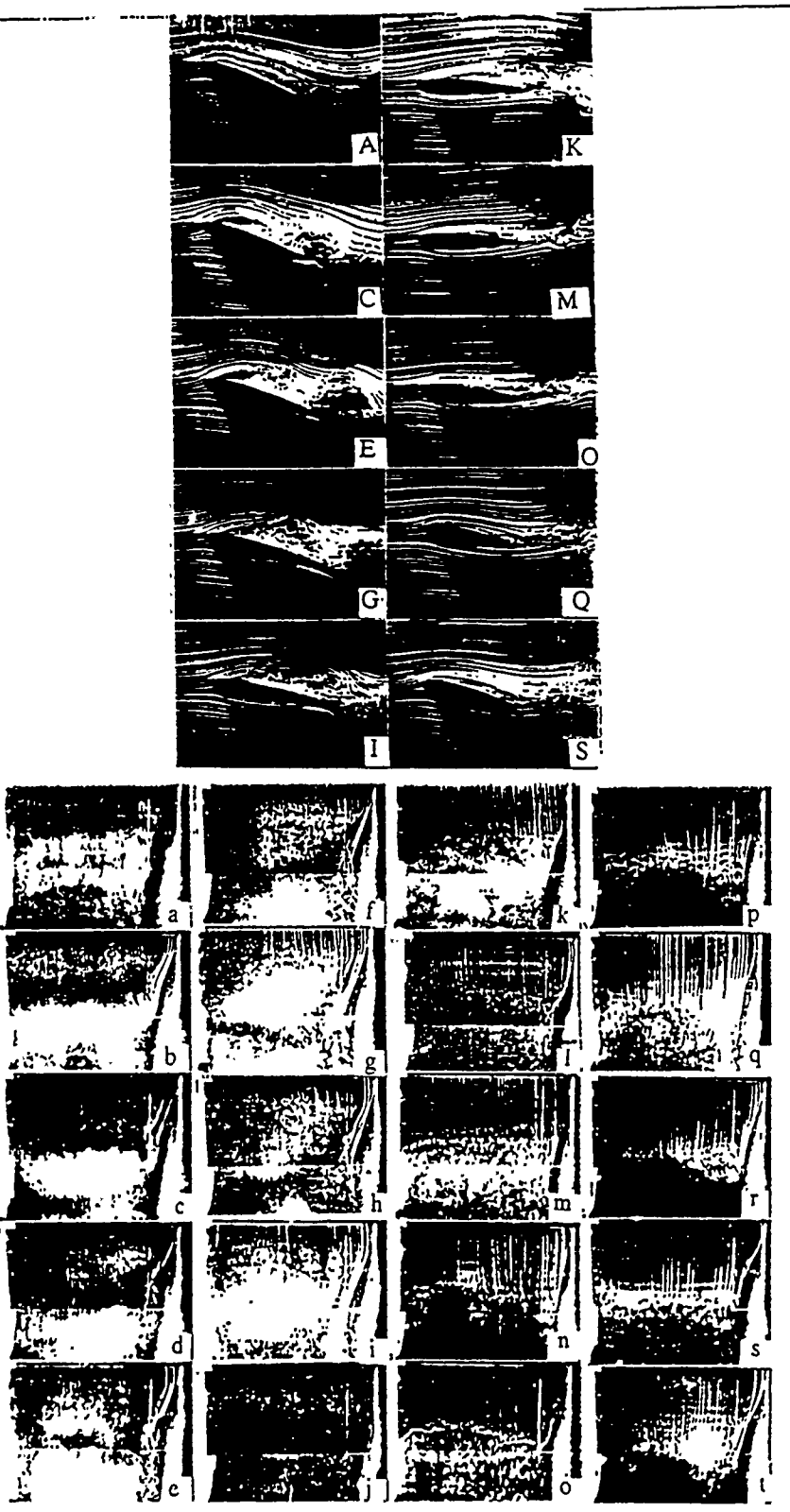

Fig. 5 Visualizations of sinusoidal oscillation pitch motion. K=0.5, $a_m=10^o$. Upper sequence shows centerline flows (airflow from left to right), lower shows near surface flows (airflow from top to bottom, splitter plate at left).

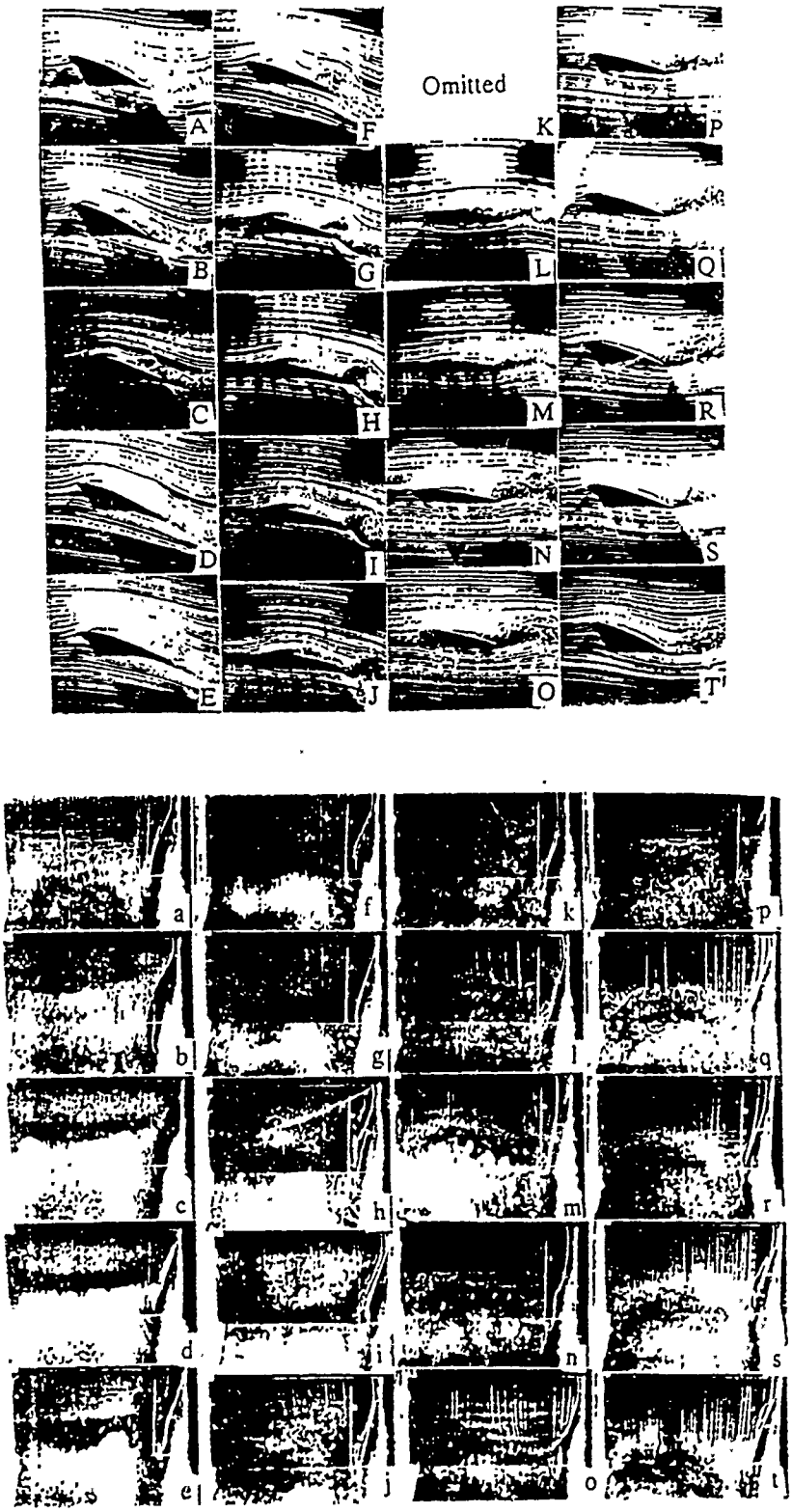

Fig. 6 Visualizations of sinusoidal oscillation pitch motions. $K = 0.75$, $a_m = 10^o$. Upper sequence shows centerline flows (airflow from left to right), lower shows near surface flows (airflow from top to bottom, spitter plate at left).

Frame	Alpha(deg)	% cycle	Delay times (ms) K = 0.25	K = 0.50	K = 0.75
A	20	0	0	0	0
B	18	10	64	32	21
C	16	15	93	47	31
D	14	18	116	58	37
E	12	22	137	69	46
F	10	25	157	79	52
G	8	28	177	89	59
H	6	31	198	99	66
I	4	35	221	111	74
J	2	40	250	125	83
K	0	50	314	157	105
L	2	60	378	189	127
M	4	65	407	204	136
N	6	69	430	215	144
O	8	72	451	226	151
P	10	75	471	236	158
Q	12	78	491	246	164
R	14	82	512	256	173
S	16	85	535	268	179
T	18	90	564	282	189

Oscillation Periods
K = 0.25, 0.628 s
K = 0.50, 0.314 s
K = 0.75, 0.209 s

Table 1 Instantaeous a and per cent cycle for sinusoidal oscillation pitch motion of the airfoil.

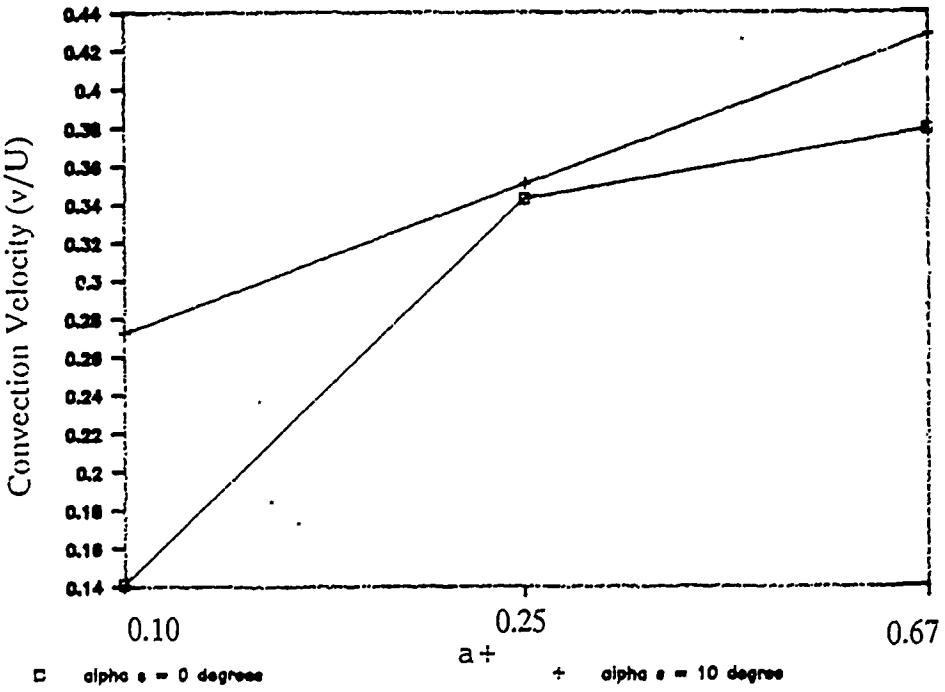

Fig. 7 Averaged DSV convection velocities for constant rate pitching airfoil (convection velocity normalized by U)

Luttges and Kennedy (1988), Schreck and Luttges (1988) and Schreck (1989) offer a model for the sinusoidal case which, qualitatively, fits the constant rate pitching motion as well. This model states that a number of phenomena can account for the three effects noted above. First, the delayed initiation of the LEV (and presumably the DSV) is caused by the lower volume flow rate of fluid passing over the leading edge during the faster wing motions; hence, the amount of time required for the leading edge accumulate a presumed threshold level of vorticity at the leading edge increases. Second, the issue of relative vortex cohesiveness can be addressed by stating that at larger values of the respective dynamic parameters, the DSV/LEV tends to be more energetic, thus causing it to be better formed and, by definition, more cohesive (Walker et al, 1985; Adler and Luttges, 1985).

The model comparability, however, seems to break down when mechanisms of vortex convection are compared. The model states that convection rates for LEV's increase because of the LEV's increased exposure to the freestream which is a result of the decreased shadowing effect by the wing while it is pitching down, compounded by the LEV's delayed initiation. The net effect is an overall increase of the freestream's accelerating influence on convection velocity. It is obvious, however, that in the constant rate pitch circumstance, shadowing can not be reduced once the motion begins. But by comparing Fig.'s 1 and 2 or 3 and 4, it is readily seen in the centerline views that the DSV tends to be shed in a more vertical direction in the higher $a+$ circumstance, thus increasing the effect of the freestream on vortex convection rates for this motion type, although via a different mechanism.

In similar fashion to the dynamic parameters' effects on the DSV and LEV, variation of a_s and a_m also affect DSV and LEV behavior. Although during the data taking process the camera's location was not ideal for observing DSV initiation directly, it appears through correlation of the vortex's size with respect to its temporal position in Fig's 1-4 (and others not included) that the DSV does initiate earlier with increasing a_s. Furthermore, the DSV has a higher magnitude average convection velocity (Fig. 7) and greater qualitative cohesiveness that its counterpart formed at the lower a_s. Likewise, LEV's formed during increased a_m's also tend to initiate earlier in the motion and are more cohesive, but move at a lessened convection velocity than its counterpart in a lower a_m.

As before, some correlation between the fluid mechanical mechanisms at work can be inferred. The hastened DSV/LEV initiation can be attributed once again to vorticity production at the wing's leading edge (Luttges and Kennedy, 1988; Schreck and Luttges, 1988: Schreck, 1989). In these instances, the wing is either beginning at or moving beyond its static stall point (see Fig.'s 3 and 4 frames A and B). Thus, two phenomena are present on the suction surface: first, the airfoil progresses through its motion with a greater net quantity of vorticity being produced at the leading edge

throughout the motion; and second, the adverse pressure gradient along the suction surface is greater throughout the motion than for a lower value of a_s/a_m. The combination of these two factors serve to hasten vortex initiation and development. In addition, the increase in available vorticity serves to strengthen these leading edge structures, increasing its relative energy level at a higher a_s/a_m and thereby increasing its cohesiveness (see argument above).

Finally, the issue of convection velocity must be addressed. For the sinusoidally oscillating airfoil, the shielding from the freestream influences by the airfoil becomes greater with increased a_m, thus decreasing the over riding flow's influence on vortex convection, resulting in a lower convection velocity. Conversely, at higher values of a_s, the DSV is shed with an increasing vertical component, and therefore convects at a higher rate.

B. Secondary and Ancillary Structure Comparability

Besides the DSV/LEV produced by the airfoil motions, secondary and ancillary vortical structures form in the presence of a dynamically stalling airfoil. For the constant rate pitching airfoil, a system consisting of a trailing edge vortex closely followed by a second vortex at the leading edge is most readily observed in Fig. 4, but is better defined in larger amplitude pitch motions, such as those performed by Walker et al (1985) and Helin et al (1986). Furthermore, as best demonstrated in Fig's 2 and 4 (centerline views), a second vortex approximately the size of the DSV forms downstream of the DSV from within the separated region in the vicinity of the trailing edge, but convects much more rapidly downstream than the DSV. In contrast to these large structures, smaller structures can also be found in constant rate pitch visualizations, as detailed in Fig. 3 by a rapidly growing and convecting structure which passes the trailing edge by frame E. These smaller structures appear to be largely dependent on two factors: first, the pitching rate; and second, the phase relationship of the high frequency shedding from the leading or trailing edge at the time of pitch motion initiation.

Conversely, ancillary structures formed during sinusoidal oscillations tend to be much more repeatable and orderly. Klinge et al (1990) have shown that three distinct types of ancillary structures form in the wake of a sinusoidally oscillating flat plate. Similar, although much less well defined, structures can be observed in Fig's 5 and 6. These structures, in both instances, are much smaller than the LEV and tend to be more repeatable and shed at a higher frequency, unlike those associated with constant rate pitch motions. Hence, the comparability of the secondary and ancillary structures formed by the two motions is not great.

C. Three-Dimensional Flowfield Comparability

The elicited three-dimensional flows characterized by the near surface flow visualizations reveal another level of comparability between the two motion types. Fig.'s 1 through 4 (planform views), and the visualizations not included, show that in all of the cases examined, the following sequence of events occur during a constant rate pitch motion:

1. Initial lines appear orthogonal to the streaklines. Correspondence between these lines and the position of the DSV and other vortical structures visualized in the centerline views are easily reached.
2. As pitching continues, a significant spanwise flow is observed, pulsing the dense smoke toward the splitter plate. Simultaneously, the growth of the b-angle, as defined in Fig. 8, is observed as tip flow strength presumably increases.
3. A swirling motion can be seen in the smoke inboard of the tip after the DSV is shed and tip flows apparently come to dominate the post-stall flowfield.

Fig. 10 shows that the b-angle increases and peaks earlier (with respect to per cent cycle) as $a+$ decreases or as increases.

In contrast, the three-dimensionality elicited by an airfoil in sinusoidal pitch is quite different than that found in constant rate pitch systems. As characterized by Schreck (1989) and Horner et al (1990), the LEV forms into an omega-shaped structure, the three-dimensionality of which becomes significantly more pronounced with increased K and a_m, an effect which can be observed in Fig.'s 5 and 6 (the effect is partially blocked out by the presence of the splitter plate). Measurements of the b-angle show that the wingtip flows decrease slightly with increases in K (see Fig.'s 5, 6 and 9). Furthermore, it has been reported (Walker and Luttges, 1985) that decreases in a_m also decrease wingtip flows, and thus would presumably decrease the b-angle.

Walker and Luttges (1985) present a model which may explain these wingtip phenomena. This model proposes that the wingtip vortices feed on the vorticity generated at the leading edge during a sinusoidal motion. As stated earlier, increases in K and decreases in a_m decrease the net vorticity produced at the leading edge, therefore decreasing the overall quantity of vorticity for the wingtip structures to feed upon, thus reducing their strength and size. This feeding is also a likely cause for the b-angle trends observed for the constant rate pitch motion. Freymuth (1989) further confirms this hypothesis through his assertion that the DSV/LEV vortex systems couple with the wingtip vortices for both types of motions, which results in a direct link between the vorticity produced at the leading edge and wingtip flow structure strength.

VI. CONCLUSIONS

The results of this study indicate that there exists a considerable amount of comparability between the fluid mechanical phenomena experienced by a constant rate pitching and a sinusoidally

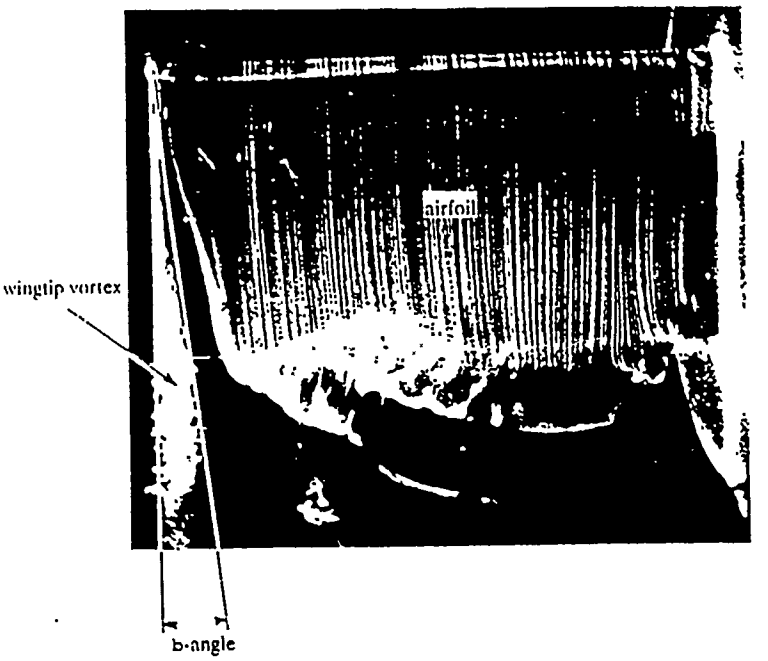

Fig. 8 Definition of b-angle

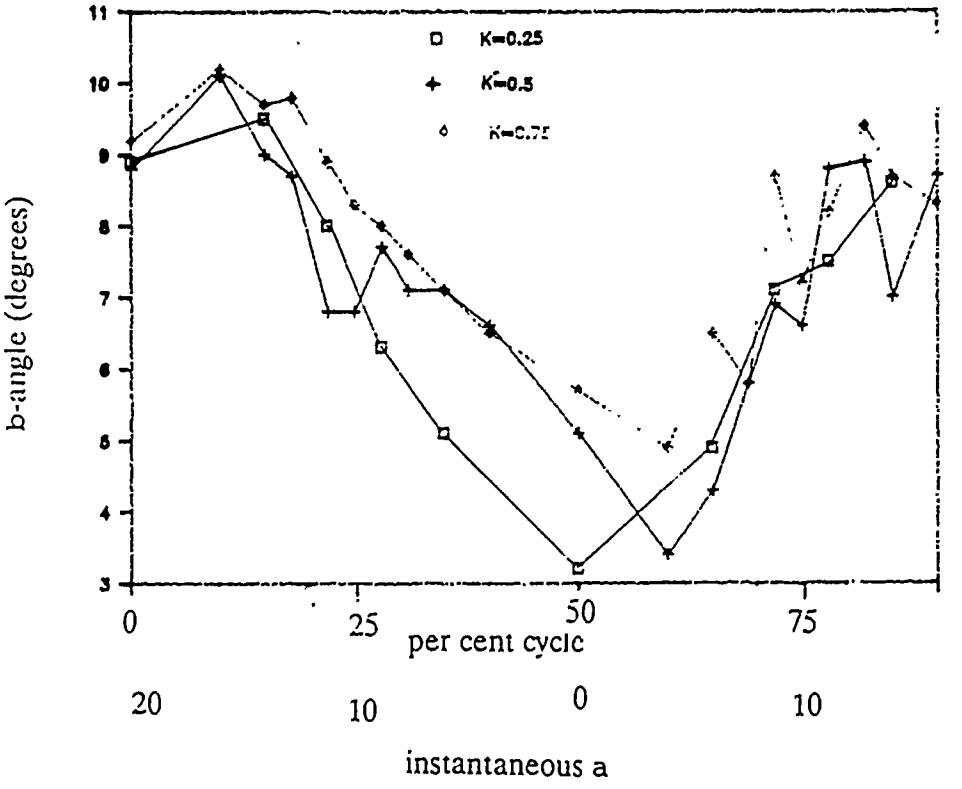

Fig. 9 b-angles for the airfoil in sinusoidal oscillation given as a function of per cent cycle and instantaneous a.

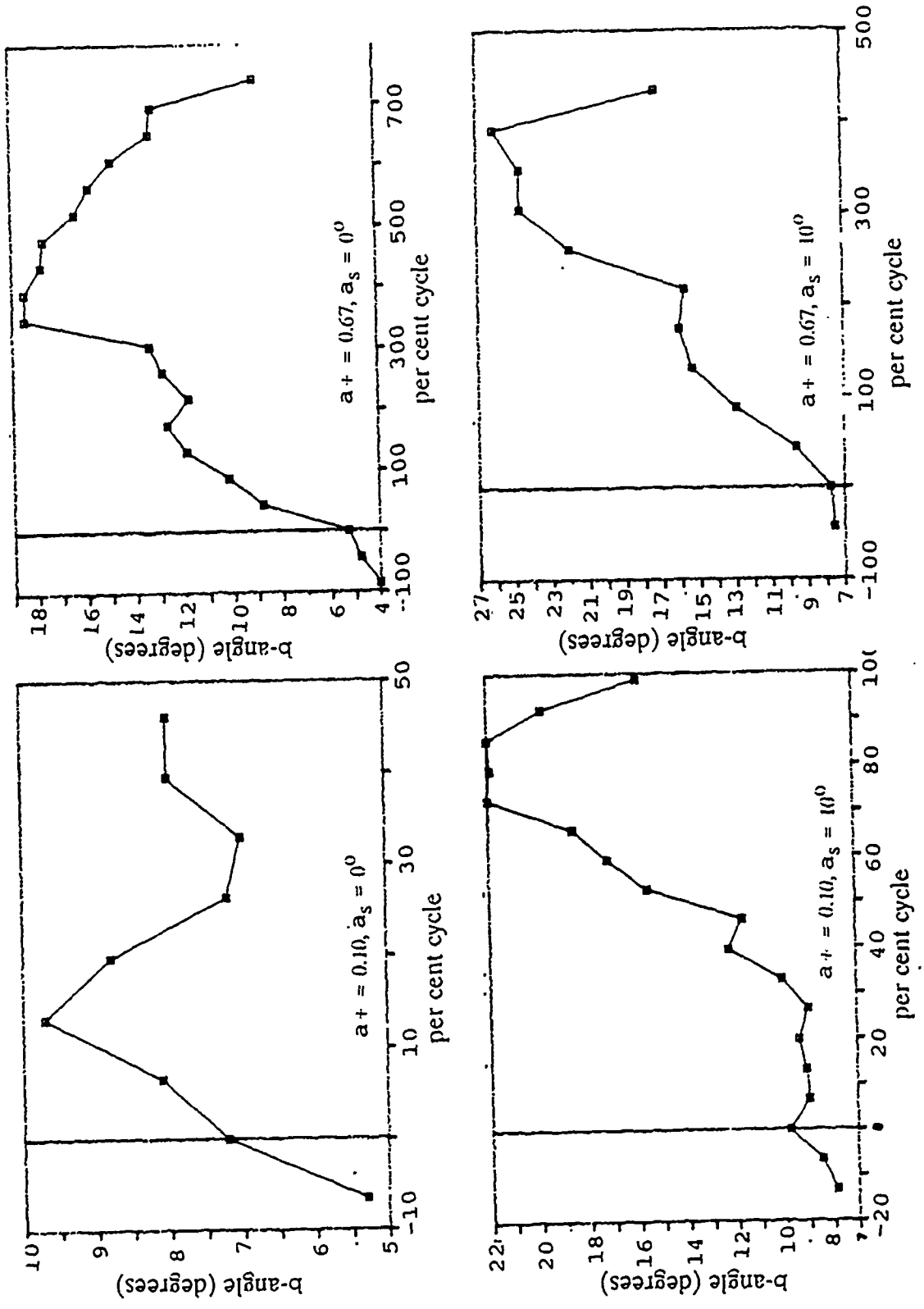

Fig. 10 b-angles for the airfoil in constant rate pitch given as a function of per cent cycle (100% cycle is full pitch up).

oscillating airfoil after taking into account the differences caused by the flow hysteresis effect and airfoil motion implicit with the sinusoidal oscillation. The comparability of alterations in the flowfields after variations in the variables of K and $a+$, and a_s and a_m is significant and should be used to form a basis for further comparative work.

VII. RECOMMENDATIONS

In order to further along the comparisons of constant rate pitching and sinusoidal oscillating with the eventual goal of developing an explicit protocol for their comparison, the following is recommended:

1. A wider array of the variables $a+$, a_s, K and a_m to give a more broadly based data base for such comparisons.
2. Quantitative measurements of flowfields elicited are required to confirm the flow visualization's more qualitative results. These quantifications may take the form of surface pressure measurements, hot wire velocimetery, or other such techniques.
3. Variance of the values of a_m and da are required so to complete the array of parameters which are variable in the motion and to assess their influence on the elicited flowfields. By not assessing these influences for this study, a complete prototype for a matching protocol is not possible at this time.

Acknowledgements

The sponsorship of this research by the USAF Systems Command, Office of Scientific Research and Frank J. Seiler Research Laboratory is greatly appreciated as well as the professional administration of this program by Universal Energy Systems, Inc. The use of sinusoidal flow visualizations collected by J. Klinge is gratefully acknowledged, as is the technical assistance provided by Captains S. Schreck and D. Bunker, USAF, and that of M. Robinson, M. Luttges, and B. Hatfield.

REFERENCES

Adler, J. N., and Luttges, M. W., "Three-Dimensionality in Unsteady Flow About a Wing", AIAA 23rd Aerospace Sciences Meeting, Reno, NV, Paper No. AIAA-85-0132, Jan., 1985.

Freymuth, P., "Visualizing the Connectivity of Vortex Systems for Pitching Wings," Journal of Fluids Engineering, Vol. 111, June, 1989, pp 217-20.

Helin, H. E., and Walker, J. M., "Interrelated Effects of Pitch Rate and Pivot Point on Airfoil Dynamic Stall," AIAA 23rd Aerospace Sciences Meeting, Reno, NV, Paper No. AIAA-85-0130, Jan., 1985.

Helin, H. E., Robinson, M. C., and Luttges, M. W., "Visualizations of Dynamic Stall Controlled by Large Amplitude Interrupted Pitching Motions," AIAA Atmospheric Flight Mechanics Conference, Williamsburg, VA, Paper No. AIAA-86-2281-CP, Aug., 1986.

Herbst, W. B., "Future Fighter Technologies," AIAA Journal of Aircraft, Vol. 17, Aug. 1980, pp 561-66.

Horner, J. B., Addington, G. A., Young, J. W., and Luttges, M, W., "Controlled Three-Dimensionality in Unsteady Separated Flows About a Sinusoidally Oscillating Flat Plate," AIAA 28th Aerospace Sciences Meeting, Reno, NV, Paper No. AIAA-90-0689, Jan., 1990.

Klinge, J.D., Schreck, S. J., and Luttges, M. W., "Dynamic Effects on High Frequency Unsteady Flow Structures," AIAA 28th Aerospace Sciences Meeting, Reno, NV, Paper No. AIAA-90-0690, Jan., 1990.

Luttges, M. W., and Kennedy, D. A., "Initiation and Use of Three-Dimensional Unsteady Separated Flows," Proceedings of Workshop II on Unsteady Separated Flows, United States Air Force Academy, CO, 1988.

Schreck, S. J., and Luttges, M. W., "Unsteady Separated Flow Structure: Extended K Range and Oscillations Through Zero Pitch Angle," AIAA 26th Aerospace Sciences Meeting, Reno, NV, Paper No. AIAA-88-0325, Jan., 1988.

Schreck, S. J., "Experimental Investigation of the Mechanics Underlying Vortex Kinematics in Unsteady Separated Flows," Doctoral Thesis, University of Colorado, 1989.

Walker, J. M., Helin, H. E., and Strickland, J. H., "An Experimental Investigation of an Airfoil Undergoing Large Amplitude Pitching Motions," AIAA 23rd Aerospace Sciences Meeting, Reno, NV, Paper No. AIAA-85-0039, Jan., 1988.

1990 USAF-UES SUMMER FACULTY RESEARCH PROGRAM/

GRADUATE STUDENT RESEARCH PROGRAM

Sponsored by the

AIR FORCE OFFICE OF SCIENTIFIC RESEARCH

Conducted by the

Universal Energy Systems, Inc.

FINAL REPORT

CONTROL OF A COMPLEX FLEXIBLE STRUCTURE UTILIZING SPACE-REALIZABLE LINEAR REACTION MASS ACTUATORS

Prepared by:	Ephrahim Garcia, Ph.D. Brett James Pokines Robert Alan Carlin
Academic Rank:	Visiting Assistant Professor
Department and	Department of Mechanical and Aerospace Engineering
University:	State University of New York at Buffalo
Research Location:	Frank J. Seiler Research Laboratory Laser and Aerospace Mechanics Division US Air Force Academy, Colorado
USAF Researchers:	Major John Duke, Division Chief Frank J. Seiler Research Laboratory
	Captain Steven Webb, Assistant Professor Department of Engineering Mechanics

Date:	September 7, 1990
Contract No:	F49620-88-C-0053

Same Report as
Prof. Ephrahim Garcia
(Report # 41)

1990 USAF-UES SUMMER FACULTY RESEARCH PROGRAM

/GRADUATE STUDENT RESEARCH PROGRAM

Sponsored by the

AIR FORCE OFFICE OF SCIENTIFIC RESEARCH

Conducted by the

Universal Energy Systems, Inc.

FINAL REPORT

Particle Image Displacement Velocimetry (PIDV) Measurements in Dynamic Stall Phenomena

Prepared by:	Ngozi Kamalu, Ph.D.	Rand Conger
Academic Rank:	Lecturer	Masters Candidate
Department:	Mechanical Engineering	Mechanical Engineering
University:	California Polytechnic State University	Washington State University

Research Location: Frank J. Seiler Research Lab
U. S. Air Force Academy

USAF Researcher: Capt. Scott Shreck

Date: 28 September 1990

Contract No.: F49620-88-C-0053

Same Report as
Prof. Ngozi Kamalu
(Report # 42)

1990 USAF-UES SUMMER FACULTY RESEARCH PROGRAM/
GRADUATE STUDENT RESEARCH PROGRAM

Sponsored by the
AIR FORCE OFFICE OF SCIENTIFIC RESEARCH
Conducted by the
Universal Energy Systems, Inc.

FINAL REPORT
A PRELIMINARY ANALYSIS OF SYMBOLIC COMPUTATIONAL TECHNIQUE FOR PREDICTION OF UNSTEADY AERODYNAMIC FLOWS

Prepared by:	S. A. Kassemi G. M. Cunning
Academic Rank:	Faculty Fellow Graduate Student
Department and University:	Aerospace Engineering University of Colorado at Colorado Springs
Research Location:	Frank J. Sieler Laboratory United States Air Force Academy Colorado Springs, CO 80840
USAF Researchers:	Major Robert Rielman Lt. Colonel Skip Dieter
Date:	August 30, 1990
Contract No.:	F49620-88-C-0053

Same Report as
Prof. Siavash Kassemi
(Report # 43)

1990 USAF-UES SUMMER FACULTY RESEARCH PROGRAM

AND GRADUATE STUDENT RESEARCH PROGRAM

Sponsored by the

AIR FORCE OFFICE OF SCIENTIFIC RESEARCH

Conducted by the

Universal Energy Systems, Inc.

FINAL REPORT

Transition Metal Carbonyl Complexes in Ambient-Temperature Molten Salts

and

Alkali Metal Reductions at Tungsten and Mercury Film Electrodes in Buffered Neutral Aluminum Chloride:1-Methyl-3-Ethylimidazolium Chloride Molten Salts

Prepared by:	Richard T. Carlin and Joan Fuller
Academic Rank:	Assistant Professor (RTC) and Graduate Student (JF)
Department and	Chemistry
University	University of Alabama
Research Location:	Frank J. Seiler Research Laboratory USAF Academy, CO 80840-6528
USAF Researcher:	John S. Wilkes
Date:	August 17, 1990
Contract No.:	F49620-88-C-0053

Same Report as
Prof. Richard Carlin
(Report # 39)

1990 USAF-UES SUMMER FACULTY RESEARCH PROGRAM / GRADUATE STUDENT RESEARCH PROGRAM

Sponsored by the

AIR FORCE OFFICE OF SCIENTIFIC RESEARCH

Conducted by

Universal Energy Systems, Inc.

FINAL REPORT

The Effect of Wall Dynamics on the Flow Field near the Root of an Oscillating Wing

Prepared by:	John D. Klinge
Academic Rank:	Master's Candidate
Department and University:	Dept. of Aerospace Engineering Sciences University of Colorado at Boulder
Research Location:	Frank J. Seiler Research Laboratory, U.S. Air Force Academy
USAF Researcher:	Capt. Scott J. Schreck
Date:	Sept. 25, 1990
Contract No:	F49620-88-C-0053

The Effect of Wall Dynamics on the Flow Field near the Root of an Oscillating Wing

by

John D. Klinge

ABSTRACT

A NACA 0015 airfoil, oscillated sinusoidally in pitch about its quarterchord, was configured with either a static splitter plate at the designated root or a dynamic splitter plate affixed to the airfoil in the same location. Qualitative characterizations of the three-dimensional unsteady separated flow fields generated in the experiments were accomplished using flow visualization and multi-exposure photography. Leading edge vortex and secondary vortex cross-sectional areas were greatly attenuated in the root vicinity of the wing. Static and Dynamic splitter plate configurations yielded no significant difference in flow field three-dimensionality over the upper surface of the wing.

I. INTRODUCTION:

Forced unsteady flow separation about an airfoil has long been studied with the intent of exploiting the high transient lift forces and reduced drag effects associated with this phenomenon. The practical use of unsteady separated flows has been demonstrated in insect flight mechanics (Kliss, 1989) and established helicopter control technology (Prouty, 1986). Large scale vortical structures incorporated into unsteady flow fields and associated transient forces on lifting surfaces have been observed and quantified in two and three-dimensional studies (Robinson, 1988).

Preliminary investigations of unsteady separated flows conducted at the University of Colorado have revealed strong asymmetries in flows produced from wing geometries (Horner, 1990). Vortical flows produced from the separated boundary layer exhibit different initiation and growth characteristics when examined at the wing root and wing tip. These asymmetric growth patterns indicate skewed loading distributions on wing planforms. High performance aircraft which enter post-stall maneuvering flight regemes may be adversely affected structurally and suffer control difficulties.

II. OBJECTIVES OF THE RESEARCH EFFORT

Currently, little is known about flow field structure near the root of a wing undergoing oscillations in pitch. A basic understanding of this region during forced unsteady flow separation would be adventageous to the successful design and utilization of aircraft lifting and control surfaces used for unconventional flight mavuevers. The purpose of this research effort was to aquire qualitative and quantitative data in the root vicinity of a wing in a forced unsteady separated flow environment. Though time restrictions precluded anticipated static pressure measurements, multiexposure photography phase locked to the pitch oscillation cycle of the wing provided excellent visual data for qualitative analysis. Two and three-dimensional flow visualization techniques were

utilized in this study to qualitatively assess flow field variations along the span of the wing and to identify wall/vortex interactions taking place at the root.

III.

a. For this investigation, a NACA 0015 airfoil with a 6 inch chord length and a 12 inch span was oscillated sinusoidally in pitch about its quarterchord. The reduced frequencies used in conjunction with the oscillatory motion were 0.25, 0.5 and 0.75. The mean pitch angle, oscillation amplitude and freestream velocity were maintained at 10 degrees, +/- 10 degrees and 10 feet/second, respectively, for all experiments.

A circular splitter plate -- with a diameter of 12 inches, a thickness of 0.25 inch and a 0.625 inch taper around the outer edge -- was mounted orthogonally to one end of the airfoil to form the root of the wing. The airfoil crossection was centered on the splitter plate so that the root of the wing had 3 inches of splitter surface upstream from the leading edge and 3 inches of splitter surface downstream from the trailing edge. The splitter plate was mounted in two different configurations. In the first configuration, it was affixed to the root of the airfoil so that the entire planform moved when driven with the oscillatory motion described above. This will be referred to as the dynamic splitter plate configuration throughout the following text. In the second configuration, the splitter plate was statically oriented (referred to as the static splitter plate configuration), with a sliding fit maintained between the airfoil and the splitter surface during the applied motion.

For all tests, the wing was roughly centered in the 3.0 X 3.0 foot test section of the low speed wind tunnel at Frank J. Seiler Research Lab. The wing was mounted on end in the tunnel, so that the leading edge of the airfoil was vertical with respect to the horizontal test section floor. A 1.0 inch diameter drive shaft protruded through the test

section floor, connecting the wing planform inside the tunnel to a scotch yoke mechanism mounted outside the tunnel test section. A 3/4 horsepower D.C. motor was used to drive the scotch yoke mechanism which transferred a sinusoidal oscillatory motion to the drive shaft.

A time reference for any phase angle in the pitching motion was provided by a delay circuit which was triggered by an electronic impulse from a magnet/reed-switch assembly mounted on a flywheel in the scotch yoke mechanism. The flywheel phase was such that reed-switch pulse generation took place at maximum pitch up in the wing oscillation cycle.

Flow visualization was accomplished by introducing smoke into the flow using an ohmic heated, oil-coated 0.013 cm diameter tungsten wire. The smoke-wire was successively mounted in three different configurations. In the first configuration the wire was stretched horizontally across the test section, 4 chord lengths upstream from the wing planform, orthogonal to the airfoil leading edge at center span. In the second configuration the wire was oriented similarly, but at a span location 0.125 inch outboard from the splitter surface, near the root of the wing. In the third configuration the wire position was fixed with respect to the wing, mounted parallel to and upstream from the leading edge stagnation point, bent around the leading edge corner of the tip and run chordwise to the trailing edge of the wing tip. Three high-intensity stroboscopic arc-lamps, phase locked to the plate oscillation, were used to illuminate the smoke. The highly repeatable flow patterns generated and illuminated at any given oscillation phase angle allowed for the use of multiexposure photography (typically 4 to 6 exposures).

b. The general organization of the temporal flow field encompassing the wing configurations used in these experiments was similar for all parameter combinations

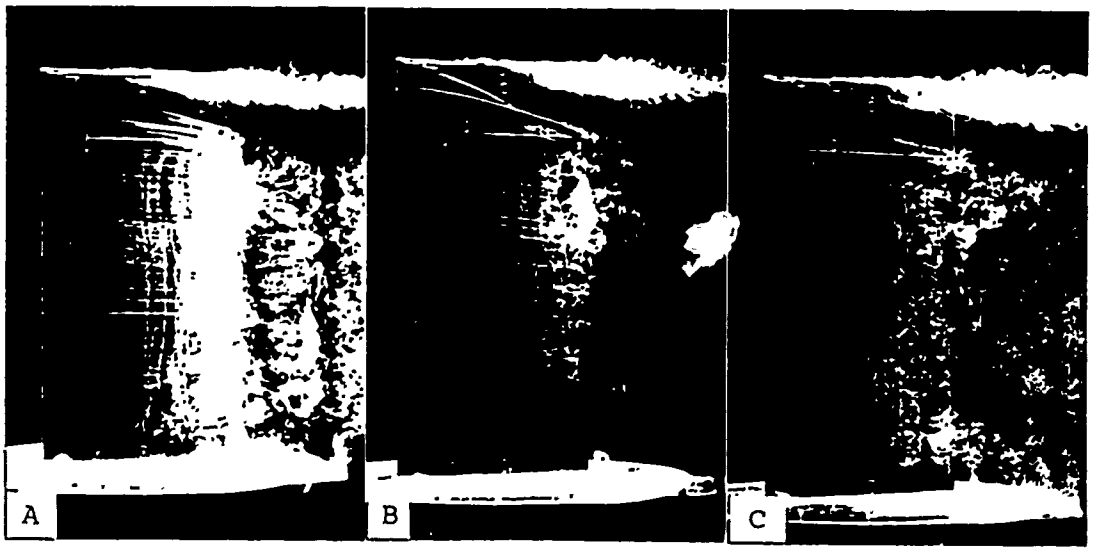

Fig. 1: The top surface of the oscillating wing (dynamic splitter plate configuration) is shown for three different reduced frequencies during mid-chord vortical structure initiation. Flow is moving from left to right in each photo. The root of the wing is at the bottom of the photographs and the wing tip is at the top. The wing in photo "A" is oscillating at a reduced frequency of 0.25. Photo "B" depicts a reduced frequency of 0.5. Photo "C" depicts a reduced frequency of 0.75.

studied (i.e. reduced frequencies of 0.25, 0.5, and 0.75, with both static and dynamic splitter plates). In every case, a leading edge vortex initiated on the upper surface of the wing simultaneously with midchord vortical structures. These midchord vortical structures appeared to initiate as Tollmein-Schlichting instabilities (fig. 1). This initiation took place near the beginning of the oscillation cycle when the the wing was at its maximum instantaneous angle of attack. As the cycle progressed, some of the midchord vortical structures coalesced into a large singular vortex (designated the secondary vortex). The secondary vortex then grew and convected over the surface of the wing simultaneously with the upstream leading edge vortex (fig.2). The pair of vortices were then shed into the wake consecutively.

As the leading edge vortex convected downstream over the upper surface of the wing, smooth surface flow stretched from the leading edge of the wing to the separation line bounding the upstream side of the leading edge vortex. This separation line lost on a

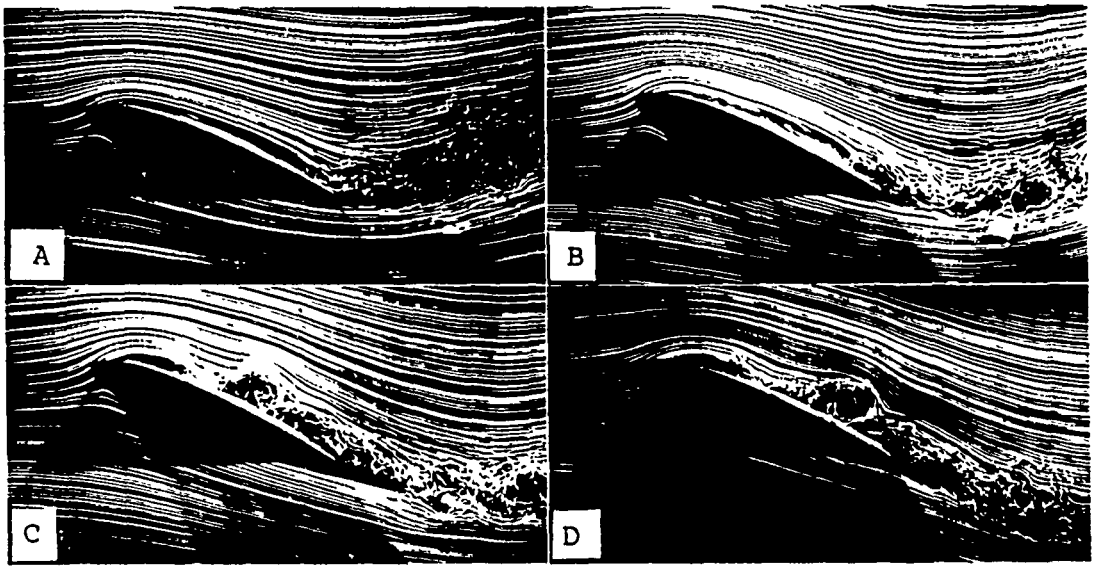

Fig. 2: This sequence of photographs shows early leading edge vortex and secondary vortex development over the center span of the oscillating wing (dynamic splitter plate configuration). The wing is oscillating at a reduced frequency of 0.75. These photos were shot in instantaneous angle of attack increments of 2 degrees with maximum pitch up occuring in photo "B".

universal shape that was observed in all conditions investigated. Photographs of the wing maintained at a constant angle of attack revealed that asymmetric Karman vortex type shedding from the lower surface of the airfoil at the trailing edge could have affected three-dimensionality in the flow field on the upper surface. Fig. 3 shows two photographs that depict the separation line as it appeared on the upper surface of the oscillating wing, and one photograph of the Karman vortex type shedding described above. The presence of a wing tip vortex was also believed to be a cause of the curved separation line shape. Characterization of the flow field in the tip region, however, remains for future investigations.

A sketch of the three-dimensional orientation of the leading edge vortex and the secondary vortex as they commonly appeared on the upper surface of the airfoil is shown in fig. 4. The flow field on the upper surface maintained a constant asymmetry due to the presence of a tip vortex on one side and a flat wall on the other. Both the

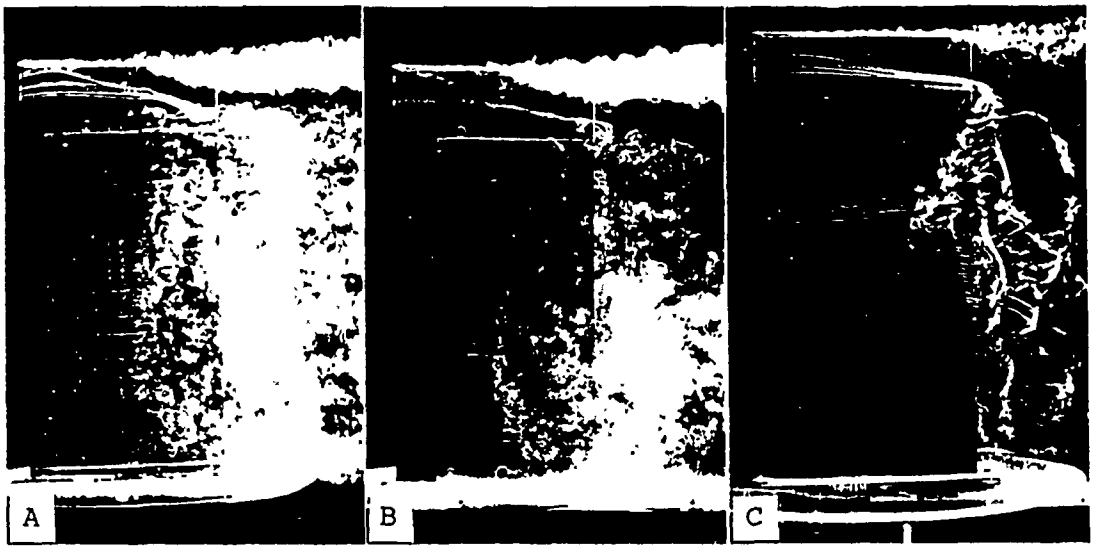

Fig. 3: The top surface of the wing is shown for three different cases. Conditions are as follows. Photo "A": reduced frequency = 0.5, static splitter plate configuration. Photo "B": reduced frequency = 0.75, dynamic splitter plate configuration. Photo "C": reynolds number = 26000, wing is at constant 0 degree angle of attack.

---

leading edge vortex and the secondary vortex exhibited "pinned" characteristics in which the ends of the vortex lines could be traced back to the leading edge tip and root corners of the airfoil. In all cases, the pinned root sections of these vortices were less evident in the flow visualization than the pinned tip sections. As the leading edge vortex and secondary vortex convected over the upper surface, the secondary vortex maintained relative two-dimensionality at midspan locations, while the leading edge vortex developed prominent three-dimensional characteristics after passing the center chord position.

IV.

a. In order to asses temporal flow field characteristics that were a result of the specific oscillation period used to drive the wing, three reduced frequencies were examined: 0.25, 0.5 and 0.75. These values were limited by the structural capabilities of the scotch yoke mechanism used to drive the wing, and by the minimum achievable speed of the wind tunnel. Differences that appeared between the three reduced frequencies were

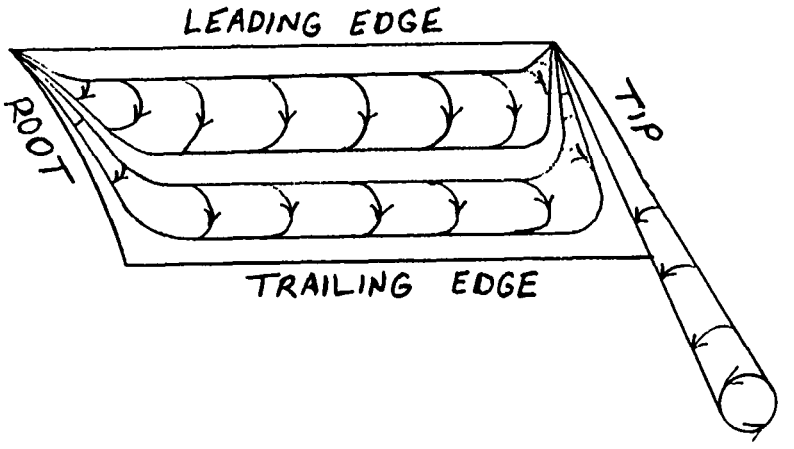

Fig. 4: A sketch of the three-dimensional orientation of the leading edge vortex, secondary vortex, and tip vortex as they commonly appeared in upper surface photographs of the oscillating wing.

---

apparent in the leading edge vortex growth rate and in the secondary vortex initiation point. Other characteristics such as flow field three dimensionality and midchord vortical structure initiation time were similar from case to case.

b. The leading edge vortex nondimensionalized growth is plotted in fig. 5. Two measurements of leading edge vortex cross-sectional area at the center span were taken for each reduced frequency. These measurements were made on the dynamic splitter plate configuration only. The first measurement took place at leading edge vortex initiation time which was 85% into the oscillation cycle for all cases. The second measurement took place at the beginning of the cycle (maximum instantaneous angle of attack). The graph in fig. 5 indicates an inverse relationship between leading edge vortex growth rate and reduced frequency during the early stages of leading edge vortex development.

Fig. 6 shows the photographs used for measurements plotted in fig. 5. The relative position of secondary vortex formation (indicated by arrows) is also shown by this set of

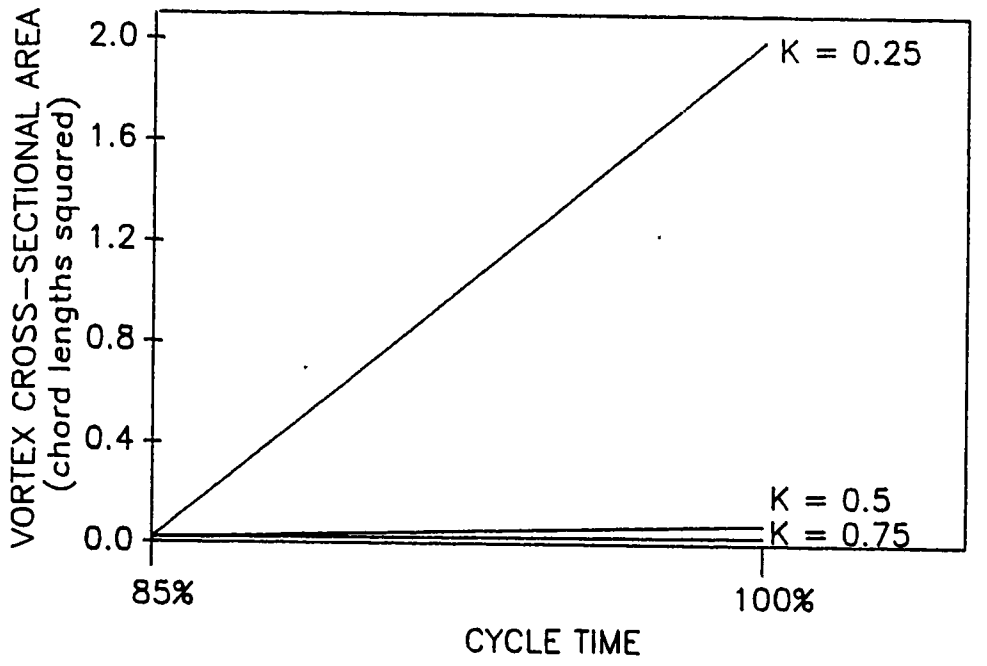

Fig. 5: A graph of non-dimensionalized leading edge vortex growth is plotted for three reduced frequencies (K's).

---

photographs. Secondary vortex formation occurred farther upstream on the surface of the wing as the reduced frequency was increased.

V.

a. Static and dynamic splitter plates were used in an attempt to more fully understand any wall/vortex interactions or flow instabilities that appeared in the flow field near the root of the wing. The splitter plate configuration appeared to have no significant effect on flow field three dimensionality over the upper surface of the wing. Some differences did exist between the two configurations, however, in flow disturbance characteristics in the region of the splitter plate surface.

b. Visualization of the flow field near the root of the oscillating wing revealed few identifiable differences between static and dynamic splitter plate configurations in terms of leading edge vortex and secondary vortex characteristics. These vortices were not as

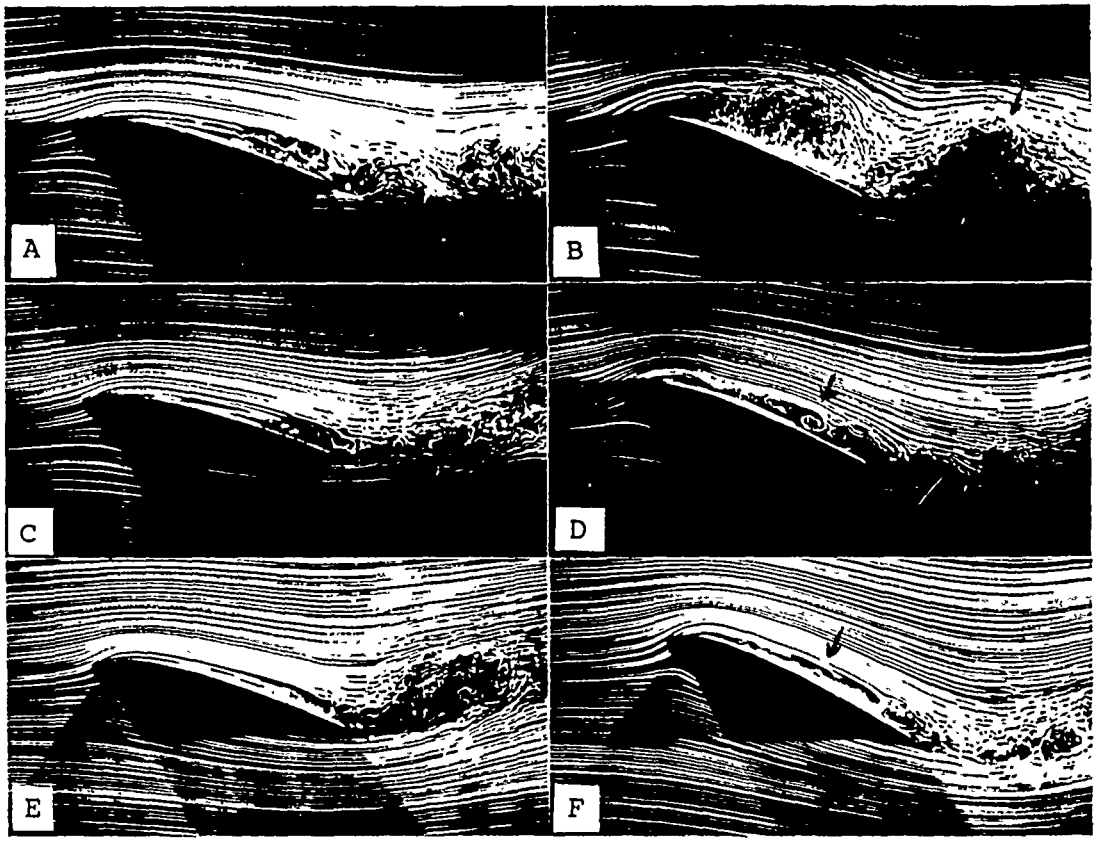

Fig. 6: Photographs of the oscillating wing during leading edge vortex initiation and early development at the center span of the dynamic splitter plate configuration. Photos "A" and "B" represent a reduced frequency of 0.25 and were taken at 85% and 100% into the oscillation cycle, respectively. Photos "C" and "D" represent a reduced frequency of 0.5 and were taken at 85% and 100% into the cycle, respectively. Photos "E" and "F" represent a reduced frequency of 0.75, and were also taken at 85% and 100% into the cycle.

---

dicernable as they appeared at the center span of the wing, and the cross-sectional areas of what appeared to be the leading edge vortex and secondary vortex at the wing root were appreciably attenuated compared to their center span counterparts. Fig. 7 shows photos taken at two different reduced frequencies at the same respective points in the oscillation cycle with static and dynamic splitter plates. These photos depict the leading edge vortex and secondary vortex at the center span of the wing with the dynamic

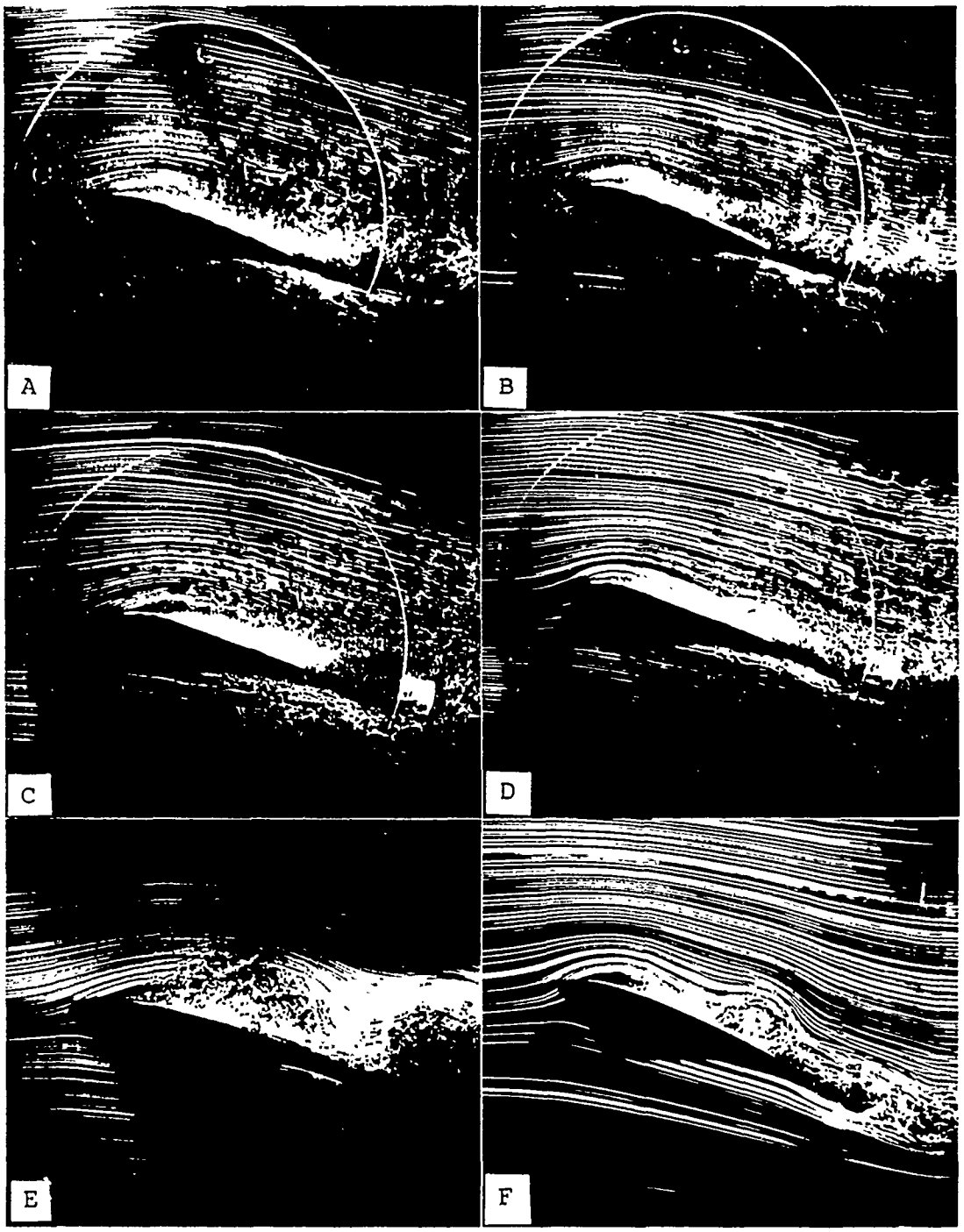

Fig. 7: Photographs of the oscillating wing near the root and at the center span. All photos on the left side of the page represent a reduced frequency of 0.5 and a cycle time of 22%. All photos on the right side of the page represent a reduced frequency of 0.75 and a cycle time of 18%. Photos "A" and "B" show the root of the static splitter plate configuration. Photos "C" and "D" show the root of the dynamic splitter plate configuration. Photos "E" and "F" show the center span of the dynamic splitter plate configuration.

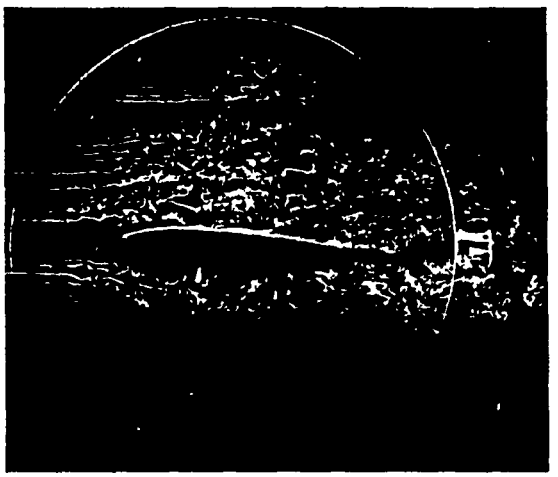

Fig. 8: This photograph shows the root of the wing at a 0 degree constant angle of attack.

splitter plate, and the flow field at the same point in the oscillation cycle near the root of both splitter plate configurations.

Differences in splitter plate surface flows that were unrelated to the vortical structures seen on the airfoil surface were apparent between the two splitter plate configurations. The static splitter plate photographs in fig. 7 show erratic flow over a certain area of the plate. The boundary locations of this area were presumably governed by the shape of the splitter plate, the characteristic motion of the wing, and the Reynolds number. Photographs taken with the wing at a constant angle of attack displayed a similarly shaped area of erratic flow near the splitter plate surface (fig. 8). Careful scrutiny of the oscillating wing (static splitter plate configuration) revealed a very faint periodic nature to the "erratic" part of the flow field over the splitter plate. This faint periodicity appeared in the form of loosely organized vorticity lines (reminiscent of the T-S waves shown in fig. 1) which extended from the upper part of the disturbed area to the lower part, repeating downstream into the wake.

The dynamic splitter plate photographs in fig. 7 depict erratic flow which appears slightly different from the static splitter plate flows, but over the same general area of the plate. The extension of the oscillatory motion to the splitter plate added additional components ot vorticity periodically to the region, but didn't significantly change the boundary positions. Vorticity lines that were observed faintly in the static splitter plated experiments appeared more prominently in dynamic splitter plate conditions.

It is possible that the loosely organized vorticity lines that appear in the disturbed region of the flow over the splitter plate surface were generated by smokewire or splitter plate vibration at a frequency equal or harmonic to that of the wing oscillation. With the assumption that these voricity lines convected at free stream velocity, wavelength measurements of these lines taken on various photographs corresponded to a frequency that was approximately twice that of the wing oscillation.

During experiments in which the flow field near the wing root was visualized with the smokewire 0.125 inches outboard from, and parallel to, the splitter plate surface, an interesting phenomenon was observed. The portion of the smoke sheet that travelled over the surface of the splitter plate abruptly shifted to a different wing span location approximately 0.25 inch further outboard from the splitter plate surface at the leading edge of the plate. This abrupt shift in the smoke sheet position is observable in the photographs presented in fig. 7 and fig. 8. A bend in the smokelines at the leading edge of the splitter plate is evident above and below the position of the airfoil in these photographs. The "bend" indicates the location of the shift in the smoke sheet's position. The shift was common to all conditions investigated except for one. When the wing was statically oriented at a 20 degree angle of attack, the smokesheet shifted in the opposite direction and passed under the splitter plate. This behavior was believed to be related to a tunnel blockage effect caused by the high static angle of attack.

VI. RECOMMENDATIONS:

a. Flows over the root surface on an oscillating wing exhibited a reduction of vortical structure size and dicernability. The "hazy" appearance of the leading edge vortex and the secondary vortex in multi-exposure photographs indicated that the vorex positions were not precisely phase-locked to the oscillation cycle of the wing. This phenomenon is characteristic to airfoils with large thickness variations like the one used. Leading edge and secondary vortex strength characterizations and associated wing loading measurements require hot wire anemometry and surface pressure tapping techniques.

b. Wall dynamics did not appear to play a role in wing surface vortical structure characteristics. Differences in the flow field generated with the dynamic and static splitter plate configurations were observable only near the surface of the splitter plate, and were unrelated to wing surface vortical structure integrity. Any further experimentation with wall conditions at the root of an oscillating airfoil should be done at greater oscillation amplitudes and greater angles of attack to exaggerate and bring to light any vortex/wall interactions that were overlooked in this investigation.

REFERENCES

Horner, M.B., Addington, G.A., Young III, J.W., and Luttges, M.W., "Controlled Three-Dimensionality in Unsteady Separated Flows About a Sinusoidally Oscillating Flat Plate". 28th Aerospace Sciences Meeting, Reno, NV, Paper No. 90-0689, January 1990.

Kliss, M., Somps, C., and Luttges, M.W., "Stable Vortex Structures: A Flat Plate Model of Dragonfly Hovering". J. Theor. Biol. 1989, Vol. 136, pp. 209-228.

Robinson, M., Walker, J., Wissler, J., "Unsteady Surface Pressure Measurements on a Pitching Rectangular Wing". Workshop II on Unsteady Separated Flow, Proceedings. Frank J. Seiler Research Laboratory, USAF Academy, CO, September 1988.

Prouty, R.W., Helicopter Performance, Stability, and Control. PWS Publishers, Boston, Massachusetts, 1986, pp. 142-153.

ACKNOWLEDGEMENTS

This work was sponsored, in part, by the United States Air Force Office of Scientific Research and Frank J. Seiler Research Lab. Universal Energy Systems, Inc. performed the administrative tasks necessary to make this project possible. The guidance and technical assistance of M. Luttges, M. Robinson, S. Schreck, G. Addington, B. Hatfield and G. Riker were greatly appreciated.

1990 USAF-UES SUMMER FACULTY RESEARCH PROGRAM/

GRADUATE STUDENT RESEARCH PROGRAM

Sponsored by the

AIR FORCE OFFICE OF SCIENTIFIC RESEARCH

Conducted by the

Universal Energy Systems, Inc.

FINAL REPORT

CONTROL OF A COMPLEX FLEXIBLE STRUCTURE UTILIZING SPACE-REALIZABLE LINEAR REACTION MASS ACTUATORS

Prepared by:	Ephrahim Garcia, Ph.D. Brett James Pokines Robert Alan Carlin
Academic Rank:	Visiting Assistant Professor
Department and	Department of Mechanical and Aerospace Engineering
University:	State University of New York at Buffalo
Research Location:	Frank J. Seiler Research Laboratory Laser and Aerospace Mechanics Division US Air Force Academy, Colorado
USAF Researchers:	Major John Duke, Division Chief Frank J. Seiler Research Laboratory
	Captain Steven Webb, Assistant Professor Department of Engineering Mechanics

Date:	September 7, 1990
Contract No:	F49620-88-C-0053

Same Report as
Prof. Ephrahim Garcia
(Report # 41)

1990 USAF-UES SUMMER FACULTY RESEARCH PROGRAM
GRADUATE STUDENT RESEARCH PROGRAM

Sponsored by the
AIR FORCE OFFICE OF SCIENTIFIC RESEARCH
Conducted by the
Universal Energy Systems, Inc.

FINAL REPORT
Calculated Plasma Drift Velocities and Comparison with DE-2 Satellite Data

Prepared by:	Leonard N. Carter Jr.
Academic Rank:	Research Assistant
Department and	Div. of Engrg. and Applied Science
University:	Boston University
Research Location:	Geophysics Laboratory/LIM
	Hanscom AFB, MA 01731
USAF Researcher:	David N. Anderson
Date:	24 August 90
Contract:	F49620-88-C-0053

Calculated Plasma Drift Velocities and Comparison with DE-2 Satellite Data

by

Leonard N. Carter Jr.

ABSTRACT

Nighttime zonal plasma drifts in the equatorial region are calculated from a simplified expression involving Pedersen conductivity, geomagnetic field strength, and zonal neutral wind, integrating along flux tubes having apex altitudes of 250 to 1500 km. The ambient conditions cover solar minimum and maximum at equinox over the American sector (zero declination), with vertical electron density profiles derived from Jicamarca-measured drift at average strength, one-half average, and zero drift. Five neutral wind models are evaluated for overall consistency and compared to similar data from the DE-2 satellite. Plasma drift velocities are displayed as contour plots versus apex altitude and local time (1700 to 0700), for both model output and DE-2 measurements. Model inputs of solar maximum, half average drift, and a wind model from Anderson et al (1987) is found to give the best agreement with the DE-2 plot. Minor modifications to this model allowed for very good agreement to be realized, neglecting fine structure in the DE-2 data. The implicit conclusion is that this final, sixth wind model is most representative of actual thermospheric winds, for the conditions of solar maximum at equinox in the nighttime sector.

ACKNOWLEDGEMENTS

I would like to thank the Air Force Office of Scientific Research and Universal Energy Systems for their sponsorship and administrative assistance in making this research program available.

I would also like to thank Dr. David Anderson for his supervisory and technical assistance, Dr. Jeffrey Forbes for his encouragement and assistance in my entry into this program, Mrs. Pat Doherty for her very generous and helpful programming assistance, and Dr. Dwight Decker and Mr. Jack Klobuchar for discussions concerning several fine points of ionospheric physical theory.

Finally, I am indebted to Drs. W.R. Coley and R.A. Heelis of the Center for Space Sciences, University of Texas at Dallas, for the DE-2 satellite data which has been invaluable in my completion of this project.

I. INTRODUCTION

An active area of research in ionospheric physics is the study of coupling processes between the neutral thermosphere and the ionosphere, because the thermosphere can strongly affect the dynamics of the ionosphere. One facet of this research is the development and validation of computer models for detailed investigation of the underlying coupling mechanisms.

The Ionospheric Physics Division of the USAF Geophysics Laboratory at Hanscom Air Force Base has an extensive involvement in modelling and simulation of the ionosphere, and in analyzing experimental data collected by satellites, rocket probes, and ground-based sites. The primary concern of the Air Force in this area is the effects of the ionosphere on operational systems, especially on the performance and reliability of communication/navigation systems.

My research interest is in space physics, primarily in the ionosphere/thermosphere domain. Previous work while at Boston University has been on neutral wind/plasma coupling processes at high latitudes, specifically on correlating plasma drift and neutral wind patterns for different ambient conditions. The work being reported here is a natural adjunct, with the focus being on low-latitude/equatorial processes.

II. OBJECTIVES OF THE RESEARCH EFFORT

As originally envisioned, the objective of this project was to carry an earlier investigation a step further by incorporating a new neutral wind model in the calculations yielding nighttime zonal plasma drift. The earlier work by Anderson et al (1987) employed a very simple wind model to facilitate computations and maximize the contrast between a latitude-dependent wind and one independent of latitude. The local times input to the model were 2100 (for maximum velocities) and 2300 (for comparison with satellite data). Initially, it was planned that this project would incorporate the NASA high-altitude wind model (called HWM87 for Horizontal Wind Model, 1987) and compare the two models for relative agreement with DE-2 satellite data at 2100 LT, and at additional time points to be decided as the work developed.

Fortunately, the above objectives were met with considerable time remaining, and the scope of the project was expanded: A total of five wind models were selected, and plasma drifts for the entire nighttime sector of 1700 to 0700 LT were simulated, to be compared with DE-2 drift data from Coley and Heelis (1989).

The net result of this effort is that a direct, comparative analysis of thermospheric neutral winds and corresponding plasma drifts has been made available, using the most recent in situ data and theoretical models of thermosphere-ionosphere coupling. This analysis has provided a quick, direct method for the development and validation of a new wind model which has been found to be in very good agreement with the DE-2 data and can therefore be considered as most representative of thermospheric neutral winds, given the ambient conditions during which DE-2 data was collected.

III.

a. The coupling of neutral winds in the thermosphere to the ions and electrons (plasma) of the ionosphere has been a topic of active research for many years. Zonal (east-west) plasma flows can be directly measured by polar-orbiting satellites and by ground-based incoherent-scatter radars, such as the one at Jicamarca, Peru. Concurrently, the development and refinement of computer models simulating flow coupling processes makes possible the direct comparison of theory and experiment. This allows for the validation of detailed theoretical models that would otherwise require a much larger effort. The work being discussed here follows earlier research along this path of inquiry: Given the experimental data of plasma velocities gathered by satellite, what type of thermospheric neutral wind model yields the best agreement, within the context of current theory?

b. The theoretical model relating neutral wind to plasma drift is quite simple and straightforward (Anderson and Mendillo, 1983; Anderson et al, 1987; Kelley, 1989). A fundamental parameter on which this type of coupling depends is the Pedersen conductivity, σ_p, which is appreciable only in the lower ionosphere (90 to 200 km), where the neutral molecules and ions are both of significant density. This parameter is given by

$$\sigma_p = \frac{Nq\nu\omega}{B(\nu^2+\omega^2)} \qquad (1)$$

where N is the electron/ion density, q the electron charge, B the geomagnetic field strength, and ν and ω are the ion-neutral collision and ion gyromagnetic frequencies. The former frequency is proportional to the density of the sum of neutral molecules plus ions divided by the square root of

molecular mass, and the latter is simply qB/m, m being ion mass. The full expression for σ_p includes terms for ion-electron and electron-neutral collisions but, at the altitudes of interest, the electrons are in a virtually collisionless regime. Within this altitude region, ν is large enough that a neutral wind will force the ions along, giving rise to a zonal flow which cuts across geomagnetic field lines, thereby generating an electric, or **E**, field (this is known as the **u** X **B** or dynamo effect). Due to the helical motion of charged particles in a magnetic field, the conductivity along field lines is extremely high, so that a potential due to a motion-induced **E** field at one point is free to propagate throughout the given region of a field line (also called a flux tube). Since the zonal wind flow u is to some extent latitude-dependent, and since each flux tube is anchored at a different latitude, the potential from this ion flow will be different for each flux tube. The potential difference between flux tubes gives rise to an **E** field directed normal to the field lines, for the entire length of each field line. This can be equivalently expressed as causing a current $\mathbf{J}_u$ to flow, where

$$\boldsymbol{J}_u=\sigma\boldsymbol{E}_u=\sigma(\boldsymbol{u}\times\boldsymbol{B}) \qquad (2)$$

σ being the conductivity tensor. For F region altitudes at night, with an eastward wind and northward **B**, the equation for $\mathbf{J}_u$ simplifies to

$$\boldsymbol{J}_u=\sigma_p uB\boldsymbol{a}_z \qquad (3)$$

where $\mathbf{a}_z$ is the upward-pointing unit vector and $\mathbf{J}_u$ is strictly an ion flow due to ion-neutral collisions.

However, this is only the neutral wind-induced current; as it begins to flow, an **E** field is set up to oppose the flow in order to maintain the divergence-free current pattern ($\nabla*\mathbf{J} = 0$), which must hold in free space. That is,

the total vertical current must sum to zero, resulting in an opposing **E** field current to balance J_u, or

$$J_{tot}=J_u+J_e=a_z(\sigma_p uB+\sigma_p E_z)=0. \quad (4)$$

The presence of the **E** and **B** fields together produce what is termed a guiding-center drift; that is, both ions and electrons move in an epicycloidal fashion with the same direction and magnitude given by

$$V_p=\frac{(ExB)}{B^2} \quad (5)$$

Therefore, the vertically-downward directed E_z and the northward-directed **B** result in a plasma velocity V_p directed east, similar to the neutral wind. Converting eqn.(5) to scalar form gives $V_{px} = -E_z/B_y$ (E_z is negative since it is downward-directed).

A final step in deriving the relationship between plasma drift V_p and neutral wind u is integration of eqn.(4) over flux tube length, since this is considered a region of equipotential (infinite conductivity):

$$\int[\sigma_p uB+\sigma_p E_z]\,ds=0, \quad (6)$$

with ds representing an increment of flux tube length. This yields, with $E_z = -B_y*V_{px}$ from eqn.(5),

$$\int\sigma_p uBds=-\int\sigma_p E_z ds=\int V_p\sigma_p Bds \quad (7)$$

The drift expression (**E** X **B**)/B^2 can be considered constant along the flux tube, since the electric field can be expected to vary as the magnetic field varies; therefore V_p can be taken out of the integral, leaving

$$V_p = \frac{\int \sigma_p u B ds}{\int \sigma_p B ds} \qquad (8)$$

c. Measurements of plasma drift velocities perpendicular to field lines should show their best agreement to eqn.(8) at the field line apex, considering that guiding center drift assumes no collisions with neutrals and any differences in the northern and southern ends of the flux tube would balance out in the region of the apex. The above equation was converted to a summation over flux tube segments and embodied in a computer code which generated arrays of plasma drift values for apex altitudes from 250 to 1500 km, and for local times of 1700 to 0700. The assumed longitude was 70 degrees west, allowing for B to be treated as north-south aligned, ie, zero declination. Since the output values are a function of the two independent variables of time and altitude, it was decided that contour plots of the output arrays would be the most effective display medium, both for visual analysis and for publication.

d. Besides the plasma drift output, the key input of electron density and the resultant σ_p values were contour plotted to reveal the contrasts and similarities among the six cases of solar minimum and solar maximum, each with zero, one-half, and average equatorial drifts. These are displayed as Figure 1,a-f (electron density, n_e), and Figure 2,a-f (σ_p). The numbers identifying contour lines are $\log_{10}(n_e)$, in cm^{-3}, and $\log_{10}(\sigma_p)$, in μmhos/meter. The differences from one panel to another are not great, but a quick inspection shows that increasing drift raises the respective contours to higher altitudes, and shifting from solar min to solar max has a much stronger effect on raising the contours, as well as reducing the gradient (contours

spaced farther apart). These general characteristics of n_e and σ_p are in line with general theoretical expectations.

e. The neutral wind models used in the comparative evaluation are as follows:

(1) The NASA-GSFC Horizontal Wind Model, 1987 (HWM87), developed by A.E. Hedin. This model is intended for altitudes above 220 km and latitudes between 50 degrees north and south. It is latitude and local time dependent but is independent of altitude.

(2) The latitude-independent empirical wind of Anderson et al (1987), based on altitude (A) and local time (LT) only: For A>300, u = 200*cos((21-LT)*15deg/hr); for 200<A<300, $u = u_{300}*(0.01(A-200))$; for 140<A<200, u = -50; and for A<140, u = 0, with A in km, LT in hours, and u in meters/sec.

(3) The latitude-dependent form of wind (2) is simply $u_{lat} = u*\cos(4\theta_d)$, where θ_d is the dip latitude in degrees, measured from the geomagnetic equator.

(4) The HWM87 model was given the altitude dependence of wind (2), ie, the value was unchanged for A>300 km and was multiplied by 0.01(A-200) for 200<A<300; for A<200 km, the values were identical to wind (2).

(5) A solar diurnal/semidiurnal tidal wind dependent on latitude, altitude, local time, and season, covering the altitude range of surface to 400 km (Forbes and Gillette, 1982).

The six ambient condition cases were run for each of the five wind models, generating thirty contour plots of plasma drift velocity vs. apex altitude (250 to 1500km) and local time (1700 to 0700). For the sake of brevity, the plots included in this report are those for models (1), (2), and (5) only, arranged as Figures 3a-f, 4a-f, and 5a-f, the latter suffix identifying the ambient case.

Inspection of Figures 3 to 5 makes apparent the basic differences among the wind models: The HWM87 model is altitude-independent with a shallow dependence on latitude (note that as the apex altitude increases, the respective flux tubes terminate at latitudes further from the magnetic equator). Because of this mild dependence, the contour plots for this model are predominantly vertical, with the characteristic bulge at 2100LT, the diurnal peak for electron density. In this case, the bulge is more of a vertical ridge due to the lack of a strong dependence on latitude/altitude. The Anderson/Heelis/McClure (A/H/M) latitude-independent wind, being a strong function of altitude, displays a much more sharply peaked bulge at 2100LT, and at a lower altitude than for HWM87. However, the late nighttime (0100-0500LT) contours shift to almost vertical, due to the sharp decrease in electron density at those times. The reversal from eastward to westward flow at 0400-0500 is the result of solar heating to the immediate east at the dawn terminator. Finally, the Forbes/Gillette wind, based on diurnal and semidiurnal solar heating effects, shows an essentially flat region for a good portion of the nighttime sector, with vertical contours indicating the shift to westward flow for early morning local times.

As one progresses from a to f on each Figure, thus going to increasing electron densities and greater solar activity, the result is that the drift velocity bulge at 2100LT shifts to a higher altitude and increases in magnitude, with the rate of increase of both effects highly dependent on wind model. The A/H/M model shows the greatest change, with the other two being much less pronounced. Again, this is the result of the explicit altitude dependence of the A/H/M model.

f. With the data thus far being computer model output, a direct comparison with experimental data was needed to develop a basis for model validation. In the modelling work

of Anderson et al (1987), the authors compared their wind models ((2) and (3) above) with data obtained from the Dynamics Explorer 2 satellite, launched into a polar orbit in August, 1981. The ion drift meter (IDM) on DE-2 provided drift velocities accurate to within 20 m/sec, for the velocity component perpendicular to the satellite orbit, thereby recording zonal (and vertical) drift values. The observed drifts from one orbit (#6184, 2300LT on 18 September 1982) were plotted vs. calculated drifts for wind models (2) and (3), and showed that fair agreement obtained between DE-2 data and wind (3).

Subsequent to publication of this work, Coley and Heelis (1989) presented an update of their processing of the IDM data transmitted from DE-2. This later work covered 810 equatorial passes of the satellite, over the period August 1981 through February 1983, with a post-processed accuracy of plus or minus 2 m/sec. This period of data acquisition coincided with maximum or near-maximum solar activity. Upon request, an updated file of drift velocities, covering 300 to 980 km altitude at two hour intervals, was transmitted to us; the data for the nighttime sector of 1700 to 0700 was contour plotted and compared to the model data plots described above. A brief phase of comparative analysis led to the formulation of a new wind model, essentially a modification of wind (3), which produced plasma drift contours in generally good agreement with the DE-2 values.

This new model is of the following functional form:
Altitude/Local Time dependence:

For A>300, $u = 190*\cos(\alpha(21-LT)*15deg/hr)$,
where $\alpha = 1.45$ for LT<2100, $= 0.67$ otherwise;
for 50<A<300, $u = u_{300}*(0.004(A-50))$;
for A<50, $u = 0$.

Latitude dependence:

$u_{lat} = u*\cos(2\theta_d)$,

A, LT, and θ_d having been defined above. A comparison of this model and the DE-2 data is shown on Figure 6a-b.

Although the DE-2 plot (Fig.6a) shows significant fine structure not present in Fig.6b, this difference can be attributed mostly to the measurement process as a result of finite sampling time and large-scale fluctuations from idealized behavior. Comparing the location, spatial extent, and magnitude of the 2100LT bulge and the orientation and spacing of the isotach contours on each side, the overall agreement can be considered quite good.

IV. RECOMMENDATIONS

This brief study has shown that the current theory of thermosphere-ionosphere coupling can be soundly validated with a large set of in situ measurements gathered over a long time period. Research should continue in this area to better define and specify the full details of the coupling processes that govern much of the dynamical behavior of the ionosphere/thermosphere system.

REFERENCES

Anderson, D.N., and M. Mendillo, Ionospheric Conditions Affecting the Evolution of Equatorial Plasma Depletions, Geophysical Research Ltrs., 1983, Vol.10, pp.541-544.

Anderson, D.N., R.A. Heelis, and J.P. McClure, Calculated Nighttime Eastward Plasma Drift Velocities at Low Latitudes and their Solar Cycle Dependence, Annales Geophysicae, 1987, Vol.5A, pp.435-442.

Coley, W.R., and R.A. Heelis, Low-Latitude Zonal and Vertical Ion Drifts seen by DE-2, J. of Geophysical Research, 1989, Vol.94, pp.6751-6761.

Forbes, J.M., and D.F. Gillette, A Compendium of Theoretical Atmospheric Tidal Structures, Part I: Model Description and Explicit Structures due to Realistic Thermal and Gravitational Excitation, AFGL-TR-82-0173(I), Hanscom AFB, MA, 1982.

Kelley, M.C., The Earth's Ionosphere, Academic Press, San Diego, CA, 1989.

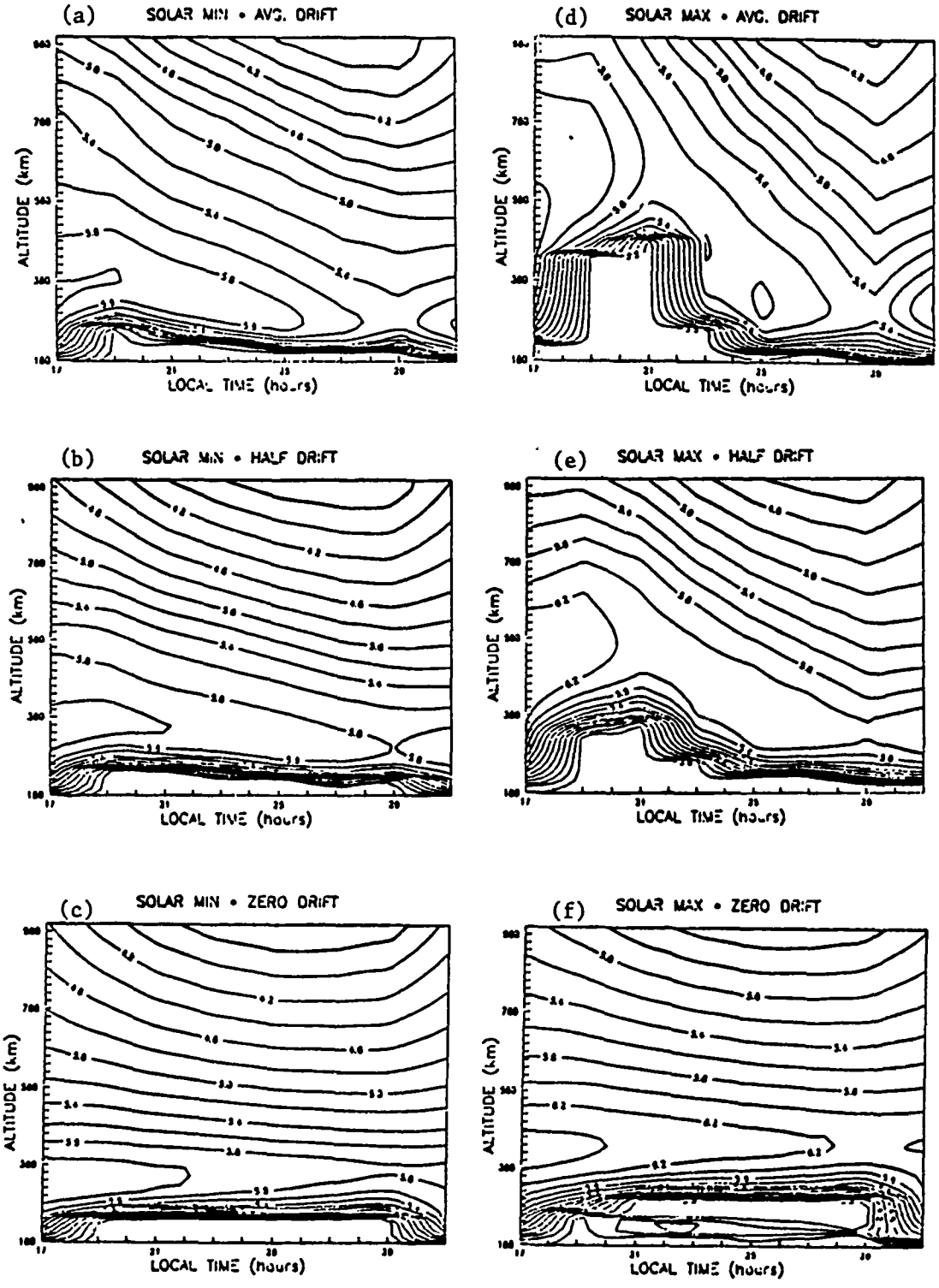

Figure 1. Electron densities, in $\log_{10}(n_e(cm^{-3}))$ vs. altitude and local time (local time of 25/29 is 0100/0500).

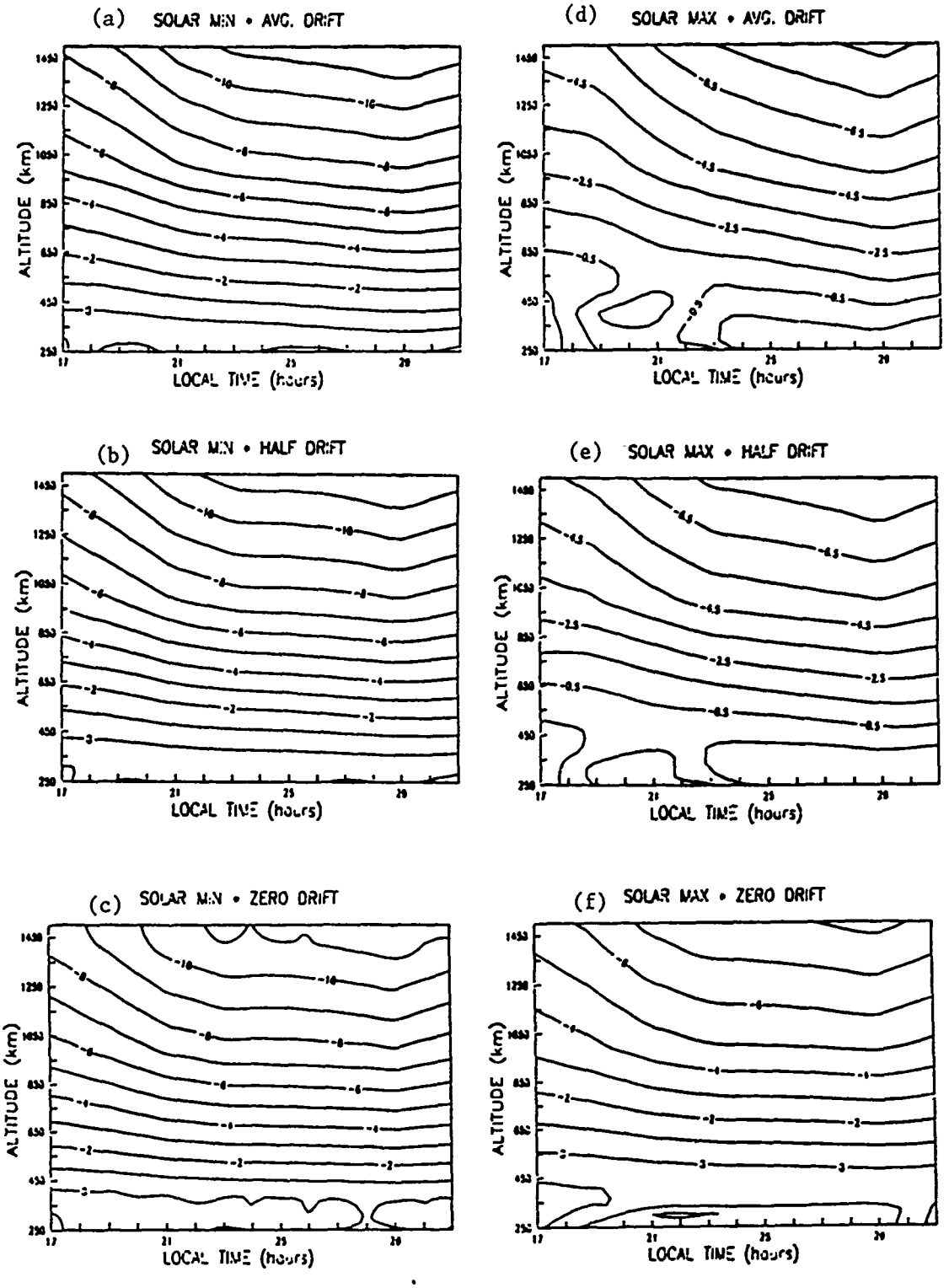

Figure 2. Pedersen conductivity, in $\log_{10}(\mu mhos/m)$ vs. altitude and local time.

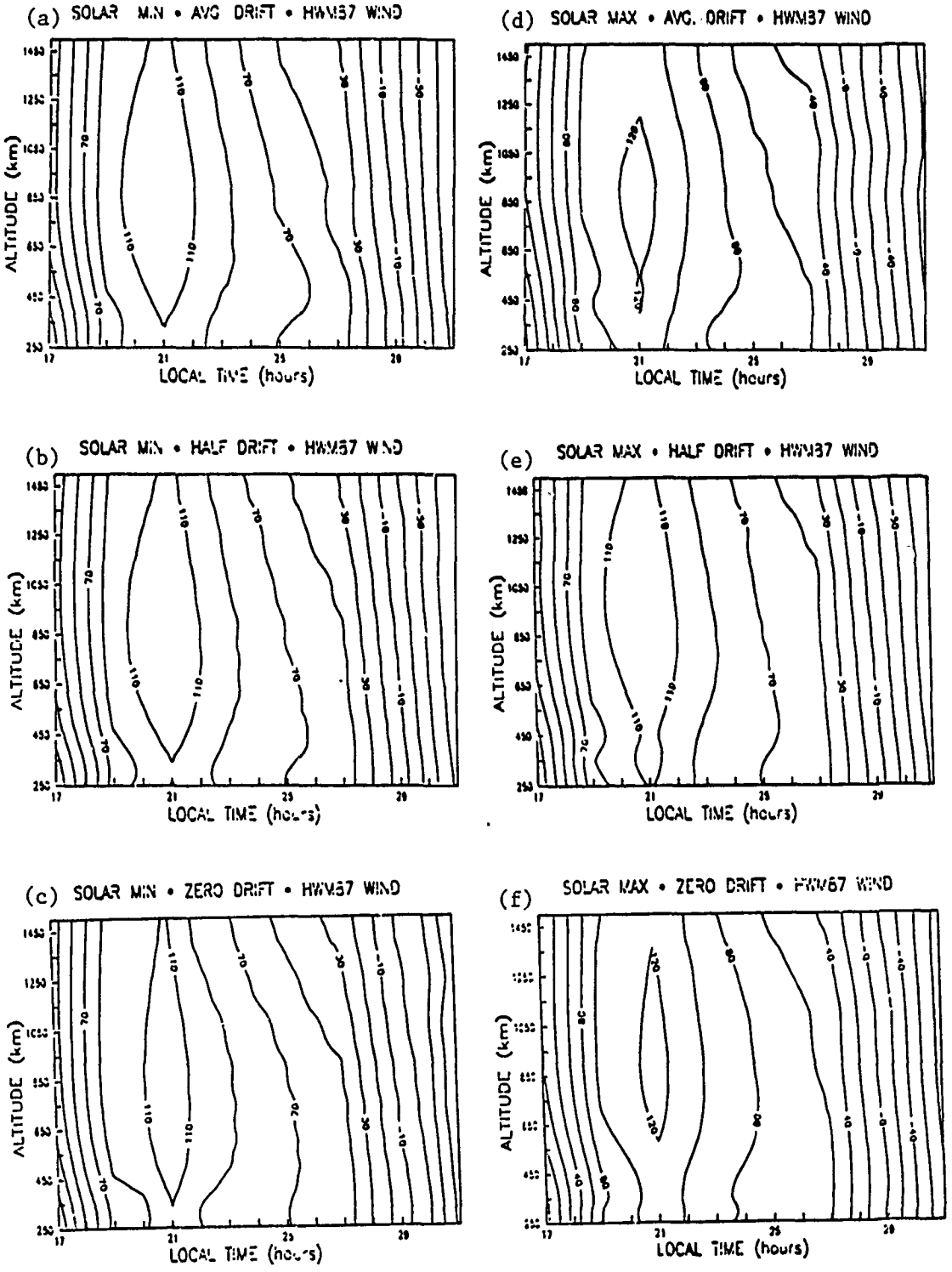

Figure 3. Plasma drift velocities in m/sec vs. altitude and local time with HWM87 model as input wind.

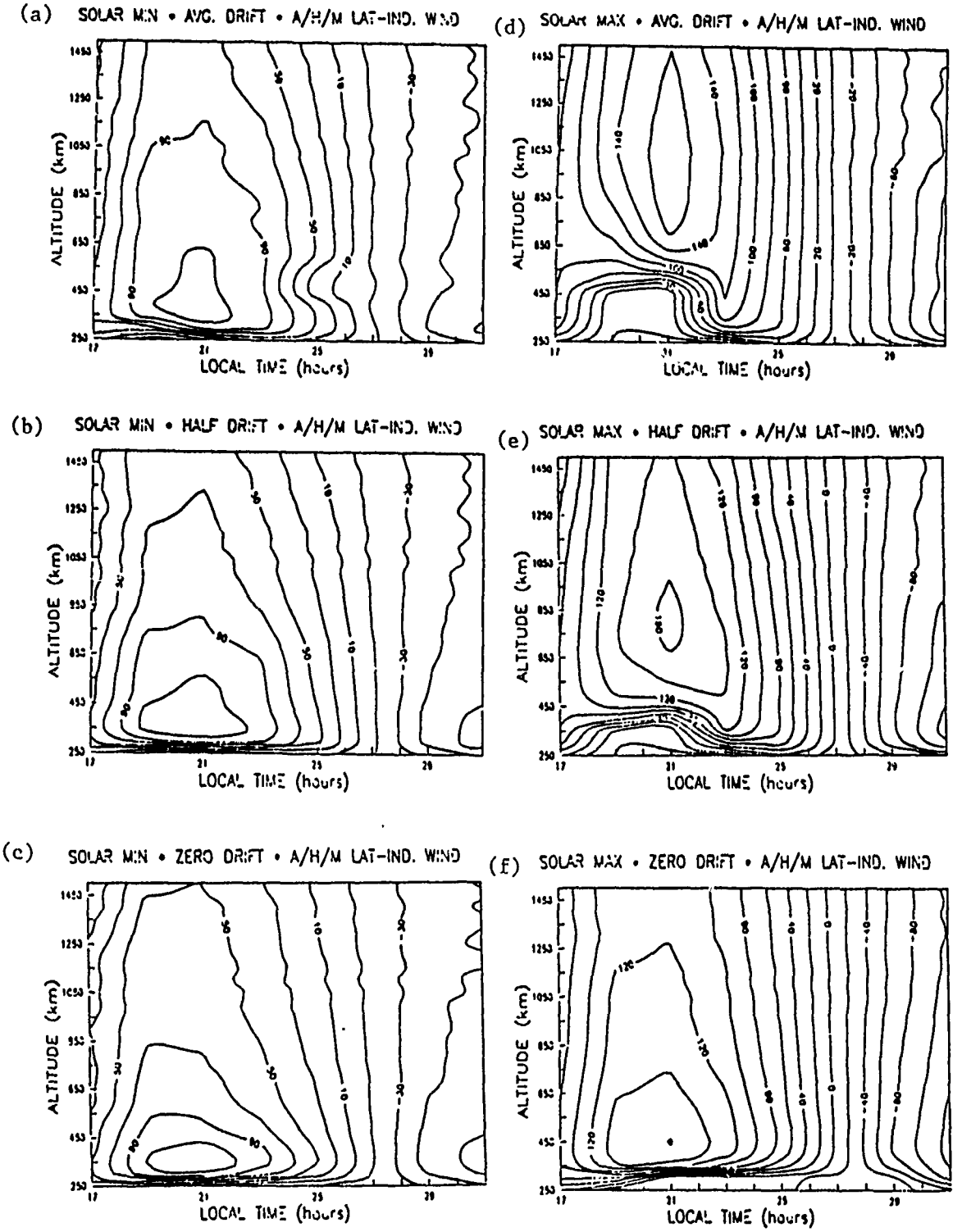

Figure 4. Plasma drift velocities in m/sec vs. altitude and local time with A/H/M latitude-independent model as input wind.

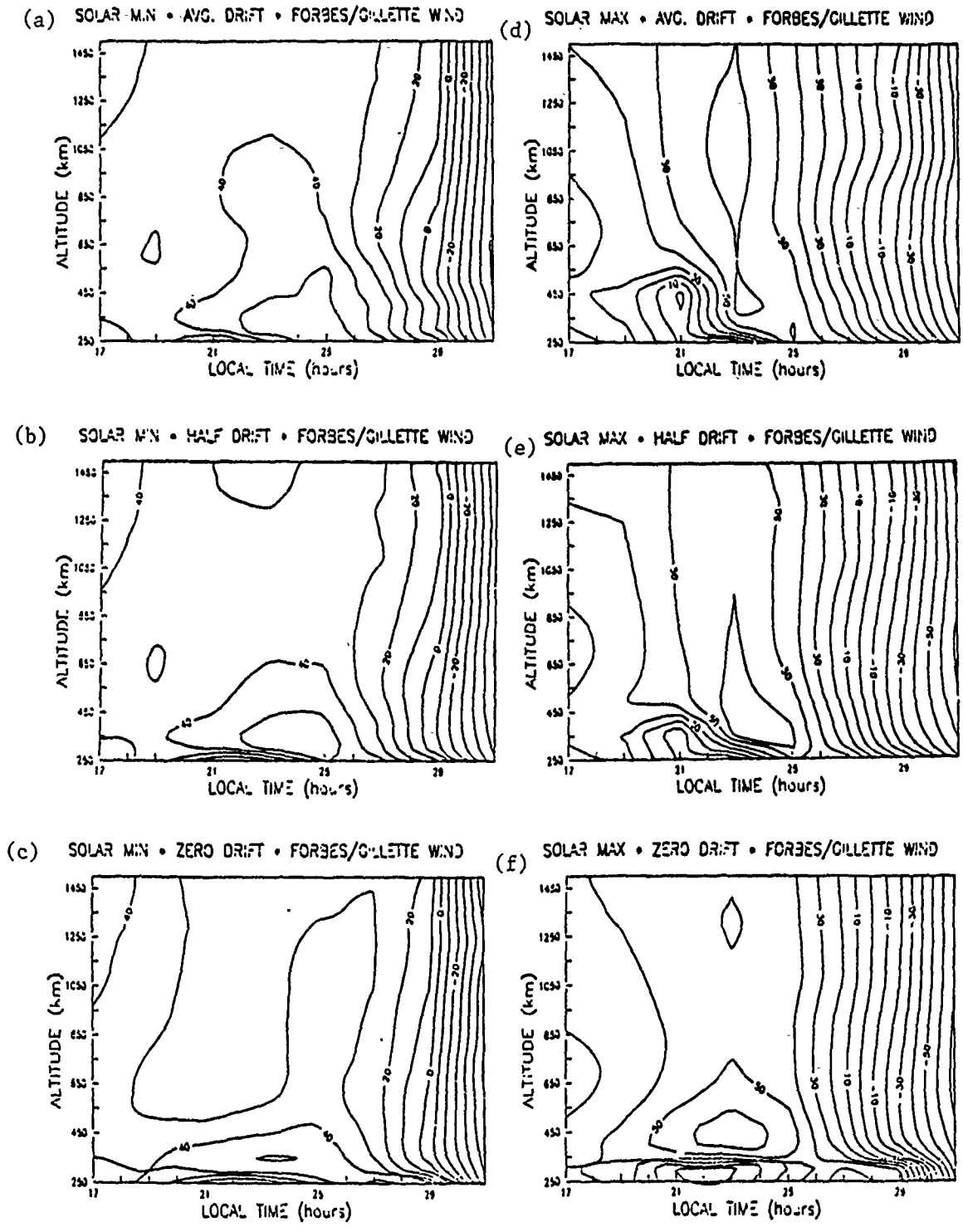

Figure 5. Plasma drift velocities in m/sec vs. altitude and local time with Forbes/Gillette model as input wind.

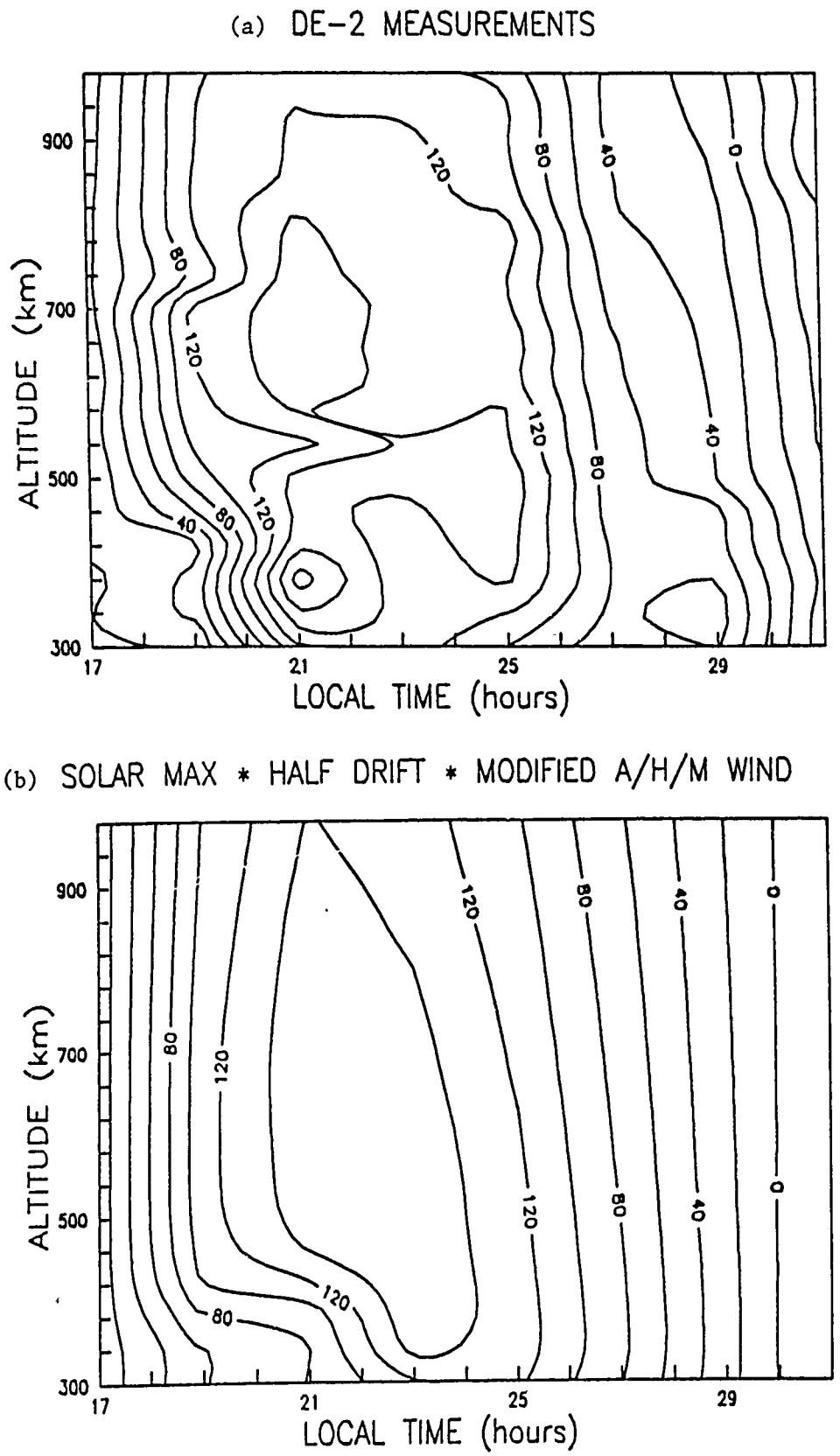

Figure 6. DE-2 plasma drift velocity measurements compared to modified A/H/M wind model (in m/sec) for solar maximum, half equatorial drift ambient case.

1990 USAF-UES SUMMER FACULTY RESEARCH PROGRAM/

GRADUATE STUDENT RESEARCH PROGRAM

Sponsored by the

AIR FORCE OFFICE OF SCIENTIFIC RESEARCH

Conducted by the

Universal Energy Systems, Inc.

FINAL REPORT

Optimum Observing Techniques for Detection of OH

Prepared by:	James C. Day
Academic Rank:	Graduate Student
Department and University:	Department of Physics and Astronomy University of Kentucky
Research Location:	AFGL/OPC Hanscom AFB, MA 01731
USAF Researcher:	Frank O. Clark
Date:	July 20, 1990
Contract No:	F49620-88-C-0053

Optimum Observing Techniques for Detection of OH

by

James C. Day

ABSTRACT

Measurement of trace gasses is necessary for validation of atmospheric models; yet, accurate measurements are difficult due to the low abundance of these gasses. Therefore, optimization of observational techniques is necessary. Emission of atmospheric hydroxyl was modeled using FASCOD3, an atmospheric code developed at the AFGL. Output from FASCOD3 was used to determine the optimum observing configuration for the detection of OH emission lines using a 140ft parabolic astronomical microwave antenna. Optimum frequency resolution, antenna position and method of background subtraction were selected based on minimizing integration time and system effects.

ACKNOWLEDGEMENTS

Without the efforts of many people this research would not have been possible. For help in everything from finding temporary housing to protecting my fixed disk, I owe Frank O. Clark of the Geophysics Lab (Air Force Systems Command) much thanks. Jim Chetwynd's endless help with the running of FASCOD3 has been greatly appreciated, as has the help from fellow student participants, Tom Kuchar and John Noto.

Much thanks is also due the Air Force Systems Command and the Air Force Office of Scientific Research for sponsoring this research, and to Universal Energy Systems for performing all of the administrative details.

I. INTRODUCTION

Understanding the complex chemistry of the Earth's atmosphere is of great strategical importance. For instance, in target detection it is necessary to be able to accurately predict the obscuring spectral features of the atmosphere. Therefore, the Air Force's Geophysics Laboratory (AFSC) produces and maintains accurate models of the detailed effects of the Earth's atmosphere at all relevant wavelengths. Often, the chemistry of trace atmospheric gases is not well understood, and these models must rely on limited physical data for input, as measurements are scarce and have large uncertainties.

The hydroxyl radical (OH) is a highly reactive chemical species which, despite its low abundance, plays a significant role in many critical reactions occurring in the atmosphere. OH is a participant in the removal of numerous trace gasses, both of natural and anthropogenic origin, and is also a catalyst in the formation of smog. Since it is involved in so many different reactions in the atmosphere, measurements of OH could be an excellent test of the accuracy of the atmospheric models on which the Air Force is dependent for planning and testing of detection systems. However, because of its low abundance and short lifetime, OH has been particularly difficult to measure.

Dr. F. O. Clark, a physicist involved in research and codes on both the celestial background and the atmosphere for the AFGL has recognized that the microwave spectral lines of atmospheric OH are detectable, and may be used to monitor the vertical profile of this radical. Through a process known as deconvolution, the shapes of emission lines detected by ground-based telescopes may be used to determine density as a function of pressure, and thus altitude.

My involvement with Dr. Clark began while he was serving as a professor at the University of Kentucky, where I am currently attending graduate school. Knowing of my interest in atmospheric physics, he contacted me regarding this research, which led ultimately to my participation in the Graduate Student Research Program.

II. OBJECTIVES OF RESEARCH EFFORT

The overall objective of the study of OH is to improve the GL atmospheric codes by enabling the measuring and monitoring of this sensitive indicator about which little is known.

Clark has proposed using a 140ft radio antenna located at the National Radio Astronomy Observatory in Green Bank, WV, for a preliminary detection experiment. Information gathered regarding the strength and detectability of the OH microwave lines would then be used to aid in the design of an instrument dedicated solely to the measurement of OH. This instrument would allow accurate measurements and temporal monitoring of OH.

Originally, my summer duties were to include assisting in the collection and reduction of data of this preliminary experiment. The experiment was, however, scheduled in late August, after the termination of my summer appointment. Therefore, because OH has such a low density and the microwave signal was expected to be difficult to detect with existing instrumentation not designed for the task, it was decided that my work should focus on the optimizing of observational variables, such as frequency resolution, background subtraction methods and antenna position for observing. These parameters not only ensure optimum detectability of the OH spectral lines, but also provide a ready basis for subsequent interpretation.

III. FREQUENCY RESOLUTION

a. The rms system noise, or minimum detectable signal (Smin), of a telescope is inversely proportional to the square root of the frequency resolution (dv) and the integration time (t):

$$Smin = \frac{Ks\ Tsys}{\sqrt{dv\ \ t}} \qquad (1)$$

where Ks is a sensitivity constant, and Tsys is the system temperature. However, while the system noise increases with finer resolution, the peak line strength of a species which is most abundant in the upper atmosphere, as is OH, increases as well. Therefore, it is beneficial to know how the line heights behave with respect to changes in resolution, in order that an optimum frequency resolution may be determined.

In order to accomplish this task, FASCOD3, an AFGL atmospheric transmission/radiance code was used to model OH emission in the microwave. Clark had previously determined that the 6GHz line was the best candidate for observation. Therefore, the line height of the 6GHz line was determined for various resolutions by using

FASCOD3's scanning option. Then, setting the line heights equal to the minimum detectable signal, the integration times required for a detection were calculated.

b. Figure 1 displays the results of the optimum frequency resolution study. A definite minimum in the integration time is seen occurring around dv = 30 KHz. Integration times were calculated for a zenith angle of eighty degrees (from vertical), using an estimated value for Ks of 1.2 (unitless) and a value for Tsys reported by a system engineer. The values should lie within a constant factor of two or less of the actual integration times; however, the relative minimum is independent of the scaling.

IV. BACKGROUND SUBTRACTION

a. Because the system noise is considerably stronger than the signal sought, it is customary in such an experiment to subtract a measurement which does not contain the signal, to effectively remove the system noise. Three methods of background subtraction were considered for the experiment: day/night switching, zenith angle switching, and frequency switching.

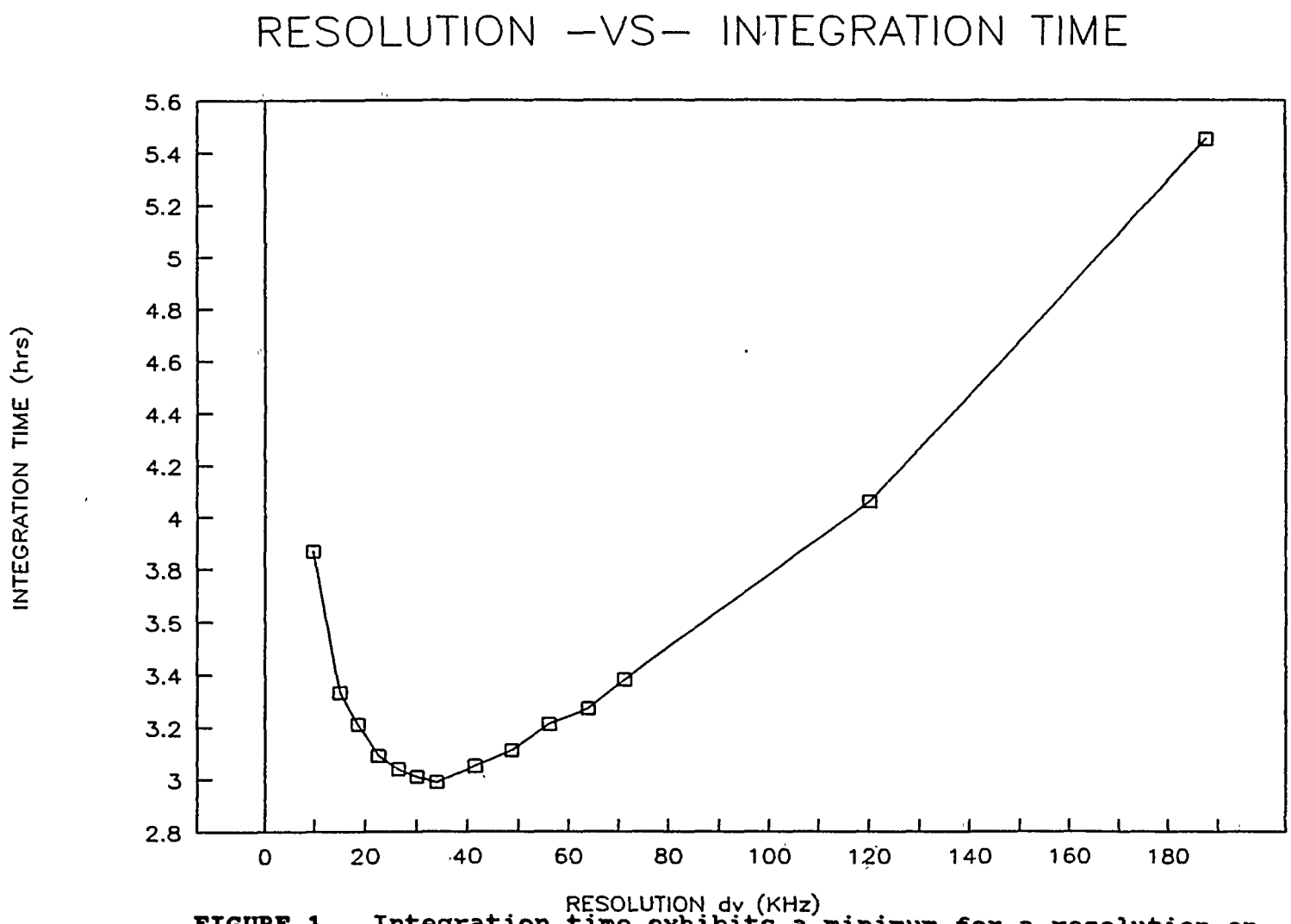

FIGURE 1. **Integration time exhibits a minimum for a resolution on the order of dv = 30 KHz.**

Again, FASCOD3 was used to model the output for various situations. ASCII output files from FASCOD3 runs were imported into Lotus 123 worksheets where the data were easily manipulated.

b. Day/night switching takes advantage of diurnal effects by subtracting a night spectrum (when OH concentrations are low) from a day spectrum. Fabian et al. have predicted stratospheric nighttime OH concentrations to drop by two orders of magnitude from the daytime maximum. Hard et al. have actually measured tropospheric diurnal variations of this magnitude. Therefore, day/night switching should prove to be a suitable method of background subtraction for the dedicated receiver when it is built. Receiver stability is a problem, however, for the 140ft NRAO scope which will be used for the preliminary detection, as the system is only stable over roughly a thirty minute period.

Because a horizontal path to space passes through more of the atmosphere than does a vertical path, a telescope viewing the atmosphere near the horizon will receive a stronger signal than when viewing near the zenith. Zenith angle switching involes subtracting a spectrum recorded near the zenith from one recorded near the horizon. FASCOD3 predicted line heights at eighty

degrees zenith angle to be about four times stronger than at zero degrees. Therefore, zenith angle switching for these angles should result in a loss of roughly 25% of the actual line height. Switching for other angles should reduce the line height even more.

Frequency switching appears to be the optimum method for the preliminary detection. This method subtracts an identical spectrum which has been shifted by a few channels, since the systematic effects do not vary appreciably over a small region. Figure 2 shows the 6GHz OH line, its frequency shifted inverse, and the addition of the two. It was found that a relatively minor frequency shift produced a strong inflection which should be easily discernable from noise. The height of this feature reaches a maximum quickly, allowing for very minute frequency shifts, resulting in better subtraction of systematic background.

V. DIRECTIONAL CONSIDERATIONS

a. Hard et al. have shown that hydroxyl abundance is strongly correlated with solar UV radiation. Therefore, both diurnal, seasonal and latitudinal variations exist. Furthermore, the antenna which will be used for the detection experiment has a system temperature (Tsys, see eq. 1) which increases non-linearly with zenith

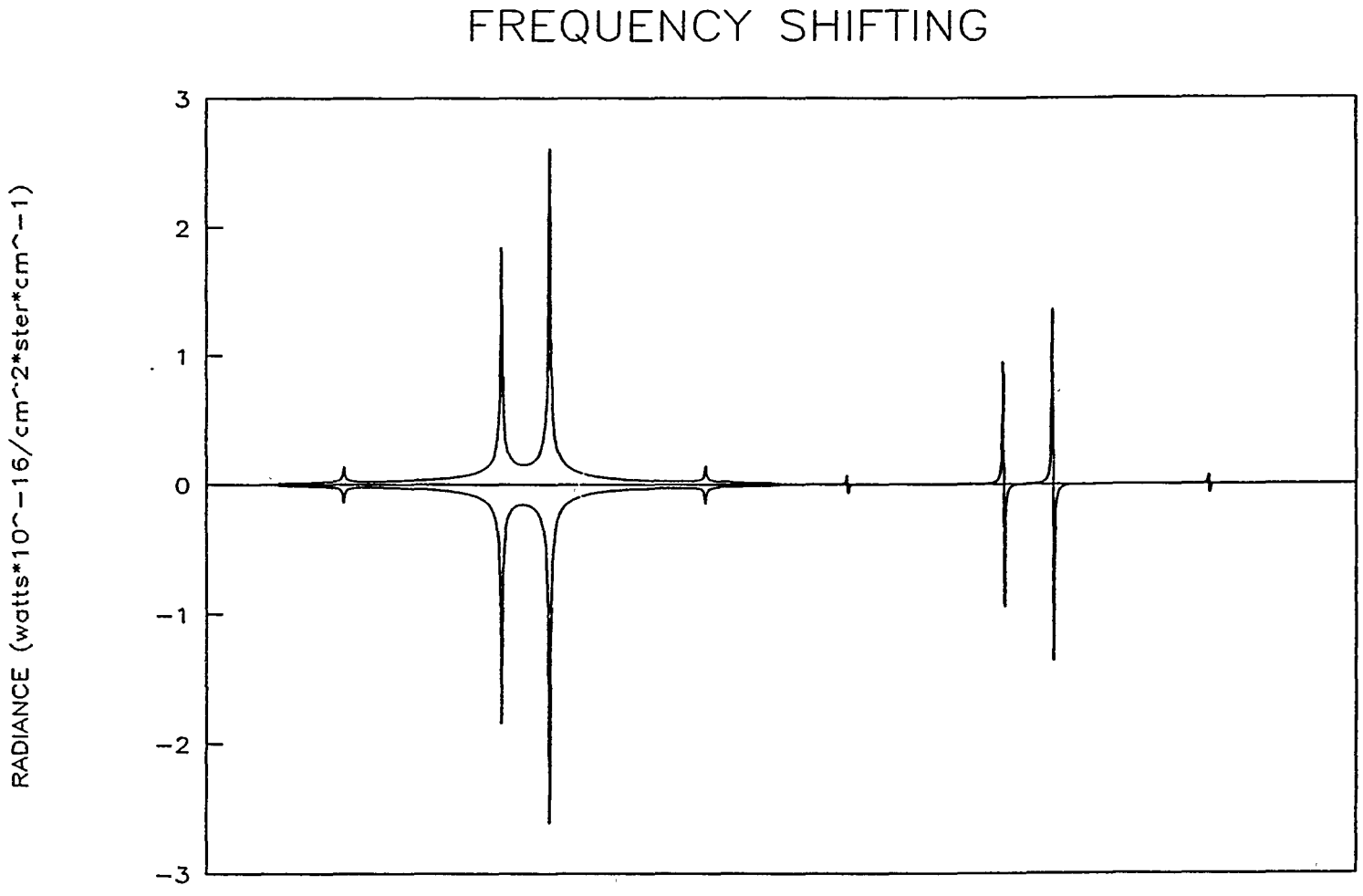

FIGURE 2. The OH 6GHz line and its frequency shifted inverse are added to produce a distinctive inflection.

angle. Thus, while the OH signal will grow with zenith angle, the system noise may swamp it if one observed all the way on the horizon. Additionally, the bright sun may produce systematic effects in the spectra even in the far-field pattern of the antenna. All of these factors must considered when selecting the optimum viewing direction.

b. Fabian et al. predict that the summer maximum OH concentration occurs at 30 to 40 degrees latitude (north of equator) at local noon. In autumn, the maximum occurs at -10 to -20 degrees latitude. NRAO is located at 38.4 degrees latitude, within the region of summer maximum.

Using system temperatures provided by a system engineer, integration times were calculated using FASCOD3 output for the line heights at various angles. Even though the system temperature increases rapidly for angles near the horizon, the minimum integration time occurred for an eighty degree zenith angle. Angles greater than eighty were not considered due to problems with ground pick up.

It appears that an optimum viewing method is to sweep the sky at eighty degrees zenith distance such that the angle of the sun and telescope is kept constant, thus

stabilizing systematic noise, and minimizing the necessary integration time.

VI. RECOMMENDATIONS

a. By optimizing the observing methods prior to conducting the experiment, the likelihood of a successful detection should be increased significantly. There will be no time wasted experimenting with variables at the site, and more time may be spent actually observing.

b. A preliminary calculation of the slew rate necessary to keep the angle between the sun and telescope constant has been performed; yet, it is hoped that either myself or Dr. Clark can perform a more detailed calculation prior to the experiment.

If the preliminary detection experiment indicates that such a method is feasible, a dedicated instrument will be built which will continuously monitor the concentration of OH. Observations made using this instrument will provide an excellent check for model accuracy, and will also allow monitoring of the effects of human activity on the chemistry of Earth's atmosphere.

REFERENCES

Fabian, P., et. al. Diurnal Variations of Minor Constituents in the Stratosphere as a Function of Latitude and Season. J.G. R. 1982, Vol. 87, pp. 4981--5000

Hard, T. M., Diurnal Cycle of Tropospheric OH. Nature. 1986, Vol. 322, pp. 617-620.

1990 USAF-UES SMMUER FACULTY RESEARCH PROGRAM/

GRADUATE STUDENT RESEARCH PROGRAM

Sponsored by the

AIR FORCE OFFICE OF SCIENTIFIC RESEARCH

Conducted by the

Universal Energy Systems, Inc.

FINAL REPORT

IRAS Correlations With Galactic H II Regions

Prepared by:	Thomas A. Kuchar
Academic Rank:	Graduate Student
Department and University:	Department of Astronomy Boston University
Research Location:	Geophysics Laboratory Hanscom AFB, MA 01731
USAF Researcher:	Dr. Frank O. Clark
Date:	6 September 1990
Contract No:	F49620-88-C0053

IRAS Correlations With Galactic H II Regions

by

Thomas A. Kuchar

ABSTRACT

Target detection and tracking in the infrared must deal with clutter from natural backgrounds. A major source of such clutter is the galactic plane, the brightest part of which is not yet well characterized. The galactic plane can be probed with ionized regions surrounding hot stars, H II regions, to improve models of the galactic plane. The far infrared emission from H II regions was studied using the data from the Infrared Astronomy Satellite (IRAS) in the form of dust color temperature maps. This emission was subsequntly compared to the Boston University–Arecibo Galactic H I Survey. A cross-correlation technique was devloped to identify the interstellar neutral hydrogen cloud associated with the dust emission. The BU–Arecibo Survey can, in principle, determine the distances to the H II regions and thus determine the absolute IR luminosity of the emission.

ACKNOWLEDGEMENTS

I wish to thank the Air Force Systems Command and the Air Force Office of Scientific Research Office for allowing me to participate in this program, especially at this time of tight funding for graduate student research.

The Geophysics Laboratory at Hanscom AFB must also be thanked for the research atmosphere that they provided and especially Dr. Frank Clark for his helpful guidance in contributing to my thesis research. I also wish to thank Dr. René Laureijs of IPAC for his help and insight in reducing the IRAS data.

The Infrared Astronomy Satellite (IRAS) was developed and operated by the Netherlands Aerospace Programs (NIVR), the US National Aeronautics and Space Administration (NASA), and the UK Science and Engineering Council (SERC).

The Infrared Processing and Analysis Center (IPAC) is funded by NASA as part of the IRAS extended mission program under contract to the Jet Propulsion Laboratory.

I. INTRODUCTION

Target detection and tracking in the infrared must deal with clutter from natural backgrounds. A major source of such clutter is the Galactic plane, which is not obscured by dust in the infrared, as in the optical, but instead shines brightly. Targets which cross the galactic plane may be totally lost if allowance is not made for this bright emission, with a variety of scale sizes and spectral components. The brightest central part of the galactic plane is not yet well characterized observationally, and therefore models of this compo- nent of the celestial background clutter are not yet ideal. This central envi- ronment of the galactic plane can be probed with ionized regions, H II regions, which surround hot stars, to improve models of the galactic plane.

Large scale surveys of the infrared sky have recently become available to the astronomical community, most notably in the form of the Infrared Astronomy Satellite (IRAS) database (Explanatory Supplement, 1985; Neugebauer et al., 1984; Rowan-Robinson et al., 1984). Perhaps the most complete survey of the infrared sky to date, the IRAS survey, is characterized by insufficient spatial resolution to adequately characterize these components of the galactic plane. Although 'standard' data reduction techniques for IRAS data already permeate the astronomical literature, analysis and interpretation of the results are still in its infancy.

The Celestial Backgrounds Division of the Geophysics Laboratory at Hanscom AFB has a continuing interest in modeling and interpreting the infrared sky. Thus methods already developed at the Geophysics Lab can be readily applied to infrared data provided by the IRAS mission.

Currently I am conducting research toward a doctorate degree in astrophysics. The dissertation involves the analysis of a portion of the Boston University–Arecibo Galactic H I Survey (Bania and Kuchar 1990), specifically the H II regions contained within the region mapped by the Survey. A pilot study involving emission-absorption

experiments toward 19 H II regions has already be conducted (Kuchar and Bania 1990). My goal is to expand the analysis of these H II regions to include the dust component as revealed by the IRAS data. The correlation of the dust with the gas component (as provided by the Survey) of H II regions can reveal a more complete picture of the physical conditions associated with H II regions.

II. OBJECTIVES OF THE RESEARCH EFFORT

This research effort seeks to study the properties of dust emission associated with cool, diffuse H I clouds detected by the BU–Arecibo Survey using the IRAS Super Skyflux Images. If correlations can be made between IRAS sources and the Survey clouds, some of the spatial confusion associated with the IRAS fields near the Galactic plane could be resolved. The Survey data base can be used to determine the distances to these IR sources. This effort attempted to find correlations between IRAS sources and a sample of H I clouds associated with H II regions whose positions, distances, velocities, and spin temperatures are known (Kuchar and Bania, 1990).

IRAS images near the galactic plane show complex structures in the infrared emission. These images are basically two-dimensional intensity maps and contain no absolute spatial information (i.e. the line of sight distances to the objects responsible for the emission cannot be determined directly from the IRAS images). The initial goals of this effort was to determine the dust temperatures of the IRAS sources and to correlate the dust properties with the H I properties of the H II region sample and thus help unravel the confusion associated with IRAS data in the Galactic plane. Two broad approaches to the identification problem were made:

1. calculation of two-dimensional spatial correlations between the IRAS brightness images (at 60 and 100μm) and the individual Survey velocity channel

position-position maps. This approach would look for characteristic signatures of these objects in the 2D spatial correlations.

2. comparison of color temperature maps with Survey maps. A simultaneous correlation of these maps might prove to be necessary, since the color temperature may be more directly related to the H I parameters.

This assumption, however, must be tested to see what correlations exist between H I spin temperatures, (as provided by Kuchar and Bania, 1990) and IRAS emission. The derivation of the dust parameters is not unique, since these parameters are based on the assumed form and value of the dust emissivity and differ for 60 and 100 μm emitters.

III. Data Sets and Reduction Techniques

a. IRAS

The Infrared Astronomy Satellite operated from January to November 1983. As part of its mission, the satellite conducted three surveys of the infrared sky in four wavebands centered at 12, 25, 60, and 100 μm. The three surveys are referred to HCONs, for Hours CONfirmed observations. The separate HCONs were to confirm structures that persisted over timescales of more than an hour. HCON2 observed the same portion of the sky 100 minutes after HCON1 had observed it. Both of these surveys covered 96% of the sky. HCON3 was conducted six months later and observed only 60% of the sky.

The Infrared Processing and Analysis Center (IPAC) of the Jet Propulsion Laboratory is responsible for the maintenance and distribution of the IRAS products. Recently (May 1990) IPAC began to offer super skyflux images to the astronomical community. These images are superior to the previous skyflux products by

improving the calibration, positional reconstruction, de-striping, and zodiacal emission subtraction.

Both versions of the skyflux images consist of co-adds of all three HCONs. The co-adds improve the signal-to-noise of the images as well as the effective resolution of the IR sources. However there are two major improvements in these images other than the improvements to the data processing algorithms. The original skyflux images did not correct for calibration differences of the adjacent detectors. These differences show up as 'stripes' in the images. Also, the original images did not remove the emission caused by solar system dust, the zodiacal emission. The super skyflux images are corrected for both of these effects before the HCONs are co-added. This is especially important for removing the zodiacal emission. Each HCON was observed through a different path length of dust and therefore observed a differing amount of zodiacal emission. Removing this emission after the co-adds has been shown compromise the data by removing structure from the images (IPAC Newsletter Vol. 5, No. 1).

This effort needed regions surveyed within the Galactic plane, encompassing Galactic longitudes $30° < \ell < 60°$. Eight separate super skyflux fields were obtained from IPAC in all four wavebands. The images are mapped as gnomonic projections of the celestial sphere. Thus there is some distortion away from the image center. However, the images were chosen to be 4° square to minimize this effect. Also, the positional inaccuracies of the distortion are small when compared to the spatial resolution of the H I data (see §II.b). The image centers are located at the Galactic equator and are spaced every 4° in longitude starting at $\ell = 30°$. The images have an effective resolution of 2.'5 and a pixel size of 1'.

Before correlations of the IR data can be made, IR emission extraneous to the the H II regions needed to be removed. This was necessary two reasons: (1) to insure that no spurious correlations are made with the background and (2) to estimate color

temperatures of the dust associated only with the H II regions. Therefore an algorithm had to be developed to remove the contribution of the Galactic IR background. Such algorithms have been applied to data at high Galactic latitudes for removing zodiacal emission ($| b | \gtrsim 30°$, Laureijs, 1989) and have been adapted for this work.

The general algorithm basically removes the contribution of point and extended sources from the images and smooths the resulting data. The resulting image is thus an estimate of the background. The original intensity map, I, is convolved with a Gaussian beam, G:

$$C = I * G \tag{1}$$

With the appropriate choice of the beam size, this procedure removes high spatial frequencies from the image. The size of the beam is usually chosen to be larger than the largest object in the field. However the Galactic plane images show crowded regions. A beam size of 1° (FWHM) proved to be an adequate choice, since there are many extended sources within a few arcminutes of each other. The resulting map, C, is then subtracted from I:

$$I' = I - C. \tag{2}$$

The map I′ contains point sources, extended object smaller than the above beamsize, and structures of high spatial frequencies. This map is then subtracted from the original image:

$$I'' = I - I'. \tag{3}$$

The map I′ may contain negative valued pixels. Since it is undesirable to increase the emission at these positions, the negative pixel in I′ are set to zero at these locations. The map I″ is then smoothed with a 20′ Gaussian beam to remove any remaining high spatial frequency structures. Thus I″ is an estimate of the emission from the Galactic background.

Figure 1 shows an example of this procedure for the 100μm image centered at Galactic longitude $\ell = 30°$. The figure shows three profiles taken at a constant galactic longitude of $\ell = 28.^{\circ}8741$. The vertical scale is in the IRAS flux units of MJy sr^{-1}. The horizontal scale is in pixels, but is directly translatable into galactic latitude. The top frame of the figure shows the original data, the middle frame the estimate of the galactic background, and the lower frame the resulting subtraction. The baselines of the profiles show rms fluctuations in range of $\sim$ 10 MJy sr^{-1} after subtraction of the background. These fluctuations are consistent with the fluctuations seen at high Galactic latitudes where the Galactic background emission is small.

Since the dust temperatures are to be compared to the gas temperatures, it is necessary to extract the dust temperatures from the IRAS images. The fluxes quoted in the IRAS survey assume a flat spectrum ($F_\nu \propto \nu^{-1}$). Thus the images need to be corrected the for the proper spectral distribution:

$$F_\nu[\text{actual}] = F_\nu[\text{quoted}]/K \tag{4}$$

where K is the color correction factor. The IRAS Explanatory Supplement (§VI.C.3) lists the color correction factors for all four wavebands for various spectral distributions as well as the algorithm for computing them.

The actual physical temperature of the dust cannot be extracted without some modeling, but the color temperatures can. If the dust emits like a blackbody, then measuring the relative brightness at two different wavelengths will indicate the temperature of the blackbody. The color temperature can be assumed to be a physical temperature if the emitter is of uniform density and optically thin. The assumption of uniform density is generally not true. However, since IRAS data have low angular resolution compared to the small the scale of these types density variations, the observations basically measure the average properties of the dust emission.

For IRAS data the ratio of the 60 to 100 μm fluxes is often used to determine

the dust color temperature. For calculating dust temperatures, however, two additional assumptions must be made if one wishes to consider the color temperature as representing a physical temperature. First, the same grain population is assumed to be responsible for both the 60 and 100μm emission. For dark clouds this assumption is not valid, since the color temperatures overestimate the physical temperatures of the dust (Clark et al., 1990). This may not be the case for H II regions, since the physical conditions are very different. However, this needs to be demonstrated.

Second, an emissivity law must be assumed for the grain population. In general the flux at a specific wavelength, F_λ, emitted be a grain in thermal equilibrium at temperature, T, is:

$$F_\lambda = B_\lambda(T)(1 - e^{-\tau_\lambda}) \tag{5}$$

where B is the Planck function and τ is the optical depth of the grain population. The optical depth is a function of wavelength and is usually assumed to be represented by a power law:

$$\tau_\lambda = \tau_0 \left(\frac{\lambda}{\lambda_0}\right)^\alpha \tag{6}$$

where α can range from -2 to -1 (Cox and Mezger 1989). For an optically thin dust component the 60/100 flux ratio is simply:

$$\frac{F_{60}}{F_{100}} = \left(\frac{60\mu m}{100\mu m}\right)^\alpha \frac{B_{60}(T_{dust})}{B_{100}(T_{dust})}. \tag{7}$$

For this effort a λ^{-1} emissivity law was used to compute the dust color temperatures, T_{dust}.

b. H I

The first phase of the BU–Arecibo Survey recently completed mapping 21cm line radiation of a portion of the inner Galaxy visible from the Arecibo Observatory

(Bania and Kuchar 1990). Currently the Survey consists of $\sim$ 11,000 spectra in the range $\mid b \mid < 0.^{\circ}5$, $30^{\circ} < \ell < 60^{\circ}$. The Survey will eventually cover $\sim$ 70 square degrees in the Galactic plane. In addition to the Galactic plane, H I maps were also made of star clusters, bi-polar flows, and H II regions. Since the Arecibo Observatory provides the smallest beamwidth for 21cm H I of any single dish antenna (HPBW = $4'$), absorption features can be detected that would be missed by H I surveys of coarser angular resolution (Bania and Lockman 1984, BL hereafter). The BL survey showed that cold diffuse H I clouds could be seen in the first Galactic quadrant as small angular sized ($\sim$8 arcmin on average) absorption features with a surface density of $\sim$20 clouds per square degree. Moreover, BL found the cool H I absorbing not only continuum radiation (from H II regions and supernova remnants) but also background 21cm line radiation. As discussed below, absorption of either type can be used to measure the kinematic distance to the cold atomic gas. BL compiled a catalog of distances to nearly 200 diffuse H I clouds and provided the impetus for the BU–Arecibo Survey.

When the analysis of absorption (against continuum sources) and self-absorption (against 21cm line radiation) is completed, the BU–Arecibo Survey is expected to have set kinematic distances to $\sim$1,000 cool ($T_{spin} \lesssim$ 100 K) H I clouds. These distances will provide an important new data base for the statistical study of interstellar clouds. Already it is clear that these absorbing clouds are associated with Galactic star clusters, H II regions, and molecular clouds. Thus the BU–Arecibo cloud distances can in principle be used to determine the intrinsic properties of the gas (neutral and ionized as well as molecular) and dust for interstellar clouds in the inner Galaxy.

As part of the BU–Arecibo Survey a detailed study was made of 19 H II regions in the Galactic plane in the form of emission-absorption experiments (Kuchar and Bania). Many of their properties were determined including H I spin temperatures, optical depths, and kinematic distances.

IV. CROSS – CORRELATION TECHNIQUE

To determine the range in velocities that the IR emission might be associated with H I absorption, a cross-correlation function was calculated. Scoville and Good (1989) used this technique for correlating CO with IRAS data. Adapting their notation for this effort, the cross-correlation function is defined by:

$$CCF(v) = \sum \frac{[T(v)T_{IR}]}{N} \times \left[\frac{1}{N} \sum T(v)T_{IR} - \sum \frac{T(v)}{N} \sum \frac{T_{IR}}{N} \right]. \qquad (8)$$

Here T_{IR} is the dust color temperture determined from the IRAS images and T(v) is the antenna temperature of the H I spectra at velocity v. The sums are taken over a square region centered on the H II region position, N is the total number of pixels involved in the summation. The size of the region is determined from the velocity integrated H I maps. This technique was originally used by Scoville and Good to correlate emission with IRAS data, rather than absorption. In this effort, correlations were made with H I absorption. Therefore it was necessary to model IR and H I emission to determine the form that the CCF would take for the case of absorption.

The IR emission was modeled as a two-dimensional Gaussian on a constant background. The parameters of the emission were based on the typical appearance of H II regions in the IRAS color temperature maps calculated from §III.a. The FWHM of the 2D Gaussian was 5′. The peak temperature of the emission was 48 K superimposed on a background of 30 K.

A single H I cloud was also modeled as a 2D Gaussian in position-position space with its centroid of emission coincident with the peak of the modeled IR emission. The half brightness contour of the H I emission was chosen as 20′. The cloud has a peak brightness temperature of 60 K, a velocity width (FWHM) of 15 $\mathrm{km\,s^{-1}}$ centered at 25 $\mathrm{km\,s^{-1}}$ in velocity space.

The parameters of the H I absorption feature were based on those typically associated with H II regions (see Kuchar and Bania). This feature, too, is Gaussian

shaped with a velocity width of $5\,\mathrm{km\,s^{-1}}$ centered at $24\,\mathrm{km\,s^{-1}}$. The absorption decreases H I emission by 10K. The absorption feature has a spatial extent of 4′, since the absorption features in Kuchar and Bania do not extend beyond the beamwidth of the Arecibo observations.

Figure 2 shows the cross-correlation as a function of velocity (in $\mathrm{km\,s^{-1}}$). The top frame of the figure shows the CCF of the IR emission and the H I emission with no absorption feature. The CCF is Gaussian shaped and peaks at the H I cloud's velocity. The lower frame includes both the H I emission and absorption features. The dip in CCF occurs precisely at the velocity of the absorption feature. Therefore the absorption manifests itself as a 'negative' peak (or relative minimum) in the correlation function.

The above case is somewhat oversimplified since there is more than one H I cloud along any line of sight traversing the Galactic plane. The above simulation was repeated with two additional model H I clouds. However, these clouds were separated in positional and velocity space from the cloud of the original simulation. The cloud centers were located 5′ from the original cloud's center and placed at 0 and 45 $\mathrm{km\,s^{-1}}$ in velocity space. The physical parameters of the original cloud were used for the two new clouds as well.

Figure 3 shows the CCF of the second simulation. Again, the top frame shows the cross-correlation of the IR emission with with only the H I emission. The CCF shows a peak at 0 $\mathrm{km\,s^{-1}}$, however, it shows a minimum at the second cloud's velocity, 45 $\mathrm{km\,s^{-1}}$. Without prior knowledge of the clouds' velocities, one could misinterpret the minimum at 45 $\mathrm{km\,s^{-1}}$ as a correlation with an absorption feature. Here the H I emission fluctuations over the region included in the summation caused by the presence of another cloud 'mimics' an absorption feature in the CCF. The lower frame of Figure 3 shows the cross-correlation with both the H I emission and absorption. The difference of these two frames thus picks out the true correlation with the absorption.

The above, somewhat simplified, simulations show that it may be necessary to correlate the emission as well as the absorption, otherwise misidentifications may result. This analysis is possible to do with the BU–Arecibo Survey database. Figure 4 shows both the emission (broken line) and absorption (solid line) CCFs for the H II region G42.4−0.3 from Kuchar and Bania. The vertical line in the figure flags the velocity of the H I absorption associated with the H II region. All the H I spectra within 4′ of the H II region position went into the calculation of both CCFs. However, the emission CCF calculation excluded the spectrum at the position nearest the H II region. In this example, there is no confusion between absorption and emission features as was demonstrated in the above simulation. Figure 4, however, reveals another complication: it shows several minima, each of which could be responsible in part for the observed IR emission. Thus an additional constraint is necessary to make a certain correlation.

V. RECOMMENDATIONS

The cross-correlation technique developed above is capable determining the velocities at which infrared emission may occur. In most cases the cross-correlation function reveals absorption features at several velocities that may be responsible for the infrared emission. To identify the feature that occurs at or near the H II region velocity as the velocity of the infrared emission requires additional information.

The dust color temperature may provide the additional constraint necessary for distinguishing among the possible absorption features. The temperature implied by the IRAS 60 to 100 μm flux ratios are relatively high for H II regions when compared to color temperatures of other infrared sources (e.g. molecular clouds). Heyer et al., 1989 examined the IRAS images of H II regions located in the Galactic anti-center. They determined an average color temperature T(60/100) = 35 K for the complex

they examined. This temperature is consistent with that found for the sample of 19 H II regions of this effort. Thus examining a more complete sample of H II regions may be needed to make solid identifications. This would involve modeling the dust emission associated with the H II regions to reproduce the color temperatures that are observed.

REFERENCES

Bania, T. M. and Lockman, F. J. 1984, Ap. J.Suppl., Vol. 54, 513.

Bania, T. M. and Kuchar, T. A. 1990, in preparation.

Beichman, C.A., Neugebauer, G., Habing, H.J., Clegg, P.E., and Chester, T.J. (eds.), IRAS Catalogs and Atlases Explanatory Supplement, Washington, D.C. U.S. Government Printing Office. 1985.

Clark, F. O., Laureijis, R. J. and Prusti, T. 1990, in preparation.

Cox, P. and Mezger, P. G. 1989, Astronomy and AstrophysicsReview, Vol. 1, 49.

Heyer, M.H., Snell, R.L., Morgan, J., and Schleorb, F.P. 1989, Ap. J., Vol. 346, 220.

Laureijs, R. Infrared Properties of Dust in Interstellar Clouds, Groningen, Netherlands, University of Groningen, 1989.

Leene, A. IRAS Studies of the Nature of Interstellar Dust and Planetary Nebulae, Groningen, Netherlands, University of Groningen, 1987.

Lockman, F.J. 1989, Ap. J.Suppl., Vol. 71, 469.

Neugebauer, G. et al.1984, Ap. J.(Letters), Vol. 278, L1.

Kuchar, T.A. and Bania, T.M. 1990, Ap. J., Vol. 352, 192.

Rowan-Robinson, M., et al.1984, Ap. J.(Letters), Vol. 278, L7.

Scoville, N.Z. and Good J.C. 1989, Ap. J., Vol 339, 149.

FIGURE 1

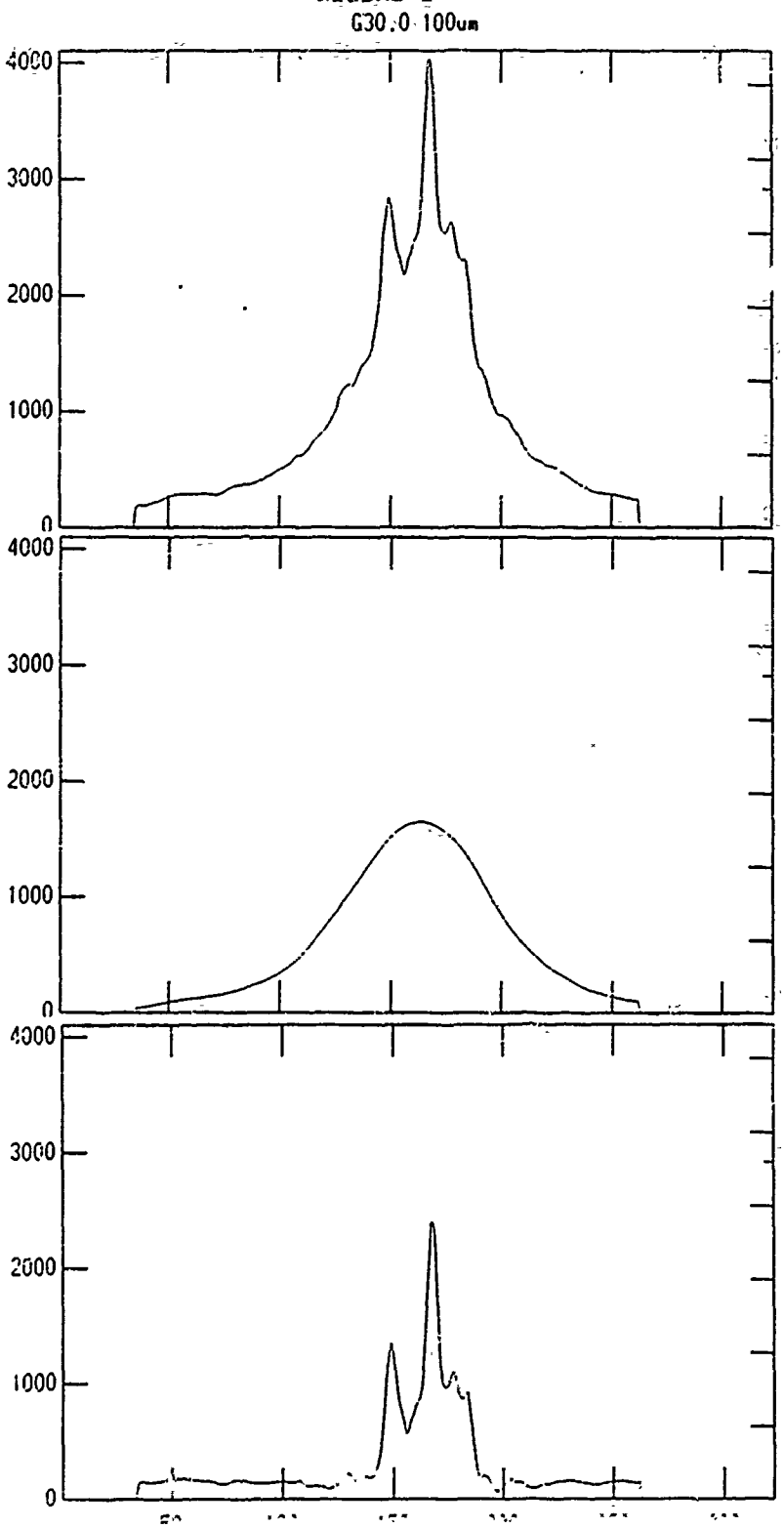
G30.0 100um
4000
3000
2000
1000
0
4000
3000
2000
1000
0
4000
3000
2000
1000
0

FIGURE 2

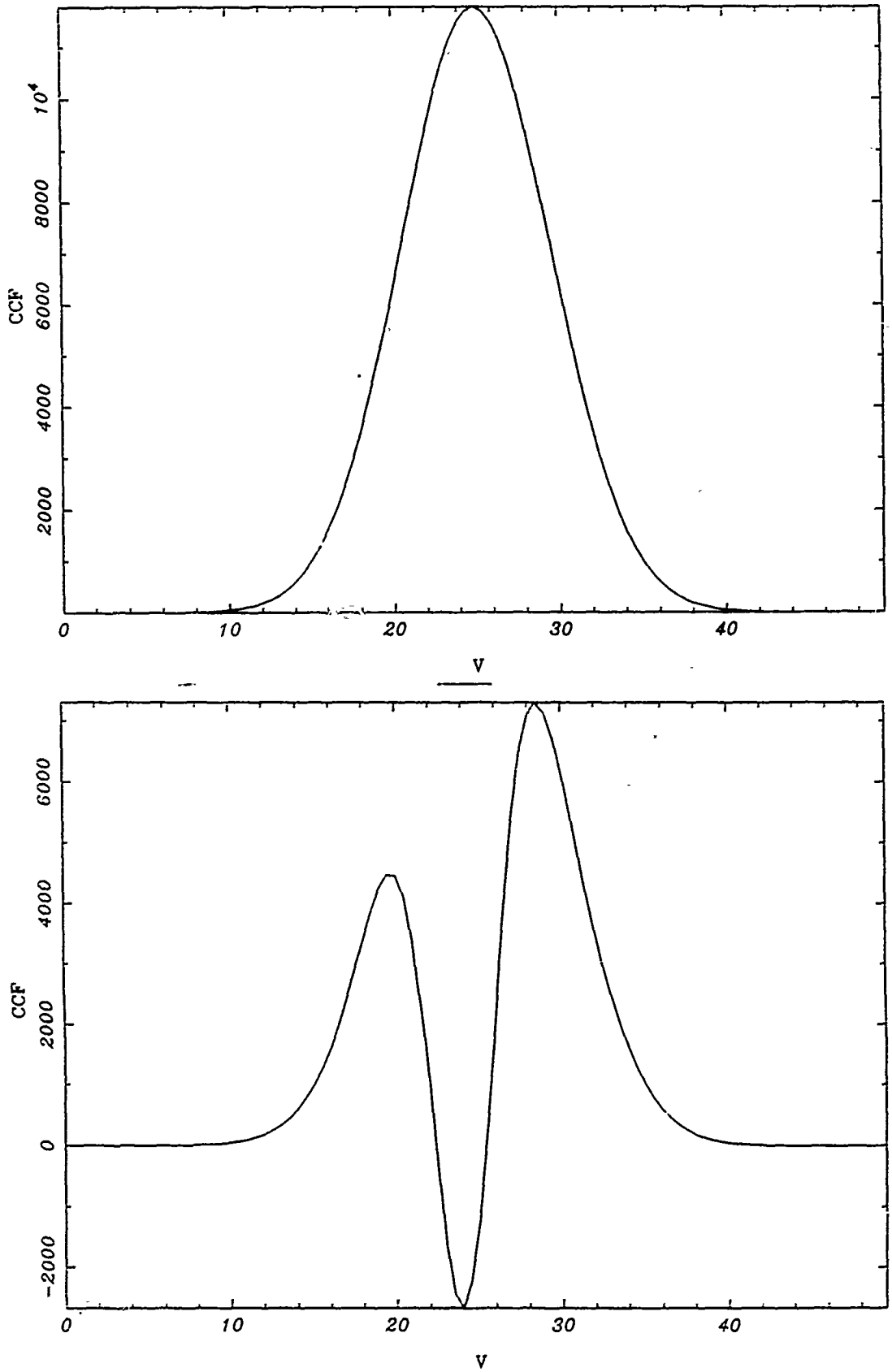
CCF
10^4
8000
6000
4000
2000
0
10
20
30
40
V
CCF
6000
4000
2000
0
-2000
0
10
20
30
40
V

FIGURE 3

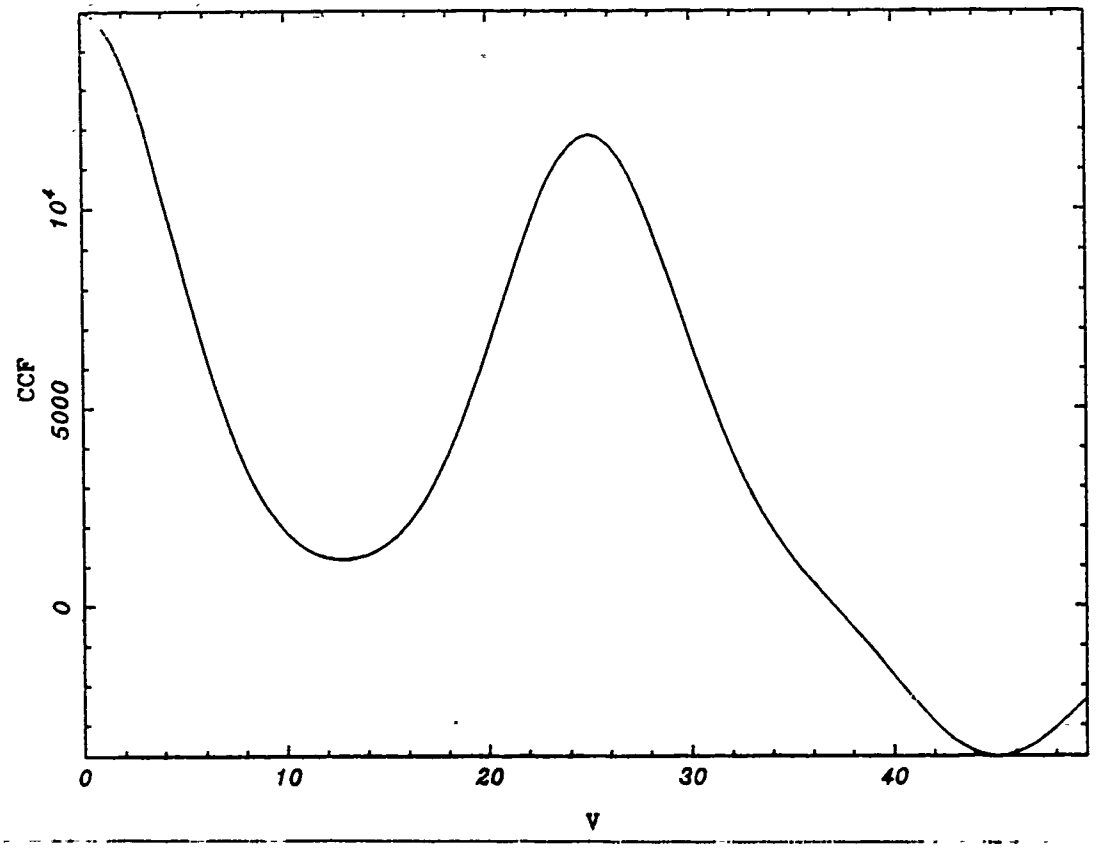

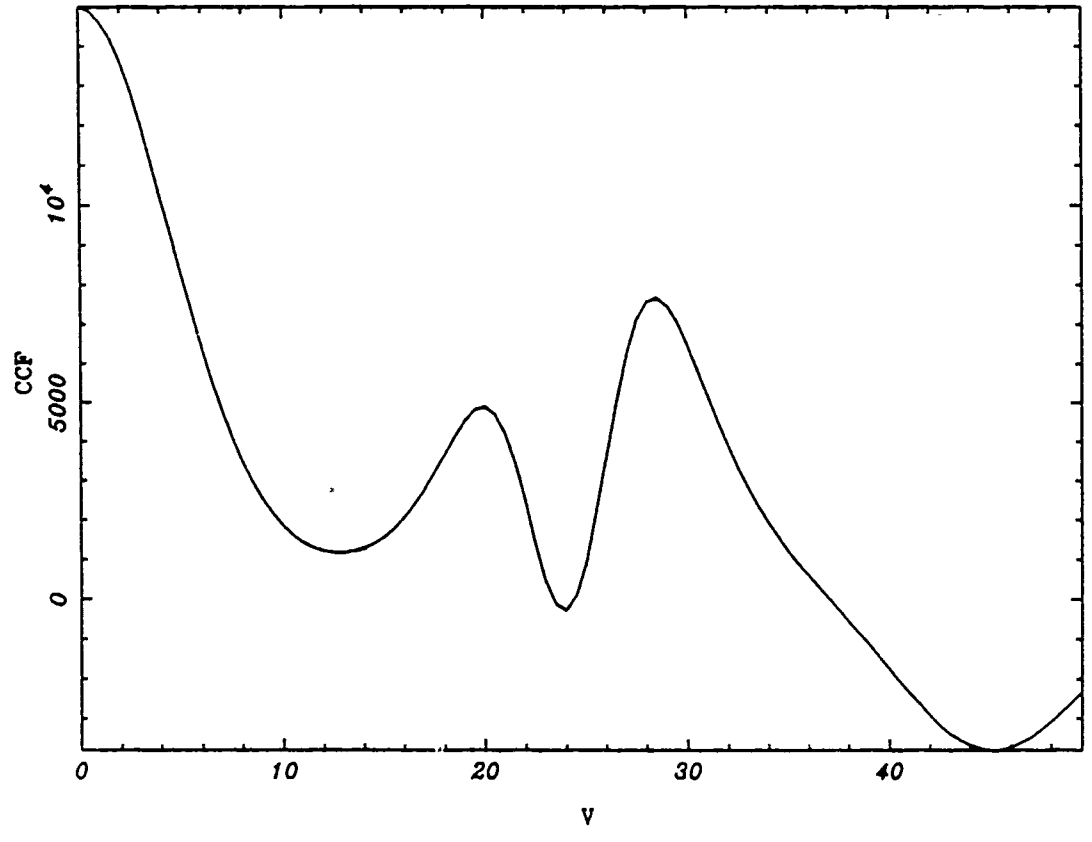

FIGURE 4

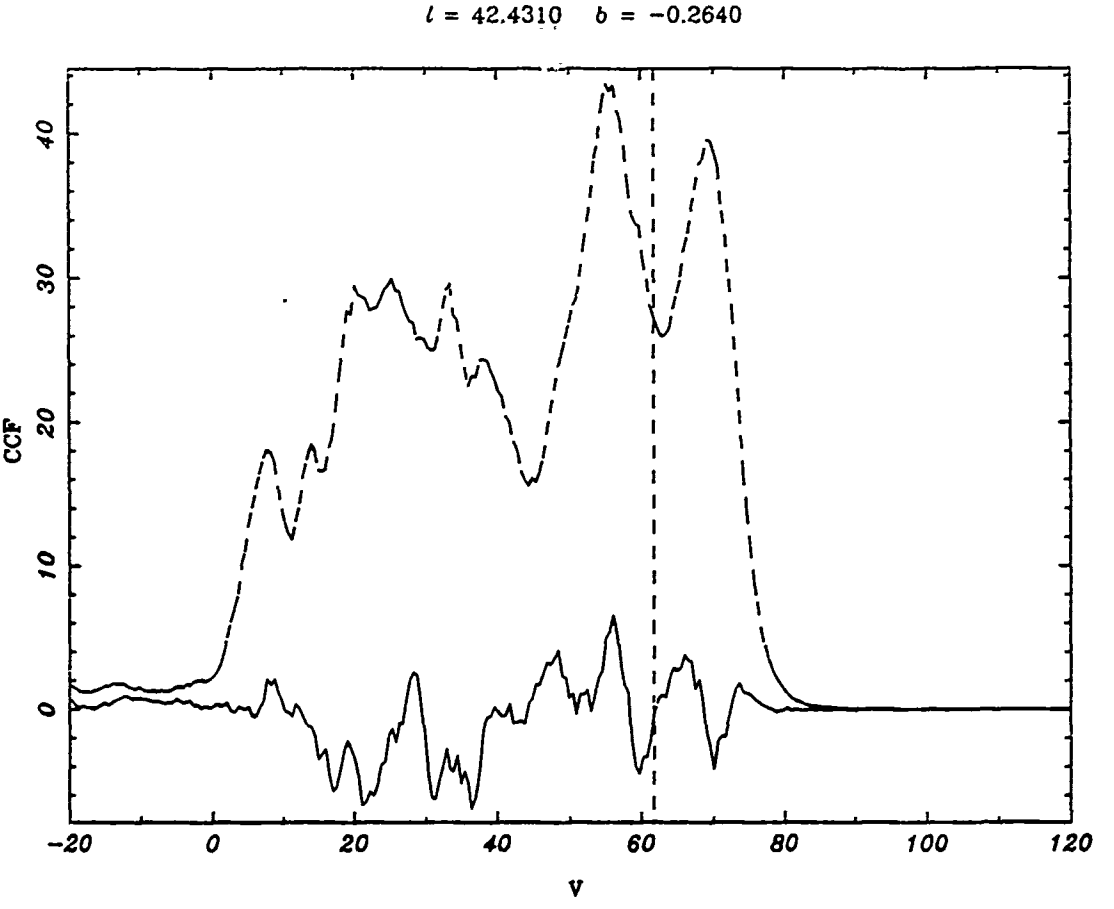

1990 USAF UES SUMMER FACULTY RESEARCH PROGRAM/

GRADUATE STUDENT SUMMER SUPPORT PROGRAM

Sponsored by the

AIR FORCE OFFICE OF SCIENTIFIC RESEARCH

conducted by the

Universal Energy systems, Inc.

Final Report

Infrared Spectroscopy of the Becklin-Neugebaurer object and Omicron Ceti

Prepared by:	John Noto
Academic Rank:	Graduate Student
Department and University:	Department of Physics and Astronomy, Tufts University
Research Location:	Air Force Geophysics Laboratory, Optical Physics Division, Infrared Branch
USAF Researcher	Paul LeVan
Date:	10 August 1990
Contract No:	F49620-88-C-0053

Infrared Spectroscopy of the Becklin-Neugebauer object and Omicron Ceti

by

John Noto

ABSTRACT

Infrared spectral images of the Becklin-Neugebauer object in Orion were analyzed for a circumstellar shell or halo. Previous speckle interferometric measurements have indicated the possible presence of a core star surrounded by an extended halo. No shell was detected with GLADYS at a statistically significant level. A decrease in silicate feature emission strength and probable circumstellar dust loss was confirmed for Omicron Ceti.

I. Introduction:

The Becklin-Neugebauer object (BN) and Omicron Ceti are two very unusual infrared objects. BN is in the closest region of high mass star formation, the Orion Molecular Cloud complex or OMC. Past observations have found evidence indicating that BN is a young star surrounded by a large cloud of dust, undergoing ~100 magnitudes of extinction in the visible. A circumstellar shell ~2" is believed to surround BN and should be detectable with large ground based telescopes

Omicron Ceti or Mira is the defining star of a class of irregular variable stars known as mira type variables. Past observations have introduced the possibility of both a secular as well as periodic change of strength in the silicate emission feature of Omicron Ceti.

GLADYS, the array spectrometer at the Air Force's Geophysics Laboratory is an excellent device to study both objects. The spectrometer is composed of a 58x62 Si:Ga array detector and is used in the 8-14μ region. Silicate emission peaks at 9.8μ and gradually falls off until about 13μ, which is perfect for the study of BN and Omicron Ceti.

Previously I have researched BN at the University of Rochester in the Infrared Astronomy group. My senior thesis involved the reduction and analysis of near infrared (1.2-4μ) CCD data taken at the IRTF in the winter of 1984. While my previous worked involved two dimensional images and some aperture photometry, the method of data reduction was similar to the method used to reduce and analyze GLADYS data. This previous experience in infrared astronomy contributed to my assignment in the Optical Physics Division.

II. Objectives of the Research Effort:

The first major goal was to use the GLADYS spectrometer to study the extended emission around the Becklin-Neugebauer source in Orion (BN). The circumstellar shell and accompanying silicate emission feature should be visible to GLADYS. Techniques for the reduction and analysis of two dimensional spectra would be developed for application to other extended sources such as planetary nebula and supernova remnants. IRAF, the NOAO image processing software package, was used to look at profiles of the BN image in an attempt to measure spatial extent. An interactive fitting program was used to fit the points along the spatial axis for a variety of wavelengths and then the widths of the half and eighth maxima points were measured. The widths were compared with those a standard star. No extended emission was detected and my other project was to be the analysis of the infrared spectrum of Omicron Ceti.

On July 10, 1990 Omicron Ceti was observed and the data was reduced using the standard one dimensional techniques. Comparison of our spectra with spectra taken from 1968-1973 showed the confirmation of a possible secular decrease in the amount of dust surrounding Omicron Ceti as well as the possibility of a periodic decrease as well.

III. The Becklin-Neugebauer object:

The Becklin-Neugebauer object in Orion (BN) is believed to have a circumstellar shell or halo and speckle interferometric observations seem to indicate the presence of an unresolved core star surrounded by a shell or halo of ~1.5". GLADYS has a spatial resolution of 1-1.5", so it was hoped that BN's shell could be resolved directly.

The BN data was reduced using IRAF, an image processing package developed by the National Optical Astronomical Observatories (NOAO), the only difference between the reduction of BN data and previous GLADYS spectra was an attempt to preserve the spatial extent. Normally spectra are reduced to one spatial dimension with 62 pixels along the wavelength axis. A standard star and polystyrene film are then used to determine the pixel number to wavelength correspondence. The final spectra are fluxed using assumed values of standard star fluxes.

IRC +10216 was the first reference star we looked at and various methods were used to try to compare BN to IRC +10216. The BN data was maintained as a 10x62 image, spatial peaks were found by making a series of cuts or spatial profiles along the spatial axis at a number of different wavelength positions. Ideally a point source would exhibit a perfect gaussian profile, unfortunately the optics and the atmosphere conspire to distort the perfect gaussian.

A two dimensional "combined" spectrum for each object was generated by spatially aligning the individual frames of each object and coadding. The combined spectra of BN and IRC +10216 were than aligned with each other by using the peak of the spatial profiles as a center. Subtracting the

two images would result in a spectrum of just the extended region of BN. Unfortunately, this method did not yield any sort of conclusive result.

The standard star, α Taurii, was chosen for another attempt using a different method. Although α Taurii has a lower signal to noise ratio than IRC +10216, the IRC +10216 frames were taken during a different night of the observing run and it was hoped that α Taurii could clarify the results.

In the alternate method using α Taurii, a six piece cubic spline was fit to the data points along the spatial dimension of both the BN and α Taurii frames. The widths of the full width one-half and one-eighth maxima points, FWHM and FWEM respectively, were then measured on the fitted curve. The results for both BN and α Taurii are in tables 1&2.

Six curves were measured for each of the BN frames and for the six brightest α Taurii frames. Figure one shows one such curve fitted to a BN frame with the FWHM and FWEM points labeled on the figure. Three measurements were made in the long wavelength region, near the 10μ peak of the silicate emission, and three in the short wavelength region. An average and standard deviation was calculated for the FWHM and the FWEM in both the long and short wavelength regions. Then the ratio of the widths of the long to short wavelength regions of the array for both BN and α Taurii, and for both the FWHM and FWEM, was calculated. Atmospheric and diffraction effects would cause the ratio to be greater than unity for a point source. A ratio removes the average of atmospheric seeing effects from the comparison since both ends of the array experience the same seeing conditions. An extended source would show a ratio different than the ratio of a non-extended source, since the temperature at unit optical depth might be different at the peak wavelength of the silicate emission feature.

Our results show that the FWHM and FWEM widths of α Taurii are larger than the FWHM and FWEM widths of BN, which we interpret as a difference in the effective atmospheric seeing disks. The measurements show that the ratio of long to short wavelength FWEM of BN is ~1σ smaller than that of α Taurii, and while this is not statistically significant it is still an interesting result.

IV. Omicron Ceti:

Omicron Ceti is the defining star of the mira class variable and has a ten month asymmetric period. The July 1990 observations of Omicron Ceti were reduced using the usual techniques into a one dimensional spectrum. Figure two shows just the GLADYS Omicron Ceti spectra with 3σ statistical error bars, and a 1100° K blackbody curve has been included as a reference. The blackbody has a positive curvature while the Omicron Ceti spectrum has a negative curvature. This is known as an infrared excess, the star is emitting more energy in the infrared than a blackbody. An infrared excess can be caused by dust surrounding the star reemitting stellar light at a longer wavelength.

The GLADYS Omicron Ceti spectrum is very flat in the short wavelength region but does have a slightly increasing slope beginning at 9.8μ and then falls off rapidly starting at 12.5μ. This effect is known as the silicate emission feature and is noticed in many stars with an infrared excess.

GLADYS is a long slit spectrometer with a slit width of 2" so there would be some light lost if the atmospheric seeing disk were larger than 2". Nevertheless, night to night repeatability in the absolute flux levels of stars

measured with GLADYS is at the level of 15%. Our reference star, ß Pegasi, is variable at the 15% level so we can expect an accuracy of ~25% for our photometry of Omicron Ceti. Our spectra can be used only to compare shapes and relative strengths of spectral features and as a flag for any major secular changes. In Figure three one can see our spectra of Omicron Ceti with 3σ statistical error bars and absolute flux levels ±25% of the true spectrum (not shown). Included for comparison is the spectrum of Gillett et al.

We observed Omicron Ceti at a phase or point on it's light curve, of 0.78, corresponding to 72 days before maximum. Gillett et al. observed Omicron Ceti with a phase of 0.96, one week before maximum. Gillett et al.'s photometry was done using older values for the fluxes of his reference star, either α Herculis or α Bootes. Gillett et al.'s assumed fluxes for his standard stars is about 12% too low on α Bootes and 6.5% too large for α Herculis causing their Omicron Ceti absolute flux level to be uncertain by these approximate amounts. The shape of their Omicron Ceti spectrum is unlikely to be incorrect since the shape shortward of the 9.7μ silicate feature of two other oxygen-rich stars (α Ori and μ Cephei) in his survey compare favorably with more recent observations.

The feature of note is the size of the silicate feature in Gillett et al.'s spectrum. GLADYS and Forrest et al.'s data is shown in Figure four. Forrest et al.'s data was taken 4 years after Gillett et al.'s spectra and spans about two-thirds of a cycle, over three separate periods. The shape of the silicate feature in both the GLADYS and Forrest et al. spectra is very similar. This means the strength of the silicate feature relative to the continuum is nearly the same in these spectra. It can also be seen in Figure four that Forrest et al.'s continuum level, the region of the spectrum

to the left of 9μ and to the right of 12.5μ, is not as steep as the GLADYS continuum.

The change in the ratio of silicate feature to the continuum since the spectrum of Gillett et al. was noticed by Forrest et al. and is most likely a single event in the temporal behavior of Omicron Ceti. The GLADYS spectra confirms this large change and we can also note that there has not been any further significant decrease in silicate emission since Forrest et al.'s observations in the early 1970's.

According to Forrest et al. the decrease in silicate feature strength corresponds to a factor of ~2 decrease in the amount of dust surrounding Omicron Ceti. Forrest et al. also mentions the possibility that there could be a slight but constant secular decrease in silicate feature strength and therefore in the amount of dust surrounding Omicron Ceti. We find no evidence of any continuing significant change in silicate feature strength or corresponding dust loss.

V. Recommendations:

Our negative results concerning the shell surrounding BN would seem to indicate that observations utilizing more complex image processing or observing techniques are needed. Speckle interferometry seems to be the way to go for this particular object. GLADYS should observe more extended objects, as it was seen during this project that IRAF has enough capabilities to allow the image processing of extended spectra without having to develop significant amounts of new software. A method needs to be developed in which single lines and sections of a set of two dimensional spectral images, each with a different relative spatial position, can be

combined into a single spectra while preserving the absolute errors. This would allow the coadding of a series of spectra of an extended object while preserving the spatial extent. This would greatly improve the sensitivity of GLADYS and enhance its usefulness for studying objects with a spatial extent.

A systematic observing program of variable stars would be an interesting GLADYS project. Mira class variables, including Omicron Ceti, could be monitored consistently using the Wyoming Infrared Observatory and GLADYS. The data should be collected over a long time period frequently enough so that a star could be studied over an entire cycle for >2 periods. Stars that are only suspected of being variables could also be observed in order to see if they are variable enough to preclude their use as reference stars.

Acknowledgements:

I would like to thank Universal Energy Systems, the Air Force Systems Command and the Air Force Office of Scientific Research for the opportunity and funding to conduct this research.

Paul LeVan was a real pleasure to work with, his support, patience (a lot of patience) and encouragement proved to be invaluable. I would also like to thank Frank Clark for many helpful and insightful discussions. Stephan Price, the director of the Geophysics Lab, Optical Physics Division, should be mentioned for informing me of this opportunity in the spring of 1990.

References:

1. Gezari, D., Schmitz, M., and Mead, J.M., 1987, Catalog of Infrared Observations, NASA Reference Publication 1196.

2. Gillett, F.C., Low F.J., and Stein, W.A., 1968, Ap. J., **154**, 677.

3. Johnson, H., 1968, Ann. Rev. Astr. Ap., **4**.

4. Forrest, W.J., Gillett, F.C., and Stein, W.A., 1975, Ap. J., **195**, 423.

5. Mattei, J., AAVSO 1990, Prediction Bulletin 53.

6. Mattei, J., AAVSO 1989, Prediction Bulletin 52.

7. LeVan, P.D., Pub. A.S.P., **102**, 648.

8. LeVan, P.D., and Sloan, G., Pub. A.S.P., **101**, 646.

Appendix A

This program was written in the command language script contained within IRAF. The language is designed for the casual programmer to give an added dimension to the image processing. The command language is similar to Fortran with the added benefit that predefined IRAF commands and logicals can be used to manipulate images without resorting to the clumsy array method of Fortran.

At the telescope data is recorded by averaging together the results of two second frame interpretations. The first "layer" contains the actual image values while the second "layer" contains the sum the squares of the values divided by the number of values. This program is used to convert the layer2 numbers into the standard deviation of the mean.

$$\mu=\sqrt{\frac{\sum(X_i-<X>)^2}{N-1}}$$

N is the number of frames

μ is the deviation of the population

$$\mu^2=\left(\frac{N}{N-1}\right)\left(\frac{1}{N}\sum X_i^2 - <X>^2\right)$$

$$\mu=\sqrt{\frac{N\left(\frac{\sum X_i^2}{N}-<X>^2\right)}{N-1}} \quad \text{with the} \quad sd_{mean}=\frac{\mu}{\sqrt{N}}$$

$$\text{so } \mu=\sqrt{N}\sqrt{\frac{\frac{\sum X_i^2}{N}-<X>^2}{N-1}} \quad \text{therefore} \quad sd_{mean}=\sqrt{\frac{(layer2)-(layer1)^2}{N-1}}$$

This is implemented in the following program and the comments should make the program entirely self explanatory.

```
procedure sdmimages (images,nframes)

int    nframes
string images        { prompt = 'list of imput images' }
struct *list

begin
   string   l_images, temp, temp2, tmp, s1
   char     sec1,sec2
# sec1 is the image slice, sec2 in the noise slice
#                    of a 62x30x2 array
   sec1 = '[*,*,1]'
   sec2 = '[*,*,2]'

# explicit prompt for inputs
    tmp    = mktemp ("tmp$junk")
    temp   = 'garb1'
    temp2  = 'garb2'

# begin scanning image list
   sections (l_image,option="root",>tmp)
   list =tmp
   while (fscan(list,s1) != EOF) {

# removes the .imh suffix
   i =strlen(s1)
   if (substr(s1,i-3,i) ==".imh") {
     s1=substr(s1,1,i-4)
   }

# gets the number of frames from the fits header
#       and places the value in x
   imgets (s1,'frames')
   x=real(imgets.value)

# then x is printed along with the image name
   print (s1//"  frames="//x)

# the pixel type is changed to 'real'
   chpixtype (s1,s1,"real")

# the appropriate arithmetic is done
   imar (s1//sec1,'*',s1//sec1,temp)
   imar (s1//sec2,'-',temp,temp)
   imar (temp,'/',(x-1.0),temp)
   imsqrt (temp,temp2)

# the original noise is replaced with the rms values
   imcopy (temp2,s1//sec2)

# all temporary files are deleted
   imdel (temp//','//temp2,ver-,>& "dev$null")
   }
   del (tmp,ver-,>& "dev$null")

# the end
end
```

TABLE 1

alpha Tau-FW(1/2)M

IMAGE	NPIX	MEAN	STDDEV	MIN	MAX
tau040	3	2.119	0.4251	1.758	2.588
tau040	3	1.898	0.2235	1.729	2.152
tau042	3	1.964	0.1923	1.757	2.138
tau042	3	1.847	0.1197	1.757	1.983
tau043	3	2.161	0.3161	1.814	2.433
tau043	3	1.603	0.06149	1.533	1.646
tau044	3	2.447	0.08546	2.348	2.503
tau044	3	1.941	0.073	1.856	1.983
tau047	3	3.080	0.1288	2.939	3.192
tau047	3	1.875	0.2617	1.631	2.152

alpha Tau-FW(1/8)M

IMAGE	NPIX	MEAN	STDDEV	MIN	MAX
tau040	3	5.170	2.047	3.586	7.481
tau040	3	3.572	1.257	2.77	5.02
tau042	3	4.055	1.57	2.939	5.85
tau042	3	3.469	0.3667	3.066	3.783
tau043	3	4.988	0.9676	3.909	5.78
tau043	3	3.258	0.32	2.995	3.614
tau044	3	3.816	0.1057	3.713	3.924
tau044	3	3.311	0.1317	3.182	3.445
tau047	3	*	*	*	*
tau047	3	4.359	1.845	2.981	6.455

IMAGE	FWEM RATIO	FWHM RATIO
tau040	1.45	1.11
tau042	1.16	1.06
tau043	1.53	1.35
tau044	1.15	1.26
tau047	*	1.64
average	1.32 +/- .20	1.28 +/- .23
average	1.25 +/- .17 w/o tau043	1.20 +/- .13 w/o tau047

* the image was too noisy for a FWEM to be measured

TABLE 2

BN-FW(1/2)M

IMAGE	NPIX	MEAN	STDDEV	MIN	MAX
bn050	3	2.536	0.1071	2.419	2.629
bn050	3	2.423	0.2619	2.179	2.7
bn051	3	3.295	1.189	2.602	4.669
bn051	3	2.635	0.1897	2.447	2.827
bn052	3	2.053	0.4289	1.631	2.489
bn052	3	1.781	0.1181	1.645	1.856
bn053	3	1.856	0.02433	1.828	1.87
bn053	3	2.17	0.6438	1.434	2.629
bn054	3	2.25	0.1837	2.039	2.377
bn054	3	1.964	0.5607	1.364	2.475

BN-FW(1/8)M

bn050	3	5.405	1.921	4.078	7.608
bn050	3	5.288	0.6169	4.585	5.738
bn051	3	7.013	0.8079	6.539	7.945
bn051	3	5.606	1.764	4.345	7.622
bn052	3	4.852	1.137	4.092	6.159
bn052	3	2.784	1.112	1.505	3.515
bn053	3	3.717	0.4178	3.248	4.05
bn053	3	3.563	1.043	2.405	4.43
bn054	3	4.139	0.5722	3.684	4.782
bn054	3	3.647	1.356	2.082	4.444

IMAGE	FWEM RATIO	FWHM RATIO
bn050	1.022	1.047
bn051	1.251	1.251
bn052	1.743	1.153
bn053	1.043	0.855
bn054	1.135	1.146
average	1.23 +/- .30	1.09 +/- .15
average	1.11 +/- .10 w/o bn052	1.15 +/- .08 w/o bn053

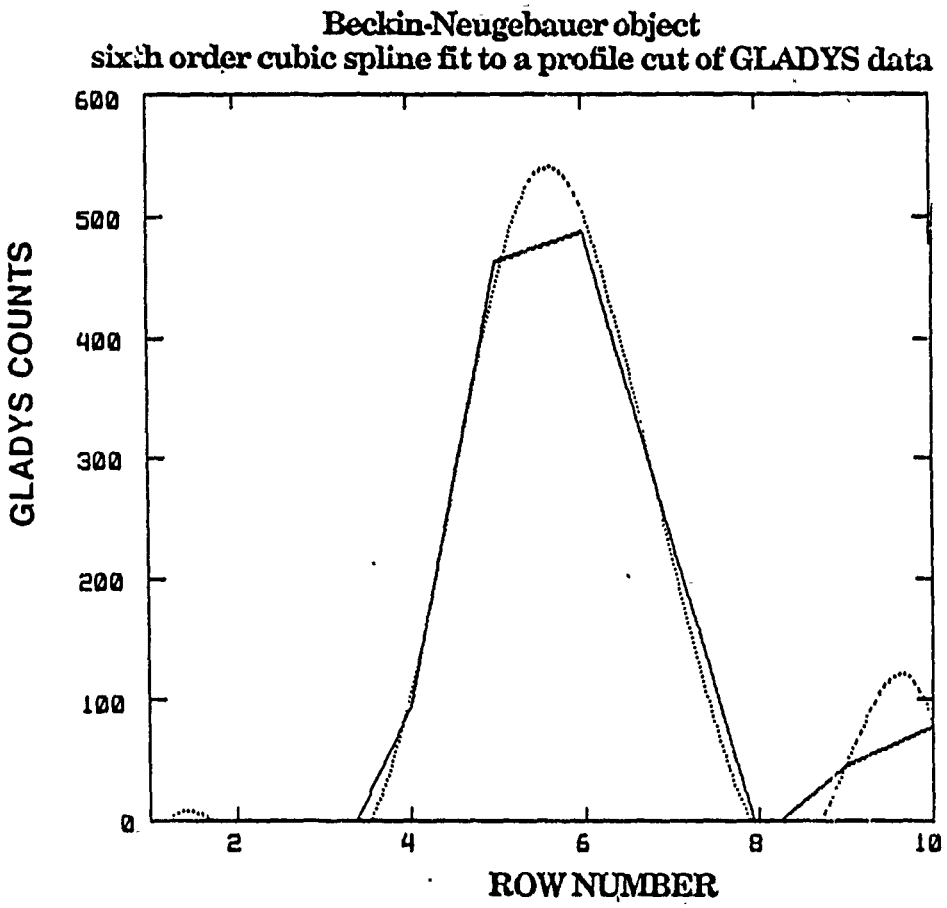

Fig. 1. This type of fit was used to determine the Full Width Half and Eighth Maxima of the "gaussian" profile of BN.

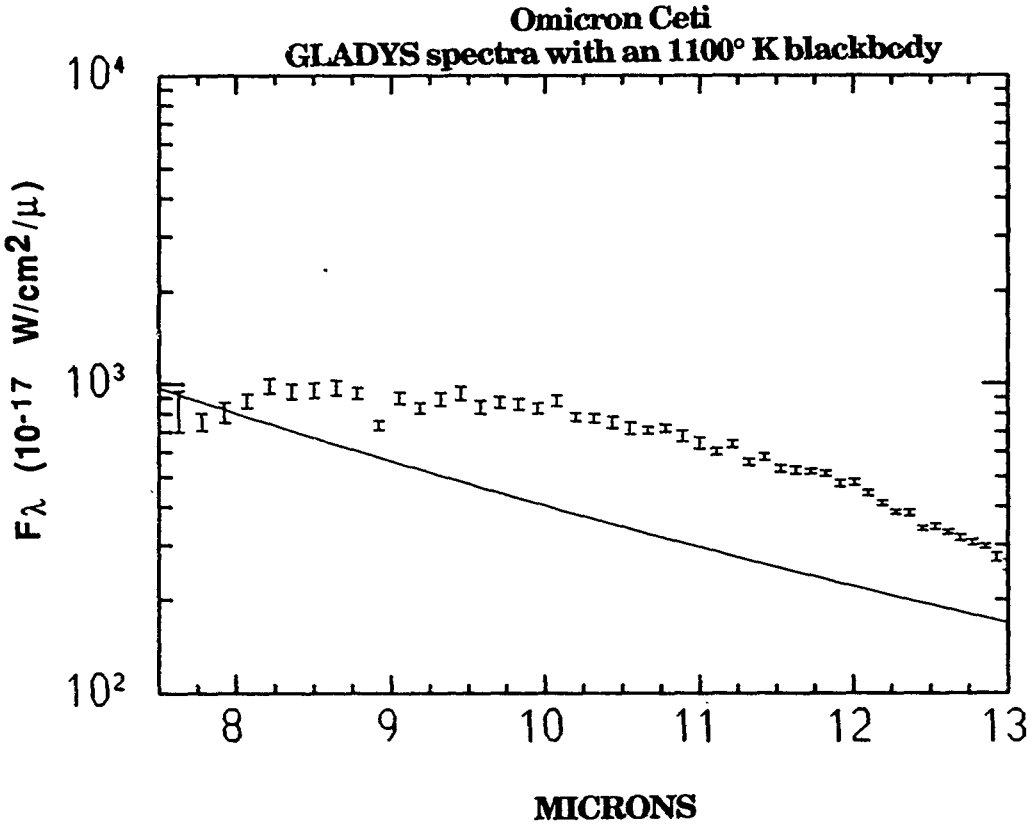

Fig. 2. This shows the GLADYS spectrum with 3σ statistical error bars. Notice the shape of the 1100°K blackbody in comparison to Omicron Ceti. The flux is correct for Omicron Ceti but not for the blackbody, which is included for shape comparison only.

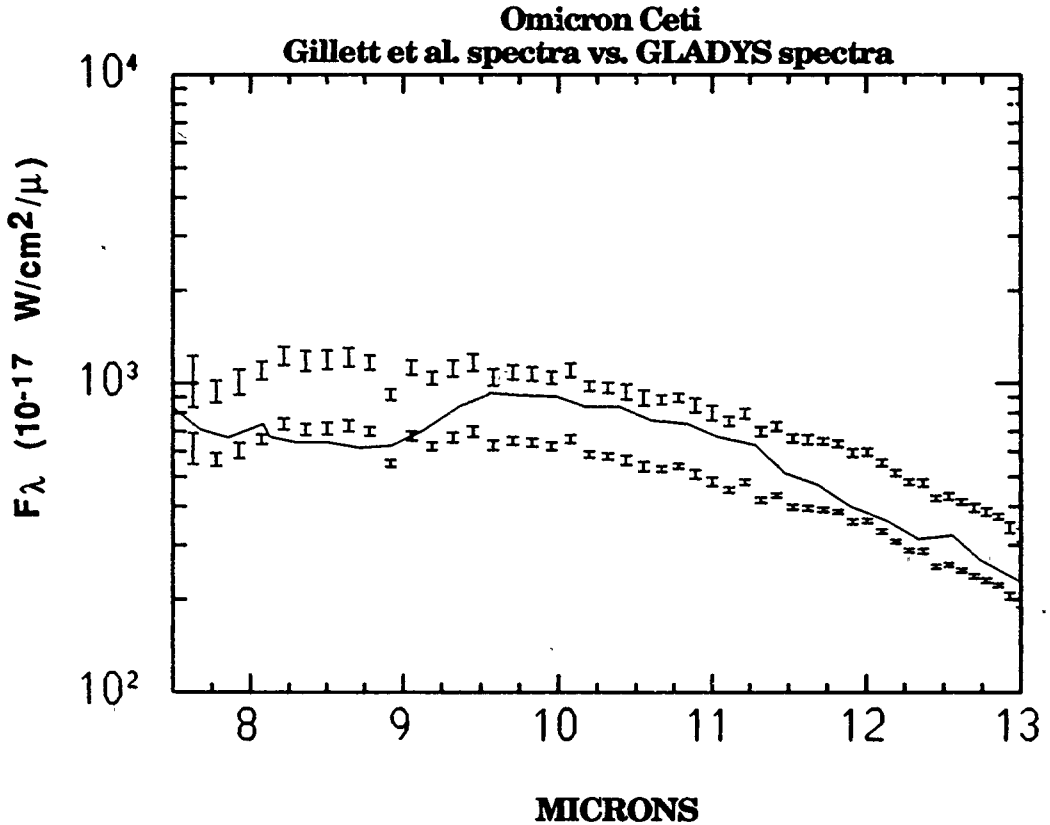

Fig. 3. This is a comparison of Gillett et al. flux for Mira with ours. The upper and lower spectra are ours ± 25% with 3σ absolute error bars. The solid line spectra is from Gillett et al. The difference in shape can also be seen in spectra from Forrest et al.

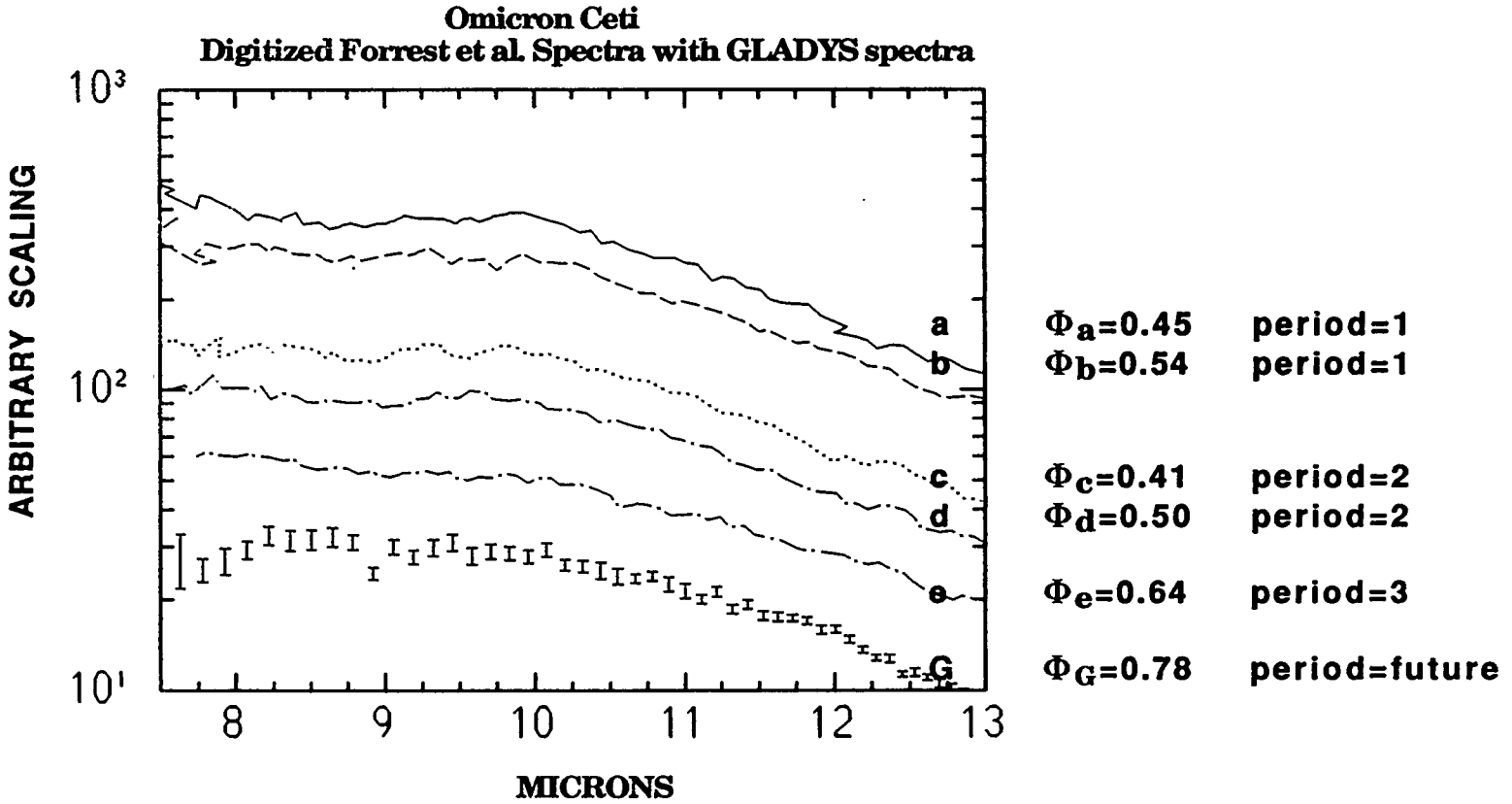

Fig. 4. This shows five of Forrest's spectra of Mira each at a different point on Mira's light curve, superimposed on his data is the GLADYS spectra with 3σ absolute error bars. Notice the similarity in the shape of the silicate emission (9.7μ-12.5μ) feature, also notice the steeper continuum in the GLADYS data.

1990 USAF-UES GRADUATE STUDENT RESEARCH PROGRAM

Sponsored by the

AIR FORCE OFFICE OF SCIENTIFIC RESEARCH

Conducted by the

Universal Energy Systems, Inc.

FINAL REPORT

A New Formal Hierarchy for Multiple Scattering

Prepared by:	Brahm A. Rhodes
Academic Rank:	PhD Candidate
Department and	Division of Engineering
University:	Boston University
Research Location:	USAF Geophysics Laboratory/LY
	Hanscom AFB
	Bedford MA 01731
USAF Researcher:	Dr. Jean King
Date:	27 Sept 90
Contract No:	F49620-85-C-0013

A New Formal Hierarchy for Multiple Scattering

Brahm A. Rhodes

Abstract

A formal hierarchy for multiple scattering theory is developed for wave propagation in an infinitely extended isotropic, homogeneous medium containing a statistical distribution of scatterers. The formalism developed is analogous to hierarchical approaches of non-equilibrium statistical mechanics. Dimensional analysis of the hierarchy displays the significance of three dimensionless parameters representing the dilution, scattering strength, and scatterer size. Perturbation techniques are used to solve the system of equations. To first order, agreement with the multiple scattering theories of Twersky and Foldy is established. The connection with radiative transfer is shown in this first order solution. Recommendations for future research are presented.

Acknowledgments

I wish to thank the Air Force Systems Command and the Air Force Office of Scientific research for sponsorship of this research. I am grateful to the staff at Universal Energy Systems for their concern and assistance in the adminstrative aspects of this program.

The author wishes to acknowledge the inspiration and guidance of the late Prof. Asim Yildiz, and extend my sincere gratitude to Dr. Jean King for his willingness to listen to my ideas and his encouragement and to Vin Falcone for his suggestions and support. Thanks to my advisor, Dr. G. v.H. Sandri, whose guidance throughout this project was invaluable. I express gratitude to Dr. M. K. Hinders, T. W. Drueding and S. D. Bogan for our many hours of discussions.

I Introduction

The Atomospherics Sciences division of the Air Force Geophysics Laboratory is currently intersted in determination of temperture profiles from remotely sensed data. The equation for radiative transfer is recast as a convolution equation and utilizing the method of differential inversion (DI), developed by Dr. Jean King [8], it is solved to obtain a unique temperature profile. The result thus obtained is significant in that it does not require an initial guess for the temperture profile.

My research interests have been in the areas of multiple scattering and new mathematical structures known as hyperdistributions, developed by Prof. Guido Sandri, at Boston University. Hyperdistributions form an algebraic field closed under the convolution product, and thus they provide a convenient way to solve convolution type integral equations. Essentially, a hyperdistribution is an expansion in the derivatives of the **Dirac delta-function**. Hyperdistributions have some distinct advantages over Fourier transform techniques for determining the convolution inverse of various kernels and it can be shown that the differential inversion formula are a special case of hyperdistribution expansions. My work in scattering and basic research on hyperdistributions and their application for solving integral equations of the type that arise in radiative transfer and image processing contributed to my assignment to the Atmospheric Sciences Division of the Geophysics Laboratory.

II Objectives of the Research Effort

Current methods for determining the temperature profile from remotely sensed radiance data rely on an iterative solution, which requires an initial guess or constraint for the temperature profile that does not depend on the current radiance measurements. Thompson et.al. [11] state that the validity of the temperature profile solution from any given iterative solution depends fundamentally on the validity of the particular additional contraints or initial guess. It is noted that different guesses produce dif-

ferent profiles from the same radiance data. The DI solution of the convolution form of the radiative transfer equation can be shown to be unique within a certain class functions and does not require an initial guess. Namely, a unique solution is available only for kernels with exponential decay, i.e. $K(x) \sim e^{-|x|}$.

My initial goal was to extend the DI method to include functions with algebraic decay $K(x) \sim |x|^{-1}$. This was to be accomplished by utilizing an expansion in **Cauchy's Principal Value** distribution. However it was determined that the differential inversion series arises as a special case of a hyperdistribution expansion only due to the simple behavior of the Dirac delta function under integration.

Since it appears that the DI method cannot be extended to include non-exponential type functions, it was decided to utilize my experience with multiple scattering and conduct basic research into wave propagation in random media. Starting from first principles, I have recently developed a hierarchy of equations, as part of my dissertation research at Boston University, to describe multiple scattering of waves propagating in a medium consisting of a random distribution of scatterers. The hierarchy is analogous to approaches which have been sucessful in the field of non-equilibrium statistical mechanics. The solution of the hierarchy describes the average total field (coherent wave) due to a wave propagating through a distribution of scatterers embedded in an isotropic, homogeneous medium. Note that the method developed in this report is applicable to discrete or continuous random media and can be applied to acoustic, electromagnetic and elastic wave propagation.

Dimensional analysis of the hierarchy displays the significance of three dimensionless parameters. A **functional assumption** is made for the reduced wave functions, to be defined in the next section. which along with perturbation or asymptotic expansions in the dimensionless parameters is used to investigate solutions for various limiting cases. By considering these limiting cases we can determine agreement with and correction to other multiple scattering theories. In particular, to first order in the dilute limit, agreement with the multiple scattering formalisms of Foldy [1] and

Twersky [12]-[14] is obtained and the connection to radiative transfer is established.

Of particular significance is the goal of obtaining the equations of **transport theory**[1]. It is hoped that a Mini-grant can be obtained to continue this research, since multiple scattering and radiative transfer play significant roles in many areas of interest to the Air Force. The overall goal of this research is to formulate and investigate a new approach to multiple scattering, based on techniques and concepts from non-equilibrium statistical mechanics.

III The Complete Multiple Scattering Problem

The problem of multiple scattering can be considered as a linear version of the many-body problem. Its relation to the single scattering problem is analogous to the relation between the many-body problem and the two-body problem. The wave that propagates through a discrete random media satisfies the **complete** wave equation,

$$\left(\nabla^2 + n^2(\vec{r})k^2\right)\psi^N = 0 \tag{1}$$

where we define the square index of refraction by

$$n^2(\vec{r}) \equiv 1 - \sum_{i=1}^{N} \mu(\vec{r} - \vec{r}_i) \tag{2}$$

μ is a function that vanishes outside the scatterer centered at $\vec{r}_i$. The wave function, ψ^N, has an explicit dependence on the position vector and an implicit dependence on the scatterer locations and properties. We rewrite this equation as

$$(\nabla^2 + k^2)\psi^N = U^N\psi^N \tag{3}$$

with

$$U^N \equiv -k^2 \sum_{i=1}^{N} \mu(\vec{r} - \vec{r}_i) \tag{4}$$

We note that this formulation is valid for a continuous random media, with the appropriate choice for μ.

[1] Radiative transfer is included in the generic term **transport theory**.

The solution of (1) or (3) is generally intractable, since boundary conditions must be satisfied on all the scatterers and N is typically a very large number. Keller [6] describes "honest " and "dishonest" methods for the solution of random equations such as (3). Honest methods entail finding the exact or approximate solution to (3) and then averaging the solution to find mean values and other statistics. In solving the complete problem randomness plays no role.

Dishonest methods take advantage of the randomness in order to simplify the equation before solving it. For example, (3) is averaged over an ensemble and an equation for the mean value, $< v^N >$, is obtained. The "dishonest" part comes about through the use of some unproven assumption about the statistics of the solution. These assumptions are generally necessary, so as to make the equations for $< \psi^N >$ determinate. Most of the major results in multiple scattering are derived from dishonest methods, since exact solutions are difficult to obtain. One goal of this field of mathematics is to show that dishonest solutions are approximations of honest ones.

We will be using a dishonest method to obtain solutions to (3). The complete wave equation will be averaged over the phase space of $N - s$ scatterers, resulting in a set of coupled equations for the reduced wave functions, defined in the next section.

IV Statistical Mechanics Formalism

Statistical Preliminaries

We simply state here the relevant statistical functions necessary to develop the hierarchy. The N-scatterer distribution function, p_N, is defined by the probability that the set of scatterers is in a particular configuration,

$$p_N(\zeta_1, \ldots, \zeta_N) d\zeta_1 \ldots d\zeta_N \tag{5}$$

where ζ_i represents the position and all scattering variables (size, material properties, orientation, etc) of the i^{th} scatterer. We use the following normalization for p_N

$$\int p_N \prod_{i=1}^{N} \frac{d\zeta_i}{V} = 1 \tag{6}$$

where V is the volume accesible to the scatterers. With this normalization, the probablility density has the normal form, $V^{-N} p_N$. Correlation functions, g_{21} are given by the standard definition

$$p_2(\zeta_1, \zeta_2) = p_1(\zeta_1) p_1(\zeta_2) + g_{12}(\zeta_1, \zeta_2) \tag{7}$$

We define the reduced wave functions, ψ^s, in terms of a **projection operator**, $\mathcal{P}$

$$\mathcal{P}^s \psi^N = \psi^s = \int \psi^N p^N \prod_{i=s+1}^{N} \frac{d\zeta_i}{V} \tag{8}$$

It is easy to see that $\mathcal{P}^s$ satisfies the condition,

$$\mathcal{P}^s \mathcal{P}^s = \mathcal{P}^s \tag{9}$$

The Statistical Hierarchy

Applying (8) to (3) and assuming that the wave function and probability distributions are symmetric with respect to particle positions we obtain a hierarchy of N coupled equations[2]. The s^{th} equation is given by

$$(\nabla^2 + k^2)\psi^s = U^s \psi^s - \frac{N-s}{V} \int U(\vec{r} - \vec{r}_{s+1}) \psi^{s+1} \, d^3 r_{s+1} \tag{10}$$

Taking the **thermodynamic** or **bulk** limit,

$$\lim_{N,V \to \infty} \frac{N}{V} = n_0 \tag{11}$$

where n_0 is a finite number and gives the average number of scatterers per unit volume, we obtain (10) as

$$(\nabla^2 + k^2)\psi^s = U^s \psi^s + n_0 L^s \psi^{s-1} \tag{12}$$

[2]We have averaged over all scattering variables and thus are left with a configuration of identical scatterers allowing us to assume the reduced wave functions are symmetric in the position variables.

The operator L^s is defined as

$$L^s\psi^{s-1} \equiv \int U(\vec{r} - \vec{r}_{s+1})\psi^{s+1}\, d^3r_{s+1} \tag{13}$$

The hierarchy equations in the form given by (12), exhibit only the effect of the parameter, n_0. In order to highlight all the possible dimensionless parameters in (12) we define the nondimensional variables

$$\vec{r} = a\vec{r} \qquad\qquad \vec{r}_i = a\vec{r}_i \tag{14}$$

where a is some characteristic length of the system, such as average scatterer size. Dropping the tilde notation, we write the nondimensional form of the hierarchy as

$$(\nabla^2 - \kappa^2)\psi^s = \kappa^2 U^s \psi^s + \kappa^2 \alpha L^s \psi^{s-1} \tag{15}$$

$$\alpha \equiv n_0 a^3, \qquad \kappa \equiv ka, \qquad U^s \equiv \sum_{i=1}^{s} -\mu(\vec{r} - \vec{r}_i) \tag{16}$$

There are clearly three relevant physical parameters: ka the dimensionless wave number, n_0a^3 the dilution parameter and μ the scattering strength parameter. All regimes of physical interest are represented by letting these parameters cover the orders of magnitude: $(\epsilon^{-1}, 1, \epsilon)$ where ϵ is an infintesimal. There are many possible combinations, some of which are nonphysical. The most interesting include the Rayleigh (low frequency) regime $\kappa \sim \epsilon$, dilute $\alpha \sim \epsilon$. Born (weak scattering) $\mu \sim \epsilon$ and the geometric optics (high frequency) regime $\kappa \sim \epsilon^{-1}$. These various regimes can be explored to find agreement with and correction to current theories of multiple scattering.

Functional Assumption and the Dilute Limit

We make two assumptions that have found success in non-equilibrium statistical mechanics. The first assumption is known as the "functional **ansatz**" and is simply stated as follows: the reduced wave functions ψ^s depend on position, $\vec{r}$, only through the $s = 0$ wave function, that is

$$\psi^s(r; r_1 \ldots r_s) \equiv \psi^s(r_1 \ldots r_s \mid \psi^0(r)) \tag{17}$$

where we have supressed the vector notation, $\vec{r} = r$ for convenience. We assume that this assumption applies on a length scale which is large compared to the smallest characteristic length associated with the system. A rigorous proof of the validity of this assumption is not available, but it appears reasonable since the higher order wave functions vary on a scale proportional to a while the coherent wave varies on a scale proportional to $V^{\frac{1}{3}}$, where V is the volume of the system and a is a characteristic dimension of a scatterer. We have, in effect, **coarse-grained** the length scale of the problem, where distances are now measured on a scale $\chi \sim r/\epsilon \gg r$.

The second assumption requires us to expand the reduced wave functions, for $s \geq 1$, in powers of a small parameter ϵ,

$$\psi^s = \sum_{n=0}^{\infty} \epsilon^n \psi_n^s \tag{18}$$

These assumptions are direct analogs to assumptions made by Bogolibov [2], [5], [16] in his analysis of the BBGKY hierarchy in the theory of non-equilibrium statistical mechanics[3]

Using the expansion (18) in the $s = 0$ equation and the ordering $\alpha \sim \epsilon$ gives

$$(\nabla^2 + \kappa^2)\psi^0 = \epsilon\kappa^2 L^0 \psi_0^1 + \epsilon^2 \kappa^2 L^0 \psi_1^1 + \cdots \tag{19}$$

The coherent wave, ψ^0, propagates through an "effective medium" with dimensionless wavenumber K without scattering, but with attenuation and thus should satisfy a homogeneous wave equation given by,

$$(\nabla^2 + K^2)\psi^0 = 0 \tag{20}$$

Clearly a solution to this equation is

$$\psi^0 = e^{iK \cdot r} \tag{21}$$

[3]The analogous assumption in statistical mechanics is that the s-particle distribution functions depend on time only through the 1-body distribution function after a time period long compared to the time of a collision of two particles. Bogoluibov's expansion is in terms of inverse powers of the specific volume.

Turning our attention to the full hierarchy, we substitute (18) into (15), with $\alpha \sim \epsilon$ and collect terms in powers of ϵ to obtain the following set of equations

$$\begin{aligned} \epsilon^0: \quad (\nabla^2 + \kappa^2)\psi_0^s &= \kappa^2 U^s \psi_0^s \\ \epsilon^1: \quad (\nabla^2 + \kappa^2)\psi_1^s &= \kappa^2 U^s \psi_1^s + \kappa^2 L^s \psi_0^{s+1} \\ &\vdots \\ \epsilon^m: \quad (\nabla^2 + \kappa^2)\psi_m^s &= \kappa^2 U^s \psi_m^s + \kappa^2 L^s \psi_{m-1}^{s+1} \end{aligned} \tag{22}$$

We mention here several interesting observations, the first being that the effects of the higher order wave functions are "ordered" in powers of epsilon. Specifically, we note that the zeroth order perturbation for $s = 1$, ψ_0^1, is simply the equation for a single scatterer located at position r_1. Also, the first order perturbation, ψ_1^1 requires the solution of the equation for ψ_0^2. This is a two-body problem and correlations may be present, but the term in (19) that contains ψ_1^1 is of second order in ϵ, thus suggesting that two-body correlations are a second order effect. The same argument can be used to show that higher order correlations are also higher order effects in ϵ. It is important to note that these correlations cannot, in general, be neglected.

V First Order Solution

We now carry out a solution to first order and show agreement with the theories of Foldy [1] and Twersky [12]-[14] for negligible correlations. To obtain a first order solution we adopt a formalism due to Twersky [15] in which we consider a "two-space scatterer". A two-space scatterer is one in which the incident wave propagates in a medium with wave number k_1, impinges upon a scatterer characterized by wave number k_2, which then radiates into a space with wave number k_3. Details of this formalism are available in Twersky [15] who has used it in multiple scattering problems [14].

The two-space method requires three different wave equations, one for the interior of the scatterer and two for the exterior region plus appropriate boundary conditions.

The required equations are given as follows:

$$(\nabla^2 + \kappa^2)\phi = 0 \tag{23}$$

$$(\nabla^2 + K^2)\psi^0 = 0 \tag{24}$$

$$(\nabla^2 + \kappa_2^2)\psi_0^1 = 0 \tag{25}$$

where $\kappa_2^2 = \kappa^2(1 + \mu)$ and $\mu \equiv U^1$.

Equations (23) and (24) are assumed to hold in all space, while (25) is valid only inside the scatterer. In addition, we need (19), to first order

$$(\nabla^2 + \kappa^2)\psi^0 = \epsilon\kappa^2 L^0 \psi_0^1 \tag{26}$$

To proceed we need to make a further assumption, which is that for negligible correlations the reduced wave function is simply a product of the reduced proability distribution and a suitable wave function, this is expressed mathematically as

$$\psi^1 = \hat{\psi}^1 p_1(r_1) \tag{27}$$

Inserting (27) into (26) gives

$$\left(\nabla^2 - \kappa^2\right)\psi^0 = \epsilon\kappa^2 L^0 \hat{\psi}_0^1 p_1 \tag{28}$$

Following Twersky [15], we consider the case where the incident wave propagates in the z-direction and satisfies (24). Assuming we have "tenuous scatterers" ($K \approx \kappa_2 \approx \kappa \gg 1$) large compared to wavelength and neglecting reflection and refraction effects we use the leading term in the WKB approximation [3], [9], [15] with the transmission coefficient set to unity, to obtain

$$\hat{\psi}_0^1 \approx e^{iKz_s'} e^{i\kappa_2(z_0' - z_s')} \tag{29}$$

where z_s' is a point on the surface of the scatterer from which the incident ray reaches the interior point z_0' as measured from the center of the scatterer. Essentially we

have treated the internal field by approximating it as a straight ray with the phase modified by the scatterer medium it has traversed. We write (29) in the form

$$\hat{\psi}_0^1(r_0') \approx \psi^0(r_s)\Phi(r' - r_s) \tag{30}$$

Applying the Green's function,

$$G(r - r') = \frac{e^{i\kappa|r-r'|}}{-4\pi \mid r - r' \mid} \tag{31}$$

to (28) we obtain the integral equation

$$\psi^0 = \phi_{in} + \epsilon \int G(r - r')\kappa^2\mu(r' - r_1)\hat{\psi}_0^1(r')p_1(r_1)\, dr_1 dr' \tag{32}$$

where ϕ_{in} is the incident wave in free κ-space. Making a change of variables under the integral sign (wrt dr') to $r' = r_0' + r_1$ and using (30) gives

$$\psi^0 = \phi_{in} + \epsilon \int G(r - r_1 - r_0')\kappa^2\mu(r_0')\psi^0(r_s')\Phi(r_0' - r_s')p_1(r_1)\, dr_0' dr_1 \tag{33}$$

Taking a far-field limit, i.e. $R = r - r_1 \gg r_0'$ we write the Green's function as, $G(R - r_0') \sim G(R)e^{-i\kappa\hat{o}\cdot r_0'}$. Using this in (33) gives

$$\psi^0 = \phi_{in} - \epsilon \int G(R)\psi^0 p_1 \left[\int e^{-i\kappa\hat{o}\cdot r_0'}\kappa^2\mu(r_0')\Phi\, dr_0'\right] dr_1 \tag{34}$$

The form of the integral in brackets is simply the form of a scattering amplitude with internal field Φ [3],[4], that is,

$$f(\hat{o},\hat{\imath}) = f(\theta) = \frac{1}{4\pi}\int e^{-i\kappa r_0'\cos\theta}\kappa^2\mu(r_0')\Phi\, dr_0' \tag{35}$$

where $\hat{\imath}$ and $\hat{o}$ are unit vectors in the direction of incidence and observation, respectively and θ is the angle between the two vectors. Using this result we can write (34) as

$$\psi^0(r) = \phi_{in} + \alpha \int u_1^s \psi^0(r_1)p_1(r_1)\, dr_1 \tag{36}$$

where

$$u_1^s = \frac{e^{i\kappa|r-r_1}}{\mid r - r_1 \mid} f(\theta) \tag{37}$$

The result given in (36) is identical to the equation for the coherent field, first obtained by Foldy [1] and later by Twersky [4], [12] [4]

The physical significance of (36) is clear if we apply the wave operator $(\nabla^2 + \kappa^2)$ to both sides, assuming a uniform distribution of scatterers ($p_1 = 1$), we obtain

$$(\nabla^2 + \kappa^2)\psi^0 = -4\pi\alpha f(\theta)\psi^0 \tag{38}$$

comparing with (20) we find

$$K = \kappa + 2\pi\alpha f(\theta)/\kappa \tag{39}$$

Since $f(\theta)$ is in general complex, even for lossless scatterers, the coherent wave propagates with attenuation, but no scattering.

The **total cross-section** of a scatterer is related to the forward scattering amplitude by the "forward scattering" theorem

$$\frac{4\pi}{\kappa}\Im f(0) = \sigma_s + \sigma_a = \sigma_t \tag{40}$$

where σ_s, σ_a, σ_t are the scattering, absorbtion and total crossections of the particle and $f(0)$ is the scattered amplitude in the forward direction[5]. Since the imaginary part of K is given by, $\Im K = \frac{1}{2}\alpha\sigma_t$ we see that the coherent intensity attenuates according to $I_c = \mid \psi^0 \mid^2 = e^{-\alpha\sigma_t z}$.

With these results in hand we now show the connection between Twersky's results and radiative transfer.

VI Connection to Radiative Transfer

The fundamental quantity in radiative transfer is the **specific intensity**, $I(r, \hat{s})$. Ishimaru [4] has shown that the the correlation function, $< \psi(r_a)\psi^*(r_b) >$ is related

[4]Note: Here we use the symbol ψ^0 to represent the coherent wave where Foldy uses $< v >$.

[5]Since our analysis is in terms of dimensionless parameters we note that these cross-sections are actually "efficiencies", $Q_i = \sigma_i/\sigma_g$, where σ_g is the geometric cross section of a scatterer and $i = s, a$ or t.

to the specifc intensity by

$$< \psi_a \psi_b^* >= \int I(r_c, \hat{s}) e^{iK_r \hat{s} \cdot r_d} \, d\Omega \tag{41}$$

where $r_c = \frac{1}{2}(r_a + r_b)$, $r_d = r_a - r_b$ and K_r is the real part of K. This simply states that the correlation function is the Fourier transform of the specific intensity.

It has also been shown that, by using (41), Twersky's equations for multiple scattering are equivalent, under certain assumptions, to the equation of transfer [3],[4], which is given by

$$\frac{d}{ds} I(r, \hat{s}) = -\rho \sigma_t I(r, \hat{s}) + \frac{1}{4\pi} \rho \sigma_t \int p(\hat{s}, \hat{s}') I(r, \hat{s}') \, d\omega' \tag{42}$$

where the phase function, $p(\hat{s}, \hat{s}') = \frac{4\pi}{\sigma_t} \mid f(\hat{s}, \hat{s}') \mid^2$ and $\rho = \alpha a^{-3}$ is the density. In conventional form we write the transfer equation as

$$\frac{dI}{dz_1} = k\rho(B - I) \tag{43}$$

where the absorbtion coefficient k is proportional to the total cross-section and the source term, B is the integral in (42).

VII Conclusion

A formal hierarchy of integro-differential equations, analogous to hierarchies in non-equilibrium statistical mechanics, has been developed from first principles. The solution of this hierarchy describes the coherent wave propagation through a random media (discrete or continuous). Dimensional analysis highlights three dimensionless parameters which characterize several limiting regimes for wave propagation and scattering. Making a functional ansatz and expanding the reduced wave functions in a small parameter we can use the simplified set of equations to obtain solutions, good to various orders of ϵ, for the coherent wave. To first order, we have obtained the results of Twersky and Foldy and shown the connection to radiative transfer.

We make several interesting observations: In the simple illustration above we have essentially neglected backscattering[6]. Twersky [12] showed that Foldy's result was obtained from the expanded representation by neglecting repeated scattering (backscattering) between scatterers. Second, correlations are only negligible in very dilute or very weak scattering systems and Foldy's results only apply in the case of negligible correlations. The fact that, by making two approximations, (dilute limit and no backscattering) we arrive at Foldy's result suggests that the hierarchy has validity for a multiple scattering formalism. Third, we note that standard approaches to multiple scattering generally attempt to find the ensembled average of the Green's function representation for the field of a fixed configuration of scatterers, where we have obtained the ensembled average of the governing differential equation and then obtained the Green's function representation for the average field. The intermediate steps should highlight the differences. Fourth, our functional ansatz, at least to first order, is similar to the assumption made by Foldy, who assumed that the field averaged over all but one scatterer was the same as the total averaged field. To first order, our assumption plus the application of the two space method is essentially the same as Foldy's, although, in general, it should be less restrictive, since the functional form is yet to be specified for higher wave functions.

VIII Recommendations

The above results and observations combined with the success of similar techniques and ideas in non-equilibrium statistical mechanics, suggests that this formalism can provide a accurate description of multiple scattering in random media and should be investigated further. We note that the method used to obtain the first order solution is a relatively simple perturbation expansion. There exist several other, more sophisticated, methods available that should be attempted. Most notably is

[6]Note: For scatterers large compared to wavelength it is well known that most of the scattering is in the forward direction.

the method of **multiple scales**. In this method, successively longer length (or time scales) are introduced serving to produce a set of equations that are presumably easier to solve than the original. This method has found wide spread use in the field of non-linear mechanics and kinetic theory [2], [9]. Keller [7] describes a general method based on two distinct length scales, that has been applied to the problem of porous media.

The true test of the method will be to include two-body correlations and consider higher order wave functions. We note that correlations are generally considered via a Mayer cluster expansion based on a summation decomposition [5], [16]. In order to deal with the long correlation lengths in a plasma, Ramanathan [10] proposed a cluster expansion based on a product decomposition, this approach may prove useful in dense systems. In addition to these analytic investigations, preliminary work is being carried out leading to the direct simulation of the hierarchy on a massively parallel computer. This work should provide insight into the behavior of the higher order wave functions and may provide a quantitative measure for the functional assumption.

The connection to radiative transfer should be more direct from the hierarchy than it is from Twersky [4]. A consistent set of equations for the correlation functions needs to be developed, in order to establish this connection via the hierarchy. The radiative transfer equation can be expected, a priori, to apply in a high frequency, dilute limit, but a satisfactory justification for this type of treatment lies in showing that a consistent wave treatment leads to the same results.

In many problems of wave propagation and scattering, the medium in which the wave travels may be classified as a discrete or continuous random media, for example, the atmosphere, ocean, composite materials, geological and biological media. These natural and man-made media vary randomly in space and time and the waves in such media vary randomly in amplitude and phase. These random fluctuations and scattering present a variety of practical problems in many areas, such as communications, remote-sensing, detection and non-destructive test & evaluation. An accurate means

of describing, predicting and simulating the effects of these random fluctuations can be applied to a variety of problems in the above areas.

References

[1] Foldy, L.L., **The Multiple Scattering of Waves** Phys Rev. **67**, 107 (1945)

[2] Goldberg, P. and Sandri, G. **Power Series of Kinetic Theory. I. Perturbation Expansions**, Phys. Rev. **154** 188 (1967)

[3] Ishimaru, A. **Wave Propagation and Scattering in Random Media**, vol. 1, Academic Press, New York (1978)

[4] Ishimaru, A., **Wave Propagation and Scattering in Random Media**, vol. 2, Academic Press, New York (1978)

[5] Liboff, R., **Introduction to the Theory of Kinetic Equations**, John Wiley & Sons, New York (1969)

[6] Keller, J.B., **Wave Propagation in Random Media**, Proc. Symp. Appl. Math. **13**, 227, Amer. Math Soc., Providence. Rhode Island (1964)

[7] Keller. J.B., **Statistical Mechanics and Statistical Methods in Theory and Application**, (Uzi Landman ed.), Plenum Press, New York (1976)

[8] King J.I.F, Hohlfeld. R.G.. and Killian, J. C., **Application and Evaluation of a Differential Inversion Technique for remote Temperature Sensing**, Met and Atmos Phys. **41**. 115 (1989)

[9] Nayfeh, A., **Perturbation Methods**, John Wiley & Sons, New York (1973)

[10] Ramanthan, G.V., **A New Cluster Scheme in Statistical Physics**, J Math Phys. **7**, 1507 (1966)

[11] Thompson, O. E., Dazlich, D. D., and Hou, Y., **The Ill-posed Nature of the Sattellite Temperature Retrieval Problem and the Limits of Retrievability**, JAOT **3** 643 (1986)

[12] Twersky, V., **On Propagation in Random Media of Discrete-Scatterers**, Proc. Symp. Appl. Math. **16**, 84, Aner. Math Soc., Providence, Rhode Island (1964)

[13] Twersky, V., **On Scattering of Waves by random Distributions. I. Free Space Scatterer Formalism**, J Math Phys. **3**, 700 (1962)

[14] Twersky, V., **On Scattering of Waves by random Distributions. II. Two-Space Scatterer Formalism** J Math Phys. **3**, 724 (1962)

[15] Twersky, V., **On a General Class of Scattering Problems**, J Math Phys. **3**, 716 (1962)

[16] Wu, T., **Kinetic Equations of Gases and Plasmas**, Addison-Wesley, Reading, MA (1966)

1990 USAF-UES SUMMER FACULTY RESEARCH PROGRAM/

GRADUATE STUDENT RESEARCH PROGRAM

Sponsored by the

AIR FORCE OFFICE OF SCIENTIFIC RESEARCH

Conducted by the

Universal Energy Systems, Inc.

FINAL REPORT

Low Temperature Properties of Dilute Tunneling Quadrupoles

Prepared by:	Andrew D. Galasso
Academic Rank:	Graduate Student
Department and	Department of Physics
University:	Worcester Polytechnic Institute
Research Location:	Rome Air Development Center
	Solid State Directorate
	Hanscom Air Force Base
USAF Researcher:	Alfred Kahan
Date:	27 August 1990
Contract No:	F49620-88-C-0053

Low Temperature Properties of Dilute Tunneling Quadrupoles

by

Andrew D. Galasso

ABSTRACT

The thermal conductivity and the thermal expansion are calculated for dilute concentrations of four orientational tunneling quadrupoles (TQ's) in a non-polar host crystal. The exact eigenfunctions for TQ pairs are used to calculate the relaxation times from resonance scattering. The partition function for the TQ pairs is used to calculate the thermal expansion. We find that: (i) only those TQ pairs which interact ferroelastically contribute to the thermal conductivity at very low T; (ii) the thermal conductivity is proportional to T^2 at very low T, the same T dependence observed in glasses; (iii) the TQ-TQ interaction leads to a negative term in the thermal expansion analogous to what is observed in dilute quadrupolar glasses.

I. INTRODUCTION

In a recent paper[1] it was shown that dilute concentrations of four-orientational interacting tunneling elastic quadrupoles (TQ's) give low energy excitations similar to those observed in glasses. For glasses it has been proposed[2,3] that the low energy excitations arise from two level tunneling states (TLS) with a random potential barrier between the potential wells. An ad-hoc constant density of states gave some of the experimentally measured low temperature properties of glasses. However, the origin of the TLS has not been determined, and the constant density of states is generally assumed without microscopic justification. The TQ model allows one to derive the constant density of states from fundamental considerations.

The distinctive feature of the TQ model is the seemingly paradoxical fact that the strain interaction of strongly coupled TQ pairs leads to the smallest energy excitations.[1] The fact that flux creep in high T_c superconductors is believed also to be dominated by strain interactions leads one to believe that aspects of the TQ model could be relevant to the problem of the tunneling of vortices in superconductors. Thus, in addition to clarifying the glass problem, a better understanding of the TQ model could lead to a theoretical explanation of certain aspects of superconductivity which are not presently well understood.

As an undergraduate at Worcester Polytechnic Institute I had the opportunity to work with Professor Michael Klein for my Major Qualifying

Project (senior thesis). Professor Klein has been working under a Mini-Grant from the Faculty Research Program. At that time, my task was to calculate the eigenfunctions for interacting TQ pairs. These eigenfunctions are needed to calculate the relaxation times and the thermal conductivity for the TQ's. Since understanding the relaxation process may help clarify the behavior of the low temperature sound velocity in some high T_c superconductors, the results of that effort contributed to my assignment to the present research. Professor Klein, in conjunction with Dr. Alfred Kahan of the Rome Air Development Center became interested in the applicability of the TQ model to the motion of vortices in the presence of random barriers, and I was interested in assisting in the calculations.

II. OBJECTIVES OF THE RESEARCH EFFORT

My assignment in the 1990 Summer Graduate Student Research Program (GSRP) was to provide calculations for the thermal and relaxation properties of interacting TQ's, thus hopefully clarifying the nature of the TQ-TQ interaction and how it affect glassy properties. After becoming familiar with the concepts of the model and with the computer calculations necessary to evaluate the integrals which arise, the objectives of the research were to calculate the relaxation times, the thermal conductivity and the thermal expansion for dilute four-orientational TQ's. The relaxation times may help clarify the behavior of the low temperature sound velocity in some high T_c superconductors.[4]

At low temperatures T glassy materials[1] are found experimentally to have a thermal conductivity which is proportional to T^2. One research objective is to determine whether the TQ model predicts such a T dependence and, if so, over what T regions the T^2 dependence is valid.

It is often mentioned in the literature in connection with TLS in glasses that there are two types of tunneling units.[5] Since the fundamental nature of the tunneling states has not been determined, this observation is justifiable only on a phenomenological basis. However, it is hoped that the current model, which begins with a microscopic Hamiltonian, should contribute some understanding to this question.

Experiments with quadrupolar glasses[6] have shown that the thermal

expansion becomes negative at very low T. Previous models, which do not start from a microscopic Hamiltonian, have not been successful in explaining the negative thermal expansion. Thus, in using the TQ model to calculate the thermal expansion one would like to examine particularly whether one obtains a negative thermal expansion.

III. THE RELAXATION TIMES AND THE THERMAL CONDUCTIVITY

a. approach

Since at low T resonance scattering is the dominant mechanism for phonon scattering,[7] it is sufficient to calculate the relaxation times from resonance scattering by the TQ's. Having a matrix representation for the Hamiltonian for TQ pairs[1] allows one to calculate the exact eigenfunctions for interacting TQ pairs. One may then use the phonon perturbed Hamiltonian to calculate the matrix elements of transition. The Golden Rule allows one to then find the relaxation times from resonance scattering.[7] Integrating a function which depends on the relaxation times gives the thermal conductivity.

b. results

Our results show that for very low phonon energies the relaxation times from resonance scattering are inversely proportional to the phonon frequency ω. For higher phonon energies, of the order of the tunneling matrix element, the relaxation times become proportional to ω^{-2}.

These results yield a thermal conductivity for the TQ's which is proportional to T^2 at very low T, becoming linear in T at higher T. The tunneling matrix element determines the upper limit for the T^2 dependence.

We find also that, at least for this system, there is only one type of tunneling state. We find that there is a selection rule which prohibits transitions at very low energies for those TQ's which are not coupled ferrorelastically. However, all TQ's contribute to the specific heat.[1] This could provide an explanation for the experimental observation[8] that only a fraction of the impurities in dilute quadrupolar glasses contribute to the phonon scattering at low T .

IV. THE THERMAL EXPANSION

a. approach

The free energy for dilute interacting four orientational TQ's may be represented in a virial expansion.[1] For very low TQ concentrations it is assumed that all but the first two terms of the expansion may be neglected. This allows one to obtain exact expressions for the thermal expansion due to the first and second virial coefficients. The first term has a simple form and represents the Schottky peak. The Schottky term becomes exponentially small for very low T, thus the contribution from the second virial coefficient should dominate at very low T. The eigenvalues of the Hamiltonian for the TQ pairs allow one to derive the

partition function from which the thermal expansion due to the second virial coefficient may be obtained.

b. results

Two parameters are found to enter into the expression for the thermal expansion due to the second virial coefficient, and the resulting two terms must be integrated numerically. The first term arises from the TQ-TQ interaction and is negative at very low T. The second term arises from the tunneling matrix element and is positive at very low T. The manner in which these terms contribute relative to each other determines whether the thermal expansion is negative. At this time, the relative contributions of the two terms has not been determined. However, the fact that there is a negative contribution arising from the TQ-TQ interaction is quite significant and unexpected in light of previous models.

V. RECOMMENDATIONS

a. suggestions for follow-on research

The present research calculated the thermal conductivity due to resonance scattering and thus was valid only for very low temperatures. It would be of interest to investigate the thermal conductivity at higher temperatures. At higher T it is necessary to include the contribution of the resonance relaxation processes[7] in addition to

resonance scattering. This calculation would be significant since it seems likely that an additional scattering mechanism could give the plateau in the thermal conductivity which is observed experimentally, and which is not yet understood theoretically.

The calculation of the thermal expansion also raised several new questions. In particular, one would like to determine if the TQ strain interaction is responsible for a negative thermal expansion. This would require a more detailed examination of the parameters entering into the calculation of the thermal expansion.

b. Conclusion

Substantial progress has been made towards understanding the TQ strain interaction and how it affects glassy properties. However due to time constraints progress in applying the current work towards the flux creep problem has not reached the point where any actual calculations could be performed. It is the author's hope that this work will contribute to a better understanding of the nature of the TQ strain interactions so that the flux creep problem may soon be addressed.

ACKNOWLEDGEMENTS

I wish to thank the Air Force Office of Scientific Research for sponsorship of this research. Universal Energy Systems must be mentioned for their concern and help to me in all administrative aspects of the program.

I wish to thank Dr. Alfred Kahan for his kindly help and advice and for his dedicating time to this project. I thank Professor Michael Klein for providing me with the opportunity to participate in such stimulating and enriching research.

REFERENCES

1. M. W. Klein. To be published.

2. P. W. Anderson, B. I. Halperin, and C. M. Varma. Philos. Mag. 25, 1 (1972).

3. W. A. Phillips. J. Low Temp. Phys. 7, 351 (1972).

4. M. J. McKenna, A. Hikata, J. Takeuchi, C. Elbaum, R. Kershaw, and A. Wold. Phys. Rev. Lett. 62, 1556 (1989).

5. J. L. Black and B. I. Halperin. Phys. Rev. B 16, 2879 (1977).

6. J. N. Dobbs, M. C. Foote, and A. C. Anderson. Phys. Rev. B 33, 4178 (1985).

7. S. Hunklinger and W. Arnold. In W. P. Mason and R. N. Thurston, editors, Physical Acoustics, volume 12, page 155. Academic, New York, 1976.

8. J. J. DeYoreo, W. Knaak, M. Meissner and R. O. Pohl. Phys. Rev. B 34, 8828 (1986).

1990 USAF-UES SUMMER FACULTY RESEARCH PROGRAM/
GRADUATE STUDENT RESEARCH PROGRAM

Sponsored by the

AIR FORCE OFFICE OF SCIENTIFIC RESEARCH

Conducted by the

Universal Energy Systems, Inc.

Final Report

Absolute surface temperature calibration in semiconductor processing

Prepared by: David A. LaGraffe, Ph. D.

Academic Rank: Formerly, Graduate Student

Department and University: Physics Department, Syracuse University

Research Location: RADC/ESME, Hanscom AFB, MA 01732

USAF Researcher: Dr. David Weyburne

Date: 30 Aug 90

Contract No: F49620-88-C-0053

ABSOLUTE SURFACE TEMPERATURE CALIBRATION IN SEMICONDUCTOR PROCESSING

by

David A. LaGraffe

ABSTRACT

There are a number of semiconductor processes in which wafers must be heated uniformly to a given temperature. The wafer temperature is typically monitored with either an optical pyrometer or a thermocouple. Each of these methods has inherent uncertainties which makes absolute temperature determination of the wafer problematical. Hence, process temperatures are normally optimized emperically for any given system. This makes it difficult to compare results from one system to another. To overcome this problem we have developed a simple method for calibrating temperature control systems on an absolute scale. This method utilizes the eutectic transition points of binary metal, semiconductor systems, as determined by reflectance measurements, to reference temperature control with universal, absolute temperatures.

I. INTRODUCTION AND OBJECTIVES OF THE RESEARCH EFFORT

Many important semiconductor processes require the wafer to be heated uniformly to a given temperature. It is well known that the wafer surface temperature is one of the most important parameters determining growth of epitaxial semiconductors in either molecular beam epitaxy (MBE) or organometallic vapor phase epitaxy (OMVPE). Growth rate, in particular, is a strongly temperature dependent quantity.[1] Good temperature control is important to optimize growth rate and temperature uniformity across the growth wafer is essential for uniform layers. Unfortunately, this parameter has been difficult to determine accurately. Substrate temperature monitoring is normally accomplished with an optical pyrometer, thermister or a thermocouple junction. Each of these methods has inherent uncertainties that produce discrepancies from chamber to chamber. Normally, process temperatures are optimized empirically on a relative scale for any given system. However, this makes it difficult to compare results from one system to another. For example, the wide variety of reported optimum growth temperatures for identical systems may be at least partially traced to a lack of absolute temperature calibration.

Optical pyrometers suffer from real limitations in knowledge of spectral and total emissivities.

Emissivities depend on wavelength and more importantly for growth, temperature.[2] Many commercial pyrometers operate at wavelengths that are transparent to growth wafers. This means that the temperature being monitored is actually the platter (heater) temperature, not the wafer surface. This problem can be solved by using a wavelength tuned to a particular substrate.[3] Even with a tuned wavelength device, it has been shown that emissivities can depend on the doping levels and that pyrometric measurements of different termination layers can give temperature variations of 20 C.[3,4] Transmission effects of optical windows must also be considered. Some of the problems with emissivities can be avoided by using a two color pyrometer. Two color pyrometers are independent of emissivity as long as the sample can be considered a greybody source. However, even this assumption is unreliable for most materials.[5]

Thermocouples and thermisters are limited by the inability to directly probe the surface. The presence of a thermocouple or thermister in the platter can also cause temperature inhomogeneities in the platter. Different thermal conductivities and placement geometries will also produce vagaries from system to system.

In spite of their problems, optical pyrometers,

thermisters and thermocouples can be carefully calibrated to reproducibly and reliably control growth temperatures on a relative scale. Any given system can be optimized for the best growth parameters particular to that system. Unfortunately this produces a significant barrier to translating information and techniques learned on one system to another. The relative parameters for each system are different. What is needed is to have the carefully determined relative parameters referenced to a universal, absolute temperature scale that all researchers can access. There have been attempts to use native oxide evaporation or the limiting temperature of congruent evaporation as an absolute temperature standard, but with poor results.[6,7,8]

This universal temperature can be provided by the eutectic points of binary alloys. The choice of alloy systems is influenced by several considerations. The system should be compatible with use in an MBE, OMVPE, or similar processing system. A simple eutectic transition is desirable to ensure that only one sharp transition temperature is present. Finally, of course, one wants transition temperatures in the range of semiconductor process temperatures, typically 300 to 1000 C. Binary systems satisfying these criteria are Al, Au, and Ag alloys with Si and Ge. Although for simplicity we did not attempt any, systems with complex eutectics can in

principle be used as well by applying the Walser-Bene rule.[9] This rule states that the first silicide to grow is the highest congruently melting phase next to the lowest melting eutectic. This rule is only correct about 80-90% of the time, but could be used with care to calibrate other temperature ranges.[10]

In this report, we use the fact that the reflectance properties of thin metal films deposited on semiconductors will change drastically when the wafer is heated above the metal, semiconductor eutectic point. Measurement of the reflectance and platter temperature determines the platter temperature at the precise points of the known eutectic transitions. These reflectance measurements will accurately calibrate the relative platter temperature scale with an absolute, universal temperature scale; the known eutectic points of alloys.

III. EXPERIMENTAL

Films of Al, Ag, and Au were deposited from 99.9999% pure sources in a high vacuum evaporator on chemically etched Si(111) and Ge(111) single crystal wafers. The film thickness was measured by a calibrated oscillating quartz crystal monitor (Inficon). The reflectance

measurements were made in a low vacuum, 5-10 mtorr, silica bell jar configured as a typical OMVPE chamber. The residual atmosphere was a static background of forming gas ($Ar+H_2$). Light from a He-Ne laser was reflected at near normal incidence off of wafers placed on a graphite platter. The platter acted as a susceptor for an RF heating source. The as deposited films were exposed to atmosphere while transferring from the evaporator to the reflectance system. The reflected signal was measured by a Si detector.

The graphite platter temperature was measured with a (Vanzetti) two color optical pyrometer. A two color pyrometer utilizes band ratio radiometry to attempt to eliminate any emissivity dependence. This type of measurement is as accurate as the assumption that the emissivity of the object at two different wavelengths remains in a fixed ratio with temperature (a greybody source). For graphite this is a very good assumption and we consider measurements of the platter temperature to be accurate. The two color pyrometer was used in conjunction with an Omega temperature controller and the RF source to control the platter temperature. The system was carefully tuned so that temperature control of +-1 C of the platter was achieved. We could also independently measure temperatures with a one color IR camera, but the strong dependence of emissivity with temperature makes these

measurements very suspect.[4]

Actual changes in the physical morphologies of the films through the eutectic points were determined using a rapid thermal annealing oven and low power microscope. The rapid thermal anneal oven had a small (1-2 C) overshoot in the controller so the temperatures cited are the maximum temperatures reached.

IV. RESULTS

We first wanted to determine that the thin films were undergoing a morphological change at the eutectic temperatures cited in the binary phase diagrams.[11] The cited eutectics are given in table 1. To verify these transitions we annealed the films for 30 seconds in a rapid thermal annealing oven in 1 degree increments across the transition temperature. At each stage the sample was removed from the oven and examined with a microscope. Fig. 1 shows results for Au and Al films on Si. The as deposited films were highly reflective and flat. As evident in the photographs, the films experienced a large morphology change when annealed. The annealed films were dull and unreflective. To within the experimental uncertainties, the films showed these transitions at the eutectic points.

In fig. 2, we present representative reflectance measurements of the various films compared to the platter temperature determined by the two color pyrometer. The reflectance was measured as the platter temperature was linearly ramped. We tried several different heating rates ranging from 1 C/min to 10 C/min and different film thicknesses from 100 nm to 1um with no measurable effect on the reflectance transition. The transition widths in temperature were also measured and are shown in table 2. The widths were determined as the difference in temperature between the reflectance strength at 90% of the initial value to 10%. The heating rate for the width measurements was 5 C/min and the film thicknesses were 300 nm.

We should note that at high temperatures it is easy to oxidize the Ag films. This caused a gradual loss in reflectivity of the Ag films as the temperature increased. Almost total reflectivity was lost well before the eutectic point. To eliminate this problem, we deposited 30 nm films of Al on top of the Ag as a protective cap. Since the reaction occurs at the metal, semiconductor interface,[9] this cap has no effect on the observed eutectic transition. This is also supported by the fact that Al covered Ag films on Si and Ge show transitions at temperatures expected for Ag, Si alloys and for Ag, Ge

alloys, respectively. Al, Ag alloying effects would, of course, be largely independent of the substrate.

V. DISCUSSION

Initially, the films form a flat, highly reflective coating for the wafers.. As the films are heated to above the eutectic temperature, the metal and semiconductor will alloy and the reflectivity becomes very low. This can occur through two mechanisms. First, the alloying is confined at the interface but causes the film to crumple which will scatter light in all directions. Secondly, the metal and the semiconductor can be completely reacted and the electronic properties determining the complex dielectric function, and hence reflectivity, are drastically changed. The precise mechanism is determined by the reaction rate and the time of anneal. In either mechanism, the photoreflectance versus temperature will show a sharp transition at the eutectic point.

The sharp reflectance transitions shown in fig. 2 demonstrate the ease with which measured platter temperatures can be calibrated to an absolute, universal temperature scale. Using the change in photoreflectance due to the eutectic transition, the platter temperature is determined for a range of different wafer surface

temperatures. Although we measured the actual reflectance, the reflectance change is so strong that all that is really necessary is to view the reflected beam spot. At the transition temperature, the reflected spot becomes extremely diffuse. This is beneficial for operating systems were a minimum amount of intrusion is desirable. Other methods of accurate surface temperature determination using interference techniques[13] or precise emissivity measurements[4,14] have been done but generally require greater effort and sophistication.

Actually, using the change in reflectance at the eutectic point determines the precise temperature of the metal, semiconductor interface; not the bare wafer surface. The prescence of the thin film will affect the radiative loss properties of the substrate. The different emissivities of the metal surface compared to the uncovered semiconductor means that the radiative heat loss, Q^{rad}, will be different. This is determined by the Stefan-Boltzmann equation,

$$Q^{rad} = e \, o \, T^4,$$

where e is the emissivity, o the Stefan-Boltzmann constant and T the temperature. Of the other heat mechanisms, the thermal conductivity will be the same and the convective surface-gas losses will be almost the same. It has been

demonstrated for OMVPE systems that radiative heat loss accounts for roughly two-thirds of the total heat loss.[12] Clearly, for MBE it will be the dominant mechanism.

So, we are measuring the platter temperature for a given metal, semiconductor interface temperature. What we really want to know is the uncovered surface temperature. The effect of differing emissivities on the true surface

temperature can be estimated by considering the following. We assume that the metal film is infinitely thin and only serves to alter the emissive properties of the semiconductor. The thermal conductivity is the same. Since the radiation loss acts as a heat sink, we write the classical heat flow equation as,

$$- K (T_e - T_p) = e^{metal} \, o \, T_e^4 / a,$$

with K the thermal conductivity, T_e and T_p are the eutectic and platter temperature respectively, and a is an effective emissivity factor correcting for geometric effects. This equation is used to determine a and then a similar equation is then solved using the uncovered semiconductor emissivity, and the to be determined free surface temperature, T_s:

$$- K (T_s - T_p) = e^{semi} \, o \, T_s^4 / a.$$

Solving for the true uncovered surface temperature in terms of the measured parameters yields,

$$T_s+\{(e^{semi}/e^{metal})(T_p-T_c)/T_c^4\}T_s^4 = T_p,$$

which can be solved by iteration. For example when applied to our system, this predicts a temperature 16 C lower for uncovered Si at the platter temperature (582.6 C) for the Al, Si eutectic of 577 C. This means a platter temperature of 582.6 C gives a true Si surface temperature of 561 C. For Ag on Ge we predict a change of 17.4 C.

One way to minimize the effects of the different emissivities between the metal covered and the plain semiconductor is to deposit the metal onto a small spot. We used films only slightly larger than the laser beam diameter of 1.5 mm. This provides a surface that has the identical emissivity, and hence radiation loss properties, as the plain wafer except for a very small area. This should produce a temperature much closer to the true surface temperature. Lateral thermal conductivity will help to reduce any temperature gradients at the small metal spot to the true surface temperature.

This procedure increased the temperature difference measured between the platter and the wafer surface

consistent with the larger emissivity of the semiconductor than the metal; higher emissivity causing greater radiative heat loss. For Al on Si, the measured difference was 23.9 C. For Ag on Ge, the difference was 30 C. These results show that the argument used above underestimates the effect of metallization, but is a reasonable estimate if measuring small spot depositions is not feasible.

VI. CONCLUSIONS

We have demonstrated the utility of the eutectic transition in metal, semiconductor alloys for temperature calibration of semiconductor processing systems. This provides a reliable calibration standard that all research groups can use, eliminating temperature differences due solely to artifacts of any particular chamber design. The sharpness of the transitions and the large change in reflectivity strength means the calibration is also simple to employ. Although we estimate the true surface temperature accuracy is about +-15 C, this is far superior to oxide evaporation or congruent evaporation temperatures showing system to system variations of 140 C.[4] It is also a quick and easy technique to employ compared to interference techniques or precise emissivity measurements.

VII. RECOMMENDATIONS

There are some further aspects of this research effort that should be explored that time and circumstances did not allow to be finished. The first of these is to conduct the same experiments in an actual OMVPE system. This was an original goal of the project, but replacement of a faulty heater platter in the OMVPE system has delayed this for several weeks. Dr. Weyburne and Mr. Tripathi of RADC have indicated they will continue this project when the replacement is installed.

The second recommendation involves studying compound semiconductors more thoroughly. The idea of placing the well behaved binary system, such as Al on Si, on a compound semiconductor could be pursued. Initial measurements were conducted on aluminum films on Si on GaAs with little success. The films showed sharp reflectivity transitions, but at erratic temperatures. I believe this is due to limitations in the Si evaporation system. The present resistive heating evaporator is not well suited for Si and SiO_2 was most likely deposited. The electron beam evaporator at RADC is much better suited for Si deposition. However, at present this system is under renovation.

ACKNOWLEDGEMENTS

I am indebted to the Air Force Systems Command and the Air Force Office of Scientific Research for selecting me as an Air Force Summer Fellow.

I would particularly like to thank Dr. David Weyburne for his sponsorship and enthusiasm of this project. This research was also greatly aided by the help of Mr. Ken Vacarro and Mr. Alok Tripathi. I thank Dr. Brian Ahern for the fruitful and lively discussions. Finally, I would like to thank the staff at RADC for making me feel welcome, especially Dr. Mike Alexander and Dr. John Larkin.

The body of this final report was submitted for publication to the Journal of Vacuum Science and Technology.

REFERENCES

1. Gerald B. Stringfellow, Organometallic Vapor-Phase Epitaxy (Harcourt Brace Jovanovich, London, 1989).

2. see for example E. L. Dereniak and D. G. Crowe, Optical Radiation Detectors (Wiley, New York, 1984).

3. A. J. SpringThorpe, T. R. Humphrey, A. Majeed, and W. T. Moore, J. Appl. Phys. **55**, 2138 (1989).

4. T. Mizutani, J. Vac. Sci. Technol. B 6(6), 1671 (1988).

5. We measured with the eutectic transition a false temperature difference of 40 C between readings from a molybdenum and a graphite platter even with a two color pyrometer.

6. A. Y. Cho and M. B. Panish, J. Appl. Phys. **43**, 5118 (1972).

7. F. S. Hellman and J. S. Harris, Jr., J. Cryst. Growth 81, 38 (1987).

8. A. J. SpringThorpe, S. J. Ingrey, B. Emmerstorfer, and P. Mandeville, Appl. Phys. Lett. **50**, 77 (1987).

9. R. Walser and R. Bene, Appl. Phys. Lett. **23**, 624 (1976).

10. M.-A. Nicolet and S. S. Lau in VLSI Electronics, ed. by N. G. Einspruch and G. B. Larrabee (Academic, NY, 1983).

11. Binary Alloy Phase Diagrams, ed. by Thaddeus B. Massalski (American Society for Metals, Metals Park, OH, 1986).

12. D. I. Fotiadis, Shigekazu Kieda, and Klaus Jensen, J. Cryst. Growth 102, 441 (1990).

13. H. Sankur and W. Gunning, Appl. Phys. Lett. 56, 2651 (1990).

14. J. Nulman, S. Antonio, and W. Blonigan, Appl. Phys. Lett. 56, 2513 (1990).

FIGURES AVAILABLE FROM

AUTHOR OR

UES

1990 USAF-UES SUMMER FACULTY RESEARCH PROGRAM

GRADUATE STUDENT RESEARCH PROGRAM

Sponsored by the

AIR FORCE OFFICE OFFICE OF SCIENTIFIC RESEARCH

Conducted by the

Universal Energy Systems, Inc.

FINAL REPORT

Optical Simulations of Guided-Wave Structures

Prepared by: Lionel Friedman, Professor

Richard Lareau, Graduate Student

Department and University: Department of Electrical Engineering, Worcester Polytechnic Institute

Research Location: RADC/ESO, Hanscom AFB, MA 01731

USAF Researcher and focal point: Dr. Richard A. Soref

Date: July 20, 1990

Contract Number: F49620-88-C-0053

Same Report as
Prof. Lionel Friedman
(Report # 59)

1990 USAF-UES SUMMER FACULTY RESEARCH PROGRAM/

GRADUATE STUDENT RESEARCH PROGRAM

Sponsored by the

AIR FORCE OFFICE OF SCIENTIFIC RESEARCH

Conducted by the

Universal Energy Systems, Inc.

FINAL REPORT

Spectral Integral Formulation Applied to Scattering by Conductor-Backed Dielectric Gaps

Prepared by:	John Moore, M.S.
Academic Rank:	Graduate Student
Department and University:	Department of Electrical and Computer Engineering The University of Texas at Austin
Research Location:	RADC/EECT Hanscom AFB Bedford, MA 01731
USAF Researcher:	Major Keith Trott
Date:	August 1, 1990
Contract No:	F49620-88-C-0053

Spectral Integral Formulation Applied to Scattering by Conductor-Backed Dielectric Gaps

by

John Moore

ABSTRACT

The electromagnetic scattering from two-dimensional conductor-backed dielectric gaps is studied using a spectral integral formulation. This formulation utilizes the Green's function of the conductor-backed dielectric in a volume integral equation. Both far-fields and surface waves excited by the gap are extracted. The results of this approach for the E-polarized case have been validated against an alternative boundary integral formulation. Excellent agreement is observed between the two methods. The spectral integral approach can potentially be extended to treat more complicated structures including (i) three-dimensional gaps, (ii) gaps in multi-layered coatings, and (iii) multiple gaps on complex targets.

Acknowledgements

I wish to thank the Air Force Systems Command and the Air Force Office of Scientific Research for sponsorship of this research. Thanks go also to Major Keith Trott, my technical focal point, whose leadership made the summer research effort quite fruitful. Dr. Arthur Yaghjian taught me several concepts of mathematical physics. Thorkild Hansen and Marc Cote were also sources of useful information. Finally, my supervising professor, Hao Ling, provided me with the technical advice and moral support to successfully complete the research.

I. INTRODUCTION

As the electromagnetic scattering community has developed methods to reduce the radar cross section (RCS) due to major external scatterers such as corners or edges in complex targets, the scattering from cavities and gaps have become an important factor in the overall RCS of these targets. Cavities and gaps are natural models for interior structures such as inlet cavities, antenna windows, and air frame seams, and their contributions to the RCS need to be critically addressed.

One mission of the Target Characterization Branch under the Electromagnetic Sciences Division of the Rome Air Development Center at Hanscom Air Force Base is to perform the electromagnetic characterization of complex targets. Two popular RCS prediction codes, MISCAT and NEC, maintained by the branch facilitate this on-going mission. In the past two years, there has been active research in the area of scattering from gaps and cracks based on novel numerical/asymptotic methods. The finite-difference time-domain (FDTD) method has been used to model small gaps [1]. Also, recent in-house research in the area of gaps and cracks includes utilizing the incremental diffraction coefficient concept to analyze cracks on reflector surfaces [2] and extracting low frequency solutions of scattering from conducting semicircular gaps [3].

One of my past research projects involved the solution of a surface integral equation for scattering from non-uniform dielectric bodies. A volume integral equation approach can be applied to the gap in a conductor-backed dielectric. This alternative approach shares some common threads with the surface integral equation approach. Both my interest in studying what to me is a new problem within my realm of expertise and the interest of the Target Branch at RADC in validating existing "scattering from gaps" codes led to my appointment at Hanscom Air Force Base this summer.

II. OBJECTIVES OF THE RESEARCH EFFORT

The primary objective of my summer research is to perform a preliminary study of the scattering physics of conductor-backed dielectric gaps. Another objective is to validate other techniques, such as the FDTD [1], and thus establish accurate benchmark solutions.

To achieve the above goals, two different approaches have been implemented. The first approach involves a volume integral equation formulation which requires the computation of the Green's function for layered media. Calculation of this Green's function requires the evaluation of a spectral integral, and phenomena such as surface waves are included in the Green's function. The second approach is based on a novel boundary-integral formulation. This approach was carried out by my supervising professor, Hao Ling, who accompanied me to Hanscom AFB under the Summer Faculty Research Program.

Results generated by the two approaches have been validated against each other, and excellent agreement was obtained for various gap dimensions. This report describes the formulation of the gap problem using the first approach and the numerical validation of the results with the second approach. The detailed formulation of the second approach is documented in Hao Ling's final report.

III. FORMULATION OF THE PROBLEM

Fig. 1 shows a rectangular gap in a dielectric slab backed by an infinite conductor. The gap is of width **w** and thickness **d** and is embedded in a dielectric with material parameters (μ,ε). The dielectric and gap are infinite in the z-direction. The problem at hand is to determine the scattering contribution from the gap, defined as the difference between the total scattered field from the structure shown in Fig. 1 and that from the same coated conductor without the gap.

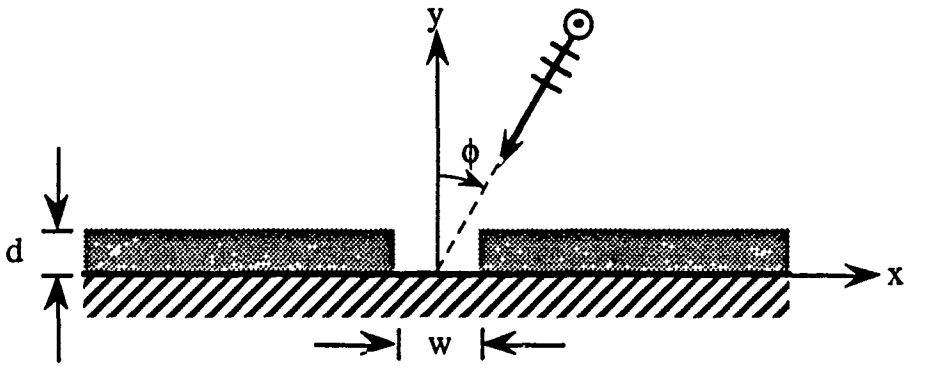

Fig. 1. The gap geometry.

The first conceptual step in solving this problem is shown for the E-polarized case in Fig. 2. For the case shown, all electric currents and fields are z-directed. When the gap is excited by a source, polarization currents are induced in it and are given in terms of the total electric field **E** by

$$\mathbf{J} = j\omega(\varepsilon_0-\varepsilon)\mathbf{E} = j\omega(\varepsilon_0-\varepsilon)[\mathbf{E}^i+\mathbf{E}^s] \tag{1}$$

where $\mathbf{E}^i$ is the electric field of the source, and $\mathbf{E}^s$ is the scattered electric field produced by the excited gap [4]. In the above equation, the only known quantity is $\mathbf{E}^i$. The objective is to solve for the two unknowns $\mathbf{J}$ and $\mathbf{E}^s$.

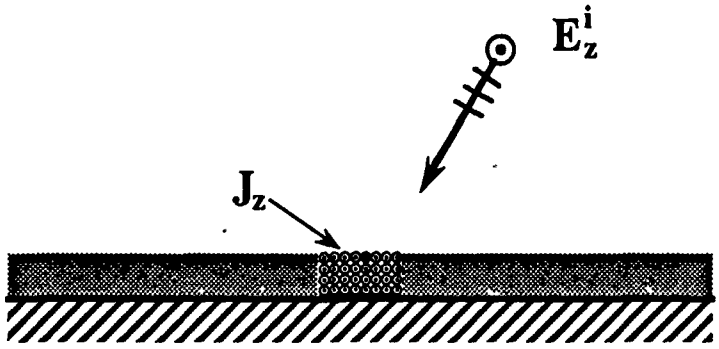

Fig. 2. Induced volume currents in the gap due to an E-polarized incident electric field.

The scattered field $\mathbf{E}^s$ at any point is related to the polarization currents in the gap through the Green's function of a line source of electric current by the volume integral

$$\mathbf{E}^s(x,y)=\int_{gap} G(x,y;x',y')\mathbf{J}(x',y')dx'dy' \tag{2}$$

If $\mathbf{E}^s$ is expressed in terms of $\mathbf{J}$, then $\mathbf{J}$ can then be expressed solely as a function of the incident field $\mathbf{E}^i$. Through application of the moment method via point-matching and rectangular pulse functions, (1) and (2) may be combined and recast into the following matrix equation.

$$[J]=\left[[Z]+\frac{j}{\omega(\varepsilon_0-\varepsilon)}[I]\right]^{-1}[E^i] \tag{3}$$

where [I] is the identity matrix, and [Z] is an impedance matrix resulting from integrating the Green's function over the area of a rectangular pulse of dimensions Δx by Δy.

$$[Z] = \int_{\Delta x} \int_{\Delta y} G(x',y')dy'dx' \tag{4}$$

Once the Green's function is calculated, (3) and (4) are used to solve for the unknown currents. G(x, y; x',y') which is the Green's function due to a point source is most easily found by first Fourier transforming the point source in the x-direction ($x \rightarrow k_x$). This results in a Green's function due to an infinite sheet of currents which shall be named $g(k_x, y; x',y')$. The transformed problem is analogous to a transmission line problem, so **g** is found easily. **G** is found by simply inverse transforming **g**. [Z] in terms of **g** is given by

$$[Z] = \int_{\Delta x} \int_{\Delta y} dy'dx' \left[\int_0^{\infty} g(k_x,y;x',y')\cos(xk_x)dk_x \right] \tag{5}$$

The triple integration can be reduced to a single integration by first interchanging the order of the variables of integration and then performing the integration over the pulse analytically:

$$[Z] = \int_0^{\infty} \int_{\Delta x} \int_{\Delta y} dy'dx'g(k_x,y;x',y')\cos(xk_x)dk_x \tag{6}$$

The end result is a multiplicative factor within the Fourier integral.

$$[Z] = \int_0^{\infty} \left[\frac{4\sin(\frac{\Delta x k_x}{2})\sin(\frac{\Delta y k_{y1}}{2})}{k_x k_{y1}} \right] g(k_x,y;x',y')\cos(xk_x)dk_x \tag{7}$$

Since **g** contains singularities for some values of k_x, the path of integration is deformed to avoid any possible singularities. One singularity is a branch point located at $k_x=k_0$. There may be one or more poles lying between $k_x=k_0$ and k_1, each corresponding to a surface wave mode supported by the dielectric slab. Fig. 3 shows the deformed path that a computer program could use to perform the integration.

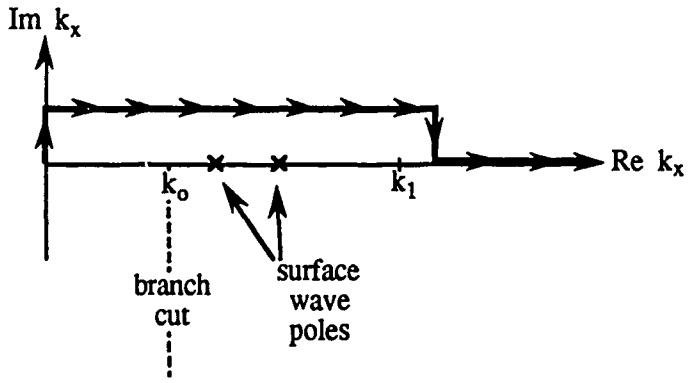

Fig. 3. The path of integration.

Since the upper integration limit is infinity, it is possible that a computer program may need to evaluate the integrand over an extremely large number of points before it converges. By employing the "Method of Averages" [5], the convergence of the integral may be significantly accelerated.

By calculating [**Z**] using (7), the polarization currents may be determined. From this the far-fields may be evaluated. Evaluating the far-fields requires evaluation of the Green's function for infinite values of **x** and **y**. An asymptotic approximation to the Green's function is found using the Method of Steepest Descents. This far-field approximation is not easily applied to observation angles of $\pm 90^o$ when surface waves are present. At these angles, reciprocity is

used to relate this problem to a similar problem where the source and observation points have been interchanged. Fig. 4 shows the two situations to be related through the following reciprocity formula by which the unknown surface wave coefficient contained in $\mathbf{E}^a$ is calculated.

$$\int_{\substack{\text{point}\\ \text{source}}} \mathbf{J}^a\mathbf{E}^b ds = \int_0^{\infty} \mathbf{J}^b\mathbf{E}^a dy \tag{8}$$

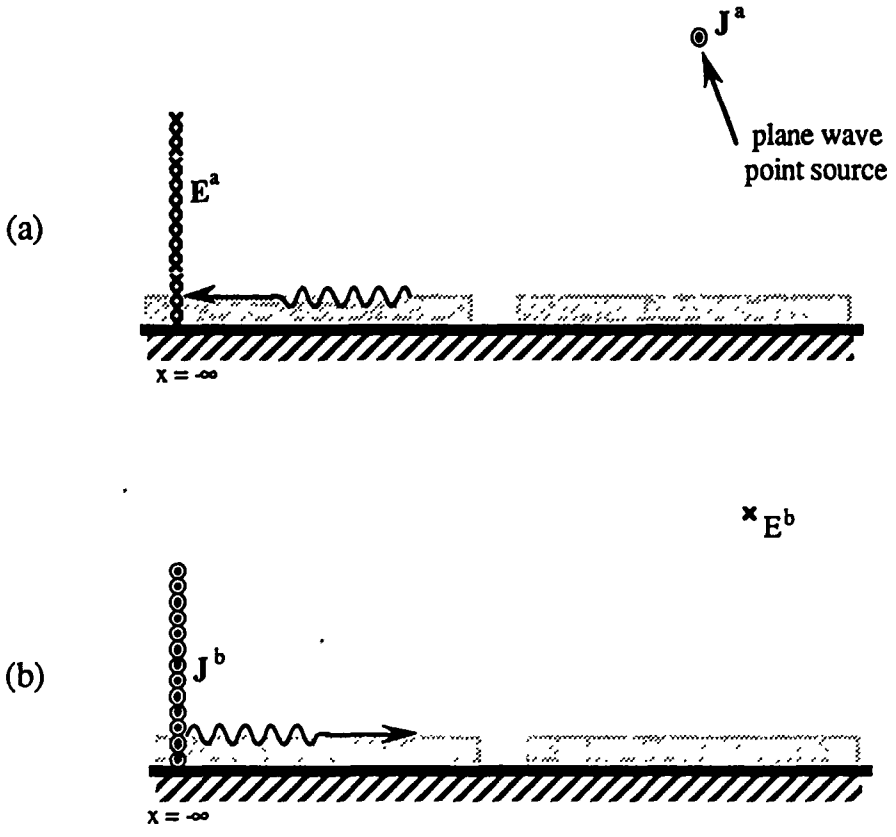

Fig. 4. (a) The original problem in which the surface wave $\mathbf{E}^a$ is the unknown;
(b) An alternative to (a) in which the source and observation points are interchanged.

IV. RESULTS AND DISCUSSION

Numerical results have been generated using the spectral integral method just described (SIM) and compared with those generated using the boundary integral method (BIM) for various gap dimensions. Also, the results are compared against a crude physical optics (PO) approximation (i.e., the physical optics integral is applied over the gap region).

Shown in Fig. 5(a) is a comparison in echo width between the three solutions for E-polarized incidence, coating thickness $\mathbf{d}=0.2\ \lambda_0$, $\varepsilon=2$ and gap width $\mathbf{w}=0.1\ \lambda_0$. No surface wave is excited. Excellent agreement between the SIM and the BIM solutions is observed. Note also that the crude PO approximation is surprisingly accurate, especially near normal incidence. Fig. 5(b) is a comparison of echo widths for the same geometry but with $\varepsilon=2\text{-}j2$. The SIM and BIM solutions still maintain excellent agreement, but the PO approximation is not at all accurate.

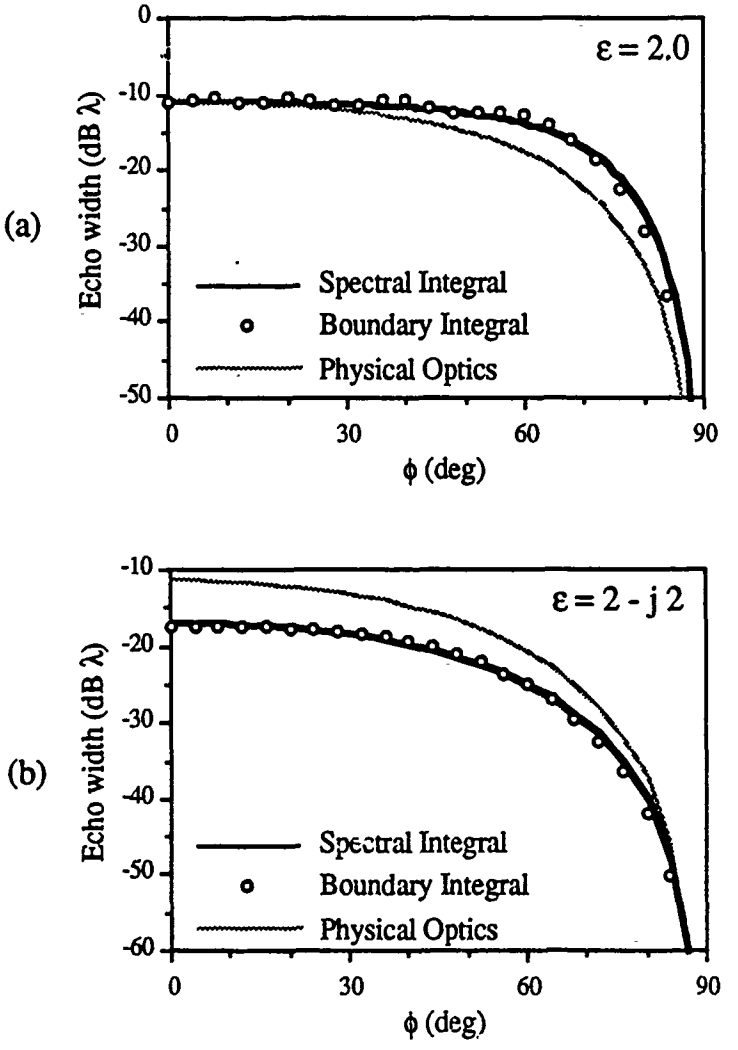

Fig. 5. Echo widths versus angle for w=.1 λ_0, d=.2 λ_0, and

(a) $\varepsilon = 2$; (b) $\varepsilon = 2\text{-}j2$.

Fig. 6(a) is a plot of the echo width versus angle when the dielectric is thick enough to support the propagation of the lowest order E-pol surface wave. In this case, the PO solution is not accurate. The surface wave excitation is extracted via reciprocity and the magnitude of the two outgoing surface waves are plotted in Fig. 6(b). The magnitude has been normalized to the incident electric field. The magnitude of C_- (the -x travelling wave) is always greater

than or equal to that of C_+. The surface wave coefficients predicted by the SIM and BIM are also in excellent agreement.

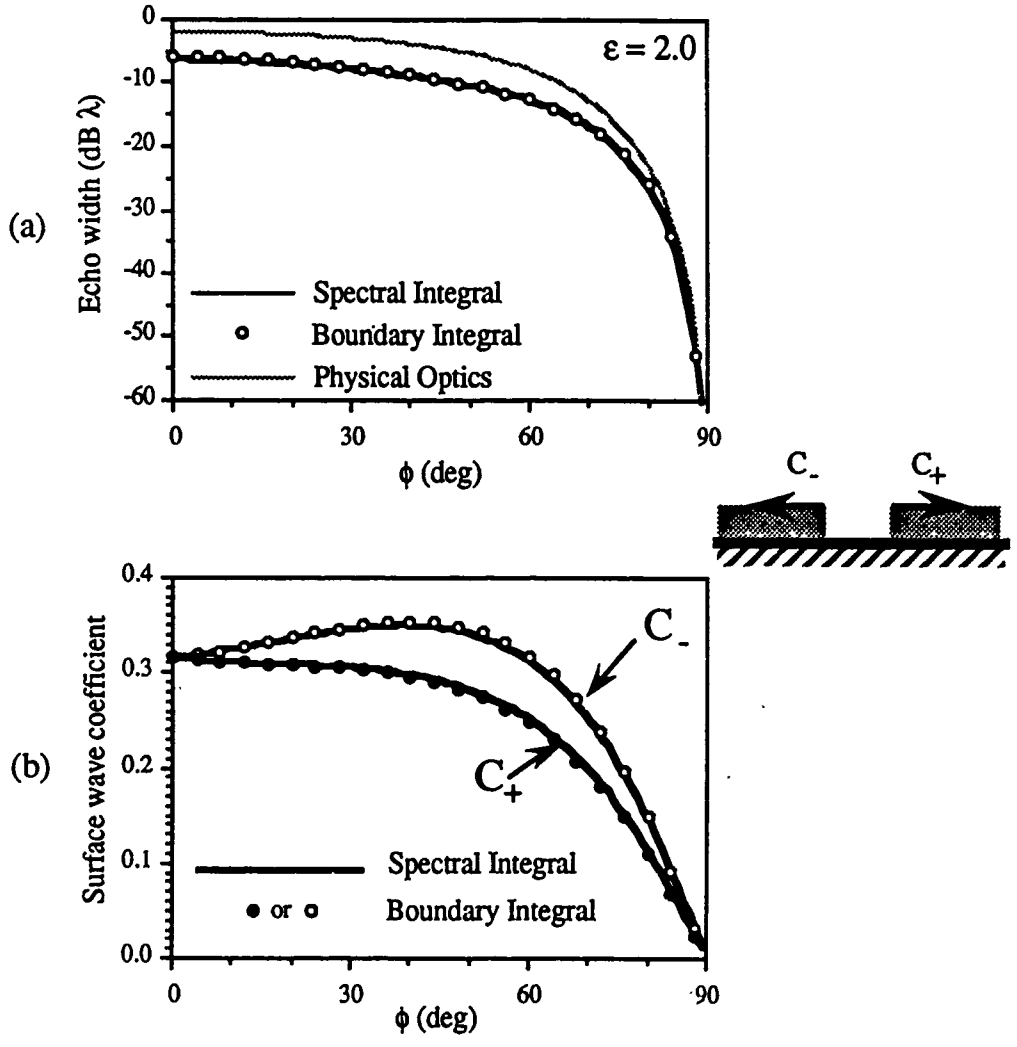

Fig. 6. (a) Echo width versus angle for w=.2 λ_0, d=.4 λ_0, and $\varepsilon = 2$; (b) Surface wave coefficients.

I also generated results for a two-gap case. The two gap geometry is shown in Fig. 7. The parameter s is the separation distance between the centers of the two gaps. One could solve the integral equation for two gaps. This full solution would include all interactions between

the two gaps, but would be rather time consuming and not general enough to be implemented into a general RCS prediction code. A first order approximation to the two-gap problem is to solve for a single gap and sum two isolated gap solutions. This solution does not account for interactions due to surface waves. A second order approximation is to include surface wave interactions in the first order approximation . The surface waves leaving one gap are simply injected into the second gap where they then re-radiate. (Multiple reflections of surface waves are ignored.) Fig. 8 shows results of the three solution methods just outlined. The first approximation when compared to the full solution does not do well at the null located near 30°. The second approximation exhibits good agreement with the full solution at all scan angles.

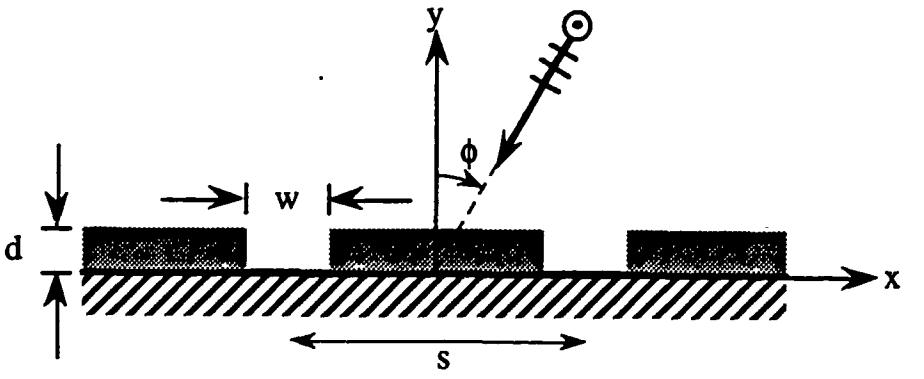

Fig. 7. The two-gap geometry.

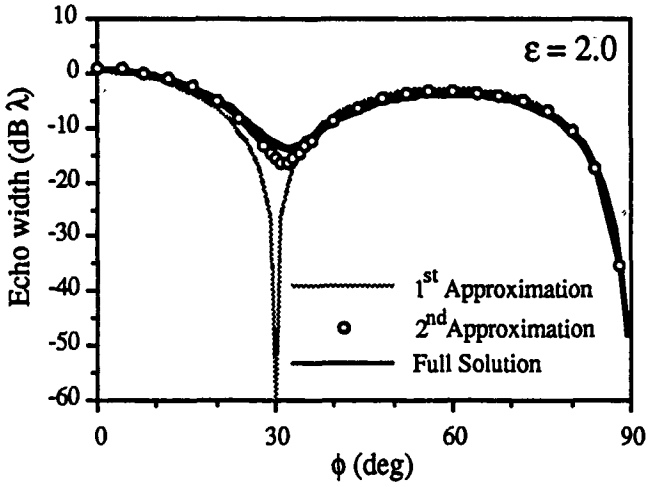

Fig. 8. Results for the two-gap geometry.

$w=.2\ \lambda_o$, $d=.3\ \lambda_o$, $s=.5\ \lambda_o$, and $\varepsilon=2$

V. SUMMARY AND RECOMMENDATIONS

The problem of 2-dimensional E-polarized scattering by a conductor-backed dielectric gap has been successfully addressed by a spectral integral formulation. This formulation is based upon a volume integral equation which utilizes the Green's function for the dielectric slab. The results of this approach have been validated against an alternative boundary integral formulation. The two solutions agree very well. Preliminary results for multiple scatterers were also shown. Several possible extensions to this study are described below.

(a) The results contained in this report are for the E-pol incident field case only. The solution method for the H-pol case is slightly more complicated than the E-pol solution method. The induced polarization currents will have components pointing in both the x and y-direction. The resulting Green's function will be a dyadic (a matrix) rather than a scalar. The spectral integral solution for the H-pol case will not converge as quickly as the E-pol case and thus will require more computation time.

(b) The present analysis can be extended to treat scattering from 3-dimensional dielectric gaps (Fig. 9). One approximation to the 3-D solution is to couple the 2-D solution with an equivalent current method [6]. This approximation requires that both the 2-D E-pol and H-pol solutions be available and would work best when the curvature of the gap varies smoothly in the third dimension.

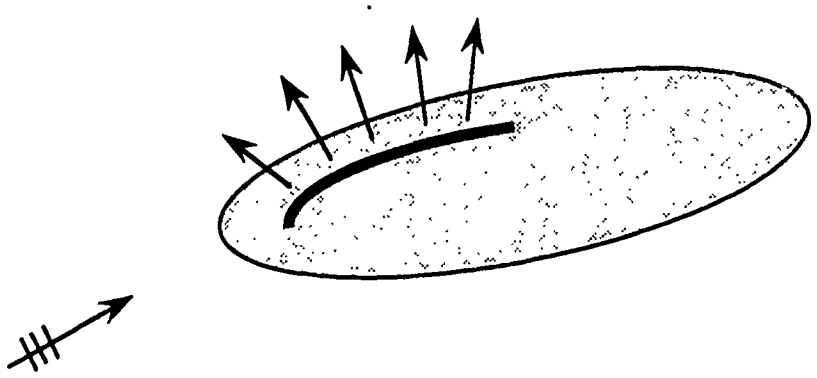

Fig. 9. Scattering from a 3-D gap.

(c) The present approach can be extended to study gaps in multi-layered coatings (Fig. 10). This extension would involve only changing the spectral green's function **g** to account for multiple layers.

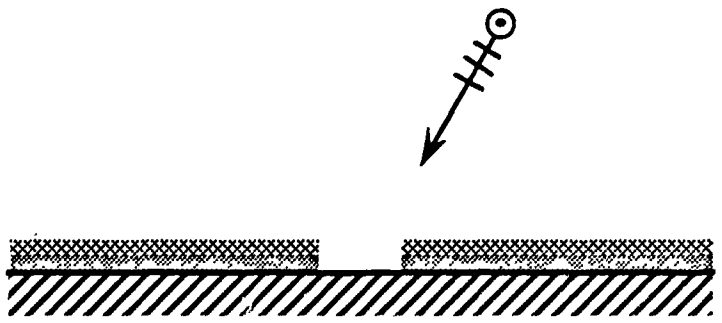

Fig. 10. Gaps in multi-layered coatings.

REFERENCES

1. Demarest, K. R., "Scattering from Thin Apertures in Coated Conductors Using FDTD," Univ. of Kansas, Radar Systems and Remote Sensing Laboratory Tech. Rep. 8090-3, Oct. 1989.

2. Shore, R. A. and A. D. Yaghjian, "Incremental Diffraction Coefficients for Planar Surfaces, Part III: Pattern Effects of Narrow Cracks in the Surface of a Paraboloid Antenna," Rome Air Development Center Tech. Rep. 88-119, May 1988.

3. Hinders, M. K., "Scattering of a Plane Electromagnetic Wave from a Semicircular Crack in a Perfectly Conducting Ground Plane," Rome Air Development Center Tech. Rep. 89-12, April 1989.

4. Harrington, Roger, Time Harmonic Electromagnetic Fields, New York, New York, McGraw-Hill, 1961.

5. Mosig, J. R. and F. E. Gardiol, "Analytic and numerical techniques in the Green's function treatment of microstrip antennas and scatterers," IEE Proc., Part H: Microwaves, Opt. Antennas, vol. 130, pp. 175-182, 1983.

6. Dominek, A. K., "Analysis of Gaps and Cracks," The Ohio State Univ., ElectroScience Laboratory Tech. Rep. 717067-2, May 1985.

1990 USAF-UES SUMMER FACULTY RESEARCH PROGRAM/
GRADUATE STUDENT RESEARCH PROGRAM

Sponsored by the
AIR FORCE OFFICE OF SCIENTIFIC RESEARCH
Conducted by the
Universal Energy Systems, Inc.

FINAL REPORT

Exploiting Parallel Architectures within a Distributed Computational Environment

Prepared by:	Gary L. Craig
Academic Rank:	Assistant Professor
and	Charles K. Shank
Academic Rank:	Graduate Fellow
Department and	Electrical and Computer Engineering
University	Syracuse University
Research Location:	Rome Air Development Center
	Griffiss AFB, NY 13441
USAF Researcher	Richard Metzger
Date:	July 26, 1990
Contract No.	F49620-88-C-0053

Same Report as
Prof. Gary Craig
(Report # 58)

1990 USAF-UES SUMMER FACULTY RESEARCH PROGRAM/

GRADUATE STUDENT RESEARCH PROGRAM

Sponsored by the

AIR FORCE OFFICE OF SCIENTIFIC RESEARCH

Conducted by the

Universal Energy Systems, Inc.

FINAL REPORT

A Phenomenological Model for the Magnetic Reconnection in Compact Toroid Formation

Prepared by:	Melissa R. Dittmar
Academic Rank:	Graduate Student
Department and University:	Physics and Astronomy University of New Mexico
Research Location:	High Energy Plasma Division Weapons Laboratory (WL/AWX) Albuquerque, NM 87110-6008
USAF Researcher:	Dr. Norman Roderick
Date:	21 September 90
Contract No:	F49620-88-C-0053

A Phenomenological Model for the Magnetic Reconnection in Compact Toroid Formation

by

Melissa R. Dittmar

ABSTRACT

Magnetic Reconnection is observed to occur in the MARAUDER compact toroid formation experiment on a much shorter time scale than that predicted soley by a Spitzer diffusion. This implies that there is an additional process to the Spitzer resistivity which enhances the growth rate of reconnection. Simulations using the MACH2 MHD code were first run on the simple field geometry of a magnetic shear. The results indicate that that the normal component of the current drives the instability which causes the reconnection. Treating this current-related diffusion as an anomalous resistivity, a phenomenological model of the reconnection process was developed and incorporated into the compact toroid simulations. To determine the extent to which microinstabilities and the toroidal electron drift velocity influence the reconnection rate produced by the anomalous resistivity, a parameter search will need to be done.

Acknowledgements

I would like to thank the Air Force Systems Command and the Air Force Office of Scientific Research for sponsorship of this research. I also wish to thank Universal Energy Systems in their assistance with the administrative portion of this program.

Working with the group in the High Energy Plasma Division was a truly enjoyable experience for me. As a graduate student about to embark on her dissertation research, I found their enthusiam toward their work and their willingness to help facilitate my understanding of the current projects very encouraging and refreshing. There were a number of people who were particularly helpful in the area of my research project. Dr. Peter Turchi provided me with many interesting ideas and stimulated alot of rethinking. The encouragement and help of Captain Carl Sovinec was not only greatly appreciated but very much needed. During the ten week period, I learned an incredible amount about the computational and theoretical aspects of plasma physics. This would not have been possible without the unending patience and guidance of Dr. Norman Roderick. His experience and genuine understanding of plasma physics was an invaluable asset to every aspect of this research project.

I. INTRODUCTION:

Magnetic reconnection is a physical process often connected with astrophysical phenomena such as solar flares and the acceleration of energetic charged particles at the earth's bow shock and in the magnetotail. Over the past two decades, however, it has become an increasingly common factor in the context of magnetic field confinement in the laboratory, particularly in the area of fusion research. One confinement configuration which relies heavily upon the occurence of the reconnection process is the compact toroid.

The High Energy Plasma Division of the Weapons Lab at Kirtland Air Force Base has been conducting experiments on the formation of Compact Toroids (CT) as part of their MARAUDER (Magnetically Accelerated Rings to Achieve Ultra-high Density Energy and Radiation) research effort. Their method of formation utilizes a coaxial plasma gun in which a predominantly radial (poloidal) magnetic field is initially created. Gas is then puffed into the gun and a toroidal field is induced at the bottom of the gun by a formation discharge. The magnetic pressure of this induced toroidal field forces the plasma embedded poloidal field upward into an expansion region, where it forms a magnetic bubble. At some point, magnetic reconnection is observed to occur at the neck of the bubble. This results in the formation of a compact toroid.

Based on classical Spitzer resistivity and known physical

conditions, magnetic reconnection should not take place in the MARAUDER experiment because the time needed for this process to occur is much longer than the time scale defined by the experiment itself. It is apparent that a more accurate formulation of the reconnection process is needed. As a physics graduate student whose primary interest is in plasma physics, I was very interested in working on this problem. My previous research experience had included some work in the area of astrophysical plasmas and I did have a familiarity with the magnetic reconnection process that is occuring in the earth's magnetotail. I believe these factors facilitated in my assignment to the project at the High Energy Plasma Division.

II. OBJECTIVES OF THE RESEARCH EFFORT:

As mentioned, the magnetic reconnection observed in the formation of the compact toroid in MARAUDER happens on a much shorter time scale than that predicted by classical Spitzer resistivity in which the diffusion of a magnetic field in a plasma is directly related to the electrical resistivity (electron ecounter with ions) of the plasma. Elementary calculations using magnetohydrodynamic (MHD) simulations show that the time for reconnection lies somewhere between the Alfven time of the plasma and the classical diffusion time for the plasma. Consequently, there must be an additional process working with the Spitzer resistivity which enhances the growth rate of the reconnection. Determination of this process is of

significant interest since it can play an important role in the developmental aspect of future experiments.

In an attempt to specify the unknown reconnection mechanism, two distinct possibilities were originally considered, both of which essentially embody non-classical resistivity. One way to approach the problem is to view reconnection as the result of some action inherent to the plasma which intensifies any perturbation instability and hence growth. Taking this standpoint introduces the concept of anomalous resistivity and describes the interaction of magnetic field with the components of the plasma. A second approach involves taking into account the desorption of wall material from the formation vessel. This creates a macroscopic resistivity caused by electron collisions with cold neutrals ablating from the container walls.

For the ten weeks that I had to follow up on these two scenarios, I spent my time looking at plasma instabilities and the role that anomalous resistivity might play in the growth of these instabilities. Macroscopic resistivity was not addressed for the following reason. To incorporate it in the reconnection problem, the MHD code being used would need to be modified which would take some unknown amount of time. Anomalous resistivity was already implemented into the code allowing an analysis to be performed immediately. Further, once the latter study was underway, some interesting instability features surfaced from the code. I felt it was

necessary to look at the influence of the code in such instances and eventually, I decided to keep working in this area.

III.

a. To study the reconnection process, I used the MACH2 2-1/2 dimensional MHD simulation code (reference 4) at Kirtland Air Force Base. Initially, a simple field geometry which is known to result in reconnection was analyzed. The last three weeks of the project then applied any pertinent information obtained from this field geometry to the more complex geometry of MARAUDER.

The simple field topology examined first consists of a current sheet interface with a plasma-embedded constant magnetic field exterior to the interface but in opposing directions on either side. A perturbed field, denoted by a sine function, is introduced perpendicular to the embedded field. The mathematical forms of the two fields are given by

$$B_y(\text{shear}) = B_{oy} \tanh[(x-r_o)/xkff]$$

$$B_x(\text{perturbed}) = B_{ox} \sin[2\pi y\ (ykff)]$$

The perturbed field is primarily manipulated by a term in its argument called ykff, while the embedded field is mathematically described by a hyperbolic tangent function whose arguments include the distance along a box enclosing the computational

region, a position for the center of the current sheet r_o, and a distance parameter xkff. The effects that xkff and ykff have upon the configurations of the embedded and perturbed fields are shown in Figures 1 and 2. Using only classical Spitzer resistivity and allowing certain parameters of the system to be varied, the MHD code is allowed to run out to one microsecond.

The field geometry of the MARAUDER experiment is described in the introduction. Mathematically these fields are given by a force-free field configuration. The MHD code is usually run out to five microseconds

b. The MHD simulations on the uniform field configuration produced a variety of interesting results. It was found that magnetic reconnection, which often manifests itself in the form of magnetic islands, does not occur without the existence of the perturbed field. This implies that the perturbed field plays a necessary role in the reconnection process. Furthermore, the reconnection was observed to occur on time scales and with a topology indicative of a faster field spread in the plasma than should be seen with classical diffusion. Recall that only a Spitzer component of the resistivity was operating in the code; thus even in this simple geometry there was a reconnection process that should not have evolved on the times scales defined by classical resistivity. This reinforces the postulation that there might be something inherent in the plasma that stimulates the growth of reconnection.

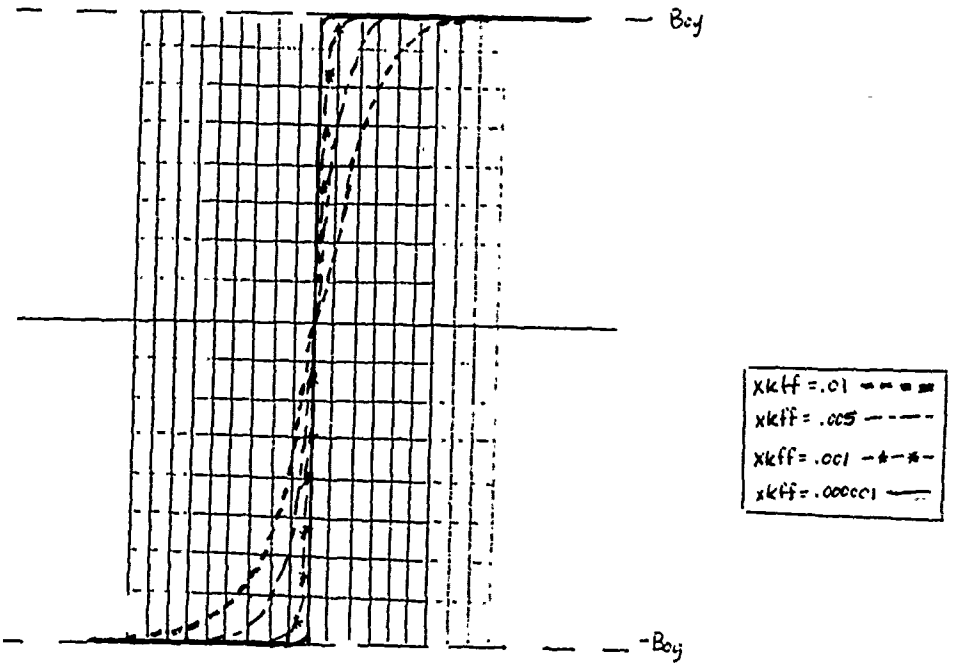

FIGURE 1 REPRESENTATION OF HOW THE VALUE xkff CHANGES THE MAGNITUDE OF THE FIELD IN THE REGION OF THE CURRENT SHEET (FIELD-REVERSAL REGION). THE BLOCKS DENOTE COMPUTATIONAL CELLS.

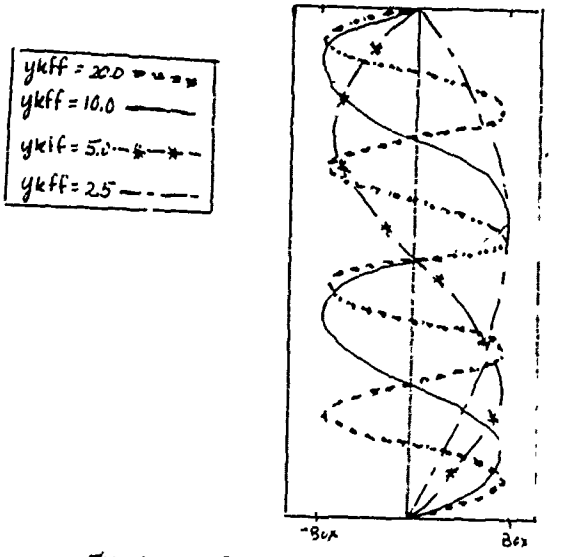

FIGURE 2. REPRESENTATION OF HOW THE VALUE ykff ALLOWS THE WAVELENGTH OF THE PERTURBED FIELD TO VARY IN A BOX.

A likely scenario is that there is an additional diffusion process working simultaneously with that caused by Spitzer resistivity. To follow up on this speculation, calculations of an effective resistivity were made from the simulation output of the code using island widths and and their corresponding development times. This value was then substituted into the MHD code in place of the Spitzer resistivity and the perturbed field set to zero. The embedded field was found to diffuse in the expected fashion but with the width of the diffusion region comparable to that of the magnetic islands. This increase in width can be interpreted as the result of an additonal component in the diffusion.

Variation of the parameters xkff and ykff also gave insight into the reconnection process. Changing the value of xkff modifies the region over which the magnetic field reverses, and, because the current is related to the curl of the field, this in turn modifies the width of the current sheet. The current width is considered to characterize the kinetic energy of the electrons, or equivalently the electron drift velocity. As a result, the manipulation of xkff portrays the effect that the motion of the electrons have on the reconnection process. For an xkff of less than .005, magnetic reconnection was initially present in the form of two islands at symmetrical locations about the center of the computational box along the current sheet. These two islands later evolved into three islands then back to two islands and eventually coagulated into one. This reconnection did not develop for an xkff above .005.

This latter value defines the region of field reversal as approximately 1/3 the size of the box. At this value, the current density profile is very wide and a factor of 10 smaller in magnitude compared to that seen for xkff below .001. This suggests that the width of the current sheet, and hence, the electron drift velocity does play a role in the reconnection process.

The parameter ykff signifies the number of wavelengths of the perturbed field which are fit into the computational box. Simulations with ykff equal to four, two, one, 1/2, and 1/4 wavelengths were examined. The most noteworthy results in these cases pertain to the numerical problems with the code. For a wavelength of four, no visible reconnection was observed because the perturbation could no longer be resolved by the code whereas less than one wavelength appeared to give reconnection caused purely by numerical diffusion. Such numerical effects were not only evident in the manipulation of the parameter ykff but also in the cell size of the computational mesh. Increasing the cell size along the perpendicular to the current sheet caused the formation time for the different island structures to shorten. This can be seen in Figures 3 through 6 which show the island formation for the cell sizes of 32, 48, 64 and 96.

This analysis of the simplified field topology proved to be very instructive in developing a phenomenological model of the reconnection process. This model was incorporated into the

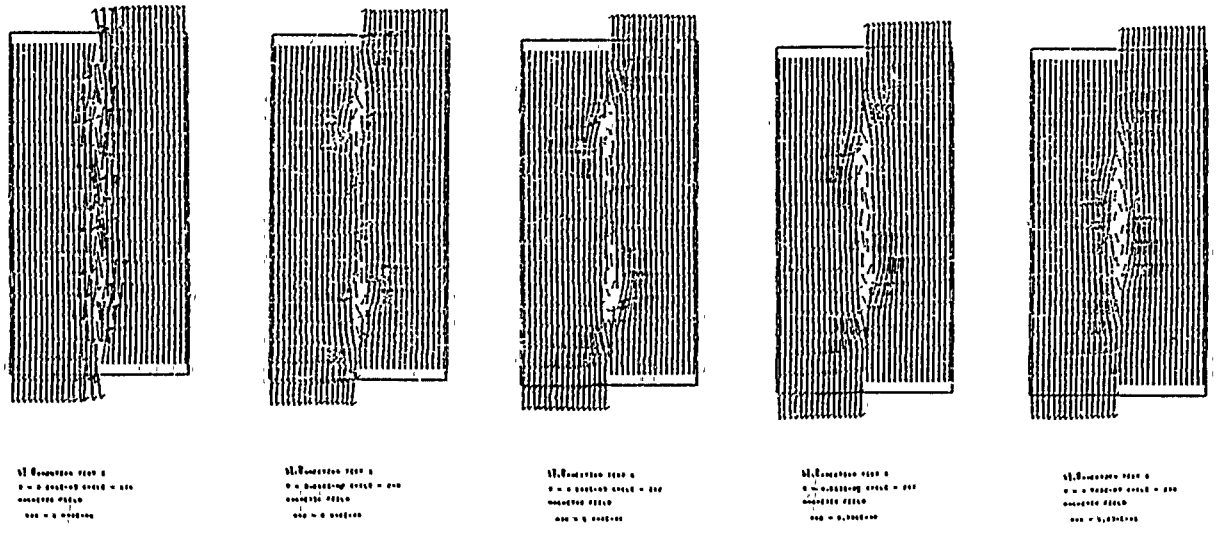

FIGURE 3. MAGNETIC RECONNECTION SIMULATION FOR 32 X 16 CELLS.

xklf = .00001
yklf = 10.0

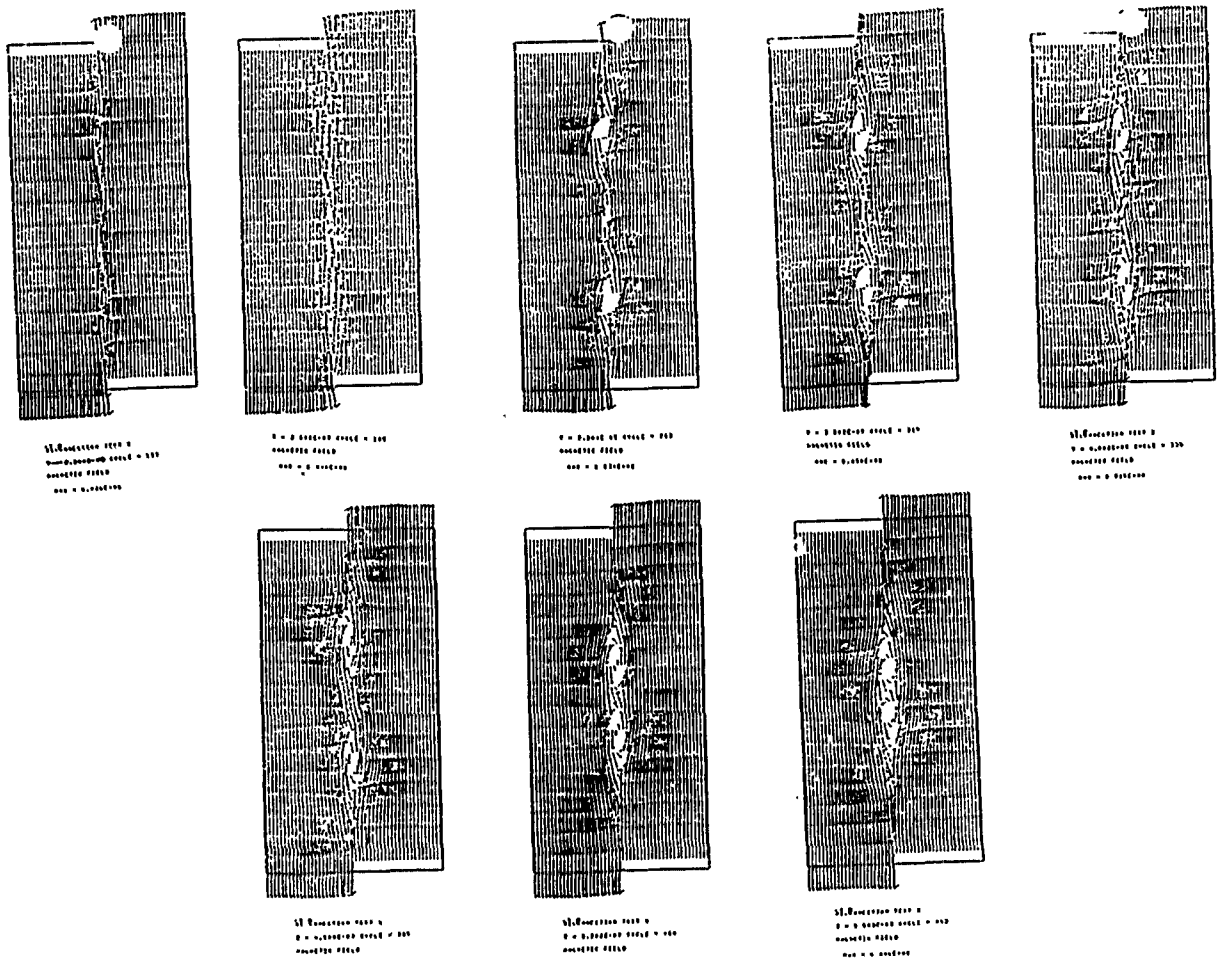

FIGURE 4. MAGNETIC RECONNECTION SIMULATION FOR 48 X 16 CELLS.

xkff = .000001
ykff = 10.0

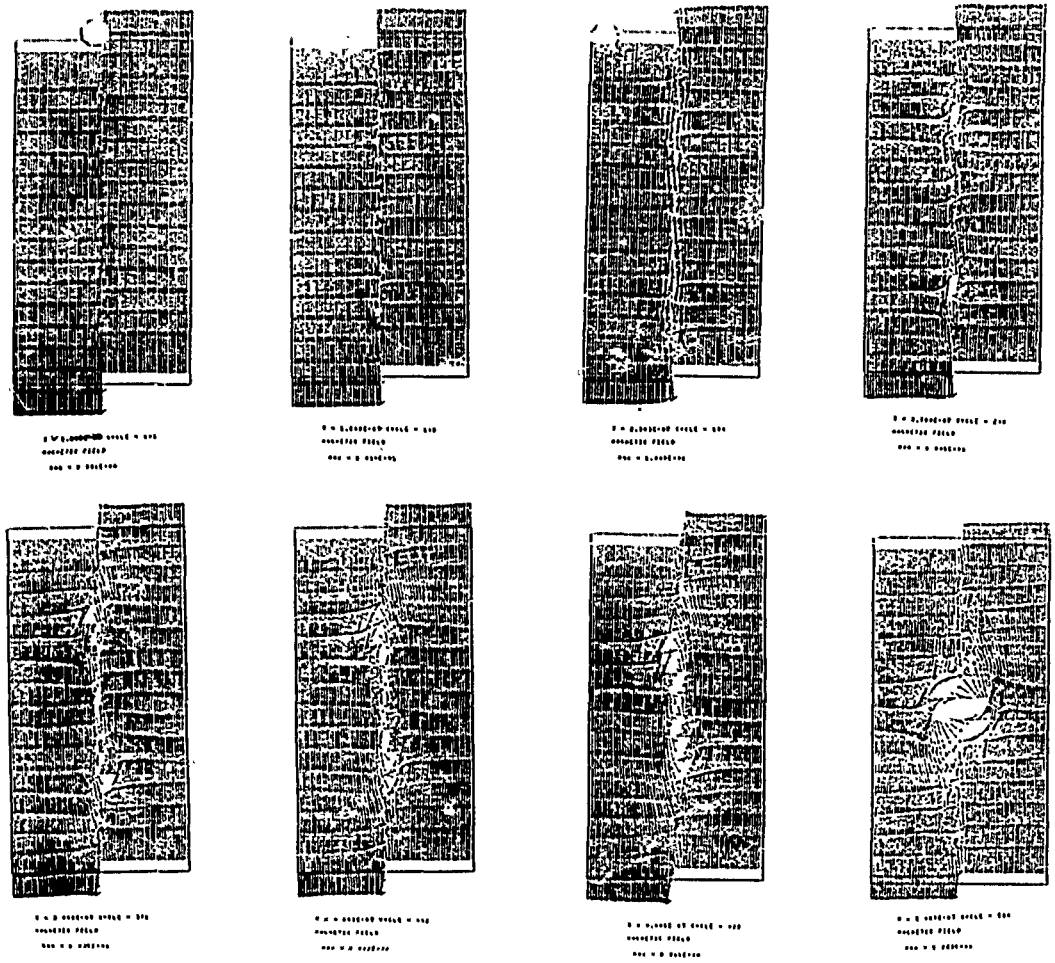

FIGURE 5 MAGNETIC RECONNECTION SIMULATION FOR 64 X 16 CELLS

akff = .cccc1
ykff = 10 0

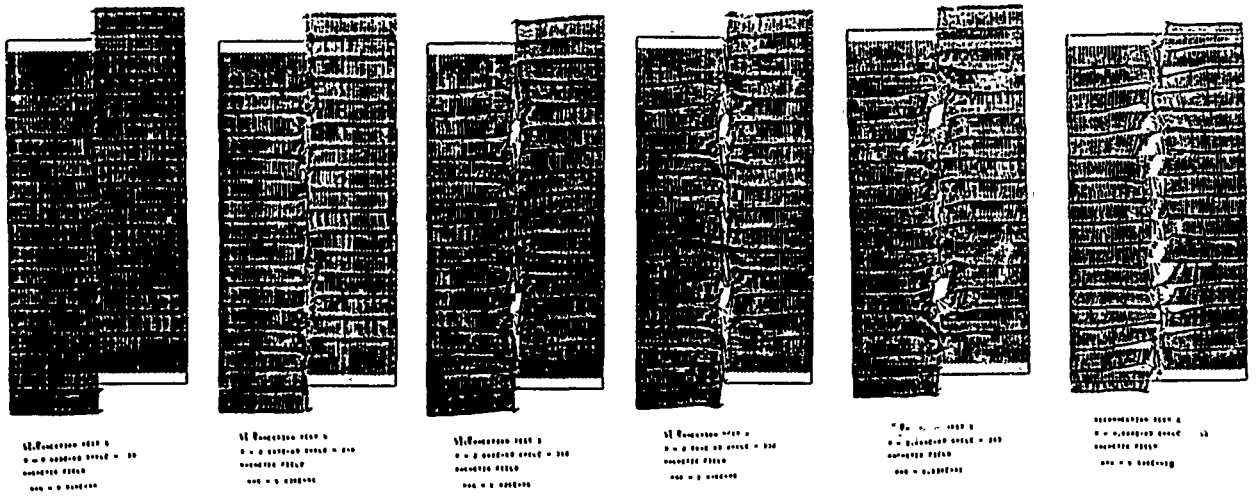

FIGURE 6 MAGNETIC RECONNECTION SIMULATION FOR 96 X 16 CELLS.

xkff = .000001
ykff = 10.0

computational description of the MARAUDER experiment by using an anomalous resistivity subroutine already present in the simulation code.

In the field-reversal geometry, the reconnection process was largely influenced by the current sheet. Not only was the spatial formation of magnetic islands always coincident with the physical position of the current sheet, but their existence and growth depended on the width of the sheet. Such conditions suggest that the growth of the instability which leads to reconnection is most likely driven by the thin sheet of current produced from the field shear. Based on this, the large resistivity which is found interior to the islands can also be explained. As the perturbation is allowed to grow, the particles in the plasma find themselves in a turbulent situation; this results in an increase in the resistivity of the reconnection region.

Because the physics of the compact toroid is no different from that of the simple field geometry, these same properties should be seen with the reconnection site of the compact toroid. To insure this, the anomalous resistivity was treated as the instigator of the instability and written in the following form

$$\frac{\eta^*}{\mu_0} \sim \text{ARESFDG} * \left\{1 - \exp\left[-v_{e0} / (\text{ARESFDG2} * v_{i.a.})\right]\right\}$$

Where $v_{i.a.}$ is the ion-acoustic velocity and v_{e0} is the electron drift velocity in the toroidal direction. Here ARESFDG is indicative of a threshold value for the electron velocity while

ARESFDG2 gives the magnitude of the microturbulence. A parameter search was then started using the values of ARESFDG and ARESFDG2 to find physically meaningful results. At the time of this report, I have run the simulations using the values of 0,1, and 10 for ARESFDG. So far this has shown that there is very little change in the reconnection properties between 1 and 10.

IV.RECOMMENDATIONS

a. The phenomenological model developed here treats the anomalous resistivity as the diffusion process responsible for the magnetic reconnection observed in compact toroid formation. Since this model was derived from a shear field configuration, it should be applicable to any physical experiment containing a field reversal geometry. Implementing the anomalous resistivity model in an existing MHD code containing all pertinent physics should not be too difficult.

b. The work accomplished in the ten week period established a foundation for future research of the reconnection process in compact toroid formation. This study is being continued at Kirtland AFB where I am working on this project as a part time co-op student. The parameter search with the anomalous resistivity is currently being pursued to find the necessary values for ARESFDG and ARESFDG2 that furnish the expected reconnection properties.

The equation used for the anomalous resistivity does not restrict the large resistivity only to the reconnection site located at the neck of the lower end of the bubble. Instead, the high resistivity is defined over the vicinity surrounding the neck. This might cause problems in emulating the actual experiment and needs to be kept in mind when performing the formation simulation.

c. In incorporating this phenomenological model for the reconnection process in an MHD code, the numerical effects to the diffusion process should not be ignored. Extreme instances of numerical effects include cases where the reconnection is a product soley of numerical diffusion or the growth rate is completely damped by the numerical resolution. Often the numerics involve an interplay between these two extremes and lead to inaccurate conclusions concerning the details of the reconnection mechanism. It is therefore imperative that numerical effects be taken into account in the simulations of the reconnection process.

REFERENCES

1. Degnan, J.H., et al., "Compact Toroid Formation Experiments", Proc. 1990 IEEE International Conference on Plasma Science, Oakland California, May 1990, 3P4-10.

2. Furth, Harold P., John Killeen and Marshall N. Rosenbluth, "Finite-Resistivity Instabilities of a Sheet Pinch", The Physics of Fluids, Volume 6, No.4, April 1963, p.459.

3. Peterkin, Robert E. Jr., "Compact Toroid Simulations with MACH2", MRC/ABQ-R-1130, December 1988.

4. Peterkin, Robert E. Jr., et al., "MACH2: A Reference Manual - Fourth Edition", MRC/ABQ-R-1207, November 1989.

5. Sovinec, Carl R., and Robert E. Peterkin, Jr., "Phase 1B MARAUDER Computer Simulations -- Formation of Plasma Torus", Proc. 1990 IEEE International Conference on Plasma Science, Oakland California, May 1990, 3P4-14.

1990 USAF-UES SUMMER FACULTY RESEARCH PROGRAM/

GRADUATE STUDENT RESEARCH PROGRAM

Sponsored by the

AIR FORCE OFFICE OF SCIENTIFIC RESEARCH

Conducted by the

Universal Energy Systems, Inc.

FINAL REPORT

SEPS: Stimulated Emission Pump Spectroscopy of IF

Prepared by:	Shawn J. Gaffney
Academic Rank:	Graduate Student
Department and University:	Electrical Engineering Notre Dame
Research Location:	USAF WL/ARDJ Kirtland AFB, NM 87117
USAF Researcher:	Capt. Mel Nowlin
Date:	20 Aug 90
Contract No:	F49620-88-C-0053

SEPS: Stimulated Emission Pump Spectroscopy of IF

by

Shawn J. Gaffney

ABSTRACT

Preliminary work was started on an experimental station to perform stimulated emission pumping on iodine monofloride. Two optical tables were prepared with the proper optical equipment to simultaneously converge the beams of two pulse dye lasers and one ring dye laser onto a reaction point . The appropriate optics and monitoring equipment was added to observe the wavelength of all beams as well as beam absorption at the reaction site. The design and fabrication of a high speed photodetector was completed. The detector allowes time shifted synchronization of two Nd:YAG to be measured and can be used to detect and signal the presence of beam intensities dangerous to other equipment.

Acknowledgements

I wish to express my appreciation to the Air Force Systems Command and the Air Force Office of Scientific Research for providing the opportunity to participate in the research efforts of the Weapons Lab's Chemical Laser division. The cooperation and encouragement among the lab's personnel made the working environment very enjoyable. In particular, Chris Berst, Lt. Matt Bohn, Capt. Bob Cranich, Dr. Dan Johnson, Capt. Bob Mack, and Marty Vias were always willing to lend both a helping hand and discuss technical matters. Dr. Ernie Dorko kept things running smoothly and could be counted on for assistance in all areas. In addition, Dr. Dorko fostered both a sense of unity among the researchers and the leadership necessary for technical excellence.

Capt. Mel Nowlin is leader of the SEPS experiment and is an excellent engineer. His combination of managerial and engineering skills, as well as, the support and encouragement he provided, made the research period very rewarding.

I. INTRODUCTION:

The stimulated emission process occurs when an excited atom is induced by an outside source to emit its excited state energy. In the case of SEPS, this outside influence is a laser pulse, and the energy emission is in the form of a photon. By tuning this laser pulse so its photons have energy exactly equal to the energy difference between the excited state of the atom and a desired lower energy state, the atom is stimulated into emitting a photon. This photon is identical to the stimulating photon in energy, direction of travel, frequency and phase; thus light produced through this process appears as a laser beam.

The Chemical Laser Facility at Kirtland AFB is particularly concerned with investigating the feasibility of using the stimulated emission process in the design of a chemical laser which would operate in the visible spectrum. It appears that certain diatomic molecules hold promise in this area. Iodine monofloride was chosen to be the first investigated, but the experimental apparatus design allows flexibility in investigation other gaseous substances.

II. OBJECTIVES:

The principal goal of the summer research was to determine the rate of vibrational energy transfer in ground state iodine. Because these values can be readily cross checked with existing literature, this data serves as a calibration source for the experimental apparatus. Once accomplished, the equipment would be ready for data acquisition of iodine monofloride.

The experimental station consists of one argon-ion laser, two pulse dye lasers (PDL), one ring dye laser, two Nd:Yag pulse lasers, assorted optics, two wave meters, and a monocrometer. Data acquisition is accomplished via a National Instruments A/D conversion board which reads the output of a photomultiplier tube used with the monocrometer and assorted signal processing equipment. The argon-ion laser serves as a pumping source for the ring dye laser and the Nd:Yag lasers pump the pulse dye lasers. The output beams from the three dye lasers converge onto a low pressure (15 mTorr) iodine cell. The iodine is placed into a

vibrationally excited state by a pulse from the first PDL. This is followed by a pulse from the second PDL which causes stimulated emission. Finally, the monochrometer is used in conjunction with the signal processing/data acquisition equipment to measure differences in absorption of the ring dye laser beam as it probes the reaction cell. From data gathered, the kinetic rate may be determined.

III.

In completing the assembly of the experimental station, the following requirements were necessary and constituted my main assignment as a participant in the 1990 Summer Graduate Student Research Program (GSRP). A pressure tune control was fabricated for controlling a pulse dye laser etalon; this included installation of a digital panel meter for monitoring pressure. Following this, a laser beam cavity/enclosure was constructed. This structure reduces the eye strain of working in the area where the pulse lasers are strobing and also serves as protection from beam reflections. A wavemeter to read the pulse lasers was repaired, aligned and calibrated. Cooling systems were repaired and installed on the two Nd:Yag lasers. Finally, a high speed photodetector-amplifier combination was designed and fabricated. This

device has application in both beam intensity monitoring and laser synchronization.

IV. RECOMMENDATIONS:

The SEPS station is at a near operational status as of summer's end; a few technical obstacles still need to be overcome. The method for accurately synchronizing the pulse laser timing is still being addressed. The photodetector designed and fabricated this summer has a decay constant which is too long for the capture of a rapid succession input. However, the rise time for a single input pulse is very rapid, and the use of two detectors would give accurate readings for comparing the start points of the two PDLs. An alternative method being investigated by Capt. Nowlin is the use of a photomultiplier tube instead of the photodetector. I would caution examining any possible delays associated with the tube before trusting it for accurate time shifted synchronizing.

1990 USAF-UES SUMMER FACULTY RESEARCH PROGRAM/

GRADUATE STUDENT RESEARCH PROGRAM

Sponsored by the

AIR FORCE OFFICE OF SCIENTIFIC RESEARCH

Conducted by the

Universal Energy Systems, Inc.

FINAL REPORT

ANALYSIS OF CENTRIFUGE CRATERING

Prepared by:	Michael A. Geer
Academic Rank:	Graduate Student
Department and University:	Civil Engineering Penn State University
Research Location:	Weapons Laboratory, Civil Engineering Division, Geological Response Branch
USAF Researcher:	Maj John Gill
Date:	13 August 1990
Contract No:	F49620-88-C-0053

ANALYSIS OF CENTRIFUGE CRATERING

by

Michael A. Geer

ABSTRACT

Data from a series of explosive crater tests performed in a centrifuge is analyzed. The raw data, in the form of photographs of before-shot and after-shot conditions, is transcribed onto full-size scales. These transcribed drawings are then digitized using a digitizing tablet and computer software. Once on a computer, the drawings are scaled and measured to generate crater data such as diameter, depth, and volume. Also using a computer, the crater profiles can be overlaid on one another and symmetry between the right and left halves of the profiles can be examined. Finally, relative movements of soil markers can be determined.

ACKNOWLEDGEMENTS

I would like to thank Maj John Gill and Capt Bill Corson for going through all the trouble and expense of enabling me to work at the Weapons Lab this summer. I'd especially like to thank Maj Gill for all of his help and guidance on this project. Additional thanks are due to Prof. Krauthammer for his help and to all of the personnel in the geological response section for their help and friendship. I would also like to acknowledge the sponsorship of Air Force Systems Command, Air Force Office of Scientific Research.

I. INTRODUCTION

Explosive cratering is of interest both to the military (structural survivability) and to civilian industry (primarily mining and construction). Full scale field data is very difficult and expensive to obtain, and shows a great deal of scatter due to a wide range of site and explosive conditions. This has led researchers to look for ways to physically model field test conditions in a more controlled and less expensive laboratory environment.

Small scale tests at one gravity have shown that true similarity between model and prototype cannot be achieved Goodings, et al., 1988). For laboratory tests to accurately model full scale events, gravitational acceleration must be changed so that similar stresses are experienced at similar points in the soil. The use of a centrifuge is the most common way of creating a high gravity environment in the laboratory. Although Soviet and European researchers have been using centrifuges for several decades to model a number of geotechnical situations, only in the last 15 years or so has the centrifuge become an important research tool in the United States.

My research interests are in the area of soil dynamics and soil liquefaction, particularly with regard to explosive sources. My thesis advisor, Prof. Krauthammer, has done extensive work with the Air Force in the area of explosive effects on structures and soils. It was he who helped me make contact with Maj Gill and learn about his centrifuge project.

II. OBJECTIVES OF THE RESEARCH EFFORT

The goal of my work this summer was to extract crater data from the series of photographs taken during the experiments. The following data was desired:

Crater diameter
Crater depth
Crater volume
Scaled plots of various craters overlaid on one another
Comparisons of scaled crater profiles to field test profiles
Comparisons of scaled crater volumes to field test volumes
Crater symmetry between the left and right halves of the profiles
Relative movements of soil markers before and after the shots

Normally, the actual crater dimensions are measured immediately after the centrifuge stops spinning. In this case, no measurements were taken; photographs were taken of the crater profiles through the plexiglass wall of the quarter-space apparatus. My assignment was to extract all of the above data from these photographs. The tools at my disposal included full-size scales, or "targets",(i.e., the same size as the scale on the plexiglass wall of the centrifuge), a mapping software package, and a digitizing tablet.

All of the required data was obtained. Further research on the effects of scaling the craters and on wind and Coriolis effects will be performed this fall and winter as part of my master's thesis at The Pennsylvania State University.

III. PROCEDURE

The objectives stated in the previous section were met in three steps. First, scale drawings of the photographs needed to be done. Because the photographs were taken from different distances and different angles, a set of drawings with consistent scale and perspective were needed. This was done by hand using the photographs of each shot and full size targets on paper. Several photographs were taken from different angles for each shot. Using the photographs, points could be matched between the target in the photograph and the full size target on paper. Once the similar points were noted, the crater profile and sand markers were sketched in.

The second step was to digitize the drawings. Once the drawings were input into a computer (through a digitizer), they could be scaled and manipulated to obtain the desired data.

The manipulation of the digitized drawings was done in step three using a commercial software package called ARC/INFO. Crater diameters, depths, and volumes are presented in Table 2 in the next section. The crater diameters and depths were found directly from ARC/INFO; these numbers were used to calculate the volumes by hand. The qualitative results (the various overlays and comparisons) were done by using ARC/INFO's graphics capabilities. Showing the complete set of these results would exceed the length limit of this report; examples of each type of result are shown in the next section.

IV. RESULTS

Table 1. Centrifuge Shots

Shot	Acceleration (g)	Scaled Charge (lb TNT)	Scaled Depth of Burst (ft)
A	26.2	500	0
B	26.2	500	0
C	33.0	1000	0
D	41.6	2000	0
E	33.0	1000	0
F	26.2	500	0
G	26.2	500	5
H	26.2	500	10
I	26.2	500	15

Table 2. ...ter Data

Crater	Scaled Diameter (ft)	Scaled Depth (ft)	Scaled Volume (ft^3)
A	20.33	3.92	542
B	21.62	3.98	612
C	26.65	4.75	1186
D	29.36	5.22	1678
E	23.17	4.55	748
F	21.45	3.85	476
G	36.30	6.46	3103
H	36.21	7.33	3453
I	32.75	6.22	1806

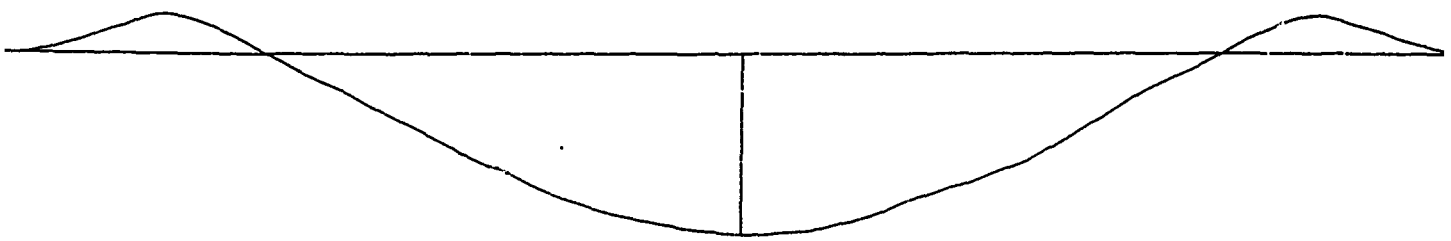

Figure 1. Profile of Crater B

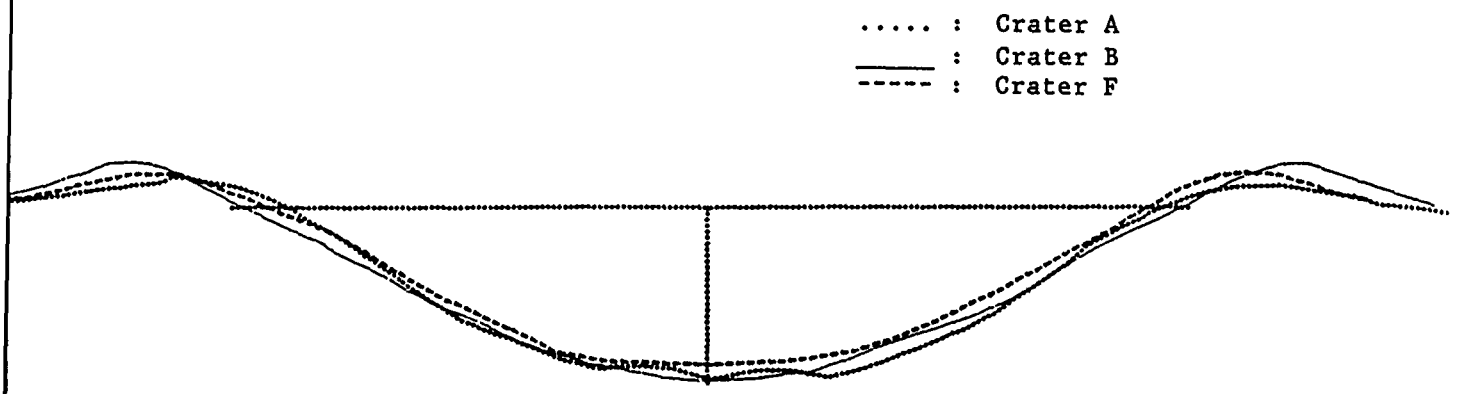

Figure 2. Overlay Comparing Craters A, B, and F

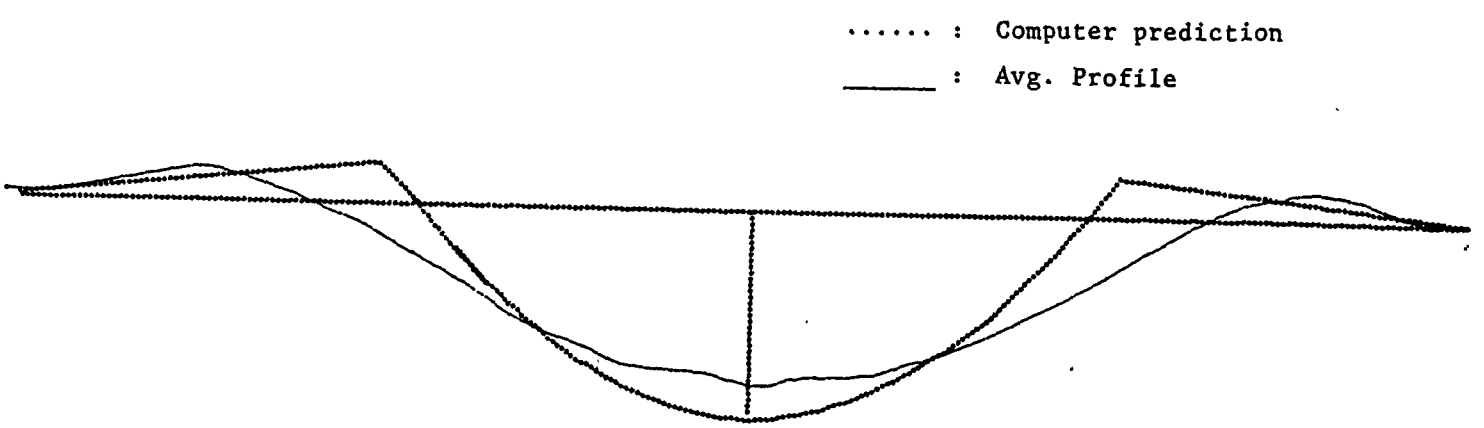

Figure 3. Overlay Comparing Computer Prediction for 500 lbs. at 0 DOB With Average Profile for Craters A, B, and F

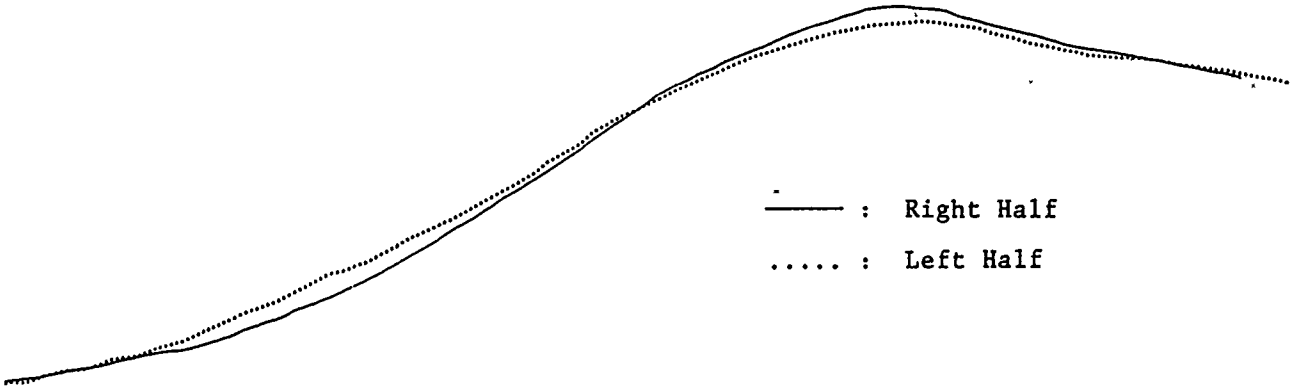

Figure 4. Overlay Comparing Left and Right Halves of Crater D

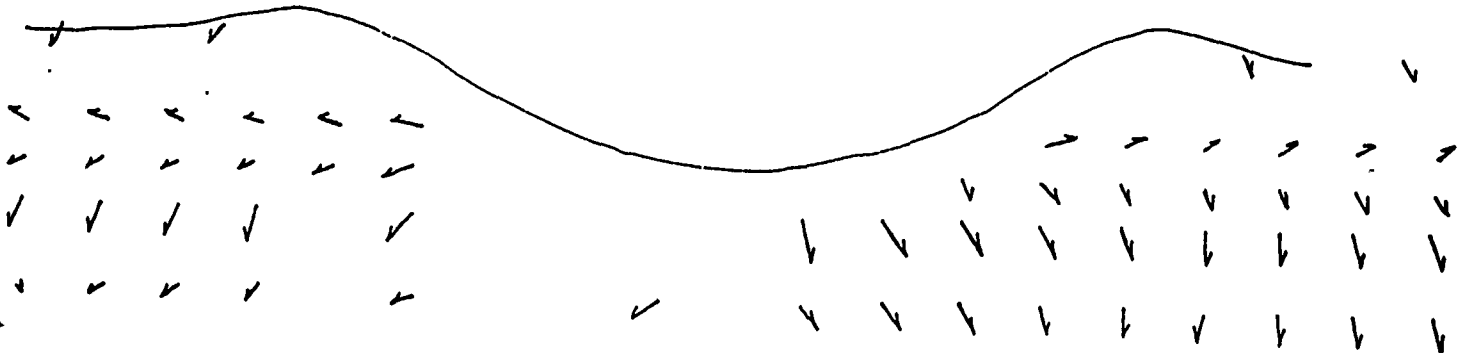

Figure 5. Crater D Relative Soil Movements

V. RECOMMENDATIONS

The results gained from this research are not of much use in and of themselves; they are meant to be used in a larger effort which will examine scaling effects of centrifuge testing and the effects of windage and Coriolis, if any. This work will be done this fall and winter as part of a master's thesis at The Pennsylvania State University. I will work closely with Maj Gill and my advisor, Prof. Theodor Krauthammer.

I feel there is a great deal that still needs to be done in the field of centrifuge cratering. Studies dedicated solely to examining the effects of windage and Coriolis would be very helpful in determining the usefulness of the centrifuge as a research tool. The experiments described in this report only consisted of nine craters. A much more extensive study, perhaps involving dozens of shots, would be a substantial addition to the current field of knowledge.

REFERENCES

Goodings, D.J., Fourney, W.L., and Dick, R.D., "Geotechnical Centrifuge Modeling of Explosion Induced Craters - A Check for Scaling Effects," Report AFOSR 86-0095, The University of Maryland, 1988.

1990 USAF-UES SUMMER FACULTY RESEARCH PROGRAM/
GRADUATE STUDENT RESEARCH PROGRAM

Sponsored by the

AIR FORCE OFFICE OF SCIENTIFIC RESEARCH

Conducted by the

Universal Energy Systems, Inc.

FINAL REPORT

SHIELD AND REFLECTOR MATERIALS FOR OUT-OF-CORE THERMIONIC SPACE NUCLEAR REACTORS

Prepared by:	Michael G. Houts
Academic Rank:	Graduate Student / PhD Candidate
Department and University:	Nuclear Engineering Department; Massachusetts Institute of Technology
Research Location:	AFWL/TAPN, Kirtland AFB, New Mexico
USAF Researcher:	Francis J. Jankowski
Date:	17 September 1990
Contract No:	F49620-88-C-0053

SHIELD AND REFLECTOR MATERIALS FOR OUT-OF-CORE THERMIONIC SPACE NUCLEAR REACTORS

by

Michael G. Houts

Out-of-core thermionic space nuclear reactor (OTR) performance and safety might be enhanced through reflector and/or shield modifications. Two topics are discussed in this report: the effect of modifying the radial reflector of a reference OTR (GA's "STAR-C") and the potential of using various metal hydrides for shielding.

The radial neutron reflector for the reference OTR is beryllium. Up to 71% of this beryllium can be replaced with an alternate material without affecting electrical or heat rejection subsystem design. Replacing 71% of the beryllium in the radial reflector with $B^{11}{}_4C$, BeO, or Diamond increases system k_{eff} and reduces onboard toxicity. OTRs can be controlled by changing neutron leakage instead of absorption by modifying the radial reflector to pivot, and using a disk radiator for heat rejection. The need for axial heat pipes between the core and the pivoting reflector reduces k_{eff} by 0.5% for the pivoting reflector system.

Shield fluences and heating rates in OTRs are lower than in other space nuclear reactor systems, allowing a wider range of potential shielding materials. Neutron and gamma linear and mass attenuation coefficients for HfH_2, HoH_3, LiH, ThH_2, Th_4H_{15}, TiH_2, UH_3, and ZrH_2 are evaluated in this study. In addition; the effect of adding 5 volume percent $B^{10}{}_4C$ to each material (except LiH) is evaluated. For the geometry studied, lithium-6 hydride has the highest effective 1.0 to 3.16 MeV gamma and neutron mass attenuation coefficient. Hafnium hydride has the highest effective 1.0 to 3.16 MeV neutron linear attenuation coefficient; and borated uranium (depleted) hydride has the highest 1.0 to 3.16 MeV gamma linear attenuation coefficient.

The addition of 0.1 volume percent $B^{10}{}_4C$ increases zirconium hydride's effective 1.0 to 3.16 MeV gamma linear attenuation coefficient by 40%. No significant improvement is obtained by increasing $B^{10}{}_4C$ concentration beyond 0.1%.

Acknowledgements

I wish to thank the Air Force's Weapons Laboratory and the Air Force Office of Scientific Research for sponsoring this project. Universal Energy Systems must also be thanked for their assistance with the administrative aspects of this program.

I would especially like to thank Prof. David Lanning, Dr. Frank Jankowski and Major Dan Mulder for their support, advice and encouragement throughout this project. Lt. Fred Nichols' knowledge of the TAPN computers was quite helpful. Harriet Foster's ability to do focused and thorough literature searches also contributed greatly.

I. INTRODUCTION

Out-of-core thermionic space nuclear reactors (OTRs) may be the best systems for providing 5 to 40 kWe to various Air Force payloads. High heat-rejection temperature and the elimination of the need for a pumped coolant loop are two OTR advantages.

There are very few in-depth designs of OTR systems, and existing designs should be optimized. Shield mass can account for 50% of OTR system mass, and should be minimized. Neutron reflectors should be designed to minimize critical mass and core size. Also, any modification of the existing designs must include consideration of the overall system safety and performance.

MIT's Space Nuclear Technology Research Group, under the leadership of Professor David D. Lanning, has spent the last two years researching potential design modifications to a reference OTR, and is also studying OTR control. My previous work with the Space Nuclear Technology Research Group; as well as two summer's experience working on space nuclear power systems at Los Alamos National Laboratory, and ten week's experience working on OTRs at WL/TAPN, contributed to my assignment to Kirtland Air Force Base.

II. OBJECTIVES OF THE RESEARCH EFFORT

The objective of this research effort is to contribute to the development of space nuclear power systems. Specifically, the research is aimed at evaluating potential design modifications to a reference OTR in order to identify potential safety and/or performance improvements. Two types of modifications are evaluated in this study: modification of the reference OTR radial neutron reflector and modification of the reference OTR shield.

III. MODIFYING THE REFERENCE OTR RADIAL NEUTRON REFLECTOR

The STAR-C (GA Technologies, 1987), is the reference out-of-core thermionic space nuclear reactor (OTR) used in this study. The STAR-C uses metallic beryllium as the radial and axial neutron reflector material. Advantages of using metallic beryllium for neutron reflection include the following:

1. Beryllium can be simultaneously used to reflect neutrons and conduct electricity generated by the thermionic converters;
2. Beryllium can be used to provide structural support; and
3. Beryllium can withstand operating temperatures of 1000 K or higher.

It may be desirable to replace all or part of the beryllium neutron reflector with an alternative reflector material for the following reasons:

1. The use of alternative reflector materials may reduce fuel loading;
2. The use of alternative reflector materials may reduce system mass;
3. The use of alternative reflector materials may reduce onboard toxicity and enhance launch safety;
4. Alternative reflector materials may provide an electrical insulator between thermionic converters;
5. The use of alternative reflector materials may reduce water immersion criticality concerns; and
6. The use of alternative reflector materials may enhance operating safety or reliability.

The STAR-C neutron reflectors operate at a temperature of 1000 K. Neutron reflectors that are stable at these temperatures include beryllium (Be), beryllium oxide (BeO), yttrium dihydride (YH_2), Boron Carbide ($B^{11}{}_4C$), graphite (C), and diamond (C). If the reflector temperature can be lowered, zirconium hydride (ZrH_2), yttrium trihydride ($YH_{2.7}$), and lithium hydride (Li^7H) may also be suitable reflector materials.

In the STAR-C design, two beryllium electrical leads conduct electricity from each thermionic converter to the outer surface of the reflector. Beryllium required for conducting electricity is retained in all modified designs. Beryllium is also used in the STAR-C to provide structural support. In all modifications, at least 10 millimeters of beryllium is retained at the base of the core to provide structural support for the STAR-C during launch and operation. A detailed structural analysis is needed to determine the exact amount of beryllium required. No modifications are made to the core/reflector inside a radius of 0.158 m.

III.a Replacing 71% of the Beryllium in the Reference Radial Reflector with BeO, $B^{11}{}_4C$, C, or YH_2

Up to 71% of the beryllium in the reference OTR's outer (15.8 - 23.0 cm) radial reflector can be replaced with an alternate reflector material without modifying the STAR-C power conversion or heat rejection system. MCNP3B (Briesmeister, 1986) was used to calculate k_{eff} for the reference radial reflector, a radial reflector containing 71% Poco graphite, a radial reflector containing 71% YH_2, a radial reflector containing 71% high density graphite, a radial reflector containing 71% B_4C (1% B^{10}), a radial reflector containing 71% B_4C (0.1% B^{10}), a radial reflector containing 71% $B^{11}{}_4C$, and a radial reflector containing 71% Diamond. The results of these calculations are presented in Table 1. The reference axial beryllium reflectors are retained in all cases. Table 1 also shows the effect of using natural tungsten heat collectors/emitters instead of depleted tungsten for the reference reflector , the 71% YH_2 reflector, and the 71% BeO reflector.

TABLE 1. Calculated k_{eff} and Standard Deviation for the Reference Beryllium Reflected OTR, and OTRs using Modified Radial Reflectors Containing 71% Alternate Reflector Material in the 0.158 to 0.23 m Radial Region.

Reflector	k_{eff} (Depleted W)	Standard Dev. (σ)	k_{eff} (Natural W)	Standard Dev. (σ)
Beryllium Metal (Reference)	1.055	0.002	1.040	0.002
71% Poco C	1.015	0.002		
71% YH_2	1.026	0.002	0.999	0.002
71% HD C	1.031	0.002		
71% B_4C (1% B^{10})	1.033	0.002		
71% B_4C (0.1% B^{10})	1.055	0.002		
71% $B^{11}{}_4C$	1.068	0.002		
71% BeO	1.070	0.002	1.055	0.002
71% Diamond	1.091	0.002		

Table 1 shows that modifying the radial reflector to contain 71% boron carbide (0.1% B^{10}); 71% boron-11 carbide; 71% beryllium oxide; or 71% diamond results in an equivalent or larger k_{eff}. Modified OTRs using boron-11 carbide, beryllium oxide, or diamond would require less U^{235} and could have a smaller core diameter. The use of boron carbide or diamond would significantly reduce onboard toxicity. The use of BeO, $B^{11}{}_4C$ or diamond would reduce water immersion criticality concerns by increasing reflector worth. For these cases, if the reflector is stripped off and replaced with water, k_{eff} decreases more for the modified design than for the reference design.

The use of a diamond reflector is at present economically impractical. Future advances in synthetic diamond technology could make the use of a diamond reflector feasible. A reflector containing a 50/50 mixture of high density graphite and diamond is neutronically superior to the reference beryllium reflector.

Depleted tungsten may be difficult and expensive to obtain. An OTR with a beryllium oxide reflector and natural tungsten heat collectors / emitters requires the same fuel loading as an OTR using depleted tungsten and the reference radial reflector. Replacing 71% of the reference radial reflector with BeO would thus allow the use of natural tungsten, with no further system modification.

III.b Modifying the Reference OTR to have a Pivoting Radial Reflector

It may be possible to modify the reference OTR to use a pivoting radial reflector for control and neutron reflection. A schematic of an OTR with a pivoting radial reflector and disk radiator is shown in Figure 1. The modified design is axially identical to the reference design, and radially identical out to a radius of 0.158 m. Heat pipes located between radius 0.158 m and radius 0.178 m transfer waste heat to a disk radiator located above the reactor. The heat pipes are 10 mm wide, 20 mm thick, and have 1.0 mm thick niobium walls (GA Technologies, 1987). The heat pipes taper in at the top of the reactor, and form a column 38 mm in radius between the top of the reactor and the disk radiator. Electrical leads located between radius 0.158 m and 0.178 m conduct electricity to a power conditioner located behind the shadow shield. The radial neutron reflector is located between radius 0.178 m and radius 0.250 m in the modified design. The modified design is controlled by pivoting the radial reflector, which varies radial neutron leakage. Potential advantages of the modified design include the following:

1. The reactor is controlled by leakage instead of absorption, eliminating the need for control rods. Due to the relatively hard neutron spectrum in the reference radial reflector, control rods must be fairly large (up to 1/2 of the available volume in reflector) to provide adequate shutdown margin;
2. Minimum radial reflector operating temperature is not limited by radiator temperature. Radial reflector operating temperatures are low enough to allow the use of ZrH_2, Li^7H, or $YH_{2.7}$; and
3. Infrared signature below the reactor is reduced.

The neutronic performance of eight potential reflector materials was evaluated using MCNP3B (Briesmeister, 1986). In each case, k_{eff} for the pivoting reflector system was calculated with the given material located in the radial (0.178 - 0.25 m radius) and axial neutron reflectors. In each case, 0.01 m of beryllium is retained at the base of the reactor to provide structural support. Table 2 gives the calculated k_{eff} for each material.

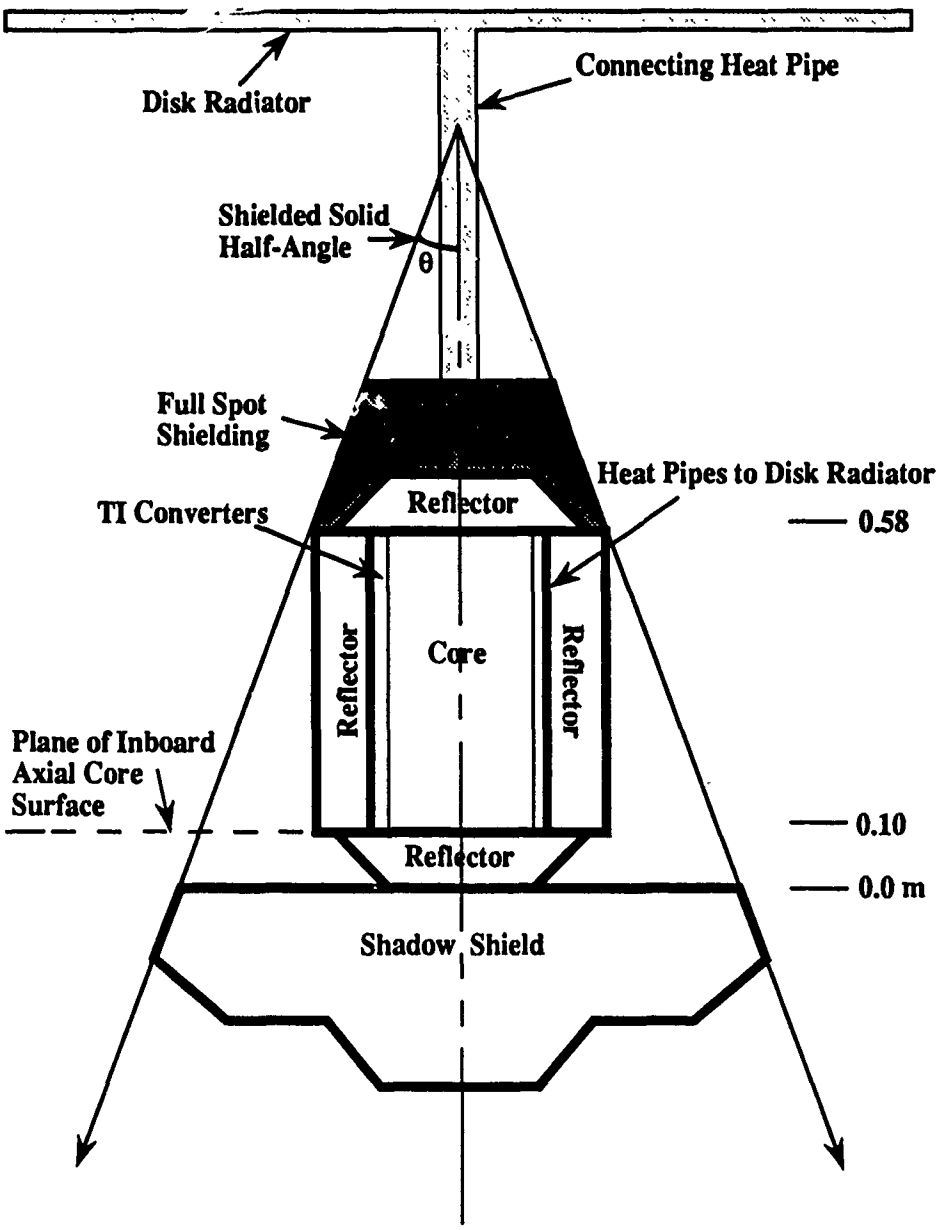

FIGURE 1. Schematic of an Out-of-Core Thermionic Reactor with Disk Radiator and Pivoting Reflector Control; Full Spot Shielding.

TABLE 2. **Calculated k_{eff} and Standard Deviation for Eight Potential Neutron Reflecting Materials and a Void; 75 kWt OTR with Pivoting Neutron Reflector.**

Material	K_{eff}	Standard Dev. (σ)
Void	0.792	0.0021
TiH_2	0.915	0.0026
Li^7H	0.983	0.0017
$YH_{2.7}$	0.993	0.0023
ZrH_2	1.016	0.0025
Be	1.046	0.0024
$B^{11}{}_4C$	1.056	0.0016
BeO	1.065	0.0023
Diamond	1.087	0.0014

Table 2 shows that for the pivoting reflector system, diamond, beryllium oxide, and boron carbide (100% B^{11}) are neutronically superior to beryllium as reflector materials. A slight reactivity penalty is associated with using the proposed pivoting radial reflector instead of the reference radial reflector, as seen by comparing the k_{eff} values in Table 2 to those in Table 1.

III.C Other Considerations

III.C.1 Dose to the Payload from Neutron Backscatter off of the Radiator

Material located outside of the shielded solid angle (i.e. material with a view of the payload) can scatter neutrons or gammas into the shielded solid angle and increase radiation dose to the payload. In

addition, capture gammas produced by neutron absorption in material outside of the shielded solid angle can increase radiation dose to the payload.

The reference OTR has a thermal power of 75 kWt, and rejects 65 kWt of waste heat. A typical shadow shield will shield a 20 degree solid angle from all points in the core and neutron reflectors. A cylindrical radiator with a radius of 0.25 m and an emissivity of 0.90 can radiate 80 kWt per meter of length assuming a radiator temperature of 1000 K and a view factor of one. To reject 65 kWt, the reference OTR radiator must be 0.81 m long. If the effect of the shield on radiator view factor is neglected, and if a 0.05 m gap is left between the shield and radiator, the required radiator will extend 0.28 m above the outboard axial core surface (Figure 2). The payload is not shielded from neutrons or photons interacting in the radiator region located above the plane of the outboard axial core surface (Figure 2).

Energy dependent neutron and photon fluences per fission source neutron were calculated at a dose plane located 5 m behind the OTR core midplane. Neutrons and photons that struck the main shadow shield were assumed to be absorbed. Neutron fluences were converted into 1 Mev equivalent N/cm^2 for a 75 kWt reactor operating for 10 years. Gamma fluences were converted into rads. Both reference and spot shielded cases were considered. Partially spot shielded cases (reference radiator) have shield material in the region located between the plane of the outboard axial core and the plane of the outboard axial reflector surface; outside the outboard axial reflector and inside the shielded solid angle (Figure 2). Fully spot shielded cases (reference radiator) have material located in the same region as the spot shielded case, as well as the region above the plane of the outboard axial reflector surface, below the outboard edge of the radiator, and inside shielded solid angle (Figure 2). Full spot shielding for the disk radiator consists of shielding located outside of the outboard axial reflector, inside the shielded solid angle, and below a plane located 0.20 m above the outboard axial reflector (Figure 1). Calculated neutron and gamma doses for each case are given in Table 3. Table 3 illustrates the importance of keeping all components inside of the shielded solid angle. Neutron fluences from backscatter may approach dose limits, even for the spot shielded cases.

For both the disk and the reference radiator, radiation dose due to backscatter is highest on the outer half of the dose plane. For the disk radiator, dose is fairly uniform across the outer half of the dose plane. For the reference radiator, however, dose is more than twice the outer-half average in the outer 0.10 m of the dose plane. If possible, the reference radiator should be tapered to stay within the shielded solid angle.

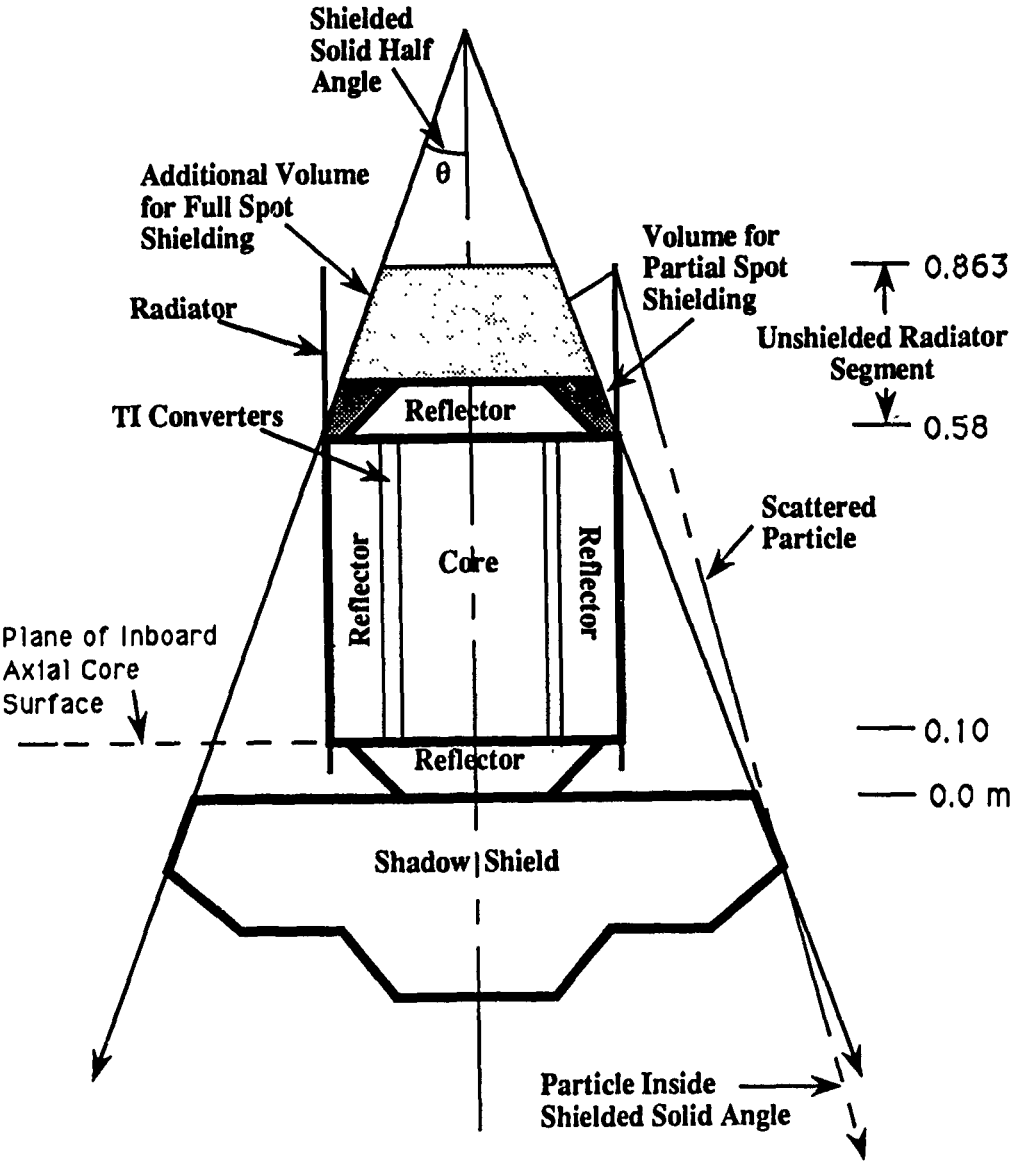

FIGURE 2. Reference Out-of-Core Thermionic Reactor Configuration with Shaded Volume Available for Spot Shielding.

TABLE 3. Average Dose Due to Backscatter off of Radiator; Outer Half (Area) of Dose Plane 5 m Behind Core Midplane; 20 Degree Shield Solid Half Angle; 10 Year Operation at 75 kWt.

Case	Neutron Dose (1 MeV eq N/cm^2)	Gamma Dose (Rads)
Reference Radiator	5.9×10^{13}	5.1×10^{4}
Reference Radiator with Partial LiH Spot Shielding	3.4×10^{13}	3.2×10^{4}
Reference Radiator With Partial HfH_2 Spot Shielding	2.8×10^{13}	2.4×10^{4}
Reference Radiator With Partial ZrH_2/B Spot Shielding	2.9×10^{13}	2.5×10^{4}
Reference Radiator with Full LiH Spot Shielding	1.4×10^{13}	2.1×10^{4}
Reference Radiator With Full HfH_2 Spot Shielding	1.0×10^{13}	9.9×10^{3}
Reference Radiator With Full ZrH_2/B Spot Shielding	1.3×10^{13}	1.1×10^{4}
Disk Radiator	4.8×10^{13}	2.3×10^{4}
Disk Radiator with Full Li^6H Spot Shielding	9.9×10^{12}	7.7×10^{3}

IV. Alternate Hydrides for OTR Neutron and Gamma Shielding

Out -of-core thermionic space reactors (OTRs) differ from other proposed space reactors in that they operate at core thermal powers below a few hundred kilowatts. Shield nuclear heating rates and fluences are thus lower for OTRs than for higher power space reactor systems. The reduced fluence and nuclear heating rates in OTR shields may enable the use of shielding materials that are not well suited for higher power reactors.

Two hydrides currently used for space reactor gamma and neutron shielding are zirconium hydride (ZrH_2) and lithium hydride (LiH). Other hydrides that may be suitable (especially at low fluences) include hafnium hydride (HfH_2), holmium hydride (HoH_3), thorium hydride (ThH_2 or Th_4H_{15}), titanium hydride (TiH_2), and uranium hydride (UH_3). MCNP3B (Briesmeister, 1986) was used to calculate effective neutron

and gamma linear attenuation coefficients for HfH_2, HoH_3, LiH, ThH_2, Th_4H_{15}, TiH_2, UH_3, and ZrH_2. In addition, the effect of adding 5 volume percent $B^{10}{}_4C$ to each material (except LiH) was studied. The addition of boron-10 reduces neutron capture gamma production in some hydrides by reducing the number of neutrons absorbed in hydrogen or in the base element. Neutron capture by boron-10 does not result in capture gamma production.

Mass attenuation coefficients are obtained for each material by dividing the linear attenuation coefficient by the material's density. Further information concerning hydride properties can be obtained from the book Metal Hydrides (Mueller et.al., 1968).

IV.A METHODOLOGY

A simplified OTR system model is used to calculate neutron and gamma attenuation coefficients for each shield material. The model consists of a UC_2/C core surrounded by a beryllium reflector, with a shadow shield located beneath the core. A schematic of the simplified system is shown in Figure 3. The core is 0.40 m long, 0.12 m in radius, and has a 0.04 m radius central annulus. The axial and radial beryllium reflectors are 0.10 m thick. The shadow shield has a radius of 0.22 m and a thickness of 0.20 m.

Neutron and gamma currents inside a shield radius of 0.12 m are tallied at axial increments of 0.02 m. MCNP3B accounts for photons produced by neutron interactions; however, photoneutrons are not taken into account. To help account for buildup, the tally region is surrounded radially with 0.10 m of shield material. Shield material (i.e. the hydride being evaluated) is assumed to be 100% theoretical density at room temperature. Attenuation coefficients are calculated from the change in current between shield depths of 0.02 m and 0.20 m, with distance effects taken into account. Plots of current versus position show the attenuation to be nearly exponential.

The attenuation coefficients calculated are effective attenuation coefficients for the neutron and gamma spectra in the shield. Attenuation coefficients at low energies are thus lower than they would be for a monoenergetic beam, as downscatter provides a continuous source of new particles. High energy gamma attenuation coefficients may also be lower than they would be for a monoenergetic beam of gamma rays due to inelastic neutron scatter and neutron capture gammas. Calculated attenuation coefficients are only valid for the stated geometry. Different geometries or applications may result in significantly different attenuation coefficients, due to buildup or spectral effects. Energy-dependent gamma and neutron linear attenuation coefficients for each evaluated hydride are given in Tables 4 and 5, respectively.

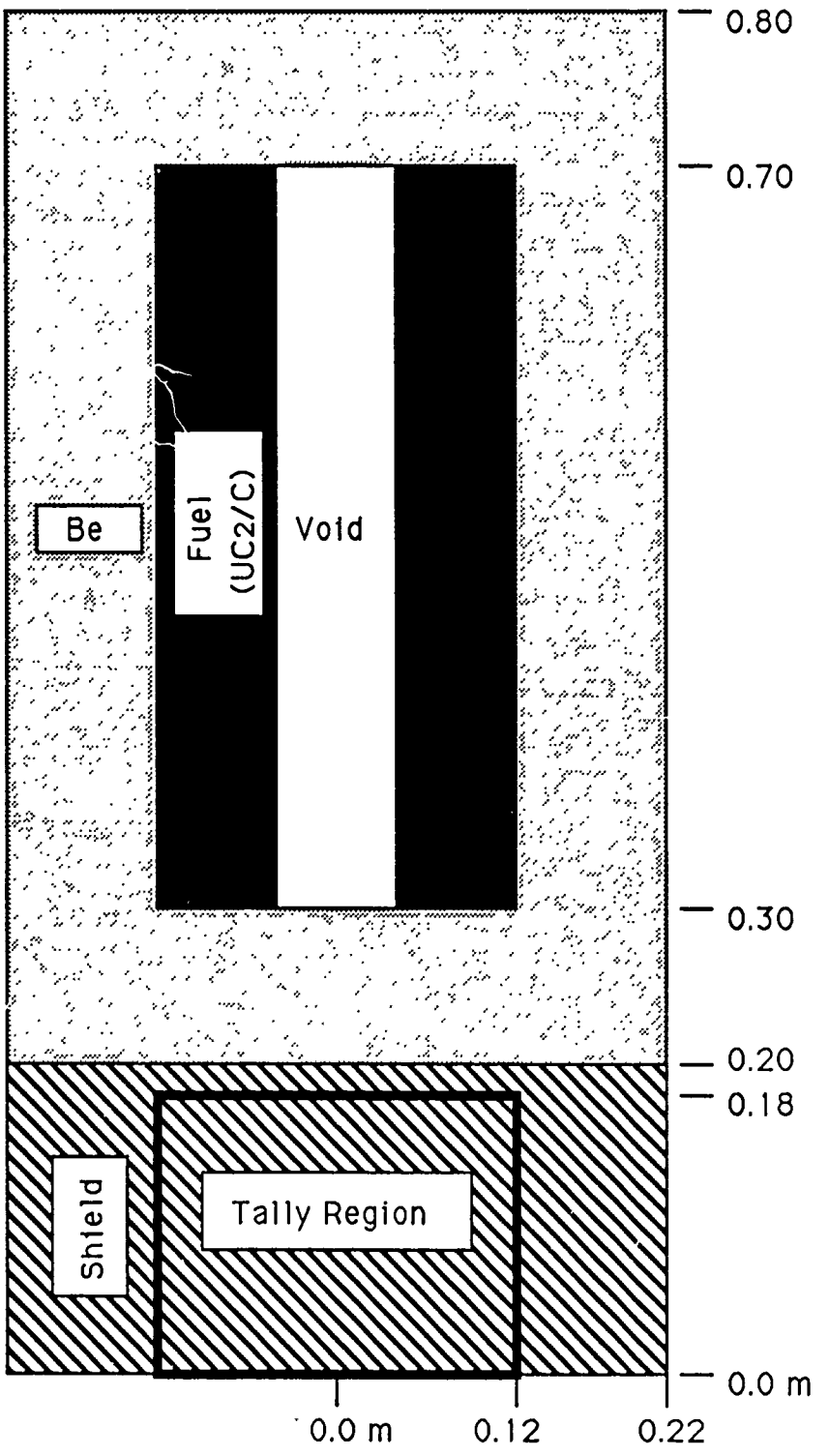

FIGURE 3. Model Used for Evaluating Potential Hydride Shielding Materials.

TABLE 4. Gamma Linear Attenuation Coefficient (cm^{-1}) as a Function of Energy (Mev) for Various Hydrides.

Material	Density ($10^3 kg/m^3$)	0.1-0.316 MeV	0.316-1.0 MeV	1.0 - 3.16 MeV	3.16-10.0 MeV
HfH_2	11.37	0.335 cm^{-1}	0.319 cm^{-1}	0.309 cm^{-1}	0.308 cm^{-1}
HfH_2 / 5%B	10.93	0.330	0.317	0.306	0.301
HoH_3	7.40	0.270	0.247	0.224	0.232
HoH_3 / 5%B	7.16	0.261	0.242	0.220	0.225
Li^6H	0.685	0.021	0.025	0.032	0.005
LiH	0.775	0.022	0.025	0.025	0.015
ThH_2	9.50	0.249	0.245	0.231	0.236
ThH_2/5%B	9.15	0.253	0.267	0.266	0.286
Th_4H_{15}	8.28	0.302	0.277	0.247	0.262
Th_4H_{15}/5%B	7.99	0.288	0.302	0.285	0296
TiH_2	3.70	0.122	0.108	0.105	0.077
TiH_2/5%B	3.64	0.154	0.156	0.118	0.092
UH_3	10.91	0.282	0.240	0.235	0.210
UH_3/5%B	10.48	0.307	0.325	0.332	0.343
ZrH_2	5.62	0.168	0.147	0.130	0.122
ZrH_2/5%B	5.47	0.232	0.217	0.180	0.170

TABLE 5. Neutron Linear Attenuation Coefficient (cm^{-1}) as a Function of Energy (Mev) for Various Hydrides.

Material	Density ($10^3 kg/m^3$)	0.1-0.316 MeV	0.316-1.0 MeV	1.0 - 3.16 MeV	3.16-10.0 MeV
HfH_2	11.37	0.323 cm^{-1}	0.314 cm^{-1}	0.309 cm^{-1}	0.251 cm^{-1}
HfH_2 / 5%B	10.93	0.310	0.302	0.297	0.236
HoH_3	7.40	0.279	0.270	0.261	0.199
HoH_3 / 5%B	7.16	0.276	0.270	0.259	0.190
Li^6H	0.685	0.214	0.194	0.188	0.162
LiH	0.775	0.214	0.198	0.199	0.163
ThH_2	9.50	0.221	0.207	0.214	0.156
ThH_2/5%B	9.15	0.219	0.206	0.206	0.152
Th_4H_{15}	8.28	0.257	0.250	0.256	0.176
Th_4H_{15}/5%B	7.99	0.271	0.263	0.248	0.183
TiH_2	3.70	0.285	0.275	0.270	0.206
TiH_2/5%B	3.64	0.284	0.272	0.265	0.202
UH_3	10.91	0.221	0.201	0.208	0.164
UH_3/5%B	10.48	0.295	0.279	0.275	0.215
ZrH_2	5.62	0.265	0.257	0.239	0.185
ZrH_2/5%B	5.47	0.266	0.252	0.241	0.184

IV.B Gamma and Neutron Attenuation in OTR Shadow Shields

Of the materials evaluated (in the specified geometry), Lithium-6 hydride has the highest effective 1.0 to 3.16 MeV gamma and neutron mass attenuation coefficients; hafnium hydride has the highest

effective 1.0 to 3.16 MeV neutron linear attenuation coefficient; and borated uranium hydride has the highest 1.0 to 3.16 MeV gamma linear attenuation coefficient. Effective attenuation coefficients may be significantly different for different geometries.

Borated uranium hydride is hazardous to work with, and did not show significant enough advantages to warrant further investigation. Lithium hydride and hafnium hydride have excellent shielding properties in the evaluated geometry, and were investigated further for use as space reactor gamma shields. Zirconium hydride containing 1% B^{10}_4C (by volume) was used as the reference shield material.

In the evaluated geometry, lithium-6 hydride is the most mass-effective material for shadow shielding a payload from both neutrons and gamma rays. In an actual shadow shield, however, several factors may reduce the desirability of using Li^6H for gamma shielding. First, because of lithium-6 hydride's low gamma linear attenuation coefficient, shield thicknesses are greater than for borated zirconium hydride. Control rod drives, electrical leads and other components that must pass through or around the shield become longer, more massive, and potentially more complicated. If the power conditioner is mounted on the rear of the shield, additional electrical losses will result from using a thicker shield. Shield volume affects stowability during launch and the mass of the vessel used to contain the shield. Second, the evaluated Li^6H shield reduces 1.0 to 3.16 MeV gamma fluence by less than a factor of three. Actual OTR shadow shields may reduce gamma fluence by a factor of a hundred, thus buildup factors will be larger in actual shields. Actual shields will also have a larger radius, further increasing buildup. Finally, shield mass increases at a rate greater than shield thickness, due to the increasing radius of the shield at increasing thicknesses. This effect is especially pronounced for large shield solid angles.

A potential advantage of using a lithium-6 hydride gamma shield is that virtually no neutrons will pass through a shield of realistic size, eliminating payload damage due to neutrons traveling directly from the reactor. This may be beneficial since neutrons scattering off components (e.g. the radiator in some OTR designs) located outside of the shielded solid angle may provide a significant fluence to the payload. A shield that uses a single material may be simpler than one that requires two or more shield materials.

Hafnium hydride may be the best material for use when shield volume is limited. For example, if a portion of the radiator is located outside of the shielded solid angle, neutrons and gammas exiting the core can backscatter off the radiator, miss the shadow shield, and hit the payload. A small volume where shielding material can be added exists above the core and inside the shielded solid angle. Shielding material added in this volume does not increase shadow-shield size but reduces backscatter off of the radiator.

IV.C Comparison Between Uncontoured ZrH_2/B, Li^6H, and HfH_2 Shadow Shields

Comparisons between ZrH_2/B shields and shields containing an equivalent mass of Li^6H or HfH_2 were made assuming shield solid half-angles of 5 degrees and 20 degrees. A 5 degree half-angle will shield a 4.9 m diameter payload located 25 m behind the core midplane, assuming a reactor diameter of 0.50 m and core length of 0.48 m. With the same assumptions, a 20 degree half-angle will shield a 4.3 m diameter payload located 5 m behind the core midplane. Energy-dependent neutron and gamma fluences were tallied at dose planes located 25.0 and 5.0 m behind the core midplane for the 5 degree and 20 degree shields, respectively. Gamma doses and neutron fluences at the dose planes (assuming 10 years of operation at 75 kWt) are given in Table 6.

TABLE 6. Gamma Dose (Rad) and Neutron Fluence (1 MeV equiv n/cm^2) at the Dose Plane for Various Shields; Assuming 10 years of operation at 75 kWt.

Shield Material	Eq Mass Shield Thick. / Angle	Distance to Dose Plane	Gamma Dose (Rad Silicon)	Neut. Fluence (1 MeV eq. n/cm2)
ZrH_2/B	0.10 m / 5 degree	25 m	6×10^5	2.2×10^{14}
Li^6H	0.59 m / 5 degree	25 m	6×10^5	6×10^{10}
ZrH_2/B	0.30 m / 20 degree	5 m	3×10^5	7.6×10^{13}
Li^6H	1.30 m / 20 degree	5 m	3×10^6	$< 10^8$
HfH_2	0.16 m / 20 degree	5 m	1.1×10^6	6×10^{14}

For the 5 degree shield case with the payload located 25 m from the core midplane, using an equivalent mass Li^6H shield results in a gamma dose equivalent to that from using a ZrH_2/B shield. Neutron fluence, however, is four orders of magnitude less for the Li^6H shielded case.

IV.D Effect of B^{10} Concentration on Gamma Attenuation in Borated Zirconium Hydride (ZrH_2/B)

As shown previously, the addition of small amounts of $B^{10}{}_4C$ to certain hydrides increases effective gamma attenuation coefficients by reducing neutron capture gamma production. An optimal boron concentration exists for zirconium hydride shields, and is dependent on the neutron spectrum within the shield and on the amount of boron that will be lost to burnup. MCNP3B was used to determine effective

energy dependent gamma linear attenuation coefficients for zirconium hydride ($ZrH_{2.0}$) containing 0.01 to 5.0 volume percent B^{10}_4C. Calculated gamma and linear attenuation coefficients are shown in Table 7. Table 7 shows that the effective attenuation coefficient for 1.0 to 3.16 MeV gamma rays rises sharply with the addition of 0.01% B^{10}_4C, and remains roughly constant for B^{10}_4C volume percents of 0.1 to 5.0.

TABLE 7. Gamma Linear Attenuation Coefficient (cm^{-1}) as a Function of Energy (MeV) and B^{10}_4C Volume Percent for Zirconium Hydride ($ZrH_{2.0}$)

Material	0.1 - 0.316 MeV	0.316 - 1.0 MeV	1.0 - 3.16 MeV	3.16 - 10.0 MeV
ZrH_2	0.168	0.147	0.130	0.122
ZrH_2/0.01%B	0.200	0.185	0.160	0.147
ZrH_2/0.03%B	0.218	0.205	0.174	0.153
ZrH_2/0.1%B	0.231	0.216	0.181	0.167
ZrH_2/0.3%B	0.236	0.221	0.183	0.170
ZrH_2/1.0%B	0.236	0.222	0.186	0.160
ZrH_2/3.0%B	0.234	0.218	0.179	0.168
ZrH_2/5.0%B	0.232	0.217	0.180	0.170

V. Recommendations

The following recommendations can be made based on the results of this project:

1. The addition of 0.1% B^{10}_4C to a ZrH_2 shield increases effective 1.0 to 3.16 MeV gamma attenuation coefficients by 40%. Increasing B^{10}_4C concentration beyond 0.1% does not significantly affect attenuation coefficients. The optimal beginning-of-life B^{10}_4C concentration may be the minimum concentration such that burnup does not cause B^{10}_4C concentration to drop below 0.1 %.
2. Neutron interactions with components located outside of the shielded solid angle can result in significant fluences to the payload. If an OTR uses a disk radiator, neutron interactions with the radiator must be considered when determining satellite configuration, radiator material, and spot shielding requirements.
3. A lithium hydride neutron/gamma shield may be well suited for applications requiring a small shielded solid angle and moderate gamma attenuation. The primary advantage of using a single material for shielding is the simplification of shield design. The primary disadvantage of a lithium hydride

neutron/gamma shield is its large thickness and volume. The effects of gamma radiation on lithium hydride need further investigation.

4. Hafnium hydride has large neutron and gamma linear attenuation coefficients, and may be useful for volume-limited shielding applications. Spot shielding to prevent backscatter off of components located outside the shielded solid angle is one example.

5. Replacing 71% of the reference radial reflector with $B^{11}{}_4C$, BeO, or Diamond increases k_{eff} and reduces onboard toxicity. The potential of using $B^{11}{}_4C$ as a reflector material should be further evaluated. The feasibility of a synthetic diamond reflector should be periodically assessed.

6. An OTR using a pivoting reflector for control (via leakage) has a slight neutronic disadvantage over the reference system. The use of pivoting reflector control may simplify the system, and would eliminate the neeed for large control rods inside the radial reflector. The infrared signature of the reactor could be reduced if a disk radiator is used in conjuction with pivoting reflector control.

References

Briesmeister, J.F. (1986) MCNP - A General Monte Carlo Code for Neutron and Photon Transport, LA-7396-M, Rev. 2, Los Alamos National Laboratory, Los Alamos, NM.

GA Technologies (1987) "Concept Definition Phase of the STAR-C Thermionic Power System for the Boost Surveillance and Tracking System (BSTS)," GA-C18676, General Atomics, San Diego, CA.

Mueller et al. (1968) Metal Hydrides, Academic Press, New York, NY.

James Lasche

Technical Memorandum Submitted

1990 USAF-UES SUMMER FACULTY RESEARCH PROGRAM

GRADUATE STUDENT RESEARCH PROGRAM

Sponsored by the

AIR FORCE OFFICE OF SCIENTIFIC RESEARCH

Conducted by the

Universal Energy Systems, Inc.

FINAL REPORT

Variable Structure Control Pointing and Tracking of Flexible Structures

Prepared by:	Toby B. Martin
Academic Rank:	Graduate Student
Department and	Aeronautical and Astronautical Engineering
University:	University of Illinois at Urbana-Champaign
Research Location:	AFWL/ARCB Kirtland AFB Albuquerque, New Mexico
USAF Reseacher:	Lt. Larry Cooper Lt. Travis Peppler
Date:	10 Aug 90
Contract No:	F49620-88-C-0053

Variable Structure Control Pointing and Tracking of Flexible Structures

by

Toby B. Martin

ABSTRACT

It is shown here a means of achieving pointing and tracking maneuvers of flexible structures in the presence of slew induced deformations, aft-body disturbances and model errors. Flexible structures pose a problem for control engineers mainly due to the difficulty in modeling such structures, following is a method of controlling these structures without a precisely known model. A sliding control technique coupled with Lyapunov stability criteria design are implemented to provide a robust control capable of performing the desired task.

A sliding surface is defined based on tracking error and remaining on this surface becomes the essence of the control problem.It is illustrated how this technique leads to a 'chattering' controller and how a modified version, implementing a boundary layer about the sliding surface, can be used to avoid this chattering behavior. This new 'non-chattering' controller trades tracking performance for control effort, thus avoiding the problems of high actuator activity and possibly non-linear dynamic excitation. Finally the dynamics within the error boundary can be represented by that of a critically damped oscillator with designer selected time constant.

ACKNOWLEDGEMENT

I wish to thank the Air Force Systems Command and the Air Force Office of Scientific Research for sponsoring this research. I also wish to thank those people at Universal Energy Systems, Inc., for their work in administering the Graduate Student Reseach Program for the U. S. Air Force.

I finally thank LT. Lawrence Cooper, LT. Travis Peppler, and Bill Wood of the Air Force Weapons Lab/ARCB for their valuable assistance in the TACOS lab. Also the men and women of Air Force Weapons Lab, Kirtland AFB, New Mexico.

I. INTRODUCTION

A problem concerning many of today's engineers is the control of flexible structures, especially with the space station and other large space structure projects getting underway. The movement of these structures involves, usually unmodeled, non-linear dynamics. Often the use of nominal trajectory or feed-back linearization methods are employed to address problems with flexible dynamics [1], [2]. These methods have their drawbacks, due to deviations from the precalculated nominal trajectories in the first case and from problems finding suitable transformations in the second, that render these methods incapable of performing the desired task [3]. And in the presence of modeling errors or parameter variations, serious robustness issues arise with each of these methods.

The Air Force Weapons Lab is interested in movement of flexible structures due to interest in large DEW systems in the planning and development stages. My research interests lie in the area of applying advanced control techniques for slewing flexible space structures. It is shown here that a control algorithm can be developed, in the presence of parameter uncertainties, to provide improved pointing and tracking performance of flexible structures. A sliding control technique along with Lyapunov stability criteria, known as Variable Structure Control (VSC) is demonstrated on a laboratory model on the TACOS testbed at the Air Force Weapons Lab, Kirtland AFB, New Mexico. The model is a simplified space-based laser or telescope beam expander. It is shown using VSC how a nominal control is generated based on, perhaps inaccurate, model parameters and a correction control is computed based on upper bounds on model errors and the tracking error. It is also demonstrated how a modified version of VSC can be implemented to reduce high actuator control effort (which may excite unmodeled non-linearities) at the expense of tracking performance [4].

II. OBJECTIVES

It is desired to develop a control scheme capable of accurate pointing and tracking of a flexible body. Once the rotational and flexible dynamics are combined, the object is to develop a control scheme capable of high precision tracking of a commanded angular trajectory. It is desired to accurately control the central body or hub angle while it is being corrupted by the elastic dynamics of a flexible appendage. It is also desirable to investigate the ability of the selected control scheme to perform with limited bandwidth actuators.

2.1 Equations of Motion

Modeling a movable flexible structure is often one of the most pressing issues when developing a control scheme for this type of system. The more precise our model, the more complex the equations of motion become, and the more difficult the entire problem becomes. Therefore in the development of the model some simplifying assumptions are employed. First, only slew induced deformations of the appendage are modelled. Second, the structure is viewed to be discrete, having point masses connected by massless links. The coupling between vibration and rotation is clearly observable in this simple model.

In this section we model a single axis rotational/vibrational system, as described by (fig. 2.1). The general planer equations are first given (without derivation) and then modified to suit the proposed problem and laboratory setup.

Using a body fixed axes system, we develop the planar equations of motion:

- Planar Rotation

$$[J + y^T M^* y]\ddot{\theta} + [b - 2\dot{y}^T M^* y]\dot{\theta} + k\theta + \delta^T \ddot{y} = \tau + e^T f \qquad (2.1)$$

where: J = axial inertia matrix, y = structural deformation vector (with respective time derivatives), M^* = associated mass matrix, b = axial damping matrix, k = axial stiffness matrix δ^T = rotational/vibrational coupling matrix, θ = angular trajectory, τ = control torque vector, e^T = force distribution (rotational influence) matrix, f = external force vector.

- Planar Vibration

$$M\ddot{y} + c\dot{y} + (k + \dot{\theta}^2 M^*)\, y + \delta\ddot{\theta} + Ef \qquad (2.2)$$

where: M = mass matrix, c = structural damping matrix, k = structural stiffness matrix, δ = rotational/vibrational coupling matrix, E = force distribution (vibrational influence) matrix

immediately we see the effects of coupling through terms like $y^T M^* y\ddot{\theta}$, $\dot{y}^T M^* y\dot{\theta}$, $\delta^T \ddot{y}$ in the rotational equation and $\dot{\theta}^2 M^* y$, $\delta\ddot{\theta}$ terms in the vibrational equation. Now the product terms $y^T M^* y\ddot{\theta}$ and $\dot{y}^T M^* y\dot{\theta}$ are small and can be neglected if we assume small deflections. Now finally, with the current laboratory setup, f = 0, since there are no actuators on the appendage. Also the motor/beam system is free to rotate, so there is no restoring spring constant, k = 0. A torsional dynamometer is used to sense the rotational/vibrational coupling. Therefore, the whole effect of the disturbance caused by the vibrating beam is captured by the torsional dynamometer signal, τ_{dyn}. So now we simply have for control purposes a linearized equation of motion given by:

- Planar Rotation

$$J\ddot{\theta} + b\dot{\theta} = u - \tau_{dyn} \tag{2.3}$$

here the control torque τ is replaced by the familiar control variable u.

III. VARIABLE STRUCTURE CONTROL TECHNIQUE

Due to problems with classical (PD, PID,...) controllers [5], we find it necessary to pursue a different design method that takes into account limited actuators modeling errors of the system. The chosen method is called Variable Structure Control, it utilizes a sliding manifold and Lyapunov stability criteria. VSC was first introduced by the Soviets in the mid-sixties (by Enelyanov) and again by Utkin and Itkis in the mid-seventies [6]. Since it's introduction, flexible robot manipulators [4] and large angle spacecraft maneuvers [7] have benefitted (if only theoretically) from VSC techniques.

3.1 Chattering Control

VSC's main feature is it's 'switching' of the control as the state variables cross predetermined surfaces in the state space. This switching allows the dynamics to stay on the desired surface without regard to disturbances or parameter variations. Generally we would define the n-th order error dynamics, s, as:

$$s(\Delta\theta,t) = \left(\frac{\partial}{\partial t} + \lambda\right)^{n-1} \Delta\theta \tag{3.3}$$

where, s, is now a new definition of the tracking error, n is the order of the dynamic system and $\Delta\theta = \theta - \theta^*$ as defined before is the true tracking error.

The definition of the switching manifold, S, is given simply by:

$$S = \{s \mid s(\Delta\theta, t) = 0\} \tag{3.4}$$

In our system (a simple second order one, n = 2) we would conclude that the surface dynamics defined by $s = 0$ and $\dot{s} = 0$ is given by (3.3) with n=2 or:

$$s = \Delta\dot{\theta} + \lambda\Delta\theta \tag{3.5}$$

Now if $s = 0$ and $\dot{s} = 0$ on the switching surface, we have:

$$\left(\frac{\partial}{\partial t} + \lambda\right)s = 0 \tag{3.6}$$

which yields:

$$\Delta\ddot{\theta} + 2\lambda\Delta\dot{\theta} + \lambda^2\Delta\theta = 0 \tag{3.7}$$

we have the error dynamics behaving as a critically damped oscillator, with designer selected λ. In actuality this second order system in $\Delta\theta$ behaves as an asymptotically stable first order system in s with a time constant λ^{-1}
Then we know that the solution to this system is given by:

$$|\Delta\theta| \leq |\Delta\theta(t_o)|e^{-\lambda(t - t_o)} \tag{3.8}$$

Therefore tracking any commanded trajectory θ^* is equivalent to staying on the switching surface, S, once we've reached it for all time $t > t_o$. This can be expressed by:

$$\left\{\begin{array}{l} \lim_{s \to 0^+} \frac{\partial}{\partial t}(s) < 0 \\ \lim_{s \to 0^-} \frac{\partial}{\partial t}(s) > 0 \end{array}\right\} \tag{3.9}$$

Now define a candidate Lyapunov function for our 2-dimensional system to be:

$$V(s) = \frac{1}{2}s^2 < 0 \tag{3.10}$$

From [6] we state the following two theorems to ensure existence of the sliding mode and reachability of the switching surface.

Theorem 1 For a system equivalent to the state space form of the combined vibrational and rotational dynamics given by:

$$\dot{x}_1 = x_2$$
$$\dot{x}_2 = -J^{-1}(-bx_2 - u + \tau_{dyn}) \tag{3.11}$$

(where mentioned before τ_{dyn} contains all the external forces applied to the appendage, if any, and all of the vibrational coupling terms)

and a multidimensional switching surface S, a sufficient condition for the existence of a sliding mode is that:

$$\frac{\partial}{\partial t} V(s) = s\dot{s} < 0 \tag{3.12}$$

in a neighborhood of $s = 0$.

Theorem 2 For a system equivalent to (3.11) and a multidimensional switching surface S, the subspace for which $s = 0$ is reachable is given by :

$$\Gamma = \{ s \mid s\dot{s} < 0 \; \forall \; t \} \tag{3.13}$$

Proofs may be found in [8]. Further, a much stronger condition is given by [4] as:

$$\frac{1}{2}\frac{\partial}{\partial t}(s^2) \leq -\eta |s| \tag{3.14}$$

where η is a positive constant.

According to [5] and [8] there exists an 'equivalent control input', the ideal control that can maintain $s = 0$ and $\dot{s} = 0$. This is when the tracking error remains on the switching surface for all time after it reaches it. This equivalent control is found by setting the equations in s and $\dot{s}$ (3.5),(3.11) equal to zero then solving for u_{equiv}.

When there are uncertain model parameters, $s = 0$ can never be maintained. So one is forced to apply the weaker condition of $\dot{s} = 0$. This fortunately yields a solution in the neighborhood of $s = 0$, which would be the same with the proper choice of a boundary layer as found on the surface itself [4]. Now to bring the s dynamics close to S, a correction control is added/subtracted to a nominal control. the nominal control is found by simply applying the weak condition, $\dot{s} = 0$, discussed above, where:

$$\dot{s} = \ddot{\Delta\theta} + \lambda\dot{\Delta\theta} \tag{3.15}$$

substituting in with (2.3) and (3.5) one gets:

$$\dot{s} = -J^{-1}(b\dot{\theta} + \tau_{dyn}) + J^{-1}u - \ddot{\theta}^{*} + \lambda(s - \lambda\Delta\theta) \tag{3.16}$$

now apply the weak condition and solve for the nominal portion of the control:

$$u_{nom} = \hat{J}\ddot{\theta}^{*} + \hat{b}\dot{\theta} - \hat{J}\lambda s + \hat{J}\lambda^2\Delta\theta + \hat{\tau}_{dyn} \tag{3.17}$$

again where $(\hat{\ })$ hats denote estimates of the prescribed parameter and $\Delta\theta = \theta - \theta^{*}$ as follows from [5]. Now with a substitution of (3.5) into (3.17) we get:

$$u_{nom} = \hat{J}\ddot{\theta}^{*} + \hat{b}\dot{\theta}^{*} + (\hat{b} - \hat{J}\lambda)\Delta\dot{\theta} + \hat{\tau}_{dyn} \tag{3.18}$$

since there are certainly model errors in the system,we need to include a correction control to the nominal control in the form:

$$u = u_{nom} + \Delta u \tag{3.19}$$

where Δu is the correction control term that changes sign (switches) as the error dynamics do. Now to get the true dynamics one substitutes (3.19) and (3.17) into (3.16) to get:

$$J\dot{s} = \Delta J\,(\ddot{\theta}^{*} + \lambda^2\Delta\theta) - \Delta J\lambda s + \Delta b\dot{\theta} + \Delta\tau_{dyn} + \Delta u \tag{3.20}$$

where $\Delta(\,) = (\hat{\ }) - (\,)$.

From [5] and [9] we choose a modified candidate Lyapunov function :

$$V(s) = \frac{1}{2}\, s^T P\, s \tag{3.21}$$

where P is a positive definite symmetric. In our study J, the axial moment of inertia is chosen for P. Therefore we have:

$$V(s) = \frac{1}{2}\, J\, s^2 \tag{3.22}$$

s is a scalar, so the transpose isn't required. The reachability condition (3.14) becomes:

$$\dot{V}(s) = sJ\dot{s} + \frac{1}{2}\dot{J}s^2 \leq -J\eta\,|s| \tag{3.23}$$

we will assume at this point that the structural deformations are small, which means the $\dot{J}$ term is small and therefore neglected. And one is reminded that the η term in this strong Lyapunov condition is designer selected. Substituting (3.20) into (3.23) to get:

$$\dot{V}(s) \approx sJ\dot{s} = s[\Delta J(\ddot{\theta}^{*} + \lambda^2\Delta\theta) - \Delta J\lambda s + \Delta b\dot{\theta} + \Delta\tau_{dyn} + \Delta u] \tag{3.24}$$

and following [6] we choose:

$$\Delta u = \Delta u^{(1)} + \Delta u^{(2)} \tag{3.25}$$

so that the reachability condition can be stated as:

$$\begin{aligned}\dot{V}(s) \approx sJ\dot{s} = s[+\Delta b\dot{\theta} + \Delta\tau_{dyn} + \Delta J(\ddot{\theta}^{*} + \lambda^2\Delta\theta) + \Delta u^{(1)}] \\ + s[-\Delta J\lambda s + \Delta u^{(2)}] \le - J\eta\,|s|\end{aligned} \tag{3.26}$$

This condition can be satisfied by the choice:

$$s[\Delta b\dot{\theta} + \Delta\tau_{dyn} + \Delta J(\ddot{\theta}^{*} + \lambda^2\Delta\theta) + \Delta u^{(1)}] \le - J\eta\,|s| \tag{3.27}$$

and

$$s[- \Delta J\lambda s + \Delta u^{(2)}] \le 0 \tag{3.28}$$

Then the correction controls that satisfy (3.27) and (3.28) can be expressed as:

$$\Delta u^{(1)} = - [\,\overline{\Delta b}\,\overline{\dot{\theta}} + \overline{\Delta\tau_{dyn}} + \overline{\Delta J}\,\overline{(\ddot{\theta}^{*} + \lambda^2\Delta\theta)} + \hat{J}\eta]\ \mathrm{sgn}(s) \tag{3.29}$$

and

$$\Delta u^{(2)} = [\overline{\Delta J}\lambda s] \tag{3.30}$$

where over-bars $(\bar{\ })$ indicate upper bounds on the associated system parameters. And where sgn(s) is the signum function defined as:

$$\mathrm{sgn}(s) = \begin{Bmatrix} 1 & \text{if } s > 0 \\ -1 & \text{if } s < 0 \end{Bmatrix} \tag{3.31}$$

so the 'chattering' control that is required to maintain s on the switching surface S is:

$$u = u_{nom} + \Delta u^{(1)} + \Delta u^{(2)} \tag{3.32}$$

the 'chattering' refers to the inherent behavior of the correction control $\Delta u^{(1)}$, which switches rapidly as the error dynamics, s, switches signs.

3.2 Non-Chattering Control

As mentioned above the control has an inherent chattering behavior. This behavior, while quite effective at keeping the error dynamics on the sliding surface, S, is undesirable since it can excite unmodeled vibrational dynamics and also requires high actuator activity. Now to avoid the chattering we must make a compromise between actuator activity and tracking error. We relax the requirement of reaching and remaining on the sliding surface

with that of reaching and remaining in a boundary layer about the sliding surface, S. It is shown next how the correction control terms change, and how to determine an optimal dead zone thickness, σ, based on model errors and actuator bandwidth. Further it is shown how this thickness can be made to behave as a decaying exponential, which drives the error dynamics, s, toward the sliding surface, S.

The new boundary layer (non-chattering) Variable Structure Control is obtained by replacing the sgn(s) function by the sat(s/σ) shown in fig. (3.2) and defined by:

$$\text{sat}(s/\sigma) = \begin{cases} \text{sgn}(s/\sigma) & \text{if } |s/\sigma| > 1 \\ s/\sigma & \text{if } |s/\sigma| \le 1 \end{cases} \tag{3.33}$$

Following [4] and [9], the selection of the Lyapunov parameter η is based on the first entry time t_1 into the boundary layer. If we look again at the reachability condition given in (3.23) as:

$$sJ\dot{s} \ge -J\eta\,|s|$$

and we require this condition to be valid at $t = t_1$. then we have the corresponding equation $\dot{s}(t_1) = -\eta\,\text{sgn}(s)$. Expanding through a first order Taylor's series about $t = t_1$ we get:

$$s(0) \approx s(t_1) - \dot{s}(t_1)t_1 \tag{3.34}$$

then by setting $|s(t_1)| = |\sigma|$ one gets for the Lyapunov parameter η in terms of t_1:

$$\eta \le \hat{J}^{-1}J\,\{|s(0)| - |\sigma|\}/t_1 \tag{3.35}$$

Looking back at (3.30) and following [9] we will choose:

$$\Delta u^{(2)} = -\hat{J}Ks \tag{3.36}$$

where K is (somewhat) designer selected. Substitution into (3.28) yields:

$$s[\Delta J\lambda - \hat{J}K]s \le 0 \tag{3.37}$$

To keep the Lyapunov stability criteria satisfied choose K such that the following inequality is holds:

$$\hat{J}K \ge \Delta J\lambda \tag{3.38}$$

it is noted here that if the $\dot{J}$ term in (3.23) had not been small the above inequality (3.38) is:

$$\hat{J}K \ge \Delta J\lambda + \frac{1}{2}\dot{J} \tag{3.39}$$

Also following [9] we redefine (3.29) with the sat(s/σ) function as follows:

$$\Delta u^{(1)} = -(\hat{J}\eta + \overline{JB})\,\mathrm{sat}(s/\sigma) \tag{3.40}$$

where

$$\overline{JB} = \overline{\Delta J(\ddot{\theta}^{*} + \lambda^2\Delta\theta)} + \overline{\Delta b\dot{\theta}} + \overline{\Delta\tau} \tag{3.41}$$

and B is implicitly defined.

We note that with definition (3.33), outside the boundary layer $|s/\sigma| > 1$ we continue to have the 'chattering' control, but when inside the boundary layer $|s/\sigma| \le 1$ the correction control is now:

$$\Delta u = -[\hat{J}K + Q]s \tag{3.42}$$

where

$$Q = (\hat{J}\eta + \overline{JB})/\sigma \tag{3.43}$$

and $\hat{J}K$ is chosen as in (3.38) or more generally (3.39). Now the sliding surface error dynamics is found to be:

$$\dot{s} + J^{-1}(\hat{J}K + Q)s = B \tag{3.44}$$

Then proceeding by choosing:

$$Q = \hat{J}\lambda' \tag{3.45}$$

where λ' is designer selected. The error dynamics in the boundary layer now takes on the from of a low pass filter with a designer selected break frequency given by choice of λ'.

Then selecting the boundary layer, σ, from (3.45) and (3.43) gives:

$$\sigma = (\eta + \hat{J}^{-1}\overline{JB})\lambda'^{-1} \tag{3.46}$$

Refining the selection, as in [4], of the envelope $|s/\sigma| \le 1$ about the sliding surface $s = 0$, is completed by: Allowing the Lyapunov bound η to vary with σ by requiring attractivity ($\eta > 0$) in (3.27) only when the envelope is narrowing ($\dot{\sigma} < 0$). So redefining η as:

$$\eta = \eta' - \dot{\sigma} \tag{3.47}$$

where $\eta' > 0$ is chosen to adjust first entry time into the boundary layer as in (3.35). Substituting into (3.46) gives σ in terms of a time varying quantity, not a constant, therefore the boundary layer is dynamic. The 'boundary layer dynamics' are then:

$$\dot{\sigma} + \lambda'\sigma = \eta' + \hat{J}^{-1}\overline{JB} \tag{3.48}$$

which, depending on the choice of λ' is stable. Choosing K in (3.38) close to zero, gives:

$$J^{-1}\hat{J}(K + \lambda') \approx J^{-1}\hat{J}\lambda' \tag{3.49}$$

the error dynamics are given by:

$$\dot{s} + J^{-1}\hat{J}\,\lambda' s \approx B \tag{3.50}$$

when comparing (3.50) to (3.48) one can see that the boundary layer dynamics, $\sigma(t)$, are given by known bounds on the unknown error dynamics, s(t). Also (3.46) gives the non-dynamic version of σ, or the steady-state solution of (3.48).

Now the correction control term becomes:

$$\Delta u = -\hat{J}[Ks + \lambda'\sigma\ \mathrm{sat}(s/\sigma)] \tag{3.51}$$

finally, it is possible to find the tracking error bounds along the predescribed commanded trajectory. Once inside the boundary layer $|s/\sigma| \le 1$ the integration of (3.5) gives:

$$|\Delta\theta| \le \{e^{[1 - \lambda(t - t_1)]}\Delta\theta(t_1) + \lambda^{-1}(1 - e^{-\lambda(t - t_1)})\}\,|\sigma| \tag{3.52}$$

then substituting (3.46) for σ yields for $t >> t_1$:

$$|\Delta\theta| \le (\lambda\,\lambda')^{-1}[\eta + \widehat{JJB}] \tag{3.53}$$

if $\lambda = \lambda'$ one finds that (3.53) corresponds to the design rule found in [4]. Where the tracking error is proportional to model error bounds and inversely proportional to the square of the control bandwidth λ.

IV. SIMULATIONS

All of the following simulations are computer generated using models developed in Matrix$_X$ control system software installed on a DEC VAXstation 3100. The controller algorithms are developed as above with $\lambda = \lambda' = 20$ and the entry time selected as 1 second. A finite element model of the cantilever beam gave flexible modes at about 5 and 10 Hz, and the simulation presumes as much. Also the controller is designed purposely with an erroneous model of the plant, the controller presumes that there is a 2% error in each of the plant parameters The simulations compare a point-to-point retarget maneuver and sinusoid tracking maneuver, using chattering and non-chattering techniques.

4.1 Pointing Maneuver

By commanding an angular acceleration profile composed of a positive step of $\pi/2$ rad/sec^2 for a duration of one second and then a negative step of $\pi/2$ rad/sec^2 for one second. The commanded angle profile results from integrating the acceleration profile, the result is a smooth, rapid repoint of π radians. The figures 4.1 and 4.2 are included for emphasizing the good performance of each of the two control techniques. Looking next at the control authority required for each technique in figs. 4.3 and 4.4, one can easily see where the terms 'chattering' and 'non-chattering' come from. And as noted the non-chattering is the more desirable, since the chatteri. g control's rapid switching can excite nonlinearities in the flexible structure and is often difficult to achieve due to physical limitations on the actuator itself. In figure 4.5, we see the trade-off made for reducing the actuator control effort, increased tracking error.

4.2 Sinusoid Tracking Maneuver

The sinusoid is generated by commanding a sinusoid acceleration, and giving the velocity profile a negative initial condition so the commanded angle profile is centered around a zero line. Looking at the figures 4.6 - 4.10, one will see the same type of results as found in the pointing maneuver. One is directed at the continuing error in the non-chattering control technique as the sinusoid changes slope.

V. RECOMMENDATIONS

It has been shown through simulation that Variable Structure Control techniques are capable of providing the desired response. But the technique still needs to be thoroughly investigated, further work should focus on robustness issues; the effects of external disturbance torques, of disturbance forces along the flexible structure itself, large beam deflections and the effects of large modelling errors (and various combinations of these). Also further investigations should show the effects of different choices for the lambda's and entry time into the boundary layer. Also one could extend the simple hub control to a line-of-sight control, where optical alignment of the hub and tip are maintained (as would be necessary in a DEW beam expander) during pointing and tracking maneuvers.

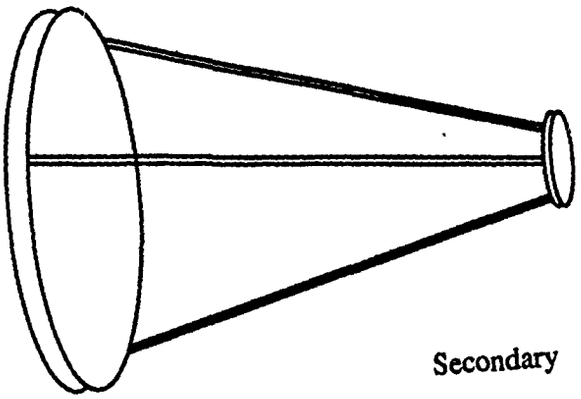
Secondary
Primary


cantilever beam
Tip
Hub

Fig. 2.1

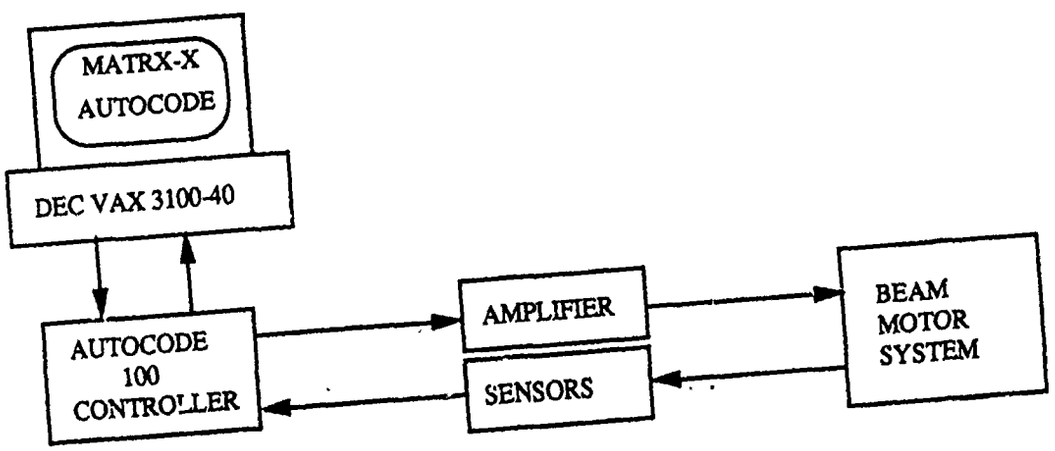
MATRX-X
AUTOCODE
DEC VAX 3100-40
AUTOCODE
100
CONTROLLER
AMPLIFIER
SENSORS
BEAM
MOTOR
SYSTEM

Fig. 2.2

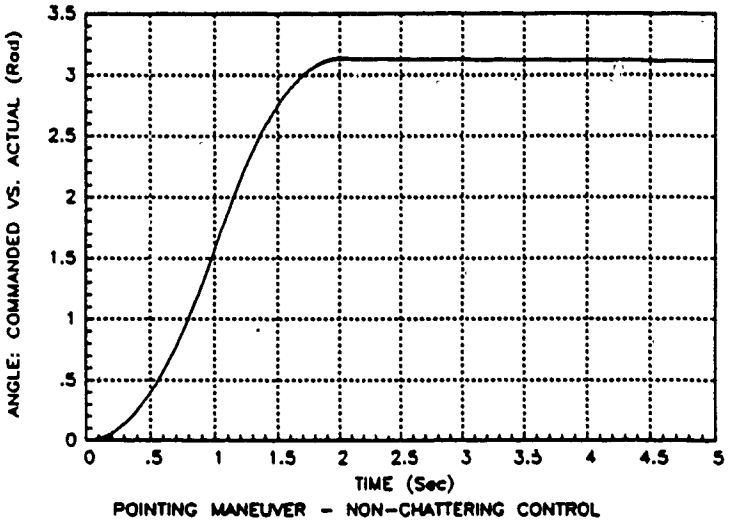

Fig. 4.1

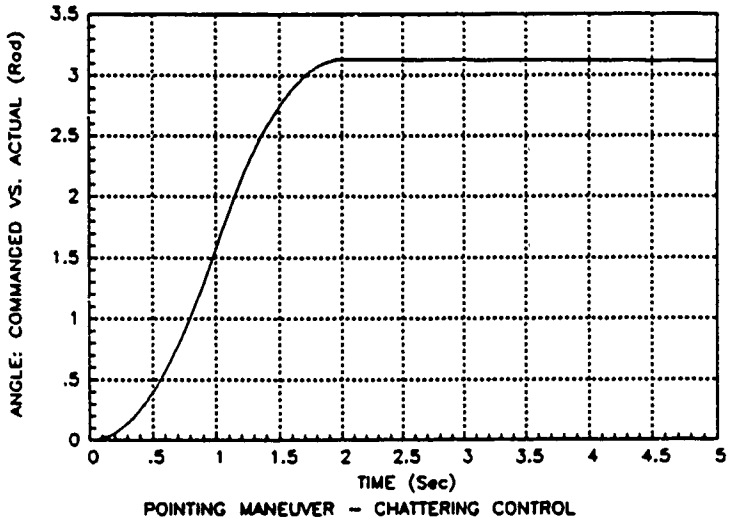

Fig. 4.2

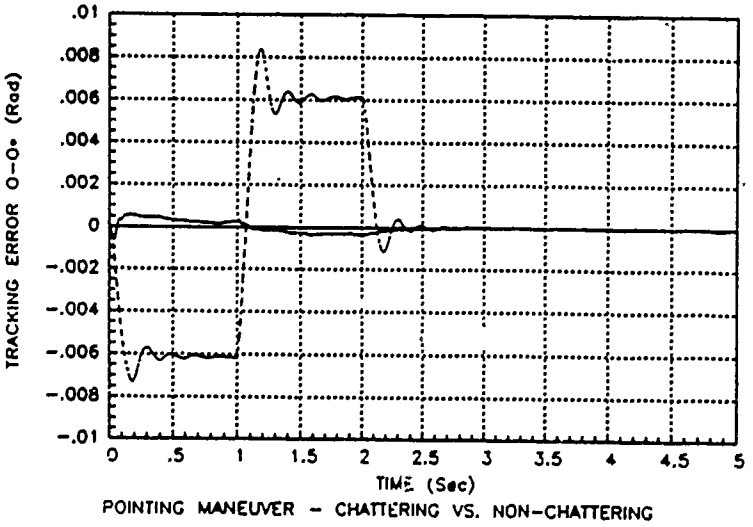

Fig. 4.5

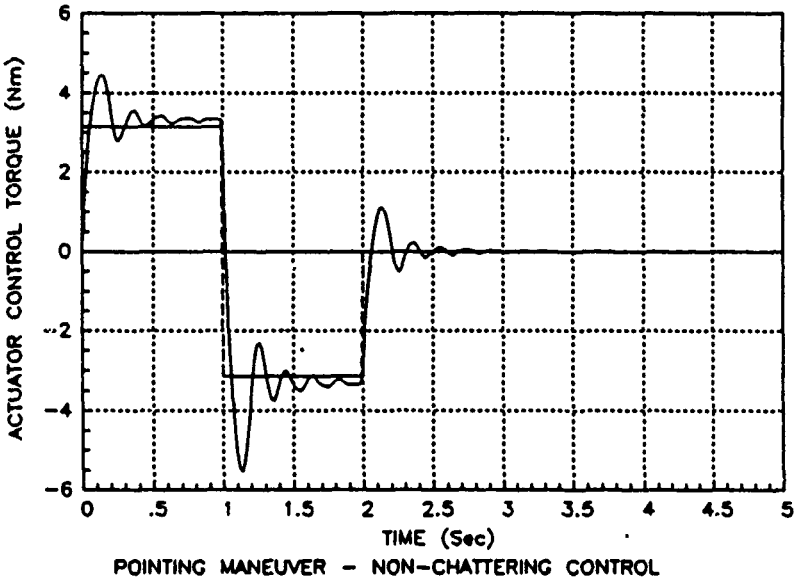
ACTUATOR CONTROL TORQUE (Nm)
6
4
2
0
-2
-4
-6
0
.5
1
1.5
2
2.5
3
3.5
4
4.5
5
TIME (Sec)
POINTING MANEUVER - NON-CHATTERING CONTROL

Fig. 4.3

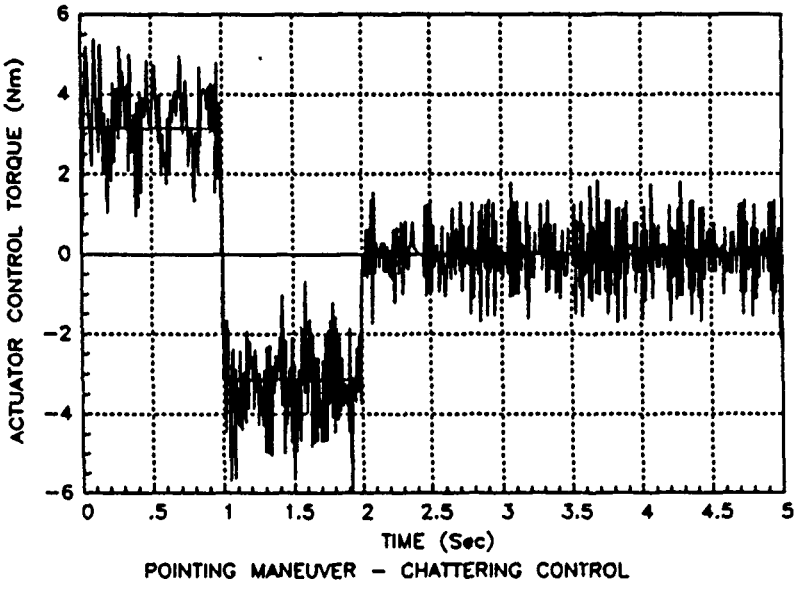
ACTUATOR CONTROL TORQUE (Nm)
6
4
2
0
-2
-4
-6
0
.5
1
1.5
2
2.5
3
3.5
4
4.5
5
TIME (Sec)
POINTING MANEUVER - CHATTERING CONTROL

Fig. 4.4

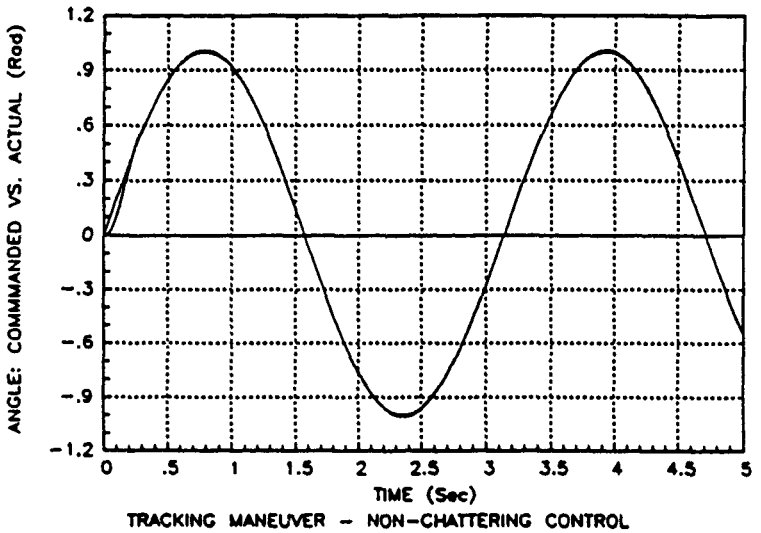

Fig. 4.6

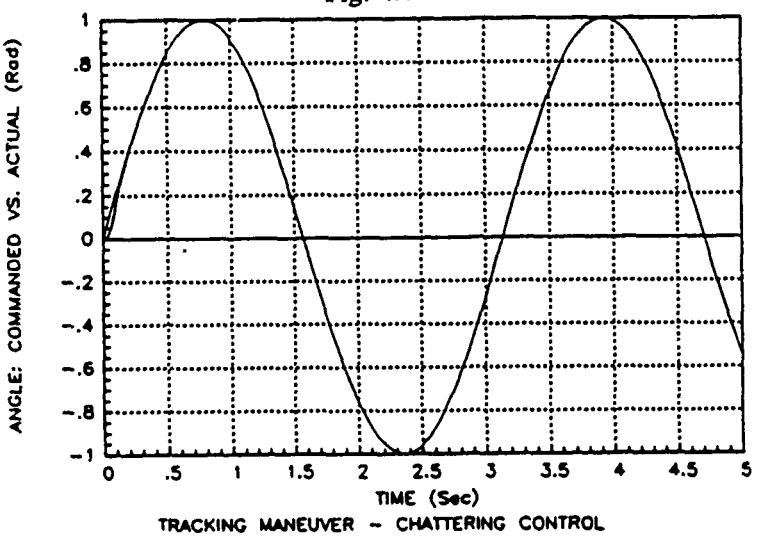

Fig. 4.7

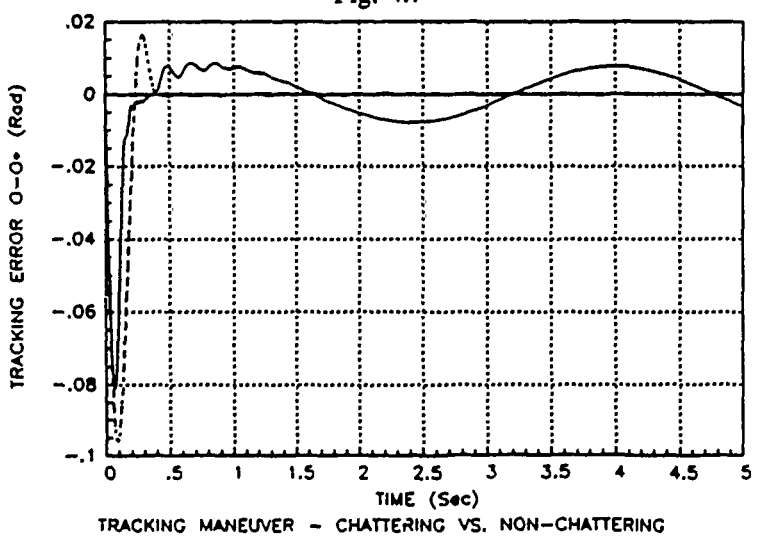

Fig. 4.10

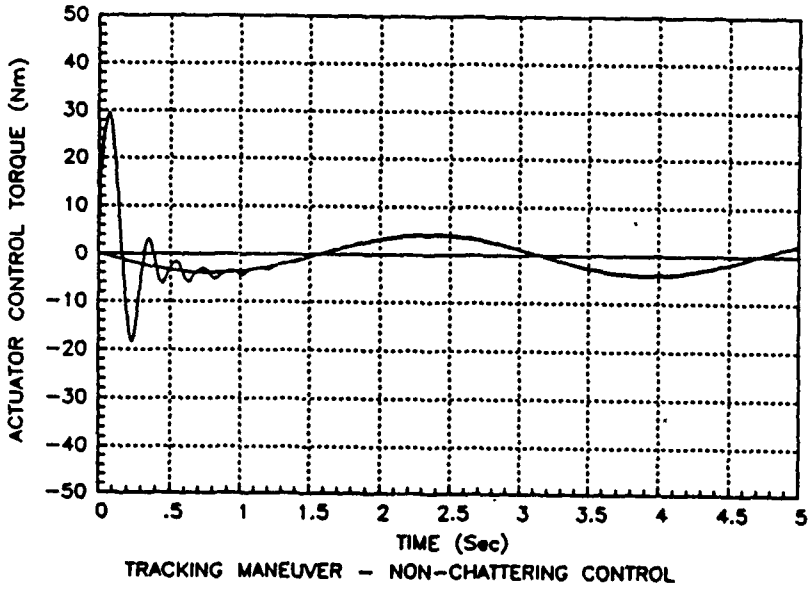
ACTUATOR CONTROL TORQUE (Nm)
50
40
30
20
10
0
-10
-20
-30
-40
-50
0
.5
1
1.5
2
2.5
3
3.5
4
4.5
5
TIME (Sec)
TRACKING MANEUVER – NON-CHATTERING CONTROL

Fig. 4.8

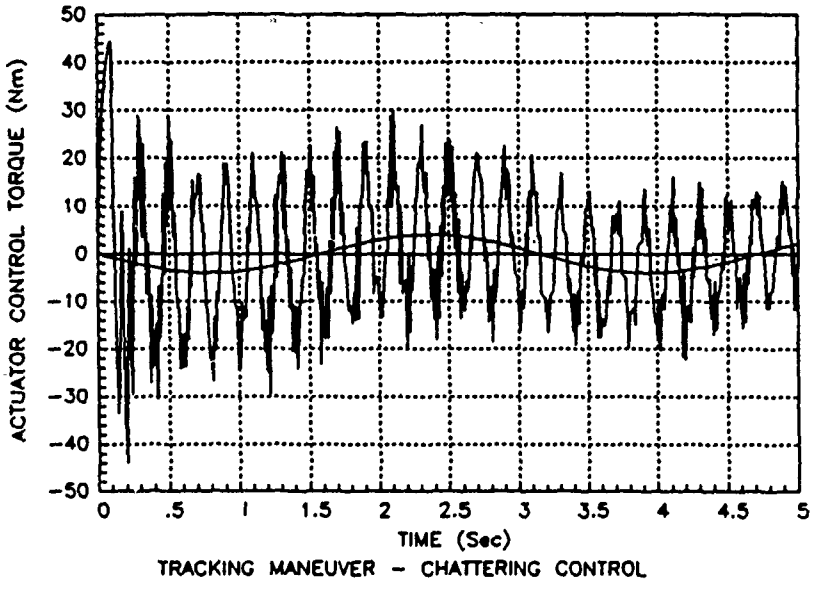
ACTUATOR CONTROL TORQUE (Nm)
50
40
30
20
10
0
-10
-20
-30
-40
-50
0
.5
1
1.5
2
2.5
3
3.5
4
4.5
5
TIME (Sec)
TRACKING MANEUVER – CHATTERING CONTROL

Fig. 4.9

REFERENCES

[1] Su, R., "On the Linear Equivalents of Nonlinear Systems," Systems and Control Letters, v. 2, 1981, pp.48-52.

[2] Hunt, L. R., R. Su, and G. Meyer,"Global Transformations of Nonlinear Systems," IEEE Transactions on Automatic Control, v. AC-28, 1983, pp.24-30.

[3] Sastry, S. S., and P. V. Kokotovic, "Feedback Linearization in the Presence of Uncertainties," International Journal of Adaptive Control and Signal Processing, v. 2, Dec 1988, pp.324-346.

[4] Slotine, J-J. E., "Sliding Controller Design for Nonlinear Systems," International Journal of Control, v. 40, 1984, pp.421-434.

[5] Karray, F., "Nonlinear Spline Operator Interpolation and Sliding Control of Deformable Maneuvering Bodies," Ph.D. Thesis, Dept. of Aeronautical and Astronautical Engineering, University of Illinois, Urbana, IL 1989.

[6] Dwyer, T.A.W., F. Karray, and J. Kim,"Robust Tracking of Fast Moving Elastic Structure by means of Sliding Control Technique combined with Nonlinear Spline Operator Interpolation," (personal draft copy) Eventually to be submitted to IEEE Transactions on Automatic Controls.

[7] Vadali, S. R., "Variable Structure Control of Spacecraft Large Angle Maneuvers," AIAA Journal of Guidance, Control and Dynamics, v. 9, Mar-Apr 1986, pp. 235-239.

[8] Utkin, V. I., Sliding Modes and Their Applications in Variable Structure Systems, MIR Publishers, Moscow, 1978.

[9] Dwyer, T. A. W., and J. Kim, "Bandwidth-Limited Robust Sliding Control of Multiaxial Spacecraft Tracking and Pointing Maneuvers," Variable Structure Control: Aerospace Applications, K.K.D. Young ed., Elsevier: Amsterdam, Holland, to appear.

Tanya Payne

Technical Memorandum Submitted